

.....

# THÈSE DE DOCTORAT

Soutenue à Aix-Marseille Université  
Le 13 décembre 2021 par

**Rogelio J. Gómez-Piñeiro**

## Experimental and Theoretical Investigation of Bioinspired Mononuclear Copper Complexes

**Discipline**

Sciences Chimiques

**Spécialité**

Chimie Bioinorganique

**École doctorale**

ED250, Sciences Chimiques de Marseille

**Laboratoire/Partenaires de recherche**

Aix-Marseille Université

Institut de Sciences Moléculaires de Marseille

• **Composition du jury**

• Dr. Carole DUBOC Rapporteuse

• Université Grenoble Alpes, CNRS

• Dr. Jean-Marie MOUESCA Rapporteur

• Université Grenoble Alpes, CEA

• Dr. Dimitrios A. PANTAZIS Examineur

• Max-Planck-Institut für Kohlenforschung

• Pr. Alexandre MARTINEZ Président du jury

• École Centrale de Marseille, CNRS

• Dr. Maylis ORIO Directrice de thèse

• Aix-Marseille Université, CNRS

• Dr. A. Jalila SIMAAN Co-directrice de thèse

• Aix-Marseille Université, CNRS



## Affidavit

Je soussigné, Rogelio J. Gómez-Piñeiro, déclare par la présente que le travail présenté dans ce manuscrit est mon propre travail, réalisé sous la direction scientifique de Dr. Maylis Orio et Dr. A. Jalila Simaan, dans le respect des principes d'honnêteté, d'intégrité et de responsabilité inhérents à la mission de recherche. Les travaux de recherche et la rédaction de ce manuscrit ont été réalisés dans le respect à la fois de la charte nationale de déontologie des métiers de la recherche et de la charte d'Aix-Marseille Université relative à la lutte contre le plagiat.

Ce travail n'a pas été précédemment soumis en France ou à l'étranger dans une version identique ou similaire à un organisme examinateur.

Fait à Marseille, le 27 octobre 2021



Cette œuvre est mise à disposition selon les termes de la [Licence Creative Commons Attribution - Pas d'Utilisation Commerciale - Pas de Modification 4.0 International](https://creativecommons.org/licenses/by-nc-nd/4.0/).







## Affidavit

I, undersigned, Rogelio J. Gómez-Piñeiro, hereby declare that the work presented in this manuscript is my own work, carried out under the scientific direction of Dr. Maylis Orio and Dr. A. Jalila Simaan, in accordance with the principles of honesty, integrity and responsibility inherent to the research mission. The research work and the writing of this manuscript have been carried out in compliance with both the French national charter for Research Integrity and the Aix-Marseille University charter on the fight against plagiarism.

This work has not been submitted previously either in this country or in another country in the same or in a similar version to any other examination body.

Place Marseille, date 27 octobre 2021



Cette œuvre est mise à disposition selon les termes de la [Licence Creative Commons Attribution - Pas d'Utilisation Commerciale - Pas de Modification 4.0 International](https://creativecommons.org/licenses/by-nc-nd/4.0/).





# Contents

Contents.....	7
Acknowledgements.....	13
Publications and Conferences.....	15
Abbreviations.....	17
Executive summary in English.....	19
Executive summary in French.....	19
Summary in English.....	20
Summary in French.....	21
 <b>Chapter I. Introduction.....</b>	<b>23</b>
<b>1 – Copper sites in biology.....</b>	<b>25</b>
1.1 – Classification of copper sites in biology.....	26
1. Type I site.....	26
2. Type II site.....	27
3. Type III site.....	27
1.2 – Mononuclear copper monooxygenases.....	28
1. Dopamine $\beta$ -Monooxygenase (D $\beta$ M) and Peptidylglycine $\alpha$ -hydroxylating monooxygenase (PHM).....	28
2. Lytic Polysaccharide Monooxygenase (LPMO).....	31
1.3 – Bioinspired models.....	41
1. Cu-superoxo.....	41
2. Cu-hydroperoxo.....	43
3. Cu-oxyl.....	44
4. Cu(III)-hydroxide.....	45
<b>2 – Theoretical calculations in bioinorganic chemistry.....</b>	<b>46</b>
2.1. Basic principles.....	47
2.2 Density functional theory.....	49

2.3 Application of DFT in copper bioinorganic chemistry.....	52
<b>3 – Ph.D. objectives and areas of research.....</b>	<b>54</b>
 <b>Chapter II. Computational EPR spectroscopy for the study of mononuclear copper(II) centers.....</b>	 <b>67</b>
<b>1 – Convergence studies of basis sets, DFT functionals, and wave-function methods for the calculation of hyperfine coupling constants.....</b>	<b>70</b>
1.1 – Computational details.....	73
1.2 – Performance assessment of basis sets, functionals and wave function methods.....	75
1.3 – Development and evaluation of a new basis set.....	76
1. Scalar relativistic corrections and the finite nucleus model .....	79
2. Basis set applicable for wave function methods.....	82
1.4 – Evaluation of commonly used functionals.....	82
1.5 – Comparison of wavefunction methods with respect to DFT.....	88
1.6 – Conclusions.....	91
<b>2 – Convergence studies of basis sets and DFT functionals for the calculation of the <i>g</i>-tensor.....</b>	<b>92</b>
2.1 – Performance assessment of basis sets.....	94
2.2 – Evaluation of functionals and scalar relativistic approaches.....	95
2.3 – Conclusions.....	99
 <b>Chapter III. Prediction of EPR parameters of the LPMO active site and an LPMO-like tripeptidic complex using model systems.....</b>	 <b>111</b>
<b>1 – Exploring the origin of the intriguing EPR signals of the LPMO active site using small model systems.....</b>	<b>114</b>
1.1 – Model systems of the <i>P/AA10</i> LPMO active site.....	117
1.2 – Geometry optimizations of the LPMO models and description of the structures.....	122
1.3 – Calculation of EPR parameters.....	131
1. Functional evaluation.....	132

2. Evaluation of EPR parameters for the LPMO models.....	134
1.4 – Conclusions.....	139
<b>2 – Correlating experiment and theory in predicting the structures of a small LPMO-like peptide.....</b>	<b>141</b>
2.1 – Investigation of possible HPH peptide structures and its modifications.....	142
2.2 – Computational studies of the model systems from sets A, B, and C: Energetic considerations.....	145
2.3 – Calculation of EPR parameters.....	148
2.4 – Calculation of UV-vis spectra.....	150
2.5 – Discussion on the study of HPH structures.....	153
2.6 – Electronic profiles of HPH and HMePH.....	154
2.7 – Conclusions.....	158
<b>Chapter IV. Bioinspired mononuclear copper complexes: synthesis, characterization, and reactivity.....</b>	<b>165</b>
<b>1 – First generation PMPA and PEPA-based complexes: synthesis, characterization, and theoretical description.....</b>	<b>169</b>
1.1 – Spectroscopic characterization: UV-vis, MS, EPR.....	172
1.2 – Electrochemical studies.....	177
1.3 – Conclusions.....	179
<b>2 – Reactivity of the [Cu(PMPA)(H<sub>2</sub>O)(NO<sub>3</sub>)] complex (1) in presence of hydrogen peroxide.....</b>	<b>180</b>
2.1 – Formation of the [Cu(POPA)(OH)(OCHO)] <sup>-</sup> complex .....	180
1. Understanding the oxidation state of the [Cu(POPA)(OH)(OCHO)] complex.....	183
2. Reactivity in Ethanol.....	186
3. Other products observed .....	187
2.2 – Quantification of formate produced.....	188

1. Influence of the oxidation of PMPA.....	192
2. Other oxidation products.....	193
2.3 – Origin of formate.....	194
1. Investigation of CO <sub>2</sub> sequestration and reduction.....	194
2. Investigation of C-H activation of solvent.....	196
2.4 – Bond dissociation energies.....	198
2.2 – Proposed reaction mechanisms.....	199
2.6 – Conclusions.....	203
<b>3 – Other reactivity of the [Cu(PMPA)(H<sub>2</sub>O)(NO<sub>3</sub>)] complex.....</b>	<b>204</b>
3.1 – Reactivity in acetonitrile .....	204
3.2 – Reactivity with the model substrate: PNPG.....	205
<b>4 – Perspectives.....</b>	<b>207</b>
<b>Closing comments and general perspectives.....</b>	<b>217</b>
<b>Materials and methods.....</b>	<b>223</b>
<b>1 – Chapter III. Prediction of EPR parameters of the LPMO active site and an LPMO-like tripeptide using models.....</b>	<b>225</b>
<b>2 – Chapter IV. Bioinspired mononuclear copper complexes, synthesis, characterization and reactivity.....</b>	<b>227</b>
1. Synthesis of the PMPA ligand.....	227
2. Synthesis of complex <b>1</b> , [Cu(PMPA)(H <sub>2</sub> O)(NO <sub>3</sub> )].....	228
3. Synthesis of the PEPA ligand.....	232
4. Synthesis of complex <b>2</b> , [Cu(PEPA)(H <sub>2</sub> O) <sub>2</sub> ] <sup>+</sup> (ClO <sub>4</sub> ) <sup>-</sup> .....	232
5. Formation of complex <b>3</b> , [Cu(POPA)(OH)(OCHO)] <sup>-</sup> .....	234
6. Synthesis of POPA ligand.....	237
7. Synthesis of complex <b>4</b> , [Cu(POPA)(H <sub>2</sub> O)(NO <sub>3</sub> )].....	237
8. GC experiments.....	239

9. GC-MS experiments.....	239
10. Formation of complex <b>5</b> , [Cu(POPA)(H <sub>2</sub> O)(NCO)].....	239
11. Oxidative cleavage of PNPG model substrate.....	240
12. Synthesis of the PMPA- <i>o</i> -NH <sub>2</sub> ligand.....	241
13. Synthesis of complex <b>6</b> , [Cu(PMPA- <i>o</i> -NH <sub>2</sub> )(X) <sub>2</sub> ] (X = NO <sub>3</sub> or H <sub>2</sub> O).....	241
14. Synthesis of the PEPA- <i>o</i> -NH <sub>2</sub> ligand.....	243
15. Synthesis of complex <b>7</b> , [Cu(PEPA- <i>o</i> -NHCO <sub>2</sub> )(H <sub>2</sub> O)] complex.....	243
16. Computational methods.....	244
17. Crystallographic data table.....	246
 <b>Supporting Information.....</b>	 <b>251</b>
<b>1 – Supporting information regarding Chapter II.....</b>	<b>254</b>
<b>2 – Supporting information regarding Chapter III.....</b>	<b>289</b>
 <b>List of Figures.....</b>	 <b>293</b>
<b>List of Schemes.....</b>	<b>300</b>
<b>List of Tables.....</b>	<b>304</b>





## Acknowledgements

Empezó todo con el alquiler de un carro y alrededor de 800 km de ruta. Pensaba que era una pequeña travesía para los trotamundos. El Salvador me enseñó lo que era la nostalgia, los Estados Unidos lo que era soñar despierto, y Francia lo que vale una amistad. Fueron tres países, tres idiomas, tres maletas. Y fueron más las cuentas bancarias, las ciudades, los apartamentos, los números celulares, las peleas con los agentes de migración, los documentos impresos, las cervezas, los vinos, los brindis.

Llegando a Marsella, vi lo movido que era la ciudad, el ruido de la gente conversando, tratando de venderte la última promoción del mercado, la brisa salada de la grandeza del Mediterráneo, la pasión por el equipo y el deslumbrar del sol. Esta ciudad me tocaría por 3 años de trabajo de doctorado en el laboratorio BiosCiencias, y me sentí afortunado.

Quiero agradecer, a todo el equipo por acogerme de una gran manera en el laboratorio. Recuerdo cuando Yolande y Elise insistieron si necesitábamos cosas tan sencillas como platos, u hojitas, para nuestros apartamentos, no dudáramos en avisarles. Un gesto sencillo que llevaba a mucho. Esta actitud se reflejaba en todos los integrantes del equipo. Agradezco a Pierre y al rugby, Cendrine y los pedidos de los compuestos, a Yasmina, sus hijas, y el viaje de champiñones, así mismo que a Olga, Christophe, Katia, Agnès, Michel, Julien, Renaud, y Mireille. Agradezco al responsable del equipo Thierry por su amabilidad y cuidado de todos los estudiantes.

En mi proyecto en particular, agradezco a Bruno por ayudarme en la síntesis, a Véronique por la cromatografía de gases, a Marius por compartir sus ideas. También a mis colaboradores Sylvain, Michel y Dimitrios. Así mismo otros profesores que me aportaron durante mis estudios: Armando, Wetzell, Ivan, Benoit, Jean-Luc y Nicolas. Quiero agradecer especialmente a mis directoras de tesis, Maylis y Jalila, por darme la oportunidad de trabajar en el proyecto, de enseñarme y guiarme a lo largo de estos 3 años. Gracias por los bonitos momentos que pudimos compartir, viajando a Alemania, degustando mezcal, conversando de la vida, y, claro, estudiando los centros mononucleares de cobre bioinspirados.

Estos duros años de estudios se hacen más amenos en compañía de colegas que pasan por lo mismo. Los doctorantes que ya se fueron te aconsejan, y los que están empezando te recuerdan del porque uno se entusiasma tanto. Agradezco a Quim y a Raul por el laboratorio de habla hispana, a Alex y Eugénie por darme la bienvenida en la oficina, así mismo a Hugo, Julie, Bernadette, Clarisse, Cheikh, Elif, Hamza, Manon, Maxime, Quijano, Francesco, Soniya, Yongxing, Karno, Guillaume, Jeffrey. Quiero agradecer a mis amigos que también emprendieron esta carrera en otros

países y universidades : Léonie, Inés, Daniela, Ismail, Silvia, Christine, Beatrice, Abhishek, Ehider y Julian.

Una vez escuche que donde se sufre, se hacen lazos de amistad más fuertes, y el doctorado no es una excepción. Quiero agradecer a mis amigos doctorantes que hicieron más de lo debido para ayudarme y apoyarme: Claudio, Michail, Alex y su familia, Robert, Alessia, Fang Fang, Elena, y Iago. Entre tanto viaje, he tenido la dicha de encontrar grandes personas, amigos envidiables que me han apoyado desde el principio y les tengo mucho cariño y aprecio. Les agradezco infinitamente : Roberto, Andrea, Simon, Salvador, Ricardo, Karen, Manuel, Roy, Jaimito.

Quiero agradecer especialmente a mi familia que aceptaron y me alentaron a cruzar el Atlántico y me vieron emprender mis estudios en Europa. Sus muestras de cariño, apoyo y aliento, nunca me faltaron : abuelita Dora, Papito, Mamita, mi mamá Irene, Julio, Caroline, Lexi y Evi, Paola y Charles, Eddy, Sonia y Olivia, Juanpi y Katie. Mi papá Julio, y mi abuelo Rogelio que nos acompañan en este momento desde el cielo. Agradezco también a todos mis tíos y tías, todos mis primos y primas, en especial a mi madrina tía Dorita, que siempre los tengo en mente. Por último, quiero agradecer a Emma y a Stefaní por brindarme su más grande amor. Con ustedes a mi lado, mi vida toma color, y desde la lluvia al sol, me hacen verdaderamente feliz.

Espero que mis pocas palabras hagan honor a lo que he querido expresar. Quiero cerrar con una reflexión que me ha marcado a lo largo de los años:

*Nacimos todos para cosas grandes*

*Pero no todo lo que vale oro brilla*

*En las pequeñas acciones del día a día*

*Nos devolveremos la alegría de antes*

- Roge

## Publications and Conferences

1) List of publications realized during the Ph.D. thesis :

1. Gómez-Piñeiro, R. J. ; Pantazis, D. A. ; Orio, M. Comparison of Density Functional and Correlated Wave Function Methods for the Prediction of Cu(II) Hyperfine Coupling Constants. *Chem. Phys. Chem.* **2020**, 21, 24, 2667-2679.
2. Gómez-Piñeiro, R. J. ; Decroos, C. ; Simaan, A. J. ; Pantazis, D. A. ; Orio, M. Decoding an ambiguous EPR signal in *PlAA10* LPMO enzyme by construction of active site models using Density Functional Theory. *Article in preparation*.

2) Conferences and Thematic Schools attended during the Ph.D. thesis :

1. INSPECTHE – Spectroscopies & Chimie Théorique : Des Approches Complémentaires pour la Chimie Inorganique Bio-Inspirée, 2018
2. 26<sup>ème</sup> Journée de la Chimie, SCF-PACA, 2019
3. Tutoriel deMon2k et deMon-nano, 2019
4. 5th Quantum Bio-Inorganic Chemistry Conference, 2019
5. Journées de Chimie de Coordination, 2020



## Abbreviations

(NAG) <sub>6</sub>	(N-acetyl-glucosamine) <sub>6</sub>
A	Hyperfine
AA	Auxiliary activity
Ac	Acetate
ACN	Acetonitrile
AcrH <sub>2</sub>	10-methyl-9,10-dihydroacridine
APD	Absolute percent deviation
BDE	Bond dissociation energy
BO	Born-Oppenheimer
BPBA	bis(2-pyridylmethyl)tert-butylamine
CD	Circular dichroism
CE	Counter electrode
CHD	1,4-cyclohexadiene
CPCM	Conductor-like polarizable continuum model
CV	Cyclic voltammetry
cw	Continuous wave
DCM	Dichloromethane
DFT	Density functional theory
DIC	N,N'-Diisopropylcarbodiimide
DIIS	Direct inversion in the iterative subspace
DIPEA	Diisopropylethylamine
DKH	Douglas-Kroll-Hess
DMPO	5,5-dimethyl-1-pyrroline-N-oxide
DOMO	Doubly occupied molecular orbital
D $\beta$ M	Dopamine $\beta$ -monooxygenase
EPR	Electronic paramagnetic resonance
ESI	Electron spray ionisation
ET	Electron transfer
FC	Fermi contact
Fc <sup>+</sup>	Ferrocenium
F <sub>HK</sub>	Hohenberg-Kohn functional
GC	Glassy carbon
GC	Gas chromatography
GEA	Generalized expansion approximation
GGA	Generalized gradient approximation
HAA	Hydrogen-atom abstraction
HEPES	2-[4-(2-hydroxyethyl)piperazin-1-yl]ethanesulfonic acid
HF	Hartree-Fock
hfc	Hyperfine coupling constants
HOBt	Hydroxybenzotriazole

HPH	His-Pro-His
HSA	Human serum albumin
IR	Infrared
KDIE	Kinetic isotope effect
LDA	Local-density approximation
LMCT	Ligand to metal charge transfer
LPMO	Lytic polysaccharide monooxygenase
MAPD	Mean absolute percent deviation
MBO	Mayer bond order
MES	2-(N-morpholino)ethanesulfonic acid
MOPS	3-morpholinopropane-1-sulfonic acid
MS	Mass spectroscopy
NHE	Normal hydrogen electrode
NMR	Nuclear magnetic resonance
NPA	Natural population analysis
PAL	Peptidyl- $\alpha$ -hydroxyglycine $\alpha$ -amidating lyase
PC	Pseudo-contact
PDB	Protein Data Bank
PEPA	N-(2-(pyridine-2-yl)ethyl)picolinamide
PHM	Peptidylglycine $\alpha$ -hydroxylating monooxygenase
pMMO	Particulate methane monooxygenase
PMPA	N-((pyridine-2-yl)methyl)picolinamide
PNPG	p-nitrophenyl- $\alpha$ -D-glucopyranoside
POPA	N-picolinoylpicolinamide
PrP <sup>c</sup>	Prion proteins
QM/MM	Quantum mechanics/Molecular mechanics
RE	Reference electrode
RHF	Restricted Hartree-Fock
RMSD	Root-mean-square deviation
SD	Spin-dipolar
SO	Spin-orbit
SOC	Spin-orbit coupling
SOMF	Spin-orbit mean-field
SOMO	Singly occupied molecular orbital
tBu	Tert-butyl
TD-DFT	Time-dependent DFT
TEA	Triethylamine
TON	Turnover number
TZVP	Triple-zeta valence polarized
UHF	Unrestricted Hartree-Fock
UNO	Unrestricted Natural Orbitals
UV	Ultraviolet
W	Water
WE	Working electrode
XRD	X-ray diffraction
ZORA	Zeroth order regular approximation

## Executive summary in English

Lytic polysaccharide monooxygenases (LPMO) break down polysaccharides and are greatly studied in the context of biomass conversion. They contain a mononuclear copper center which is studied by its magnetic properties. The mechanism of reaction and its intermediates are still unknown. We use a large set of well-known complexes to develop a protocol to predict the magnetic properties of copper systems using computational calculations. This protocol was applied to LPMO models and to an LPMO-inspired tripeptidic complex to elucidate their structural and spectroscopic properties. In addition, we produced a series of complexes to capture potential high-valent reaction intermediates of LPMO. Eventually, the reactivity of one specific complex was studied for its capacity to produce formate in alcohol solvents. Formate was produced at around 120% conversion. Future generations of ligands and complexes were also synthesized and envisioned to understand the reaction pathways of LPMO.

## Executive summary in French

Les monooxygénases polysaccharidiques lytiques (LPMO) cassent des polysaccharides et sont étudiés dans la valorisation de la biomasse. Ces enzymes contiennent un centre mononucléaire à cuivre, étudié grâce à ses propriétés magnétiques. Le mécanisme et les intermédiaires mis en jeu demeurent inconnus. On a utilisé un ensemble de complexes de la littérature pour développer un protocole pour prédire les propriétés magnétiques de systèmes à cuivre grâce aux calculs théoriques. Ce protocole a été utilisé sur des modèles de LPMO et sur un complexe tripeptidique afin de comprendre leurs propriétés. De plus, on a développé une série de complexes pour isoler des intermédiaires de haute-valence des LPMO. La réactivité d'un complexe en particulier a été étudié pour sa capacité à produire du formate dans des alcools. Le formate a été produit avec un rendement de 120%. De futures générations de complexes ont été synthétisés et seront étudiés pour mieux comprendre les chemins réactionnels des LPMOs.

## Summary in English

Lytic polysaccharide monooxygenase (LPMO) enzymes degrade recalcitrant polysaccharide and are studied for their application in biomass conversion. LPMOs contain a mononuclear copper ion in their active site which coordinates two histidine residues. One of these is the N-terminal amino acid that binds copper in a bidentate fashion and is known as the histidine brace. The complete coordination sphere has a distorted square-pyramidal geometry. The reaction mechanism of LPMOs is not yet elucidated but high-valent oxidation states of copper have been postulated as intermediates.

Within this work, we have employed experimental and theoretical approaches to investigate LPMO enzymes and get insight into their structure, spectroscopic properties, and reaction mechanism. We first set-up a theoretical protocol employing density functional theory (DFT) methods for calculating Electronic Paramagnetic Resonance (EPR) parameters of copper complexes, a technique being well adapted to probe the coordination sphere and geometry of metal centers having unpaired electrons. We selected a large set of mononuclear copper complexes with well-defined EPR parameters and calculated their metal hyperfine coupling constants (hfc). The values are determined by including three terms of which the Fermi contact was found to be the largest and most sensitive contribution. A home-made basis set was developed to better reproduce the behavior of the core electrons of the copper center, and we showed we can accurately predict the hfc values of all 20 complexes when used in combination with the hybrid functional B3PW91.

This approach was also successfully applied for the calculation of g-tensors for the same set of complexes. We applied our protocol to understand the origin of the ambiguous EPR signal recorded with some LPMO enzymes, such as the PAA10A which displays two species in solution with different EPR signatures: a major species displaying a rhombic signal and a minor species with parameters for an axial symmetry. We thus generated several models of the active site including multiple modulations of the coordinating ligands. By calculating the EPR parameters of these models, we proposed a rationale for the mixed signal experimentally observed. The “rhombic” signal is characteristic of typical LPMO active sites while the axial one is proposed to correlate with the existence of negatively charged ligands (such as hydroxyl groups) coordinating the metal center.

We applied a similar strategy to identify and elucidate the possible structures of a tripeptide-copper complex experimentally characterized in solution. A tripeptidic system was indeed previously synthesized to reproduce the histidine-brace of LPMO and investigate its implication



towards the reactivity of the system. We rationalized on the possible peptide-Cu(II) structures existing in solution by generating multiple models with various coordination spheres, computing their spectroscopic features (EPR, UV-vis) and comparing them with experimental ones. Our results highlight the existence of a major complex reproducing the structural features of the peptidic complex around pH=7.5.

Finally, we synthesized three generations of ligands and complexes to possibly capture high valent copper species. The Cu(II)(PMPA) complex was prepared and its reactivity in presence of base and hydrogen peroxide was studied in different solvents. The resulting solutions provided crystals which exhibited multiple modifications to the initial complex. A formate anion was bound to the copper center in alcohol solvents and was produced to 120% conversion. Other solvent oxidation products were identified. In acetonitrile, the complex coordinated a cyanate ligand. DFT calculations were applied to rationalize the nature of the species formed as well as the binding properties of the cyanate ligand. Labelling experiments demonstrated that formate originates from methanol or ethanol via C-H activation reactions and the same can be envisioned for cyanate produced from acetonitrile.

## Summary in French

Les monooxygénases polysaccharidiques lytiques (LPMO) sont des enzymes qui dégradent les polysaccharides récalcitrants et sont valorisés pour la conversion de la biomasse. Le site actif des LPMO contient un centre à cuivre mononucléaire qui coordonne deux résidus histidines. L'un d'entre eux est l'acide aminé N-terminal qui lie le cuivre d'une façon bidentate, appelée « histidine brace ». La sphère de coordination de l'ion cuivre se trouve dans une géométrie pyramide à base carré distordue. Le mécanisme réactionnel des LPMOs n'est toujours pas élucidé mais des espèces à hauts degrés d'oxydation du cuivre sont proposés comme intermédiaires.

Dans ce travail, on a combiné des approches expérimentales et théoriques pour étudier les enzymes LPMO et mieux comprendre leur structure, leurs propriétés spectroscopiques et leur mécanisme réactionnel. On a choisi un large panel de complexes mononucléaires à cuivre ayant des paramètres de spectroscopie de Résonance Paramagnétique Electronique (RPE) bien définis et on a réalisé le calcul des constantes de couplage hyperfin. Les valeurs sont obtenues par incorporation de trois termes dont le contact de Fermi présentait la contribution la plus importante

et sensible. Une base a été développée pour reproduire au mieux le comportement des électrons de cœur du cuivre. On a montré qu'on pouvait prédire avec précision les valeurs de couplage hyperfin des 20 complexes sélectionnés en utilisant notre base associée à la fonctionnelle hybride B3PW91.

Cette approche a aussi été appliquée pour le calcul des tenseurs-g du même groupe de complexes sélectionnés pour ce travail. On a appliqué notre protocole pour comprendre l'origine d'un signal RPE ambigu obtenu lors de l'étude de certaines enzymes LPMO. En effet, l'enzyme *P/AA10* montre deux espèces en solution avec des signatures RPE différentes, une espèce majoritaire à symétrie rhombique, et une minoritaire à caractère axial. On a donc mis au point plusieurs modèles de ce site actif incluant plusieurs modulations des ligands. En calculant les paramètres RPE de ces modèles, on a pu proposer une explication pour le signal mixte observé en expérience. Le signal à caractère rhombique est caractéristique des sites actifs des LPMOs tandis que le signal à symétrie axiale a été corrélé à l'existence d'une espèce comportant des ligands chargés négativement, comme des groupements hydroxyles.

On a appliqué une stratégie similaire pour identifier les structures possibles d'un complexe tripeptidique, caractérisé expérimentalement en solution. Le système tripeptide avait été synthétisé pour reproduire le motif « histidine brace » caractéristique des LPMO. On a pu étudier les possibles structures peptide-Cu(II) existant en solution en élaborant plusieurs modèles avec des sphères de coordination différentes, puis en calculant leurs paramètres spectroscopiques et, enfin, en les comparant avec les données expérimentales. Nos résultats montrent qu'un des modèles mis au point permet de reproduire les caractéristiques structurales du complexe peptidique à pH=7.5.

Finalement, on a synthétisé trois générations de complexes dans le but de pouvoir isoler des espèces à cuivre de haute valence. Le complexe Cu(II)(PMPA) a été préparé et on a étudié sa réactivité en présence de H<sub>2</sub>O<sub>2</sub> dans plusieurs solvants. Les milieux réactionnels ont formé des cristaux qui montrent plusieurs modifications du complexe initial. Un formate est lié au cuivre dans des alcools et a été produit jusqu'à 120% de conversion. D'autres produits d'oxydation ont été identifiés. Dans l'acétonitrile, le complexe coordonne un ligand cyanate. Des calculs DFT ont été réalisés pour comprendre la nature des espèces formées ainsi que les propriétés de fixation du ligand cyanate. Des expériences avec du marquage isotopique démontrent que le formate provient du méthanol ou de l'éthanol par activation de la liaison C-H et le même raisonnement peut être envisagé dans le cas du cyanate produit à partir de l'acétonitrile.

---

# CHAPTER I. INTRODUCTION

---



# CHAPTER I. INTRODUCTION

The present work will focus on two major approaches used when working in bioinorganic chemistry, a field that is well-known for its interdisciplinary character: 1) bioinspiration from enzymatic systems with great capabilities in reactivity and their mechanistic features, [1] and 2) theoretical methods to rationalize, distinguish, or correlate experimental observations. [2] [3] Bioinspiration follows the practice of observing what nature has learned by eons of evolution and recreating its functionalities in synthetic systems. Theoretical methods apply quantum and molecular mechanics to describe and extract information of a complex system. These methods may also be used as a tool to predict and target specific structures. The copper transition metal has attracted great interest in inorganic chemistry because of its redox properties and potential activity. [4] In addition, copper is found in many enzymatic systems and is considered a natural and biological atom which is readily available, as opposed to heavier transition metals. For instance, a simple inspection into the human body finds dopamine- $\beta$ -monooxygenase or peptidylglycine  $\alpha$ -hydroxylating monooxygenase, both copper-containing enzymes involved in the synthesis of norepinephrine and of neuropeptides, respectively. [5] This bioavailability aspect of copper makes it a safer and more environmentally friendly metal to use in catalysis, [6] medicinal chemistry, [7] and other fields. [8]

In this introduction, we will first describe copper sites found in biology with a focus on mononuclear copper monooxygenases and synthetic bioinspired models. Second, we will present an overview of theoretical methods and their use in the study of such systems, before finishing with the objectives and the research lines of this PhD work.

## 1 – Copper sites in biology

Many copper containing enzymes are found in nature carrying diverse activity such as electron transfer, O<sub>2</sub> binding, activation, and reduction, and in nitrite and nitrous oxide reduction, *etc.* [9] [4] [1] Due to their versatility and diversity, copper proteins have been classified according to their spectroscopic properties into different “Types”, which we will describe briefly. Then, we will pay a particular attention to mononuclear copper monooxygenase proteins. Finally, we will introduce bioinspired synthetic models developed to investigate copper/oxygen chemistry.

## 1.1 – Classification of copper sites in biology

### 1. *Type I site*

Proteins containing a mononuclear copper site are denoted as Type I copper sites or blue copper sites when displaying the following three characteristics: 1) An intense blue color characterized by an absorption at 600 nm with an extinction coefficient ( $\epsilon$ ) between 3000 and 6000  $\text{M}^{-1}\cdot\text{cm}^{-1}$ . This transition originates from a cysteinate to Cu(II) charge transfer. 2) An atypical Cu(II) signature with electron paramagnetic resonance (EPR) and a spectrum characterized by a remarkably decreased hyperfine splitting in the parallel region ( $A_{\parallel} = 70\text{-}100$  G) when compared to that of normal Cu(II) centers ( $A_{\parallel} = 150\text{-}200$  G) 3) High redox potentials (180-680 mV) compared to the copper aqua Cu(II)/Cu(I) redox couple. [10] [9] These centers are involved in electron transfers (ET) in fundamental processes such as photosynthesis and respiration. [11] [12] [13] This copper center is generally found in a geometry between the fully tetrahedral Cu(I) and square-pyramidal Cu(II) geometries a natural compromise to allow efficient electron transfer with a minimal reorganization around the copper ion. [14] The first coordination sphere is in the form of  $\text{CuN}_2\text{S}_2$  or  $\text{CuN}_2\text{S}$  where the copper center is bound to two sulfur atoms and two nitrogen atoms. The sulfur atoms originate from a thioether and a thiolate from a methionine and a cysteine residue, respectively. The two nitrogen atoms are both from imidazole rings coordinating from histidine residues.

As an example, plastocyanin is a Type I copper enzyme modulating electron transfers between photosystem I and photosystem II in oxygenic organisms. [15] Its crystal structure was first determined in 1978 by Freeman and co-workers (Figure 1). [16] [17]

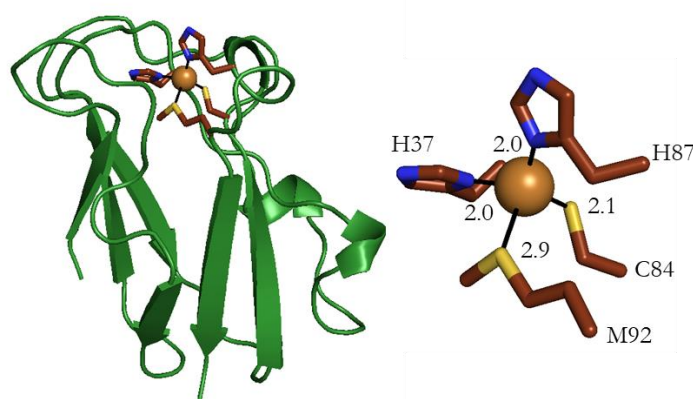


**Figure 1.** Crystal structure of Plastocyanin from spinach resolved to 1.7 Å with zoom into the active site (PDB: 1AG6). [15]

## 2. Type II site

Type II copper sites are mononuclear and are known as non-blue copper sites due to their low absorption at 600 nm attributed to forbidden d-d transitions ( $\epsilon = 50$  to  $100 \text{ M}^{-1}\text{cm}^{-1}$ ). The EPR spectrum of these sites is of axial character with a normal hyperfine splitting in the parallel region ( $A_{\parallel} = 150\text{-}200\text{G}$ ). [18] They are often involved in  $\text{O}_2$ -activation reactions. The geometry of these sites is generally square planar or square-pyramidal. They can coordinate multiple amino acid residues, such as histidine, tyrosine, methionine, and cysteine. More importantly, they all conserve a free coordinating site to allow dioxygen binding to the copper. We will discuss this type of site in more details in the following section which is about mononuclear copper monooxygenases with a special emphasis on an enzyme in particular, the lytic polysaccharide monooxygenase enzyme.

## 3. Type III site

Copper sites of coupled binuclear nature are classified as type III. They have two copper centers in the active site. In the oxidized forms (either resting or in the peroxide  $\mu\text{-}\eta^2\text{:}\eta^2(\text{O}_2)$  bridged resulting from dioxygen binding) the two copper ions are antiferromagnetically coupled. [19] [20] The copper ions are in square-pyramidal geometries, coordinating three histidine ligands each. Tyrosinase is an enzyme that contains a typical Type III site catalyzing the hydroxylation of a phenol and the subsequent oxidation to produce a quinone (Figure 2). [21]

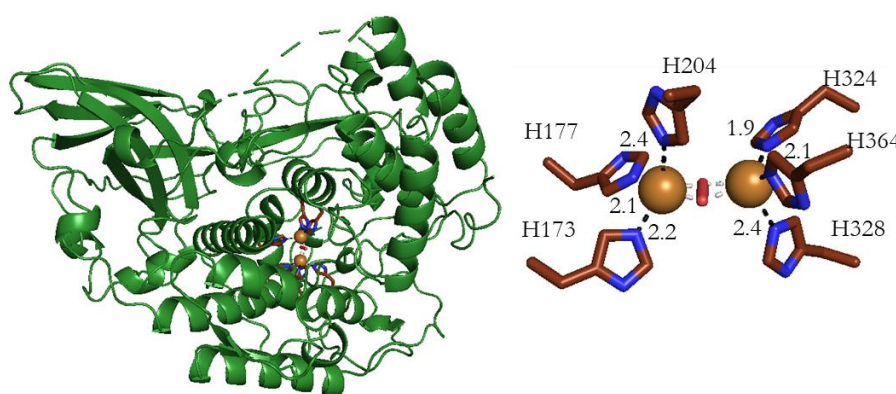


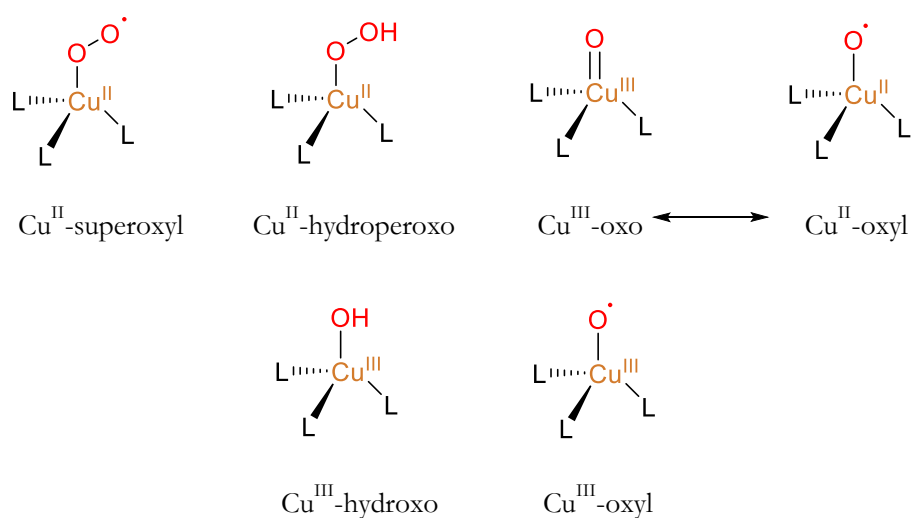
Figure 2. Crystal structure of oxyhemocyanin obtained from *Limulus polyphemus* determined at  $2.4\text{\AA}$  resolution, with zoom into the active site (PDB: 1OXY). [22]

## 1.2 – Mononuclear copper monooxygenases

Within the type II copper sites, monooxygenase enzymes activate dioxygen to catalyze an O-atom insertion into a C-H bond of the substrate (Eqn. 1).



The difficulty of this reaction lies on three different aspects: 1) splitting the dioxygen bond, 2) interacting between the triplet state of oxygen against the singlet state of the substrate, and 3) the uphill thermodynamic drive between the O-H bond in water and the C-H bond of the substrate. [23] One way Nature found to overcome these difficulties is by employing metal ions such as copper that can bind and activate dioxygen to produce active copper-oxygen species (Scheme 1). This is the case of the copper containing Dopamine  $\beta$ -Monooxygenase (D $\beta$ M), Peptidylglycine  $\alpha$ -hydroxylating monooxygenase (PHM), and Lytic Polysaccharide Monooxygenase (LPMO) enzymes.



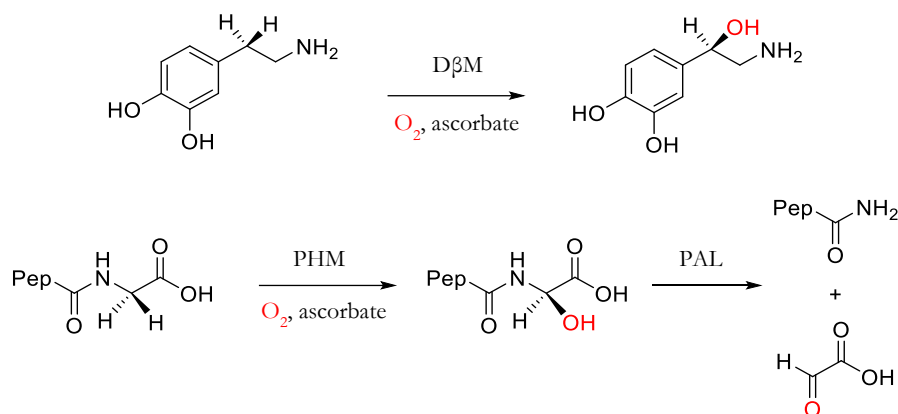
**Scheme 1. Copper-oxygen species proposed as active species in the reactivity of copper monooxygenases.**

### 1. Dopamine $\beta$ -Monooxygenase (D $\beta$ M) and Peptidylglycine $\alpha$ -hydroxylating monooxygenase (PHM)

Dopamine  $\beta$ -Monooxygenase (D $\beta$ M) and Peptidylglycine  $\alpha$ -hydroxylating monooxygenase (PHM) are two enzymes found in mammals which share 28% of sequence identity, and that share similar catalytic domains and conserved copper ligands. [5] [24] D $\beta$ M transforms dopamine into norepinephrine while PHM transforms the terminal glycine residue of peptides into



hydroxyglycine, which is in turn transformed to N-terminal amide and glyoxylic acid by peptidyl- $\alpha$ -hydroxyglycine  $\alpha$ -amidating lyase (PAL) (Scheme 2).



**Scheme 2. Reactions catalyzed by dopamine  $\beta$ -monooxygenase (D $\beta$ M) and peptidylglycine  $\alpha$ -hydroxylating monooxygenase (PHM) in presence of dioxygen and ascorbate.**

These enzymes contain two distinct and separate copper centers in their structures each having specific roles. One copper center binds three histidine residues and an external water molecule. It is proposed to perform electron transfer (ET) from the ascorbate co-factor. This site is known as Cu<sub>H</sub> for PHM and Cu<sub>A</sub> for D $\beta$ M. The second copper center binds two histidine and one methionine residues and one water molecule. The substrate coordinates this site and undergoes the hydroxylation reaction. This site is known as Cu<sub>M</sub> for PHM and Cu<sub>B</sub> for D $\beta$ M. [18] The crystal structure of PHM confirms that two separate domains are found, binding each a single copper atom, separated by 10.7 Å (Figure 3). The core of D $\beta$ M is identical to the one observed in PHM. However, it can present either an open configuration where the copper distances are estimated at 14 Å, and a close configuration where the copper distances is estimated at around 5 Å. There is still a debate on whether the open/closed configurations are linked to a specific functional role. [18]

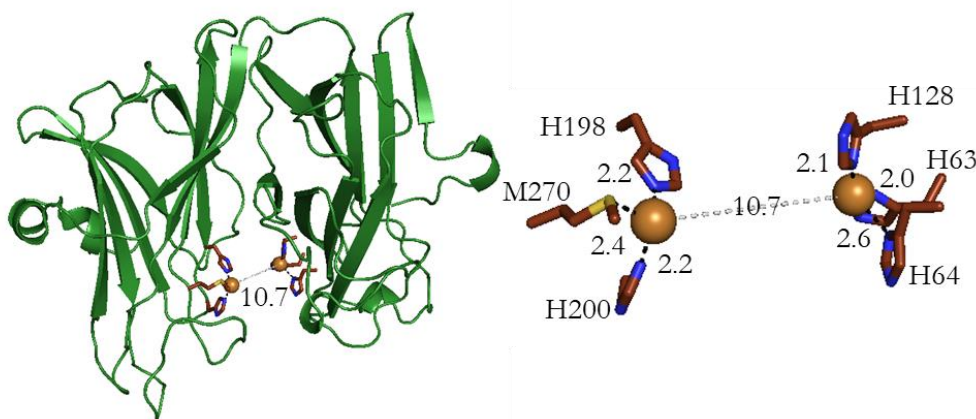
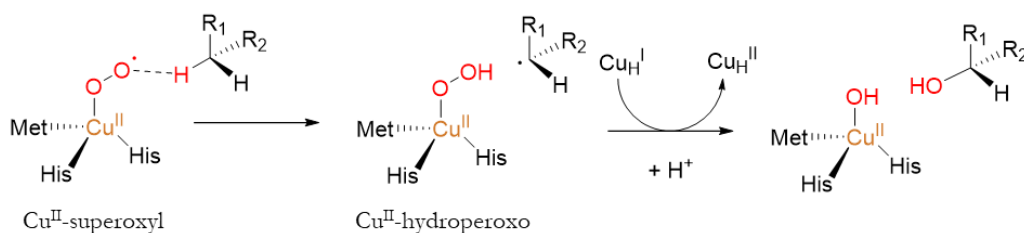


Figure 3. Crystal structure of PHM obtained from *Rattus norvegicus*, with zoom into the active site (PDB: 1OPM). [25]

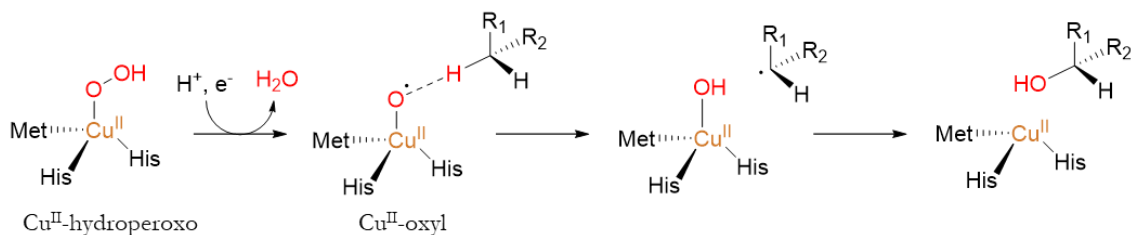
For the PHM enzyme, two crystal structures were obtained in excess dioxygen. The protein was frozen and trapped which shows two different dioxygen bindings. When substrate is in the surroundings dioxygen binds in an end-on fashion while without it, dioxygen binds side-on.

Different copper-oxygen active species, responsible for H-atom abstraction (HAA) from substrates were discussed in the case of D $\beta$ M and PHM such as the Cu(II)-superoxyl [26] or Cu(II)-oxyl [27] (Scheme 1). The nature of the copper-oxygen species involved in the reaction of D $\beta$ M and PHM is still a subject of discussion. [5] [28] The mechanism can involve either the Cu(II)-superoxyl or the Cu(II)-hydroperoxo species as being the active ones (Scheme 3). In the case of the Cu(II)-superoxyl species, HAA from the substrate generates a Cu(II)-hydroperoxo and a substrate radical. The hydroxylating mechanism is still uncertain, but many studies involving quantum mechanical methods have proposed a rebound on the proximal O-atom leading to an O-O cleavage. [29] The case of the Cu(II)-hydroperoxo species can only be considered for the PHM enzyme since irreversible inactivation was observed with the D $\beta$ M enzyme when subjected to hydrogen peroxide. In PHM, the formation of the Cu(II)-hydroperoxo species led to catalytic activity without additional reductant (peroxide shunt). The critical step would be the formation of the formal Cu(II)-oxyl species generated from the O-O cleavage of the hydroperoxo species.

A) Cu<sup>II</sup>-superoxyl as active species



B) Cu<sup>II</sup>-oxyl as active species



**Scheme 3.** Proposed mechanisms for C-H bond activation involving the Cu(II)-superoxyl (A) or the Cu(II)-oxyl (B) as active species of the Cu<sub>M</sub> and Cu<sub>B</sub> sites in PHM and DβM, respectively.

In conclusion, these enzymes have two non-coupled copper centers separated by a large distance. The ET can occur before or after the HAA step leading to different possible mechanistic pathways.

## 2. Lytic Polysaccharide Monooxygenase (LPMO)

LPMOs are enzymes capable to break recalcitrant polysaccharide, such as cellulose and chitin. Given the world's demand in energy and the societal impulse to find new sustainable alternatives, there is great interest in studying these enzymes because of their potential use in the production of biofuels from second-generation biomass. [30] [31] LPMOs are used in synergy with other enzymes to improve the production of second generation bioethanol from lignocellulosic feedstock. Nonetheless, further improvements will depend, most likely, on better understanding the enzyme's interaction with the substrates and its mechanism of action. [32]

One of the enzyme's early appearances was from a fungus, *Trichoderma Reesei*, which was discovered in the 50s. This fungus was found eating away cotton tents in the Solomon Islands during World War II. At this time, Elwyn T. Reese and co-workers proposed a paired system between a cellulolytic component and a non-cellulolytic component for this activity. A first step occurred with hydrolysis of the straight chain of cellulose, and a second step broke the shorter glucose chains into smaller molecules. [33] [34]

Fifty years later, the first LPMO enzymes were identified by Vaaje-Kolstad and co-workers as an enzyme boosting chitin degradation, called CBP21. [35] This “boosting” protein was found to catalyze the oxidative cleavage of glycosidic bonds. Its active site was found bearing two histidine ligands arranged around an unknown transition metal in a 3N-coordination so-called “histidine-brace” motif which includes the primary amine of the N-terminal histidine. [36]

It was later found by Quinlan and co-workers [37] that the recombinant *Thermoascus aurantiacus* LPMO denoted *Ta*GH61 was a mononuclear copper-containing enzyme (Figure 4). Two of the three nitrogen atoms come indeed from the postulated histidine brace motif. This motif is very rare in metalloenzymes and has been observed in one copper site (B-subunit) of particulate methane monooxygenase (pMMO) enzyme [38]. A tyrosine is present in axial position and is replaced by a phenylalanine in some sub-families. Finally, a closer inspection into *Ta*GH61 shows an N-methylated imidazole in the N-terminal histidine. This methylation is not always present.

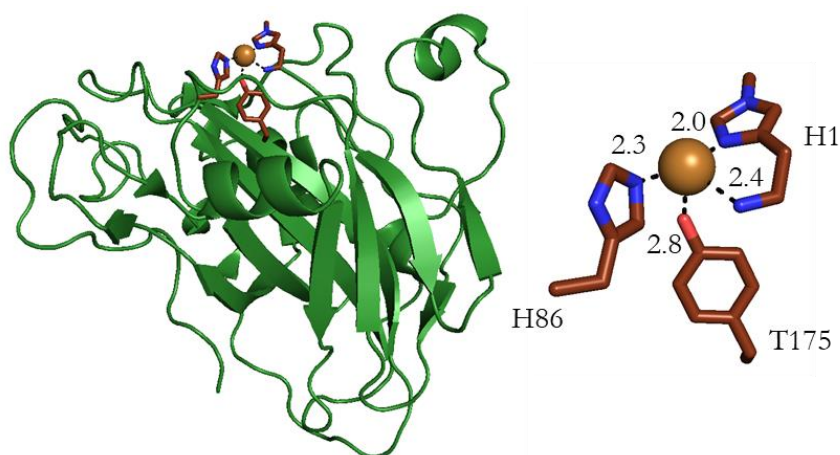


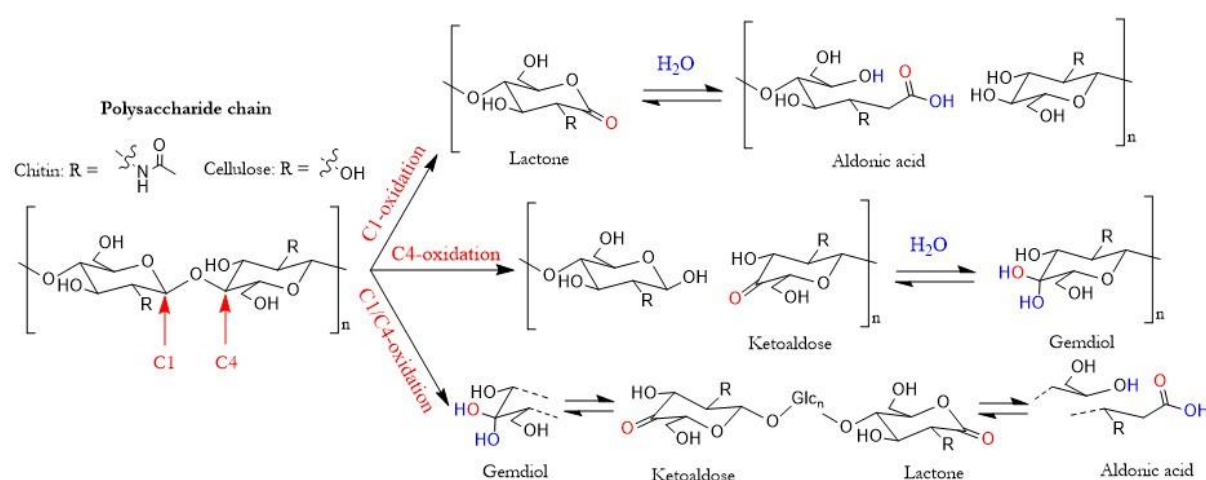
**Figure 4.** Crystal structure of *Ta*GH61 LPMO enzyme and zoom into the first and second coordination spheres of the active site. (PDB: 2YET). [37]

### *Substrate reactivity*

Differences in chemical functions, natural substrate, regioselectivity, and origin of LPMO, led to develop a classification based on Auxiliary Activity (AA) families. Nowadays, there are 7 AA families that are described: AA9, AA10, AA11, AA12, AA14, AA15, and AA16. The LPMOs described before are now known to be part of the AA9 family for *Ta*GH91 and AA10 for CBP21.

Activity assays have been expanded in recent years. Multiple substrates, other than cellulose [37] [39] [40] and chitin, [35] [41] [42] are being tested for the same goal and include xylan, [43]

xyloglucan, glucomannan, lichenan,  $\beta$ -glucan, [44] [45] and starch. [46] [47] LPMO catalyzes the hydroxylation of one C-H bond at the glycosidic linkage leading to chain breaking. Two oxidation positions are known: C1 and C4 (Scheme 4). When oxidizing the C1 position, the LPMO reaction forms 1,5- $\delta$ -lactones which are spontaneously transformed into a more stable aldonic acid ( $\text{Glc}_n\text{Glc1A}$ ) form. [48] In the case of C4 oxidation, LPMOs produce 4-ketoaldoses ( $\text{Glc4KGlc}_n$ ) which are spontaneously transformed to their corresponding gemdiol ( $\text{Glc4GemGlc}_n$ ) form. [45] Most enzymes have either a C1 or C4 regioselectivity but some LPMOs are also capable to oxidize both positions displaying a mixed C1/C4 regioselectivity. [49]



**Scheme 4. Regioselectivity on the oxidation of polysaccharide chains by LPMOs. C1 oxidation results in the formation of lactones and subsequent hydration to form aldonic acids. C4 oxidation leads to the formation of ketoaldose and the corresponding hydrated gemdiols. C1/C4 oxidations lead to oligosaccharides with both ends being oxidized. [50]**

### Electronic Paramagnetic Resonance

LPMOs have been characterized with typical spectroscopic methods used for classical type II copper systems, notably with EPR. In the case of *TaGH61*, the X-band EPR spectrum obtained in acetate buffer at pH 5.0 and 140 °K, shows an unambiguous signal for a mononuclear copper ion with tetragonal geometry. [37] From the 7 AA families, there is a well conserved first coordination sphere around the copper center. Yet, their EPR parameters can be quite different and diverse. For instance, LPMOs display in general a rather axial EPR spectrum although chitin-active LPMOs from AA10 sub-family display a rhombic spectrum indicative of significant trigonal distortion. Hemsworth and co-workers, [51] have gathered the EPR parameters ( $g_z$  and  $A_z$  values) for an extensive set of LPMOs at their resting Cu(II) state, and constructed an adapted Peisach-

Blumberg plot (Figure 5). [52] They therefore evidenced the variability of EPR parameters between AA families and within sub-families as well.

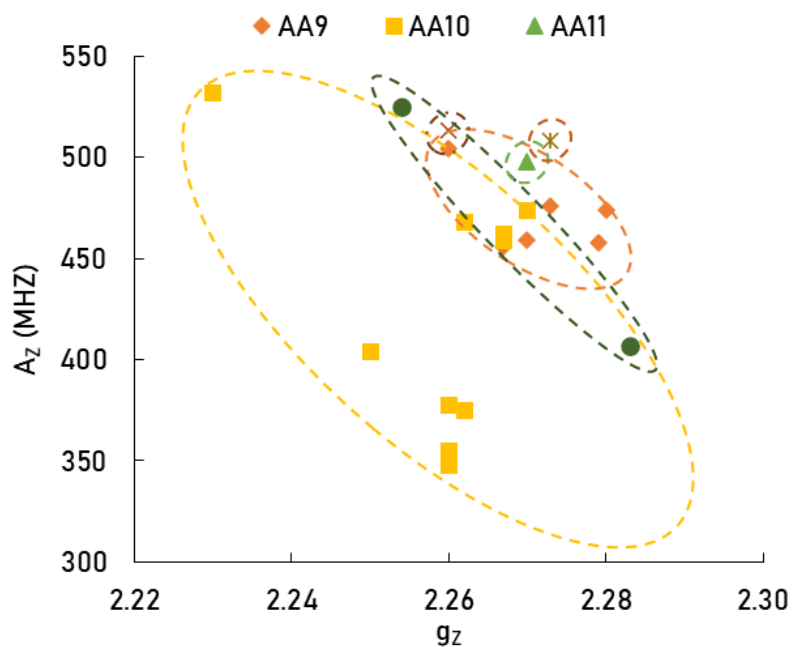


Figure 5. Peisach-Blumberg plot of selected LPMO enzymes showing variability in  $g_z$  and  $A_z$  values between and within AA families. The dash-lined circle of the corresponding family gives an idea of the potential region for expected EPR values. Data and references are reported in Table 1. [51].

**Table 1. EPR  $g_z$  and  $A_z$  values used for the Peisach-Blumberg plot.**

AA family	LPMO enzyme	$g_z$	$A_z$ (MHz)	Reference
<b>AA9</b>	<i>NcAA9C</i>	2.267	456	Borisova et al (2015) [53]
	<i>TdAA9A</i>	2.270	459	Quinlan et al. (2011) [37]
	<i>HjAA9A</i>	2.280	474	Hansson et al. (2017) [54]
	<i>MtAA9</i>	2.260	204	Span et al. (2017) [55]
	<i>CvAA9A</i>	2.273	476	Simmons et al. (2017) [56]
	<i>LsAA9A</i>	2.279	458	Frandsen et al. (2016) [57]
<b>AA10</b>	<i>BaAA10A</i>	2.250	404	Hemsworth et al. (2013) [42]
	<i>CjAA10A</i>	2.267	462	Forsberg et al. (2016) [58]
	<i>SmAA10A</i>	2.260	348	Forsberg, Rohr, et al. (2014) [59]
	<i>ScAA10C</i>	2.267	459	
	<i>B/AA10</i>	2.262	375	
	<i>TjAA10B</i>	2.262	468	
	<i>ScAA10B</i>	2.270	474	Forsberg, Mackenzie, et al. (2014) [49]
	<i>PlAA10A</i>	2.260	355	Munzone et al. (2020) [41]
	<i>SlAA10E</i>	2.260	378	Chaplin et al. (2016) [60]
		2.230	532	
<b>A11</b>	<i>AoAA11</i>	2.270	498	Hemsworth et al. (2014) [61]
<b>A13</b>	<i>AoAA13</i>	2.260	513	Lo Leggio et al. (2015) [47]
<b>A14</b>	<i>PcAA14A</i>	2.273	508	Couturier et al. (2018) [62]
<b>A15</b>	<i>TdAA15A</i>	2.283	407	Sabbadin et al. (2018) [63]
		2.254	525	

It has also been observed that in the case of some chitin-active LPMOs (including one from our laboratory), two species can be detected by EPR spectroscopy (Figure 6, Table 2). There is evidence of a major species with a “normal” rhombic EPR signature, and the formation of a second, minor species with distinct axial features. This has been assigned to a possible decoordination of the primary N-terminal amine. [41] [60] However, no in-depth study on the origin of this second species has been reported.

**Table 2.** Spin-Hamiltonian parameters for selected enzymes showing two EPR species parameters with rhombic and axial features.

Reference	Enzyme used	Species	g-tensor			A-tensor (MHz)		
			$g_x$	$g_y$	$g_z$	$A_x$	$A_y$	$A_z$
Munzone et al. [41]	P/AA10	Major (80%)	2.025	2.103	2.260	220	95	355
		Minor (20%)	2.062	2.062	2.250	< 90	< 90	537
Chaplin et al. [60]	S/LPMO10E	Major	2.033	2.067	2.260	38	38	378
		Minor	2.055	2.071	2.230	53	53	532

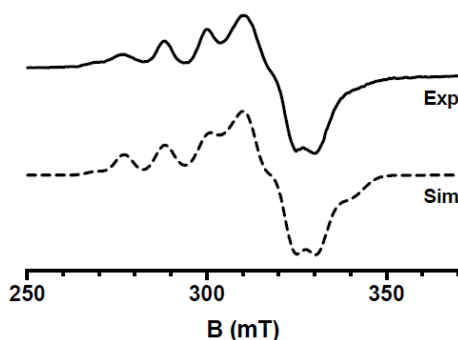


**Figure 6.** X-band EPR spectra of the LPMO enzyme *P/AA10* (plain line) and the simulated EPR spectra (dashed line) obtained with the parameters shown in Table 2. [41].

### Substrate interaction

When the substrate is added to the LPMO mixture, there is a clear change on the EPR signature and its parameters, indicating significant rearrangements of the copper site upon substrate's binding. [64] [53] [57] [56] For instance, using *SmAA10A*, Bissaro and co-workers [64] observed that after binding of substrate, the  $g_z$  values decrease and the  $A_z^{\text{Cu}}$  values increase. This trend was further rationalized using large enzyme models and QM/MM calculations. In addition, the hyperfine and superhyperfine values change depending on the presence of the substrate. The binding of an oligomer, (N-acetyl-glucosamine)<sub>6</sub>, denoted (NAG)<sub>6</sub>, resulted in a weaker  $A_z^{\text{Cu}}$  shift compared to the one with crystalline  $\beta$ -chitin. In addition, the superhyperfine features of the neighboring nitrogen atoms are considerably more apparent in the presence of  $\alpha$ - or  $\beta$ -chitin compared to (NAG)<sub>6</sub> (Table 3, Figure 7. X-band EPR spectra of the LPMO enzyme *SmAA10A* (black lines): A) without substrate, B) in the presence of (NAG)<sub>6</sub>, and C) in the presence of either  $\alpha$ - or  $\beta$ -chitin. In each case, the simulated spectra are reported as well (sim, gray line) using the experimental g- and A- values. Data obtained from Figure 7).



Table 3. Spin-Hamiltonian parameters (parallel region) for selected enzymes and in interaction with the substrate.

Reference	Enzyme			Enzyme + substrate		
	Enzyme used	$g_z$	$A_z^{\text{Cu}}$ (MHz)	Substrate used	$g_z$	$A_z^{\text{Cu}}$ (MHz)
Bissaro et al. [64]	<i>SmAA10A</i>	2.259	346	(NAG) <sub>6</sub>	2.212	560
				$\beta$ -chitin	2.216	610
Borisova et al. [53]	<i>NdLPMO9C</i>	2.267	456	Cellohexaose and xyloglucan	2.226	525
Frandsen et al. [57]	<i>Ls(AA9)A</i>	2.280	458	Cellohexaose	2.270	515
	<i>LsAA9A</i>	2.279	458	Cellohexaose	2.273	515
Simmons et al. [56]				Avicel	2.278	470
				Xylan	2.272	480
				Glucomannan	2.232	518
				Xyloglucan	2.270	515
				Cellohexaose	2.228	527

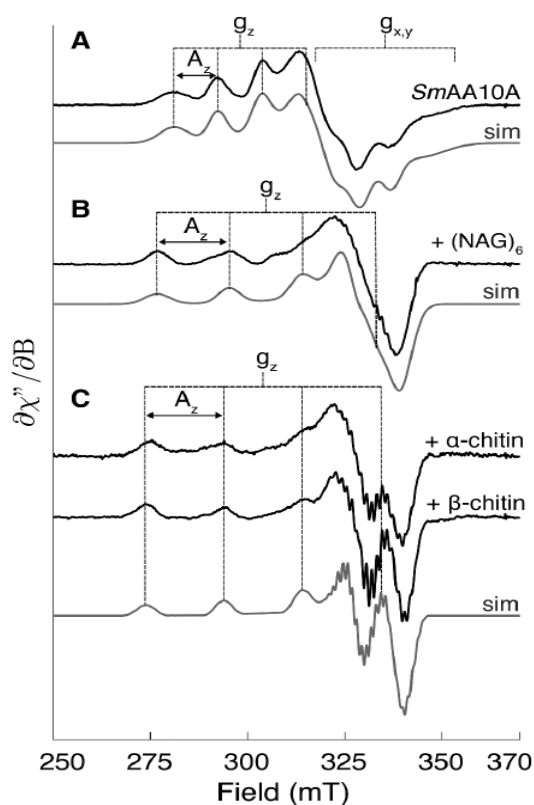


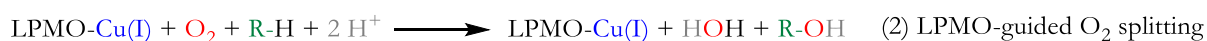
Figure 7. X-band EPR spectra of the LPMO enzyme *SmAA10A* (black lines): A) without substrate, B) in the presence of (NAG)<sub>6</sub>, and C) in the presence of either  $\alpha$ - or  $\beta$ -chitin. In each case, the simulated spectra are reported as well (sim, gray line) using the experimental  $g$ - and  $A$ - values. Data obtained from [64].

## Oxygen source

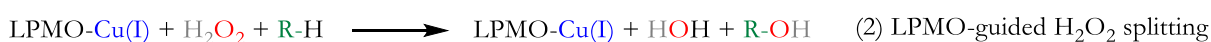
To carry the oxidation reaction on the polysaccharides, LPMOs require an oxygenated co-substrate. The nature of this co-substrate, dioxygen or hydrogen peroxide, is still debated (Scheme 5). The dioxygen was proposed as substrate since the very beginning of the studies. [36] After carrying isotope-labelled experiments, it was shown that one oxygen atom was inserted from  $^{18}\text{O}_2$ . In addition, removal of dioxygen led to the absence of reaction. Conversely, Bissaro et al. studied the  $\text{H}_2\text{O}_2$  dependence of LPMOs. [65] Under catalytic conditions and in the presence of  $\text{H}_2\text{O}_2$ , product levels were found higher than the amount of ascorbic acid used. This is not possible if the reaction was strictly dependent on  $\text{O}_2$ . Also, under anaerobic conditions, LPMO works when  $\text{H}_2\text{O}_2$  is supplied. The reaction rate is independent of  $\text{O}_2$  levels. Isotope-labelling experiments suggest that the oxygen introduced comes from  $\text{H}_2^{18}\text{O}_2$  and not from  $\text{O}_2$ , even if  $\text{O}_2$  is in large excess. Finally, to dismiss the possibility of  $\text{H}_2\text{O}_2$  being an artificial substrate (peroxide shunt), competition experiments were carried out in the presence of  $\text{H}_2\text{O}_2$ -consuming peroxidases. In this case, the LPMO activity was completely inhibited. The origin of the natural oxygenated co-substrate is still in question, and it must be noted that, in absence of substrate, LPMOs produce  $\text{H}_2\text{O}_2$  from  $\text{O}_2$  during what has been reported as “uncoupling turn-overs”. A conclusion was reached in 2019 by Eijssink and co-workers: “Perhaps the biggest complication lies in the nature of the co-substrate, which, in fact is difficult to assess experimentally. The fact that the one potential co-substrate,  $\text{O}_2$ , can be converted to another,  $\text{H}_2\text{O}_2$ , which leads to faster catalysis, makes experimental LPMO-work challenging.” [30]

Finally, ascorbate is commonly used as reductant for in-vitro studies but several molecules (including lignans derivatives) or protein-partners were described as efficient electron suppliers for LPMOs. [66]

### A) $\text{O}_2$ mediated reaction



### B) $\text{H}_2\text{O}_2$ mediated reaction



**Scheme 5.** Equations for the oxidative reaction of LPMO enzymes mediated by A)  $\text{O}_2$ , or B)  $\text{H}_2\text{O}_2$ . In either case, there is a priming reduction of the Cu(II) metal center to Cu(I).

To activate the C-H bond of the substrate and perform the hydrogen atom abstraction (HAA) step, mononuclear copper centers need to produce O<sub>2</sub>-derived species and perform copper-oxygen chemistry (Figure 8). Initially, the Cu(II) metal center of the LPMO enzyme will be reduced to Cu(I). This reduced copper ion will be oxidized to a mononuclear cupric superoxo species (LPMO-Cu<sup>II</sup>-OO<sup>•</sup>) in the presence of dioxygen, regardless of whether the substrate binds the metal before or after the oxidation. At this stage, there are several proposed pathways that could lead to the substrate's hydroxylation. These pathways can be classified based on the reactive intermediate performing the HAA step. Three distinct classes are derived:

- I. Cu<sup>II</sup>-superoxo, LPMO-Cu<sup>II</sup>-OO<sup>•</sup>, itself performs HAA
  1. Direct HAA from Cu<sup>II</sup>-superoxo produces LPMO-Cu<sup>II</sup>-OOH<sup>-</sup> and R<sup>•</sup>. The radical on the substrate will rebound to form the peroxyated substrate, R-OOH, and LPMO-Cu<sup>I</sup>. Finally, the two electron-two proton reduction takes place to produce the hydroxylated product and a water molecule.
  2. Single electron reduction from Cu<sup>II</sup>-superoxo produces LPMO-Cu<sup>II</sup>-OO<sup>2-</sup>. HAA takes place to yield LPMO-Cu<sup>II</sup>-OOH<sup>•2-</sup> and R<sup>•</sup>. Then rebound and reduction produce the hydroxylated product and a water molecule, as well as the reduced LPMO-Cu<sup>I</sup> species.
- II. Cu<sup>II</sup>-hydroperoxo, LPMO-Cu<sup>II</sup>-OOH<sup>•</sup>, performs HAA, after protonation of the superoxo species
  1. Direct HAA from Cu<sup>II</sup>-hydroperoxo produces LPMO-Cu<sup>II</sup>-OOH<sub>2</sub> and R<sup>•</sup>. After water dissociation and rebound of the radical substrate, the hydroxylated product and the initial LPMO-Cu<sup>I</sup> species are produced.
  2. Single electron reduction from Cu<sup>II</sup>-hydroperoxo produces LPMO-Cu<sup>II</sup>-OOH<sup>-</sup>. This species performs HAA to dissociate a water molecule, form the copper-oxyl, LPMO-Cu<sup>II</sup>-O<sup>•</sup>, and the radical substrate, R<sup>•</sup>. After rebound and reduction, LPMO-Cu<sup>I</sup> and the hydroxylated product are obtained.
  3. Double electron reduction from Cu<sup>II</sup>-hydroperoxo produces LPMO-Cu<sup>II</sup>-OOH<sup>•2-</sup>. This intermediate performs HAA to first obtain LPMO-Cu<sup>II</sup>-O<sup>2-</sup> and water, and then LPMO-Cu<sup>II</sup>-OH<sup>-</sup> and a hydroxyl group. After rebound and reduction, water and the products are released, as well as the initial LPMO-Cu<sup>I</sup>.
- III. Cu<sup>II</sup>-oxyl radical, LPMO-Cu<sup>II</sup>-O<sup>•</sup>, performs HAA, after double protonation of the superoxo species and dissociation of a resulting water molecule

1. Direct HAA from  $\text{Cu}^{\text{III}}$ -oxyl radical,  $\text{LPMO-Cu}^{\text{III}}\text{-O}^\bullet$ , to produce a high oxidation state  $\text{LPMO-Cu}^{\text{III}}\text{-OH}^\bullet$  and the substrate radical  $\text{R}^\bullet$ . Then, rebound of the substrate and reduction of copper center yields the initial  $\text{LPMO-Cu}^{\text{I}}$  and the hydroxylated product.
2. Single electron reduction from  $\text{Cu}^{\text{II}}$ -oxyl to produce  $\text{LPMO-Cu}^{\text{II}}\text{-O}^\bullet$ . After HAA,  $\text{LPMO-Cu}^{\text{II}}\text{-OH}^\bullet$  and the radical substrate are formed. After rebound, the  $\text{LPMO-Cu}^{\text{I}}$  species, the hydroxylated product, and the water molecule are obtained.

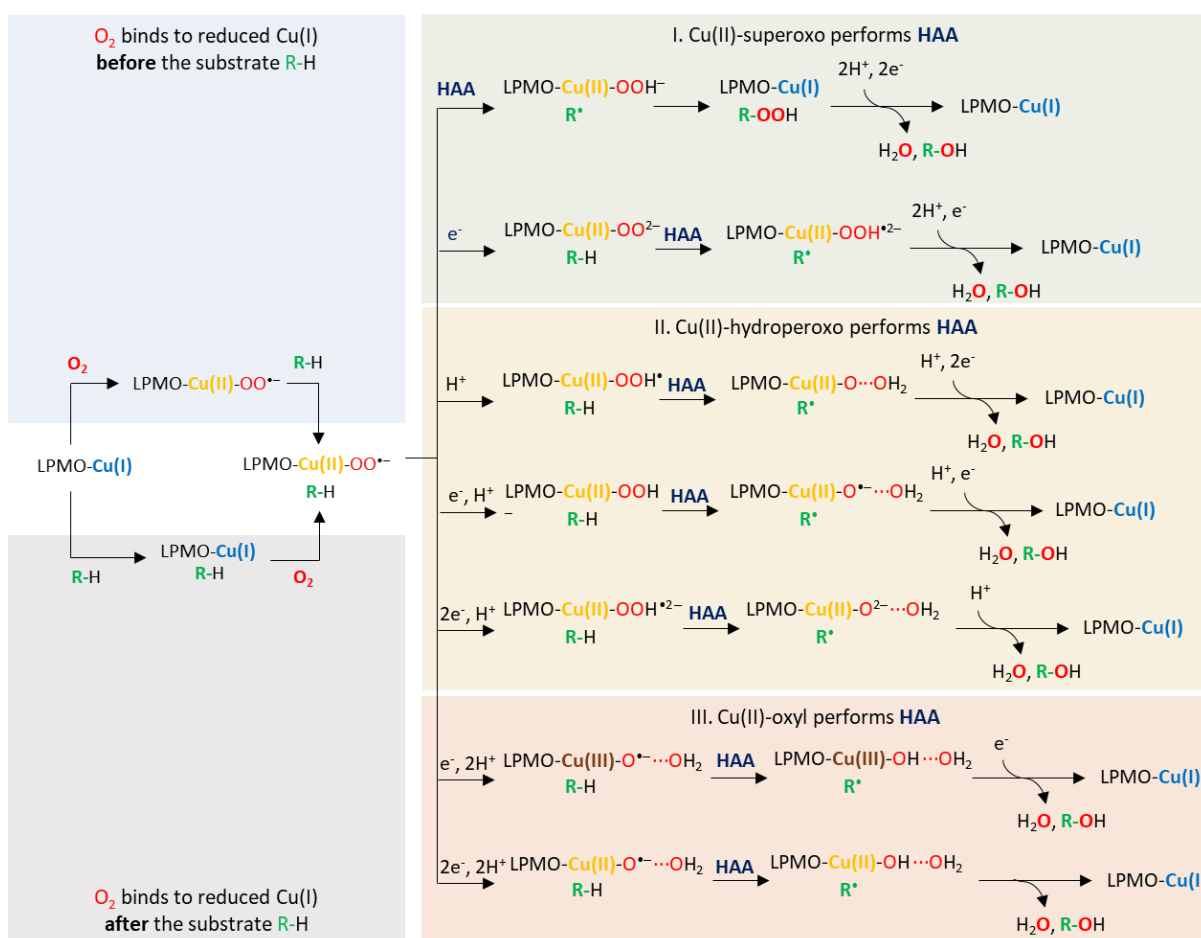


Figure 8. Overview of the possible catalytic pathways proposed for LPMOs on polysaccharide substrates ( $\text{R-H}$ ). The dark blue HAA label identifies the hydrogen atom abstraction step. The reduced  $\text{LPMO-Cu(I)}$  species can bind either dioxygen first and then the substrate (blue box), or the opposite (gray box), to produce the  $\text{LPMO-Cu(II)-superoxo}$  species. Three distinct classes are derived with respect to the HAA step: I.  $\text{Cu(II)-superoxo}$  performs HAA (green box), II.  $\text{Cu(II)-hydroperoxo}$  performs HAA (yellow box), or III.  $\text{Cu(II)-oxyl}$  performs HAA (red box). Adapted from [67].

These pathways are derived from dioxygen chemistry in the presence of the reduced mononuclear copper(I) species. However, LPMOs could be peroxygenase enzymes where hydrogen peroxide is the co-substrate instead of dioxygen (Figure 9). Binding hydrogen peroxide to the active site would follow intramolecular proton transfer and dissociation of a water molecule. This will produce the copper-oxyl, LPMO-Cu<sup>II</sup>-O<sup>•</sup>. [67] This is imitating the peroxide shunt pathway. Computational studies suggest that the C-H hydroxylation of LPMOs occurs by generation of this copper oxyl species. [68]

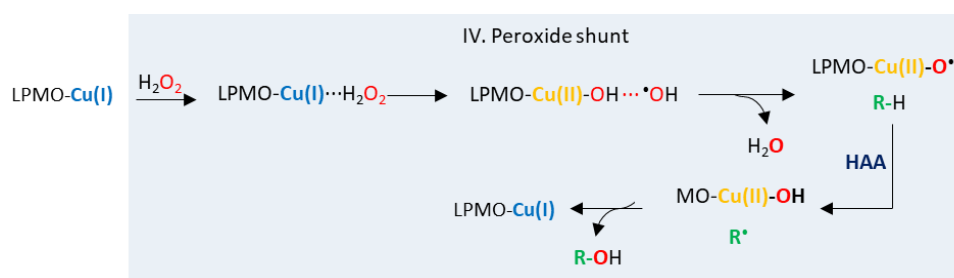


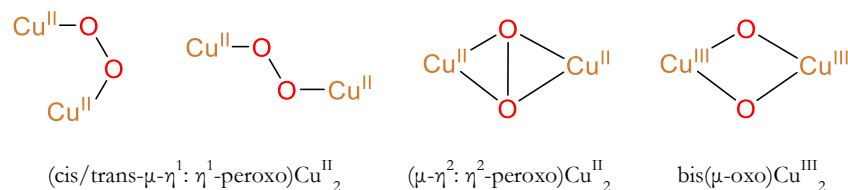
Figure 9. Proposed peroxide shunt pathway for LPMO enzymes producing the copper-oxyl intermediate.

### 1.3 – Bioinspired models

The copper oxygen species are important entities in monooxygenase enzymes. Synthetic models have been produced to stabilize and characterize different reactive intermediates. Nevertheless, their reactivity is difficult to control, and these species have generally to be isolated at low temperatures (-80°C / -135°C).

#### 1. *Cu-superoxo*

Several cupric-superoxo have been isolated in the literature. They have generally been obtained by oxygenation of Cu(I) complexes. [69] The copper-superoxo species can also undergo dimerization with a reduced copper(I) complex to produce the binuclear dicopper complexes: (cis/trans- $\mu$ -  $\eta^1$ : $\eta^1$ -peroxo)Cu<sup>II</sup><sub>2</sub>, ( $\mu$ - $\eta^2$ : $\eta^2$ peroxo)Cu<sup>II</sup><sub>2</sub>, or bis( $\mu$ -oxo)Cu<sup>III</sup><sub>2</sub> (Scheme 6). [70] This constitutes one difficulty when trying to characterize and isolate a mononuclear superoxo species and therefore, most superoxyl species were described using bulky ligands. Two crystal structures were obtained ([Cu(O<sub>2</sub>)(TMG)3tren]<sup>+</sup> and [Cu(O<sub>2</sub>)(TptBu,iPr)]) illustrating the possible end-on or side-on binding modes of the superoxo ligand (Figure 10). [71] [72]



**Scheme 6.** Dinuclear copper species formed from copper-superoxo species.

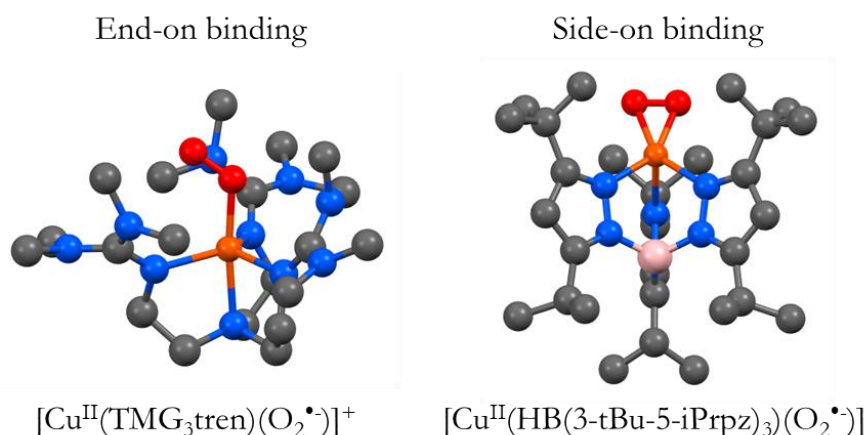
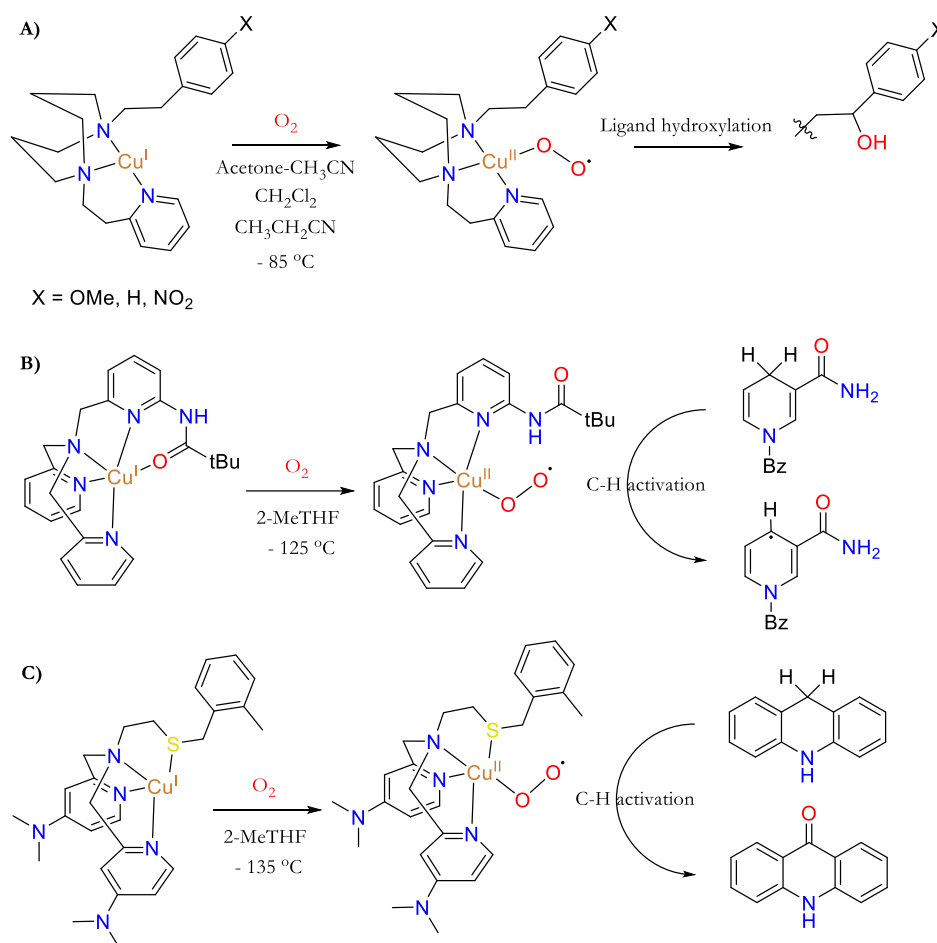


**Figure 10.** Crystal structures of  $[\text{Cu}^{\text{II}}(\text{TMG}_3\text{tren})(\text{O}_2^{\bullet})]^+$  and  $[\text{Cu}^{\text{II}}(\text{HB}(3\text{-tBu-5-iPrpz})_3)(\text{O}_2^{\bullet})]$  illustrating the end-on and side-on binding of the superoxo ligand.

The reactivity of Cu-superoxo intermediates was evaluated on different substrates. For example, Itoh and co-workers demonstrated that Cu-superoxo were capable of intramolecular benzylic C-H oxygenation (Scheme 7). [71] [72] Karlin and co-workers used intrinsic H-bonding groups to stabilize the species at  $-125^\circ\text{C}$  and evaluate their subsequent reactivity on different substrates. [73] Finally, Kim and co-workers employed a  $\text{N}_3\text{S}$  ligand with enhanced reactivity compared to those of the  $\text{N}_4$  type. [74] Overall, most of the Cu-superoxo complexes display the ability to perform various reactions that mimic the chemistry of copper oxygenases. The observed reactivity and the effects of geometry (tetrahedral versus bipyramide trigonal) and ligand variation (S- versus N-donors) led to the conclusions that they can be considered as relevant active species for the chemistry performed by D $\beta$ H and PHM enzymes but probably not by LPMOs.

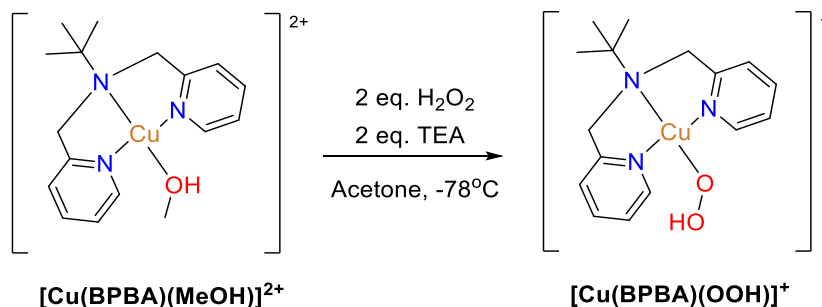


**Scheme 7.** Formation of spectroscopically characterized Cu(II)-superoxo species. **A)** Intramolecular benzylic oxygenation. [71] [72] **B)** Hydrogen bond stabilization of Cu(II)-superoxo species capable of C-H activation. [73] **C)** Different coordinating atoms,  $N_3S$ , capable of C-H activation. [74]. Modified from [75].

## 2. Cu-hydroperoxo

Several Cu(II)-OOH have been described in the literature. Most of these intermediates were generated by reaction a Cu(II) complex with hydrogen peroxide in the presence of a base and one crystal structure has been reported in the literature. [69] In most cases, the geometry around the copper is trigonal. Fujii *et al.* [76] characterize a square-planar copper-hydroperoxo species using the bis(2-pyridylmethyl)tert-butylamine, BPBA, ligand. The  $[Cu^{II}(BPBA)(MeOH)](ClO_4)_2$  complex was subjected to two equivalents of triethylamine and hydrogen peroxide in acetone at  $-78^\circ C$ . (Scheme 8) The resulting product displayed a dominant absorption band at 350 nm from UV-vis assigned to the  $HOO^-$  to Cu LMCT while maintaining a square-planar geometry as attested by EPR parameters,  $g_{//} = 2.26$ ,  $g_{\perp} = 2.06$ , and  $A_z^{Cu} = 554$  MHz. In addition, Fujii and his group studied the stability and the reaction kinetics for the oxidation of dimethyl sulfide. In general,

Cu(II)OOH intermediates have been described as sluggish oxidants towards external substrates and are rather considered as precursors of more oxidizing intermediates such as copper-oxyl ones.

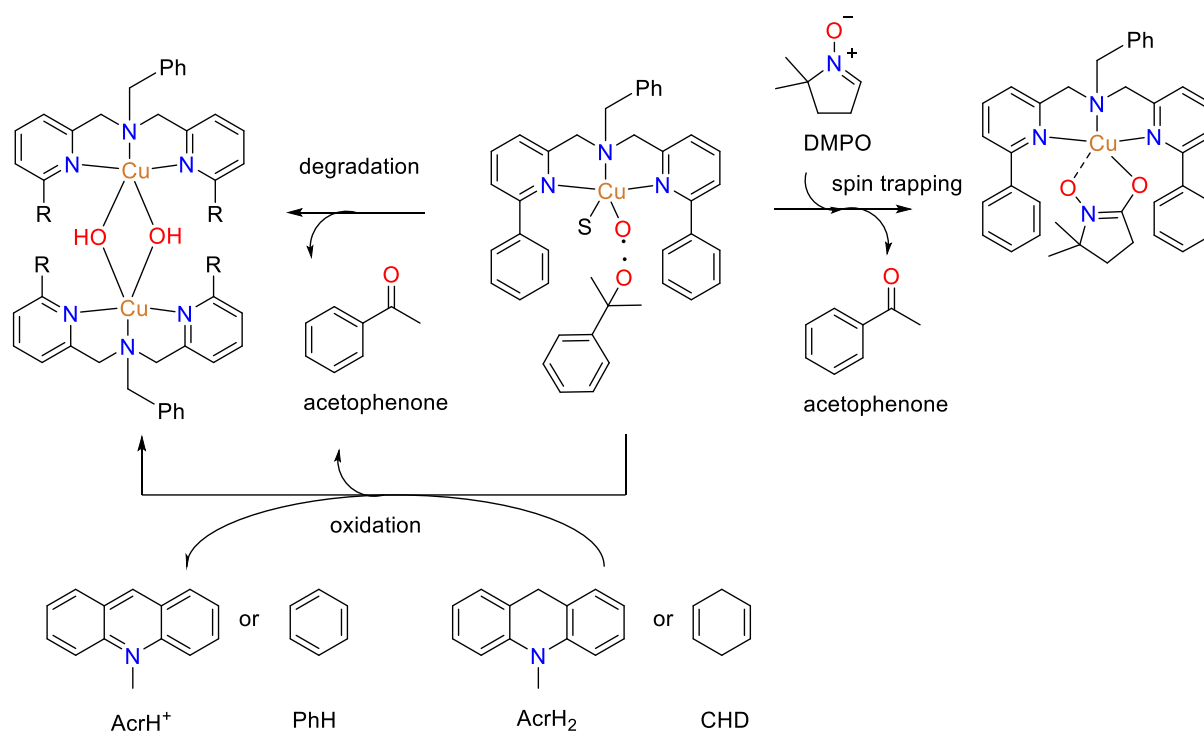


Scheme 8. Formation of the square-planar  $[\text{Cu}(\text{BPBA})(\text{OOH})]^{+}$  complex by addition of 2 equivalents of both hydrogen peroxide and triethylamine, in an acetone solution of the  $[\text{Cu}(\text{BPBA})(\text{MeOH})]^{2+}$  complex at  $-78^{\circ}\text{C}$ .

### 3. Copper-oxyl

Although no copper-oxyl was directly detected, several indirect evidence of their formation during catalysis were reported. Itoh and co-workers provided evidence of the generation of copper-oxyl species produced by O-O homolysis of a  $\text{Cu}^{\text{II}}\text{-OOR}$  complex. [77] The starting Cu(II) complex was subjected to cumene hydroperoxide in the presence of triethylamine in acetonitrile at  $-40^{\circ}\text{C}$ . This formed the copper-cumylperoxo species which exhibited a relatively intense absorption band at 465 nm (Scheme 9). It gradually decomposed to produce a dinuclear bis( $\mu$ -hydroxo)dicopper(II) complex. The O-O cleavage of the copper-cumylperoxo species is evidenced by the presence of the acetophenone by-product of the oxidation reaction of substrates, such as 10-methyl-9,10-dihydroacridine ( $\text{AcrH}_2$ ) and 1,4-cyclohexadiene (CHD). The radical copper-oxyl species was also captured by 5,5-dimethyl-1-pyrroline-N-oxide (DMPO) and identified by EPR.





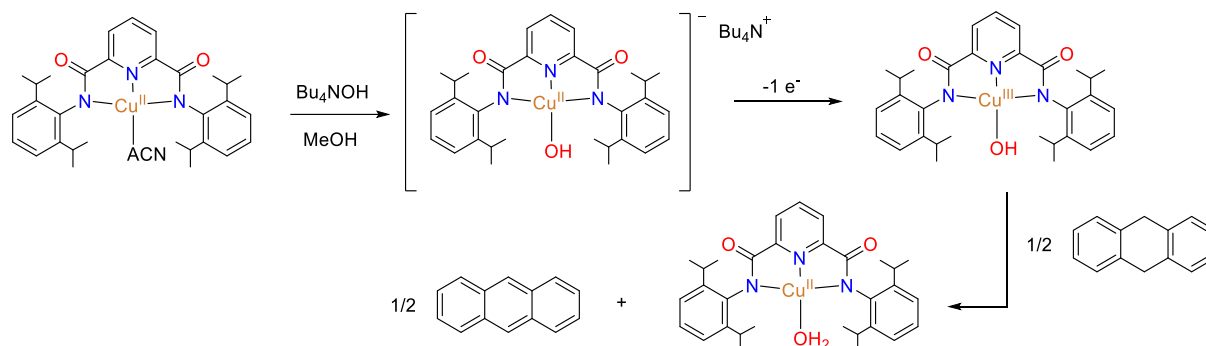
**Scheme 9. Copper-cumylperoxo and its reactivity products: gradual degradation, spin trapping with DMPO and oxidation of substrates (AcrH<sub>2</sub> and CHD). Modified from [77].**

The reaction of Cu(I) complex with PhIO was also attempted by Reglier [78] and Karlin. [79] In both cases, intramolecular oxidation of the ligand was observed. The group of Karlin reported the low-temperature ESI-MS spectrometry of the putative cupryl intermediate at the early stage of the reaction before the formation of the final oxidized complex. Finally, the group of Tolman have studied the oxidative decarboxylation of Cu(I)-2-oxoacid complexes to generate high-valent copper–oxo species that were not detected but led to intramolecular oxidation of the ligand. [80]

#### 4. Cu(III)-hydroxide

Tolman and his group generated a high-valent copper-hydroxide species using the N,N'-bis(2,6-diisopropylphenyl)-2,6-pyridinedicarboxamide ligand (Scheme 10). [81] After complexation of the ligand with copper, tetrabutylammonium hydroxide was added in a methanol solution. Then, chemical oxidation was performed using ferrocenium hexafluorophosphate (Fc<sup>+</sup>PF<sub>6</sub><sup>-</sup>) at -80°C. An intense absorption feature was observed at around 540 nm and the solution was found to be EPR silent. The high oxidation Cu<sup>III</sup>-OH species is possibly coming from a protonated state of the copper-oxyl reactive intermediate. [82] This complex was studied for its reactivity with several

substrates for C-H or O-H activation. [83] Their strong C-H bond activation ability ( $> 90$  kcal/mol) makes Cu(III)-OH species relevant for LPMO reactivity.



**Scheme 10.** Formation of the Cu(III)-hydroxide complex and its reactivity with dihydroanthracene.

The synthetic systems that were presented are capable to produce copper-superoxo, copper-hydroxide, or copper-oxyl species, at low temperatures. To perform an in-depth study, computational chemistry is often employed, especially using Density Functional Theory (DFT), to rationalize between the envisioned reaction mechanisms and the possible copper oxygen species forming during the reaction. [67] [68]

## 2 – Theoretical calculations in bioinorganic chemistry

Computational methods are widely used in chemistry to evaluate the geometrical, chemical, and physical properties of a system. In the context of bioinorganic chemistry, quantum mechanical methods are extensively employed, especially those based on density functional theory (DFT). DFT is implemented in many program packages, such as TurboMole, [84] ADF, [85] JAGUAR, [86] and ORCA, [87] among others, making this method a readily available and quite user-friendly tool. Geometries, total energies, spin-states, vibrational frequencies, electronic properties, magnetic parameters and optical spectra are some of the properties made easily accessible using DFT. The latter was first introduced by Hohenberg and Kohn in 1964 [88] and its derivation was made possible with the introduction of quantum chemistry and Hartree-Fock theory. In this

section, we will present computational methods based in quantum mechanics, *i.e.* wave-function methods and DFT, before showcasing some applications of DFT in copper bioinorganic chemistry.

### 1. Basic principles

In quantum mechanics, the uncertainty principle forbids us to know the position ( $\mathbf{r}$ ) and the momenta of a particle at a given time ( $t$ ) simultaneously. Instead, wavefunction provides us with the probability of finding this particle in a specific position at a given velocity. To calculate the wavefunction, we use the Hamiltonian concept. In quantum mechanics, it is formally a mathematical operator which eigenvalue corresponds to the total energy of the system under study and it is built from the contributions of two main operators:

$$H = T + V \quad (\text{Eqn. 2}).$$

With  $T$  the kinetic energy and  $V$  the potential energy of the system.

Introducing the spin of the electron ( $s$ ) as an extra variable in addition to the position  $\mathbf{x}$  and the time  $t$ , we can introduce the Schrödinger's equation [89]. The latter is a linear partial differential equation that governs the wave function of a quantum-mechanical system and that is written as follows:

$$\hat{t} \frac{\partial}{\partial t} \Psi(r, s, t) = H(r, s, t) \Psi(r, s, t) \quad (\text{Eqn. 3}).$$

Assuming the Hamiltonian does not depend on time, we obtain the time-independent Schrödinger equation:

$$H(r, s) \Psi(r, s) = E \Psi(r, s) \quad (\text{Eqn. 4}).$$

This equation is however far too complex to be solved and approximations are necessary. The Born-Oppenheimer (BO) approximation [90] is fundamental to quantum chemistry as it allows to neglect the kinetic energy of the nuclei. Nuclei are much heavier than electrons and therefore are much slower so that electrons will adjust immediately to the nuclear configuration. By consequence, the energy becomes a function of the nuclear coordinates and is known as the potential energy surface. Also, the Schrödinger equation separates in two distinct parts, the electrons for an arrangement of nuclei and the nuclei on a potential energy.

Unfortunately, one cannot solve the BO problem exactly, except for 1-dimensional 2-electron systems, because the task is still far too complex to account for polyelectronic systems with notably

multiple repulsive electron-electron interactions. Theoretical chemists and physicists have intensely studied this problem and have come up with different approximations. In this respect, the variational principle allows to state that the energy of any normalized and antisymmetric wavefunction ( $\Psi$ ) must be higher than or equal to the energy of the exact wavefunction ( $\Psi_0$ ):  $E(\Psi) \geq E(\Psi_0)$  with  $E_0$  representing the lowest eigenvalue associated with the exact wavefunction  $\Psi_0$ .

The Hartree-Fock (HF) approximation takes advantage of the mean-field theory to describe the electron-electron repulsion term as an average effect. The wavefunction is built with one-electron functions called spin-orbitals. These objects are employed in a Slater determinant [91] fulfilling the Pauli principle where two electrons with the same spin state cannot be in the same region in space. Two spin states of opposite values exist:  $\alpha(S) = 1/2$ , and  $\beta(S) = -1/2$ . The wavefunction is described as follows:

$$\Psi(1, \dots, N) = \frac{1}{\sqrt{N}} \begin{vmatrix} \phi_1\alpha(1) & \phi_1\beta(1) & \dots & \phi_{N/2}\alpha(1) & \phi_{N/2}\beta(1) \\ \dots & \dots & \dots & \dots & \dots \\ \phi_1\alpha(n) & \phi_1\beta(n) & \dots & \phi_{N/2}\alpha(n) & \phi_{N/2}\beta(n) \end{vmatrix} \quad (\text{Eqn. 7})$$

These auxiliary one-electron functions introduced within the Slater determinant are known as orbitals. The orbitals are expanded themselves to another set of auxiliary functions known as the basis set  $\chi_\mu$ :

$$\phi_i = \sum_{\mu} c_{\mu i} \chi_{\mu} \quad (\text{Eqn. 8})$$

Variations are carried within the molecular orbital coefficient ( $c_{\mu i}$ ) leading to the famous Hartree-Fock Roothan equations [92]:

$$F \phi_i = \epsilon_i \phi_i \quad (\text{Eqn. 10})$$

$$\sum_{\nu} F_{\mu i} (c) c_{\mu i} = \epsilon_i \sum_{\nu} c_{\nu i} S_{\mu \nu} \quad (\text{Eqn. 11})$$

Where  $\epsilon_i$  is the orbital energy of orbital  $i$ ,  $F$  is the Fock operator and  $S$  the overlap matrix.

Since  $F$  depends on the  $c$  matrix, Eqn. 11 is not linear, and the Self-Consistent Field method is used. This iterative process minimizes the energy by estimating an initial Hamiltonian, solving the Schrödinger equation to obtain a more accurate set of orbitals. The latter are reused to estimate a new Hamiltonian, and the process is restarted.

There are two variants to the HF method, the Restricted (RHF) and Unrestricted (UHF) approaches. The RHF applies to closed shell systems where opposite spins are constrained to the same orbital space. The UHF is used for open shell systems where the orbitals of spins  $\alpha$  and  $\beta$  are treated separately.

Post-HF methods have been developed to better treat the correlation effects that are highly neglected in basic HF framework. The most economical theory is the perturbative Møller-Plesset [93] method of second order (MP2). This theory is expressed in terms of the Many-Body Perturbation Theory which states that the Hamiltonian of a system can be divided into two terms: one of zeroth order ( $H_0$ ) with known functions ( $\Psi_i^0$ ) which energy values ( $E_i^0$ ) are close to the searched Hamiltonian  $H$ , and a second perturbation term ( $\lambda V$ ).

$$H = H_0 + \lambda V \quad (\text{Eqn. 12})$$

$$H_0 |\Psi_i^0\rangle = E_i^0 |\Psi_i^0\rangle \quad i = 1, 2, \dots \quad (\text{Eqn. 13})$$

Other post-HF methods are based on the Multi-Configurational approach and aim at improving the results obtained using HF. To do so, it is possible to use a wavefunction containing several determinants and employing the HF wavefunction  $\Psi_{HF}$  as the starting point. The general form of this method is the following:

$$\Psi = a_0 \Psi_{HF} + \sum_{i \neq 0} a_i \Psi_i \quad (\text{Eqn. 14}).$$

These methods vary in their way to determine the coefficients  $a$ .

## 2. Density functional theory

Hohenberg and Kohn introduced density functional theory (DFT) in 1964. [88] In DFT, the energy is a function of the electronic density ( $\rho$ ) of the many-electron system. The electronic density is defined as the probability of finding an electron in a given volume. Thus, for an electronic cloud, the electronic density gives information on the most probable positions for the electrons to be. This density is equal to 0 at infinity in space and is equal to the total number of electrons  $N$  when integrated over the complete x-y-z volume.

$$\rho(r \rightarrow \infty) = 0 \quad (\text{Eqn. 15})$$

$$\int \rho(r) dr = N \quad (\text{Eqn. 16}).$$

The first Hohenberg-Kohn theorem consists in justifying that, for one electronic density, there is a corresponding and unique external potential ( $v_{ext}(\mathbf{r})$ ). The electronic density determines the wavefunction and all electronic properties of the system. The total energy of the system is therefore a functional of the electronic density:

$$E[\rho(r)] = F_{HK}[\rho(r)] + \int \rho(r) v_{ext}(r) dr \quad (\text{Eqn. 17})$$

$$E[\rho(r)] = T_e[\rho(r)] + V_{eN}[\rho(r)] + V_{ee}[\rho(r)] \quad (\text{Eqn. 18})$$

$$F_{HK}[\rho(r)] = T_e[\rho(r)] + V_{ee}[\rho(r)] \quad (\text{Eqn. 19}).$$

The second Hohenberg-Kohn theorem is also known as the DFT variational principle. Here, the variational principle is applied as a function of the electronic density. The energy of a given density functional must be equal to or higher than the energy of the fundamental density functional:

$$E[\rho(r)] \geq E_{fund} \quad (\text{Eqn. 20}).$$

The energy of a system can therefore be minimized until the given density functional is in fact the fundamental density functional.

The Hohenberg-Kohn functional ( $F_{HK}$ ) regroups two terms dependent on the electronic density but with unknown analytical expression. Kohn and Sham simplified the electronic density by assuming a fictional non-interacting electronic density to the proper electronic density. Now, it is possible to give the energy of the non-interacting part as a functional of the electronic density. Therefore, the kinetic and potential energy are divided into classical ( $T_e^{ind}, V_e^{cla}$ ) and non-classical expressions ( $T_e, V_{ee}$ ). The classical energies are the Hartree energies, while the non-classical are grouped in the exchange-correlation energy ( $E_{xc}$ ). [94] [95] Finally, the  $F_{HK}$  is expressed with the known Hartree energies and the only unknown part is minimized within the  $E_{xc}$ .

$$E_{xc} = (T_e - T_e^{ind}) + (V_{ee} - V_e^{cla}) = T_e^{dep} + V_{ee}^{non-cla} \quad (\text{Eqn. 21})$$

The choice of Kohn and Sham is to refer to a fictional system of  $N$  non-interacting electrons which implies to solve  $N$  monoelectronic Schrödinger equations.

The Local Density Approximation (LDA) considers the exchange-correlation potential as a local quantity defined at a point ( $r$ ) with being almost independent of variations of the density around

the same point ( $r$ ). This approximation is the basis to the modern exchange-correlation functionals and is defined in the following:

$$E_{xc}^{LDA}[\rho] = \int \rho(r) \varepsilon_{xc}(\rho(r)) dr \quad (\text{Eqn. 22}).$$

The term  $\varepsilon_{xc}$  corresponds to the energy of the exchange-correlation per particle of the uniform electron gas of density  $\rho(r)$ .

To improve the precision of the LDA, the Generalized Expansion Approximation (GEA) was developed to account for the inhomogeneity of a system. In GEA, the LDA is treated as a Taylor series expansion:

$$E_{xc}^{GGA}[\rho] = \int \varepsilon_{xc}^{GEA}(\rho(r)) \rho(r) dr + \int C(\rho(r)) \frac{|\nabla \rho(r)|^4}{\rho^3(r)} dr + \dots \quad (\text{Eqn. 23})$$

Further corrections were added to the GEA to force the approximation to respect the physical limits of the system. This gave rise to the Generalized Gradient Approximation (GGA) which gave great success to DFT:

$$E_{xc}^{GGA}[\rho, \nabla \rho] = \int \varepsilon_{xc}^{GGA}(\rho(r), \nabla \rho(r)) dr \quad (\text{Eqn. 24})$$

The main issue with LDA coming from the exchange term, a particular attention was paid to the development of the individual exchange term that is expressed as follows:

$$E_x^{GGA}(\rho, \nabla \rho) = E_x^{LDA} - \int F(s(r)) \rho^{\frac{4}{3}}(r) dr \quad (\text{Eqn. 25})$$

Where  $F$  is a function of the reduced gradient density:

$$s(r) = \frac{|\nabla \rho(r)|}{\rho^{\frac{4}{3}}(r)} \quad (\text{Eqn. 26})$$

Within the GGA functionals, we can list the well-known BP86, [96] [97] and PBE [98].

To better improve the performances of GGA functionals, another type of exchange-correlation functional were developed: the meta-GGA (m-GGA). The latter consider the density of the kinetic energy of the Kohn-Sham orbitals ( $\tau$ ) in addition to the gradient approximation already included in the GGA.

$$\tau = \frac{1}{2} \sum_i^{occ} |\nabla \psi_i|^2 \quad (\text{Eqn. 27}).$$

The meta-GGA functional used in this PhD work is the TPSS functional. [99]

Kohn and Sham had already discussed the possibility to treat the exchange-correlation based on the Hartree-Fock approximation for the exact exchange term and based on the LDA for the correlation term. However, this initial approach was not as satisfying as the GGAs until Becke used part of the exact exchange ( $E_x^{exact}$ ) in the exchange-correlation energy which lead him to propose a three-parameter expression denoted as B3: [100] [101]

$$E_{xc} = E_{xc}^{LDA} + a_0(E_x^{exact} - E_x^{LDA}) + a_x\Delta E_x^{B88} + a_c\Delta E_c^{PW91} \quad (\text{Eqn. 28})$$

Where  $a_0$ ,  $a_x$ , and  $a_c$  are semi-empirical coefficients obtained from experimental data. Thanks to this approximation, the accuracy on calculated energies became superior to those obtained with GGA. This has lead to the development of many hybrid functionals by simply varying the coefficients and their origin

Within the hybrid functionals that were used in this PhD work, we can list the following: B3PW91, [100] [102] B3LYP, [100] [103] PBE0. [104] Meta-hybrid functionals also exist: M06, M06-2X, [105] TPSSH. [106]

### *3. Application of DFT in copper bioinorganic chemistry*

Nowadays, DFT is established as a powerful tool to elucidate, rationalize, and understand experimental observations as well as to predict the behavior of chemical and physical phenomena. Its resurgence in chemistry led to W. Kohn's Nobel Prize award in 1998.

DFT is very well adapted to copper chemistry in synthetic and biological models since it can handle the expected size of most systems in the field (up to around 200 atoms). DFT can also give reliable and accurate results when used to calculate and predict specific features and parameters: geometries, total energies, vibrational frequencies, and electronic, magnetic, and optical properties. The computed information can then be related to experimental observations in the form of infrared (IR), nuclear magnetic resonance (NMR), electron paramagnetic resonance (EPR), redox potentials from electrochemical measurements, absorbance UV-vis spectra, circular dichroism (CD), Raman spectra, among many others. [107]

In the next section, we will present two concrete examples of successful applications of DFT methods to study copper systems in the field of bioinorganic chemistry: (i) identification of the



structures involved in reaction mechanisms and (ii) calibration study to predict reliable magnetic observables applicable to EPR spectroscopy.

#### *Geometries and relative free energies*

In the study of the LPMO reaction mechanism, S. Kim and co-workers [68] extracted the active site of *T. aurantiacus* and compared its geometry to the calculated Cu(II), Cu(I), and Cu(II)-superoxo states. The B3LYP functional was used in combination with the 6-31G(d) basis set. The Cu-N distances were compared to experimental data as well as the electronic charge localized on the copper center. The root-mean-square deviation (RMSD) was calculated with respect to the enzyme's active site.

Two copper-oxygen intermediates were investigated for their capability to perform the hydrogen atom abstraction of the substrate, one with the copper-superoxo species and another with the copper-oxyl. Structures were constructed for three different states and two transition states within each mechanism. The free energies of each species was computed at the B3LYP/6-31G(d) level of theory. The activation barrier found for the superoxo mechanism was much higher than the overall two-step barrier obtained for the oxyl mechanism (34.9 kcal/mol vs. 18.8 kcal/mol). The authors concluded that the copper-oxyl is the reactive oxygen species in fungal LPMO, which follows an oxygen rebound mechanism.

#### *Magnetic properties and EPR*

G. Sciortino *et al.* [108] converged computational methods for predicting accurate  $g_{\max}$  and  $A_{\max}$  EPR parameters in Cu(II) complexes. To do so, they selected multiple structures with known EPR parameters as well as diverse functionals and calculated the mean absolute percent deviation (MAPD) with respect to experimental results. They selected the B3LYP and PBE0 functionals as the best for specifically calculating these two EPR parameters.

In addition, they applied DFT to the study of two copper containing proteins: the Human serum albumin (HSA) and Prion proteins (PrP<sup>c</sup>). Each structure was first delimited to the amino acids involved in the metal binding site. Then, the structures were optimized individually, and their EPR parameters were obtained with the above mentioned functionals. In the case of the HSA, the  $g_{\max}^{\text{calc}}$  had a -1.7% deviation with respect to experiment while the deviation for the  $A_{\max}^{\text{calc}}$  was -1.1%. In PrP<sup>c</sup>, two species were investigated with either a [Cu(II)L]<sup>+</sup> or [Cu(II)L] configuration. The  $g_{\max}$  and  $A_{\max}$  deviation was much higher in the case of the [Cu(II)L]<sup>+</sup> species than for the [Cu(II)L], -2.9% and -8.7% compared to -2.5% and -1.9%, respectively. The group concluded that

the calculated values were overall in close agreement with the experimental ones and that the methodology could be applied in a more general manner to copper(II) models in biology.

### 3 – Ph.D. objectives and areas of research

This Ph.D. work includes a mixed approach for the study of copper bioinorganic systems, combining theoretical methods and experimental techniques. The following chapters will therefore present data ranging from mainly theoretical, theoretical applied on experimental data, to mainly experimental topics. However, the interconversion between experiment and theory is present all throughout the manuscript.

EPR being an important method for the characterization of copper centers, the first part of my thesis (Chapter II) focuses on the development of a DFT method to obtain reliable and accurate hyperfine coupling constants. To this end, we selected a large set of copper complexes for which EPR parameters were reported. A basis set was built to properly describe the magnetic interaction between the electron and nucleus of the copper atom. Many DFT functionals were tested as well as wavefunction methods. These results were recently published in *Chem. Phys. Chem.* in 2020. This method was also applied for the calculation of g-tensors.

The second part was dedicated to the application of the above-mentioned method to experimental data obtained in the laboratory (Chapter III). We aimed at rationalizing possible structures by means of their EPR and UV-vis spectroscopic data in two experimental conundrums. First, we tried to rationalize the mixed EPR signal observed in P/AA10 LPMO enzyme and the nature of the minor species found in solution. Second, we used our methodology to propose structures for the synthetic histidine-brace containing peptide-copper complexes based on the comparison between experimental and predicted electronic and EPR spectra.

Finally (Chapter IV), we prepared LPMO-inspired Cu(II) complexes featuring N3-coordination motif and capable of stabilizing high oxidation states of copper. One of these complexes was subjected to reaction with hydrogen peroxide and its reactivity with alcohol solvents led to the production of formic acid in solution. The origin of formic acid was investigated by labelling experiments. Mechanistic features were proposed and studied by means of DFT. These complexes were shown to be good functional models of LPMO as they can activate strong C-H bonds.

## REFERENCES

- [1] K. M. Kadish, R. Guilard and M. Réglér, Series on chemistry, energy and the environment, Bioinspired Chemistry, from enzymes to synthetic models, World Scientific, 2019.
- [2] F. Neese, "A critical evaluation of DFT, including time-dependent DFT, applied to bioinorganic chemistry," *Journal of Biological Inorganic Chemistry*, vol. 11, pp. 702-711, 2006.
- [3] M. V. Putz and D. M. P. Mingos, Applications of Density Functional Theory to Biological and Bioinorganic Chemistry, Springer, 2013.
- [4] K. D. Karlin and Z. Tyeklar, Bionionorganic Chemistry of Copper, Springer Science & Business Media, 2012.
- [5] R. L. Osborne, J. P. Klinman, K. D. Karlin and S. Itoh, "Insights into the proposed copper-oxygen intermediates that regulate the mechanism of reactions catalyzed by dopamine b-monoxygenase, peptidylglycine a-hydroxylating monoxygenase, and tyramine b-monoxygenase," in *Copper-oxygen chemistry*, John Wiley & Sons Inc., 2011, pp. 1-22.
- [6] G. Anilkumar and S. Saranya, Copper Catalysis in Organic Synthesis, Wiley-VCH, 2020.
- [7] I. Iakovidis, I. Delimaris and S. M. Piperakis, "Copper and its complexes in medicine: a biochemical approach," *Molecular Biology International*, p. 13, 2011.
- [8] R. R. Conry, "Copper: inorganic & coordination chemistry," *Encyclopedia of Inorganic Chemistry*, 2006.
- [9] E. I. Solomon, D. E. Heppner, E. M. Johnston, J. W. Ginsbach, J. Cirera, M. Quayyum, M. T. Kiebbler-Emmons, C. H. Kjaergaard, R. G. Hadt and L. Tian, "Copper Active Sites in Biology.," *Chem. Rev.*, vol. 114, pp. 3659-3853, 2014.
- [10] W. Kaim, B. Schwederski and A. Klein, "Bioinorganic Chemistry: Inorganic Elements in The Chemistry of Life," 2013.
- [11] A. G. Sykes, "Active-site properties of the blue copper proteins," *Advances in Inorganic Chemistry*, vol. 36, pp. 377-408, 1991.
- [12] E. T. Adman, "Copper protein structures," *Advances in Protein Chemistry*, vol. 42, pp. 145-197, 1991.

- [13] G. W. Canters and G. Gilardi, "Engineering type 1 copper sites in proteins," *FEBS letters*, vol. 325, no. 1-2, pp. 39-48, 1993.
- [14] B. E. Ramirez, B. G. Malmstrom, J. R. Winkler and H. B. Gray, "The currets of life: the terminal electron-transfer complex of respiration," *Proceedings of the National Academy of Sciences*, vol. 92, no. 26, pp. 11949-11951, 1995.
- [15] K. Sigfridsson, "Plastocyanin, an electron-transfer protein," *Photosynthesis Research*, vol. 57, pp. 1-28, 1998.
- [16] P. M. Colman, H. C. Freeman, J. M. Guss, M. Murata, V. A. Norris, J. A. M. Ramshaw and M. P. Venkatappa, "X-ray crystal structure analysis of plastocyanin at 2.7 Å resolution," *Nature*, vol. 272, pp. 319-324, 1978.
- [17] Y. Xue, M. Ökvist, Ö. Hansson and S. Young, "Crystal structure of spinach plastocyanin at 1.7 Å resolution," *Protein Science*, vol. 7, pp. 2099-2105, 1998.
- [18] J. P. Klinman, "Mechanisms whereby mononuclear copper proteins functionalize organic substrates," *Chemical Reviews*, vol. 96, pp. 2541-2561, 1996.
- [19] E. I. Solomon, D. M. Dooley, R. H. Wang, H. B. Gray, M. Cerdonio, F. Mogno and G. L. Romani, "Susceptibility studies of laccases and oxyhemocyanin using an ultrasensitive magnetometer. Antiferromagnetic behavior of the type 3 copper in Rhus laccase," *Journal of the American Chemical Society*, vol. 98, no. 4, pp. 1029-1031, 1976.
- [20] R. S. Himmelwright, N. C. Eickman, C. D. LuBien, E. I. Solomon and K. Lerch, "Chemical and spectroscopic studies of the binuclear copper active site of Neurospora tyrosinase: comparison to hemocyanins," *Journal of the American Chemical Society*, vol. 102, no. 24, pp. 7339-7344, 1980.
- [21] E. I. Solomon, U. M. Sundaram and T. E. Machonkin, "Multicopper oxidases and oxygenases," *Chemical Reviews*, vol. 96, no. 7, pp. 2563-2606, 1996.
- [22] K. A. Magnus, B. Hazes, H. Ton-That, C. Bonaventura, J. Bonaventura and W. G. Hol, "Crystallographic analysis of oxygenated and deoxygenated states of arthropod hemocyanin shows unusual differences," *Proteins*, vol. 19, pp. 302-309, 1994.
- [23] A. Messerschmidt, "8.14 - Copper Metalloenzymes," in *Comprehensive Natural Products II*, Elsevier, 2010, pp. 489-545.
- [24] C. Southan and L. I. Kruse, "Sequence similarity between dopamine β-hydroxylase and peptide α-amidating enzyme: Evidence for a conserved catalytic domain," *FEBS Letters*, vol. 255, no. 1, pp. 116-120, 1989.

- [25] S. T. Prigge, A. S. Kolhekar, B. A. Eipper, R. E. Mains and L. M. Amzel, "Substrate-mediated electron transfer in peptidylglycine alpha-hydroxylating monooxygenase," *Nature Structural & Molecular Biology*, vol. 6, pp. 976-983, 1999.
- [26] S. M. Miller and J. P. Klinman, "Secondary isotope effects and structure-reactivity correlations in the dopamine beta-monooxygenase reaction: evidence for a chemical mechanism," *Biochemistry*, vol. 24, no. 9, pp. 2114-2127, 1985.
- [27] G. Tian, J. A. Berry and J. P. Klinman, "Oxygen-18 kinetic isotope effects in the dopamine beta-monooxygenase reaction: Evidence for a new chemical mechanism in non-heme, metallomonooxygenase," *Biochemistry*, vol. 33, pp. 226-234, 1994.
- [28] I. Blain, P. Slama, M. Giorgi, T. Tron and M. Réglér, "Copper-containing monooxygenases: enzymatic and biomimetic studies of the O-atom transfer catalysis," *Reviews in Molecular Biotechnology*, vol. 90, no. 2, pp. 95-112, 2002.
- [29] R. E. Cowley, L. Tian and E. I. Solomon, "Mechanism of O<sub>2</sub> activation and substrate hydroxylation in noncoupled binuclear copper monooxygenases," *Proceedings of the National Academy of Sciences*, vol. 113, no. 43, pp. 12035-12040, 2016.
- [30] V. G. H. Eijsink, D. Petrovic, Z. Forsberg, S. Mekasha, A. K. Rohr, A. Várnai, B. Bissaro and G. Vaaje-Kolstad, "On the functional characterization of lytic polysaccharide monooxygenases (LPMOs)," *Biotechnology for Biofuels*, vol. 15, no. 58, 2019.
- [31] G. R. Hemsworth, E. M. Johnston, G. J. Davies and P. H. Walton, "Lytic polysaccharide monooxygenases in biomass conversion," *Trends in Biotechnology*, vol. 09, no. 06, 2015.
- [32] F. C. Barbosa, M. A. Silvello and R. Goldbeck, "Cellulase and oxidative enzymes: new approaches, challenges and perspectives on cellulose degradation for bioethanol production," *Biotechnology Letters*, vol. 42, no. 6, pp. 875-884, 2020.
- [33] E. T. Reese, R. G. H. Siu and H. S. Levinson, "The biological degradation of soluble cellulose derivatives and its relationship to the mechanism of cellulose hydrolysis," *Journal of Bacteriology*, pp. 485-497, 1950.
- [34] M. Mandels and E. T. Reese, "Induction of cellulase in *Trichoderma Viride* as influenced by carbon sources and metals," *Journal of Bacteriology*, pp. 269-278, 1956.
- [35] G. Vaaje-Kolstad, S. J. Horn, D. M. F. van Aalten, B. Synstad and V. G. H. Eijsink, "The non-catalytic chitin-binding protein CBP21 from *Serratia marcescens* is essential for chitin degradation," *Journal of Biological Chemistry*, vol. 280, no. 31, pp. 28492-28497, 2005.

- [36] G. Vaaje-Kolstad, B. Westereng, S. J. Horn, Z. Liu, H. Zhai, M. Sorlie and V. G. H. Eijsink, "An oxidative enzyme boosting enzymatic conversion of recalcitrant polysaccharides," *Science*, vol. 330, pp. 219-222, 2010.
- [37] R. J. Quinlan, M. D. Sweeney, L. Lo Leggio, H. Otten, J.-C. N. Poulsen, K. S. Johansen, K. B. R. M. Kristian, C. I. Jorgensen, M. Tovborg, A. Anthonsen, T. Tryfona, C. P. Walter, P. Dupree, F. Xu, G. J. Davies and P. H. Walton, "Insights into the oxidative degradation of cellulose by a copper metalloenzyme that exploits biomass components," *Proceedings of the National Academy of Sciences*, vol. 103, no. 37, pp. 15079-15084, 2011.
- [38] S. I. Chan and S. S.-F. Yu, "Controlled oxidation of hydrocarbons by the membrane-bound methane monooxygenase: The case for a tricopper cluster," *Accounts of Chemical Research*, vol. 41, no. 8, pp. 969-979, 2008.
- [39] V. V. Vu, W. T. Beeson, C. M. Phillips, J. H. D. Cate and M. A. Marletta, "Determinants of regioselective hydroxylation in the fungal polysaccharide monooxygenases," *Journal of the American Chemical Society*, vol. 136, pp. 562-565, 2014.
- [40] W. T. Beeson, C. M. Phillips, J. H. D. Cate and M. A. Marletta, "Oxidative cleavage of cellulose by fungal copper-dependent polysaccharide monooxygenases," *Journal of the American Chemical Society*, vol. 134, pp. 890-892, 2011.
- [41] A. Munzone, B. El Kherdi, M. Fanuel, H. Rogniaux, D. Ropartz, M. Réglier, A. J. Simaan and C. Decroos, "Characterization of a bacterial copper-dependent lytic polysaccharide monooxygenase with an unusual second coordination sphere," *The FEBS Journal*, vol. 287, no. 15, pp. 3298-3314, 2020.
- [42] G. R. Hemsworth, E. J. Taylor, R. Q. Kim, R. C. Gregory, S. J. Lewis, J. P. Turkenburg, A. Parkin, G. J. Davies and P. H. Walton, "The copper active site of CBM33 polysaccharide oxygenases," *Journal of the American Chemical Society*, vol. 135, pp. 6069-6077, 2013.
- [43] A. Karnaouri, E. Topakas, I. Antonopoulou and P. Christakopoulos, "Genomic insights into the fungal linocellulolytic system of *Myceliophthora thermophila*," *Frontiers in Microbiology*, vol. 281, no. 5, 2014.
- [44] J. W. Agger, T. Isaksen, A. Vámai, S. Vidal-Melgosa, W. G. T. Willats, R. Ludwig, S. J. Horn, V. G. H. Eijsink and B. Westereng, "Discovery of LPMO activity on hemicellulose shows the importance of oxidative processes in plant cell wall degradation," *Proceedings of the National Academy of Science*, vol. 111, no. 17, pp. 6287-6292, 2014.

- [45] T. Isaksen, B. Westereng, F. L. Aachmann, J. W. Agger, D. Kracher, R. Kittl, R. Ludwig, H. Dietmar, V. G. H. Eijsink and S. J. Horn, "A C4-oxidizing lytic polysaccharide monooxygenase cleaving both cellulose and cello-oligosaccharides," *Journal of Biological Chemistry*, vol. 289, no. 5, pp. 2632-2642, 2014.
- [46] V. V. Vu, W. T. Beeson, E. A. Span, E. R. Farquhar and M. A. Marletta, "A family of starch-active polysaccharide monooxygenases," *Proceedings of the National Academy of Sciences*, vol. 111, no. 38, pp. 13822-13827, 2014.
- [47] L. Lo Leggio, T. J. Simmons, J.-C. N. Poulsen, K. E. H. Frandsen, G. R. Hemsworth, M. A. Stringer, P. von Freiesleben, M. Tovborg, K. S. Johansen, L. De Maria, P. V. Harris, C.-L. Soong, P. Dupree, T. Tryfona, N. Lenfant, B. Henrissat, G. J. Davies and P. H. Walton, "Structure and boosting activity of a starch-degrading lytic polysaccharide monooxygenase," *Nature Communications*, vol. 6, pp. 5961-5969, 2015.
- [48] B. Westereng, J. W. Agger, S. J. Horn, G. Vaaje-Kolstad, F. L. Aachmann, Y. H. Stenstrom and V. G. H. Eijsink, "Efficient separation of oxidized cello-oligosaccharides generated by cellulose degrading lytic polysaccharide monooxygenases," *Journal of Chromatography A*, vol. 1271, pp. 144-152, 2013.
- [49] Z. Forsberg, A. K. Mackenzie, M. Sorlie, A. K. Rohr, R. Helland, A. S. Arvai, G. Vaaje-Kolstad and V. G. H. Eijsink, "Structural and functional characterization of a conserved pair of bacterial cellulose-oxidizing lytic polysaccharide monooxygenases," *Proceedings of the National Academy of Sciences*, vol. 111, no. 23, pp. 8446-8451, 2014.
- [50] Z. Forsberg, B. Bissaro, J. Gullesen, B. Dalhus, G. Vaaje-Kolstad and V. G. H. Eijsink, "Structural determinants of bacterial lytic polysaccharide monooxygenase functionality," *Journal of Biological Chemistry, American Society for Biochemistry and Molecular Biology*, vol. 293, no. 4, pp. 1397-1412, 2018.
- [51] G. R. Hemsworth, L. Ciano, G. J. Davies and P. H. Walton, "Production and spectroscopic characterization of lytic polysaccharide monooxygenases," *Methods in Enzymology*, vol. 613, pp. 63-90, 2018.
- [52] J. Peisach and W. E. Blumberg, "Structural implications derived from the analysis of electron paramagnetic resonance spectra of natural and artificial copper proteins," *Archives of Biochemistry and Biophysics*, vol. 165, no. 2, pp. 691-708, 1974.
- [53] A. S. Borisova, T. Isaksen, M. Dimarogona, A. A. Kognole, G. Mathiesen, A. Várnai, A. K. Rohr, C. M. Payne, M. Sorlie, M. Sandgren and V. G. H. Eijsink, "Structural and functional characterization of a lytic polysaccharide monooxygenase with broad substrate specificity," *Journal of Biological Chemistry*, vol. 290, no. 38, pp. 22955-22969, 2015.

- [54] H. Hansson, S. Karkehabadi, N. Mikkelsen, N. R. Douglas, S. Kim, A. Lam, T. Kaper, B. Kelemen, K. K. Meier, S. M. Jones, E. I. Solomon and M. Sandgren, "High-resolution structure of a lytic polysaccharide monooxygenase from *Hypocrea jecorina* reveals a predicted linker as an integral part of the catalytic domain," *Journal of Biological Chemistry*, vol. 292, no. 46, pp. 19099-19109, 2017.
- [55] E. A. Span, D. L. M. Suess, M. C. Deller, R. D. Britt and M. A. Marletta, "The role of the secondary coordination sphere in fungal polysaccharide monooxygenase," *ACS Chemical Biology*, vol. 12, no. 4, pp. 1095-1118, 2017.
- [56] T. J. Simmons, K. E. H. Frandsen, L. Ciano, T. Tryfona, N. Lenfant, J. C. Poulsen, L. F. L. Wilson, T. Tandrup, M. Tovborg, K. Schnorr, K. S. Johansen, B. Henrissat, P. H. Walton, L. Le Leggio and P. Dupree, "Structural and electronic determinants of lytic polysaccharide monooxygenase reactivity on polysaccharide substrates," *Nature Communications*, vol. 8, no. 1, pp. 1064-1076, 2017.
- [57] K. E. H. Frandsen, T. J. Simmons, P. Dupree, J.-C. N. Poulsen, G. R. Hemsworth, L. Ciano, E. M. Johnston, M. Tovborg, K. S. Johansen, P. von Freiesleben, L. Marmuse, S. Fort, S. Cottaz, H. Driguez, B. Henrissat, N. Lenfant, F. Tuna, A. Baldansuren, G. J. Davies, L. Lo Leggio and P. H. Walton, "The molecular basis of polysaccharide cleavage by lytic polysaccharide monooxygenases," *Nature Chemical Biology*, vol. 12, pp. 298-303, 2016.
- [58] Z. Forsberg, C. E. Nelson, B. Dalhus, S. Mekasha, J. S. M. Loose, L. I. Crouch, A. K. Rohr, J. G. Gardner, V. G. H. Eijsink and G. Vaaje-Kolstad, "Structural and functional analysis of a lytic polysaccharide monooxygenase important for efficient utilization of chitin in *Cellvibrio japonicus*," *Journal of Biological Chemistry*, vol. 291, no. 14, pp. 7300-7312, 2016.
- [59] Z. Forsberg, A. K. Rohr, S. Mekasha, K. K. Andersson, V. G. H. Eijsink, G. Vaaje-Kolstad and M. Sorlie, "Comparative study of two chitin-active and two cellulose-active AA10-Type lytic polysaccharide monooxygenases," *Biochemistry*, vol. 53, pp. 1647-1656, 2014.
- [60] A. K. Chaplin, M. T. Wilson, M. A. Hough, D. A. Svistunenko, G. R. Hemsworth, P. H. Walton, E. Vijgenboom and J. A. R. Worrall, "Heterogeneity in the histidine-brace copper coordination sphere in auxiliary activity family 10 (AA10) lytic polysaccharide monooxygenases," *The Journal of Biological Chemistry*, vol. 291, no. 24, pp. 12838-12850, 2016.



- [61] G. R. Hemsworth, B. Henrissat, G. J. Davies and P. H. Walton, "Discovery and characterization of new family of lytic polysaccharide mono-oxygenases," *Nature Chemical Biology*, vol. 10, no. 2, pp. 122-126, 2014.
- [62] M. Couturier, S. Ladevèze, G. Sulzenbacher, L. Ciano, M. Fanuel, C. Moreau, A. Villares, B. Cathala, F. Chaspoul, K. E. Frandsen, A. Labourel, I. Herpoël-Gimber, S. Grisel, M. Haon, N. Lenfant, H. Rogniaux, D. Ropartz, G. J. Davies, M.-N. Rosso, P. H. Walton, B. Henrissat and J.-G. Berrin, "Lytic xylan oxidases from wood-decay fungi unlock biomass degradation," *Nature Chemical Biology*, vol. 14, pp. 306-314, 2018.
- [63] F. Sabbadin, G. R. Hemsworth, L. Ciano, B. Henrissat, P. Dupree, T. Tryfona, R. D. S. Marques, S. T. Sweeney, K. Besser, L. Elias, G. Pesante, Y. Li, A. A. Dowle, R. Bates, L. D. Gomez, R. Simister, G. J. Davies, P. H. Walton, N. C. Bruce and S. J. McQueen-Mason, "An ancient family of lytic polysaccharide monooxygenases with roles in arthropod development and biomass digestion," *Nature Communication*, Vols. 756-768, p. 9, 2018.
- [64] B. Bissaro, I. Isaksen, G. Vaaje-Kolstad, V. G. H. Eijsink and A. K. Rohr, "How a lytic polysaccharide monooxygenase binds crystalline chitin," *Biochemistry*, vol. 57, no. 12, pp. 1893-1906, 2018.
- [65] B. Bissaro, A. K. Rohr, G. Muller, P. Chylenski, M. Skaugen, Z. Forsberg, S. J. Horn, G. Vaaje-Kolstad and V. G. H. Eijsink, "Oxidative cleavage of polysaccharides by monocopper enzymes depends on H<sub>2</sub>O<sub>2</sub>," *Nature Chemical Biology*, vol. 13, pp. 1123-1130, 2017.
- [66] E. I. Solomon and S. S. Stahl, "Introduction: Oxygen reduction and activation in catalysis," *Chemical Reviews*, vol. 118, no. 5, pp. 2299-2301, 2018.
- [67] L. Bertini, R. Breglia, M. Lambrugh, P. Fantucci, L. De Gioia, M. Borsari, M. Sola, C. A. Bortolotti and M. Bruschi, "Catalytic mechanism of fungal lytic polysaccharide monooxygenases investigated by first-principles calculations," *Inorganic Chemistry*, vol. 57, pp. 86-97, 2018.
- [68] S. Kim, J. Stahlberg, M. Sandgren, R. S. Paton and G. T. Beckham, "Quantum mechanical calculations suggest that lytic polysaccharide monooxygenases use a copper-oxyl, oxygen-rebound mechanism," *Proceedings of the National Academy of Sciences*, vol. 111, no. 1, pp. 149-154, 2014.
- [69] A. L. Concia, A. Munzone, M.-C. Kafentzi, A. Kochem, M. Réglie, C. Decroos and A. J. Simaan, "8: Modeling the mononuclear copper monooxygenase active site," in *Bioninspired Chemistry*, World Scientific, 2019, pp. 185-263.

- [70] E. A. Lewis and W. B. Tolman, "Reactivity of dioxygen-copper systems," *Chemical Reviews*, vol. 104, no. 2, pp. 1047-1076, 2004.
- [71] C. Würtele, E. Gaoutchenova, K. Harms, M. C. Holthausen, J. Sundermeyer and S. Schindler, "Crystallographic characterization of a synthetic 1:1 end-on copper dioxygen adduct complex," *Angewandte Chemie International Edition*, vol. 45, pp. 3867-3869, 2006.
- [72] K. Fujisawa, M. Tanaka, Y. Moro-oka and N. Kitajima, "A monomeric side-on superoxocopper(II) complex:  $\text{Cu}(\text{O}_2)(\text{HB}(3\text{-tBu-5-iPrpz})_3)$ ," *Journal of the American Chemical Society*, vol. 116, no. 26, pp. 12079-12080, 1994.
- [73] A. Kunishita, M. Kubo, H. Sugimoto, T. Ogura, K. Sato, T. Takui and S. Itoh, "Mononuclear copper(II)-superoxo complexes that mimic the structure and reactivity of the active centers of PHM and DBM," *Journal of the American Chemical Society*, vol. 131, pp. 2788-2789, 2009.
- [74] A. Kunishita, M. Z. Ertem, Y. Okubo, T. Tano, S. Hideki, K. Ohkubo, N. Fujieda, S. Fukuzumi, C. J. Cramer and S. Itoh, "Active site models for the CuA site of peptidylglycine  $\alpha$ -hydroxylating monooxygenase and dopamine- $\beta$ -monooxygenase," *Inorganic Chemistry*, vol. 51, pp. 9465-9480, 2012.
- [75] R. L. Peterson, R. A. Himes, H. Kotani, T. Suenobu, L. Tian, M. A. Siegler, E. I. Solomon, S. Fukuzumi and K. D. Karlin, "Cupric superoxo-mediated intermolecular C-H activation chemistry," *Journal of the American Chemical Society*, vol. 133, pp. 1702-1705, 2011.
- [76] S. Kim, J. Y. Lee, R. E. Cowley, J. W. Ginsbach, M. A. Siegler, E. I. Solomon and K. D. Karlin, "A N3S(thioether)-ligated Cu(II)-superoxo with enhances reactivity," *Journal of the American Chemical Society*, vol. 137, no. 8, pp. 2796-2799, 2015.
- [77] J. Y. Lee and K. D. Karlin, "Elaboration of copper-oxygen mediated C-H activation chemistry in consideration of future fuel and feedstock," *Current Opinion in Chemical Biology*, vol. 25, pp. 184-193, 2015.
- [78] T. Fujii, A. Naito, S. Yamaguchi, A. Wada, Y. Funahashi, K. Jitsukawa, S. Nagatomo, T. Kitagaza and H. Masuda, "Construction of a square-planar hydroperoxo-copper(II) complex inducing a higher catalytic reactivity," *Chemical Communications*, no. 21, pp. 2700-2701, 2003.
- [79] A. Kunishita, H. Ishimaru, S. Nakashima, T. Ogura and S. Itoh, "Reactivity of mononuclear alkylperoxo copper(II) complex. O-O bond cleavage and C-H bond activation," *Journal of the American Chemical Society*, vol. 130, pp. 4244-4245, 2008.

- [80] M. Réglér, E. Amadei, R. Tadayoni and B. Waegell, "Pyridine nucleus hydroxylation with copper oxygenase models," *J. Chem. Soc., Chem. Commun.*, no. 8, pp. 447-450, 1989.
- [81] D. Maiti, A. A. Narducci Sarjeant and K. D. Karlin, "Copper-hydroperoxo-mediated N-debenzylation chemistry mimicking aspects of copper monooxygenases," *Inorg. Chem.*, vol. 47, no. 19, pp. 8736-8747, 2008.
- [82] S. Hong, S. M. Huber, L. Gagliardi, C. C. Cramer and W. B. Tolman, "Copper(I)- $\alpha$ -ketocarboxylate complexes: Characterization and O<sub>2</sub> reactions that yield copper-oxygen intermediates capable of hydroxylating arenes," *J. Am. Chem. Soc.*, vol. 129, no. 46, pp. 14190-14192, 2007.
- [83] P. J. Donoghue, J. Tehranchi, C. J. Cramer, R. Sarangi, E. I. Solomon and W. B. Tolman, "Rapid C-H bond activation by a monocopper(III)-hydroxide complex," *Journal of the American Chemical Society*, vol. 133, pp. 17602-17605, 2011.
- [84] D. Dhar and W. B. Tolman, "Hydrogen atom abstraction from hydrocarbons by a copper(III)-hydroxide complex," *Journal of the American Chemical Society*, vol. 137, no. 3, pp. 1322-1329, 2014.
- [85] D. Dhar, G. M. Yee, T. F. Markle, J. M. Mayer and W. B. Tolman, "Reactivity of the copper(III)-hydroxide unit with phenols," *Chemical Science*, vol. 8, pp. 1075-1085, 2017.
- [86] S. G. Balasubramani, G. P. Chen, S. Coriani, M. Diedenhofen, M. S. Frank, Y. J. Franzke, F. Furche, R. Grotjahn, M. E. Harding, C. Hattig, A. Hellweg, B. Helmich-Paris, C. Holzer, U. Huniar, M. Kaupp, A. M. Khah, S. K. Khani, T. Muller, F. Mack, B. D. Nguyen, S. M. Parker, E. Perlt, D. Rappoport, K. Reiter, S. Roy, M. Ruckert, G. Schmitz, M. Sierka, E. Tapavicza, D. P. Tew, C. van Mullen, V. K. Voora, F. Weigend, A. Wodynski and J. M. Yu, "TURBOMOLE: Modular program suite for ab initio quantum chemical and condensed-matter simulations," *Journal of Chemical Physics*, vol. 152, pp. 184107-36, 2020.
- [87] G. te Velde, F. M. Bickelhaupt, E. J. Baerends, C. Fonseca Guerra, S. J. A. van Gisbergen, J. G. Snijders and T. Ziegler, "Chemistry with ADF," *Journal of Computational Chemistry*, vol. 22, p. 931, 2001.
- [88] A. D. Bochevarov, E. Harder, T. F. Hughes, J. R. Greenwood, D. A. Braden, D. M. Philippi, D. Rinaldo, M. D. Halls, J. Zhang and R. A. Friesner, "Jaguar: A high-performance quantum chemistry software program with strengths in life and materials sciences," *Journal of Quantum Chemistry*, vol. 113, no. 18, pp. 2110-2142, 2013.

- [89] F. Neese, F. Wenmohs, U. Becker and C. Riplinger, "The ORCA quantum chemistry program package," *Journal of Chemical Physics*, vol. 152, p. 224108, 2020.
- [90] P. Hohenberg and W. Kohn, "Inhomogeneous electron gas," *Physical Review*, vol. 136, no. 3B, pp. B864-871, 1964.
- [91] E. Schrodinger, "An undulatory theory of the mechanics of atoms and molecules," *Annalen der Physik*, vol. 28, p. 1049, 1926.
- [92] M. Born and J. R. Oppenheimer, "On the quantum theory of molecules," *Annalen der Physik*, vol. 84, p. 458, 1927.
- [93] J. C. Slater, "The Theory of Complex Spectra," *Physical Review*, vol. 34, p. 1293, 1923.
- [94] C. C. J. Roothan, "New developments in molecular orbital theory," *Reviews of Modern Physics*, vol. 23, p. 69, 1951.
- [95] C. Moller and M. S. Plesset, "Note on an approximation treatment for many-electron systems," *Physical Review*, vol. 46, p. 618, 1934.
- [96] J. Harris and R. O. Jones, "The surface energy of a bounded electron gas," *Journal of Physics F: Metal Physics*, vol. 4, p. 1170, 1974.
- [97] R. A. Harris, "Induction and dispersion forces in the electron gas theory of interacting closed shell systems," *Journal of Chemical Physics*, vol. 81, p. 2403, 1984.
- [98] A. D. Becke, "Density-functional exchange-energy approximation with correct asymptotic-behavior," *Physical Review A*, vol. 38, no. 6, pp. 3098-3100, 1988.
- [99] J. P. Perdew, "Density-functional approximation for the correlation-energy of the inhomogeneous electron-gas," *Physical Review B*, vol. 33, no. 12, pp. 8822-8824, 1986.
- [100] J. P. Perdew, K. Burke and M. Ernzerhof, "Generalized gradient approximation made simple," *Physical Review Letters*, vol. 77, no. 18, pp. 3865-3868, 1996.
- [101] J. M. Tao, J. P. Perdew, V. N. Staroverov and G. E. Scuseria, "Climbing the density functional ladder: Nonempirical meta-generalized gradient approximation designed for molecules and solids," *Physical Review Letters*, vol. 91, no. 14, p. 146401, 2003.
- [102] A. D. Becke, "Density-functional thermochemistry. III. The role of exact exchange," *Journal of Chemical Physics*, vol. 89, p. 5648, 1993.
- [103] A. D. Becke, "A new mixing of Hartree-Fock and local density-functional theories," *Journal of Chemical Physics*, vol. 98, p. 1372, 1993.

- [104] J. P. Perdew and Y. Wang, "Accurate and simple analytic representation of the electron-gas correlation-energy," *Physical Review B*, vol. 45, no. 23, pp. 13244-13249, 1992.
- [105] C. T. Lee, W. T. Yang and R. G. Parr, "Development of the Colle-Salvetti correlation-energy formula into a functional of the electron-density," *Physical Review B*, vol. 37, no. 2, pp. 785-789, 1988.
- [106] C. Adamo and V. Barone, "Toward reliable density functional methods without adjustable parameters: The PBE0 model," *Physical Review B*, vol. 45, no. 23, pp. 13244-13249, 1992.
- [107] Y. Zhao and D. G. Truhlar, "The M06 suite of density functionals for main group thermochemistry, thermochemical kinetics, noncovalent interactions, excited states, and transition elements: two new functionals and systematic testing of four M06-class functionals and 12 other function," *Theoretical Chemistry Accounts*, vol. 120, no. 1-3, pp. 215-241, 2008.
- [108] V. N. Staroverov, G. E. Scuseria, J. M. Tao and J. P. Perdew, "Comparative assessment of a new nonempirical density functional: Molecules and hydrogen-bonded complexes," *Journal of chemical Physics*, vol. 119, no. 23, pp. 12129-12137, 2003.
- [109] A. C. Tsipis, "DFT/TDDFT insights into the chemistry, biochemistry and photophysics of copper coordination compounds," *Royal Society of Chemistry Advances*, vol. 4, p. 32504, 2014.
- [110] G. Sciortino, G. Lubinu, J.-D. Maréchal and E. Garriga, "DFT protocol for EPR prediction of paramagnetic Cu(II) complexes and application to protein binding sites," *Magnetochemistry*, vol. 4, no. 4, p. 55, 2018.
- [111] S. T. Prigge, B. A. Eipper, R. E. Mains and L. M. Amzel, "Dioxygen binds end-on to mononuclear copper in a pre-catalytic enzyme complex," *Science*, vol. 304, no. 5672, pp. 864-867, 2004.
- [112] B. Hazes, K. A. Magnus, C. Bonaventura, J. Bonaventura, Z. Dauter, K. H. Kalk and W. G. Hol, "Crystal structure of deoxygenated *Limulus polyphemus* subunit II hemocyanin at 2.18 Å resolution: clues for a mechanism for allosteric regulation," *Protein Science*, vol. 2, no. 4, pp. 597-619, 1993.
- [113] K. A. Magnus, H. Ton-That and J. A. Carpenter, "Three-dimensional structure of the oxygenated form of the hemocyanin subunit II of *Limulus polyphemus* at atomic resolution," in *Bioinorganic Chemistry of Copper*, New York, Chapman & Hall, 1993, pp. 143-150.



---

# CHAPTER II. COMPUTATIONAL EPR SPECTROSCOPY FOR THE STUDY OF MONONUCLEAR COPPER(II) COMPLEXES

---





## CHAPTER II. COMPUTATIONAL EPR SPECTROSCOPY FOR THE STUDY OF MONONUCLEAR COPPER(II) COMPLEXES

The redox behavior of copper is an important characteristic naturally exploited in biology but also used and developed in synthetic chemistry. [1] [2] [3] Changing redox states can affect the coordinating environment and the geometric properties of any given system. In the case of mononuclear Cu(II), electron paramagnetic resonance (EPR) spectroscopy is the most prevalent method for probing the local electronic structure. [4] This spectroscopic technique encodes the information in the gyromagnetic factor,  $g$ , and hyperfine tensors,  $A$ . The  $g$ -tensor originates from the Zeeman interaction of the unpaired electron density with the applied magnetic field. The  $A$ -tensor originates from the hyperfine interaction of the unpaired electron density with the nuclear spin of copper. [5] [6] Obtaining accurate and reliable calculation of these spin Hamiltonian parameters is a formidable challenge in quantum chemistry. [7] [8] [9] This is particularly true for the hyperfine coupling constants, HFCs, in which three different contributions with distinct physical origins need to be predicted:

1. The Fermi Contact term,  $A^{FC}$ , a first-order property which is proportional to the spin density at the nucleus and represents an isotropic contribution.
2. The Spin-Dipolar term,  $A^{SD}$ , corresponding to the magnetic dipole-dipole interaction between electron and nuclear spins. The  $A^{SD}$  term is also a first-order property but of anisotropic nature.
3. The Spin-Orbit coupling,  $A^{SO}$ , a second-order contribution involving excited states of the same spin as the ground state. The  $A^{SO}$  term is composed of two terms itself:
  - a. The isotropic Pseudo-Contact,  $A^{PC}$ , term, and
  - b. The anisotropic dipolar tensor,  $A^{SO,dip}$ , term.

Predicting the hyperfine coupling constants is a difficult task, albeit a consensus in the use of hybrid functionals within density functional theory, DFT, has been reached in a wide array of studies. [10] [11] [12] [13] [14] [15] [16] However, these studies demonstrate a large spread in terms of quality of results. Unexpected failures are not uncommon and there is no clear superior choice that guarantees consistent predictability and performance. Recently, hyperfine coupling constants of the first-order,  $A^{FC}$  and  $A^{SD}$ , are becoming accessible by the means of wave function methods

for systems of “realistic” size, complexes incorporating ligands with tens of atoms. [17] [18] [19] [20] Smart algorithmic approximations and cost-effective implementations facilitate the use of wave-function methods. In literature, two examples have been discussed: the orbital-optimized second-order Moller-Plesset perturbation theory (OO-MP2), [17] [18] and the domain-based local pair natural orbital coupled cluster method with single and double excitations (DLPNO-CCSD). [19] These methods are known to perform more systematically and with better control of errors. This has been observed and accepted for energetics and one can envision that this will hold true for the calculation of hyperfine couplings.

In Chapter II entitled “Theoretical methods and their application in EPR spectroscopy of mononuclear copper(II) centers”, we define and evaluate a crucial methodological component that may be a source of unsystematic errors in calculating HFCs when different theoretical methods are compared, i.e. the basis set used for the copper atom. Additionally, we compare a series of DFT methods that represent all families of functionals, as well as several wave function-based methods. Part 1 focuses the study on HFCs whereas Part 2 deals with the prediction of g-tensors. Both are necessary for a complete study of more realistic models.

## 1 – Convergence studies of basis sets, DFT functionals, and wave-function methods for the calculation of hyperfine coupling constants

Work published: Rogelio J. Gómez-Piñeiro, Dr. Dimitrios A. Pantazis, Dr. Maylis Orio. Comparison of Density functional and Correlated Wave Function Methods for the Prediction of Cu(II) Hyperfine Coupling Constants. *Chem. Phys. Chem.* **2020**, 21, 24, 2667-2679.

To study the A- tensors in mononuclear copper centers, we first defined an extensive set of complexes that fulfill the criteria of being molecular entities with well-defined crystallographic structures, as well as having reliable resolved experimental EPR components. The complex set is depicted in Figure 1 below, with their corresponding A-values in Table 1. The complexes encompass a wide range of ligands and coordinating atom types so that the set is sufficiently varied. The coordinating sites around the copper centers comprise either one type of coordinating atom: 4N, 4S, 4O, 5N, 6S, or a combination of these: 2N2S, 2N2O, 3N1O. This ensures that both the electronic properties of the complexes and their coordinating geometries are varied: square planar, distorted square planar, tetrahedral, distorted square base pyramidal, and octahedral. Also, some

ligands have chelating effects, with bidentate, tridentate, or tetradentate configurations. These differences in coordination chemistry provide a complete set of small mononuclear Cu(II) complexes with distinct intrinsic properties.

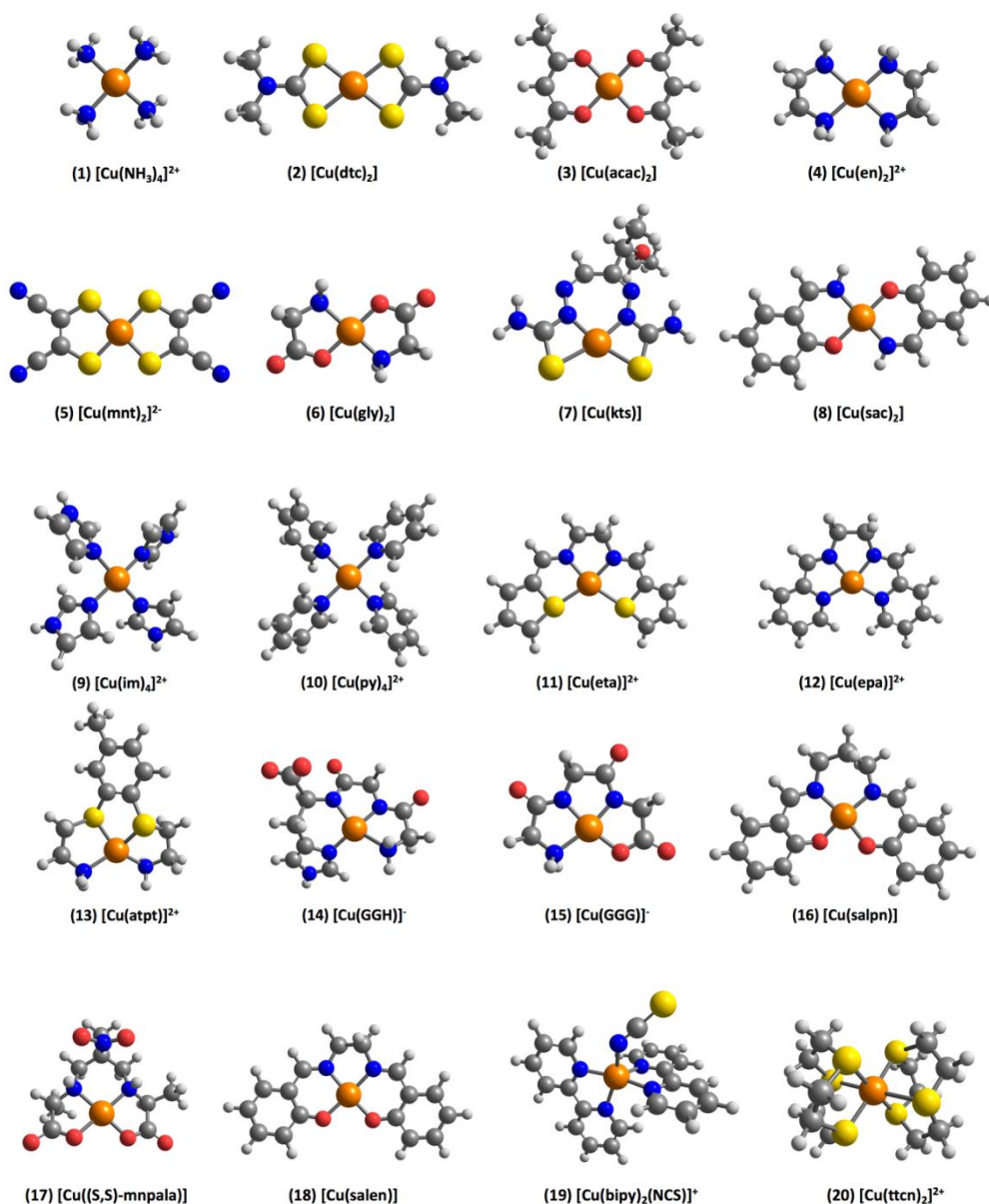


Figure 1. Molecular structures of the Cu(II) complexes considered in the present study. Definition of ligand abbreviations: dtc = dimethyldithiocarbamate, acac = acetylacetone; en = ethylenediamine; mnt = maleonitriledithiolate; gly = glycine; kts = 2-keto-3-ethoxybutyraldehyde-bis(thiosemicarbazone); sac = salicylaldehyde imine; im = imidazole; py = pyridine; eta = N,N'-ethylenebis(thiophene-2-alimine); epa = N,N'-ethylenebis(pyridine-2-alimine); atpt = 3,4-bis(3-amino-1-thiopropyl)toluene; GGH = glycine-glycine-histidine; GGG = glycine-glycine-glycine; salpn = N,N'-bis(salicylidene)-1,2-propanediamine; (S,S)-mnpala = 2,5,8-trimethyl-5-nitro-3,7-diazanonanedioate; salen = bis(salicylidene)ethylenediamine; bipy = 2,2'-bipyridine; ttcn = 1,4,7-trithiacyclononane.

**Table 1. List of the Cu(II) complexes considered in the present study and their experimentally determined  $^{63}\text{Cu}$  hyperfine coupling constants (absolute values, in MHz).**

Entry	Complex	$A_x$	$A_y$	$A_z$	Ref.
1	$[\text{Cu}(\text{NH}_3)_4]^{2+}$	68.8	68.8	586.5	[21]
2	$[\text{Cu}(\text{dtc})_2]$	140.1	140.1	487.3	[22]
3	$[\text{Cu}(\text{acac})_2]$	35.0	35.0	520.0	[23]
4	$[\text{Cu}(\text{en})_2]^{2+}$	78.0	82.0	602.0	[24]
5	$[\text{Cu}(\text{mnt})_2]^{2-}$	118.0	118.0	500.0	[25]
6	$[\text{Cu}(\text{gly})_2]$	43.1	43.1	529.9	[21]
7	$[\text{Cu}(\text{kts})]$	92.9	92.9	575.1	[26]
8	$[\text{Cu}(\text{sac})_2]$	60.0	60.0	470.7	[27]
9	$[\text{Cu}(\text{im})_4]^{2+}$	63.2	63.2	563.8	[21]
10	$[\text{Cu}(\text{py})_4]^{2+}$	48.8	48.8	563.5	[21]
11	$[\text{Cu}(\text{eta})]^{2+}$	90.5	90.5	531.8	[28]
12	$[\text{Cu}(\text{epa})]^{2+}$	92.9	92.9	524.6	[29]
13	$[\text{Cu}(\text{atpt})]^{2+}$	54.0	54.0	320.8	[30]
14	$[\text{Cu}(\text{GGH})]^-$	66.0	66.0	620.0	[13]
15	$[\text{Cu}(\text{GGG})]^-$	63.0	63.0	602.6	[13]
16	$[\text{Cu}(\text{salpn})_2]$	47.1	47.1	526.7	[31]
17	$[\text{Cu}(\text{S,S-mnpala})_2]$	66.0	66.0	581.6	[32]
18	$[\text{Cu}(\text{salen})_2]$	100.4	100.4	613.7	[33]
19	$[\text{Cu}(\text{bipy})_2(\text{NCS})]^+$	44.1	44.1	468.0	[34]
20	$[\text{Cu}(\text{ttcn})_2]^{2+}$	60.0	60.0	458.7	[35]

Crystallographic coordinates of all complexes were obtained from the Cambridge Structural Database and were individually edited for completeness, chemical correctness and to remove solvent molecules and other non-coordinating counter-ions. Theoretical calculations were performed with ORCA. [36] Geometry optimizations were performed with the BP86 functional [37] [38] and the def2-TZVP basis sets, [39] in combination with corresponding auxiliary basis sets. [40] Increased integration grids were employed (Grid4 in ORCA nomenclature. Vibrational frequencies were computed for all optimized structures and the absence of imaginary modes confirmed that the true minima were obtained.

## 1.1 – Computational details

DFT methods evaluated in the present work include multiple functional types: GGAs and meta-GGAs (PBE, [41] TPSS, [42] and SCAN [43]), hybrids and range-separated hybrids (B3LYP, [44] [45] B3PW91, [44] [46] PBE0, [47] and CAM-B3LYP [48]), as well as meta-hybrids and double hybrids (TPSSH, [49] M06, [50] M06-2X, [50] and B2PLYP [51]). Computation of hyperfine coupling constants used increased general integration grids (Grid6 in ORCA convention), further increased radial integration accuracy (IntAcc 6.0) and specially enhanced grids for copper (SpecialGridIntAcc 11). For all ligand atoms, the def2-TZVP basis sets [39] were used. A large variety of basis sets were tested for Cu and further details will be provided in the corresponding section. No approximations to two-electron integrals were used when calculating hyperfine coupling constants to exclude any potential error related to density fitting approximations. Spin-orbit contributions were included through mean-field and effective potential approaches. The spin-orbit coupling operator was treated by an accurate mean-field (SOMF) approximation to the Breit–Pauli operator. [52] [53] The potential was constructed to include one-electron terms, compute the Coulomb term in a semi-numeric way, incorporate exchange via one-center exact integrals including the spin-other orbit interaction, and include local DFT correlation. It is worth noting that the Coulomb term can also be computed semi-numerically using the RI approximation or exactly. [52] The former approach exhibited unreasonable HFC values with hybrid functionals, mainly affecting the spin-orbit contribution, while the latter did not show any difference with the semi-numeric approach except for a longer running time (Table 2). Scalar relativistic calculations were performed with the second-order Douglas–Kroll–Hess (DKH2) [54] [55] [56] [57] [58] [59] [60] and the zeroth-order regular approximation (ZORA) [61] [62] [63] Hamiltonians. Given the different behavior of these methods close to the nucleus, [64] the appropriateness of the basis set for Cu was carefully studied and purpose-made basis sets were used where available. In the case of DKH2 calculations, both a point nucleus and a finite nucleus model with a Gaussian charge distribution [65] were tested. Picture change effects were applied as appropriate. The effect of considering the solvent via a continuum solvation model was investigated and found to be non-essential for calculating HFCs (Table 3).

**Table 2.** Calculated HFCs (individual components and detailed contributions, in MHz) of  $[\text{Cu}(\text{NH}_3)_4]^{2+}$  obtained with the PBE0 functional with selected basis sets and varying the computational approach to compute the Coulomb term.

<i>Semi-Numeric</i>	$A_{11}$	$A_{22}$	$A_{33}$	$A^{FC}$	$A^{PC}$	$A_{11}^{SD}$	$A_{22}^{SD}$	$A_{33}^{SD}$	$A_{11}^{S,dip}$	$A_{22}^{S,dip}$	$A_{33}^{S,dip}$	<i>Run Time</i>
aug-cc-pVTZ-Junc	-26.3	-26.8	-610.3	-360.8	139.7	257.3	256.7	-514.0	-62.4	-62.3	124.7	00:13:37
aug-cc-pVTZ-J	-24.8	-25.2	-607.4	-359.9	140.8	257.2	256.7	-513.9	-62.9	-62.8	125.6	00:15:16
CP(PPP)	-33.2	-33.6	-602.4	-357.8	134.7	249.6	249.1	-498.8	-59.7	-59.6	119.5	00:06:12
aug-cc-pVTZ-Jmod	-23.8	-24.3	-606.4	-359.5	140.8	258.0	257.4	-515.4	-62.9	-62.7	125.7	00:14:38
<i>Semi-Numeric with RI approx.</i>	$A_{11}$	$A_{22}$	$A_{33}$	$A^{FC}$	$A^{PC}$	$A_{11}^{SD}$	$A_{22}^{SD}$	$A_{33}^{SD}$	$A_{11}^{S,dip}$	$A_{22}^{S,dip}$	$A_{33}^{S,dip}$	<i>Run Time</i>
aug-cc-pVTZ-Junc	-100.5	-101.1	-870.0	-360.8	3.6	257.3	256.7	-514.0	-0.6	-0.6	1.1	00:40:29
aug-cc-pVTZ-J	-99.6	-100.2	-869.1	-359.9	3.6	257.2	256.7	-513.9	-0.6	-0.6	1.2	00:13:48
CP(PPP)	-105.4	-105.9	-854.6	-357.8	2.5	249.6	249.1	-498.8	0.3	0.3	-0.5	00:11:00
aug-cc-pVTZ-Jmod	-98.4	-99.0	-870.1	-359.5	3.6	258.0	257.4	-515.4	-0.5	-0.5	1.2	00:16:41
<i>Exact term</i>	$A_{11}$	$A_{22}$	$A_{33}$	$A^{FC}$	$A^{PC}$	$A_{11}^{SD}$	$A_{22}^{SD}$	$A_{33}^{SD}$	$A_{11}^{S,dip}$	$A_{22}^{S,dip}$	$A_{33}^{S,dip}$	<i>Run Time</i>
aug-cc-pVTZ-Junc	-26.3	-26.7	-610.2	-360.8	140.8	257.3	256.7	-514.0	-62.9	-62.7	125.7	03:21:27
aug-cc-pVTZ-J	-24.7	-25.2	-607.3	-359.9	140.9	257.2	256.7	-513.9	-62.9	-62.8	125.7	06:07:38
CP(PPP)	-33.2	-33.6	-602.3	-357.8	134.8	249.6	249.1	-498.8	-59.8	-59.7	119.5	00:22:02
aug-cc-pVTZ-Jmod	-24.8	-25.2	-610.9	-359.5	139.2	258.0	257.4	-515.4	-62.5	-62.4	124.8	05:03:36

**Table 3.** Calculated HFCs (individual components and detailed contributions, in MHz) of  $[\text{Cu}(\text{NH}_3)_4]^{2+}$  obtained with the B3PW91 functional and the aug-cc-pVTZ-J-mod basis set, using different solvents and the CPCM model.

<i>Solvent</i>	<i>Dielectric Constant</i>	<i>Refractive Index</i>	$A_{11}$	$A_{22}$	$A_{33}$	$A^{FC}$	$A^{PC}$	$A_{11}^{SD}$	$A_{22}^{SD}$	$A_{33}^{SD}$	$A_{11}^{S,dip}$	$A_{22}^{S,dip}$	$A_{33}^{S,dip}$
THF	7.25	1.407	-13.9	-14.3	-588.4	-335.5	129.9	249.6	249.0	-498.6	-57.9	-57.8	115.8
$\text{CH}_2\text{Cl}_2$	9.08	1.424	-13.7	-14.1	-588.2	-335.4	130.0	249.6	249.1	-498.7	-58.0	-57.9	115.8
Methanol	32.63	1.329	-13.1	-13.5	-587.9	-335.1	130.3	249.8	249.3	-499.1	-58.0	-57.9	116.0
Acetonitrile	36.60	1.344	-13.0	-13.5	-587.9	-335.1	130.3	249.8	249.3	-499.1	-58.0	-57.9	116.0
DMSO	47.20	1.479	-13.0	-13.4	-587.9	-335.0	130.3	249.8	249.3	-499.1	-58.0	-57.9	116.0
Water	80.40	1.330	-12.9	-13.3	-587.8	-335.0	130.3	249.8	249.3	-499.1	-58.1	-57.9	116.0

Wave function methods used in this work include second-order Møller–Plesset (MP2), orbital-optimized MP2 (OO-MP2) and its spin-component scaled version, OO-SCS-MP2. [17] [66] [67] Relaxed densities were used for MP2; the densities of OO methods are by definition relaxed densities. The Calculations using Domain based Local Pair Natural Orbital Coupled Cluster method with single- and double perturbative excitations (DLPNO-CCSD) were initiated with unrestricted Kohn–Sham orbitals and followed the standard DLPNO procedure. [68] [69] The thresholds used for the DLPNO-CCSD calculations of hyperfine coupling constants were all tighter than default cutoffs, in line with previous recommendations for spin densities. [19] In detail, the various settings were as follows:  $\text{TCutMKN} = 1.0 \times 10^{-4}$ ,  $\text{TCutDO} = 5.0 \times 10^{-3}$ ,  $\text{TCutPNO} = 1.0 \times 10^{-7}$ ,  $\text{TCutPNOSingles} = 0.00$ ,  $\text{TScalePNOCore} = 1.0 \times 10^{-3}$ , and  $\text{TScalePNOSOMO} = 1.0 \times 10^{-1}$ . In the wave function based calculations of hyperfine coupling constants, all electrons were set as active. “Unrelaxed” spin densities are used for DLPNO-CCSD, as defined by Saitow

and Neese, [19] i.e. where the effect of orbital relaxation is recovered only through the action of  $\exp(T_1)$  onto the reference. Only the  $A^{FC}$  and  $A^{SD}$  components can be computed with these methods. The lack of the  $A^{SO}$  component means that final values for comparison with experiment must combine the wave function values of the first-order components with the second-order contribution obtained from a different method. The def2-TZVP basis sets with their corresponding auxiliary basis sets for correlated calculations [69] were used for all light atoms. For Cu, we employed our tailor-made basis set described in the following section and based on the primitives of the aug-cc-pVTZ-J basis set of Hedegård et al. [70] Since our modified basis set, denoted aug-cc-pVTZ-Jmod, does not have a specific auxiliary counterpart, we generated a very large auxiliary basis set with the “AutoAux” procedure of ORCA. [71]

## 1.2 – Performance assessment of basis sets, functionals and wave function methods

To assess the performance of the calculated HFCs using different parameters such as basis sets, functionals and wave function methods, the absolute percent deviations (APDs) are evaluated with respect to experimental results for relevant parameters. Three quantities are evaluated:  $A_{33}$ ,  $A_{iso}$ , and  $\Delta A$ .  $A_{33}$  represents the largest component of the hyperfine tensor,  $A_{iso}$  the average between all three total hyperfine values  $[(A_{11}+A_{22}+A_{33})/3]$  and  $\Delta A$  the anisotropic difference  $[(A_{33}-A_{11})]$ . The APDs are evaluated as percentage in the following manner:

$$APD(A_{33}^{(M)}) = \left| \frac{A_{33}^{(M)} - A_{33}^{exp}}{A_{33}^{exp}} \right| \times 100,$$

$$APD(A_{iso}^{(M)}) = \left| \frac{A_{iso}^{(M)} - A_{iso}^{exp}}{A_{iso}^{exp}} \right| \times 100,$$

where  $A_{iso}^{(M),exp} = (A_{11}^{(M),exp} + A_{22}^{(M),exp} + A_{33}^{(M),exp})/3$ , and

$$APD(\Delta A^{(M)}) = \left| \frac{\Delta A^{(M)} - \Delta A^{exp}}{\Delta A^{exp}} \right| \times 100, \text{ where } \Delta A^{(M),exp} = A_{max}^{(M),exp} - A_{min}^{(M),exp}.$$

For a complete evaluation of the whole set of complexes, the mean absolute percent deviation (MAPD) is reported. In this case, a MAPD for an evaluated component,  $x$ , is taken over all 20 complexes such as:

$$MAPD(x) = \frac{\sum APD(x)}{20}.$$

### 1.3 – Development and evaluation of a new basis set

In typical applications, such as reactivity studies, general-purpose basis sets are large and flexible in the frontier orbital region but lack a range of  $s$  functions with high exponents. This construction is inadequate for calculating hyperfine coupling constants because the intrinsic nature of this property requires a high flexibility in the core region, i.e. the inner Cu  $s$  orbitals so that the sensitive variations of spin density on and close to the nucleus are adequately captured. This directly affects the calculation of the dominant Fermi contact term. Therefore, the choice of basis set for the copper atom is a critical methodological parameter for the calculation of the HFCs.

The basis set must not be treated as an adjustable parameter that can be used to distort the performance by the means of error compensation. It should provide converged and reliable results for all components. Therefore, the basis set should be flexible for the calculated target property. It should also be robust enough to be used in non-relativistic as well as scalar relativistic frameworks. Additionally, the basis set should remain small enough to avoid numerical instabilities.

Two types of basis sets are proposed as particularly appropriate for the calculation of core properties: the CP(PPP), which was originally engineered for the calculation of Mössbauer parameters, [72] and the aug-cc-pVTZ-J, that specifically targets the calculation of the HFCs. [70] [73] They both feature the increased flexibility of the  $s$  subset and the inclusion of steep  $s$  functions, even though their overall design is different. CP(PPP) is a [17s7p3d1f] basis set with a total of 60 contracted functions. It is based on the primitives of the original 1994 Ahlrichs [8s5p3d] VTZ basis set. [74] The aug-cc-pVTZ-J basis set of Hedegard et al. [70] is a [17s10p7d3f2g] generally contracted set with 121 functions, using primitives from the original aug-cc-pVTZ. Its fully decontracted version version, denoted aug-cc-pVTZ-Junc, corresponds to a [25s18p10d3f2g] set with a total of 168 primitives. This is the largest and most flexible basis set presented in this study and is used as a reference for all others. Finally, our modified version of aug-cc-pVTZ-J, denoted aug-cc-pVTZ-Jmod, includes decontracted  $s$  functions and removal of the three innermost  $s$  primitives [22s10p7d3f2g].



**Table 4. Calculated HFCs (individual components and detailed contributions, in MHz) for  $[\text{Cu}(\text{NH}_3)_4]^{2+}$  obtained with the PBE0 functional using different basis sets.**

<i>Basis Set</i>	Total			Isotropic		Anisotropic					
	$A_{11}$	$A_{22}$	$A_{33}$	$A^{FC}$	$A^{PC}$	$A_{11}^{SD}$	$A_{22}^{SD}$	$A_{33}^{SD}$	$A_{11}^{SO,dip}$	$A_{22}^{SO,dip}$	$A_{33}^{SO,dip}$
aug-cc-pVTZ-Junc	-26.3	-26.8	-610.3	-360.8	139.7	257.3	256.7	-513.9	-62.4	-62.3	124.7
aug-cc-pVTZ-J	-24.8	-25.2	-607.4	-359.9	140.8	257.2	256.7	-513.9	-62.9	-62.7	125.7
CP(PPP)	-33.2	-33.6	-602.4	-357.8	134.7	249.6	249.1	-498.8	-59.7	-59.6	119.5
aug-cc-pVTZ	-276.6	339.6	339.0	-9.7	143.7	-536.7	268.1	268.7	127.2	-63.5	-63.6
aug-cc-pwCVTZ	211.2	211.6	-372.4	-122.3	139.1	256.6	257.1	-513.7	-62.2	-62.3	124.5
cc-pwCVTZ	212.6	213.0	-370.5	-120.5	138.9	256.2	256.8	-513.0	-62.0	-62.1	124.2
def2-TZVP	-249.5	345.8	346.2	4.8	143.2	-521.6	260.5	261.1	124.6	-62.3	-62.4
def2-TZVP-uncS	-3.2	-3.7	-599.1	-345.4	143.3	261.2	260.7	-521.9	-62.4	-62.3	124.9
aug-cc-pVTZ-Jmod	-23.8	-24.3	-606.4	-359.5	139.1	258.0	257.4	-515.4	-62.4	-62.3	124.8
<i>Exp.</i>	68.8	68.8	586.5								

**Table 5. Core and valence-shell spin contributions to the isotropic HFCs (in MHz) for  $[\text{Cu}(\text{NH}_3)_4]^{2+}$  obtained with the PBE0 functional using different basis sets.**

<i>Basis Set</i>	1s	2s	3s	Core	Valence	$A_{iso}$	$\langle S^2 \rangle$	$APD(\langle S^2 \rangle)$
aug-cc-pVTZ-Junc	-17.5	-622.7	437.4	-202.9	-18.3	-221.1	0.7527	0.36
aug-cc-pVTZ-J	-17.9	-622.9	438.7	-202.2	-16.9	-219.1	0.7527	0.36
CP(PPP)	-17.9	-610.1	430.1	-198.0	-25.1	-223.1	0.7526	0.34
aug-cc-pVTZ	-19.6	-347.9	506.8	139.3	-5.3	134.0	0.7527	0.36
aug-cc-pwCVTZ	-17.5	-433.6	489.9	38.7	-21.9	16.8	0.7527	0.36
cc-pwCVTZ	-17.4	-433.6	491.5	40.5	-22.1	18.4	0.7527	0.36
def2-TZVP	-19.3	-361.6	537.8	156.8	-9.3	147.5	0.7527	0.36
def2-TZVP-uncS	-24.7	-589.1	423.6	-190.2	-11.8	-202.0	0.7527	0.36
aug-cc-pVTZ-Jmod	-17.9	-620.7	436.3	-202.3	-15.9	-218.2	0.7527	0.36
<i>Exp.</i>						241.4	0.7500	

Table 4 presents a comparison of these basis set as well as other standard ones for the computation of the copper HFC for the  $[\text{Cu}(\text{NH}_3)_4]^{2+}$  complex obtained with DFT using the PBE0 [47] functional. Note that the results discussed below have been confirmed with both the  $[\text{Cu}(\text{dtc})_2]$  and the  $[\text{Cu}(\text{acac})_2]$  complexes, as well as with the TPSSh [49] and B3PW91 [44] [46] functionals (Tables S1-S16 and Figures S1-S8).

Several points become immediately apparent from this. First, the Fermi contact term is extremely sensitive to the  $s$  functions of the basis set. The aug-cc-pVTZ-J (or Junc) and CP(PPP) basis sets are in close agreement with respect to  $A^{FC}$  which is due to an important core-shell spin polarization contribution of negative sign (Table 5). In contrast, the standard aug-cc-pVTZ and def2-TZVP basis sets produce essentially useless results and display positive contributions for core-shell spin polarization, the  $2s$  contribution being underestimated, leading to a poor description of the isotropic term of the Cu HFCs. The situation is identical for the aug-cc-pwCVTZ and cc-pwCVTZ basis sets that contain core-correlating functions, confirming that the use of basis sets not explicitly

adjusted for HFCs should be avoided. For these latter basis sets, the core-shell spin polarization contributions are again affected with underestimated  $2s$  contributions and leading to low and positive  $A_{iso}$  values. The importance of the flexibility of the  $s$  subset on the  $A^{FC}$  term becomes apparent by testing a version of def2-TZVP where the  $s$  functions are simply decontracted (denoted def2-TZVP-uncS in Table 4): The Fermi contact term is now drastically improved and the overall differences from the reference values are due to differences in the other terms as much as the  $A^{FC}$ . Indeed, there is complete remediation of the core-shell spin polarization contribution, both in sign and magnitude (Table 5). This observation justifies the concept behind the original creation of the CP(PPP) basis sets as well as the use of similarly “core property” modified versions of scalar-relativistic def2-TZVP basis sets in practical applications. [75] A second important observation is that CP(PPP) underestimates slightly but non-negligibly the reference values for  $A^{SD}$  and for the largest component of  $A^{SO}$ . Given that the values of these components are predicted consistently between the fully decontracted reference basis set and others that have a similar coverage of the valence space, this deviation is ascribed to a suboptimal coverage of the  $p$  subspace in CP(PPP), deficiency likely inherited from the parent Ahlrichs VTZ basis set.

To assess the performance of the basis sets, the APDs are evaluated with respect to experimental results as described before. The APD calculations for  $[\text{Cu}(\text{NH}_3)_4]^{2+}$  (Table 6 and Figure 2) is also presented for  $[\text{Cu}(\text{dte})_2]$  and  $[\text{Cu}(\text{acac})_2]$ , using PBE0, B3PW91, and TPSSh functional in Tables S1-S16 and Figures S1-S8, and supports the above analysis regarding the necessity of high flexibility for the basis set in the core region and the relevance of the aug-cc-pVTZ-J (or -Junc) basis set to predict copper HFCs.

All these results advocate the use of the purpose-made basis set, denoted as aug-cc-pVTZ-Jmod, for the calculation of copper HFCs, since it produces results indistinguishable from its fully decontracted version.

**Table 6.** APD values of  $A_{33}$ ,  $A_{iso}$ , and  $\Delta A$  for calculated HFCs of  $[\text{Cu}(\text{NH}_3)_4]^{2+}$  obtained with the PBE0 functional using different basis sets and compared with experimental data.

<i>Basis set</i>	$A_{33}$	$A_{iso}$	$\Delta A$	$APD(A_{33})$	$APD(A_{iso})$	$APD(\Delta A)$
aug-cc-pVTZ-Junc	-610.3	221.1	584.0	4.1	8.4	12.8
aug-cc-pVTZ-J	-607.4	219.1	582.6	3.6	9.2	12.5
CP(PPP)	-602.4	223.1	569.2	2.7	7.6	9.9
aug-cc-pVTZ	339.0	134.0	616.2	42.2	44.5	19.0
aug-cc-pwCVTZ	-372.4	16.8	584.0	36.5	93.0	12.8
cc-pwCVTZ	-370.5	18.4	583.5	36.8	92.4	12.7
def2-TZVP	346.2	147.5	595.7	41.0	38.9	15.1
def2-TZVP-uncS	-599.1	202.0	595.9	2.1	16.3	15.1
aug-cc-pVTZ-Jmod	-606.4	218.2	582.6	3.4	9.6	12.5
<i>Exp.</i>	<i>586.5</i>	<i>241.4</i>	<i>517.7</i>			

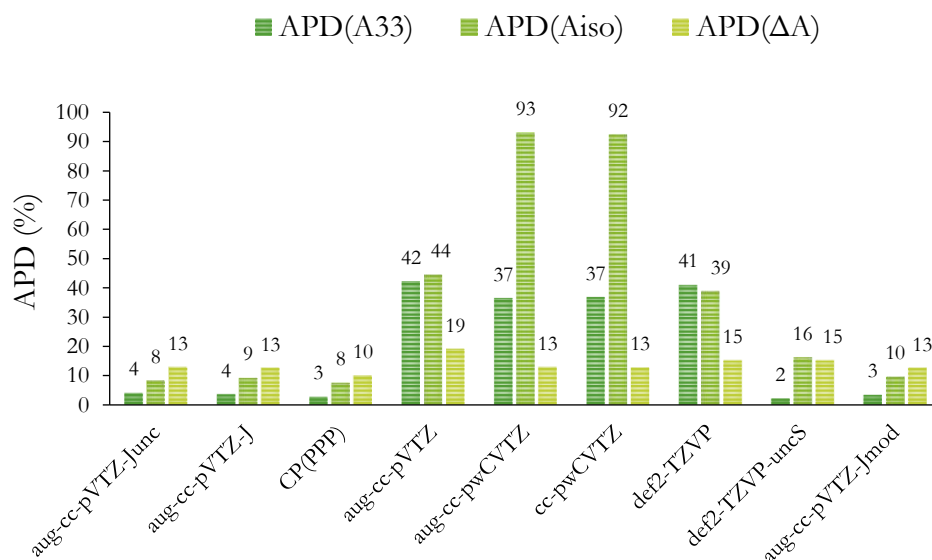


**Figure 2.** Graphical representation of the APD values of calculated  $A_{33}$ ,  $A_{iso}$ , and  $\Delta A$  for  $[\text{Cu}(\text{NH}_3)_4]^{2+}$  obtained with the PBE0 functional using different basis sets.

### 1. Scalar relativistic corrections and the finite nucleus model

An additional point concerns the robustness of the basis set with respect to scalar relativistic effects, which result in spatial contraction of  $s$  and  $p$  orbitals. [64] These data, obtained with the PBE0 functional, are presented in Table 7 below and propose a similar comparison for  $[\text{Cu}(\text{NH}_3)_4]^{2+}$  using the DKH2 Hamiltonian and appropriate corresponding basis sets. Here again, the aug-cc-pVTZ-Junc basis set serves as the reference. DKH-adapted versions of the standard cc-type basis sets fail to reproduce the  $A^{\text{FC}}$  term, but the DKH-adapted version [76] of def2-TZVP,

[39] developed to be used in conjunction with the SARC family of all-electron basis sets, [76] [77] [78] [79] [80] [81] performs very well for all components, owing to the DKH-optimized contraction coefficients and the partially decontracted  $s$  and  $p$  shells. CP(PPP) can be considered as adequate for the  $A^{FC}$  term but it shows the same type of deviation as seen in the non-relativistic calculations for both  $A^{SD}$  and  $A^{SO}$  components. Importantly, the contracted aug-cc-pVTZ-J version deviates from the reference for the crucial Fermi contact term showing that it suffers from the contraction of  $s$  functions, whereas the  $A^{SD}$  and  $A^{SO}$  terms are practically the same as the reference values. [82] The finite nucleus model available with the ORCA program package was applied with the DKH2 Hamiltonian for  $[\text{Cu}(\text{NH}_3)_4]^{2+}$ , employing the PBE0 functional, as shown in Table 8. Applying the finite nucleus model has a very limited effect on the computed HFCs. Regardless of the functional used, the DK version of the cc basis sets still underperform, and the aug-cc-pVTZ-J keeps deviating from the Junc analogue while predicted HFCs with both CP(PPP) and DKH-def2-TZVP are close to those obtained with the reference. Overall, the finite nucleus model has a very limited effect on the calculated HFCs, and we recover the main trends obtained without using it. Identical conclusions are reached when the ZORA Hamiltonian is used instead of DKH2 for the inclusion of scalar relativistic effects (Table 9). Considering the results with aug-cc-pVTZ-Junc as reference, the CP(PPP) and the ZORA version of the def2-TZVP perform identically and provide computed HFCs of similar sign and magnitude. The above observations combined with the evaluation of the APDs for both DKH2 and ZORA Hamiltonians (Table S20 and Figure S9) finally support that inclusion of scalar relativistic corrections is not statistically crucial for an accurate prediction of Cu HFCs, the limiting parameter here being the definition of appropriate basis sets. These results were also obtained with the B3PW91 functional yielding an identical conclusion (Tables S17-S20 and Figure S10). While scalar relativistic effects are usually important to model the properties of transition metal complexes, it does not seem to clearly improve the prediction of copper HFCs in an average sense. Therefore, for the sake of simplicity, the next results of our study do not incorporate scalar relativistic corrections.

**Table 7. Calculated HFCs (individual components and detailed contributions, in MHz) for  $[\text{Cu}(\text{NH}_3)_4]^{2+}$  obtained with the PBE0 functional and the DKH2 Hamiltonian with different basis sets.**

<i>Basis set</i>	$A_{11}$	$A_{22}$	$A_{33}$	$A^{FC}$	$A^{PC}$	$A_{11}^{SD}$	$A_{22}^{SD}$	$A_{33}^{SD}$	$A_{11}^{S,dip}$	$A_{22}^{S,dip}$	$A_{33}^{S,dip}$
aug-cc-pVTZ-Junc	-19.6	-20.1	-607.9	-356.4	140.6	258.7	258.1	-516.8	-62.5	-62.4	124.8
aug-cc-pVTZ-J	5.7	6.3	-580.7	-330.8	141.3	257.9	258.5	-516.5	-62.6	-62.7	125.4
CP(PPP)	-24.7	-25.1	-598.1	-351.0	135.0	250.7	250.3	-501.0	-59.5	-59.4	118.9
aug-cc-pVTZ-DK	-295.5	323.9	324.4	-27.0	144.6	-540.3	269.8	270.4	127.2	-63.6	-63.7
aug-cc-pwCVTZ-DK	194.3	194.7	-393.7	-141.4	139.9	258.1	258.6	-516.7	-62.3	-62.4	124.5
cc-pwCVTZ-DK	195.7	196.2	-391.8	-139.7	139.7	257.4	258.3	-516.0	-62.0	-62.1	124.2
DKH-def2-TZVP	-18.9	-19.4	-606.2	-353.2	138.4	257.3	256.8	-514.1	-61.4	-61.3	122.8
def2-TZVP-uncS	4.2	4.7	-596.9	-340.5	144.4	262.7	263.3	-526.0	-62.5	-62.6	125.2
aug-cc-pVTZ-Jmod	-17.8	-18.3	-604.7	-354.9	141.3	258.5	257.9	-516.5	-62.7	-62.6	125.4
<i>Exp.</i>	<i>68.8</i>	<i>68.8</i>	<i>586.5</i>								

**Table 8. Calculated HFCs (individual components and detailed contributions, in MHz) for  $[\text{Cu}(\text{NH}_3)_4]^{2+}$  obtained with the PBE0 functional, DKH2 Hamiltonian, and finite nucleus model with different basis sets.**

<i>Basis set</i>	$A_{11}$	$A_{22}$	$A_{33}$	$A^{FC}$	$A^{PC}$	$A_{11}^{SD}$	$A_{22}^{SD}$	$A_{33}^{SD}$	$A_{11}^{S,dip}$	$A_{22}^{S,dip}$	$A_{33}^{S,dip}$
aug-cc-pVTZ-Junc	-4.5	-5.0	-592.7	-341.3	140.6	258.7	258.1	-516.8	-62.5	-62.4	124.8
aug-cc-pVTZ-J	6.5	7.1	-579.9	-330.1	141.3	257.9	258.5	-516.5	-62.6	-62.7	125.4
CP(PPP)	-22.9	-23.3	-596.2	-349.2	135.0	250.7	250.3	-501.0	-59.5	-59.4	118.9
aug-cc-pVTZ-DK	-295.5	323.8	324.3	-27.0	144.6	-540.3	269.8	270.5	127.2	-63.6	-63.7
aug-cc-pwCVTZ-DK	194.5	195.0	-393.5	-141.2	139.9	258.1	258.6	-516.7	-62.3	-62.4	124.5
cc-pwCVTZ-DK	195.9	196.4	-391.5	-139.4	139.7	257.7	258.3	-516.0	-62.0	-62.1	124.3
DKH-def2-TZVP	-18.8	-19.2	-606.0	-353.1	138.4	257.3	256.8	-514.1	-61.4	-61.3	122.8
def2-TZVP-uncS	4.4	4.9	-596.8	-340.3	144.4	262.7	263.3	-526.0	-62.5	-62.6	125.2
aug-cc-pVTZ-Jmod	-11.0	-11.5	-603.4	-348.3	139.7	260.0	259.4	-519.3	-62.3	-62.2	124.5
<i>Exp.</i>	<i>68.8</i>	<i>68.8</i>	<i>586.5</i>								

**Table 9. Calculated HFCs (individual components and detailed contributions, in MHz) for  $[\text{Cu}(\text{NH}_3)_4]^{2+}$  obtained with the PBE0 functional and ZORA Hamiltonian with different basis sets.**

<i>Basis set</i>	$A_{11}$	$A_{22}$	$A_{33}$	$A^{FC}$	$A^{PC}$	$A_{11}^{SD}$	$A_{22}^{SD}$	$A_{33}^{SD}$	$A_{11}^{S,dip}$	$A_{22}^{S,dip}$	$A_{33}^{S,dip}$
aug-cc-pVTZ-Junc	-66.5	-67.0	-655.7	-403.4	140.4	258.9	258.4	-517.2	-62.4	-62.3	124.6
aug-cc-pVTZ-J	-41.9	-42.3	-629.8	-379.1	141.1	258.8	258.2	-517.0	-62.6	-62.5	125.2
CP(PPP)	-68.9	69.2	-643.2	-395.3	134.8	251.0	250.5	-501.5	-59.4	-59.3	118.7
aug-cc-pVTZ	-281.5	340.0	340.4	-12.1	145.1	-542.2	270.8	271.3	127.7	-63.8	-63.9
aug-cc-pwCVTZ	234.4	234.8	-356.0	-101.6	139.3	258.7	259.2	-517.8	-62.0	-62.0	124.1
cc-pwCVTZ	237.0	237.4	-353.0	-98.7	139.2	258.3	258.8	-517.1	-61.8	-61.9	123.7
ZORA-def2-TZVP	-58.1	-58.5	-646.2	-392.3	138.0	257.4	257.0	-514.4	-61.3	-61.2	122.4
def2-TZVP-uncS	-30.9	-31.3	-633.5	-376.2	144.4	263.6	263.1	-526.6	-62.6	-62.5	125.0
aug-cc-pVTZ-Jmod	-63.0	-63.5	-651.0	-400.3	141.1	258.8	258.2	-517.0	-62.6	-62.5	125.2
<i>Exp.</i>	<i>68.8</i>	<i>68.8</i>	<i>586.5</i>								

## 2. Basis set applicable for wave function methods

A further consideration in the context of the present study is how appropriate a basis set is for use with correlated wave function methods. Simple test calculations with MP2 and CCSD approaches on  $[\text{Cu}(\text{NH}_3)_4]^{2+}$  confirmed the expectation that aug-cc-pVTZ-J and aug-cc-pVTZ -Junc recover massively more correlation energy than the CP(PPP), in line with the absence of appropriate correlation functions in the latter. All the above observations taken together would seem to suggest that the reference aug-cc-pVTZ -Junc basis set would be the safest choice, however this would be computationally cumbersome. Moreover, it is clear from Table 4 and Table 5 that decontraction of shells with angular momenta higher than  $s$  is unnecessary. This led us to investigate modifications of the -J basis sets that bring the results as close as possible to the reference while constraining the computational cost. The decontraction of  $s$  functions assures converged  $A^{\text{FC}}$  values both in non-relativistic and scalar relativistic calculations. However, close inspection of the Cu  $1s$  orbital revealed that the three innermost  $s$  primitives remain practically unused and have near-zero coefficients. The only condition under which we saw these functions making a noticeable, yet not significant, difference in HFC results was in DKH2 calculations that made use of the finite nucleus model, an approach that will not be further explored here. For the present purposes, we therefore define a modified version of aug-cc-pVTZ-J with decontracted  $s$  functions and removal of the three innermost  $s$  primitives. This leads to the the aug-cc-pVTZ-Jmod basis set  $[22s10p7d3f2g]$ , which is a computationally optimal basis set for the calculation of Cu HFCs that is applicable to all methods considered in the present study.

### 1.4 – Evaluation of commonly used functionals

Now that an optimal basis set has been defined, density functional methods are evaluated in the prediction of reliable and accurate copper hyperfine coupling constants. For that purpose, we exclusively employ our modified basis set, aug-cc-pVTZ-Jmod, and conduct calculations on the complete set of copper complexes. Diverse density functionals are considered such as: GGA (PBE), hybrid (PBE0, B3LYP, B3PW91) and range-separated hybrid (CAM-B3LYP); meta-GGA (TPSS, SCAN) and hybrid meta-GGA (M06, M062X, TPSSH); and double hybrid (B2PLYP). As shown in the previous section, no scalar relativity corrections will be included in the calculations as they were proven to make no difference on average.

On a more technical note, we observed that hybrid functionals seemed to be sensitive to the method used for calculating the spin-orbit contribution. When the SOC operator was set to

compute the Coulomb term with the RI approximation, the calculated HFCs deviated remarkably from the experimental values. Setting this SOC operator to compute the Coulomb term exactly leads to good agreement between calculated and experimental results. When, the Coulomb term was computed semi-numerically, the calculated hyperfine values did not change significantly compared to those obtained with the exact computation of the Coulomb term.

**Table 10.** Calculated HFCs (total values and individual components, in MHz) for  $[\text{Cu}(\text{NH}_3)_4]^{2+}$  obtained with the aug-cc-pVTZ-Jmod basis set using different functionals.

<i>Functional</i>	Total		Isotropic			Anisotropic					
	$A_{II}$	$A_{22}$	$A_{33}$	$A^{FC}$	$A^{PC}$	$A_{II}^{SD}$	$A_{22}^{SD}$	$A_{33}^{SD}$	$A_{II}^{SO,dip}$	$A_{22}^{SO,dip}$	$A_{33}^{SO,dip}$
B3LYP	-2.0	-2.4	-576.6	-320.2	126.5	248.2	247.7	-495.8	-56.5	-56.4	112.9
B3PW91	-19.2	-19.6	-591.2	-337.9	127.9	248.1	247.6	-495.7	-57.3	-57.2	114.4
CAM-B3LYP	-56.0	-56.6	-768.3	-338.7	45.0	259.0	258.5	-517.5	-21.4	-21.3	42.8
M06	-91.0	290.2	290.6	-72.9	236.2	-509.8	254.6	255.2	255.6	-127.7	-127.9
M062X	-241.6	-241.9	-518.5	-675.0	341.0	276.0	275.4	-551.4	-183.6	-183.2	366.9
PBE	6.3	6.5	-502.5	-254.8	91.6	210.9	211.2	-422.0	-41.3	-41.4	82.8
PBE0	-23.8	-24.3	-606.4	-359.5	139.1	258.0	257.4	-515.4	-62.4	-62.3	124.8
SCAN	31.4	33.1	-627.6	-254.0	64.6	246.9	248.7	-495.6	-26.2	-26.2	57.4
TPSS	11.4	11.7	-534.2	-254.5	84.1	218.5	218.8	-437.3	-36.7	-36.8	73.5
TPSSh	-5.4	-5.8	-586.3	-298.0	98.8	236.5	236.0	-472.5	-42.7	-42.6	85.3
<i>Exp.</i>	<i>68.8</i>	<i>68.8</i>	<i>586.5</i>								

**Table 11.** Core and valence-shell spin contributions (in MHz) for  $[\text{Cu}(\text{H}_3)_4]^{2+}$  obtained with the aug-cc-pVTZ-Jmod basis set using different functionals.

<i>Functional</i>	1s	2s	3s	Core	Valence	$A_{iso}$	$\langle S^2 \rangle$	$APD(\langle S^2 \rangle)$
B3LYP	-18.6	-554.4	409.3	-163.7	-30.0	-193.7	0.7524	0.32
B3PW91	-18.0	-567.9	403.0	-182.9	-27.1	-210.0	0.7524	0.32
CAM-B3LYP	-17.9	-578.0	424.9	-171.0	-122.7	-293.6	0.7526	0.35
M06	-6.4	-217.8	286.6	62.3	100.9	163.3	0.7527	0.36
M062X	-9.1	-1420.6	813.5	-616.2	282.2	-334.0	0.7531	0.41
PBE	-9.7	-439.5	297.1	-15.0	-11.2	-163.2	0.7511	0.15
PBE0	-17.9	-620.7	436.3	-202.3	-15.9	-218.2	0.7527	0.36
SCAN	-9.1	-679.1	622.4	-65.8	-121.9	-187.7	0.7526	0.34
TPSS	-8.8	-409.1	283.2	-65.8	-35.7	-170.4	0.7514	0.18
TPSSh	-12.2	-477.0	335.5	-153.7	-45.5	-199.2	0.7520	0.26
					<i>Exp.</i>	<i>241.4</i>	<i>0.7500</i>	

Looking at Table 10, we observe that hybrid functionals (PBE0, B3LYP and B3PW91) reproduce quite well the experimental hyperfine coupling constants of the reference complex  $[\text{Cu}(\text{NH}_3)_4]^{2+}$ . This is not the case for both GGA (PBE), meta-GGA (TPSS, SCAN) and range-

separated (CAM-B3LYP) functionals which deviate from experiment. While PBE and TPSS indeed provide a low  $A_{iso}$  term due to the underestimation of the core-shell spin polarization contributions, the case of CAM-B3LYP is quite different as it suffers from an incorrect description of the spin-orbit contribution with underestimation from both pseudo-contact and second-order dipolar terms. The Minnesota functionals (M06 and M062X) do not reproduce the experimental values at all and behave quite erratically as no trend can be extracted from the predicted individual contributions. These observations are in line with previous studies [13] [83] which reported the inadequate behavior of the Minnesota functionals due to the incorrect description of core spin-densities. From Table 11, it also appears that the second-order dipolar contributions obtained with M06 and M06-2X are poorly predicted both in sign and magnitude. [84] Finally, the individual components calculated with the hybrid meta-GGA (TPSSh) are in fair agreement with experiment and compare well with those obtained with hybrid functionals. Overall, the performances of the above functionals are directly connected to their ability to predict adequate isotropic terms. Indeed, there is a strong diversity of results for  $A_{iso}$  (Table 11) and the performances of the functionals may be related to either core- (M06, PBE, SCAN, TPSS) or valence-shell spin polarization (CAM-B3LYP, M06, M06-2X, SCAN). However, very little spin contamination is observed in general with GGA and meta-GGA functionals having the least deviation from the ideal value of 0.75 for a half-spin system. On the contrary, the Minnesota functionals deviate the most from this value, in line with core contributions being not described properly. This performance evaluation becomes obvious when analyzing the data on absolute percent deviations reported in Table 12 and graphically presented in Figure 3.

**Table 12.** APD values of  $A_{33}$ ,  $A_{iso}$  and  $\Delta A$  for calculated HFCs obtained with the aug-cc-pVTZ-Jmod basis set using different functionals with respect to experimental HFCs for  $[\text{Cu}(\text{NH}_3)_4]^{2+}$ .

<i>Functional</i>	$A_{33}$	$A_{iso}$	$\Delta A$	$APD(A_{33})$	$APD(A_{iso})$	$APD(\Delta A)$
B3LYP	-576.6	193.7	574.6	1.7	19.8	11.0
B3PW91	-591.2	210.0	572.0	0.8	13.0	10.5
CAM-B3LYP	-768.3	293.6	712.3	31.0	21.7	37.6
M06	290.6	163.3	381.6	50.5	32.4	26.3
M062X	-518.5	334.0	276.9	11.6	38.4	46.5
PBE	-502.5	163.2	509.0	14.3	32.4	1.7
PBE0	-606.4	218.2	582.6	3.4	9.6	12.5
SCAN	-627.6	187.7	660.7	7.0	22.2	27.6
TPSS	-534.2	170.4	545.9	8.9	29.4	5.4
TPSSh	-586.3	199.2	580.9	0.0	17.5	12.2
<i>Exp.</i>	<i>586.5</i>	<i>241.4</i>	<i>517.7</i>			



At first glance, hybrid functionals reproduce well the magnitude of the largest hyperfine components,  $A_{33}$ , with an average of 1.5% deviation. The best match is found for the hybrid meta-GGA TPSSh in the case of  $[\text{Cu}(\text{NH}_3)_4]^{2+}$ . For this parameter, the meta-GGA functionals are also competitive with an average of 8% deviation. As previously mentioned, the other functionals are of poor quality for the prediction of  $A_{33}$ . Interestingly, similar trends are observed for the average value of the HFC,  $A_{\text{iso}}$ , where deviations do increase to about 15% for the (PBE0, B3LYP and B3PW91) group of functionals. Finally, the anisotropic parameter,  $\Delta A$ , is also in good agreement with experiment with an average of 11% deviation when looking at the hybrid functionals. The performances of the hybrid meta-GGA, TPSSh, remain correct for both isotropic,  $A_{\text{iso}}$ , and anisotropic,  $\Delta A$ , parameters. The worst performing functionals are M06 and M062X while the GGA and meta-GGA functionals underperform compared to their hybrid counterpart.

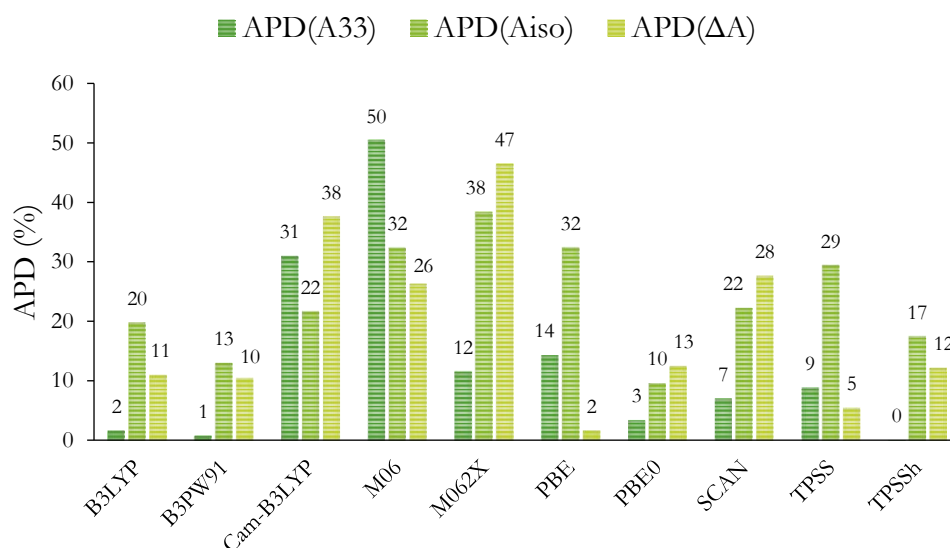


**Figure 3.** Graphical representation of the APD values of calculated  $A_{33}$ ,  $A_{\text{iso}}$  and  $\Delta A$  for  $[\text{Cu}(\text{NH}_3)_4]^{2+}$  obtained with the aug-cc-pVTZ-Jmod basis set using different functionals and compared to experimental results.

From the mean absolute percent deviations shown in Table 13 and Figure 4, we evaluate the ability of a given functional to predict reliable and accurate hyperfine coupling constants over the complete set of complexes (Tables S21-S39). Using our aug-cc-pVTZ-Jmod basis sets, we obtain the following trend: B3PW91 < TPSSh < B3LYP < PBE0 < TPSS < PBE < CAM-B3LYP < SCAN < M062X < M06, with B3PW91 having the lowest deviation from experiment and M06 the largest. Table 13 and Figure 4 both show that B3PW91 is the best performing functional, a

conclusion in line with a previous study. [13] This behavior can be extended to the other hybrid (PBE0 and B3LYP) and hybrid meta-GGA (TPSSh) functionals which feature moderate MADP values with respect to experimental data. On the other hand, and consistently to previous observations, GGA and meta-GGA functionals underperform compared to their hybrid counterparts, while the Minnesota functionals cannot be considered applicable for the prediction of HFCs.

**Table 13.** MAPD values of  $A_{33}$ ,  $A_{iso}$  and  $\Delta A$  with respect to experimental results for the complete set of complexes obtained with the aug-cc-pVTZ-Jmod basis set while using different functionals.

<i>Functional</i>	<i>MAPD(<math>A_{33}</math>)</i>	<i>MAPD(<math>A_{iso}</math>)</i>	<i>MAPD(<math>\Delta A</math>)</i>
B3LYP	6.9	12.5	17.8
B3PW91	8.1	9.0	17.3
CAM-B3LYP	17.5	13.0	28.7
M06	53.3	61.0	14.3
M062X	29.4	76.0	19.9
PBE	14.3	31.1	8.2
PBE0	13.0	9.3	21.7
SCAN	17.0	29.3	27.4
TPSS	10.3	29.1	9.2
TPSSh	6.6	14.2	15.9

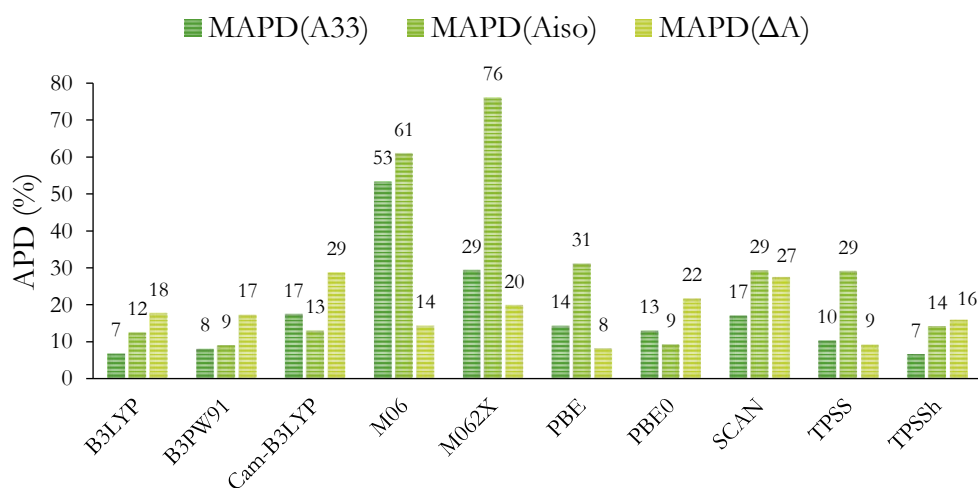


**Figure 4.** Graphical representation of the mean APD values of calculated  $A_{33}$ ,  $A_{iso}$  and  $\Delta A$  for the complete set of complexes obtained with the aug-cc-pVTZ-Jmod basis set using different functionals and compared to experimental results.

To finalize the comparison of DFT methods, we included the double hybrid functional B2PLYP to our study and computed the HFCs for the complete set of complexes. This functional was first evaluated using the mean absolute percent deviations for the Fermi contact term and the three components of the spin dipolar contribution with respect to the ones obtained using the B3PW91 functional and the aug-cc-pVTZ-Jmod basis set. In the specific case of  $[\text{Cu}(\text{NH}_3)_4]^{2+}$ , Table 14 shows that B2PLYP provide calculated values for the spin-dipolar terms close to those obtained with B3PW91, but deviates in a non-negligible manner for the Fermi contact term.

**Table 14.** Hyperfine contributions  $A^{FC}$  and  $A^{SD}$  (total values and individual components, in MHz) using the aug-cc-pVTZ-Jmod basis set and the B2PLYP functional and absolute APD values for  $[\text{Cu}(\text{NH}_3)_4]^{2+}$  with respect to B3PW91 values.

	$A^{FC}$	$A_{11}^{SD}$	$A_{22}^{SD}$	$A_{33}^{SD}$	$APD(A^{FC})$	$APD(A_{11}^{SD})$	$APD(A_{22}^{SD})$	$APD(A_{33}^{SD})$
B2PLYP	-382.7	261.7	261.2	-522.9	13.2	5.5	5.5	5.5
B3PW91	-337.9	248.1	247.6	-495.7				

Looking at the entire set of complexes (Table 14 and Table S40-S41), the following mean absolute percent deviations were obtained:  $\text{MAPD}(A^{FC}) = 16$ ,  $\text{MAPD}(A_{11}^{SD}) = 12$ ,  $\text{MAPD}(A_{22}^{SD}) = 8$ , and  $\text{MAPD}(A_{33}^{SD}) = 10$ . On average, the value that deviates the most is for the Fermi contact term while the predicted spin-dipolar terms remain within an acceptable range of deviation, i.e. 10% on average. This initial comparison between B2PLYP with B3PW91 only gives an estimate on the ability of this double hybrid functional to predict HFCs. However, due to the lack of the spin-orbit contribution, which is not implemented for the B2PLYP method, the total hyperfine coupling constants cannot be directly calculated. To overcome this, we simply added the individual spin-orbit terms,  $A^{SO}$ , calculated with B3PW91 to the remaining B2PLYP components and obtain fully comparable hyperfine tensors for the entire set of complexes.

**Table 15.** Mean APDs of  $A_{33}$ ,  $A_{iso}$  and  $\Delta A$  with respect to experimental results for the complete complex set obtained with B2PLYP using B3PW91  $A^{SO}$  values and the aug-cc-pVTZ-Jmod basis set.

<i>Functional</i>	<i>MAPD(<math>A_{33}</math>)</i>	<i>MAPD(<math>A_{iso}</math>)</i>	<i>MAPD(<math>\Delta A</math>)</i>
B2PLYP	19.4	19.5	24.7
B3PW91	8.1	9.0	17.3

While it seems promising for the case of  $[\text{Cu}(\text{NH}_3)_4]^{2+}$ , the HFCs obtained with B2PLYP using the SOC contributions from B3PW91 are well above an acceptable error range for the complete set of complexes (Table S40-S41). Finally reports the mean absolute percent deviations for the 20 complexes and we observe that the errors are evenly distributed between the studied parameters,  $A_{33}$ ,  $A_{iso}$  and  $\Delta A$ , and much greater than B3PW91, making B2PLYP an unfit DFT functional to predict Cu hyperfine coupling constants.

### 1.5 – Comparison of wavefunction methods with respect to DFT

Most of the correlated wave function calculations required an auxiliary basis set for the resolution of the identity approximations that are used either optionally or by default, as for example in the OO methods and in DLPNO-CCSD. Standard main basis sets often have custom-made auxiliary bases for correlation fitting, denoted as /C. This is the case for the def2 family and the correlation consistent (cc-pVnZ) series of basis sets. However, neither the standard basis sets identified in the benchmark DFT calculations as potential candidates for the calculation of copper hyperfine coupling constants, nor our final choice defined above (aug-cc-pVTZ-Jmod) have dedicated auxiliary basis sets. It is noted that for the aug-cc-pVTZ-J basis set it appears that the standard aug-cc-pVTZ/C is sufficient, both in non-relativistic and DKH2 scalar relativistic calculations. In comparison, the aug-cc-pwCVTZ/C and the larger aug-cc-pVQZ/C auxiliary basis perform less well, demonstrating the low tolerances involved in adapting a correlation fitting basis set to a specific size and type of main basis. It is also noted that the def2/C basis sets are inadequate when either the aug-cc-pVTZ-J or the smaller CP(PPP) were used as main basis sets for Cu. Modifications of standard basis sets to make them more appropriate for aug-cc-pVTZ-Jmod did not show a systematic trend, therefore we opted instead for the automatic generation procedure encoded in ORCA, [64] which led to a [38s37p37d35f35g7h5i] auxiliary that reproduced exactly the non-RI energies and properties.

The wave function methods studied here for the evaluation of hyperfine coupling constants can only provide the  $A^{FC}$  and the  $A^{SD}$  terms. A first evaluation was therefore carried out with respect to the corresponding terms obtained from the best performing DFT method, B3PW91. The resulting data are presented in Table 16 and Figure 5 for the mean absolute percent deviations and detailed contributions are reported in Supplementary Information (Table S42).

**Table 16.** Mean APDs for the complete set of complexes using the aug-cc-pVTZ-Jmod basis set and different wave function methods, with respect to B3PW91 values.

<i>Wave function method</i>	<i>MAPD(<math>A^{FC}</math>)</i>	<i>MAPD(<math>A_{11}^{SD}</math>)</i>	<i>MAPD(<math>A_{22}^{SD}</math>)</i>	<i>MAPD(<math>A_{33}^{SD}</math>)</i>
DLPNO-CCSD	13.7	24.1	19.1	21.4
HF	56.1	49.4	42.2	45.8
MP2	47.6	36.8	44.1	37.6
OO-MP2	61.5	54.5	47.4	51.4
OO-SCS-MP2	56.7	33.2	22.7	27.8

The Fermi contact term appears to be the most sensitive parameter for HF, MP2, OO-MP2 and OO-SCS-MP2 methods. Except for OO-SCS-MP2, the calculated spin-dipolar contributions also deviate quite significantly from the B3PW91 reference values. On the other hand, the opposite trend is observed for DLPNO-CCSD which is the best performing wave function based method since it displays the smallest mean deviations.

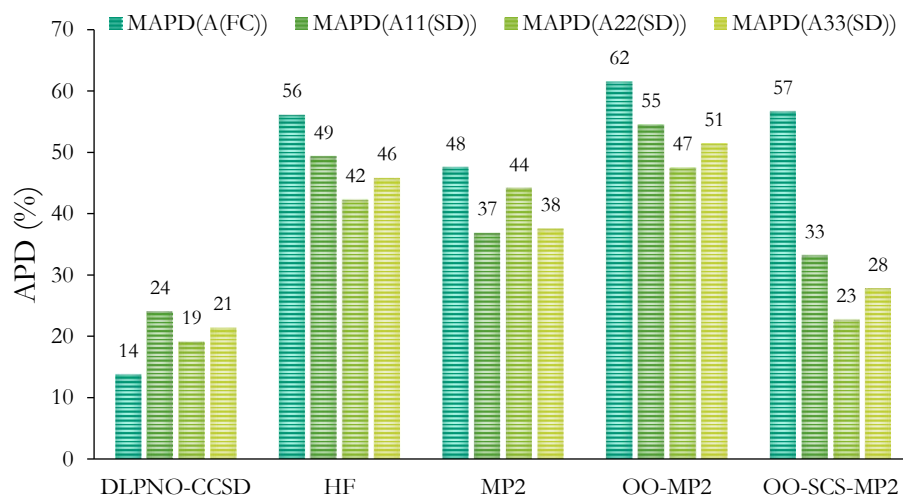


**Figure 5.** Graphical representation of the mean APD values of calculated  $A^{FC}$  and  $A^{SD}$  for the complete set of complexes using the aug-cc-pVTZ-Jmod basis set and different wave function methods with respect to B3PW91 values.

A second evaluation was conducted with respect to experimental results. In this case, the  $A^{SO}$  obtained from B3PW91 is applied to each wave function method to yield complete hyperfine coupling constants. Table 17 and Figure 6 finally reports the mean absolute percent deviations for the calculated HFCs of the 20 complexes.

Table 17. MAPD values of  $A_{33}$ ,  $A_{iso}$  and  $\Delta A$  with respect to experimental results for the complete complex set obtained with different wave function methods using B3PW91  $A^{SO}$  values and the aug-cc-pVTZ-Jmod basis set.

Wave function method	MAPD( $A_{33}$ )	MAPD( $A_{iso}$ )	MAPD( $\Delta A$ )
DLPNO-CCSD	26.4	12.8	41.0
HF	77.4	74.6	83.9
MP2	54.4	50.4	72.9
OO-MP2	68.7	70.4	56.2
OO-SCS-MP2	59.6	75.1	33.8
B3PW91	8.1	9.0	17.3

Once the SOC terms have been added and the total components evaluated against experimental values, a general trend in absolute percent deviation can be extracted: B3PW91 < DLPNO-CCSD < OO-SCS-MP2 < MP2 < OO-MP2 < HF, with B3PW91 having the lowest deviation from experiment and HF the largest. B3PW91 continues to perform much better as a DFT method compared to any other *ab initio* methods.

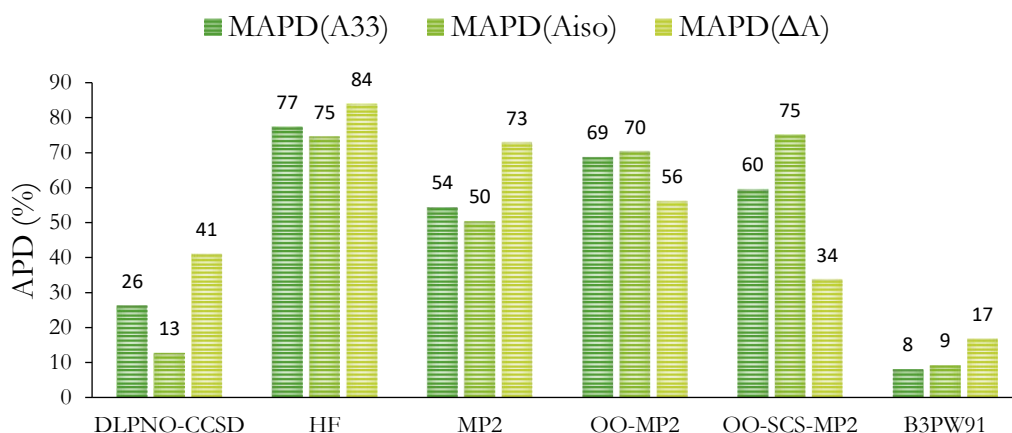


Figure 6. Graphical representation of the mean APD values of calculated  $A_{33}$ ,  $A_{iso}$  and  $\Delta A$  for the complete set of complexes obtained with the aug-cc-pVTZ-Jmod basis set and different wave function methods, using  $A^{SO}$  contributions from B3PW91, with respect to experimental results.

A closer look at these data also shows that DLPNO-CCSD offers the best results with a reasonably low deviation for the prediction of the isotropic hyperfine contribution. The OO-SCS-MP2 is the second-best performing method due to its low  $\Delta A$  deviation. On the contrary, the MAPD deviation of both the  $A_{33}$  and  $A_{iso}$  terms is quite high and of similar magnitude than the ones obtained with OO-MP2. The opposite trend is found for the MP2 case: the  $\Delta A$  deviation is

greater than the one obtained for  $A_{33}$  and  $A_{iso}$ . The simple HF calculation is consistent throughout the terms but highly inaccurate. Overall, none of the wave-function based methods can compete with B3PW91 for the prediction of accurate HFCs. The only promising approach among the methods examined here is DLPNO-CCSD, but this still lags behind DFT on average. It will be interesting to see whether future developments, for example by incorporating the effects of triples excitations, can offer better control of errors and thereby improve the performance of this approach.

## 1.6 – Conclusions

In this section, we evaluated the performance of DFT and modern wave function based methods for the prediction of Cu hyperfine coupling constants, using a large set of 20 complexes with experimentally known structures and resolved EPR parameters. We defined a computationally optimal basis set for Cu, the aug-cc-pVTZ-Jmod basis set, a modified version of aug-cc-pVTZ-J with decontracted  $s$  functions and removal of innermost  $s$  primitives, as a robust, flexible and generally applicable basis set that can be used with all quantum chemical methods tested in the present study. With this basis set we carried out an unbiased evaluation of a series of DFT methods representing all families of functionals, and of wave function based methods. Our results indicated that the hybrid functional B3PW91 performs best, as it features the lowest mean absolute percent deviation of the total HFC with respect to experimental data. It was also shown that, to a lesser extent, hybrid and hybrid meta-GGA functionals such as TPSSH, B3LYP and PBE0 are also able to provide accurate and reliable hyperfine tensors. On the contrary, more modern functionals, such as the range-separated CAM-B3LYP or both Minnesota functionals, yielded poor estimations of the total HFCs. Consistently with previous reports, net underestimations were observed with GGA while meta-GGA functionals underperform compared to their hybrid counterparts. The double hybrid functional B2PLYP was also included in the prediction of HFCs and when evaluated against the reference functional B3PW91, the resulting mean error showed that B2PLYP cannot deliver a reliable prediction of Cu HFCs. A similar conclusion is reached when investigating the performance of wave function based methods. Currently these approaches only calculate the Fermi contact and spin-dipolar terms. To overcome this limitation, the SOC contribution from B3PW91 was added to generate complete hyperfine coupling constants. Within this approximation, the DLPNO-CCSD method provided the best results, but does not compete with hybrid and hybrid meta-GGA functionals. In conclusion, and despite its shortcomings, DFT remains the method of choice for the calculation of Cu(II) hyperfine coupling constants.

## 2 – Convergence studies of basis sets and DFT functionals for the calculation of the $g$ -tensor.

To conduct our calibration study for the calculation of  $g$ -tensors of mononuclear copper complexes, we used the extensive set of systems selected for the first part of this chapter. The set of complexes is depicted in Figure 1, and their corresponding  $g$ -tensors are reported in Table 18. Encompassing the wide range of coordinating atoms, ligands, and general variability in coordination chemistry, it ensures a wide range of Cu(II) complexes with distinct properties.

Table 18. List of the Cu(II) complexes considered in this study together with their experimental  $g$ -tensors.

Entry	Complex	$g_x$	$g_y$	$g_z$	Ref.
1	[Cu(NH <sub>3</sub> ) <sub>4</sub> ] <sup>2+</sup>	2.047	2.047	2.241	[21]
2	[Cu(dtc) <sub>2</sub> ]	2.025	2.025	2.085	[22]
3	[Cu(acac) <sub>2</sub> ]	2.060	2.060	2.285	[23]
4	[Cu(en) <sub>2</sub> ] <sup>2+</sup>	2.040	2.046	2.202	[24]
5	[Cu(mnt) <sub>2</sub> ] <sup>2-</sup>	2.023	2.023	2.093	[25]
6	[Cu(gly) <sub>2</sub> ]	2.052	2.052	2.267	[21]
7	[Cu(kts)]	2.030	2.030	2.140	[26]
8	[Cu(sac) <sub>2</sub> ]	2.050	2.050	2.240	[27]
9	[Cu(im) <sub>4</sub> ] <sup>2+</sup>	2.047	2.047	2.262	[21]
10	[Cu(py) <sub>4</sub> ] <sup>2+</sup>	2.053	2.053	2.263	[21]
11	[Cu(eta)] <sup>2+</sup>	2.030	2.030	2.160	[28]
12	[Cu(epa)(H <sub>2</sub> O)] <sup>2+</sup>	2.053	2.053	2.213	[29]
13	[Cu(atpt)] <sup>2+</sup>	2.100	2.100	2.235	[30]
14	[Cu(H <sub>2</sub> GGH)] <sup>-</sup>	-	-	2.173	[13]
15	[Cu(H <sub>2</sub> GGG)] <sup>-</sup>	-	-	2.202	[13]
16	[Cu(salpn) <sub>2</sub> ]	2.060	2.060	2.261	[31]
17	[Cu(S,S-mnpala) <sub>2</sub> ]	2.060	2.060	2.240	[32]
18	[Cu(salen) <sub>2</sub> ]	2.052	2.052	2.192	[33]
19	[Cu(bipy) <sub>2</sub> (NCS)] <sup>+</sup>	2.088	2.088	2.259	[34]
20	[Cu(ttcn) <sub>2</sub> ] <sup>2+</sup>	2.045	2.045	2.117	[35]



To assess the performance of the calculations of  $g$ -tensors, we evaluated the  $g$ -shift,  $\Delta g$ , which is the difference between the calculated  $g$  value and the  $g$  of a free electron multiplied by 1000 ( $\Delta g = (g_{calc} - g_e) \times 1000$  with  $g_e = 2.0023$ ). [85] Then, the absolute percent deviation (APD) is calculated with respect to the experimental  $g$ -shift. The APD values will be determined for the  $g_L$ ,  $g_{//}$ , and  $g_{iso}$  parameters. The  $g_L$  value is obtained as the average between the two lowest calculated  $g$  values while the  $g_{//}$  value is the largest calculated  $g$  one. The  $g_{iso}$  parameter is the average of all three  $g$  values. The APD values are evaluated in the following manner:

$$APD(\Delta g_L^{(M)}) = \left| \frac{\Delta g_L^{(M)} - \Delta g_L^{exp}}{\Delta g_L^{exp}} \right| \times 100,$$

$$APD(\Delta g_{//}^{(M)}) = \left| \frac{\Delta g_{//}^{(M)} - \Delta g_{//}^{exp}}{\Delta g_{//}^{exp}} \right| \times 100, \text{ and}$$

$$APD(\Delta g_{iso}^{(M)}) = \left| \frac{\Delta g_{iso}^{(M)} - \Delta g_{iso}^{exp}}{\Delta g_{iso}^{exp}} \right| \times 100.$$

The mean APD (MAPD) values are thus used to evaluate the performance of a given computational method to predict a specific  $g$  parameter over the complete set of complexes.

The computational details for the calculation of  $g$ -tensors are essentially identical to those used for evaluating the hyperfine coupling constants in the first part of the chapter. In summary, DFT methods evaluated in the calculation of  $g$ -tensors include the following functionals: PBE, [41] TPSS, [42] SCAN, [43] B3LYP, [44] [45] CAM-B3LYP, [48] B3PW91, [44] [46] PBE0, [47] TPSSh, [49] M06, [50] M06-2X, [50]. The calculations used increased general integration grids (Grid6 in ORCA convention), further increased radial integration accuracy (IntAcc 6.0) and specially enhanced grids for copper (SpecialGridIntAcc 11). For all ligand atoms, the def2-TZVP basis sets [39] were used. The spin-orbit coupling operator was treated by an accurate mean-field (SOMF) approximation to the Breit–Pauli operator (SOCType 3 in ORCA). [52] [53] The potential was constructed to include one-electron terms, compute the Coulomb term in a semi-numeric way, incorporate exchange via one-center exact integrals including the spin-other orbit interaction, and include local DFT correlation (SOCFlags 1,2,3,1 in ORCA). Scalar relativistic calculations were performed with the second-order Douglas–Kroll–Hess (DKH2) [54] [55] [56] [57] [58] [59] [60] and the zeroth-order regular approximation (ZORA) [61] [62] [63] Hamiltonians. Given the different behavior of these methods close to the nucleus, [64] the appropriateness of the basis set

for Cu was carefully studied and purpose-made basis sets were used where available. Picture change effects were applied as appropriate.

## 2.1 – Performance assessment of basis sets

Comparative studies were first carried using selected basis sets for the computation of the copper  $g$ -tensors. Using the  $[\text{Cu}(\text{NH}_3)_4]^{2+}$  complex as reference, the  $g$ -tensors were obtained with DFT employing the PBE0 [47] functional. Looking at Table 19 and graphically presented in Figure 7, the  $\Delta g_L$ ,  $\Delta g_{//}$  and  $\Delta g_{iso}$  values do not vary much when changing the basis set. It is obvious that there is little influence of the basis set in the calculation of  $g$ -tensors. This is especially important when considering our home-made basis set, aug-cc-pVTZ-Jmod, which is found to produce similar results for the calculation of  $g$ -tensors with respect to those obtained with the reference basis aug-cc-pVTZ-Junc and its parent basis set aug-cc-pVTZ-J. These results were reproduced using the B3PW91, [44] [46] functional and led to the same conclusion (Table S43 and Figure S11).

**Table 19. Calculated  $g$ -tensors of  $[\text{Cu}(\text{NH}_3)_4]^{2+}$  obtained with PBE0 functional and selected basis sets.**

<i>PBE0</i>	$g_x$	$g_y$	$g_z$	$\Delta g_L$	$\Delta g_{//}$	$\Delta g_{iso}$	$APD(\Delta g_L)$	$APD(\Delta g_{//})$	$APD(\Delta g_{iso})$
aug-cc-pVTZ	2.053	2.053	2.189	50.7	186.7	96.0	13.4	21.8	12.2
aug-cc-pVTZ-J	2.053	2.053	2.189	50.7	186.7	96.0	13.4	21.8	12.2
aug-cc-pVTZ-Jmod	2.053	2.053	2.190	50.7	187.7	96.3	13.4	21.4	11.9
aug-cc-pVTZ-Junc	2.053	2.053	2.189	50.7	186.7	96.0	13.4	21.8	12.2
aug-cc-pwCVTZ	2.053	2.053	2.189	50.7	186.7	96.0	13.4	21.8	12.2
cc-pwCVTZ	2.053	2.053	2.188	50.7	185.7	95.7	13.4	22.2	12.5
CP(PPP)	2.053	2.053	2.184	50.7	181.7	94.3	13.4	23.9	13.7
def2-TZVP	2.053	2.052	2.185	49.7	182.7	94.0	11.2	23.5	14.0
<i>Exp.</i>	<i>2.047</i>	<i>2.047</i>	<i>2.241</i>	<i>44.7</i>	<i>238.7</i>	<i>109.3</i>			

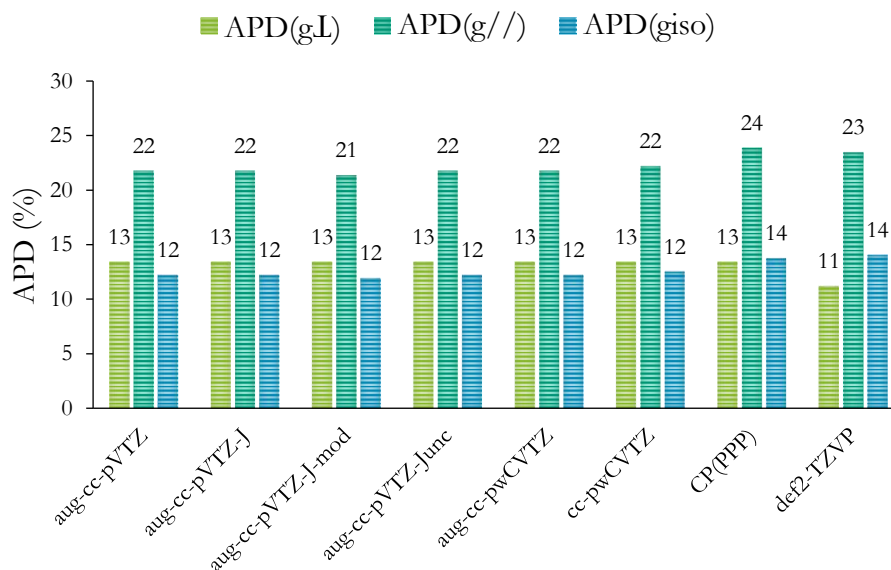


**Figure 7.** Graphical representation of the APD values of calculated  $g$ -tensors for  $[\text{Cu}(\text{NH}_3)_4]^{2+}$  obtained with the PBE0 functional and selected basis sets.

## 2.2 – Evaluation of functionals and scalar relativistic approaches

The performances of density functional methods were also evaluated in the prediction of  $g$ -tensors. For that purpose, we exclusively employ our modified basis set, aug-cc-pVTZ-Jmod, and conduct calculations on the selected set of copper complexes. The same library of density functionals is considered: GGA (PBE), hybrid (PBE0, B3LYP, B3PW91) and range-separated hybrid (CAM-B3LYP); meta-GGA (TPSS, SCAN) and hybrid meta-GGA (M06, M062X, TPSSh).

We started our investigation by considering two scalar relativistic Hamiltonians, DKH2 and ZORA, using the complete library of functionals and the  $[\text{Cu}(\text{NH}_3)_4]^{2+}$  complex. Table 20, Table 21, and Table 22 show that there is no significant improvement in the predicted  $g$ -tensors whether we vary the nature of the functional used or include relativistic corrections (Figures S12, S13, and S14). For instance, the greatest deviation obtained with hybrid functionals is roughly 3% which will not affect the  $g$ -tensors in terms of absolute values. More important deviations are seen in the case of M06 or M062X functionals and tend to worsen the results when applying scalar relativistic corrections. Considering the small improvement for the calculation of both copper HFCs and  $g$ -tensors, these methods will not be further employed in the present study. It is worth noting that these results are also confirmed with both the  $[\text{Cu}(\text{dtc})_2]$  and the  $[\text{Cu}(\text{acac})_2]$  complexes and are reported in the Supplementary Information (Tables S44-S49 and Figures S15-S20).

When evaluating the  $g$ -tensors without any scalar relativistic corrections (Table 20), an initial trend can be deduced in terms of functional performances by comparing the computational results with experimental values. In general, hybrid functionals (B3LYP, B3PW91, PBE0) and meta-hybrids (TPSSh) have the lowest deviation with respect to experimental values rendering them the most suitable DFT methods to predict  $g$ -tensors. These results are in line with other computational studies focusing on the prediction of  $g$ -tensors in transition metal complexes. [86] Hybrid functionals are better at predicting the  $\Delta g_L$  values rather than the  $\Delta g_{//}$ . The origin of such discrepancy lies in the underestimation of the largest  $g$  component which has been also observed in previous computational studies and could be due to a poor modeling of the metal-ligand covalency effects. The  $g$ -shifts being proportional to the excitation energy, metal–ligand covalency in both the ground and the excited states must be well reproduced if one wants to obtain realistic excitation energies and accurate  $g$ -shifts [87]

Therefore, there is an ease in the calculation of small values within the  $\Delta g_L$  and a difficulty to produce the larger component of the  $\Delta g_{//}$  which ends up being usually lower than the experimental one, leading to greater deviations.

**Table 20.** Calculated  $g$ -tensors (individual components,  $g$ -shifts, and APDs) of  $[\text{Cu}(\text{NH}_3)_4]^{2+}$  obtained with selected functionals with the aug-cc-pVTZ-Jmod basis set without applying any scalar relativistic corrections.

<i>Functional</i>	$g_x$	$g_y$	$g_z$	$\Delta g_L$	$\Delta g_{//}$	$\Delta g_{iso}$	$APD(\Delta g_L)$	$APD(\Delta g_{//})$	$APD(\Delta g_{iso})$
B3LYP	2.048	2.048	2.170	45.4	167.9	86.2	1.7	29.7	21.1
B3PW91	2.048	2.048	2.172	45.9	169.7	87.1	2.7	28.9	20.3
CAM-B3LYP	2.020	2.020	2.073	17.5	70.3	35.1	60.9	70.6	67.9
M06	2.067	2.067	2.327	64.8	325.0	151.5	45.0	36.2	38.6
M062X	2.116	2.116	2.523	113.3	520.8	249.1	153.5	118.2	127.8
PBE	2.053	2.053	2.190	50.7	187.3	96.2	13.5	21.5	12.0
PBE0	2.053	2.053	2.190	50.7	187.3	96.2	13.5	21.5	12.0
SCAN	2.028	2.028	2.093	26.0	91.0	47.6	41.9	61.9	56.4
TPSS	2.033	2.033	2.113	30.8	110.7	57.4	31.1	53.6	47.5
TPSSh	2.039	2.039	2.133	37.0	130.9	68.3	17.2	45.2	37.6
<i>Exp.</i>	<i>2.047</i>	<i>2.047</i>	<i>2.241</i>	<i>44.7</i>	<i>238.7</i>	<i>109.3</i>			

**Table 21** Calculated  $g$ -tensors (individual components,  $g$ -shifts, and APDs) of  $[\text{Cu}(\text{NH}_3)_4]^{2+}$  obtained with selected functionals with the aug-cc-pVTZ-Jmod basis employing the DKH2 Hamiltonian.

<i>Functional</i>	$g_x$	$g_y$	$g_z$	$\Delta g_{\parallel}$	$\Delta g_{\perp}$	$\Delta g_{\text{iso}}$	$APD(\Delta g_{\parallel})$	$APD(\Delta g_{\perp})$	$APD(\Delta g_{\text{iso}})$
B3LYP	2.049	2.049	2.174	46.7	171.3	88.2	4.4	28.2	19.3
B3PW91	2.049	2.049	2.175	47.1	173.1	89.1	5.4	27.5	18.5
CAM-B3LYP	2.020	2.020	2.073	17.5	70.6	35.2	60.9	70.4	67.8
M06	2.070	2.070	2.348	68.1	345.2	160.4	52.4	44.6	46.7
M062X	2.119	2.120	2.543	117.2	541.1	258.5	162.3	126.7	136.4
PBE	2.035	2.035	2.123	32.6	120.8	62.0	27.0	49.4	43.3
PBE0	2.054	2.054	2.193	51.8	190.5	98.0	16.0	20.2	10.3
SCAN	2.029	2.029	2.093	26.3	90.7	47.7	41.2	62.0	56.3
TPSS	2.034	2.034	2.114	31.6	112.0	58.4	29.3	53.1	46.6
TPSSh	2.040	2.040	2.135	37.7	132.6	69.3	15.7	44.5	36.6
<i>Exp.</i>	<i>2.047</i>	<i>2.047</i>	<i>2.241</i>	<i>44.7</i>	<i>238.7</i>	<i>109.3</i>			

**Table 22.** Calculated  $g$ -tensors (individual components,  $g$ -shifts, and APDs) of  $[\text{Cu}(\text{NH}_3)_4]^{2+}$  obtained with selected functionals with the aug-cc-pVTZ-Jmod basis employing the ZORA Hamiltonian.

<i>Functional</i>	$g_x$	$g_y$	$g_z$	$\Delta g_{\parallel}$	$\Delta g_{\perp}$	$\Delta g_{\text{iso}}$	$APD(\Delta g_{\parallel})$	$APD(\Delta g_{\perp})$	$APD(\Delta g_{\text{iso}})$
B3LYP	2.049	2.049	2.173	46.6	170.9	88.0	4.4	28.4	19.5
B3PW91	2.049	2.049	2.175	47.1	172.6	88.9	5.4	27.7	18.7
CAM-B3LYP	2.020	2.020	2.073	17.6	70.6	35.2	60.7	70.4	67.8
M06	2.070	2.071	2.347	68.1	345.1	160.4	52.5	44.6	46.7
M062X	2.119	2.119	2.541	116.7	538.5	257.3	161.1	125.6	135.3
PBE	2.035	2.035	2.123	32.6	120.5	61.9	27.0	49.5	43.4
PBE0	2.054	2.054	2.192	51.8	190.0	97.9	16.0	20.4	10.5
SCAN	2.029	2.029	2.093	26.3	90.6	47.7	41.1	62.0	56.3
TPSS	2.034	2.034	2.114	31.7	111.8	58.4	29.1	53.2	46.6
TPSSh	2.040	2.040	2.135	37.7	132.3	69.3	15.6	44.6	36.7
<i>Exp.</i>	<i>2.047</i>	<i>2.047</i>	<i>2.241</i>	<i>44.7</i>	<i>238.7</i>	<i>109.3</i>			

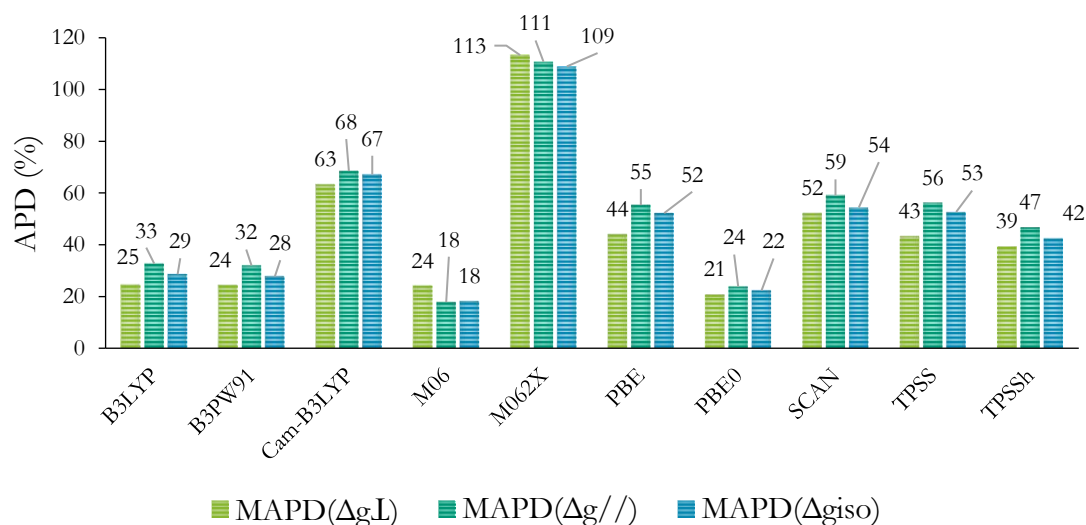
We extend the calculation of the  $g$ -tensors for all complexes using the selected functionals and assess their performance. (Supplementary Information, Tables S50-SS66) From the mean absolute percent deviations shown in Table 23 and Figure 8 obtained using our aug-cc-pVTZ-Jmod basis sets, we observe the following trend in performance evaluation:  $\text{M06} < \text{PBE0} < \text{B3PW91} < \text{B3LYP} < \text{TPSSh} < \text{PBE} < \text{TPSS} < \text{SCAN} < \text{CAM-B3LYP} < \text{M062X}$ , with M06 having the lowest deviation from experiment and M062X the largest. While M06 appears as the best performing functional to reproduce experimental  $g$ -shifts, it is unable to predict accurate hyperfine coupling constants which makes it an unreliable method if one wants to use it to calculate the full set of

EPR parameters in mononuclear copper complexes. Hybrid functionals (PBE0, B3PW91, and B3LYP) and hybrid meta-GGA (TPSSh) are next in line, predicting  $g$  values within reasonable MAPDs when compared to experimental data. On the contrary, GGA and meta-GGA functionals underperform compared to their hybrid counterparts and in general, the  $\Delta g_{\perp}$  is better predicted than the  $\Delta g_{\parallel}$  value due to the observed underestimation of  $g_{\parallel}$  when compared to experiment.

**Table 23.** Calculated MAPD values for  $\Delta g_{\perp}$ ,  $\Delta g_{\parallel}$  and  $\Delta g_{iso}$  of the complete complex set of complexes obtained with selected functionals using the aug-cc-pVTZ-Jmod basis sets.

<i>Functional</i>	<i>MAPD(<math>\Delta g_{\perp}</math>)</i>	<i>MAPD(<math>\Delta g_{\parallel}</math>)</i>	<i>MAPD(<math>\Delta g_{iso}</math>)</i>	<i>Avg. MAPD</i>
B3LYP	24.6	32.7	28.6	28.6
B3PW91	24.4	32.0	27.8	28.1
Cam-B3LYP	63.3	68.5	67.2	66.3
M06	24.1	17.8	18.2	20.1
M062X	113.3	110.7	108.9	111.0
PBE	44.0	55.3	52.2	50.5
PBE0	20.7	23.8	22.3	22.3
SCAN	52.1	59.1	54.4	55.2
TPSS	43.3	56.3	52.7	50.7
TPSSh	39.3	46.7	42.5	42.8

### A) MAPD( $\Delta g_L$ , $\Delta g_{//}$ , $\Delta g_{iso}$ )



### B) Avg. MAPD

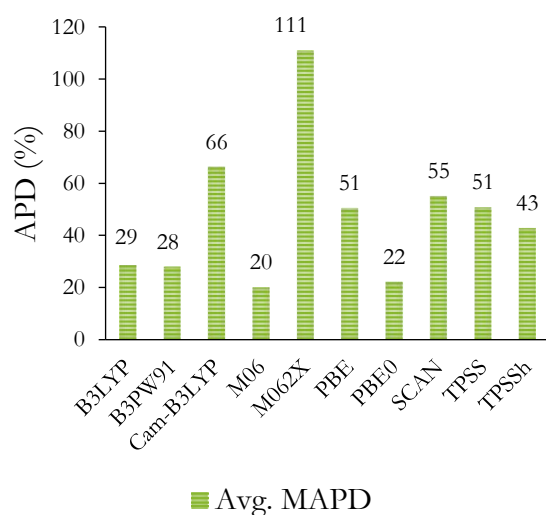


Figure 8. Graphical representation of the calculated MAPD values for  $\Delta g_L$ ,  $\Delta g_{//}$  and  $\Delta g_{iso}$  (A) and the average MAPD (B) of the complete set of complexes using selected functionals and the aug-cc-pVTZ-Jmod basis sets.

## 2.3 – Conclusions

In this section, we evaluated the performance of DFT for the prediction of Cu  $g$ -tensors, using a large set of 20 complexes with experimentally known structures and resolved EPR parameters. We tested the computationally optimal basis set for Cu, the aug-cc-pVTZ-Jmod basis set, and other commonly used basis sets, but we did not observe any real effect for the calculation of the  $g$ -tensor. Our results indicated, however, that the use of various functionals clearly affects the accuracy of the calculation. Interestingly, M06 was the best performing functional in predicting  $g$ -

tensors, probably linked to the increased Hartree-Fock admixture employed in the functional. Following in line, hybrid functionals such as PBE0, B3PW91, B3LYP and the meta-hybrid, TPSSH, also provide accurate and reliable  $g$ -tensor values. On the contrary, more modern functionals, such as the range-separated CAM-B3LYP or the M062X, yielded poor estimations of the total  $g$  values. Consistently with previous reports, net underestimations were observed with GGA and meta-GGA functionals that were found to underperform when compared to their hybrid counterparts. It was observed that the  $\Delta g_L$  is better predicted than the  $\Delta g_{//}$  due to a probable underestimation of the metal-ligand covalency that is reflected in the excitation energies making it easier to predict the small values represented in  $g_L$  and difficult for the larger one,  $g_{//}$ .

To obtain a complete prediction of the EPR signature of a given copper complex, both the  $g$ -tensor and  $A$ -tensors need to be properly evaluated. The  $g$ -tensors are less sensitive to the basis set, whereas the opposite is true in the case of the HFCs. The M06 functional is best performing in the calculation of  $g$ -tensors but provides very poor predictions in the case of the HFCs. In both cases, scalar relativistic methods were not significant in improving the DFT modeling.

All in all, a compromise is met, with the use of the hybrid DFT methods like PBE0 or B3PW91 while employing the purpose made aug-cc-pVTZ-Jmod. This methodology will be applied in the study of more realistic systems as it will be discussed in the following chapter: Chapter III. Prediction of EPR parameters for the LPMO active site and a synthetic LPMO-like peptide.

## REFERENCES

- [1] E. I. Solomon, U. M. Sundaram and T. E. Machonkin, "Multicopper oxidases and oxygenases," *Chemical Reviews*, vol. 96, no. 7, pp. 2563-2605, 1996.
- [2] R. L. Peterson, S. Kim and K. D. Karlin, "Comprehensive Inorganic Chemistry II," Amsterdam, Elsevier, 2013, pp. 149-177.
- [3] R. Trammell, K. Rajabimoghadam and I. Garcia-Bosch, "Copper-promoted functionalization of organic molecules: from biologically relevant Cu/O<sub>2</sub> model systems to organometallic transformations," *Chemical Reviews*, vol. 119, no. 4, pp. 2954-3031, 2019.



- [4] E. Garriba and G. Micera, "The determination of the geometry of Cu(II) complexes - An EPR spectroscopy experiment," *Journal of Chemical Education*, vol. 83, no. 8, pp. 1229-1232, 2006.
- [5] P. Bertrand, *Electronic paramagnetic resonance spectroscopy: fundamentals*, Springer International Publishing, 2020.
- [6] P. Bertrand, *Electron paramagnetic resonance spectroscopy: applications*, Springer International Publishing, 2020.
- [7] M. Kaupp, M. Buhl and V. G. Malkin, *Calculation of NMR and EPR parameters: Theory and applications*, Weinheim: Wiley-VCH, 2004.
- [8] F. Neese, "Metal and ligand hyperfine couplings in transition metal complexes: The effect of spin-orbit coupling as studied by coupled perturbed Kohn-Sham theory," *Journal of Chemical Physics*, vol. 118, no. 9, pp. 3939-3948, 2003.
- [9] F. Neese, "Prediction of molecular properties and molecular spectroscopy with density functional theory: From fundamental theory to exchange-coupling," *Coordination Chemistry Reviews*, vol. 253, no. 5-6, pp. 526-563, 2009.
- [10] M. Munzarova and M. Kaupp, "A critical validation of density functional and coupled-cluster approaches for the calculation of EPR hyperfine coupling constants in transition metal complexes," *Journal of Physical Chemistry A*, vol. 103, no. 48, pp. 9966-9983, 1999.
- [11] E. Malkin, I. Malkin, O. L. Malkina, V. G. Malkin and M. Kaupp, "Scalar relativistic calculations of hyperfine coupling tensors using the Douglas-Kroll-Hess method with a finite-size nucleus model," *Physical Chemistry Chemical Physics*, vol. 8, no. 35, pp. 4079-4085, 2006.
- [12] S. Kossmann, B. Kirchner and F. Neese, "Performance of modern density functional theory for the prediction of hyperfine structure: meta-GGA and double hybrid functionals," *Molecular Physics*, vol. 105, no. 15-16, pp. 2049-2071, 2007.
- [13] G. Sciortino, G. Lubinu, J. D. Marechal and E. Garriba, "DFT protocol for EPR prediction of paramagnetic Cu(II) complexes and application to protein binding sites," *Magnetochemistry*, vol. 4, no. 5, 2018.

- [14] D. A. Pantazis, "First-principles calculation of transition metal hyperfine coupling constants with the strongly constrained and appropriately normed (SCAN) density functional and its hybrid variants," *Magnetochemistry*, vol. 5, no. 4, 2019.
- [15] C. Remenyi, R. Reviakine, A. V. Arbuznikov, J. Vaara and M. Kaupp, "Spin-orbit effects on hyperfine coupling tensors in transition metal complexes using hybrid density functionals and accurate spin-orbit operators," *Journal of Physical Chemistry A*, vol. 108, no. 23, pp. 5026-5033, 2004.
- [16] W. M. Ames and S. C. Larsen, "DFT calculations of the EPR parameters for Cu(II) DETA imidazole complexes," *Physical Chemistry Chemical Physics*, vol. 11, no. 37, pp. 8266-8274, 2009.
- [17] S. Kossmann and F. Neese, "Correlated ab Initio spin densities for larger molecules: Orbital-optimized spin-component-scaled MP2 method," *Journal of Physical Chemistry A*, vol. 114, no. 43, pp. 11768-11781, 2010.
- [18] B. Sandhoefer, S. Kossmann and F. Neese, "Derivation and assessment of relativistic hyperfine-coupling tensors on the basis of orbital-optimized second-order Moller-Plesset perturbation theory and the second-order Douglas-Kroll-Hess transformation," *Journal of Chemical Physics*, vol. 138, no. 10, p. 104102, 2013.
- [19] M. Saitow and F. Neese, "Accurate spin-densities based on the domain-based local pair-natural orbital coupled-cluster theory," *Journal of Chemical Physics*, vol. 149, no. 3, p. 034104, 2018.
- [20] T. Shiozaki and T. Yanai, "Hyperfine coupling constants from internally contracted multireference perturbation theory," *Journal of Chemical Theory and Computation*, vol. 12, no. 9, pp. 4347-4351, 2016.
- [21] H. J. Scholl and J. Huttermann, "ESR and ENDOR of Cu(II) complexes with nitrogen donors - probing parameters for prothetic group modeling of superoxide-dismutase," *Journal of Physical Chemistry*, vol. 96, no. 24, pp. 9684-9691, 1992.
- [22] Y. Suzuki, S. Fujii, T. Tominaga, T. Yoshimoto, T. Yoshimura and H. Kamada, "The origin of an EPR singal observed in dithiocarbamate-loaded tissues copper(II)-dithiocarbamate complexes account for the narrow hyperfine lines," *Biochimica Et Biophysica Acta - General Subjects*, vol. 1335, no. 3, pp. 242-245, 1997.

- [23] N. Ritterskamp, K. Sharples, E. Richards, A. Folli, M. Chiesa, J. A. Platts and D. M. Murphy, "Understanding the coordination modes of  $[\text{Cu}(\text{acac})(2)(\text{imidazole})(n=1,2)]$  adducts by EPR, ENDOR, HYSCORE, and DFT analysis," *Inorganic Chemistry*, vol. 56, no. 19, pp. 11862-11875, 11862-11875.
- [24] E. Carter, E. L. Hazeland, D. M. Murphy and B. D. Ward, "Structure, EPR/ENDOR and DFT characterisation of a  $[\text{Cu-II}(\text{en})(2)](\text{OTf})(2)$  complex," *Dalton Transaction*, vol. 42, no. 42, pp. 15088-15096, 2013.
- [25] K. Bader, D. Dengler, S. Lenz, B. Endeward, S. D. Jiang, P. Neugebauer and J. van Slageren, "Room temperature quantum coherence in a potential molecular qubit," *Nature Communications*, vol. 5, p. 5304, 2014.
- [26] W. E. Antholine, R. Basosi, J. S. Hyde, S. Lyman and D. H. Petering, "Immobile-phase and mobile-phase electron-spin-resonance spectroscopy of copper-complexes - studies on biologically interesting bis(thiosemicarbazonato)copper(II) chelates," *Inorganic Chemistry*, vol. 23, no. 22, pp. 3543-3548, 1984.
- [27] I. Kuzniarska-Biernacka, K. Kurzak, B. Kurzak and J. Jezierska, "Spectrochemical properties of noncubical transition metal complexes in solutions. XV. Solution properties of bis(salicylideneaniline)copper(II)," *Journal of Solution Chemistry*, vol. 32, no. 8, pp. 719-741, 2003.
- [28] J. Garcia-Tojal, A. Garcia-Orad, J. L. Serra, J. L. Pizarro, L. Lezema, M. I. Arriortua and T. Rojo, "Synthesis and spectroscopic properties of copper(II) complexes derived from thiophene-2-carbaldehyde thiosemicarbazone. Structure and biological activity of  $[\text{Cu}(\text{C}_6\text{H}_6\text{N}_3\text{S}_2)(2)]$ ," *Journal of Inorganic Biochemistry*, vol. 75, no. 1, pp. 45-54, 1999.
- [29] N. Singh, J. Niklas, O. Poluektov, K. M. Van Heuvelen and A. Mukherjee, "Mononuclear nickel (II) and copper (II) coordination complexes supported by bispicen ligand derivatives: Experimental and computational studies," *Inorganica Chimica Acta*, vol. 455, pp. 221-230, 2017.
- [30] S. Sarkar, S. Sen, S. Dey, E. Zangrando and P. Chattopadhyay, "Coordination behavior of 3,4-bis(2-pyridylmethylthio)toluene with copper(II) ions Synthesis, structural characterization and reactivity, and DNA binding study of the dinuclear copper(II) complex," *Polyhedron*, vol. 29, no. 17, pp. 3157-3163, 2010.

- [31] K. Ananth, M. Kanthimathi and B. U. Nair, "An e.p.r. study of tetradentate Schiff base copper complexes with an N-(CH<sub>2</sub>)<sub>n</sub>-N, n=3-6 backbone," *Transition Metal Chemistry*, vol. 26, no. 3, pp. 333-338, 2001.
- [32] P. Comba, T. W. Hambley, G. A. Lawrance, L. L. Martin, P. Renold and K. Varnagy, "Template syntheses of chiral tetradentate ligands derived from L-amino-acids - Structural and spectroscopic characterization of the free ligands and of their copper(II) complexes," *Journal of the Chemical Society - Dalton Transactions*, no. 2, pp. 277-283, 1991.
- [33] M. M. Bhadbhade and D. Srinivas, "Effects on molecular association, chelate conformation, and reactivity toward substitution in Cu(5-X-salen) complexes, salen<sup>2-</sup> = N,N'-ethylenebis(salicylideneaminato), x = H, CH<sub>3</sub>O, and Cl - Synthesis, X-ray structures, and EPR investigations," *Inorganic Chemistry*, vol. 32, no. 24, pp. 5458-5466, 1993.
- [34] B. Balaiah, B. A. Sastry, M. N. Chary, G. Ponticelli and M. Massaccesi, "IR, electron-paramagnetic-res and optical-absorption studies of some 2,2'-bipyridine complexes of copper(II)," *Journal of Molecular Structure*, vol. 78, no. 3-4, pp. 289-297, 1982.
- [35] R. S. Glass, L. K. Steffen, D. D. Swanson, G. S. Wilson, R. Degelder, R. Degraff and J. Reedijk, "Bis(trithiacyclononane)metal(II) compounds and Jahn-Teller distortions from octahedral geometry, electrochemistry, spectroscopy, and crystal-structures of the copper bis(tetrafluoroborate) bis(acetonitrile) complex at 177-K," *Inorganica Chimica Acta*, vol. 207, no. 2, pp. 241-252, 1993.
- [36] F. Neese, F. Wennmohs, U. Becker and C. Riplinger, "The ORCA quantum chemistry program package," *Journal of Chemical Physics*, vol. 152, no. 22, 2020.
- [37] A. D. Becke, "Density-functional exchange-energy approximation with correct asymptotic behavior," *Physical Review A*, vol. 38, no. 6, pp. 3098-3100, 1988.
- [38] J. P. Perdew, "Density-functional approximation for the correlation-energy of the inhomogeneous electron-gas," *Physical Review B*, vol. 33, no. 12, pp. 8822-8824, 1986.
- [39] F. Weigend and R. Ahlrichs, "Balanced basis sets of split valence, triple zeta valence and quadruple zeta valence quality for H to Rn: Design and assessment of accuracy," *Physical Chemistry Chemical Physics*, vol. 7, no. 18, pp. 3297-3305, 2005.

- [40] F. Weigand, "Accurate Coulomb-fitting basis sets for H to Rn," *Physical Chemistry Chemical Physics*, vol. 8, no. 9, pp. 1057-1065, 2006.
- [41] J. P. Perdew, K. Burke and M. Ernzerhof, "Generalized gradient approximation made simple," *Physical Review Letters*, vol. 77, no. 18, pp. 3865-3868, 1996.
- [42] J. M. Tao, J. P. Perdew, V. N. Staroverov and G. E. Scuseria, "Climbing the density functional ladder: Nonempirical meta-generalized gradient approximation designed for molecules and solids," *Physical Review Letters*, vol. 91, no. 14, p. 146401, 2003.
- [43] J. W. Sun, A. Ruzsinsky and J. P. Perdew, "Strongly constrained and appropriately normed semilocal density functional," *Physical Review Letters*, vol. 115, no. 3, p. 036402, 2015.
- [44] A. D. Becke, "Density-functional thermochemistry .3. The role of exact exchange," *Journal of Chemical Physics*, vol. 98, no. 7, pp. 5648-5652, 1993.
- [45] C. T. Lee, W. T. Yang and R. G. Parr, "Development of the Colle-Salvetti correlation-energy formula into a functional of the electron-density," *Physical Review B*, vol. 37, no. 2, pp. 785-789, 1988.
- [46] J. P. Perdew and Y. Wang, "Accurate and simple analytic representation of the electron-gas correlation-energy," *Physical Review B*, vol. 45, no. 23, pp. 13244-13249, 1992.
- [47] C. Adamo and V. Barone, "Toward reliable density functional methods without adjustable parameters: The PBE0 model," *Journal of Chemical Physics*, vol. 110, no. 13, pp. 6158-6170, 1999.
- [48] T. Yanai, D. P. Tew and N. C. Handy, "A new hybrid exchange-correlation functional using the Coulomb-attenuating method (Cam-B3LYP)," *Chemical Physics Letters*, vol. 393, no. 1-3, pp. 51-57, 2004.
- [49] V. N. Staroverov, G. E. Scuseria, J. M. Tao and J. P. Perdew, "Comparative assessment of a new nonempirical density functional: Molecules and hydrogen-bonded complexes," *Journal of Chemical Physics*, vol. 119, no. 23, pp. 12129-12137, 2003.
- [50] Y. Zhao and D. G. Truhlar, "The M06 suite of density functionals for main group thermochemistry, thermochemical kinetics, noncovalent interactions, excited states, and transition elements: two new functionals and systematic testing of four M06-class functionals and 12 other function," *Theoretical Chemistry Accounts*, vol. 120, no. 1-3, pp. 215-241, 2008.

- [51] S. Grimme, "Semiempirical hybrid density functional with perturbative second-order correlation," *Journal of Chemical Physics*, vol. 124, no. 3, p. 034108, 2006.
- [52] F. Neese, "Efficient and accurate approximations to the molecular spin-orbit coupling operator and their use in molecular g-tensor calculations," *Journal of Chemical Physics*, vol. 122, no. 3, p. 034107, 2005.
- [53] B. A. Hess, C. M. Marian, U. Wahlgren and O. Gropen, "A mean-field spin-orbit method applicable to correlated wavefunctions," *Chemical Physics Letters*, vol. 251, no. 5-6, pp. 365-371, 1996.
- [54] M. Douglas and N. M. Kroll, "Quantum electrodynamical corrections to fine-structure of helium," *Annals of Physics*, vol. 82, no. 1, pp. 89-155, 1974.
- [55] B. A. Hess, "Applicability of the no-pair equation with free-particle projection operators to atomic and molecular-structure calculations," *Physical Review A*, vol. 32, no. 2, pp. 756-763, 1985.
- [56] B. A. Hess, "Relativistic electronic-structure calculations employing a 2-component no-pair formalism with external-field projection operators," *Physical Review A*, vol. 33, no. 6, pp. 3742-3748, 1986.
- [57] G. Jansen and B. A. Hess, "Revision of the Douglas-Kroll transformation," *Physical Review A*, vol. 39, no. 11, pp. 6016-6017, 1989.
- [58] A. Wolf, M. Reiher and B. A. Hess, "The generalized Douglas-Kroll transformation," *Journal of Chemical Physics*, vol. 117, no. 20, pp. 9215-9226, 2002.
- [59] M. Reiher, "Douglas-Kroll-Hess theory: a relativistic electrons-only theory for chemistry," *Theoretical Chemistry Accounts*, vol. 116, no. 1-3, pp. 241-252, 2006.
- [60] T. Nakajima, "The Douglas-Kroll-Hess approach," *Chemical Reviews*, vol. 112, no. 1, pp. 385-402, 2012.
- [61] E. van Lenthe, E. J. Baerends and J. G. Snijders, "Relativistic regular 2-component hamiltonians," *Journal of Chemical Physics*, vol. 99, no. 6, pp. 4597-4610, 1993.

- [62] E. van Lenthe, E. J. Baerends and J. G. Snijders, "Relativistic total-energy using regular approximations," *Journal of Chemical Physics*, vol. 101, no. 11, pp. 9783-9792, 1994.
- [63] E. van Lenthe, J. G. Snijders and E. J. Baerends, "The zero-order regular approximation for relativistic effects: The effect of spin-orbit coupling in closed shell molecules," *Journal of Chemical Physics*, vol. 105, no. 15, pp. 6505-6516, 1996.
- [64] D. A. Pantazis and F. Neese, "All-electron basis sets for heavy elements," *Wiley Interdisciplinary Reviews - Computational Molecular Science*, vol. 4, no. 4, pp. 363-374, 2014.
- [65] L. Visscher and K. G. Dyall, "Dirac-Fock atomic electronic structure calculations using different nuclear charge distributions," *Atomic Data and Nuclear Data Tables*, vol. 67, no. 2, pp. 207-224, 1997.
- [66] R. C. Lochan and M. Head-Gordon, "Orbital-optimized opposite-spin scaled second-order correlation: An economical method to improve the description of open-shell molecules," *Journal of Chemical Physics*, vol. 126, no. 16, p. 164101, 2007.
- [67] F. Neese, T. Schwabe, S. Kossmann, B. Schirmer and S. Grimme, "Assessment of orbital-optimized, spin-component scaled second-order many-body perturbation theory for thermochemistry and kinetics," *Journal of Chemical Theory and Computation*, vol. 5, no. 11, pp. 3060-3073, 2009.
- [68] C. Riplinger and F. Neese, "An efficient and near linear scaling pair natural orbital based local coupled cluster method," *Journal of Chemical Physics*, vol. 138, no. 3, p. 034106, 2013.
- [69] M. Saitow, U. Becker, C. Riplinger, E. F. Valeev and F. Neese, "A new near-linear scaling, efficient and accurate, open-shell domain-based local pair natural orbital coupled cluster singles and doubles theory," *Journal of Chemical Physics*, vol. 146, no. 16, p. 164105, 2017.
- [70] E. D. Hedegard, J. Kongsted and S. P. A. Sauer, "Optimized basis sets for calculation of electron paramagnetic resonance hyperfine coupling constants: aug-cc-pVTZ-J for the 3d atoms Sc-Zn," *Journal of Chemical Theory and Computation*, vol. 7, no. 12, pp. 4077-4087, 2011.
- [71] G. L. Stoychev, A. A. Auer and F. Neese, "Automatic generation of auxiliary basis sets," *Journal of Chemical Theory and Computation*, vol. 13, no. 2, pp. 554-562, 2017.

- [72] F. Neese, "Prediction and interpretation of the Fe-57 isomer shift in Mossbauer spectra by density functional theory," *Inorganica Chimica Acta*, vol. 337, pp. 181-192, 2002.
- [73] E. D. Hedegard, J. Kongsted and S. P. A. Sauer, "Improving the calculation of electron paramagnetic resonance hyperfine coupling tensors for d-block metals," *Physical Chemistry Chemical Physics*, vol. 14, no. 30, pp. 10669-10676, 2012.
- [74] A. Schafer, C. Huber and R. Ahlrichs, "Fully optimized contracted gaussian-basis sets of triple zeta valence quality for atoms Li to Kr," *Journal of Chemical Physics*, vol. 100, no. 8, pp. 5829-5835, 1994.
- [75] H. S. Shafaat, J. J. Griesse, D. A. Pantazis, K. Roos, C. S. Andersson, A. Popovic-Bijelic, A. Graslund, P. E. M. Siegbahn, F. Neese, W. Lubitz, M. Hogbom and N. Cox, "Electronic structural flexibility of heterobimetallic Mn/Fe cofactors: R2lox and R2c proteins," *Journal of the American Chemical Society*, vol. 136, no. 38, pp. 13399-13409, 2014.
- [76] D. A. Pantazis, X. Y. Chen, C. R. Landis and F. Neese, "All-electron scalar relativistic basis sets for third-row transition metal atoms," *Journal of Chemical Theory and Computation*, vol. 4, no. 6, pp. 908-919, 2008.
- [77] D. A. Pantazis and F. Neese, "All-electron scalar relativistic basis sets for the lanthanides," *Journal of Chemical Theory and Computation*, vol. 5, no. 9, pp. 2229-2238, 2009.
- [78] D. A. Pantazis and F. Neese, "All-electron scalar relativistic basis sets for the actinides," *Journal of Chemical Theory and Computation*, vol. 7, no. 3, pp. 677-684, 2011.
- [79] D. A. Pantazis and F. Neese, "All-electron scalar relativistic basis sets for the 6p elements," *Theoretical Chemistry Accounts*, vol. 131, no. 11, 2012.
- [80] D. Aravena, F. Neese and D. A. Pantazis, "Improved segmented all-electron relativistically contracted basis sets for the lanthanides," *Journal of Chemical Theory and Computation*, vol. 12, no. 3, pp. 1148-1156, 2016.
- [81] J. D. Rolfes, F. Neese and D. A. Pantazis, "All-electron scalar relativistic basis sets for the elements Rb-Xe," *Journal of Computational Chemistry*, vol. 41, no. 20, pp. 1842-1849, 2020.



- [82] A. C. Saladino and S. C. Larsen, "Relativistic DFT calculations of copper hyperfine coupling constants: Effect of spin-orbit coupling," *Journal of Physical Chemistry A*, vol. 107, no. 29, pp. 5583-5587, 2003.
- [83] C. J. Schattenberg, T. M. Maier and M. Kaupp, "Lessons from the spin-polarization/spin-contamination dilemma of transition-metal hyperfine couplings for the construction of exchange-correlation functionals," *Journal of Chemical Theory and Computation*, vol. 14, no. 11, pp. 5653-5672, 2018.
- [84] A. Wodynski and M. Kaupp, "Noncollinear relativistic two-component X2C calculations of hyperfine couplings using local hybrid functionals. Importance of the high-density coordinate scaling limit," *Journal of Chemical Theory and Computation*, vol. 16, no. 1, pp. 314-325, 2020.
- [85] S. K. Singh, M. Atanasov and F. Neese, "Challenges in multireference perturbation theory for the calculations of the g-tensor of first row transition metal complexes," *Journal of Chemical Theory and Computation*, vol. 14, no. 9, pp. 4662-4677, 2018.
- [86] M. Kaupp, R. Reviakine, O. L. Malkina, A. Arbuznikov, B. Schimmelpfennig and V. G. Malkin, "Calculation of electronic g-tensors for transition metal complexes using hybrid density functionals and atomic meanfield spin-orbit operators," *Journal of Computational Chemistry*, vol. 23, no. 8, pp. 794-803, 2002.
- [87] E. R. Sayfutyarova and G. K.-L. Chan, "Electron paramagnetic resonance g-tensors from state interaction spin-orbit coupling density matrix renormalization group," *The Journal of Chemical Physics*, vol. 148, p. 184103, 2018.



---

CHAPTER III.  
PREDICTION OF EPR  
PARAMETERS OF THE LPMO  
ACTIVE SITE AND AN LPMO-  
LIKE TRIPEPTIDIC COMPLEX  
USING MODEL SYSTEMS

---



## CHAPTER III. PREDICTION OF EPR PARAMETERS OF THE LPMO ACTIVE SITE AND AN LPMO-LIKE TRIPEPTIDIC COMPLEX USING MODEL SYSTEMS

In the study of enzymatic systems, active sites can be probed with the means of electronic paramagnetic resonance (EPR) spectroscopy. This is possible if there is an unpaired electron present in the system. This unpaired electron can either belong to a transition metal center from the enzyme [1] [2] or to an organic radical. [3] In the case of the LPMO enzyme in the resting state, the active site contains a mononuclear copper center which oxidation state is +2, forming a  $3d^9$  entity and leading to a  $S = 1/2$  spin state. [4] EPR is a technique of predilection that gives great insight in the electronic configuration and the redox state of the metal center, copper in this case, its geometry, and its coordination environment. [5] The information is encoded in two main parameters: the  $g$  matrix, and the hyperfine tensor  $A$ . After an extensive study in establishing a theoretical protocol, based on DFT, to reliably predict these EPR parameters, especially in the case of the sensitive hyperfine coupling constants, [6] we can apply it to a real example to rationalize the experimental observations to better understand the behavior of a biological system. Moreover, we can use it as a prediction tool by postulating structures that may exist in certain conditions.

Many studies on LPMO have been focused on the coordination of the substrate to the active site. Approaching the polysaccharide to the active site will affect the coordinating geometry of the copper metal center and therefore its EPR values. [7] [8] [9] [10] For example, Bissaro and co-workers [7] observed that after binding of substrate on the *SmAA10A* enzyme induces a shift of both the  $g_z$  and the  $A_z^{Cu}$  values. In the case of the  $g_z$ , there is a significant decrease from 2.259 to 2.216 when the substrate used was  $\beta$ -chitin, and to 2.212 when it was (N-acetyl-glucosamine)<sub>6</sub>. Conversely, the  $A_z^{Cu}$  value increased from 346 MHz to 610 MHz with  $\beta$ -chitin, and to 560 MHz with (N-acetyl-glucosamine)<sub>6</sub>. Interestingly, similar EPR characteristics have been observed simultaneously, in a few cases, with the enzyme alone. In these cases, there is a mixture of EPR signals suggesting the presence of two species in a major/minor distribution. [11] [12] This situation has not been clearly studied in literature, but the symmetry change in the EPR signal, evolving from rhombic to axial, and kinetics studies point towards structural changes directly related to the metal center and its coordination sphere.

In the group, two peptides have been prepared inspired by the LPMO active site to reproduce the histidine-brace ligation. Again, EPR was used to probe the copper ion and understand the

coordination properties of the peptide. With the means of DFT, we seek to propose susceptible structures and to rationalize between experimental spectroscopic data to gain greater insight into the system at hand.

In this chapter, we first studied synthetic models of the active site of LPMO from the AA10 subfamily which structure has been solved in the group to understand the origin of the mixed signal observed at the resting state of the enzyme. We rationalize on the EPR spectroscopic features using small active site models extracted from *P/AA10* crystal structure. [11] We also present the use of our DFT methods for the prediction of the structural and functional properties of histidine-brace modelling copper-peptides.

## **1 – Exploring the origin of the intriguing EPR signals of the LPMO active site using small model systems**

The active site of LPMO is comprised of two histidine amino acids coordinating a mononuclear copper center. One of these histidines is coordinating the copper center through the N-atom of the imidazole ring. The second histidine is the N-terminal amino-acid and coordinates in a bidentate fashion. First through the N-atom of the imidazole ring, and second by the terminal primary amine. This motif is known as the histidine brace and is not common in metal containing enzymes. Particulate methane monooxygenase, pMMO, is another enigmatic enzyme featuring this motif. [13] [14] The three N-atoms coordinate forming a plane with the mononuclear copper, and two water molecules complete the metal coordination sphere in a trigonal bipyramidal geometry in most cases. (Figure 1) [11] This first coordination sphere of LPMO is very conserved. [15] [16] [17] [7] In chitin active enzymes from AA10 family, the geometry of the resting Cu(II) state is different and the copper is found in a rhombic environment between square-pyramidal and trigonal geometries.

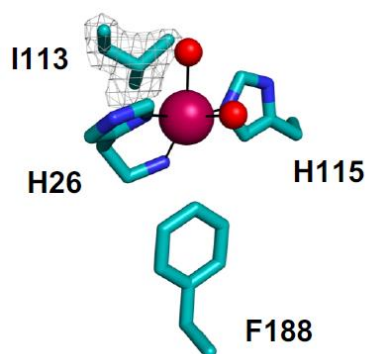


**Figure 1.** X-ray crystal structure of the active site of *P/AA10* and selected residues in the second coordination sphere. C-atoms are shown in teal, N-atoms in blue, O-atoms in red and Cu-atom in magenta. The amino acid residues are shown with their corresponding code and number with respect to the PDB structure. The isoleucine 113 is simulated with a contoured map at  $2.8\sigma$ . Adapted from [11].

Recently, a chitin active *P/AA10* LPMO enzyme was characterized and found to feature and isoleucine in place of the highly conserved second-coordination sphere alanine within this sub-family of enzyme. Munzone and co-workers have recorded the continuous wave (cw) EPR, at 120 °K, in 50 mM MES buffer at pH 6.5, using 10 % v/v glycerol as a glassing agent. The spectrum obtained is a rhombic signal. After simulation of the EPR spectrum, the g-tensors values are the following:  $g_x = 2.025$ ,  $g_y = 2.103$ , and  $g_z = 2.260$ , and the A-tensors are:  $A_x^{\text{Cu}} = 220$  MHz,  $A_y^{\text{Cu}} = 95$  MHz, and  $A_z^{\text{Cu}} = 355$  MHz.

The use of a glassing agent, in this case glycerol, can affect the quality of the EPR spectrum. [18] [19] This led to a new level of complexity for *P/AA10* LPMO when removing the glassing agent. [11] In the latter case, the EPR spectrum exhibits the contribution of two copper species in solution. First, a major species (around 80%) corresponding to the one obtained in presence of glycerol is found. But then, a minor species (around 20%) is observed having a lower  $g_z$  and a much larger  $A_z^{\text{Cu}}$  values. The spectrum is of axial type and simulated g-tensor values are 2.062 for both  $g_x$  and  $g_y$ , and 2.250 for  $g_z$ . The A-tensor values are found as  $< 90$  MHz for both  $A_x^{\text{Cu}}$  and  $A_y^{\text{Cu}}$  and 537 MHz for  $A_z^{\text{Cu}}$  (Table 1).

The presence of two species has been previously reported in another AA10 LPMO. Chaplin et al. [12] recorded the EPR spectrum of *SliAA10E* LPMO enzyme at 10K and pH 7.0 in 150 mM NaCl buffer. Two species were also found in solution with very different sets of EPR parameters (Table 1). Species 1 shows more rhombic character and  $g_x$ ,  $g_y$  and  $g_z$  equal to 2.033, 2.067 and 2.260, respectively, and  $A_x^{\text{Cu}}$ ,  $A_y^{\text{Cu}}$ , and  $A_z^{\text{Cu}}$  equal 13.5, 13.5 and 135 G (38, 38 and 378 MHz), respectively. Species 2, on the contrary, is more axial specially with an increase of the hyperfine

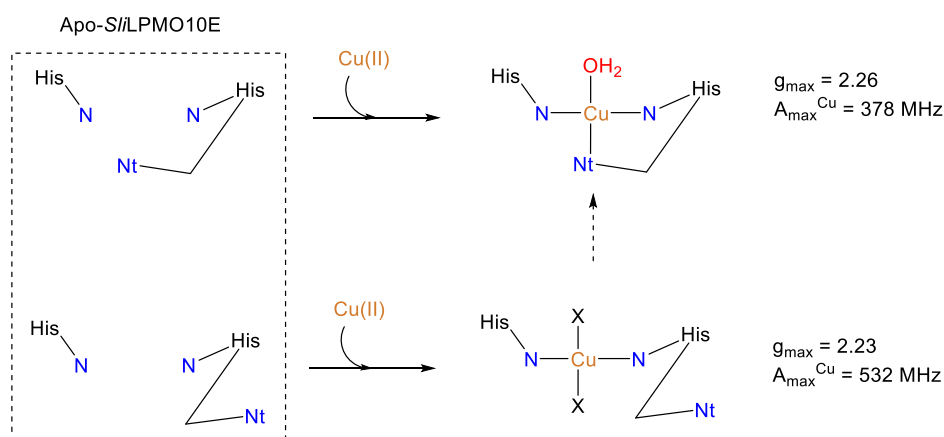
maximum value:  $g_x = 2.055$ ,  $g_y = 2.071$ , and  $g_z = 2.230$ ;  $A_x^{\text{Cu}} = 19 \text{ G}$  (53 MHz),  $A_y^{\text{Cu}} = 19 \text{ G}$  (53 MHz), and  $A_z^{\text{Cu}} = 190 \text{ G}$  (532 MHz).

**Table 1.** EPR simulation parameters of *P/AA10* [11] and *S/AA10E* [12] for both the rhombic and axial species.

<i>Enzyme</i>	<i>P/AA10</i> [11]		<i>S/AA10E</i> [12]	
<i>Species 1</i> <i>“rhombic”</i>	<i>g</i>	$A^{\text{Cu}}$ (MHz)	<i>g</i>	$A^{\text{Cu}}$ (MHz)
x	2.025	220	2.033	38
y	2.103	95	2.067	38
z	2.260	355	2.260	378
<i>Species 2</i> <i>“axial”</i>	<i>g</i>	$A^{\text{Cu}}$ (MHz)	<i>g</i>	$A^{\text{Cu}}$ (MHz)
x	2.062	< 90	2.055	53
y	2.062	< 90	2.071	53
z	2.250	537	2.230	532

Both cases may present the same rationale on the origin of this secondary species. Chaplin et al. suggested the two species may be due to the decoordination or to a movement of the primary amine in the N-terminal amino acid leading to a different coordination sphere around the copper center. In the absence of the glassing agent, decoordination may occur during freezing of the sample creating a heterogeneous solution of the *P/AA10* LPMO. [11] [19] In the case of *S/AA10E* LPMO, the mixed signal may not only originate from the decoordination of the primary amine but also from a possible binding of chloride ion to the copper center, since chloride is present in excess in the sodium chloride buffer. The authors suggested that the apo-protein is folded in a way that the N-terminal amino acid is not in a coordinating position when copper binds (Scheme 1). [12] It is worth adding that Chaplin and co-workers illustrate this heterogeneity as an innate flexibility of the histidine brace that can affect copper loading. [12] However, neither one of these hypotheses has been investigated further.





**Scheme 1. Proposed copper coordination to the apo-S/LPMO10E with and without the N-terminal (Nt) amine in the coordination sphere. X represents either H<sub>2</sub>O or chloride ligands. The  $g_z$  and  $A_z^{\text{Cu}}$  determined by EPR are reported the right-hand side of each structure. Adapted from [12].**

In the following, we used density functional theory with our previously established methodology for obtaining reliable and effective EPR parameters [6] in model systems of the active site of LPMO based on P/AA10. [11] We defined multiple sets of models by changing coordination spheres and we investigate their ability to reproduce experimental EPR values and capture the rhombic/axial species distribution in an effort to elucidate the origin of the mixed signals. To this end, each model was subjected to possible modifications of its coordination sphere. First, we proposed deprotonation of one or two water molecules to produce hydroxy anionic ligands bound to the copper metal center. Second, we explored the distortion of the imidazole rings. Third, we investigated the decooordination of the primary amine from the copper center. Finally, we tested the coordination of other possible ligands, such as chloride or water molecules. These modifications were applied individually or in different combinations to include a maximum number of structures in the study.

### 1.1 – Model systems of the P/AA10 LPMO active site

To evaluate the relationship between the mixed EPR signal and the heterogeneous coordination sphere of the LPMO active site, we proposed various models with or without modifications of the ligands. These models are divided by structure sets and are classified with respect to the coordinating atoms around the copper center. Note that the oxidation state of copper remains (+2) to generate an  $S = \frac{1}{2}$  spin state which is EPR active. We focused primarily on the P/AA10 enzyme and its native coordination sphere. It was suggested that decooordination of the primary

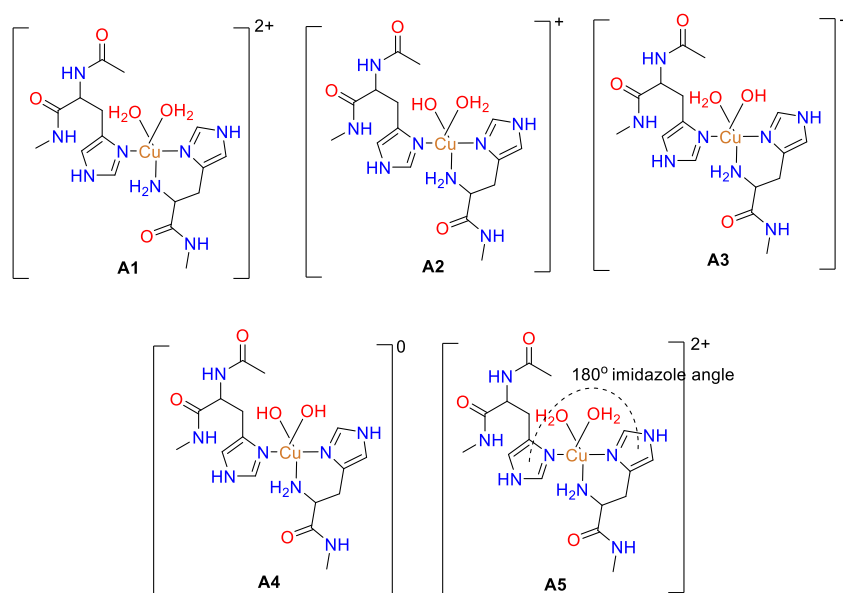
amine may result in the production of the minor species, in combination with the coordination of a chloride anion. [12] This latter proposal is not envisioned in the case of *P/AA10* since there is no reason to be any Cl-atom from experimental conditions. However, we investigated possible hydroxyl groups coordinating the metal which may be present in solution. [20] Also, we investigated modifications of the angle between the imidazole rings.

#### *Structure set A*

As mentioned earlier the LPMO active site in its resting state is comprised of two histidine residues and two water molecules binding the Cu(II) center. This 5-member coordination sphere can be described as a Cu<sub>3</sub>N<sub>2</sub>O entity, originating from one N-atom of the imidazole ring of a first histidine, two N-atoms from the imidazole ring and the primary amine of the N-terminal of the histidine brace, and two O-atoms from two water molecules. This structure is referred as the “normal” LPMO with a rhombic geometry considered in *P/AA10* [11] and denoted as structure A1. The following modifications envisioned for this structure set are:

- Deprotonation of either one of the water molecules (A2 and A3),
- Deprotonation of both water molecules (A4), and
- Distortion of the imidazole rings (A5).

The structure set A consists of 5 structures in a Cu<sub>3</sub>N<sub>2</sub>O configuration (Scheme 2).



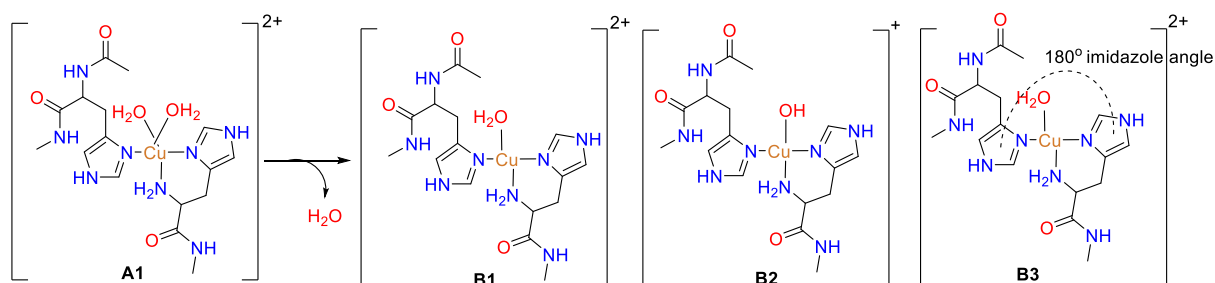
**Scheme 2.** LPMO models from structure set A, bearing a Cu<sub>3</sub>N<sub>2</sub>O coordinating environment and the corresponding modifications of the ligands: single deprotonation (A2 and A3), double deprotonation (A4), and imidazole distortion (A5).

### Structure set B

A 4-member coordination sphere can also be obtained by decooordination of a water molecule from structure A1. This square planar configuration is described as Cu<sub>3</sub>N<sub>1</sub>O and denoted as structure B1. Following the same line of modifications, two additional structures were envisioned:

- Deprotonation of the single water molecule (B2)
- Distortion of the imidazole rings (B3).

Structure set B consists of 3 structures in a Cu<sub>3</sub>N<sub>1</sub>O configuration. Scheme 3.



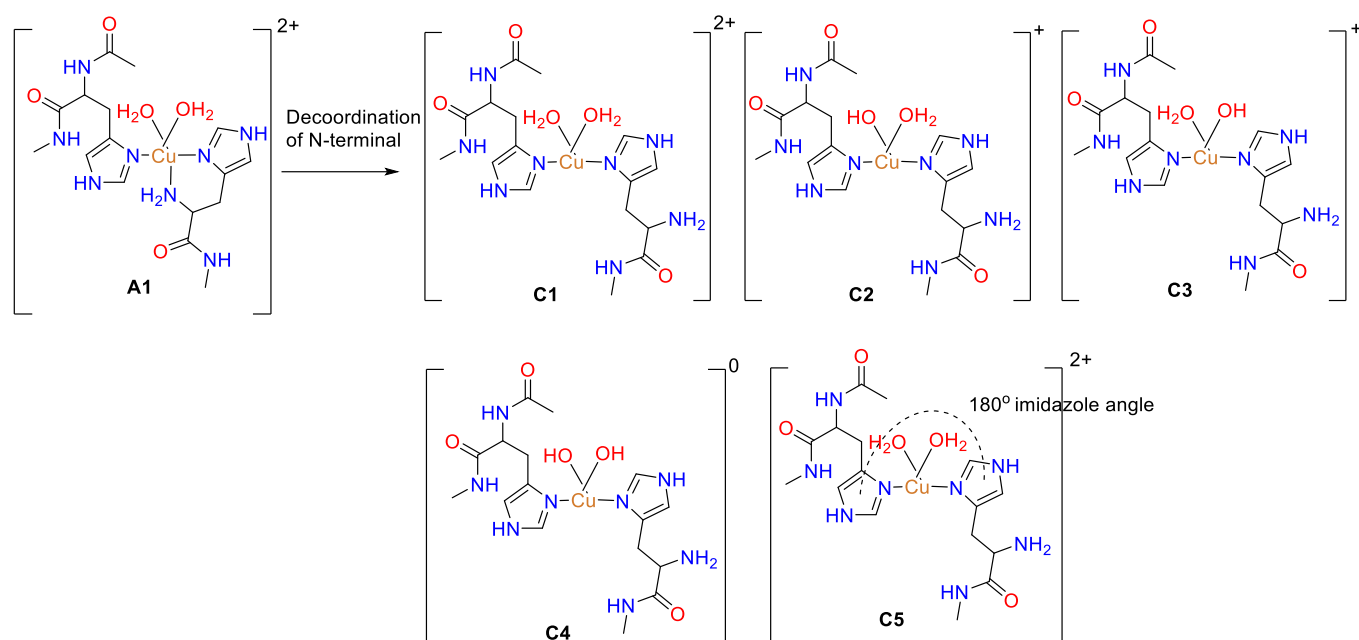
**Scheme 3.** LPMO models depicted in structure set B, bearing a Cu<sub>3</sub>N<sub>1</sub>O coordination sphere, originating from the decooordination of a water molecule from A1, and its subsequent modifications by deprotonation of the water molecule (B2) and imidazole distortion (B3).

### Structure set C

Another 4-member coordination sphere can be obtained by decooordination of the primary amine from structure A1, as proposed by Chaplin and co-workers. [12] This configuration is also square planar and is described as Cu<sub>2</sub>N<sub>2</sub>O, denoted as structure C1. Once again, we envisioned modifications of the C1 geometry to generate 4 more possible structures:

- Deprotonation of either one of the water molecules (C2 and C3),
- Deprotonation of both water molecules (C4), and
- Distortion of the imidazole rings (C5).

Structure set C consists of 5 structures in a Cu<sub>2</sub>N<sub>2</sub>O configuration (Scheme 4).



Scheme 4. LPMO models depicted in structure set C, bearing a Cu<sub>2</sub>N<sub>2</sub>O coordination sphere, originating from the decooordination of the N-terminal from A1, and its subsequent modifications: deprotonation of the water molecule(s) (C2, C3, and C4) and imidazole distortion (C5).

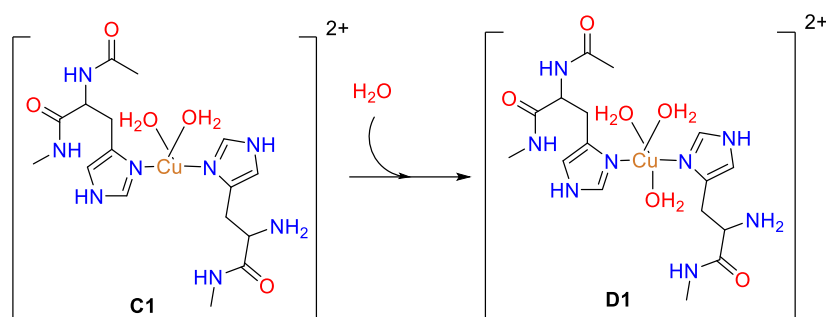
### Structure set D

The decooordination of the primary amine in structure C1 leaves an open coordinating site for another ligand. This empty space is suggested to be replaced by either a water molecule in the *P*/AA10 case or a chloride anion in the case of *S*//LPMO10E. [12] In the present case, the coordination of a water molecule leads to a 5-member coordination sphere and a Cu<sub>2</sub>N<sub>3</sub>O species.

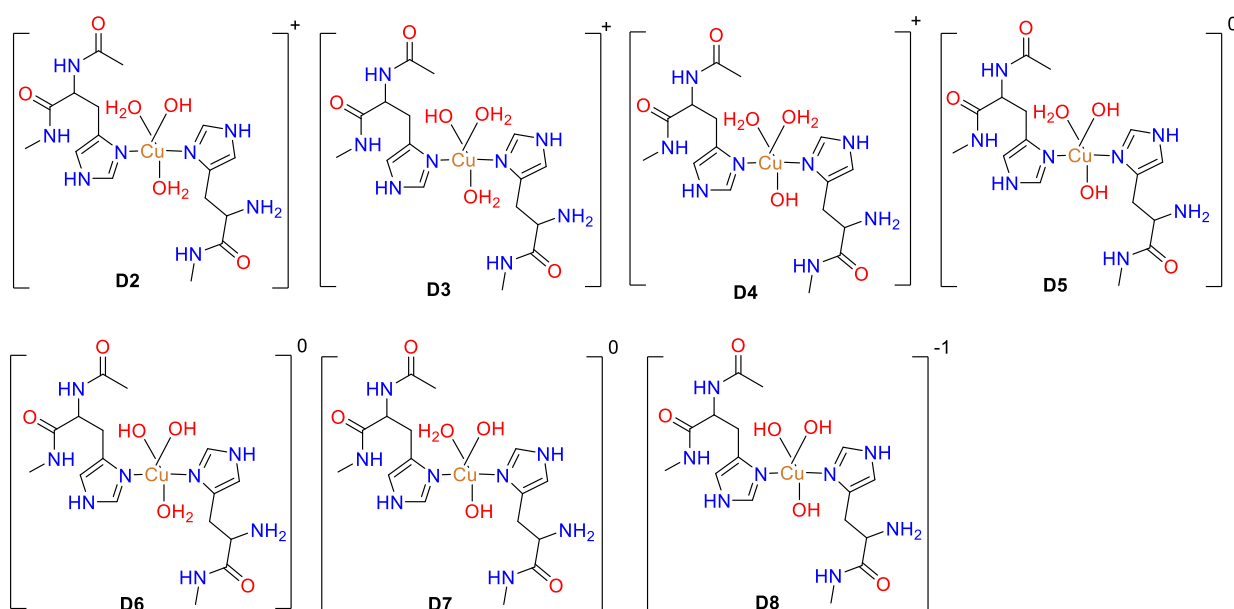
This structure is denoted as D1 (Scheme 5). This structure set was also modified by deprotonation only, such as:

- Single deprotonation of either one of the water molecules (D2, D3, and D4),
- Double deprotonation combining two water molecules (D5, D6 and D7), and
- Triple deprotonation of all three water molecules (D8).

Structure set D consists of 8 structures in a Cu<sub>2</sub>N<sub>3</sub>O configuration (Scheme 6).



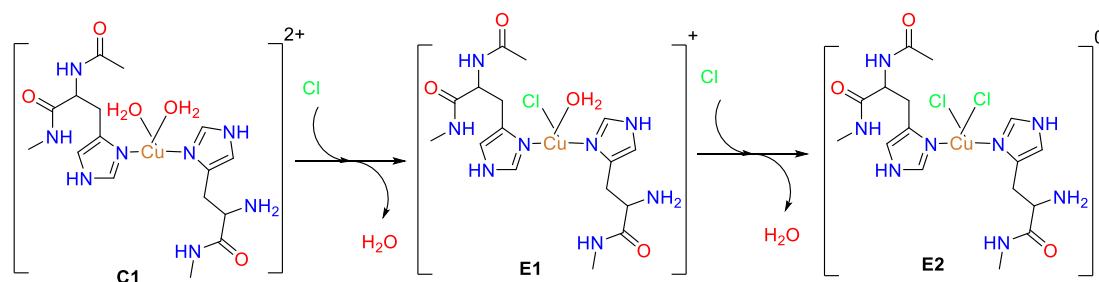
Scheme 5. LPMO models leading to structure set D, bearing a Cu<sub>2</sub>N<sub>3</sub>O coordination sphere, originating from the coordination of an extra water ligand from structure C1 (structure D1).



Scheme 6. LPMO models from structure set D, bearing a Cu<sub>2</sub>N<sub>3</sub>O coordination sphere, originating from structure D1 followed by a series of deprotonation of either one, two or all three water molecules.

### Structure set E

To complete this study, we also investigated the effect of the chloride anion binding using structure set C, *i.e.* after decoordination of the primary amine in the histidine brace motif. Simply, we replaced one or both water molecules by the Cl-atom to form Cu<sub>2</sub>N1O1Cl (E1) or Cu<sub>2</sub>N2Cl (E2) entities (Scheme 7).



**Scheme 7.** LPMO models from structure set E, bearing a Cu<sub>2</sub>N1O1Cl and Cu<sub>2</sub>N2Cl coordination sphere, originating from replacing once or twice a water molecule by a Cl-anion from structure C1.

### 1.2 – Geometry optimizations of the LPMO models and description of the structures

With the previous proposed structures, we investigated their possible relevance by simple geometry minimizations performed with the ORCA program package. [21] These geometry optimizations were carried with the BP86 functional [22] [23] and the def2-TZVP basis set, [24] in combination with corresponding auxiliary basis sets. [25] Increased integration grids were employed (Grid4 in ORCA convention), tight energy and slow convergence settings were applied in combination with the Direct Inversion in the Iterative Subspace (DIIS) algorithm (DIISmaxequation 15 in ORCA convention) and recalculation of the full Fock matrix for each iteration (directresetfreq 1 in ORCA convention). The calculation is considered heavy to run but great for converging difficult systems. The C-, N-, and O- atoms of the main amino acid chain were constrained during optimization. These optimizations were initially carried in the gas phase unless stated. In some cases, the effect of the solvent was investigated using the conductor-like polarizable continuum model (CPCM).

### Structure set A

Structure A1 was optimized without any major issues (Figure 2). The expected trigonally distorted square-pyramidal-derived geometry is obtained with appropriate Cu-N distances compared to those found in the X-ray crystal structure (Table 2). The experimental distances are  $d(\text{Cu-N}_{\text{H26}}) = 2.0 \text{ \AA}$ ,  $d(\text{Cu-NH}_{2, \text{H26}}) = 2.2 \text{ \AA}$ , and  $d(\text{Cu-N}_{\text{H115}}) = 2.0 \text{ \AA}$ , whereas the theoretical ones are  $d(\text{Cu-N}_{\text{H26}}) = 1.97 \text{ \AA}$ ,  $d(\text{Cu-NH}_{2, \text{H26}}) = 2.14 \text{ \AA}$ , and  $d(\text{Cu-N}_{\text{H115}}) = 1.99 \text{ \AA}$ . A greater difference is found in the angle between the histidine rings. This dihedral angle is found to be  $62^\circ$  in the crystal structure and  $78^\circ$  in the optimized structure. Lastly, the N-Cu-N angles of the plane are in good agreement with the experimental structure as well:  $(\text{N}_{\text{H26}}\text{-Cu-NH}_{2, \text{H26}}) = 97^\circ \text{ exp. vs. } 93^\circ \text{ calc.}$ ,  $(\text{N}_{\text{H26}}\text{-Cu-N}_{\text{H115}}) = 166^\circ \text{ exp. vs. } 174^\circ \text{ calc.}$ , and  $(\text{NH}_{2, \text{H26}}\text{-Cu-N}_{\text{H115}}) = 96^\circ \text{ exp. vs. } 93^\circ \text{ calc.}$  The optimized A1 structure is properly reproducing the geometrical features of the copper metal center bound the N-atom ligands. This structure was then used as reference to perform optimization of the rest of the modified structures within the set. It is also important to reproduce this structure *in silico* since it is considered as the one and only species found without glassing agent.

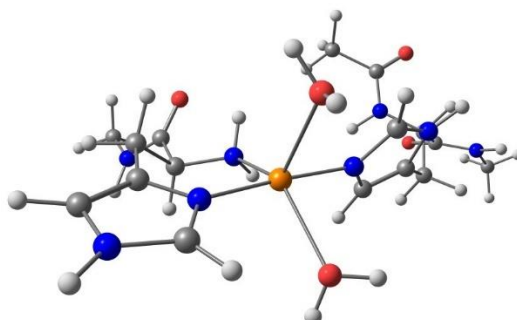


Figure 2. Optimized structure of the A1 model of the *PIAA10* enzyme's active site. H-, C-, N-, and O-atoms are presented in white, gray, blue, and red, respectively. Copper is presented in orange.

**Table 2.** Selected geometrical parameters of the copper coordination sphere of the *PIAA10* enzyme and comparison with those for the calculated model structure A1.

<i>Geometrical parameters</i>	<i>PIAA10 [11]</i>	<i>Calculated</i>
<b>Distances in Å</b>		
d(Cu-N <sub>H26</sub> )	2.0	1.97
d(Cu-NH <sub>2, H26</sub> )	2.2	2.14
d(Cu-N <sub>H115</sub> )	2.0	1.99
<b>Angles in degrees</b>		
(N <sub>H26</sub> -Cu-NH <sub>2, H26</sub> )	97	93
(N <sub>H26</sub> -Cu-N <sub>H115</sub> )	166	174
(NH <sub>2, H26</sub> -Cu-N <sub>H115</sub> )	96	93
<b>Dihedral angle in degrees</b>		
(C <sub>H26</sub> -N <sub>H26</sub> -N <sub>H115</sub> -C <sub>H115</sub> )	62	75

After optimization of the single hydroxy structures denoted A2 and A3, the models yielded 4-member coordination spheres of type Cu<sub>3</sub>N<sub>1</sub>O, similar to those of model set B (Figure 3). The hydroxyl group moved into the plane to produce a square planar geometry while the water molecule decoordinated the copper center and approached the hydroxyl group to create some stabilizing H-bonding interaction (Figure 3). The double hydroxy structure, A4, was optimized properly and lead to a square base pyramidal geometry. Both hydroxy groups moved away from each other and from the N(His)-Cu-N(His) plane.

The initial structure to start optimizing A5 was obtained by rotating the non-histidine brace ligand of the optimized structure A1 so that the imidazole rings are in the same plane. After minimization, the final angle between these rings is 29°, which is half of what was found experimentally for *PIAA10*. [11] This structure remains highly distorted with both water molecules coordinating the copper center (Figure 3).



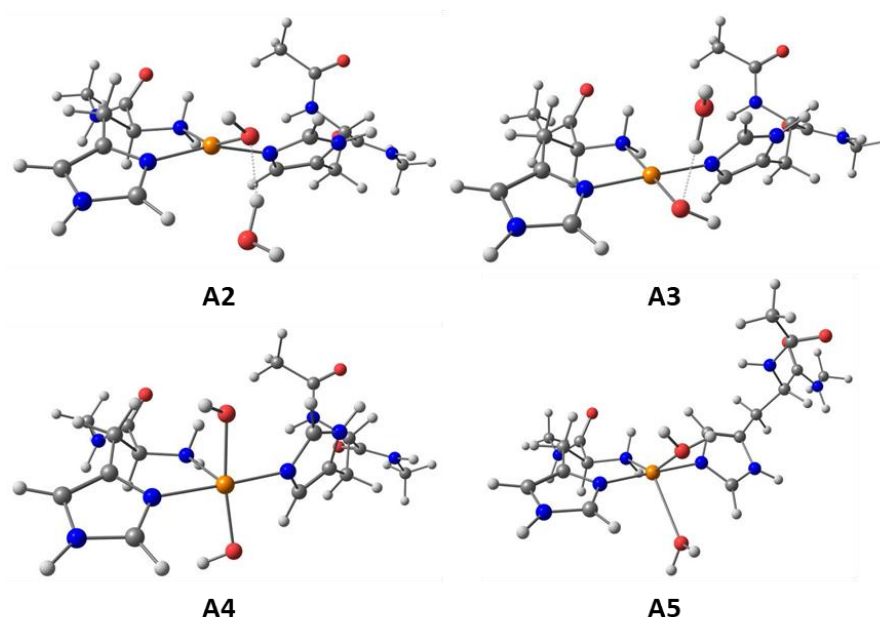


Figure 3. Optimized structures of the models from structure set A.

#### *Structure set B*

Structure B1 was optimized after removal of one water molecule from structure A1 (Figure 4). It converged to a distorted square planar structure. Slightly shorter Cu-N bond distances were obtained in comparison to those obtained for A1:  $d(\text{Cu-N}_{\text{H26}}) = 1.94$ ,  $d(\text{Cu-NH}_{2, \text{H26}}) = 2.11$  and  $d(\text{Cu-N}_{\text{H115}}) = 1.96$  (Table 3). The distortion angle of the imidazole rings falls in between the experimental value and that of the A1 structure:  $62^\circ$  experimentally,  $67^\circ$  for B1, and  $78^\circ$  for A1. Finally, the angles around the copper and the N-atom ligands are also reproduced when compared to experimental data:  $(\text{N}_{\text{H26}}\text{-Cu-NH}_{2, \text{H26}}) = 96^\circ$ ,  $(\text{N}_{\text{H26}}\text{-Cu-N}_{\text{H115}}) = 159^\circ$ , and  $(\text{NH}_{2, \text{H26}}\text{-Cu-N}_{\text{H115}}) = 97^\circ$ . This structure is used as reference for the optimizations of the modified structures with the B set.

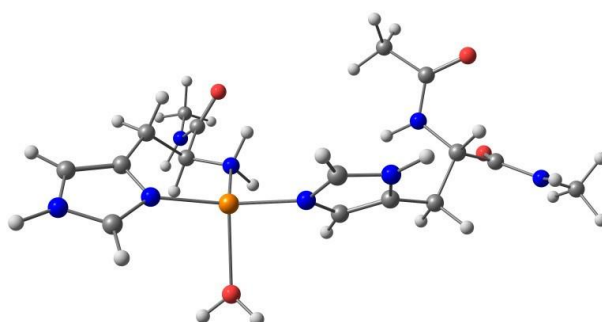


Figure 4. Optimized structure of the B1 model upon decoordination a water molecule from structure A1.

**Table 3.** Geometrical values surrounding the copper center involving the N-atom ligands of the *PIAA10* enzyme, the optimized model structure A1, and structure B1.

<i>Geometrical parameters</i>	<i>PIAA10 [11]</i>	<i>Optimized structure A1</i>	<i>Optimized structure B1</i>
<b>Distances in Å</b>			
d(Cu-N <sub>H26</sub> )	2.0	1.97	1.94
d(Cu-NH <sub>2, H26</sub> )	2.2	2.14	2.11
d(Cu-N <sub>H115</sub> )	2.0	1.99	1.96
<b>Angles in degrees</b>			
(N <sub>H26</sub> -Cu-NH <sub>2, H26</sub> )	97	93	96
(N <sub>H26</sub> -Cu-N <sub>H115</sub> )	166	174	159
(NH <sub>2, H26</sub> -Cu-N <sub>H115</sub> )	96	93	97
<b>Dihedral angle in degrees</b>			
(C <sub>H26</sub> -N <sub>H26</sub> -N <sub>H115</sub> -C <sub>H115</sub> )	62	75	67

Structure B2 was optimized after removal of one proton from the water molecule to generate the hydroxy anionic ligand. This optimization yielded a much less distorted square-planar structure compared to B1, albeit it is slightly more distorted (Figure 5).

The distortion of the imidazole rings was initially set at 0° from the initial structure of B1. After optimization, structure B3 displays an angle between these rings of 4°, which means that the imidazole distortion was maintained in the B3 model and resulted in a distorted square planar geometry (Figure 5).

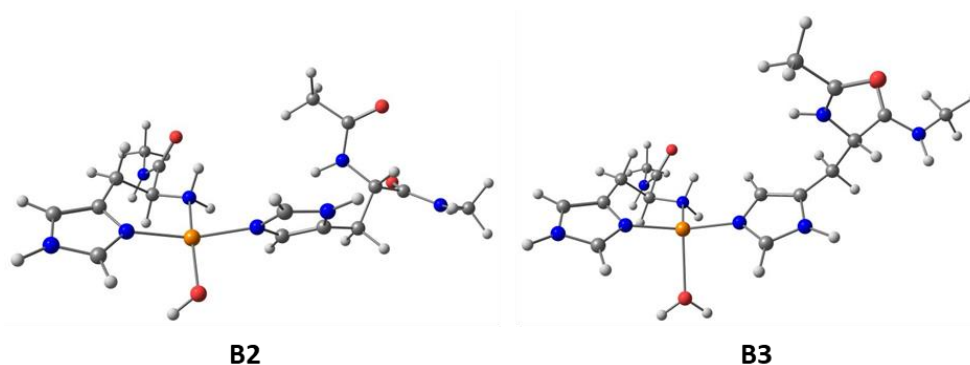


**Figure 5.** Optimized structures of the modifications brought to structure B1. Structure B2 has a single deprotonated water molecule and optimized to a distorted square planar geometry. Structure B3 has a distortion around the imidazole dihedral angle leading to a distorted square planar geometry as well.

### Structure set C

To initiate the decooordination of the primary amine from the metal center leading to structure C1, we rotated 180° along the C-C bond of the histidine brace side chain from structure A1. An optimized structure converged; however, it was not the expected one (Figure 6). The copper center is found to only coordinate a single water molecule. The second water molecule decoordinates from the copper atom and was further stabilized by H-bonding to the N-H moiety of the imidazole ring. The resulting copper center is coordinating only to both N-atoms of the imidazole rings and a single water molecule. After multiple failed attempts to stabilize this water molecule, possibly due to the need of considering solvent dielectric effect, C1 could not be produced and used as reference for the following modified structures.

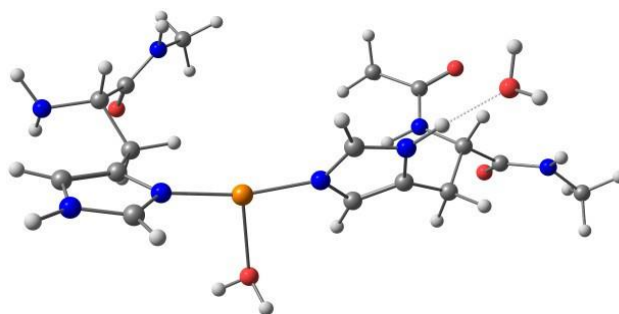


Figure 6. Optimized structure of the C1 model decoordinating the primary amine from structure A1.

Due to the above-mentioned difficulty to generate model C1, the singly deprotonated structure C2 was obtained by substituting the Cl anion from structure E1 (see section on structure set E) by a hydroxy group. This structure optimized properly into a strict square-planar geometry (Figure 7). It was then used as initial structure to optimize C3 by exchanging the positions of the remaining water molecule and the hydroxy group. This structure optimized into a distorted square planar geometry. The double-hydroxy structure, C4, was produced from C2 by deprotonation of the remaining water molecule. This structure optimized to a square planar geometry as well.

The structure of this set displaying the imidazole distortion, C5, was also produced from C2 by protonating the hydroxy group and changing the angle of interest to 0°. This structure optimized properly resulting in the imidazole rings angle having a value equal to 11° (Figure 7). For comparison, the imidazole ring angle found for C1 is 61°.

Note that an attempt was made to optimize C1 from C2 by protonating the hydroxyl group, initially obtained by replacing the Cl anion from the E1 structure. However, the same results were obtained and one of the water molecules decoordinates from the copper center. Finally, it is worth noting that this model set exhibits high complexity in both SCF convergence and geometry optimizations.

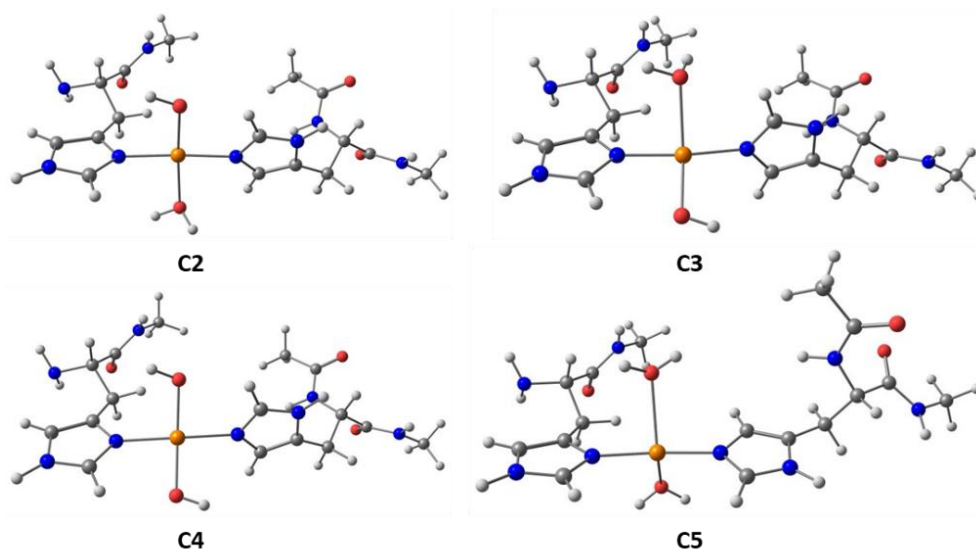


Figure 7. Optimized structures of the models from structure set C.

#### *Structure set D*

Following the same lines of structure set C, addition of an extra water molecule to produce structure D1 led to calculation problems. Indeed, when this structure was optimized, two of the three water molecules decoordinate from the copper center (Figure 8). A similar coordination sphere to C1 is obtained where copper coordinates two histidines from the N-atom and a single water ligand. The other two water molecules are stabilized by H-bonding with the remaining coordinated water molecule and with an amine on the main chain of the histidine. Due to difficulty in SCF convergence and geometry optimization, the deprotonated counterparts were not investigated further.

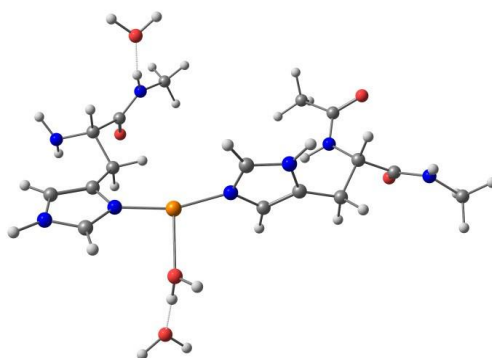


Figure 8. Optimized structure of the model D1 coordinating a water molecule from structure C1.

### *Structure set E*

Structures E1 and E2 were produced from structure C1 by removing one water molecule and adding the Cl-anion coordinate the copper center. E1 optimized to a square planar geometry with shorter and identical Cu-N distances (1.98 Å) and longer Cu-Cl (2.25 Å) and Cu-O (2.23 Å) ones. E2 optimized to a distorted square planar geometry with slightly longer Cu-N (1.99 Å and 2.00 Å) and Cu-Cl (2.30 Å and 2.32 Å) bonds than E1 (Figure 9).

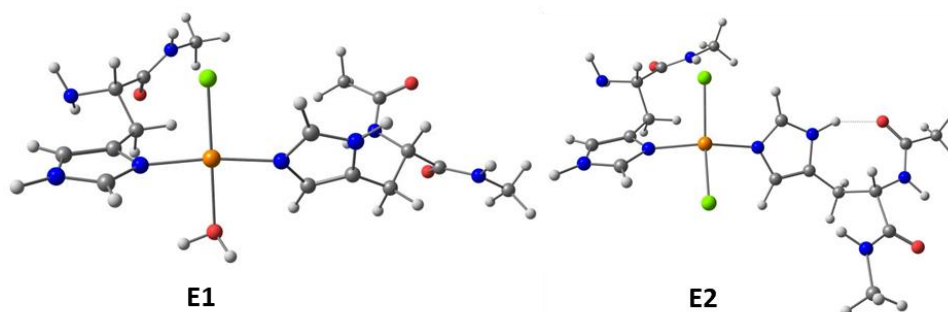


Figure 9. Optimized structure of models E1 and E2 coordinating one or two Cl-anions and decoordinating the N-terminal amine.

### *Influence of a solvation model in problematic systems*

To finalize this computational study of the structures, we accounted for a solvation model based on the conductor-like polarizable continuum model, CPCM, to circumvent problematic systems, i.e. A2, A3, C1 and D1. The solvent used was water with a dielectric constant of 80.4 and refractive index of 1.33. Adding this layer on top of the calculation greatly improves the optimization convergence. In the case of the A2/A3 pair, only one of these optimized to the Cu<sub>3</sub>N<sub>2</sub>O

configuration with the A3 structure still having one of the water molecules decoordinating the metal center. The C1 and D1 systems converged properly, and the optimized structures were the expected square planar and square base pyramidal geometries, respectively (Figure 10).

These calculations show that additional information is necessary to guide the optimization of models towards the expected behavior of the enzyme. Therefore, greater models are being built to provide the best geometrical and structural correlations between the experimental observations and the theoretical models. To this end, a cap of water molecules will be added by molecular mechanic simulations and will help to maintain the appropriate number of water molecules around the coordination site. Also, other amino acids which interact and stabilize the two histidine residues coordinating the metal center will be added. This line of work will be done in collaboration with Dr. Dimitrios A. Pantazis from Max-Planck-Institut für Kohlenforschung, in Mülheim an der Ruhr, Germany.

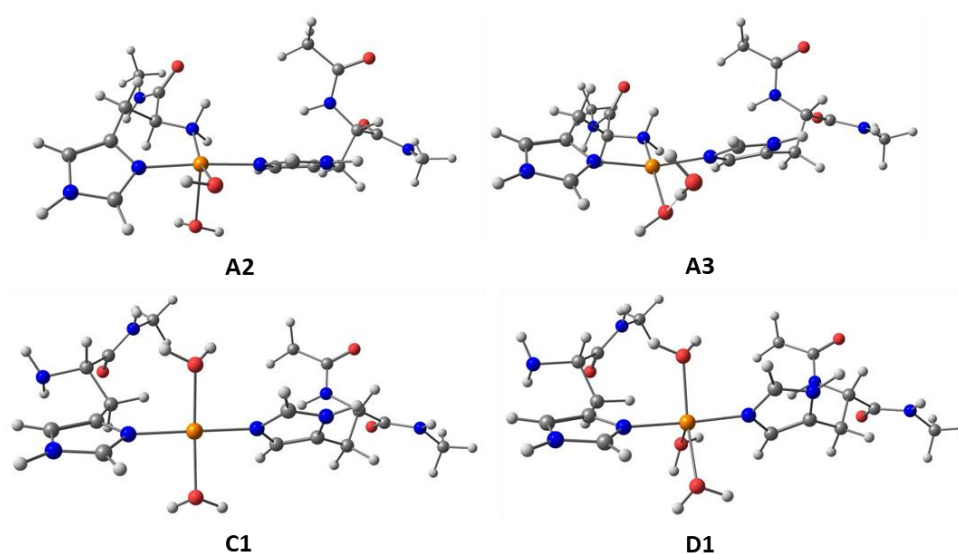


**Figure 10.** Optimized structures of models A2, A3, C1 and D1 obtained by inclusion of the water solvent through the CPCM solvation model.

Since structure D1 was properly optimized with the CPCM solvation model, we used this level of calculation to obtain the modified structures within the set (Figure 11). Firstly, we optimized the single deprotonation of each water molecule, *i.e.* structures D2, D3, and D4. Secondly, we optimized the double deprotonated models, structures D5, D6, and D7, by modifying two water molecules and keeping one protonated. Finally, we attempted an optimization of the triply deprotonated structure of the complete model set, structure D8.

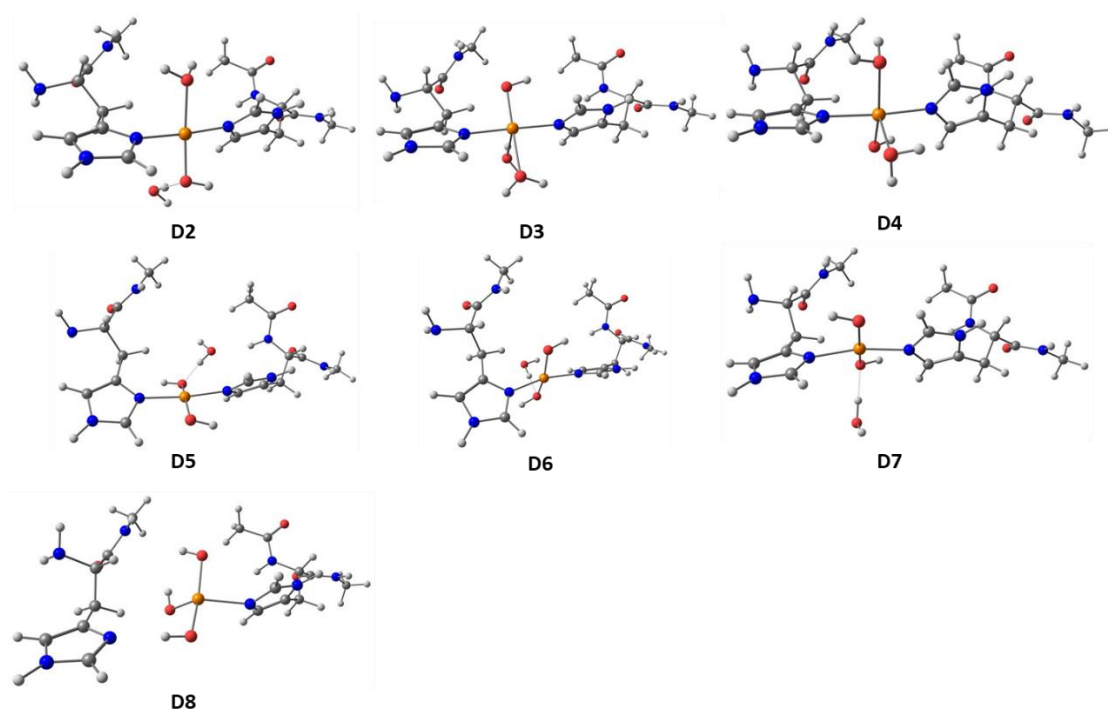


**Figure 11. Optimized structures of models D2 to D8 obtained with inclusion of the water solvent through the CPCM solvation model.**

Optimization of several D models did not converge to the expected structure. In one singly deprotonated and all the doubly deprotonated structures, the remaining water molecule decoordinates from the metal center, *i.e.* structures D2, D5, D6, and D7. In the case of the triply deprotonated structure, with the most negatively charged ligands, the histidine terminal amino acid was found completely decoordinated from the metal (D8). CPCM alone is not enough to secure the geometries of some structures from the model set. As mentioned earlier, greater models including explicit solvation would be needed to investigate this Cu<sub>2</sub>N<sub>3</sub>O geometry.

### 1.3 – Calculation of EPR parameters of the LPMO models

DFT functionals used in the following work include BP86 [22] [23], B3PW91, [26] [27] PBE0, [28], and M06. [29] Computation of hyperfine coupling constants used increased integration grids (Grid6 in ORCA convention), increased radial integration accuracy (IntAcc 6.0) and specially enhanced grids for the copper center (SpecialGridIntAcc 11). For all ligand atoms, the def2-TZVP basis sets [24] were used. In the case of Cu, a homemade basis set was used. This basis set, named aug-cc-pVTZ-Jmod, consists of a modified version of aug-cc-pVTZ-J [30] [31] with decontracted

s functions and removal of innermost s primitives. It was found to be robust, flexible, and generally applicable for the calculation of hyperfine coupling constants [6] and g-factors. No approximations to calculate two-electron integrals were used when calculating hyperfine coupling constants to exclude any potential error related to density fitting approximations. Spin-orbit contributions were included through mean-field and effective potential approaches. The spin-orbit coupling operator was treated by an accurate mean-field (SOMF) approximation to the Breit–Pauli operator (SOCType 3 in ORCA). [32] [33] The potential was constructed to include one-electron terms, compute the Coulomb term in a semi-numeric way, incorporate exchange via one-center exact integrals including the spin-other orbit interaction, and include local DFT correlation (SOCFlags 1,2,3,1 in ORCA). Scalar relativistic calculations were performed with the zeroth-order regular approximation (ZORA) [34] [35] [36] Hamiltonians. Picture change effects were applied as appropriate. The effect of an implicit solvent via a continuum solvation model was investigated using CPCM. [37]

### 1. Functional evaluation

To obtain the most reliable method for calculating the EPR parameters of the LPMO models, we assessed the performance of functionals with respect to the experimental values of the major species of the *PlAA10* [11] enzyme. It has to be noted that the experimental EPR x, y, and z notations have been changed to min., mid., and max. since the orientation cannot be properly determined unless we are in solid state.

The major species supposedly corresponds to the geometrical structure of model A1. Our previous study on a large set of small Cu(II) complexes pointed to the use of hybrid functionals for the calculation of both the hyperfine coupling constants [6] and the g-factor. The best performing one for calculating the HFCs was the B3PW91 functional, [26] [27] followed by PBE0. [28] For the g-factor, however, both fell short compared to M06. [29] In addition, the use of a scalar relativistic correction using ZORA, [34] [35] [36] and inclusion of a solvation model, CPCM, [37] were investigated (Table 4).



**Table 4.** Evaluation of EPR parameters for structure A1 using different functionals, methods, and accounting for the solvation effect during optimization. Experimental values reported are for the major species of the *P/AA10* enzyme.

Optimization method	Functional and method for EPR	$g_{\min}$	$g_{\text{mid}}$	$g_{\max}$	$A_{\min}^{\text{Cu}}$ (MHz)	$A_{\text{mid}}^{\text{Cu}}$ (MHz)	$A_{\max}^{\text{Cu}}$ (MHz)
BP86	B3PW91	2.024	2.104	2.188	118	226	375
	M06	2.030	2.171	2.374	334	511	710
	PBE0	2.025	2.119	2.214	105	272	375
	PBE0 + ZORA	2.027	2.121	2.218	109	278	405
BP86 + CPCM	B3PW91	2.041	2.070	2.180	50	174	492
	M06	2.054	2.107	2.350	40	389	497
	PBE0	2.044	2.077	2.198	36	170	514
	PBE0 + ZORA	2.046	2.077	2.199	13	140	547
<b>Exp.</b>		2.025	2.103	2.260	95	220	355

The structure optimized with CPCM seem to yield slightly more axial values, in both the  $g$ - and  $A$ - tensors, than the ones obtained without it. In general, there is a decrease of the  $g_{\text{mid}}$  and an increase of the  $g_{\min}$  values, pointing towards the  $g_{\min} \approx g_{\text{mid}}$  association. Similarly, for the hyperfine values, both the  $A_{\min}^{\text{Cu}}$  and  $A_{\text{mid}}^{\text{Cu}}$  decrease whereas the  $A_{\max}^{\text{Cu}}$  increases drastically. Naturally, this leads to large deviations with respect to experimental results obtained for the major species. It displays rhombic EPR parameters which is thus expected for structure A1. A closer inspection into the structures reveals that A1 features a square-pyramidal structure when CPCM is used, while a distorted trigonal bipyramidal geometry is expected experimentally and obtained with calculations in gas-phase (Figure 12). Again, larger models, accounting for the interaction of other amino acids would be needed to produce a model capable of better capturing the enzyme's structural parameters.

Using the gas-phase structure, the B3PW91 functional reproduces well the experimental values obtained for *P/AA10*. However, it underestimates on the calculation of the  $g_{\max}$  component. On the contrary, PBE0 seems to reproduce the magnitude of this component properly but starts failing in the calculation of the hyperfine couplings and displays a slightly larger  $A_{\text{mid}}^{\text{Cu}}$  component. This effect can be seen on the hyperfine ratios:  $A_{\max}^{\text{Cu}}/A_{\text{mid}}^{\text{Cu}} = 1.64 \text{ exp.}$  vs.  $1.66 \text{ calc.}$  with B3PW91 vs.  $1.38 \text{ calc.}$  with PBE0, and  $A_{\text{mid}}^{\text{Cu}}/A_{\min}^{\text{Cu}} = 2.32 \text{ exp.}$  vs.  $1.92 \text{ calc.}$  with B3PW91 vs.  $2.59 \text{ calc.}$  with PBE0. Both are reproducing the overall experimental EPR values quite well. However, we decided to use B3PW91 as the functional of choice for the calculation of all the EPR parameters of the models since the hyperfine values are the most sensitive and presents the best agreement with experiment when looking at all individual contributions. When evaluating all models, we will thus expect the  $g_{\max}$  component to be smaller than the actual value. The M06 functional does not

reproduce the experimental g-tensor components and overshoots in general. As observed before, it is not adapted to the calculation of hyperfine coupling constants.

This initial evaluation of the EPR parameters supports that structure A1 is the geometry observed in solution as the major species of *P/AA10*. The Cu(II) center is a 5-member coordinating complex within an intermediate geometry between square-pyramidal and trigonal bipyramidal.

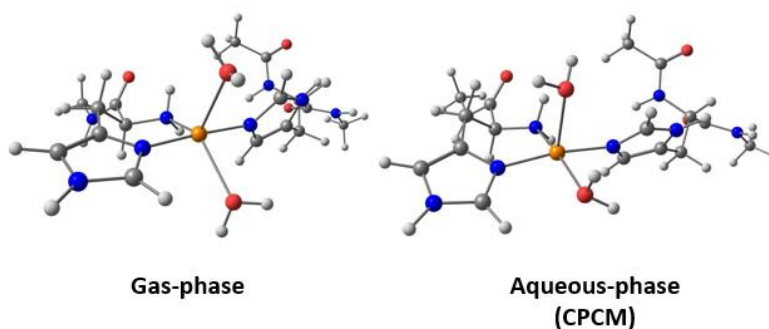


**Figure 12.** Optimized structures of model A1 in gas-phase and in aqueous-phase using CPCM and water as solvent.

## 2. Evaluation of EPR parameters for the LPMO models

From the optimized structures described previously, we evaluated the EPR parameters for all the sets of models. Note that for the structures which initially failed to optimize without the solvation model, the coordinates obtained with CPCM were used. However, the structures were kept for those who optimized successfully without CPCM. First, we investigated those structures with neutral charge and without forced distortion on the imidazole ring angles, i.e. A1, B1, C1, and D1 (Table 5).

**Table 5.** Calculated EPR parameters (B3PW91/aug-cc-pVTZ-Jmod) for structures A1, B1, C1 and D1. Experimental values of the major and minor species found in *P/AA10* [11] are reported as axial and rhombic, respectively.

Structure	$g_{\min}$	$g_{\text{mid}}$	$g_{\max}$	$A_{\min}^{\text{Cu}}$ (MHz)	$A_{\text{mid}}^{\text{Cu}}$ (MHz)	$A_{\max}^{\text{Cu}}$ (MHz)
<b>A1</b>	2.024	2.104	2.188	118	226	375
<b>B1</b>	2.028	2.096	2.189	155	162	314
<b>C1</b>	2.047	2.059	2.181	203	250	304
<b>D1</b>	2.030	2.106	2.206	152	219	527
<i>Exp. major species</i>	2.025	2.103	2.260	95	220	360
<i>Exp. minor species</i>	2.062	2.062	2.250	< 90	< 90	537

Table 5 shows the EPR parameters predicted for structures A1, B1 C1 and D1. As mentioned earlier, structure A1 probably reproduces the major species found in *P/AA10*, corresponding to the “normal” coordination sphere and the rhombic EPR signal. For this calculation, we rather adequately reproduced the experimental values despite a small underestimation of the  $g_{\max}$  term. Decoordinating a water molecule to produce a 4-member coordination sphere of the type  $\text{Cu}_3\text{N}_1\text{O}$  (structure B1) does not modify the rhombic character whatsoever even if there is a decrease in both the  $g_{\text{mid}}$  and  $A_{\text{mid}}^{\text{Cu}}$  values. A greater effect is observed in the proposed structure with decoordinated primary amine leading to a coordination sphere of type  $\text{Cu}_2\text{N}_2\text{O}$  (structure C1). This modification seems to create an axial g-tensor but with almost axial hyperfine values. Due to this large deviation for the hyperfine couplings, we do not consider that this modification alone produces the minor species with a complete axial character even if there is an influence when compared to B1. Finally, coordinating an external ligand, such as water, to produce D1 in a  $\text{Cu}_2\text{N}_3\text{O}$  coordination sphere swings the g- and A- tensors which are now more rhombic. The  $A_{\text{min}}^{\text{Cu}}$  and  $A_{\text{mid}}^{\text{Cu}}$  are still large and greater than 90 MHz. All the values obtained are generally consistent with the rhombic character.

This first comparison of the structures for the set of models reported in Table 5 only leads to rhombic tensors. This means that the modifications among them and originating from a  $\text{Cu}_3\text{N}_2\text{O}$  environment in a trigonal bipyramidal do not form and capture the minor species found in solution for the *P/AA10* [11] and *S/AA10E* [12] enzymes. Therefore, forming square planar 4-member species, decoordinating the primary amine alone, or coordinating an external water molecule does not produce at this stage any species having a computed EPR signal that resembles the experimental one.

Each water molecule found in structures A1, B1 and C1 were individually transformed by deprotonation into hydroxyl groups to produce A2, A3, B2, C2 and C3 structures. This compilation of structures presents a coordination sphere which is overall negative due to the presence of the hydroxyl anion. The EPR values were computed and are presented in the following table. Since A3 did not optimize properly, it was discarded from the group (Table 6).

**Table 6.** Calculated EPR parameters (B3PW91/aug-cc-pVTZ-Jmod) for structures A2, B2, C2, and C3. Experimental values of the major and minor species found in P/AA10 [11] are reported.

Structure	$g_{\min}$	$g_{\text{mid}}$	$g_{\max}$	$A_{\min}^{\text{Cu}}$ (MHz)	$A_{\text{mid}}^{\text{Cu}}$ (MHz)	$A_{\max}^{\text{Cu}}$ (MHz)
<b>A2</b>	2.041	2.044	2.150	27	49	613
<b>B2</b>	2.036	2.046	2.154	23	52	561
<b>C2</b>	2.036	2.045	2.151	55	118	649
<b>C3</b>	2.038	2.045	2.154	50	99	607
<b>D3</b>	2.047	2.054	2.179	15	35	620
<b>D4</b>	2.051	2.055	2.183	14	24	607
<i>Exp. major species</i>	2.025	2.103	2.260	95	220	360
<i>Exp. minor species</i>	2.062	2.062	2.250	< 90	< 90	537

Table 6 shows the EPR values obtained for structure A2, B2, C2, C3, D2, D3, and D4 which all have a single hydroxyl group coordinating the copper center. With this set, structure B2 is the closest to the experimental values obtained for the minor species of P/AA10, specially for the hyperfine values. Structure A2 has larger  $A_{\max}^{\text{Cu}}$  than B2 but is quite similar when other EPR parameters are considered. Structures C2 and C3 also exhibit a larger  $A_{\max}^{\text{Cu}}$  ones but also an increase on the  $A_{\text{mid}}^{\text{Cu}}$ . Structures D3 and D4 exhibit axial EPR parameters with low *min.* and *mid.* values, compared to a large *max.* value in both g- and A-tensors. In this group of structures, we observe that the EPR values calculated mainly displays axial characters and are well conserved throughout. In all cases, the *min.* and *mid.* g values are not exactly equal as observed in the experimental simulations but are very close to each other with the largest calculated difference between  $g_{\min}$  and  $g_{\text{mid}}$  being 0.010. For both the g-tensor and A-tensor, we obtain axial trends within this set of structures.

The deprotonation of the water molecule from structures A1, B1, C1, and D1, provided structures A2, B2, C2, C3, D2, D3 and D4 and leads to axial EPR parameters. The presence of the hydroxy ligand in the coordination sphere is driving the EPR tensors from rhombic to axial. The minor species may have a similar coordination sphere as B2, meaning that a hydroxyl group would be found coordinating the copper center of P/AA10 in the solution and a water molecule would be deccordinated. Water molecules bound to Cu(II) ions generally display pKa values ranging from 7-10. The presence of minor species bearing deprotonated copper-bound water molecules at pH 6.5 therefore appears plausible.

Following the first deprotonation, a second deprotonation can occur in the case where at least two water molecules are within the coordination sphere of copper. To this end, structures A4, C4, D5, D6, and D7 were modeled. This group has two hydroxyl ligands coordinating the copper center in different arrangements. Structural modifications between them comprise the decoordination of

the primary amine (C4) and also involve the coordination of an external water molecule in its place (D5, D6 and D7). To this series, we included the triple deprotonated structure which can only be obtained from structure set D. With the addition of an external water molecule after the decoordination of the primary amine, the Cu<sub>2</sub>N<sub>3</sub>O can sustain a triple hydroxy coordination sphere (D8). Unfortunately, only structures A4 and C4 could be optimized to lead to the expected species. Most of the models in structure set D featured a decoordinated water molecule (Table 7).

**Table 7. EPR parameters (B3PW91/aug-cc-pVTZ-Jmod) for structures A4 and C4. Experimental values of the major and minor species found in *P/AA10* [11] are reported.**

Structure	$g_{\min}$	$g_{\text{mid}}$	$g_{\max}$	$A_{\min}^{\text{Cu}}$ (MHz)	$A_{\text{mid}}^{\text{Cu}}$ (MHz)	$A_{\max}^{\text{Cu}}$ (MHz)
<b>A4</b>	2.033	2.068	2.173	99	243	412
<b>C4</b>	2.033	2.059	2.163	91	201	435
<i>Exp. Major species</i>	2.025	2.103	2.260	95	220	360
<i>Exp. Minor species</i>	2.062	2.062	2.250	< 90	< 90	537

The second deprotonation observed in structure A4 recovers slightly the original rhombicity found in structure A1. The hyperfine ratios are of the doubly deprotonated species are of similar magnitude to the deprotonated analogue:  $A_{\max}^{\text{Cu}}/A_{\min}^{\text{Cu}} = 1.66$  for A1 vs. 1.69 for A4, and  $A_{\text{mid}}^{\text{Cu}}/A_{\min}^{\text{Cu}} = 1.92$  for A1 vs. 2.03 for A4. We find however that the  $A_{\text{mid}}^{\text{Cu}}$  and  $A_{\max}^{\text{Cu}}$  are slightly larger in terms of absolute values compared to structure A1.

It is evident that the presence of charged ligands is affecting the EPR parameters of the models. By adding a hydroxyl group, we can predict highly axial g- and A- tensors. Chaplin and co-workers suggested that the minor species detected by EPR was arising from chloride binding to the copper in *SliAA10E* enzyme. For that reason, we investigated the effect of the Cl-anion by considering structures C1, E1 and E2 (Table 8).

**Table 8. EPR parameters (B3PW91/aug-cc-pVTZ-Jmod) for structures C1, E1, and E2. Experimental values of the major and minor species found in *SliAA10E* [12] are reported.**

Structure	$g_{\min}$	$g_{\text{mid}}$	$g_{\max}$	$A_{\min}^{\text{Cu}}$ (MHz)	$A_{\text{mid}}^{\text{Cu}}$ (MHz)	$A_{\max}^{\text{Cu}}$ (MHz)
<b>B1</b>	2.028	2.096	2.189	155	162	314
<b>C1</b>	2.047	2.059	2.181	203	250	304
<b>E1</b>	2.037	2.054	2.160	23	34	528
<b>E2</b>	2.041	2.061	2.172	26	30	520
<i>Exp. major species</i>	2.033	2.067	2.260	38	38	378
<i>Exp. minor species</i>	2.055	2.071	2.230	53	53	532

Structure B1 represents the proposed coordination sphere of the primary species found in *Ss*AA10E, *i.e.* coordinating the primary amine, two histidine and a single water molecule. The EPR values obtained for this structure are not exactly reproducing the experimental observation with the  $g_{\max}$  and  $A_{\max}^{\text{Cu}}$  values being lower. On the contrary, the  $g_{\text{mid}}$  and both the  $A_{\min}^{\text{Cu}}$  and  $A_{\text{mid}}^{\text{Cu}}$  are larger than experimental results. We are aware about the difficulty to adequately reproduce  $g_{\max}$  values, but due to the other offsets, we cannot confirm structure that B1 is a relevant model for the chloride-bound species in solution. Moreover, we have to remind that the EPR parameters of Cl-bound LPMO were reported for another AA10 enzyme. Nevertheless, the decoordination of the primary amine (structure C1) also leads to a set of rhombic EPR parameters, meaning that this effect alone will not yield the species with an axial EPR signal as proposed in the reaction scheme (Scheme 1). When one of the water ligands is exchanged by a Cl-anion as in structure E1, the EPR values are shifted and become axial. The  $A_{\max}^{\text{Cu}}$  hyperfine value is drastically increased and the  $g_{\max}$  value is slightly decreased with respect to structure C1. The EPR values obtained here are much closer to the experimental ones, especially in the case of the hyperfine tensor. Replacing the second water molecule for another Cl-anion yields structure E2 and varies the EPR parameters very slightly compared to those of structure E1. In general, the  $g$ -tensor values increase, and the  $A$ -tensor values slightly decrease while remaining mostly axial. It is not possible to distinguish which structure, E1 or E2, might be predominant in solution, but the effect of Cl-anion coordination leading to axial EPR parameters is clear.

Finally, we investigated the series of structures which possess neutral ligands but display a distortion around the imidazole rings. In the enzyme, this distortion may arise from strains from other amino acids. Structures A5, B3 and C5 were obtained from structures A1, B1 and C1, by optimization of an initial geometry having a completely flat angle between the imidazole rings. The original imidazole angles were found to be 75°, 67°, and 51° in A1, B1 and C1, respectively. After optimization, the dihedral angle between the rings was found to be 29° for A5, 4° for B3, and 11° for C5 (Table 9).

**Table 9. EPR parameters (B3PW91/aug-cc-pVTZ-Jmod) for structures A5, B3, and C5. The EPR values of the corresponding non-distorted structures are also presented: A1, B1, and C1. Experimental values of the major and minor species found in *PIAA10* [12] are reported.**

Structure	$g_x$	$g_y$	$g_z$	$A_x^{\text{Cu}}$ (MHz)	$A_y^{\text{Cu}}$ (MHz)	$A_z^{\text{Cu}}$ (MHz)
<b>A5</b>	2.031	2.092	2.188	96	309	313
<b>B3</b>	2.030	2.107	2.185	156	163	311
<b>C5</b>	2.012	2.088	2.178	166	222	360
<b>A1</b>	2.024	2.104	2.188	118	226	375
<b>B1</b>	2.028	2.096	2.189	155	162	314
<b>C1</b>	2.047	2.059	2.181	203	250	304
<i>Exp. Rhombic</i>	2.025	2.103	2.260	95	220	360
<i>Exp. Axial</i>	2.062	2.062	2.250	< 90	< 90	537

The EPR values obtained for the group display a rhombic character. For structure A5, the hyperfine values  $A_{\text{mid}}^{\text{Cu}}$  and  $A_{\text{max}}^{\text{Cu}}$  are of similar magnitude. When compared to the parent structure A1, there is an important increase of  $A_{\text{mid}}^{\text{Cu}}$  and a decrease in  $A_{\text{max}}^{\text{Cu}}$ . The EPR values obtained for B3 and B1 are essentially the same. The imidazole distortion affects very little the compared values in this case. The  $g_{\text{min}}$  component of C5 is predicted much lower than the one of C1. This decrease seems compensated by a larger  $g_{\text{mid}}$ , compared to that of C1. The  $g_{\text{max}}$  component and the hyperfine values are of the same order.

A simple distortion around the imidazole rings does not greatly affect the calculated EPR values. In all cases, the EPR parameters are rhombic with the unique exception for structure A5 with  $A_{\text{mid}}^{\text{Cu}}$  being essentially equally to  $A_{\text{max}}^{\text{Cu}}$ .

## 1.4 – Conclusions

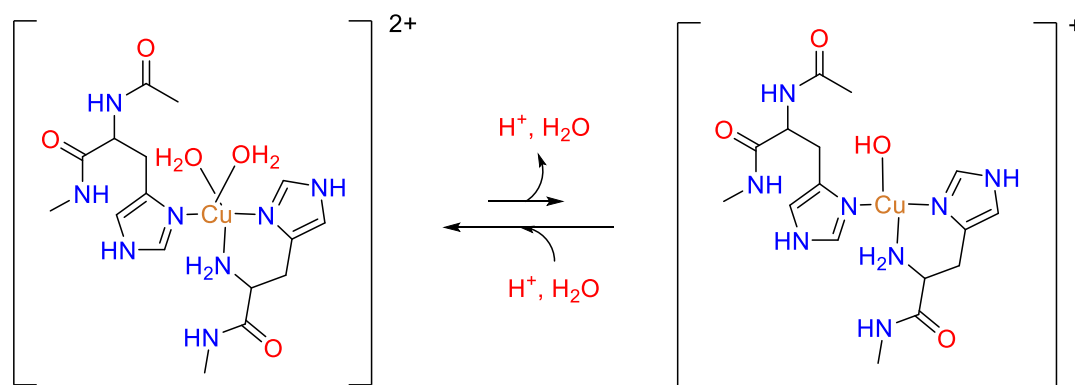
In this study, we presented small models of the LPMO enzyme based on the X-ray crystal structure of *PIAA10* [11] to rationalize the mixed species observed experimentally. [12] [11] These models have different coordination spheres around the copper center. The “normal” 5-member  $\text{Cu}_3\text{N}_2\text{O}$  complex was used as a reference before being subjected to structural modifications. First, we considered the deprotonation of one of the bound water molecules. Second, we looked into the decoordination of the N-terminal primary amine. Finally, an extra water molecule was coordinated to the latter. These changes lead to various coordination spheres around the copper center:  $\text{Cu}_3\text{N}_1\text{O}$ ,  $\text{Cu}_2\text{N}_2\text{O}$ , and  $\text{Cu}_2\text{N}_3\text{O}$ . Each of these structure sets was further modified, while keeping their respective coordination sphere, by performing single, double, and even triple,

deprotonation of the water molecules. Also, we investigated the distortion of the imidazole rings from orthogonal to parallel geometries.

When the coordinating ligands are neutral, it was found that the EPR parameters display a rhombic character and produce values similar to those of the major species found in *P/AA10* EPR spectra. Structure A1 was best performing for reproducing this species. This structure also agrees with the experimental crystal structure for which the copper center is in a distorted coordination between square pyramidal and trigonal bipyramidal. Changing the coordination sphere, by decoordinating a single water molecule, decoordinating the N-terminal amine, or adding an extra water ligand, does not reproduce the minor species observed in experiment and maintains the rhombicity of the EPR parameters. Upon deprotonation of a bound water molecule to the corresponding hydroxyl group, the EPR parameters drastically shift in magnitude and become axial. Structure B2 is best reproducing the experimental data, meaning that the minor species found in *P/AA10* may very well be a 4-member square planar structure of type  $\text{Cu}_3\text{N}_1\text{O}$  with a coordinating hydroxyl ligand. However, the second and third deprotonations were performed, axial parameters were not obtained and the computed EPR values were all found to be rhombic. To investigate the anion binding effect, we coordinated one or two Cl<sup>-</sup> ions to the copper center in the structure having a decoordinated N-terminal amine, as proposed by Chaplin and co-workers. [12] We found that the simple decoordination of the amine does not converge to the species with axial EPR parameters as they all remain rhombic. However, adding one or two Cl<sup>-</sup> anions did and in this case the second anion does not recover the initial rhombic character. These observations support the hypothesis of Chaplin *et. al.* in the case of chloride-containing buffers. Finally, distortion of the imidazole rings was not found to have significant effects when comparing the resulting EPR parameters to their orthogonal counterpart.

In conclusion, we found that the main reason for a mixed EPR signal in *P/AA10* might be the presence of a hydroxyl group coordinating the metal center producing the observed minor species (Scheme 8). The major species was found to be a 5-member  $\text{Cu}_3\text{N}_2\text{O}$  complex with a distorted trigonal bipyramidal structure with computed EPR values close to the experimental ones. The minor species forms from the decoordination of a water molecule, and deprotonation of the remaining water molecule to produce a hydroxyl group. Decoordinating the primary amine, distortion of the imidazole rings, and coordination of an extra water molecule does not lead to structures with computed EPR parameters comparable to the experimental ones for minor species.



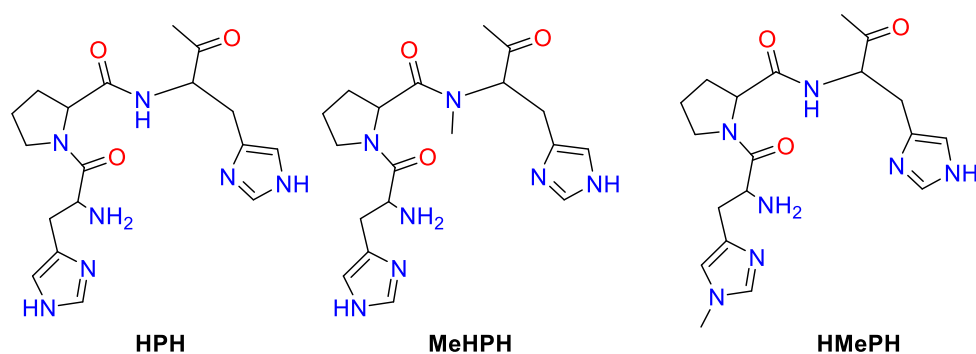


Scheme 8. Proposed structures for major and minor species referring to model system A1 and B2.

## 2 – Correlating experiment and theory in predicting the structures of a small LPMO-like peptide

The His-Pro-His (HPH) peptide was designed by Dr. Alda Lisa Concia, a former postdoc in the lab, to imitate the active site of LPMO and in particular, its histidine brace motif (Scheme 9). Four potential N-donor atoms are present: the N-terminal primary amine, two imidazole rings, and an amide moiety of the peptidic bond. In order to study the possibility of amide-binding, an amide-methylated analogue, named MeHPH, was also synthesized. In addition, some fungal LPMOs bear a methyl group at the N position of the imidazole ring within the histidine brace. [4] [38] [39] [40] This modification is called the  $\tau$ -methylation. To mimic the latter, an analogue of the HPH peptide, named HMePH, was thus synthesized, bearing the methylated group.

The functional roll of this modification remains uncertain although it was suggested that it may be related to the redox potential of the active site and its affinity for copper. It has also been proposed that the  $\tau$ -methylation could decrease the oxidative self-inactivation observed in LPMO. [41] [42] [43] [16] [44]



**Scheme 9.** Synthesized **HPH** peptide and its methylated analogues mimicking the coordination sphere of the LPMO's active site with the histidine brace and the imidazole ring. The **MeHPH** and **HMePH** are N-methylated analogues of **HPH** with methyl groups at the peptidic amide and at the imidazole ring of the histidine brace positions.

Coordination of Cu(II) to these tripeptide system was studied as a function of pH and under various experimental conditions. In particular, different copper salts were used: Cu(NO<sub>3</sub>)<sub>2</sub> and Cu(OAc)<sub>2</sub>. The species formed were analyzed by different techniques including potentiometric titrations, UV-vis, circular dichroism and EPR spectroscopies as well as electrochemistry. Coordination of the amide function at pH <12 was not observed. From potentiometric titrations, it appears that a major mononuclear species (60-80%) is formed at pH 7-9 and that the species are highly similar in the case of HPH-Cu and HMePH-Cu. No significant changes of redox properties were observed upon methylation of the N-terminal imidazole.

To further investigate the structure of the HPH-Cu and HMePH-Cu complexes formed at pH 7-9, we relied on theoretical methods based on Density Functional Theory (DFT). Multiple coordination spheres were envisioned for which we extracted spectroscopic information, mainly EPR parameters for comparison with experimental results. This investigation gave insight into the possible structures existing in solution under certain conditions. In addition, we tried to rationalize the redox properties and a comparative study of the different electronic configurations was conducted using selected structures.

## 2.1 – Investigation of possible HPH peptide structures and its modifications

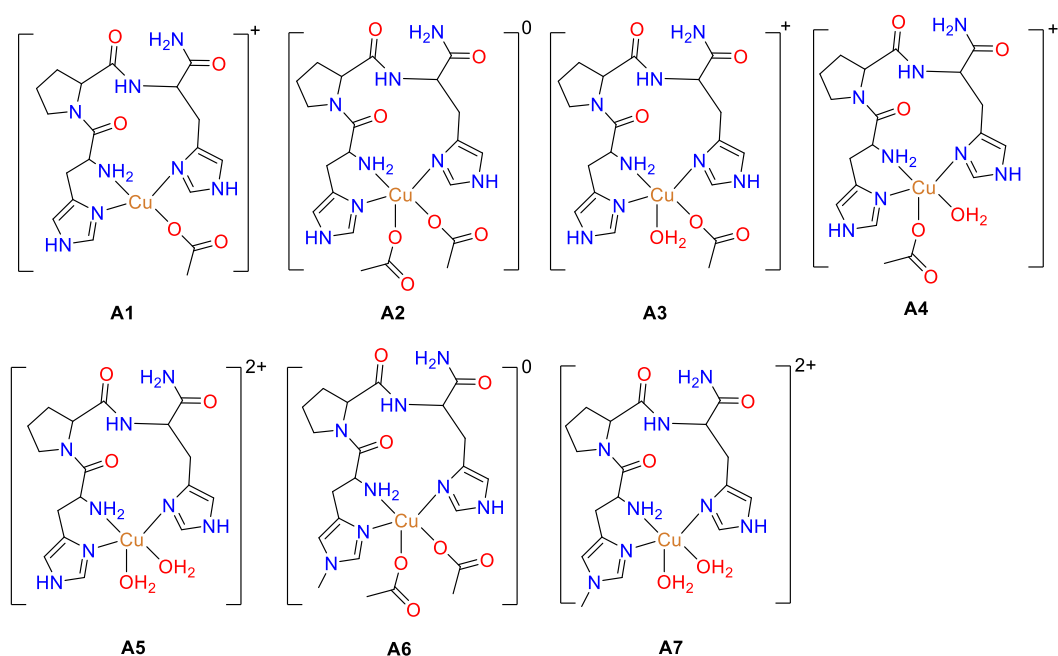
To study the structure of the HPH complex in solution, we constructed various models with multiple modifications of the coordination sphere. These models are divided in sets of structures and are based on the coordinating atoms around the copper center and the origin of the exogenous ligands. The following structures and corresponding modifications were considered in this study:

- LPMO-like coordination sphere, *i.e.* coordination of histidine brace and imidazole ring,
- Decoordination of the monodentate histidine,
- Protonation of the decoordinated histidine,
- N-methylation of the imidazole ring within the histidine brace.

Given the nature of the HPH peptide, the copper center was built to keep a 4- or 5-member coordination sphere. Additionally, the possible external ligands investigated are of different electronic charge: the acetate anion and the neutral water molecule. In all cases, the oxidation state of copper is set at +II to maintain an  $S = 1/2$  spin state which is EPR active.

### Structure set A

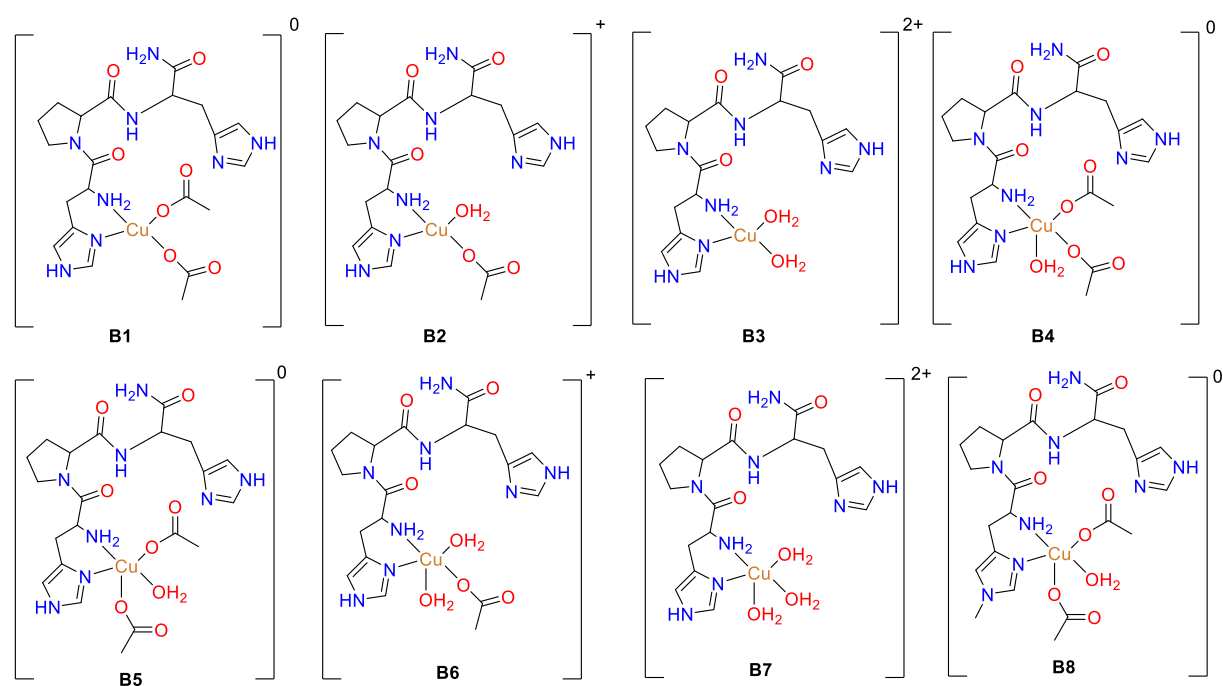
The set A considers the complete coordination of the ligand through the histidine brace and the free imidazole ring. In addition, two O-based ligands of external origin, namely water and/or acetate, have been introduced as coordinating entities to produce either a 4- or 5-member coordination sphere around the copper center. This set thus includes either a Cu<sub>3</sub>N<sub>1</sub>O or a Cu<sub>3</sub>N<sub>2</sub>O coordinating environment. In addition, two 5-member structures were investigated for the N-methylated counterpart (Scheme 10).



Scheme 10. Structures included in set A. Structure A1 has a 4-member coordination sphere of the Cu<sub>3</sub>N<sub>1</sub>O type bearing an acetate ligand. Structures A2 to A5 have a 5-member coordination sphere of the type Cu<sub>3</sub>N<sub>2</sub>O with a combination of acetate and water molecule coordinating the copper center. Structures A6 and A7 are the N-methylated counterparts of structures A2 and A5.

### Structure set B

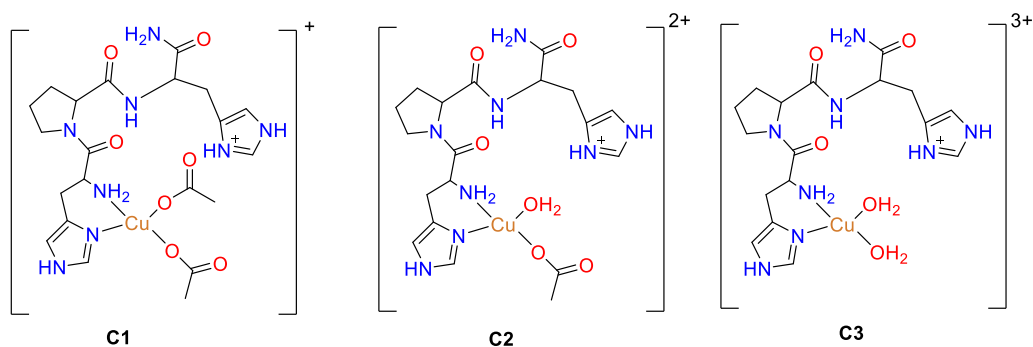
Within set B, we considered the decoordination of the second imidazole ring while keeping the coordination of the histidine brace. This decoordination has been suggested to occur at lower pH values based on spectroscopic and potentiometric experiments. This decoordination provides an empty site for coordination of another external ligand. We considered both a 4- or 5-member coordination spheres around the copper center producing either a Cu<sub>2</sub>N<sub>2</sub>O or a Cu<sub>2</sub>N<sub>3</sub>O environment. Also, one 5-member structure was investigated for its N-methylated counterpart (Scheme 11).



**Scheme 11.** Structures included in set B. Structures B1 to B3 have a 4-member coordination sphere of the Cu<sub>2</sub>N<sub>2</sub>O type. Structures B4 to B7 have a 5-member coordination sphere of the type Cu<sub>3</sub>N<sub>2</sub>O with a combination of acetate and water molecules coordinating the copper center. Structure B8 is the N-methylated counterpart of structure B5.

### Structure set C

Within set C, we considered a different protonation state of the free imidazole ring. Indeed, if this imidazole is decoordinated, it is likely protonated at acidic pH values. We intended to understand the effect of this protonation on the properties of the copper complex, and we thus only considered a 4-member coordination sphere producing a Cu<sub>2</sub>N<sub>2</sub>O environment (Scheme 12).



**Scheme 12.** Structures included in set C. All structures have a 4-member coordination sphere of the Cu<sub>2</sub>N<sub>2</sub>O type, with a combination of acetate and water molecules coordinating the copper center.

## 2.2 –Computational studies of the model systems from sets A, B and C: Energetic considerations

The Gibbs free energies (G) obtained from optimizations were calculated for all structures in each set, except for the methylated counterparts since these models are exclusively investigated for their electronic properties. In addition, the free energy was also calculated for the ligands alone (acetate and water), as well as the complexes without any external ligand coordinating the metal center, denoted as LCu. Finally, we evaluated the binding energy by calculating the free energy difference between the full complex and its individual components. For example, in the case of structure A1, we have:  $\Delta G = G_{A1} - (G_{LCu} + G_{Ac})$ . The obtained values are presented in Table 10 for set A, Table 11 for set B, and Table 12 for set C. Finally, the relative free energy differences,  $\Delta\Delta G$ , were computed with respect to the lowest binding energy and graphically reported in Figure 13.

**Table 10.** Gibbs free energies and binding energies for structures in set A. LCu represents the common coordination sphere shared between all structures.

Structure set A	Coordination sphere	Free Energy, G (Eh)	Free Energy Difference, $\Delta G$ (kJ/mol)	Relative Free Energy Difference, $\Delta\Delta G$ (kJ/mol)
<b>A1</b>	Cu <sub>3</sub> N(Ac)	-3193.55	-139.3	31.4
<b>A2</b>	Cu <sub>3</sub> N(Ac) <sub>2</sub>	-3422.02	-165.7	5.0
<b>A3</b>	Cu <sub>3</sub> N(Ac)(H <sub>2</sub> O)	-3269.94	-155.6	15.1
<b>A4</b>	Cu <sub>3</sub> N(Ac)(H <sub>2</sub> O)	-3269.95	-170.7	0.0
<b>A5</b>	Cu <sub>3</sub> N(H <sub>2</sub> O) <sub>2</sub>	-3117.84	-99.2	71.5
LCu	Cu <sub>3</sub> N	-2965.03		
Acetate	Ac	-228.47		
Water	H <sub>2</sub> O	-76.39		

### Structure set A

Structure A4 is the most stable complex of this set with a binding energy at -170.7 kJ/mol. In this structure, the histidine brace and the second imidazole are coordinated to the copper center in addition to a water molecule in the basal position and an axial acetate ligand, forming a 5-member coordinating complex. The opposite complex, structure A3, featuring an acetate ligand in the basal position and an axial water molecule, has a relative binding energy of +15.1 kJ/mol. Structure A2 with two acetate anions has a binding energy of -165.7 kJ/mol, which results in a +5.0 kJ/mol difference against the reference. This small difference does not allow us to discriminate between A2 and A4 as the most susceptible structure in solution. Structure A5 with two water molecules has the highest relative binding energy and lies at +71.5 kJ/mol with respect to A4.

**Table 11.** Gibbs free energies and binding energies for structures in set B. LCu represents the common coordination sphere shared between all structures.

Structure set B	Coordination sphere	Free Energy, G (Eh)	Free Energy Difference, $\Delta G$ (kJ/mol)	Relative Free Energy Difference, $\Delta\Delta G$ (kJ/mol)
<b>B1</b>	Cu2N(Ac) <sub>2</sub>	-3422.04	-356.5	20.1
<b>B2</b>	Cu2N(Ac)(H <sub>2</sub> O)	-3269.94	-301.0	77.4
<b>B3</b>	Cu2N(H <sub>2</sub> O) <sub>2</sub>	-3117.83	-205.0	173.6
<b>B4</b>	Cu2N(Ac) <sub>2</sub> (H <sub>2</sub> O)	-3498.43	-378.7	0.0
<b>B5</b>	Cu2N(Ac) <sub>2</sub> (H <sub>2</sub> O)	-3498.42	-352.3	26.4
<b>B6</b>	Cu2N(Ac)(H <sub>2</sub> O) <sub>2</sub>	-3346.34	-333.1	45.6
<b>B7</b>	Cu2N(H <sub>2</sub> O) <sub>3</sub>	-3194.23	-237.7	141.0
LCu	Cu2N	-2965.03		
Acetate	Ac	-228.47		
Water	H <sub>2</sub> O	-76.39		

### Structure set B

Structure B4, another 5-member coordinating complex, is the most stable with a binding energy at -378.7 kJ/mol Table 11. It coordinates the histidine brace to the copper center in addition to two acetate ligands leading to a square pyramidal geometry with a water molecule in axial position. Removing this water molecule destabilizes the system by +20.1 kJ/mol, as seen with structure B1, while putting the water molecule in the basal position, interchanging with an acetate ligand, structure B5, increases the system energy by +26.4 kJ/mol. Square planar structures B2 and B3 contain at least one water molecule while B7 features three water molecules. Structures B3, B7 and

B2 are the highest in energy and lie at +173.6, +141.0 and +77.4 kJ/mol, respectively, when compared to B4.

**Table 12.** Gibbs free energies and binding energies for structures in set C. LCu represents the common coordination sphere shared between all structures.

Structure set C	Coordination sphere	Free Energy, G (Eh)	Free Energy Difference, $\Delta G$ (kJ/mol)	Relative Free Energy Difference, $\Delta\Delta G$ (kJ/mol)
<b>C1</b>	Cu2NH(Ac) <sub>2</sub>	-3422.49	-369.5	0.0
<b>C2</b>	Cu2NH(Ac)(H <sub>2</sub> O)	-3270.40	-219.2	150.3
<b>C3</b>	Cu2NH(H <sub>2</sub> O) <sub>2</sub>	-3118.28	-318.8	50.6
LCu	Cu2NH	-2965.42		
Acetate	Ac	-228.47		
Water	H <sub>2</sub> O	-76.39		

### Structure set C

The calculated 4-member structures from C1 to C3, show greater stability when the same ligand is used to coordinate the copper center. The most stable structure coordinates two acetate anions. The most unstable structure coordinates one acetate and one water molecule. The two water molecule complexes fall in between these two structures. Overall, the negatively charged ligands greatly reduces the complex's relative free energy difference.

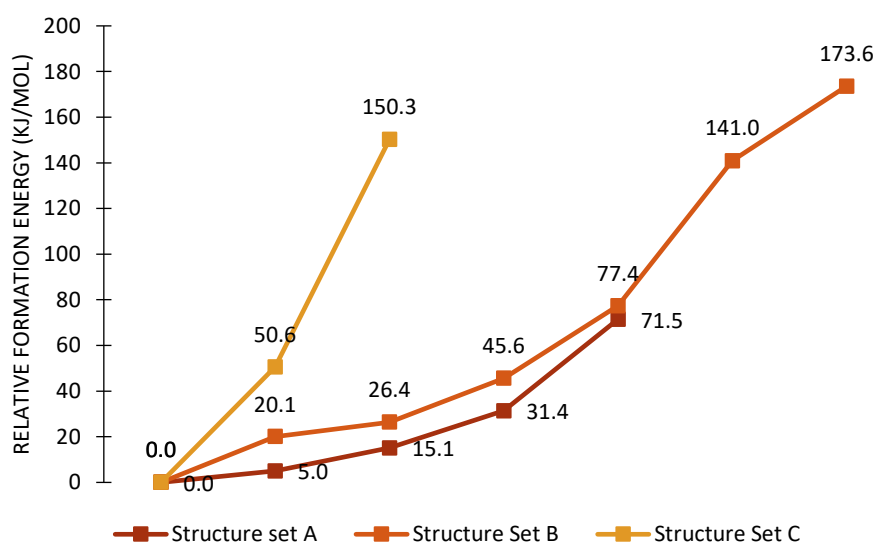


**Figure 13.** Relative binding energies calculated for selected structures in sets A (dark red), B (orange), and C (yellow). The corresponding structures and their relative free energies are indicated.

This comparative study provides a great insight on plausible structures that can exist in solution. In general, we observe that square planar geometries in 4-member coordination spheres (A1 and B2-3) display a greater relative free energy difference than the ones obtained with an extra ligand to produce the 5-member coordination sphere (A2-5 and B4-7). Also, it was shown that as the number of water molecules increases in the coordination sphere, the binding energy increases as well. It is easier for this complex to coordinate an acetate anion than the neutral water molecule. Structures A4, A3, A2, and structure B4 appear as the most interesting species regarding their relative energy and coordination spheres. Further investigations based on spectroscopic studies are pursued with these models.

### 2.3 – Calculation of EPR parameters

Using all structures in sets A and B, except the ones bearing the methylated imidazole, we calculate the EPR parameters to reproduce the experimental values and look to narrow down on the most probable structure existing in solution at given conditions. The experimental EPR values obtained for the HPH peptidic complex in acetate buffer at pH 7, are the following:  $g_x = g_y = 2.058$ ,  $g_z = 2.243$ , and  $A_z^{\text{Cu}} = 535$  MHz. This EPR signature displays an axial symmetry with a much larger parallel component compared to the perpendicular ones. Table 13 presented below reports the computed g-tensors and hyperfine values for structures A1 to A5, and B1 to B7.

**Table 13. DFT-calculated (B3PW91/aug-cc-pVTZ-Jmod) EPR parameters of selected structures in sets A and B. Experimental values are reported MOPS buffer at pH 7.5.**

Structure	Coordination sphere	$g_x$	$g_y$	$g_z$	$A_x^{\text{Cu}}$ (MHz)	$A_y^{\text{Cu}}$ (MHz)	$A_z^{\text{Cu}}$ (MHz)
<b>A1</b>	Cu3N(Ac)	2.045	2.046	2.164	22	28	617
<b>A2</b>	Cu3N(Ac) <sub>2</sub>	2.050	2.068	2.196	3	90	562
<b>A3</b>	Cu3N(Ac)(H <sub>2</sub> O)	2.049	2.051	2.178	3	5	597
<b>A4</b>	Cu3N(Ac)(H <sub>2</sub> O)	2.052	2.058	2.185	31	68	563
<b>A5</b>	Cu3N(H <sub>2</sub> O) <sub>2</sub>	2.045	2.060	2.178	31	109	539
<b>B1</b>	Cu2N(Ac) <sub>2</sub>	2.048	2.053	2.173	4	12	608
<b>B2</b>	Cu2N(Ac)(H <sub>2</sub> O)	2.042	2.061	2.171	3	89	561
<b>B3</b>	Cu2N(H <sub>2</sub> O) <sub>2</sub>	2.047	2.049	2.168	11	29	642
<b>B4</b>	Cu2N(Ac) <sub>2</sub> (H <sub>2</sub> O)	2.052	2.059	2.187	16	32	592
<b>B5</b>	Cu2N(Ac) <sub>2</sub> (H <sub>2</sub> O)	2.053	2.071	2.199	8	98	555
<b>B6</b>	Cu2N(Ac)(H <sub>2</sub> O) <sub>2</sub>	2.049	2.062	2.183	3	53	596
<b>B7</b>	Cu2N(H <sub>2</sub> O) <sub>3</sub>	2.055	2.064	2.189	26	57	594
<b>Exp.</b>		2.058	2.058	2.243	-	-	535



### *Structure set A*

Considering the g-tensor, all calculated values seem relatively close to the experimental ones. A better insight is obtained by filtering through the comparison of the hyperfine coupling constants. Three structures best reproduce the experimental value of 535 MHz: structure A2 with a computed value of 562 MHz, structure A4 at 563 MHz, and structure A5 at 539 MHz, the latter leading to the best agreement with experimental. The other structures have larger deviations with computed hyperfine coupling constants of around 600 MHz. Considering structures A2, A4 and A5, we can now look at their predicted the g-tensor in more detail. Structure A5 falls short in reproducing the  $g_x$  value at 2.178 compared to the larger values obtained for A2 and A4 e.g. 2.196 and 2.185, respectively. Similarly, the computed  $g_x$  and  $g_y$  values for A5 are somewhat smaller on average than those obtained for A2 and A4. In terms of coordination geometry, structures A2, A4 and A5 cover the complete array of possibilities with 5-member coordinating systems. Structure A2 coordinates two acetate anions, structure A4 coordinates one acetate anion and one water molecule, and structure A5 coordinates two water molecules. It is difficult to distinguish between all three structures which would be best representing the one found in solution since, for instance, the computed hyperfine coupling constant for A5 best reproduces the experimental  $A_z^{\text{Cu}}$  value but not the g-tensor. On the other hand, A2 displays a computed g-tensor close to the experimental one but with a  $A_z^{\text{Cu}}$  value in poor agreement with experiment. Finally, structure A4 seems to fall in an in-between situation and might represent the best compromise to describe the HPH peptidic complex.

### *Structure set B*

Following the analysis of the DFT-predicted hyperfine coupling constants, only two structures fall below 590 MHz: structure B2 with a computed value of 561 MHz and structure B5 at 555 MHz. Looking at their corresponding g-tensors, structure B5 has the largest  $g_z$  component at 2.199, whereas structure B2 falls short at 2.171. Similarly, the average  $g_x$  and  $g_y$  components of structure B2 are found to be smaller than those obtained for B5. Looking at their geometries, structure B2 is a 4-member Cu2N-coordinating system bearing one acetate and one water molecule. Structure B5 is a 5-member coordinating system which has two acetate anions and one water molecule as ligands. The latter thus best reproduces both the experimental g-tensor and hyperfine coupling constants within this set.

After calculating the EPR parameters of structure sets A and B, we selected the five structures capable of reproducing the experimental data. Three structures belong to structure set A with a

Cu3N2O coordination sphere. These structures differ in the origin of the oxygen-based ligands which seems to be correlated to reproducing either the g-tensor or the hyperfine values. Structure A2 coordinates two acetate anions and best reproduces the g-tensor. Structure A5 coordinates two water molecules and is in great agreement with the experimental hyperfine coupling constant. Structure A4 represents a great compromise between both cases coordinating one acetate anion and one water molecule. The two remaining structures are found in structure set B with the B2 one being a 4-member coordinating system and the B5 a 5-member system. The latter is best reproducing both the experimental g-tensor and  $A_z^{\text{Cu}}$  values within the structure set B.

## 2.4 – Calculation of UV-vis spectra

Time dependent DFT (TD-DFT) is a computational method used to predict the vertical transition energies of a given system and will be employed in the present case to further compare the molecular properties of our structures sets with the experimental data to help identifying the structure of the HPH peptidic complex in solution. Similarly to EPR, UV-vis spectroscopy is commonly used to characterize Cu(II) complexes since they exhibit specific charge transfers and d-d electron transitions. In this study, we aim to predict and reproduce the d-d electron transition found in the HPH peptidic complex. In MOPS (3-morpholinopropane-1-sulfonic acid) buffer at pH 7.5, HPH exhibits an absorption band at 620 nm. Using all non-methylated structures of sets A and B, we report the three main transitions calculated by TD-DFT in the range between 500 and 800 nm, which are sorted with respect to the computed wavelengths,  $\lambda$ , and oscillator strengths,  $f$ . We also plotted the resulting TD-DFT predicted spectra for selected structures to compare them with the experimental results. Table 14 presents the results of our computations for structure set A, and Table 15 those for structure set B. Figure 14 presents the experimental UV-vis spectrum together with those calculated by TD-DFT for selected structures.

**Table 14. TD-DFT calculated electronic transitions (PBE0/def2-TZPV) for structure set A. The experimental absorption band obtained is also reported at pH 7.5 in MOPS buffer.**

Structure	Coordination sphere	$\lambda_1$ (nm)	$f_1$	$\lambda_2$ (nm)	$f_2$	$\lambda_3$ (nm)	$f_3$
<b>A1</b>	Cu3N(Ac)	541	0.00045	619	0.00026	500	0.00023
<b>A2</b>	Cu3N(Ac) <sub>2</sub>	657	0.00235	594	0.00052	610	0.00024
<b>A3</b>	Cu3N(Ac)(H <sub>2</sub> O)	550	0.00078	571	0.00025	541	0.00023
<b>A4</b>	Cu3N(Ac)(H <sub>2</sub> O)	567	0.00066	589	0.00030	595	0.00028
<b>A5</b>	Cu3N(H <sub>2</sub> O) <sub>2</sub>	555	0.00051	574	0.00040	739	0.00024
<i>Exp.</i>		620 nm					

### Structure set A

From the results presented in Table 14, the absorption band obtained for structure A2 is in best agreement with the one observed experimentally. The oscillator strength of this 657 nm absorption which magnitude reflects the probability of absorption, is also the strongest one obtained (0.0023). The main absorptions calculated for the other structures have much lower wavelength values than the experimental one and fall in the mid 500 nm range.

**Table 15. TD-DFT calculated (PBE0, def2-TZPV) electronic transitions for structure set B. The experimental absorption band obtained is also reported at pH 7.5 in MOPS buffer.**

Structure	Coordination sphere	$\lambda_1$ (nm)	$f_1$	$\lambda_2$ (nm)	$f_2 \times 10^{-4}$	$\lambda_3$ (nm)	$f_3 \times 10^{-4}$
<b>B1</b>	Cu2N(Ac) <sub>2</sub>	566	0.00038	693	0.00032	536	1.55
<b>B2</b>	Cu2N(Ac)(H <sub>2</sub> O)	691	0.00130	543	0.00042	557	3.18
<b>B3</b>	Cu2N(H <sub>2</sub> O) <sub>2</sub>	543	0.00094	523	0.00061	568	5.30
<b>B4</b>	Cu2N(Ac) <sub>2</sub> (H <sub>2</sub> O)	587	0.00078	573	0.00049	606	0.88
<b>B5</b>	Cu2N(Ac) <sub>2</sub> (H <sub>2</sub> O)	716	0.00133	591	0.00028	640	1.06
<b>B6</b>	Cu2N(Ac)(H <sub>2</sub> O) <sub>2</sub>	566	0.00048	609	0.00038	589	2.40
<b>B7</b>	Cu2N(H <sub>2</sub> O) <sub>3</sub>	516	0.00127	612	0.00036	660	2.16
<i>Exp.</i>		620 nm					

### Structure B

The absorption bands obtained for structures B2 and B5 are the closest from experimental data (Table 15). In fact, they fall in good agreement with the maximum absorption found at lower pH (690 nm at pH 5.0 for instance) for which the non-coordination of one imidazole has been suggested based on potentiometric titration. These transitions have both the strongest oscillator strength of the series. The other structures fall short below 600 nm. Looking at the second strongest oscillator strength, the calculated absorption band for structure B1 also fits with experiment and features an oscillator strength value of the same order than for the first TD-DFT calculated transition.

### Plotted spectra and UV-vis comparison

To better visualize the calculated UV-vis spectral features, a plot is generated and superimposed with the experimental spectrum. The graph was simplified by choosing only the structures exhibiting absorptions with high oscillator strengths near the 620 nm band. Figure 14 gathers the theoretical plots for structures A2, B2 and B4. At first glance, the calculated absorption spectrum for structure A2 is best representing the experimental profile. The absorption band wavelength ( $\lambda = 657$  nm,  $f = 0.0023$ ) is in fair agreement with the experimental results. The absorption spectrum obtained for structure B4 reproduces the profile of the experimental fit albeit at a lower wavelength ( $\lambda = 587$  nm,  $f = 0.00078$ ). Structure B2 does not reproduce the experimental spectrum because the calculated absorption spectrum forms a double-bump profile since the high oscillator strengths are found for both the 1<sup>st</sup> and 2<sup>nd</sup> strongest absorptions ( $\lambda = 691$  and 543 nm,  $f = 0.00130$  and 0.00042, respectively). However, the experimental absorption band is broad, and the double-bump profile may be deconvoluted. More experimental data is needed to elucidate this case.

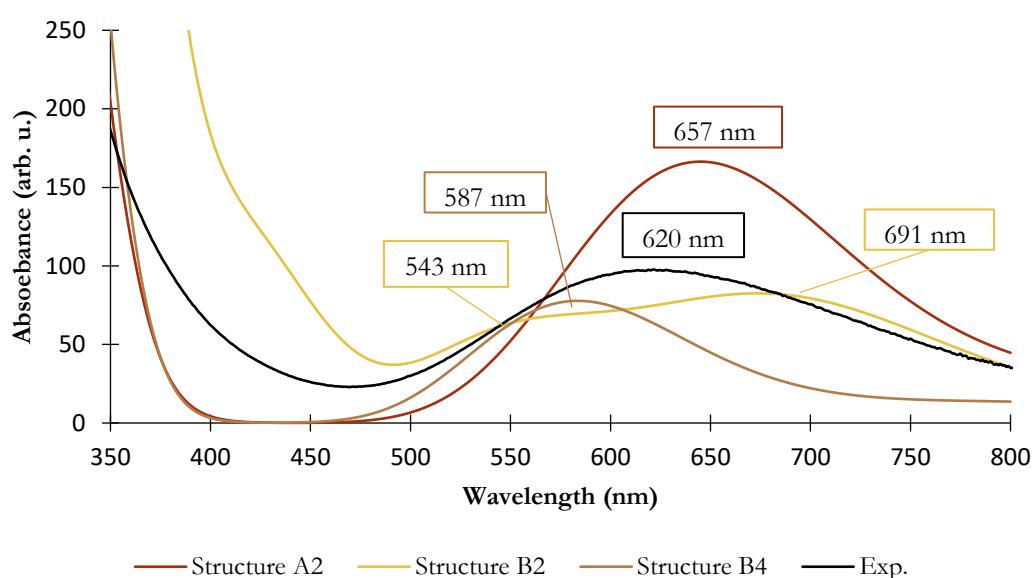


**Figure 14.** TD-DFT-calculated UV-vis spectra for structures A2 (dark red), B2 (yellow), and B4 (brown). The experimental UV-vis spectrum (black) is also plotted for comparison. The calculated graphs were normalized to improve the qualitatively comparison.

In this study, we use the non-methylated structures of sets A and B to predict their UV-vis absorption spectra and compare them with the experimental data. To this end, we calculated the first 50 excited states for each structure in the set and focused on those displaying the most important oscillator strength values for wavelengths ranging between 500 and 800 nm. A first sweep was made for structures not reproducing the experimental 620 nm wavelength absorption

with the high oscillator strengths. Out of all, three structures, A2, B2, and B4, seemed to reproduce the experimentally absorption spectrum. We plotted these theoretical UV-vis spectra using the `orca_mapspc` program to qualitatively compare them to the experimental one. The absorption spectrum obtained with structure A2 best reproduces the experimental features at  $\lambda = 657$  nm. However, structure B4 cannot be discarded since the profile is reproduced even if the calculated absorption band is at a lower wavelength ( $\lambda = 587$  nm). Structure B2 does not reproduce the general absorption profile ( $\lambda_1 = 691$  nm,  $\lambda_2 = 543$  nm). Finally, it seems difficult to distinguish between structures A2 and B4 which differ by the decoordination of the imidazole ring and the coordination of an external water ligand.

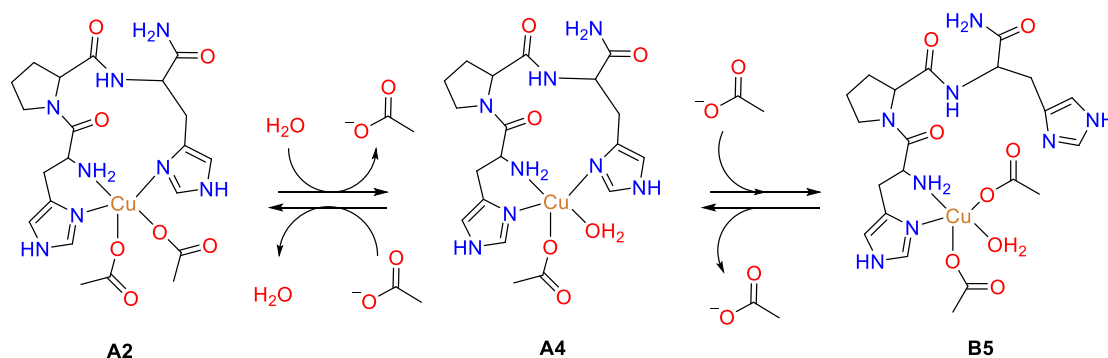
## 2.5 – Discussion on the study of HPH structures

This comprehensive study on the models of the HPH peptide concerns mainly the coordination or decoordination of the imidazole ring and the external ligands coordinating the copper center. Structure set A contains models having the imidazole ring coordinated to the metal center whereas structure set B represents the decoordinated counterpart. The investigated external ligands are either an acetate anion or a neutral water molecule. The energetic considerations reported in Tables 10 and 11 have shown that structures A4 and B4 are the lowest in relative binding energy. However, with respect to A4, structure A2 follows closely behind and lies at only +5.0 kJ/mol. The calculated EPR parameters for structures A2, A4, A5, B2 and B5 best reproduce the experimental values. The TD-DFT computed UV-vis spectra for structures A2, B2 and B4 are those best reproducing the experimental low-energy absorption.

Table 16. Calculated relative free energy differences (PBE0, def2-TZVP), predicted EPR parameters (B3PW91, aug-cc-pVTZ-Jmod), and electronic transitions (PBE0, def2-TZPV) for selected structures A2, A4, A5, B2 and B4.

Structure	Coordination sphere	Relative Free Energy Difference (kJ/mol)	$g_x$	$g_y$	$g_z$	$A_z^{Cu}$ (MHz)	$\lambda_1$ (nm)
<b>A2</b>	Cu3N(Ac) <sub>2</sub>	+5.0	2.050	2.068	2.196	562	657
<b>A4</b>	Cu3N(Ac)(H <sub>2</sub> O)	0.0	2.052	2.058	2.185	563	567
<b>A5</b>	Cu3N(H <sub>2</sub> O) <sub>2</sub>	+71.5	2.045	2.060	2.178	539	555
<b>B2</b>	Cu2N(Ac)(H <sub>2</sub> O)	+77.4	2.042	2.061	2.171	561	691
<b>B4</b>	Cu2N(Ac) <sub>2</sub> (H <sub>2</sub> O)	0.0	2.052	2.059	2.187	592	587/691
<b>B5</b>	Cu2N(Ac) <sub>2</sub> (H <sub>2</sub> O)	+26.4	2.053	2.071	2.199	555	716
		<i>Exp.</i>	2.060	2.060	2.280	531	620

The summary of these results, presented in Table 16, allows us to narrow down on possible structures susceptible to exist in solution. Structure A2 is a good representation of the HPH peptidic structure, it displays the low-energy UV-vis feature and shows good agreement with experiment for both EPR and UV-vis predicted data. We consider this structure to be the most susceptible to exist in solution, thus supporting the coordination of the imidazole ring leading to a 5-member coordinating sphere completed by two acetate anions. In this set of structures, we cannot completely discard structure A4 which also display the low energy absorption band and is in fair agreement with experiment when looking at the computed EPR parameters. This model is another 5-member coordinating complex with one acetate and one water molecule. Concerning structure set B, structures B2 and B4 model well the UV-vis and EPR properties experimentally observed. However, since the 4-member system B2 is higher energy compared B4 and B5, we considered model B5, a 5-member coordinating sphere with two acetates and one water molecule, being the best representing the HPH complex from structure set B. Interestingly, structures A4 and B5 have similar external ligands and might co-exist in solution through ligand exchange between the imidazole ring and an acetate anion. We postulate that there could be a major species present in solution which would be structure A2 but is sensitive to its environment and would undergo exogeneous ligand coordination/decoordination leading to structures A4 and B5 (Scheme 13).

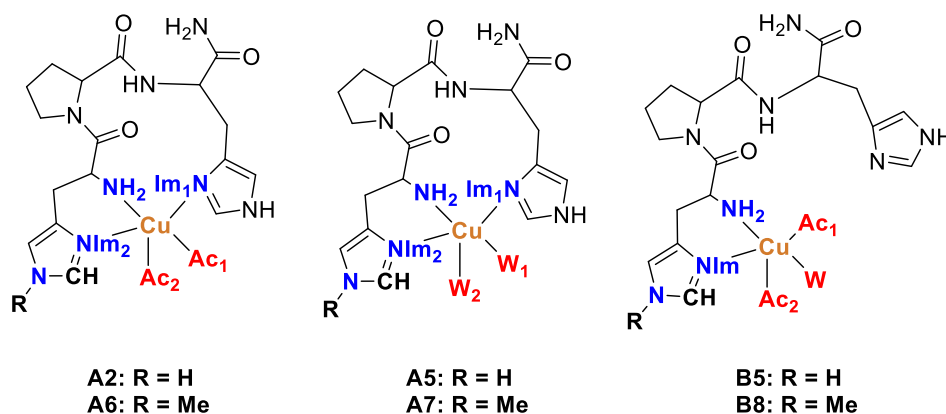


**Scheme 13. Proposed structures together with the modifications most susceptible to exist in solution.**

## 2.6 – Electronic profiles of HPH and HMePH

As mentioned earlier, some fungal LPMO have an N-methylated histidine coordinating the copper center. [4] [38] [39] [40] This modification is called  $\tau$ -methylation and the natural significance behind it remains unclear. Recent studies suggest that it may be for regulating the redox potential of the enzyme to avoid its auto-oxidation. [41] [42] [43] [16] [44] Experimentally,

it was observed that the redox potential of both HPH and HMePH complexes is the same. We tried to rationalize this observation by calculating the electronic structures of both complexes using selected structures from the computational study of HPH. In this respect, we used the Mayer bond order as a metrical tool to describe the complexation of the transition metal ion to the ligands. [45] Also, we conducted the Natural Population Analysis (NPA) of the core and valence electrons of the models. [46] In both cases, we compare the HPH complex to the modified HMePH structure. The  $\tau$ -methylated structures A6, A7, and B8 were selected for which their corresponding non-methylated version are A2, A5, and B5. Structures A2 and A6 coordinate two acetate anions with a  $\text{Cu}_3\text{N}(\text{Ac})_2$  core, structures A5 and A7 coordinate two water molecules with a  $\text{Cu}_3\text{N}(\text{H}_2\text{O})_2$  core. These structures are relevant for the species formed at pH 7.5. Structures B5 and B8 coordinate two acetate anions and one water molecule with a  $\text{Cu}_2\text{N}(\text{Ac})_2(\text{H}_2\text{O})$  core and are relevant for the species formed at pH 5.0. Specific atoms from each pair of structures are studied. These consist of the first coordination sphere of the copper center and the neighboring C-, and N- atoms of the imidazole ring with either an H- or the modified Me- group (Scheme 14).



Scheme 14. Structures considered for Mayer bond order and NPA analyses. Involved atoms and corresponding bonds are in bold and colored with Ac standing for acetate and W standing for water.

**Table 17.** Mayer bond order obtained for the selected bonding atoms in methylated and non-methylated DFT-optimized structures A2, A6, A5, A7, B5, and B8. The bonding atoms consists of those in the first coordination sphere of copper and those involved in the Me modification. \*R = H for A2, A5, and B5 and R= = Me for A6, A7 and B8.

Bonding atoms	A2	A6	Bonding atoms	A5	A7	Bonding atoms	B5	B8
<b>Cu-Ac<sub>1</sub></b>	0.564	0.558	<b>Cu-W<sub>1</sub></b>	0.360	0.358	<b>Cu-Ac<sub>1</sub></b>	0.585	0.586
<b>Cu-Ac<sub>2</sub></b>	0.295	0.306	<b>Cu-W<sub>2</sub></b>	0.209	0.213	<b>Cu-W</b>	0.447	0.445
<b>Cu-NIm<sub>1</sub></b>	0.631	0.626	<b>Cu-NIm<sub>1</sub></b>	0.703	0.712	<b>Cu-Ac<sub>2</sub></b>	0.260	0.259
<b>Cu-NH<sub>2</sub></b>	0.481	0.485	<b>Cu-NH<sub>2</sub></b>	0.608	0.608	<b>Cu-NH<sub>2</sub></b>	0.551	0.549
<b>Cu-NIm<sub>2</sub></b>	0.606	0.622	<b>Cu-NIm<sub>2</sub></b>	0.675	0.689	<b>Cu-NIm</b>	0.614	0.622
<b>NIm<sub>2</sub>-CH</b>	1.474	1.464	<b>NIm<sub>2</sub>-CH</b>	1.448	1.430	<b>NIm-CH</b>	1.469	1.448
<b>CH-N</b>	1.333	1.327	<b>CH-N</b>	1.357	1.350	<b>CH-N</b>	1.354	1.350
<b>N-R*</b>	0.884	0.908	<b>N-R*</b>	0.879	0.903	<b>N-R*</b>	0.880	0.905

Table 17 shows the Mayer bond order (MBO) of structures A2, A5, and B5, as well as their methylated counterparts, structures A6, A7, and B8, respectively. The methylation does not drastically change the MBO values initially obtained without this modification. The coordination sphere of the copper center stays essentially unchanged. A greater difference is observed, naturally, with the R substituents either being an H- or a C- from the methyl group.

The natural orbitals were computed for both the methylated and non-methylated structures. These were plotted to investigate the distribution of the unpaired electron electrons of the copper centers (3d<sup>9</sup> configuration). Looking at Figure 15, representing only structures A2 and A6, we see that there is not a great influence of the methyl modification regarding the composition and spatial distribution of the natural orbital. The energies obtained for the methylated analogue are slightly higher than those for the non-methylated structure with this difference being more obvious in the low energy DOMO set (d<sub>xz</sub>, d<sub>yz</sub>, and d<sub>xy</sub>). The SOMO remains quite similar in terms of energy (-5.061 eV for the non-methylated complex and -5.034 eV for the methylated complex). The same conclusion is obtained when looking at structures A5 and A7, as well as for B5 and B8. These orbitals and energies are presented in the Supplementary Information (Figures S21-S24).



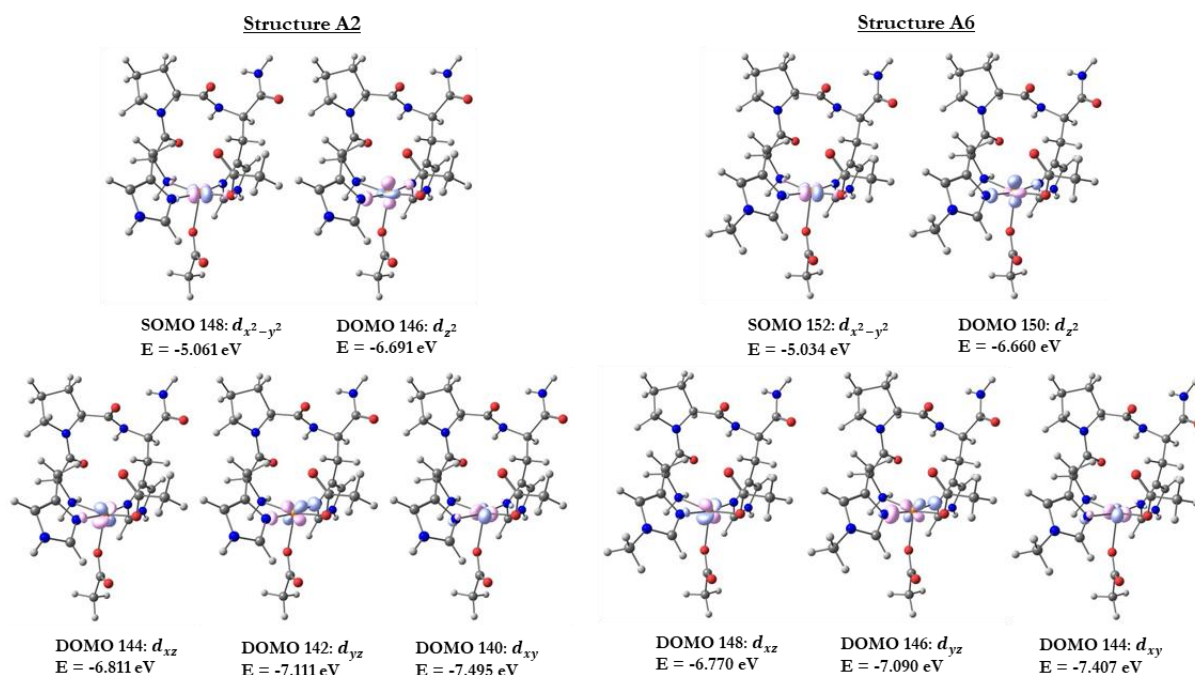


**Figure 15.** Natural orbitals of DFT-optimized structures A2 and A6 (non-methylated vs. methylated). Contour value was 1.4400 for all orbitals. The energy for each orbital is reported in eV, and their occupancy is specified (Singly occupied or Doubly occupied Molecular Orbital).

The summary of the natural population analysis conducted for structures A2 and A6 is reported in Table 18. Similar tables were placed in the Supplementary Information (Tables S67 and S68) for structure A5 and A7, and B5 and B8. A close inspection into the first coordination sphere of copper and the copper atom itself shows no change in terms of natural charge, natural population, and natural spin density. A slight change starts to be observed in the C-atom in the imidazole ring which is due to the modification. The N-atom subjected to the methylation has a greater natural charge, but the natural population is essentially the same which is consistent with the addition of the methyl group. Finally, the core of the copper center remains unchanged with respect to this modification. The methyl group affects primarily the bonded N-atom. The same conclusion is reached when comparing structures A5 with A7, and B5 with B8.

**Table 18.** Natural population analysis for selected atoms contributing to the Cu coordination sphere and to the  $\tau$ -modification in structures A2 and A6. \*R = H for A2 and R\* = Me A6.

Structure	Atom	Natural Charge	Natural Population				Natural Spin Density
			Core	Valence	Rydberg	Total	
<b>A2</b>	Cu	1.405	17.997	9.569	0.029	27.595	0.674
	Ac <sub>1</sub>	-0.805	2.000	6.782	0.024	8.805	0.083
	Ac <sub>2</sub>	-0.851	2.000	6.829	0.022	8.851	0.001
	NIm <sub>1</sub>	-0.559	1.999	5.523	0.036	7.559	0.074
	NH <sub>2</sub>	-0.862	2.000	5.835	0.027	7.862	0.081
	NIm <sub>2</sub>	-0.559	1.999	5.521	0.039	7.559	0.088
	CH	0.184	1.999	3.791	0.025	5.816	-0.006
	N	-0.477	1.999	5.458	0.020	7.477	0.002
	R*	0.457	0.000	0.542	0.001	0.543	0.001
<b>A6</b>	Cu	1.406	17.997	9.568	0.028	27.594	0.674
	Ac <sub>1</sub>	-0.809	2.000	6.786	0.023	8.809	0.082
	Ac <sub>2</sub>	-0.849	2.000	6.828	0.022	8.849	0.001
	NIm <sub>1</sub>	-0.559	1.999	5.523	0.036	7.559	0.075
	NH <sub>2</sub>	-0.860	2.000	5.834	0.027	7.860	0.080
	NIm <sub>2</sub>	-0.560	1.999	5.522	0.039	7.560	0.089
	CH	0.190	1.999	3.786	0.025	5.810	-0.006
	N	-0.296	1.999	5.275	0.021	7.296	0.002
	R*	-0.419	1.999	4.410	0.010	6.419	0.001

Upon investigating the MBOs, the natural orbitals, and the NPAs of structures A2, A5, B5 and their methylated counterparts A6, A7 and B8, no obvious difference is obtained for the copper center core. The electronic structure remains essentially the same upon the modification. This is consistent with experimental information where the redox potential of the Cu(II)/Cu(I) couple of the HPH and HMePH complexes are pretty much identical ( $E_{1/2} = 0.05$  V *vs.* NHE in MES buffer pH 7.0). This computational study together with the experimentally synthesized models do not support the suggested hypothesis regarding the influence of the methylation in LPMOs and their regulation of redox potentials.

## 2.7 – Conclusions

Many theoretical models of the HPH complex were constructed to investigate its coordination sphere and elucidate its structure in solution. To this end, two main structure sets were used which differ in the coordination and decoordination of the imidazole ring. In addition, two different external ligands were considered to complete the models with either an acetate anion or a neutral water molecule. Finally, the coordination sphere could have a total of 4- or 5- coordinating atoms.

After evaluating the binding energy concerning the possible presence of external ligands for each structure set, the most stable structures were found to coordinate at least one acetate entity. The most stable structures per structure set were identified as A4 with a  $\text{Cu}_3\text{N}(\text{Ac})(\text{H}_2\text{O})$  core, and B4 with a  $\text{Cu}_2\text{N}(\text{Ac})_2(\text{H}_2\text{O})$  core, in addition to structure A2 not far behind with a  $\text{Cu}_3\text{N}(\text{Ac})_2$  core.

We moved on to compare the complete structure set to experimental spectroscopic data obtained in acetate buffer at pH 5.0. The best representation of the experimental EPR parameters was obtained with structure set A. Structure A4 ( $\text{Cu}_3\text{N}(\text{Ac})(\text{H}_2\text{O})$  core) shows a good compromise for reproducing both the g- and A-tensor values. However, structures A2 ( $\text{Cu}_3\text{N}(\text{Ac})_2$  core), and A5 ( $\text{Cu}_3\text{N}(\text{H}_2\text{O})_2$  core), are in good agreement as well. Looking at structure set B, two candidates surge: structures B4 and B5 both with the  $\text{Cu}_2\text{N}(\text{Ac})_2(\text{H}_2\text{O})$  core. When comparing the UV-vis absorption data, the computed spectra for structure A2 is best reproducing the experiment. The computed UV-vis spectra for structure B4 is in good agreement as well. However, structure B5 best reproduced the experimental EPR values while failing to reproduce the UV-vis spectrum. Considering that their core is of the same type, we stick with structure B5 since the EPR methodology has been more developed and is more sensitive than the UV-vis method. Three structures are narrowed down when compared to experiment and those are A2, A4, and B5. The coordination sphere of the HPH complex is most likely a 5-member sphere leading to a  $\text{Cu}_3\text{N}_2\text{O}$  core with at least one acetate anion bound to copper, as seen in structure A4. Nonetheless, we cannot ignore structures A2 and B5 specially since the coordination sphere is quite similar when considering possible ligand exchanges. However, these structures might exist in very little quantity compared to the main A4 structure.

The  $\tau$ -methylation and its unaffected redox behavior of the HPH and HMePH complexes was also investigated by the means of MBO, natural orbital, and NPA analyses. Here, we evaluated each data set using the atoms involved in the first coordination sphere of copper, copper itself, and part of the imidazole ring which is subjected to the modification. In terms of bond order, natural charge, molecular orbitals, and their energies, there is no change whatsoever within the copper core. These complexes do not support the idea that  $\tau$ -methylation is naturally tuning the redox potential of LPMO to self-regulate its autooxidation.

## REFERENCES

- [1] C. More, V. Belle, M. Asso, A. Fournel, G. Roger, B. Guigliarelli and P. Bertrand, "EPR spectroscopy: A powerful technique for the structural and functional investigation of metalloproteins," *Biospectroscopy*, vol. 5, no. 5, pp. 3-18, 1999.
- [2] S. van Doorslaer and E. Vinck, "The strength of EPR and ENDOR techniques in revealing structure-function relationships in metalloproteins," *Physical Chemistry Chemical Physics*, vol. 9, no. 33, pp. 4620-4638, 2007.
- [3] G. Jeschke, "EPR techniques for studying radical enzymes," *Biochimica et Biophysica Acta - Bioenergetics*, vol. 1707, no. 1, pp. 91-102, 2005.
- [4] R. J. Quinlan, M. D. Sweeney, L. Lo Leggio, H. Otten, J.-C. N. Poulsen, K. S. Johansen, K. B. R. M. Kristian, C. I. Jorgensen, M. Tovborg, A. Anthonsen, T. Tryfona, C. P. Walter, P. Dupree, F. Xu, G. J. Davies and P. H. Walton, "Insights into the oxidative degradation of cellulose by a copper metalloenzyme that exploits biomass components," *Proceedings of the National Academy of Sciences*, vol. 103, no. 37, pp. 15079-15084, 2011.
- [5] E. Garriba and G. Micera, "The determination of the geometry of Cu(II) complexes - An EPR spectroscopy experiment," *Journal of Chemical Education*, vol. 83, no. 8, pp. 1229-1232, 2006.
- [6] R. J. Gómez-Piñeiro, D. A. Pantazis and M. Orio, "Comparison of density functional and correlated wave function methods for the prediction of Cu(II) hyperfine coupling constants," *Chem. Phys. Chem.*, vol. 21, no. 24, pp. 2667-2679, 2020.
- [7] B. Bissaro, I. Isaksen, G. Vaaje-Kolstad, V. G. H. Eijsink and A. K. Rohr, "How a lytic polysaccharide monooxygenase with broad substrate specificity," *Journal of Biological Chemistry*, vol. 290, no. 38, pp. 22955-22969, 2015.
- [8] A. S. Borisova, T. Isaksen, M. Dimarogona, A. A. Kognole, G. Mathiesen, A. Várnai, A. K. Rohr, C. M. Payne, M. Sorlie, M. Sandgren and V. G. H. Eijsink, "Structural and functional characterization of a lytic polysaccharide monooxygenase with broad substrate specificity," *Journal of Biological Chemistry*, vol. 290, no. 38, pp. 22955-22969, 2015.
- [9] K. E. H. Frandsen, T. J. Simmons, P. Dupree, J.-C. N. Poulsen, G. R. Hemsworth, L. Ciano, E. M. Johnston, M. Tovborg, K. S. Johansen, P. von Freiesleben, L. Marmuse, S. Fort, S. Cottaz, H. Driguez, B. Henrissat, N. Lenfant, F. Tuna, A. Baldansuren, G. J. Davies, L. Lo Leggio and P. H. Walton, "The molecular basis of polysaccharide cleavage by lytic polysaccharide monooxygenases," *Nature Chemical Biology*, vol. 12, pp. 298-303, 2016.
- [10] T. J. Simmons, K. E. H. Frandsen, L. Ciano, T. Tryfona, N. Lenfant, J.-C. N. Poulsen, L. F. L. Wilson, T. Tandrup, M. Tovborg, K. Schnorr, K. S. Johansen, B. Henrissat, P. H. Walton, L. Lo Leggio and P. Dupree, "Structural and electronic determinants of lytic polysaccharide monooxygenase reactivity on polysaccharide substrates," *Nature Communication*, vol. 8, no. 1, pp. 1064-1076, 2017.
- [11] A. Munzone, B. El Kherdi, M. Fanuel, H. Rogniaux, D. Ropartz, M. Réglier, A. J. Simaan and C. Decroos, "Characteriation of a bacterial copper-dependent lytic polysaccharide

- monooxygenase with an unusual second coordination sphere," *The FEBS Journal*, vol. 287, no. 5, pp. 3298-3314, 2020.
- [12] A. K. Chaplin, M. T. Wilson, M. A. Hough, D. A. Svistunenko, G. R. Hemsworth, P. H. Walton, E. Vijgenboom and J. A. R. Worrall, "Heterogeneity in the histidine-brace copper coordination sphere in auxiliary activity family 10 (AA10) lytic polysaccharide monooxygenases," *The Journal of Biological Chemistry*, vol. 291, no. 24, pp. 12838-12850, 2016.
- [13] R. L. Lieberman and A. C. Rosenzweig, "Crystal structure of a membrane-bound metalloenzyme that catalyses the biological oxidation of methane," *Nature*, vol. 434, pp. 177-182, 2005.
- [14] L. Cao, O. Caldararu, A. C. Rosenzweig and U. Ryde, "Quantum refinement does not support dinuclear copper sites in crystal structures of particulate methane monooxygenase," *Angewandte Chemie International Edition*, vol. 57, no. 1, pp. 162-166, 2017.
- [15] G. Vaaje-Kolstad, B. Westereng, S. J. Horn, Z. Liu, H. Zhai, M. Sorlie and V. G. H. Eijsink, "An oxidative enzyme boosting the enzymatic conversion of recalcitrant polysaccharides," *Science*, vol. 330, pp. 219-222, 2010.
- [16] F. L. Aachmann, M. Sorlie, G. Skjak-Braek, V. G. H. Eijsink and G. Vaaje-Kolstad, "NMR structure of a lytic polysaccharide monooxygenase provides insight into copper binding, protein dynamics, and substrate interactions," *Proceedings of the National Academy of Science USA*, vol. 109, pp. 18779-18784, 2012.
- [17] G. Vaaje-Kolstad, D. R. Houston, A. H. Riemen, V. G. H. Eijsink and D. M. F. van Alten, "Crystal structure and binding properties of the *Serratia marcescens* chitin-binding protein CBP21," *Journal of Biological Chemistry*, vol. 280, pp. 11313-11319, 2005.
- [18] F. Sabbadin, G. R. Hemsworth, L. Ciano, B. Henrissat, P. Dupree, T. Tryfona, R. D. S. Marques, S. T. Sweeney, K. Besser, L. Elias, G. Pesante, Y. Li, A. A. Dowle, R. Bates, L. D. Gomez, R. Simister, G. J. Davies, P. H. Walton, N. C. Bruce and S. J. McQueen-Mason, "An ancient family of lytic polysaccharide monooxygenases with roles in arthropod development and biomass digestion," *Nature Communications*, vol. 9, p. 756, 2018.
- [19] G. R. Hemsworth, L. Ciano, G. J. Davies and P. H. Walton, "Production and spectroscopic characterization of lytic polysaccharide monooxygenases," *Methods in Enzymology*, vol. 613, pp. 63-90, 2018.
- [20] V. G. H. Eijsink, D. Petrovic, Z. Forsberg, S. Mekasha, A. K. Rohr, B. Bissaro and G. Vaaje-Kolstad, "On the functional characterization of lytic polysaccharide monooxygenases (LPMOs)," *Biotechnology for Biofuels*, vol. 12, no. 58, 2019.
- [21] F. Neese, F. Wennmohs, U. Becker and C. Riplinger, "The ORCA quantum chemistry program package," *Journal of Chemical Physics*, vol. 152, no. 22, 2020.
- [22] A. D. Becke, "Density-functional exchange-energy approximation with correct asymptotic-behavior," *Physical Review A*, vol. 38, no. 6, pp. 3098-3100, 1988.
- [23] J. P. Perdew, "Density-functional approximation for the correlation-energy of the inhomogeneous electron-gas," *Physical Review B*, vol. 33, no. 12, pp. 8822-8824, 1986.

- [24] F. Weigend and R. Ahlrichs, "Balanced basis sets of split valence, triple zeta valence and quadruple zeta valence quality for H to Rn: Design and assessment of accuracy," *Physical Chemistry Chemical Physics*, vol. 7, no. 18, pp. 3297-3305, 2005.
- [25] F. Weigand, "Accurate Coulomb-fitting basis sets for H to Rn," *Physical Chemistry Chemical Physics*, vol. 8, no. 9, pp. 1057-1065, 2006.
- [26] A. D. Becke, "Density-functional thermochemistry .3. The role of exact exchange," *Journal of Chemical Physics*, vol. 98, no. 7, pp. 5648-5652, 1993.
- [27] J. P. Perdew and Y. Wang, "Accurate and simple analytic representation of the electron-gas correlation-energy," *Physical Review B*, vol. 45, no. 23, pp. 13244-13249, 1992.
- [28] C. Adamo and V. Barone, "Toward reliable density functional methods without adjustable parameters: The PBE0 model," *Journal of Chemical Physics*, vol. 110, no. 13, pp. 6158-6170, 1999.
- [29] Y. Zhao and D. G. Truhlar, "The M06 suite of density functionals for main group thermochemistry, thermochemical kinetics, noncovalent interactions, excited states, and transition elements: two new functionals and systematic testing of four M06-class functionals and 12 other function," *Theoretical Chemistry Accounts*, vol. 120, no. 1-3, pp. 215-241, 2008.
- [30] E. D. Hedegard, J. Kongsted and S. P. A. Sauer, "Optimized basis sets for calculation of electron paramagnetic resonance hyperfine coupling constants: aug-cc-pVTZ-J for the 3d atoms Sc-Zn," *Journal of Chemical Theory and Computation*, vol. 7, no. 12, pp. 4077-4087, 2011.
- [31] E. D. Hedegard, J. Kongsted and S. P. A. Sauer, "Improving the calculation of electron paramagnetic resonance hyperfine coupling tensors for d-block metals," *Physical Chemistry Chemical Physics*, vol. 14, no. 30, pp. 10669-10676, 2012.
- [32] F. Neese, "Efficient and accurate approximations to the molecular spin-orbit coupling operator and their use in molecular g-tensor calculations," *Journal of Chemical Physics*, vol. 122, no. 3, p. 034107, 2005.
- [33] B. A. Hess, C. M. Marian, U. Wahlgren and O. Gropen, "A mean-field spin-orbit method applicable to correlated wavefunctions," *Chemical Physics Letters*, vol. 251, no. 5-6, pp. 365-371, 1996.
- [34] E. van Lenthe, E. J. Baerends and J. G. Snijders, "Relativistic regular 2-component hamiltonians," *Journal of Chemical Physics*, vol. 99, no. 6, pp. 4597-4610, 1993.
- [35] E. van Lenthe, E. J. Baerends and J. G. Snijders, "Relativistic total-energy using regular approximations," *Journal of Chemical Physics*, vol. 101, no. 11, pp. 9783-9792, 1994.
- [36] E. van Lenthe, J. G. Snijders and E. J. Baerends, "The zero-order regular approximation for relativistic effects: The effect of spin-orbit coupling in closed shell molecules," *Journal of Chemical Physics*, vol. 105, no. 15, pp. 6505-6516, 1996.
- [37] M. Cossi and V. Barone, "Quantum calculation of molecular energies and energy gradients in solution by a conductor solvent model," *Journal of Physical Chemistry A*, vol. 102, no. 11, pp. 1995-2001, 1998.

- [38] L. Lo Leggio, T. J. Simmons, J. C. N. Poulsen, K. E. H. Frandsen, G. R. Hemsworth, M. A. Stringer, P. von Freiesleben, M. Tovborg, K. S. Johansen, L. De Maria, P. V. Harris, C.-L. Soong, P. Dupree, T. Tryfona, N. Lenfant, B. Henrissat, G. J. Davies and P. H. Walton, "Structure and boosting activity of a starch-degrading lytic polysaccharide monooxygenase," *Nature Communications*, vol. 6, p. 5961, 2015.
- [39] V. V. Vu, W. T. Beeson, C. M. Phillips, J. H. Carte and M. A. Marletta, "Determinants of regioselective hydroxylation in the fungal polysaccharide monooxygenases," *Journal of the American Chemical Society*, vol. 136, pp. 562-565, 2014.
- [40] X. Li, W. T. Beeson, C. M. Phillips, M. A. Marletta and J. H. D. Carte, "Structural basis for substrate targetting and catalysis by fungal polysaccharide monooxygenases," *Structure*, vol. 20, no. 6, pp. 1051-1061, 2012.
- [41] D. M. Petrovic, B. Bissaro, P. Chylenski, M. Skaugen, M. Sorlie, M. S. Jensen, F. L. Aachmann, G. Courtade, A. Varnai and V. G. H. Eijsink, "Methylation of the N-terminal histidine protects a lytic polysaccharide monooxygenase from auto-oxidative inactivation," *Protein Science*, vol. 27, no. 9, pp. 1636-1650, 2018.
- [42] W. T. Beeson, V. V. Vu, E. A. Span, C. M. Phillips and M. A. Marletta, "Cellulose degradation by polysaccharide monooxygenases," *Annual Review of Biochemistry*, vol. 84, pp. 923-946, 2015.
- [43] G. R. Hemsworth, E. M. Johnston, G. J. Davies and P. H. Walton, "Lytic polysaccharide monooxygenases in biomass conversion," *Trends Biotechnology*, vol. 33, pp. 747-761, 2015.
- [44] G. R. Hemsworth, B. Henrissat, G. J. Davies and P. H. Walton, "Discovery and characterization of a new family of lytic polysaccharide monooxygenases," *Nature Chemical Biology*, vol. 10, pp. 122-126, 2014.
- [45] A. J. Bridgeman, G. Cavigliasso, L. R. Ireland and J. Rothery, "The Mayer bond order as a tool in inorganic chemistry," *Journal of the Chemical Society, Dalton Transactions*, no. 14, pp. 2095-2108, 2001.
- [46] A. E. Reed, R. B. Weinstock and F. Weinhold, "Natural population analysis," *The Journal of Chemical Physics*, vol. 83, no. 2, pp. 735-746, 1985.
- [47] K. M. Kadish, R. Guillard and M. Réglér, Series on chemistry, energy and the environment: Volume 5. Bioinspired chemistry: From enzymes to synthetic models, World Scientific, 2019.





---

CHAPTER IV.  
BIOINSPIRED MONONUCLEAR  
COPPER COMPLEXES:  
SYNTHESIS,  
CHARACTERIZATION AND  
REACTIVITY

---



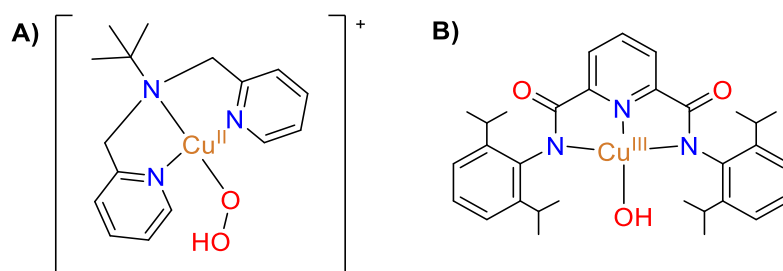
## CHAPTER IV. BIOINSPIRED MONONUCLEAR COPPER COMPLEXES: SYNTHESIS, CHARACTERIZATION AND REACTIVITY

The Lytic Polysaccharide Monooxygenase enzymes (LPMO) break down recalcitrant polysaccharides in mild conditions and can be used in the production of sustainable biofuels. [1] [2] The enzymes act on the strong C-H bonds at the glycosidic linkage of the substrate by oxidative mechanism. [3] Depending on the LPMO, two positions are known to be affected: either the C1 or the C4 carbon positions of the polysaccharide substrate. [4] [5] Some are also capable of acting on both positions. [6] The oxidation reaction requires an oxygenated co-substrate which origin is still debated. Two co-substrates have been proposed:  $O_2$  and  $H_2O_2$ . [3] [7] This opens the question on possible reaction mechanisms and reactive intermediates found with LPMO systems. [8]

The cupric superoxo species was postulated as possible intermediate responsible for H-abstraction in several enzymatic systems, including D $\beta$ H and PHM. [9] To understand this species, and its derivatives, small synthetic models have been prepared. Naturally, its high reactivity makes it difficult to control and to characterize once formed. These species have been prepared upon oxygenation of a reduced copper complex in presence of  $O_2$ , at low temperatures. Although the reactivity of these systems was evidenced, they were rather active on activated C-H bonds and based on theoretical calculations, they have been ruled out as possible substrate's activating intermediates in LPMO. [10]

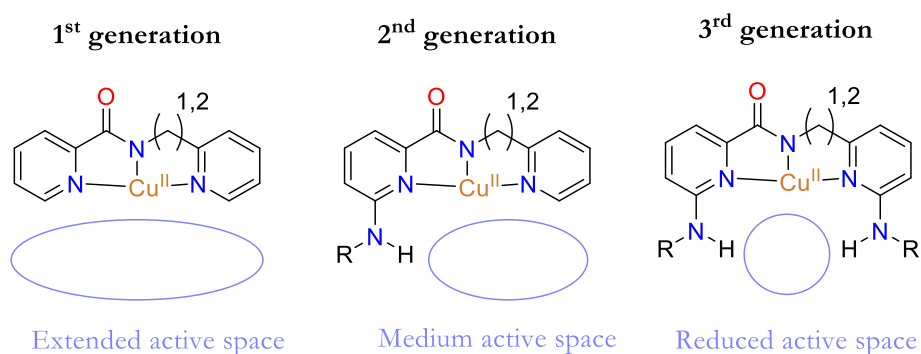
Another possible intermediate is the hydroperoxo intermediate (Cu-OOH) that can be formed by addition of  $H_2O_2$  in presence of base on a Cu(II) mononuclear complex [11] [12] with the pathway known as the peroxide shunt. Many Cu-OOH intermediates have been characterized but it has to be noted that few square-planar intermediates have been described. Fujii et al. produced a copper-hydroperoxo species at  $-78^\circ\text{C}$  with the bis(2-pyridylmethyl)tert-butylamine ligand (Scheme 1). [13] These species have displayed moderate reactivities so far and are often considered as precursors for more oxidizing intermediates. [9]

In the case of LPMO, high-valent copper species such as Cu(III)=O have been suggested as key intermediates for the strong C-H bond activation of polysaccharides. [14] The group of Tolman was able to produce a copper(III)-hydroxide complex which is considered as a protonated configuration of the copper-oxyl intermediate (Scheme 1). [15] The formal copper-oxyl species (or copper-oxo) has not been detected yet neither in proteins nor in synthetic systems.



Scheme 1. A) Square-planar copper-hydroperoxo complex [13] B) copper(III)-hydroxide species [15].

To control the reactivity and the formation of high valent copper intermediates, we designed 3 generations of ligands based on the N-((pyridine-2-yl)methyl)picolinamide, PMPA, [16] and N-(2-(pyridine-2-yl)ethyl)picolinamide, PEPA, [17] ligands (Scheme 2). These ligands were designed to provide an amide function for Cu(III) stabilization and to modulate the geometry around the copper center since PMPA and PEPA differ from the number of carbon atoms in the short alkyl chain. The 2<sup>nd</sup> and 3<sup>rd</sup> generations were envisioned by adding substituents at position 6 of the pyridine rings. The first generation has an extensive active space and can easily react in solution without any substituents around the pyridine rings. The second generation is decorated with a single modification, reducing the initial space, and providing a possible 2<sup>nd</sup> coordination sphere to the copper center. In particular, the H-bonding properties of the substituents can be modified to tune the stability of the copper intermediates that are formed. Finally, the third generation is a doubly substituted complex (one per pyridine ring) which drastically reduces the active space of the molecule. Increasing the H-bonding properties from two fronts intends to stabilize and/or activate even further the putative reactive intermediates.

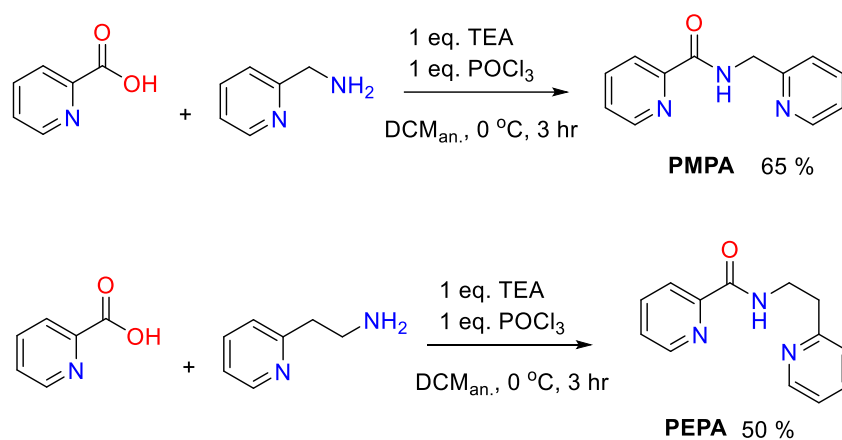


Scheme 2. Design of three generations of complexes based on PMPA ( $n=1$ ) or PEPA ( $n=2$ ) ligands with tunable space around the active metal center. R = H, COtBu.

In the following, we will first describe the 1<sup>st</sup> generation of bioinspired complexes. We will focus on the characterization of the starting Cu(II) complexes of the family with PMPA and PEPA ligands, using both experimental and theoretical methods. Then, we will present our investigations of the potential reactivity of the PMPA-based complex in oxidative reactions. Particular attention will be given to the reactivity using the peroxide shunt pathway.

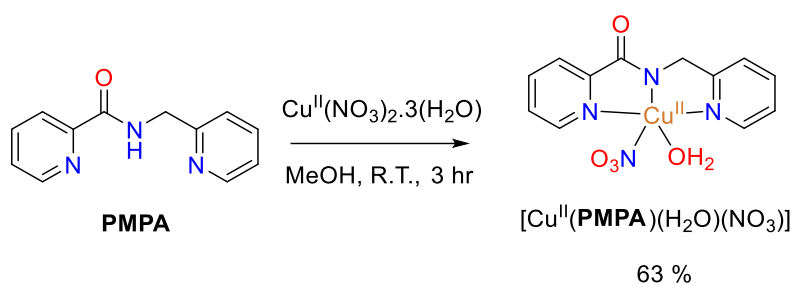
## 1. First generation PMPA and PEPA-based complexes: synthesis, characterization, and theoretical description

The PMPA and PEPA ligands were prepared by coupling picolinic acid with either 2-(aminomethyl)pyridine or 2-(2-aminoethyl)pyridine in the presence of phosphorous oxychloride and triethylamine (Scheme 3). Dichloromethane was used as solvent. The resulting mixtures yielded viscous yellow residues.



**Scheme 3.** Synthesis of PMPA and PEPA ligands via activation of picolinic acid in presence of POCl<sub>3</sub> and addition of primary amine. Anhydrous dichloromethane (DCM<sub>an.</sub>) is used as solvent in an ice bath.

Complex [Cu<sup>II</sup>(PMPA)(H<sub>2</sub>O)(NO<sub>3</sub>)] (1) was prepared by mixing copper nitrate trihydrate salt and PMPA in methanol (Scheme 4). The reaction mixture formed a dark blue precipitate. The powder was recovered and resolubilized in methanol to form suitable crystals for X-ray diffraction (XRD) by slow evaporation (Figure 1).



Scheme 4. Synthesis of  $[\text{Cu}^{\text{II}}(\text{PMPA})(\text{H}_2\text{O})(\text{NO}_3)]$  (complex 1) by addition of the PMPA ligand to a solution of copper nitrate trihydrate salt in methanol.

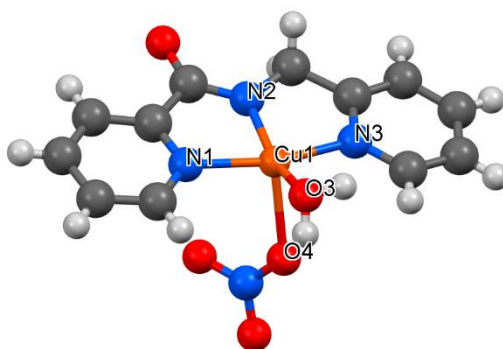
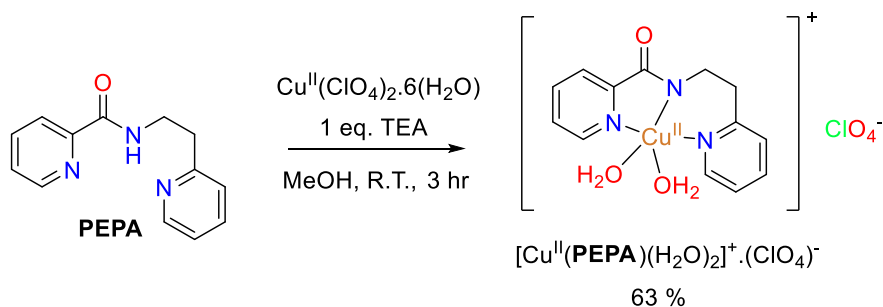
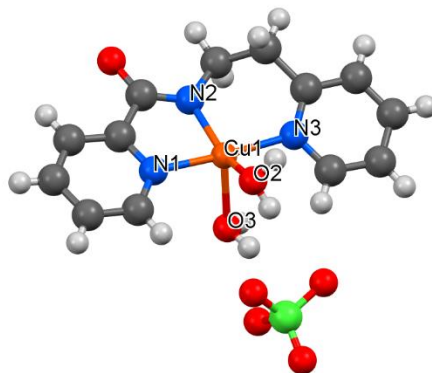


Figure 1. XRD structure of  $[\text{Cu}^{\text{II}}(\text{PMPA})(\text{H}_2\text{O})(\text{NO}_3)]$  (1) obtained by slow evaporation of a methanol solution of the complex. Empirical formula:  $\text{C}_{12}\text{H}_{12}\text{CuN}_4\text{O}_5$ , Formula weight: 355.80, Temperature: 298°K.

Similarly, complex  $[\text{Cu}^{\text{II}}(\text{PEPA})(\text{H}_2\text{O})_2] \cdot (\text{ClO}_4)$  (**2**) was prepared by mixing copper perchlorate hexahydrate salt and PEPA in methanol (Scheme 5). An equivalent of triethylamine was added to the solution to promote the deprotonation of the amide and pyridinium moieties found in PEPA. The reaction mixture formed a blue precipitate after addition of diethyl ether. The recovered powder was solubilized in a 1:1 water-methanol mixture to form suitable crystals for XRD analysis by slow evaporation (Figure 2).



Scheme 5. Synthesis of  $[\text{Cu}^{\text{II}}(\text{PEPA})(\text{H}_2\text{O})_2] \cdot (\text{ClO}_4)$  (complex 2) by addition of the PEPA ligand to a copper perchlorate hexahydrate salt in presence of 1 equivalent of triethylamine in methanol.



**Figure 2.** XRD structure of  $[\text{Cu}^{\text{II}}(\text{PEPA})(\text{H}_2\text{O})_2] \cdot (\text{ClO}_4)$  (**2**) obtained by slow evaporation. Empirical formula:  $\text{C}_{13}\text{H}_{16}\text{ClCuN}_3\text{O}_7$ , Formula weight: 452.28, Temperature: 295°K.

Once the crystallographic coordinates were obtained, theoretical calculations were performed using the ORCA program package. [18] Geometry optimizations and numerical frequencies were computed with PBE0 functional [19] and def2-TZVP basis sets, [20] in combination with the corresponding auxiliary basis sets. [21] These optimizations were carried out in solvent phase using methanol and CPCM as solvation model (Figure 3). The computed parameters are compared to the experimental ones in Table 1.

Complex **1** optimized as a square base pyramid geometry having the nitrate ligand coordinating in the basal position and the water molecule in the axial one (Figure 3). On the contrary, the crystal structure shows the water molecule in the plane and the nitrate ligand in the axial position. Besides this geometrical difference, the computed bond lengths and distances are overall similar to those of the crystal structure of complex **1** (Table 1). First, the optimized structure features slightly larger Cu-N bonds of the PMPA ligand and the Cu-O bond in the plane increases whereas the axial Cu-O bond decreases. Second, the DFT-optimized plane geometry is very similar to the one observed experimentally but a less distorted square base pyramidal geometry is observed in the optimized structure with the N2-Cu1-O4 angle being close to 180° and the N2-Cu-O3 angle approaching 90°.

Complex **2** optimized as an octahedral structure with the perchlorate anion coordinated to the copper center in axial position (Figure 3). This coordination is further stabilized by H-bonding from the basal water molecule. The Cu-N bonds are essentially similar (Table 1). Only the Cu-O3 bond found is in the axial position, is larger in the optimized structure. Again, in terms of angles,

an octahedral character is observed in the DFT-optimized structure with the N2-Cu-O3 and N2-Cu-O2 angles approaching 90° and 180°, respectively.

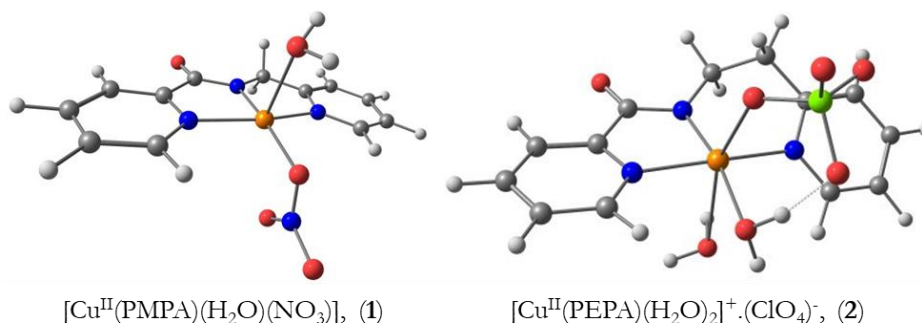


Figure 3. Optimized structures of complexes 1 and 2 obtained with PBE0 functional and def2-TZVP basis set. The crystal structure geometry was used as initial coordinates for the calculation.

Table 1. Selected bond distances and angles of XRD and DFT-optimized structures of complexes 1 and 2.

<i>Complex</i> [Cu(PMPA)(H <sub>2</sub> O)(NO <sub>3</sub> )]			<i>Complex</i> [Cu(PEPA)(H <sub>2</sub> O) <sub>2</sub> ] <sup>+</sup> (ClO <sub>4</sub> ) <sup>-</sup>		
<i>Geometrical parameters</i>	Crystal structure	PBE0/def2-TZVP optimization	<i>Geometrical parameters</i>	Crystal structure	PBE0/def2-TZVP optimization
<b>Distances in Å</b>					
Cu1-N1	2.003	2.038	Cu1-N1	2.003	2.036
Cu1-N2	1.906	1.919	Cu1-N2	1.937	1.935
Cu1-N3	2.000	2.030	Cu1-N3	2.018	2.070
Cu1-O3	1.963	2.353	Cu1-O2	2.048	2.051
Cu1-O4	2.313	2.014	Cu1-O3	2.196	2.695
<b>Angles in °</b>					
N1-Cu1-N2	82.1	81.5	N1-Cu1-N2	82.0	81.8
N2-Cu1-N3	82.0	81.5	N2-Cu1-N3	94.9	91.8
N3-Cu1-O3	98.5	96.7	N3-Cu1-O2	90.7	95.5
O3-Cu1-N1	97.4	93.4	O2-Cu1-N1	90.5	89.9
N2-Cu1-O4	117.9	172.2	N2-Cu1-O3	116.6	94.3
N2-Cu1-O3	155.2	106.3	N2-Cu1-O2	144.8	169.2

### 1.1 – Spectroscopic characterization: UV-vis, MS, and EPR

Spectroscopic methods were used to characterize the 1<sup>st</sup> generation complexes. In the following, we report on an in-depth characterization of complex **1** using common methods such as UV-vis, electronic paramagnetic resonance (EPR), and mass spectroscopies. This section will focus on complex **1** alone. In parallel, we used computational methods based on DFT to describe the



properties of the complex. Note that a back and forth between experimental and theoretical methods was carried out to fully describe the system.

### *UV-vis spectroscopy*

Solutions of either 1, 0.5, and 0.25 mM of complex **1** in methanol were prepared and examined by UV-vis spectroscopy (Figure 4). The resulting spectra exhibit a absorption bands at 640 nm which is attributed to the d-d electronic transitions. A band centered around 305 nm is also detected which can be attributed to charge-transfer events. Finally, an absorption at 272 nm is also observed.

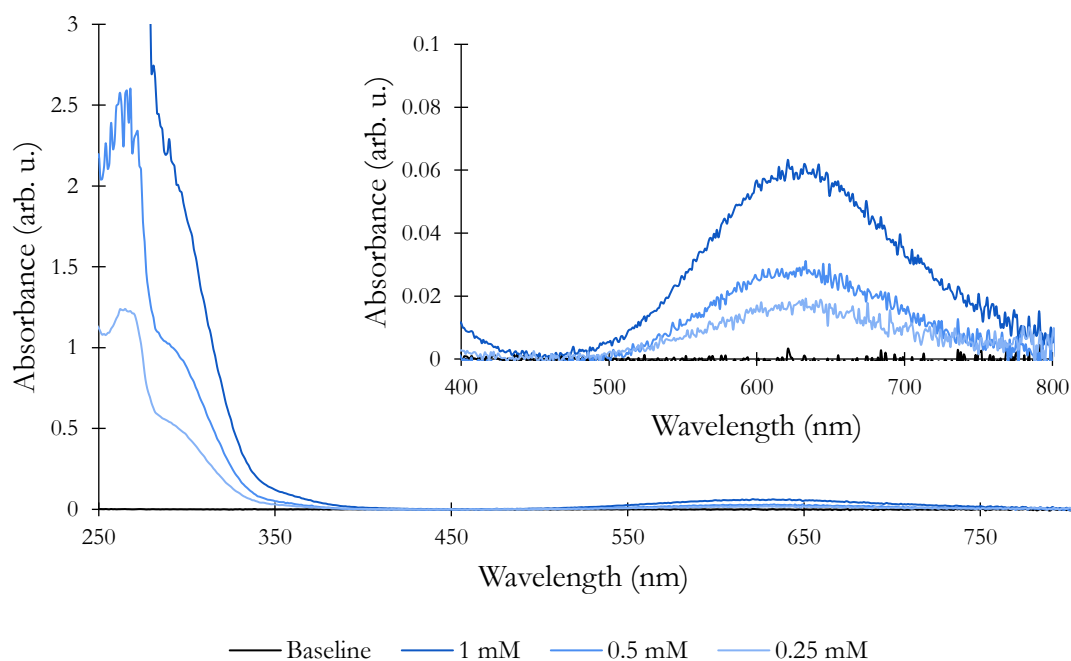


**Figure 4.** UV-vis spectra of complex **1** in methanol solutions at 1, 0.5 and 0.25 mM (dark to light blue) ranging from 200 to 800 nm. The baseline was taken with the solvent alone (black). The inset shows a magnified spectra for the 400 to 800 nm range. A 1-cm pathlength quartz cuvette was used.

Time dependent DFT (TD-DFT) was used to predict vertical transition energies and produce a theoretical UV-vis spectrum for complex **1** (Figure 5) using its DFT-optimized structure (Figure 6).

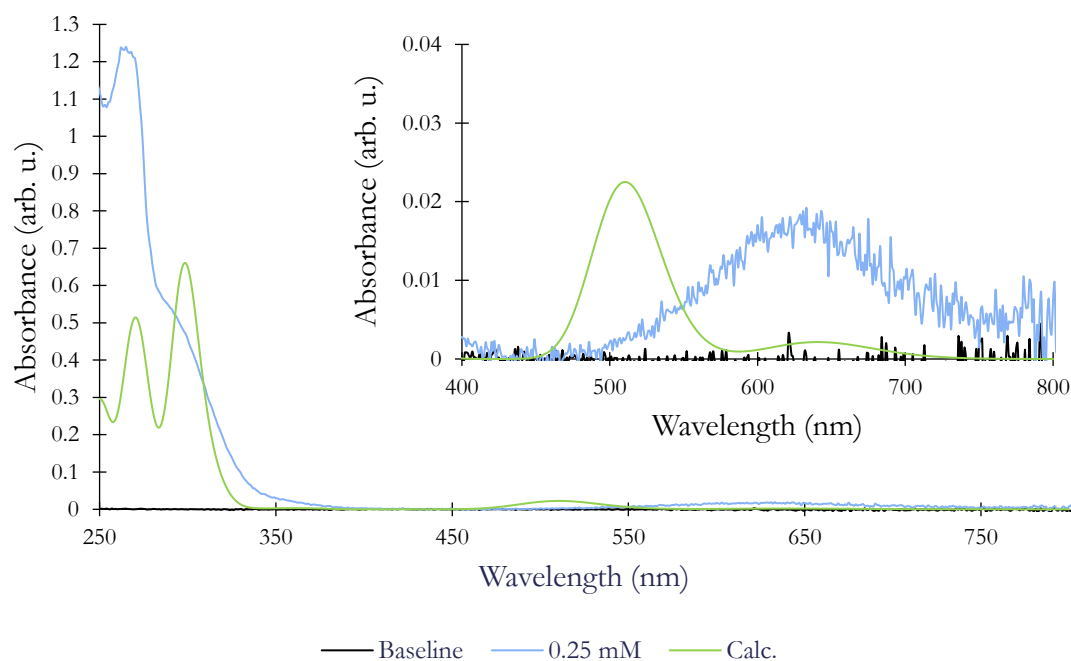


**Figure 5.** UV-vis spectrum of 0.25 mM solution of complex 1 in methanol (blue) superimposed with the calculated spectrum obtained using TD-DFT with the PBE0 functional and the def2-TZVP basis sets (green). The calculated spectrum was plotted using the `orca_plot` utility from ORCA. The inset shows magnified spectra for the 400 to 800 nm range.

The computed d-d transition is found around 510 nm whereas the experimental value is around 640 nm. This computed band is greatest in terms of oscillator strength as compared to the transition computed at 640 nm and therefore the latter was not considered. The difference density plots was generated for the 510 nm absorption band and it exclusively involves the copper center as expected for a d-d- transition(Figure 6). The experimental absorption band found at 305 nm is rather well reproduced (310 nm calc.). It is attributed to a charge transfer from the ligand to the metal (LMCT) and it involves the amide group in the donor state and the copper center in the acceptor state (Figure 6). This event also highlights the electron donating effect of the designed amide-containing ligand to the copper atom.

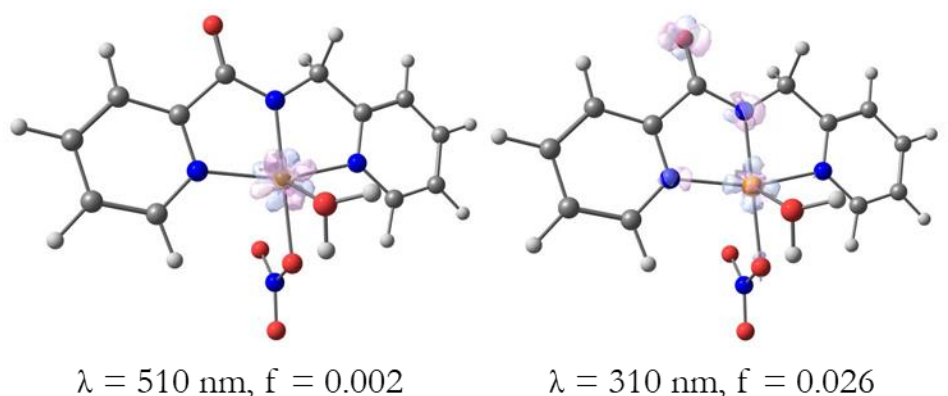


**Figure 6.** Difference electron densities sketches Active orbitals involved in the d-d transition and of the ligand to metal charge transfer for complex **1**. The corresponding wavelength and oscillator strengths,  $f$ , are reported. Contour values used are 0.011 and 0.005, respectively with the acceptor state being in light blue and the donor state in light pink.

### *Mass spectroscopy*

High resolution electron spray ionization (ESI) mass spectroscopy (MS) was used to characterize the complex and its molecular weight. The powder of the complex was solubilized in 200  $\mu\text{L}$  of acetonitrile and diluted to 1/100 in another acetonitrile solution containing 1.2 mM of sodium fluoride. The main species detected at  $m/z = 275$  is attributed to the monocharged ion  $[\text{Cu}(\text{PMPA})]^+$ . A minor species is also found at  $m/z = 612$  corresponding to a dimer with a nitrate,  $[\text{Cu}_2(\text{PMPA})_2(\text{NO}_3)]^+$ . Traces of other species were found at  $m/z = 697$  and 951, corresponding to  $[\text{Cu}_2(\text{PMPA})_2(\text{NO}_3)_2\text{Na}]^+$  and  $[\text{Cu}_3(\text{PMPA})_3(\text{NO}_3)_2]^+$ , respectively. Overall, the MS studies confirm that the structure of the complex is maintained in solution.

### *Electronic paramagnetic resonance spectroscopy*

Electronic paramagnetic resonance (EPR) was used to probe the redox state and the coordination geometry of the metal center in complex **1** (Figure 7). Samples were prepared in methanol solutions containing 1 mM of complex. The resulting EPR spectrum is typical for square-pyramidal  $\text{Cu}^{\text{II}}$  systems, with  $g_{\text{max}} > g_{\text{mid}} = g_{\text{min}}$ , and a well-defined metal hyperfine interaction  $A_{\text{max}}^{\text{Cu}}$ . The simulated values are  $g_{\text{max}} = 2.24$ ,  $g_{\text{mid}} = 2.08$ ,  $g_{\text{min}} = 2.05$ , and  $A_{\text{max}}^{\text{Cu}} = 545$  MHz.

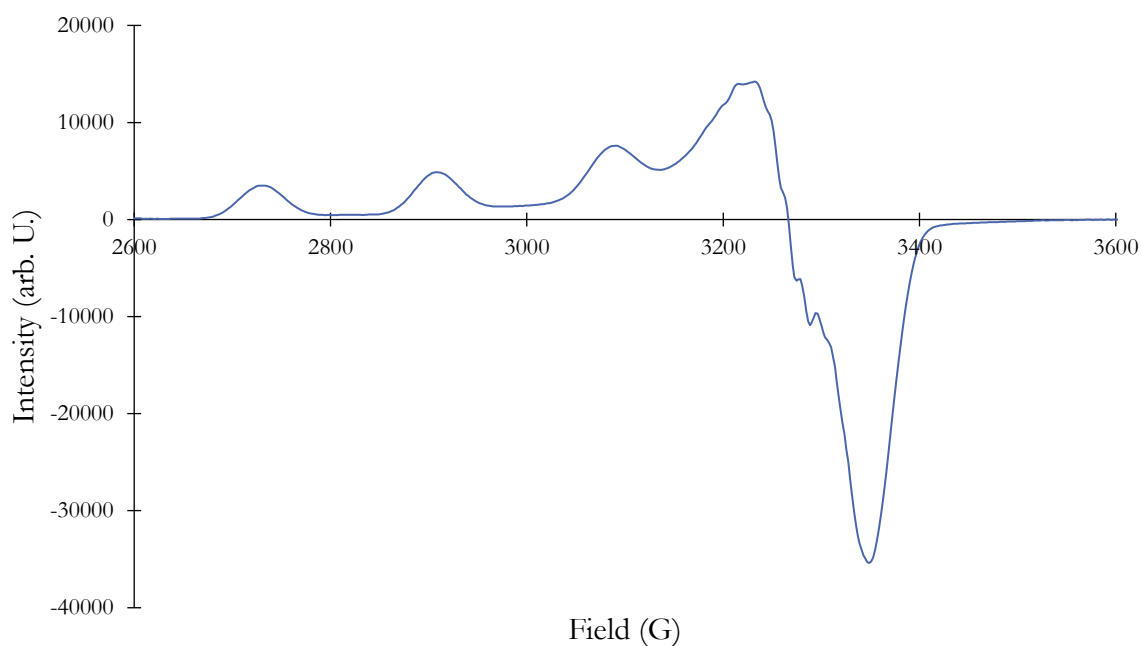


**Figure 7.** EPR spectrum of complex **1** obtained from a 1 mM solution in methanol at 120K.

The DFT method was employed for the calculation of the EPR parameters of **1** using its optimized structure and the B3PW91 [22] [23] functional in combination with the def2-TZVP basis set for the organic atoms whereas a home-made basis set (aug-cc-pVTZ-Jmod) was used for the copper center (see chapter II). [24]

**Table 2.** EPR parameters of  $[\text{Cu}^{\text{II}}(\text{PMPA})(\text{H}_2\text{O})(\text{NO}_3)]$ , complex **1**, obtained from experiment (1mM solution in MeOH) and using DFT (B3PW91 functional, aug-cc-pVTZ-Jmod basis sets).

<i>EPR parameters</i>	Experimental (1 mM, MeOH)	Calculated B3PW91/aug-cc-pVTZ- Jmod
$g_{\text{min}}$	2.05	2.04
$g_{\text{mid}}$	2.08	2.06
$g_{\text{max}}$	2.24	2.16
$A_{\text{max}}^{\text{Cu}}$	545 MHz	549 MHz

Our results show that we reproduce rather well the experimental EPR parameters of complex **1** (Table 2). The greatest difference is observed in the calculation of the  $g_z$  value which is lower than the experimental one. This computational discrepancy was observed during the convergence studies of  $g$ -tensors using a large set of 20 complexes and was attributed to a poor description of

the metal-ligand covalency (see chapter II). With this exception, the other predicted EPR are in very good agreement with the experimental ones.

## 1.2 – Electrochemical studies

Cyclic voltammetry experiments were carried to probe the complex  $\text{Cu}^{\text{II}}/\text{Cu}^{\text{I}}$  redox couple as well as other redox activity in aqueous conditions. The electrochemical cell used a glassy carbon (GC) working electrode (WE), a platinum wire as the counter electrode (CE), and Ag/AgCl as the reference electrode (RE). The electrolyte used was sodium nitrate ( $\text{NaNO}_3$ ) at 100 mM concentration. Cyclic-voltammograms were carried under argon atmosphere.

In an aqueous solution at pH 7.5, complex **1** shows a quasi-reversible wave with a half wave potential  $E_{1/2} = -0.405$  V vs. Ag/AgCl and peak separation  $\Delta E = 0.25$  V. The corresponding redox events are  $E_{\text{pa}} = -0.279$  V and  $E_{\text{pc}} = -0.531$  V vs. Ag/AgCl and current intensities:  $i_{\text{pa}} = 0.010$  mA and  $i_{\text{pc}} = -0.014$  mA, respectively. This wave is attributed to the  $\text{Cu}^{\text{II}}/\text{Cu}^{\text{I}}$  redox couple (Figure 8).

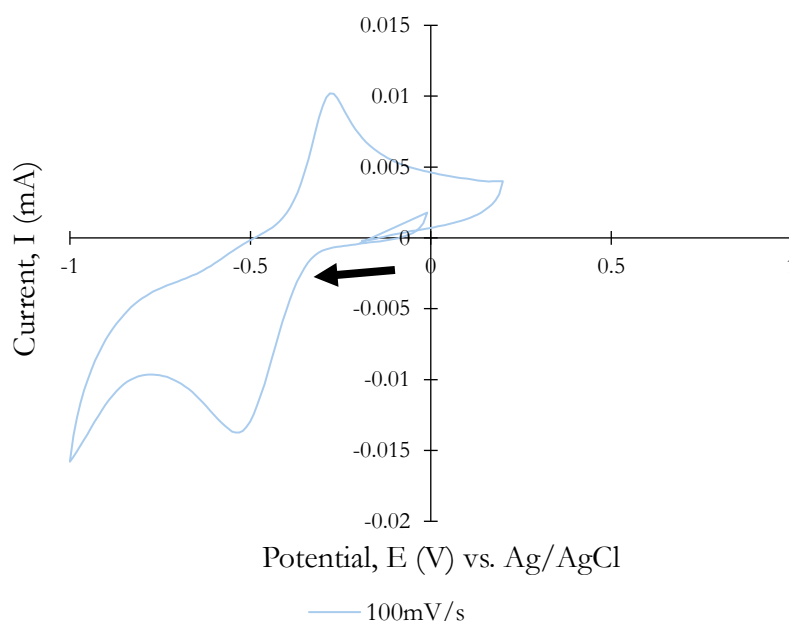


Figure 8. Cyclic voltammogram of complex **1** (5mM) in aqueous solution, pH 7.5, containing 100 mM  $\text{NaNO}_3$ , recorded under argon atmosphere and at 100 mV/s scan rate. GC was used as WE, Pt-wire as CE, and Ag/AgCl as RE. The arrow indicates the direction of the CV acquisition.

Following the Born-Haber cycle for calculating redox potentials in aqueous solutions for copper complexes, [25] we optimized the structure of complex **1** in both the Cu<sup>I</sup> and the Cu<sup>II</sup> state in both the gas and aqueous phases and calculated the numerical frequencies on the resulting structures and the functional used is PBE0, and the basis sets are def2-TZVP. The calculated potential obtained for the Cu<sup>II</sup>/Cu<sup>I</sup> redox couple is  $E_{1/2, \text{calc.}} = -0.353 \text{ V vs. Ag/AgCl}$ . This potential is slightly higher than the one obtained experimentally but fairly supports the assignment of the Cu<sup>II</sup>/Cu<sup>I</sup> redox system (Table 3).

**Table 3.** Calculated free energies used for the Born-Haber cycle to evaluate the redox potential of the Cu<sup>II</sup>/Cu<sup>I</sup> couple (PBE0/def2-TZVP/COSMO solvation model). The theoretical Ag/AgCl reference is 4.071 V.

	Gas phase (eV)	Solvation effect (eV)
<b>Reduced species</b>		
[Cu <sup>I</sup> (PMPA)(H <sub>2</sub> O)(NO <sub>3</sub> )] <sup>+</sup>	-73 442.1338	-3.0744
<b>Oxidized species</b>		
[Cu <sup>II</sup> (PMPA)(H <sub>2</sub> O)(NO <sub>3</sub> )]	-73 440.0336	-1.4580
<b><math>\Delta G_{\text{red/ox}}</math></b>	2.1002	1.6164
<b><math>\Delta E_{1/2, \text{calc.}}</math></b>	-0.353	V vs. Ag/AgCl

An oxidation wave was observed at higher potentials with greater current intensity (Figure 9). This irreversible wave is found at around +1.5 V *vs.* Ag/AgCl. The higher intensity of this peak suggests the presence of a catalytic process upon oxidation of the copper complex, possibly assigned to water oxidation.

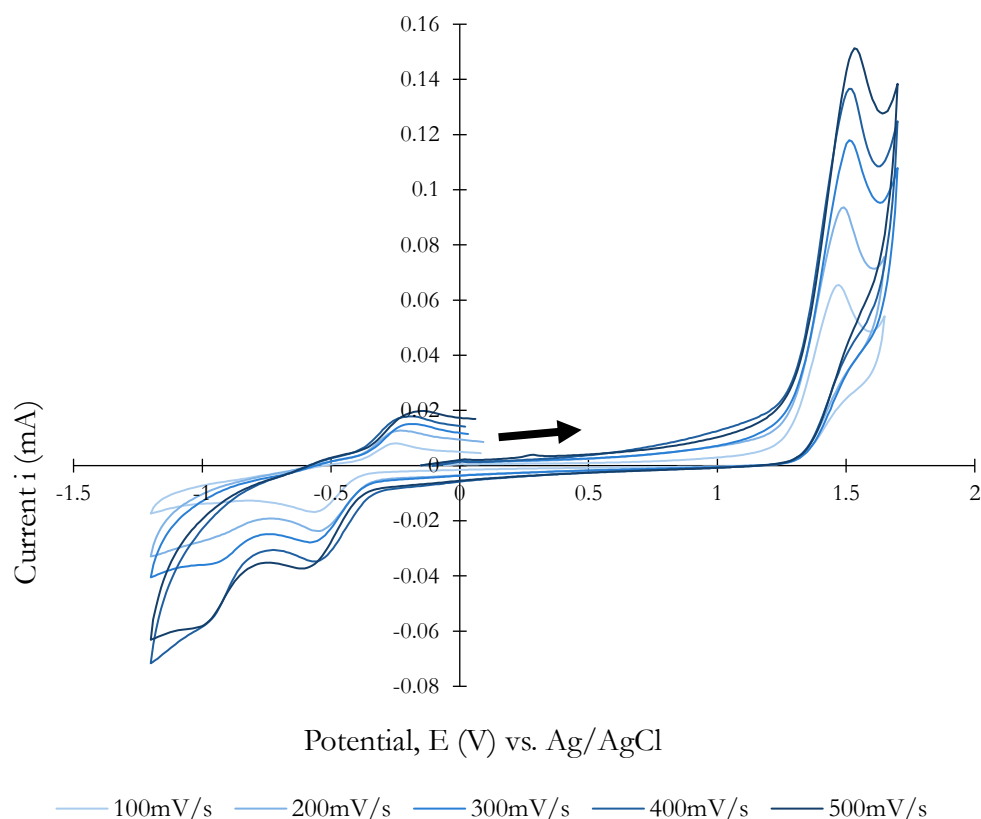


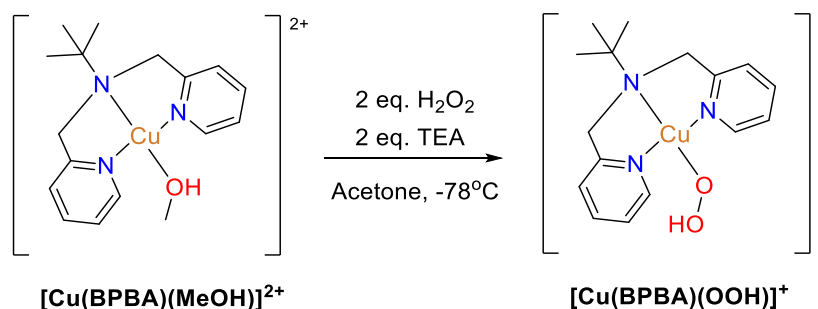
**Figure 9.** Cyclic voltammograms of complex **1** (5mM) in aqueous solution, pH 7.5, containing 100 mM NaNO<sub>3</sub>, recorded under argon atmosphere and at different scan rates (100 to 500 mV/s) The arrow indicates the direction of the CV scans.

### 1.3 – Conclusion

In this section, we have described the synthesis of the 1<sup>st</sup> generation ligands, PMPA and PEPA, and complexes, [Cu(PMPA)(H<sub>2</sub>O)(NO<sub>3</sub>)] (**1**) and [Cu(PEPA)(H<sub>2</sub>O)<sub>2</sub>].ClO<sub>4</sub> (**2**). We have also fully characterized complex **1** using spectroscopic techniques and electrochemistry. In addition, we have properly described the complex using theoretical methods which are adequately reproducing experimental results. This does not only support experimental data but can now also be used to predict and rationalize more complex observations as in the case of the next section with the reactivity studies.

## 2 – Reactivity of the [Cu(PMPA)(H<sub>2</sub>O)(NO<sub>3</sub>)] complex (1) in presence of hydrogen peroxide

The peroxide shunt pathway was used to generate a high oxidation state metal-oxo species through the formation of a hydroperoxo species. In the specific case of mononuclear copper complexes with square planar geometries, Fujii *et al.* [13] were able to stabilize and characterize a hydroperoxo species using the bis(2-pyridylmethyl)tert-butylamine, BPBA, ligand. After synthesis of the [Cu<sup>II</sup>(BPBA)(MeOH)].(ClO<sub>4</sub>)<sub>2</sub> complex, two equivalents of both triethylamine and hydrogen peroxide were added in an acetone solution of complex **1** at -78°C (Scheme 6). The resulting product displayed a great absorption band at 350 nm assigned by UV-vis to the HOO<sup>-</sup> to Cu charge transfer (LMCT) while maintaining a square-planar geometry as attested by the EPR parameters:  $g_{\parallel} = 2.26$ ,  $g_{\perp} = 2.06$ , and  $A_z^{\text{Cu}} = 554$  MHz. In addition, Fujii and his group studied the reaction kinetics for the oxidation of dimethyl sulfide.



Scheme 6. Formation of the square-planar [Cu(BPBA)(OOH)]<sup>+</sup> complex by addition of 2 equivalents of both hydrogen peroxide and triethylamine, in an acetone solution of the [Cu(BPBA)(MeOH)]<sup>2+</sup> complex at -78°C.

### 2.1 – Formation of the [Cu(POPA)(OH)(OCHO)]<sup>-</sup> complex

In the same line, we studied our [Cu(PMPA)(H<sub>2</sub>O)(NO<sub>3</sub>)] complex in presence of hydrogen peroxide and triethylamine. In a methanolic solution of complex **1** (1 mM), 2 eq. of triethylamine and 20 eq. of hydrogen peroxide were added at room temperature. The reaction was monitored by UV-vis for 20 minutes. Simultaneously, samples were taken from the reaction mixture and frozen in liquid N<sub>2</sub> for EPR analysis.



During the reaction, the original light blue solution turned light green and its evolution was followed by UV-vis spectroscopy. In the first minutes of reaction, a species displaying a absorption band at 440 nm appeared and then decreased in intensity (Figure 10). Then, the initial 305 nm band increased up to saturation and a broad absorption band appeared at around 450 nm. The absorption band at around 640 nm, which correspond to the d-d electron transition, remained unchanged. The EPR spectrum was recorded at different time intervals in the same conditions and showed a decrease in intensity and slight changes of the main features (Figure 11).

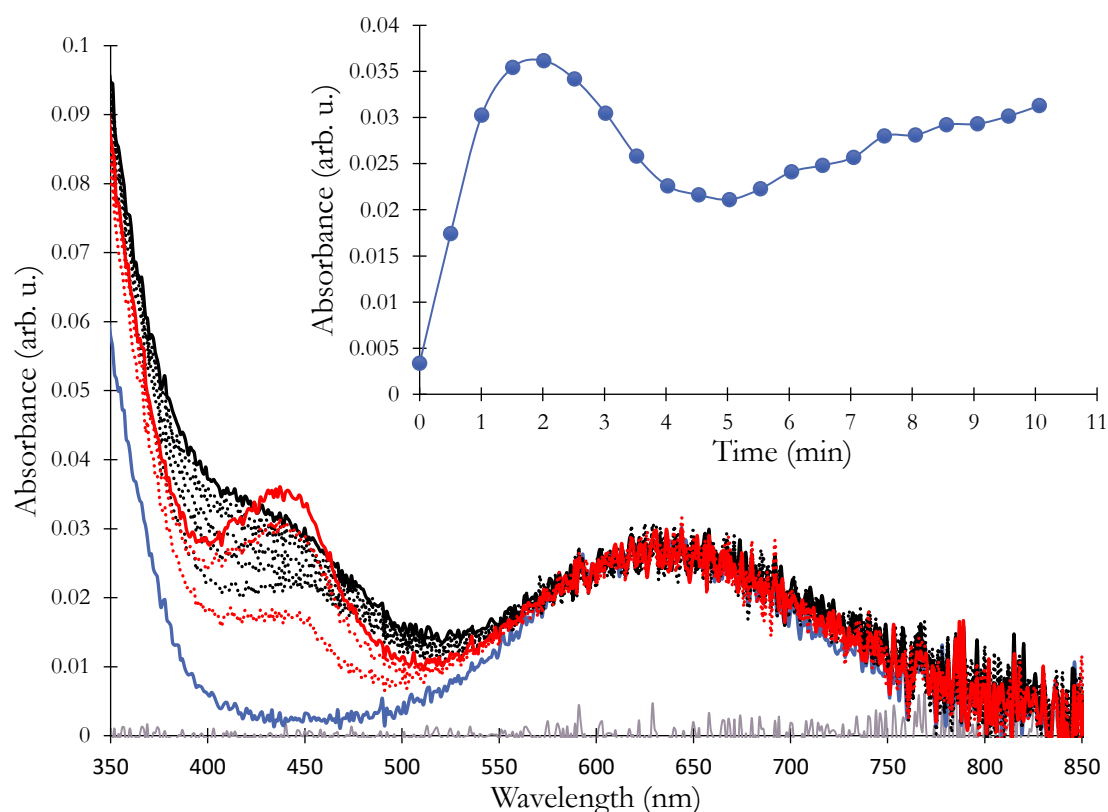


**Figure 10.** UV-vis spectrum of complex 1 in methanol before (blue) and after reaction with triethylamine and hydrogen peroxide. The red spectra was recorded right after hydrogen peroxide addition and the one in black is obtained after a few minutes of reaction. The inset shows the temporal evolution of the intensity at 440 nm. An optical fiber probe of 0.5-cm pathlength was used.

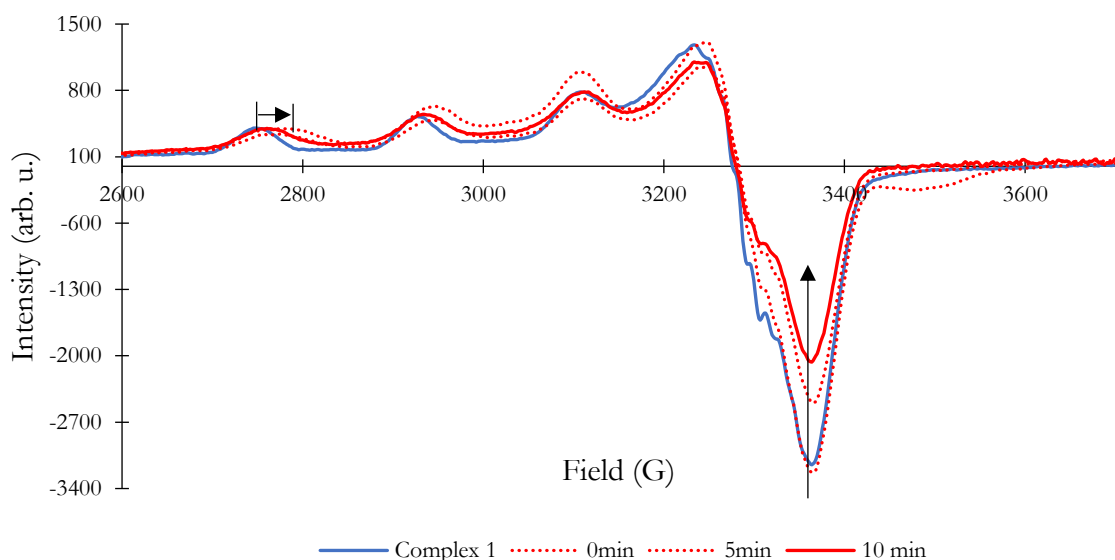


**Figure 11.** EPR spectrum of complex 1 (light blue) in methanol and upon addition of hydrogen peroxide (red) recorded at different time intervals. Black arrows indicate the evolution of the spectrum over time.

The solution of the reaction mixture was left to evaporate and suitable crystals for XRD analysis were obtained (Figure 12). The crystal structure of the resulting complex shows some modifications of the initial  $[\text{Cu}(\text{PMPA})(\text{H}_2\text{O})(\text{NO}_3)]$  complex. First, the original PMPA ligand is oxidized at the benzylic carbon to produce the N-picolinoylpicolinamide (POPA) ligand which is obtained by transformation of the amide to an imide moiety. Second, a formate anion is found coordinating the copper center in the basal position. And third, at the axial position, the original water molecule is found deprotonated forming a hydroxyl group. The resolution of the structure together with a careful analysis of the residual electronic densities and packing around the hydroxide ligand allowed us to rule out the possibility of a second proton and therefore of a bound water molecule instead of a hydroxide ligand.

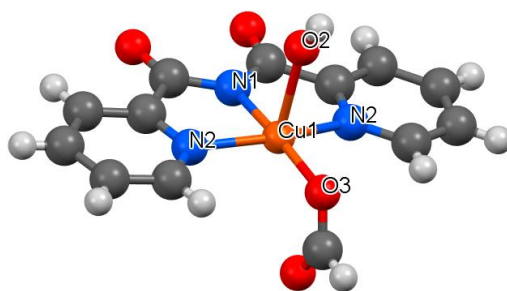


Figure 12. XRD structure of  $[\text{Cu}(\text{POPA})(\text{OH})(\text{OCHO})]$ , complex 3, obtained by slow evaporation of the reaction mixture. Empirical formula:  $\text{C}_{13}\text{H}_{10}\text{CuN}_3\text{O}_5$ , Formula weight: 351.76, Temperature: 295° K.

Since the copper metal center is coordinating three anionic ligands (imide, hydroxyl, and formate), we initially supposed the formation of a stable Cu(III) species in the form of  $[\text{Cu}(\text{POPA})(\text{OH})(\text{OCHO})]$ . To further study the oxidation state of the complex, the reaction was carried at a larger scale to produce a single crystal to be studied by EPR, SQUID and high-resolution XRD at low temperature (Figure 13).

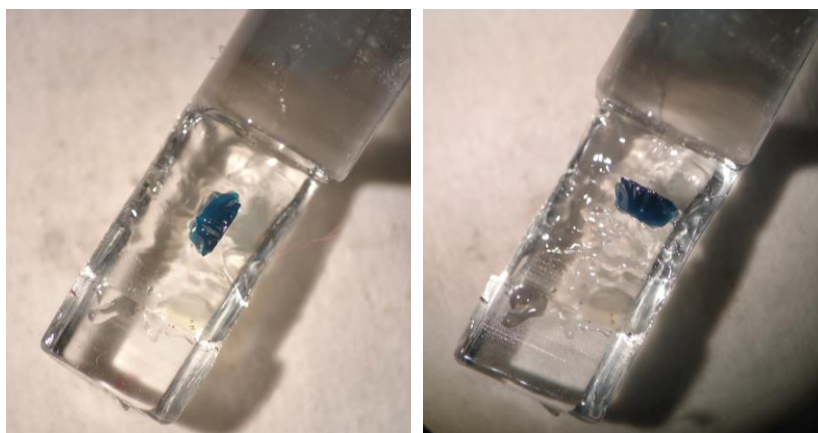


Figure 13. Image of the single crystal of complex 3 placed on the goniometer device used for solid-state EPR analysis.

#### 1. Understanding the oxidation state of the $[\text{Cu}(\text{POPA})(\text{OH})(\text{OCHO})]$ complex

In collaboration with Dr. Sylvain Bertaina of the Institut Matériaux Microélectronique Nanosciences de Provence (IM2NP), the single crystal was first studied by EPR spectroscopy using a goniometer device. A classical Cu(II) EPR signature is obtained with a well-defined g-tensor which varies with respect to the orientation of the single crystal (Figure 14). The g-tensor

values obtained are  $g_{\min} = 2.06$ ,  $g_{\text{mid}} = 2.08$ , and  $g_{\max} = 2.24$ , which are similar to those obtained for the initial  $[\text{Cu}(\text{PMPA})(\text{H}_2\text{O})(\text{NO}_3)]$  complex. Then, using a superconducting quantum interface device (SQUID), the magnetization of the crystal was extracted with respect to temperature at a constant applied field (Figure 15). The crystal's magnetization clearly coincides with that of an  $S = \frac{1}{2}$  species and is therefore consistent with a Cu(II) redox state. Both of these experiments made clear that the copper ion of the crystal produced from  $[\text{Cu}(\text{PMPA})(\text{H}_2\text{O})(\text{NO}_3)]$  in presence of triethylamine and hydrogen peroxide is a Cu(II) and that the complex is then the negatively charged  $[\text{Cu}(\text{POPA})(\text{OH})(\text{OCHO})]^-$ . We then questioned which counter cation could be stabilizing the negative charged in the crystal.

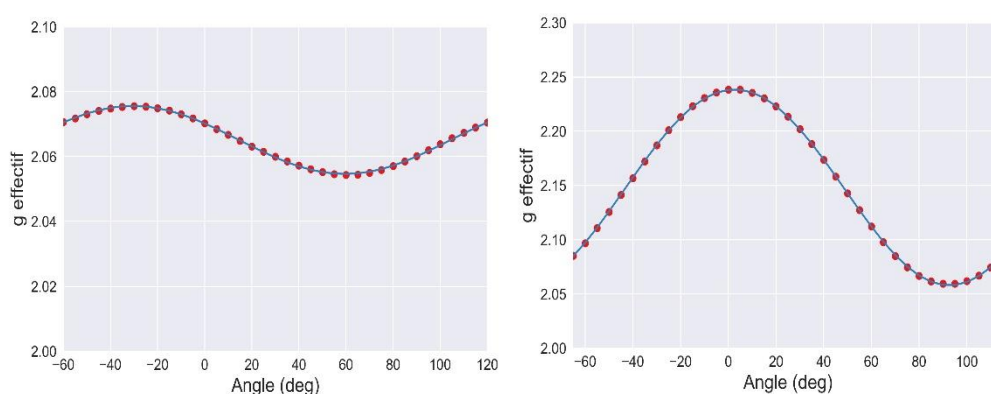


Figure 14. Effective g-value of complex 3 obtained at each rotating angle for two different orientations of the single crystal.

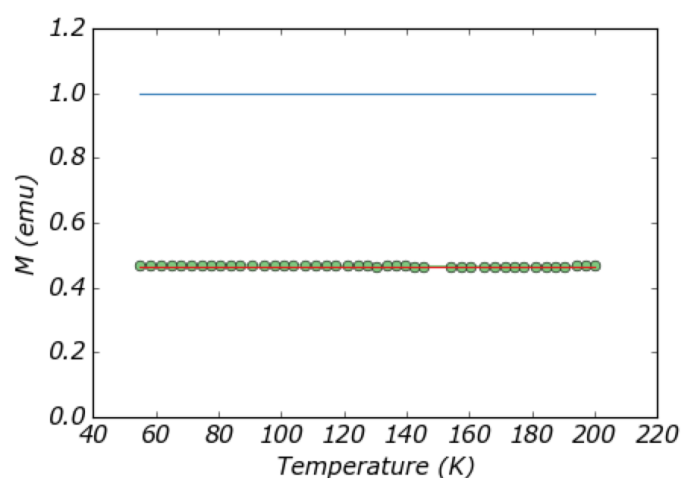


Figure 15. Magnetization of the single crystal of complex 3 (green circles) with respect to temperature. The  $S = \frac{1}{2}$  and  $S = 1$  magnetization values were simulated in red and blue, respectively.

A high resolution XRD structure was obtained for the single crystal at low temperature (Figure 16). This structure confirmed that the bound ligand is a hydroxide anion and not a water molecule. We therefore hypothesized that a mobile proton is present to compensate the charge. A deeper look into the crystal matrix exhibited channels in the structure which could be occupied by free protons that can compensate the negative charge of the complex. The presence of “mobile protons” has already been observed in the formation of metal hydrides. [26] [27] They are greatly studied for their use in hydrogen storage and in electrochemical applications. In absence of any other possible counter-ion, we thus concluded that mobile protons are present in our crystal to compensate the negative charge in the solid state.

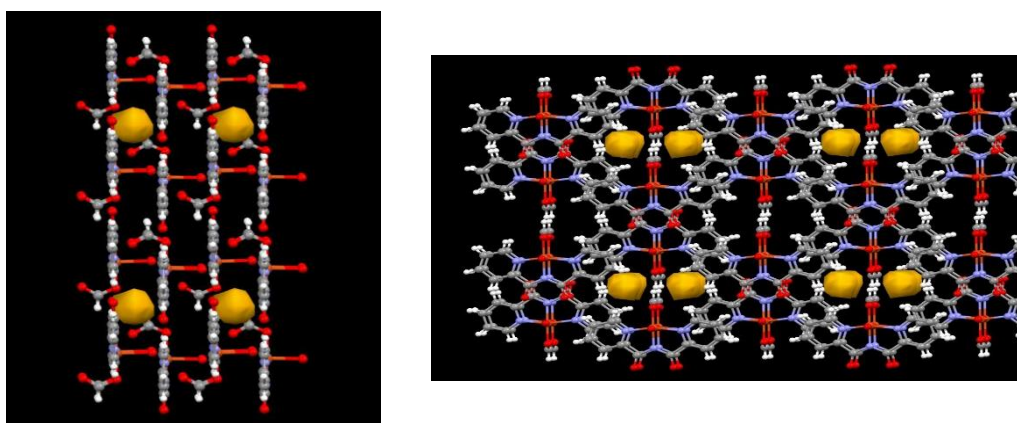
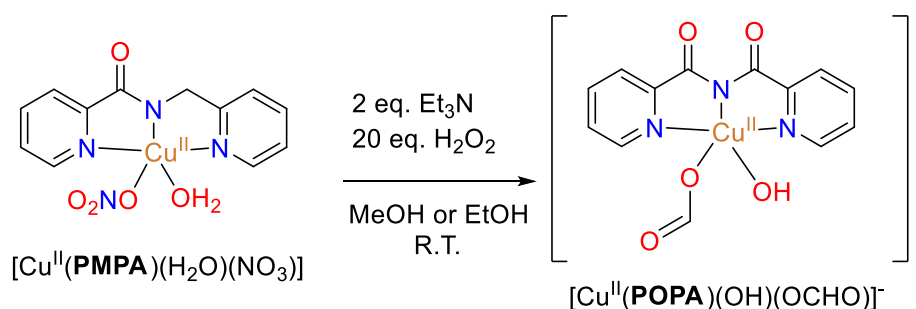


Figure 16. Tunnels present in the matrix of the crystal structure (yellow spheres) possibly occupied by protons.

The product of the reaction of complex **1** with hydrogen peroxide in the presence of Et<sub>3</sub>N is therefore complex **3**, [Cu(POPA)(OH)(OCHO)]<sup>−</sup> (Scheme 7).



Scheme 7. Formation of [Cu(POPA)(OH)(OCHO)]<sup>−</sup> in methanol or ethanol from [Cu(PMPA)(H<sub>2</sub>O)(NO<sub>3</sub>)] in presence of 2 eq. of triethylamine and 20 eq. hydrogen peroxide at room temperature.

This conclusion was further consolidated by means of DFT calculations. The open-shell system with  $S = 1/2$  was optimized as a Cu(II) with a (-1) overall charge (Figure 17, A). The spin density plot as well as the singly occupied molecular orbital (SOMO) show that the unpaired electron of the system is shared between the copper center and the hydroxyl group (Figure 17, B and C). The neutral overall charge calculation ran as a closed shell system with  $S = 0$  which considers the metal as a Cu(III) or as an open shell with  $S = 1$  where the metal is a Cu(II) coupled with an organic radical (Figure 17, D and E). The Cu(II)/radical system proved to be lower in energy than the Cu(III) system by 13.8 kcal/mol. These results point towards the presence of a Cu(II) metal center in the complex with the missing charge localized around the hydroxyl group. The hydroxyl group is thus probably found in its protonated form in solution, *i.e.* a water ligand.

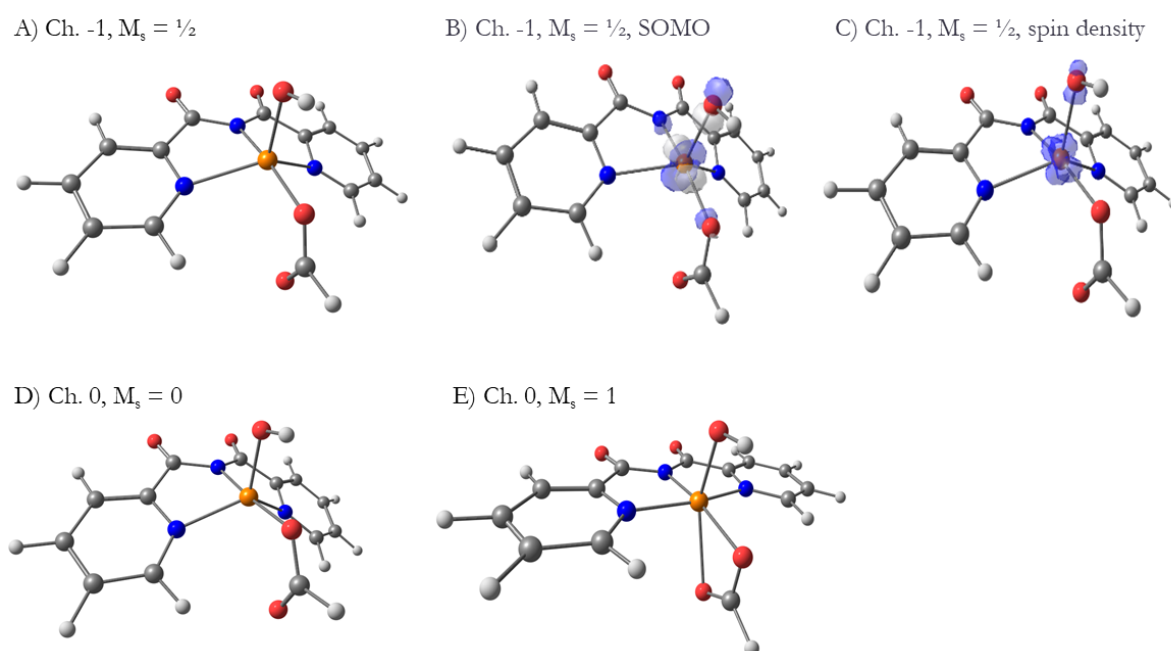


**Figure 17.** Optimized structures of complex 3 as different overall charges and spin states (A, D, and E). The singly occupied molecular orbital (SOMO) and the spin density plot are represented in B) and C).

## 2. Reactivity in Ethanol

In order to probe the origin of the formate anion, the reaction of  $[\text{Cu}(\text{PMPA})(\text{H}_2\text{O})(\text{NO}_3)]$  (1 mM) in presence of 2 eq. of triethylamine and 20 eq. hydrogen peroxide was also carried in ethanol at room temperature. This reaction was monitored by UV-vis for 20 minutes (Figure 18). A similar evolution of the absorption bands is observed. The shoulder around 300 nm becomes saturated and a new absorption band appears at 440-450 nm although the temporal evolution is less resolved.

The reaction mixture was left to evaporate to produce suitable crystals for XRD analysis. The crystal structure obtained in ethanol was found to be exactly the same as the one obtained in methanol: the  $[\text{Cu}(\text{POPA})(\text{OH})(\text{OCHO})]^-$  complex.

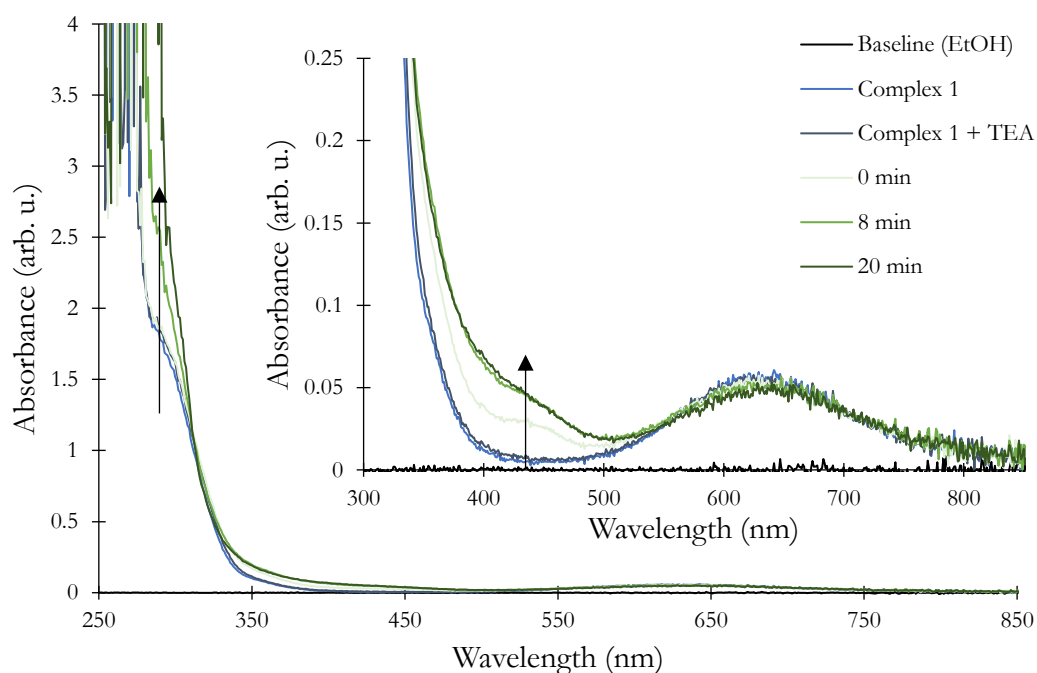
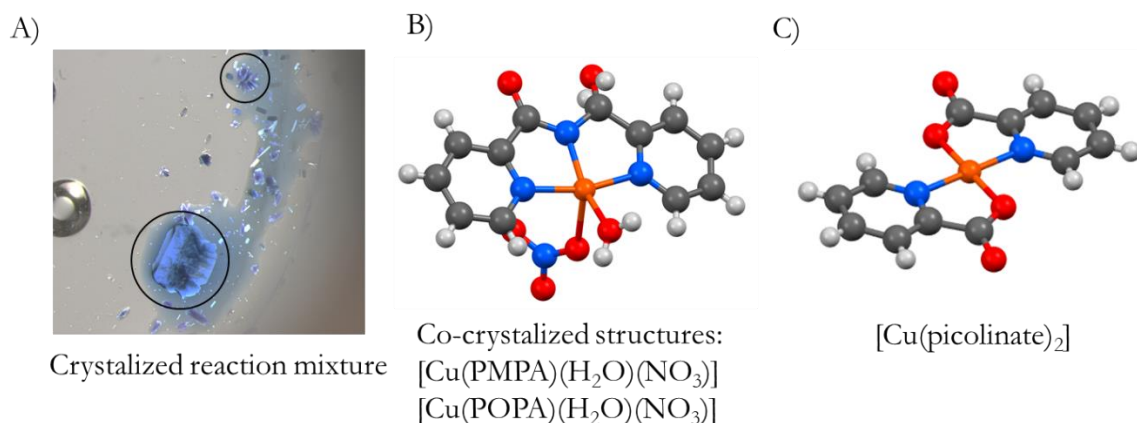


Figure 18. UV-vis spectrum of complex 1 in ethanol (light blue) and the reaction in presence of triethylamine (denoted TEA in the legend, dark blue) and hydrogen peroxide with respect to time (light to dark green). The inset zooms into the 300 to 850 nm range. The black arrows indicate the evolution of the absorbance spectrum over time. An optical fiber probe of 0.5-cm pathlength was used.

### 3. Other products observed

In both solvents, the reaction mixture exhibited multiple crystals. All were sorted out and characterized by XRD (Figure 19). The major single crystal observed (Figure 19, A) corresponds to  $[\text{Cu}(\text{POPA})(\text{OH})(\text{OCHO})]^-$ . However, other crystals are also found in the mixture. In particular, a copper complex coordinating the oxidized ligand (POPA), one water molecule and a nitrate ion (Figure 19, B). In this crystal, one of the carbonyl positions does not correspond to 100% occupancy. In fact, we observe a 2:1 ratio between the carbonyl and the alkyl moieties meaning that we have the co-crystallization of two structures, the initial  $[\text{Cu}(\text{POPA})(\text{H}_2\text{O})(\text{NO}_3)]$  complex accounting for 66% and the oxidized ligand analogue,  $[\text{Cu}(\text{PMPA})(\text{H}_2\text{O})(\text{NO}_3)]$  is found at 33%. Finally, we also obtained a complex with two picolinic acid molecules probably arising from ligand degradation (Figure 19, C).



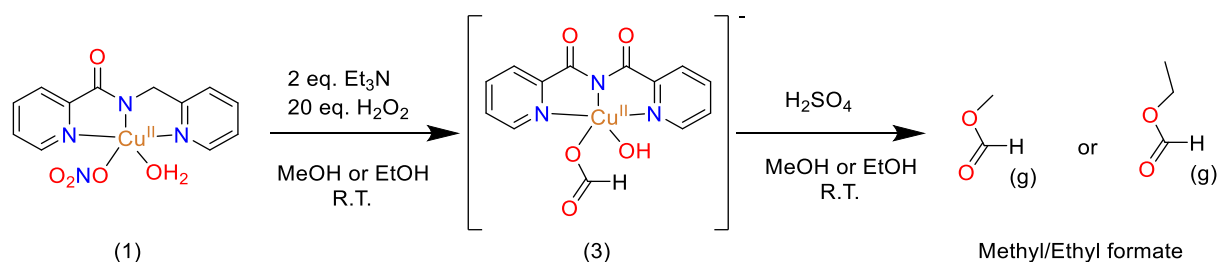


**Figure 19.** A) Crystallization of the reaction mixture displaying multiple crystal types. B) Co-crystallization of two structures with 66% of [Cu(PMPA)(H<sub>2</sub>O)(NO<sub>3</sub>)] and 33% of [Cu(POPA)(H<sub>2</sub>O)(NO<sub>3</sub>)]. C) Degraded PMPA ligand to the picolinic acid reagent to produce [Cu(picolinate)<sub>2</sub>].

## 2.2 – Quantification of formate produced

To better understand the reactivity of the system, we relied on gas chromatography (GC) to optimize the conditions of the reaction and to quantify the reaction products (formate). To do so, formate is transformed to methyl-formate or ethyl-formate by esterification upon addition of concentrated sulfuric acid in methanol or ethanol solutions, respectively (Scheme 8). This type of detection has already been reported in the context of toxicology and methanol poisoning since formate is a known metabolite of methanol in the human body. [28] [29] [30] Solutions of the complex were prepared in methanol or ethanol in gas-tight vials and reacted with hydrogen peroxide/TEA under various conditions. After the reaction, sulfuric acid was added through the septum to allow the formation of the formate esters (ethyl-formate or methyl-formate depending on the solvent used). The esters were then quantified by injecting the headspace gas to the GC using a gas-tight syringe. References were taken from pure samples of solvents, methyl and ethyl formate, and other possible oxidative products of both methanol and ethanol (formaldehyde, ethanal, ethylacetate etc.). Standard curves for methyl and ethyl formate were obtained by placing formic acid at known concentrations in methanol or ethanol and reacting with sulfuric acid following the same experimental procedure as mentioned above. The conditions of analysis were optimized in terms of column temperature, volume of injection, quantity of sulfuric acid, time of equilibrium between liquid and gas phases, *etc.* Samples were taken at least in triplicates. In the following, we report the concentration of products obtained divided by the initial number of moles of complex **1**, expressed in turnover number (TON).





**Scheme 8.** Pathway to quantify the formate produced by GC via esterification into methyl or ethyl formate.

To begin, the reaction was monitored with respect to time. Complex **1** was reacted with 2 eq. of triethylamine and 20 eq. of hydrogen peroxide. Then, 20  $\mu\text{L}$  of concentrated sulfuric acid were added at 0, 0.5, 1, 2, 3, 5, and 16 hours of reaction and the headspace was analyzed by GC (Figure 20). In both methanol and ethanol solutions, the maximum production of methyl- and ethyl-formate was obtained after 3 hours of reaction. In methanolic solution, the maximum quantity of formate obtained can roughly correspond to one TON per complex; while in ethanol, the maximum corresponds to 0.4 TON.

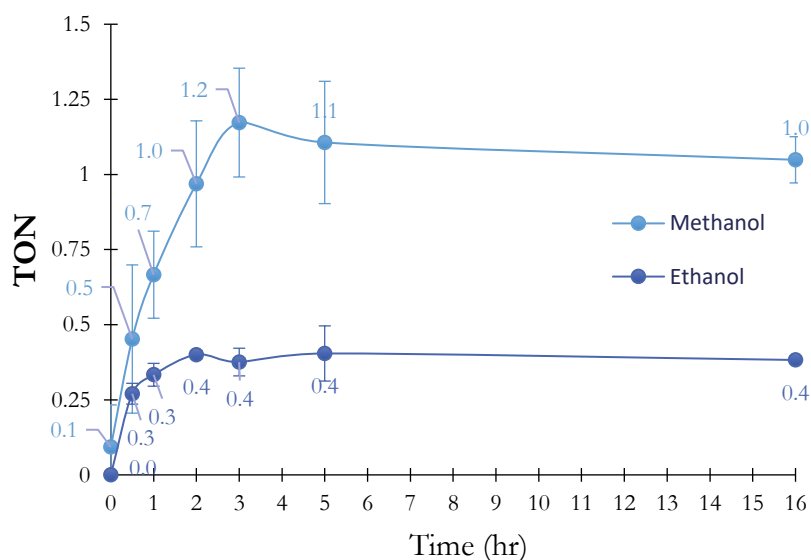
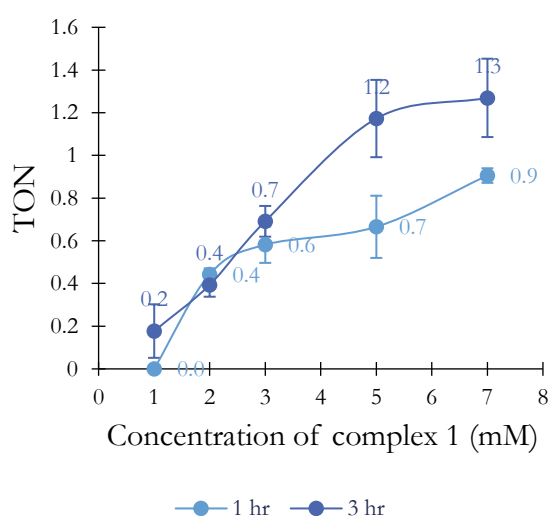


**Figure 20.** Production (in TON) of methyl/ethyl formate in either methanol (light blue) or ethanol (dark blue) as a function of time.

We then evaluated the effect of the complex concentration. Solutions of complex **1** were prepared at 1, 2, 3, 5, and 7 mM in methanol or ethanol. Triethylamine and hydrogen peroxide were added, and the reaction was left for either 1 or 3 hours. Then, the reaction mixtures were treated by concentrated sulfuric acid and the headspace gas were analyzed by GC (Figure 21). In methanol,

an increase in complex **1** concentration leads to an increase of methyl formate produced after 1- or 3-hours of reaction although a plateau is reached after 5 mM of complex and after 3 hours of reaction. In the case of ethanol, the maximum conversion is obtained for 3 mM of complex. An increase in concentration of complex **1** is detrimental to the formation of ethyl formate. This is observed both after 1- and 3-hours of reaction. Higher concentrations were not investigated because of solubility constraints. In both cases, a control was performed in the absence of complex and no evidence was found for the formation of either methyl or ethyl formate.

**A) Reaction carried out in methanol**



**B) Reaction carried out in ethanol**

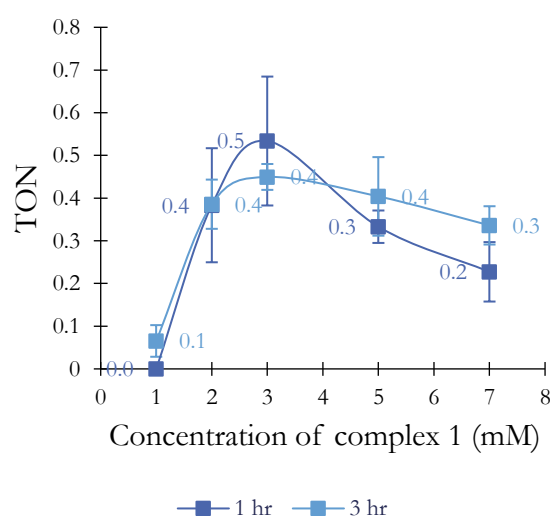


**Figure 21. Production (in TON) of methyl or ethyl formate in either methanol (graph A) or ethanol (graph B) as a function of complex 1 concentration. The reactions were carried out for 1h (light blue) or 3h (dark blue).**

In methanol, we investigated the effect of the amount of triethylamine used in the reaction mixture. We prepared solutions to add from 0 to 8 equivalents of triethylamine *vs.* the complex. The concentration of complex **1** and hydrogen peroxide were kept constants (5mM and 0.06 M respectively). The reactions ran for 3 hours, subjected to sulfuric acid, and analyzed by GC (Figure 22). The maximum conversion is found at 2 eq. of triethylamine. Above 4 equivalents, the conversion decreases. The excess of base in solution thus interferes with the reaction and might be related to a dimerization of the complex or deprotonation of bound water molecules. Note that the reaction does not occur if no triethylamine is added.

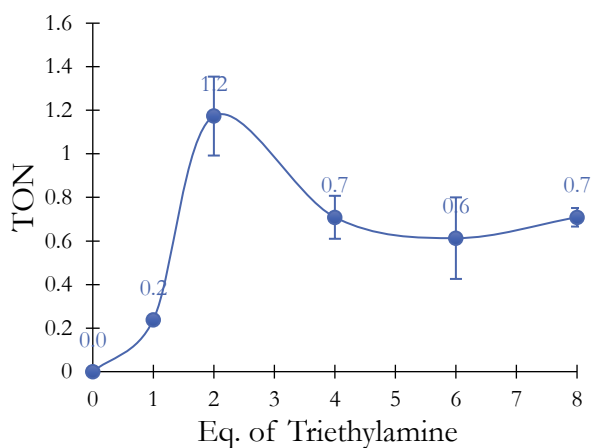


**Figure 22.** Production (in TON) of methyl formate in methanol solvent as a function of equivalents of triethylamine.

Similarly, we investigated the effect of hydrogen peroxide in the reaction. 0-80 equivalents of hydrogen peroxide were added. Again, the concentrations of the complex and of triethylamine were kept constant (5 and 10 mM respectively). The reaction was left running for 3 hours before addition of sulfuric acid and analysis by GC (Figure 23). The maximum conversion of methyl formate is found at 20 equivalents of hydrogen peroxide. Excess oxidative conditions decrease the production of methyl formate. Note that no methyl-formate is produced if hydrogen peroxide is not added to the solution.

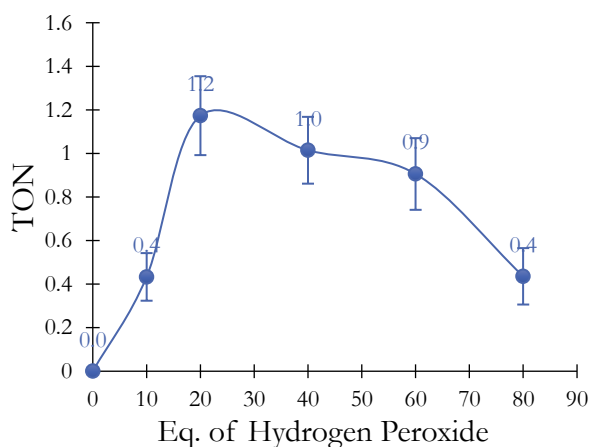
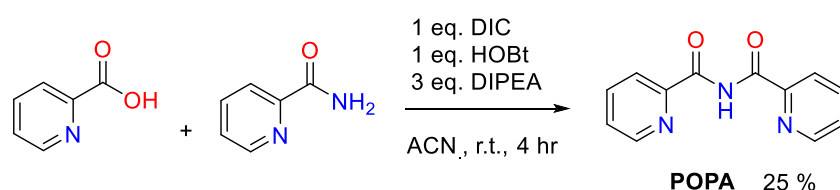


**Figure 23.** Production (in TON) of methyl-formate in methanol solvent as a function of equivalents of hydrogen peroxide.

These reactivity studies using GC gave us great insight into the reaction and the required conditions to produce formate. The maximum conversion is obtained after 3 hours of reaction in either methanol or ethanol. The reaction produces less formate in ethanol than it does in methanol. The presence of both H<sub>2</sub>O<sub>2</sub> and Et<sub>3</sub>N is necessary to produce formate.

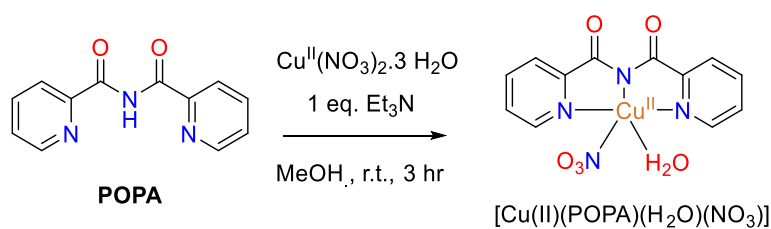
### 1. Influence of the oxidation of PMPA

During the reaction, the PMPA ligand used in complex **1** is oxidized to its POPA counterpart, where the initial amide is transformed into an imide. To investigate the influence of this oxidative reaction on formate production, we synthesized the POPA ligand by coupling picolinamide and picolinic acid in presence of *N,N'*-Diisopropylcarbodiimide (DIC), hydroxybenzotriazole (HOBt), and diisopropylethylamine (DIPEA) (Scheme 9). The yield of the reaction was found quite low around 25%.



**Scheme 9.** Synthesis of the **POPA** ligand via activation of picolinic acid in presence of **DIC**, **HOBt** and **DIPEA** and addition of primary amide. Acetonitrile (**ACN**) is used as solvent at room temperature.

Complex [Cu(POPA)(H<sub>2</sub>O)(NO<sub>3</sub>)] (**4**) was obtained by mixing the copper nitrate trihydrate salt with the POPA ligand in methanol in presence of 1 equivalent of triethylamine. The initial purple solution turned light blue. After 3 hours of reaction, diethyl ether was added to precipitate the complex (Scheme 10). The powder was solubilized in a methanol/water mixture to produce suitable crystals for XRD analysis (Figure 24).



Scheme 10. Synthesis of  $[\text{Cu}(\text{II})(\text{POPA})(\text{H}_2\text{O})(\text{NO}_3)]$ , complex **4**, by addition of POPA to a copper nitrate trihydrate salt in methanol in presence of 1 equivalent of triethylamine.

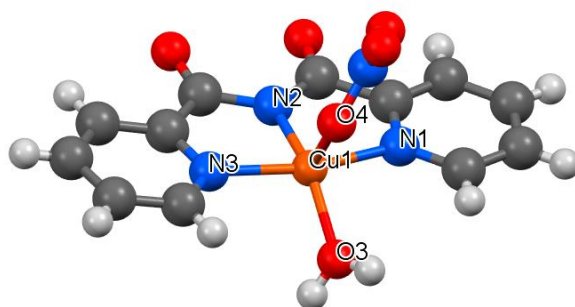
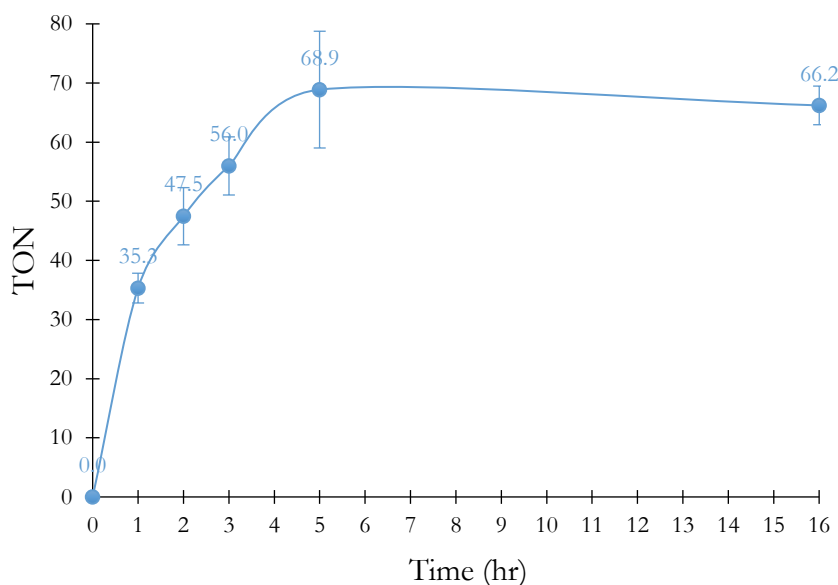


Figure 24. XRD structure of  $[\text{Cu}(\text{POPA})(\text{H}_2\text{O})(\text{NO}_3)]$  obtained by slow evaporation of the reaction mixture. Empirical formula:  $\text{C}_{13}\text{H}_{11}\text{CuN}_4\text{O}_5$ , Formula weight: 360.40, Temperature: 295°K.

Complex **4** was subjected to reaction with 2 equivalents of triethylamine and 20 equivalents of hydrogen peroxide in methanol, following the conditions used for complex **1**. The reaction was monitored over time by GC to determine if methyl-formate was produced. After 16 hours of reaction, there was no evidence of any methyl-formate in the reaction mixture. This means that the oxidation of the ligand prevents the production of methyl-formate.

## 2. Other oxidation products

In methanol, we also identified formaldehyde in the reaction mixture (Figure 25). The production of formaldehyde was quantified in presence of complex **1** (5 mM), triethylamine (2 eq.) and hydrogen peroxide (5 eq.) with respect to time. The maximum conversion (*c.a.* 69 TON) was obtained after 5 hours of reaction.



**Figure 25. Production (in TON) of formaldehyde in methanol with respect to time.**

In ethanol, multiple products were identified after 3 hours of reaction: methanol, ethanal, and ethylacetate. The importance here lies on the capabilities of the complex not only producing formate but also other oxidation products.

### 2.3 – Origin of formate

Formate is an added-value chemical specially when carbon dioxide is used as the feedstock. [31] To better understand the reaction, we need to decipher the origin of the formate formed upon reaction. There is an influence of the solvent and of the reaction conditions as well as of the oxidation of the ligand. We postulated two pathways, one where carbon dioxide is sequestered from air and reduced, and another where the solvent is oxidized.

#### 1. Investigation of CO<sub>2</sub> sequestration and reduction

Following the GC experiments previously described, we performed the reaction under different atmospheres. We bubbled either argon or CO<sub>2</sub> directly into the gas-tight vial for 5 minutes, as well as in the solutions of the reagents, *i.e.* complex **1**, triethylamine and hydrogen peroxide. Under argon atmosphere, we expect that formate is not produced if formed from CO<sub>2</sub>. On the contrary under CO<sub>2</sub>, there could be an increase in the production of formate (although not necessarily true

since the reaction might not be acting catalytically but only stoichiometrically at best). We prepared samples under air, argon, or carbon dioxide atmospheres with complex **1**, 2 equivalents of triethylamine and 20 equivalents of hydrogen peroxide (Figure 26). In the case of methanol, a great decrease in the production of formate is observed under CO<sub>2</sub> atmosphere compared to the one obtained under air. Under argon atmosphere, the quantity of methyl formate slightly increased although not significantly. In the case of ethanol, there is a slight decrease in the production of ethyl-formate under argon atmosphere. The quantity of ethyl-formate is the same under CO<sub>2</sub> than it is in air. It can therefore be concluded that adding CO<sub>2</sub> does not improve the production of formate and in fact even leads to a decrease in the production in the case of methanol. More importantly, the reaction continues to take place under argon atmosphere, suggesting that the precursor of formate is not coming from the air. Neither of these observations support CO<sub>2</sub> as the precursor to formate in the reaction.

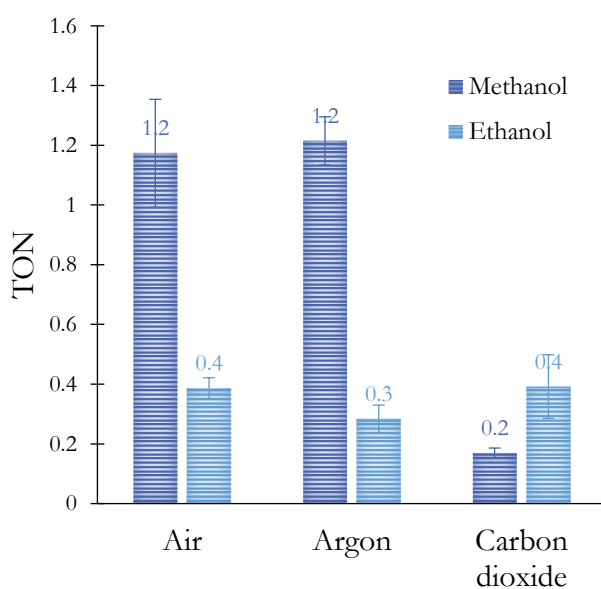


**Figure 26.** Production (in TON) of methyl- or ethyl-formate under air, argon, or carbon dioxide atmospheres after 3 hours of reaction in presence of triethylamine (2 eq.) and hydrogen peroxide (20 eq.).

Finally, we used <sup>13</sup>C-labelled CO<sub>2</sub> gas. The reaction of complex **1** (5 mM), 2 eq. of triethylamine, and 20 eq. of hydrogen peroxide was carried while bubbling <sup>13</sup>CO<sub>2</sub> in ethanol solvent. The reaction mixture was analyzed by GC-MS after 3 hours. Ethyl-formate was identified at m/z = 74 and we expected the <sup>13</sup>C labeled ethyl-formate at m/z = 75 (Figure 27). Labelled CO<sub>2</sub> does not affect the

species distribution for ethyl-formate, which unequivocally proves that CO<sub>2</sub> is not the precursor of formate in the reaction.

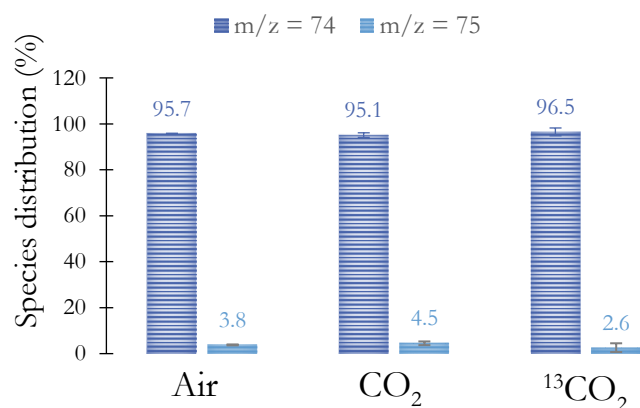


**Figure 27. GC-MS mass distribution of ethyl-formate obtained after reaction of complex 1 in presence of triethylamine (2 eq.) and hydrogen peroxide (20 eq.) in ethanol under air, carbon dioxide, and labelled carbon dioxide atmospheres.**

## 2. Investigation of C-H activation of solvent

The involvement of methanol and ethanol in the formation of formate was then investigated. We first studied the reaction in methanol and its deuterated counterpart, MeOD-d<sub>4</sub> by GC. The reaction was monitored over time under the usual conditions (2 eq. of triethylamine, 20 eq. of hydrogen peroxide, under air, in gas tight vials) (Figure 28) and formaldehyde was also quantified (Figure 29). For both formate and formaldehyde, the reaction is much slower in deuterated methanol. The initial rates were extracted for each condition (slopes) and the initial rate is admittedly 4 times faster for methyl-formate, and 6 times for formaldehyde, in methanol than in deuterated methanol. These results are indicative of C-H activation steps i rate-determining steps during the formation of formate and formaldehyde.

In addition, the kinetic isotope effect (KDIE) calculated for the formation of formate is 4.0 and for formaldehyde is 6.2. Both are greater than the KDIE for hydrogen abstraction from similar substrates by hydroxyl radicals (KDIE around 1.8 to 2.0). [32] [33] [34] This result points towards a metal-centered species involved in the hydrogen abstraction step of the reaction.



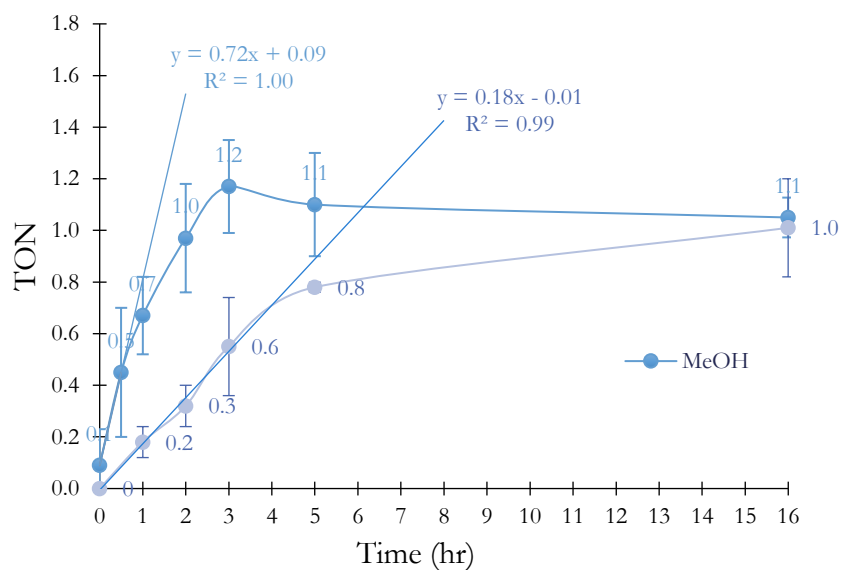


**Figure 28. Production (in TON) of methyl formate in methanol (MeOH) and deuterated methanol (MeOD-d4) with respect to time. The slopes are taken for each and the equations as well as the  $R^2$  are reported.**

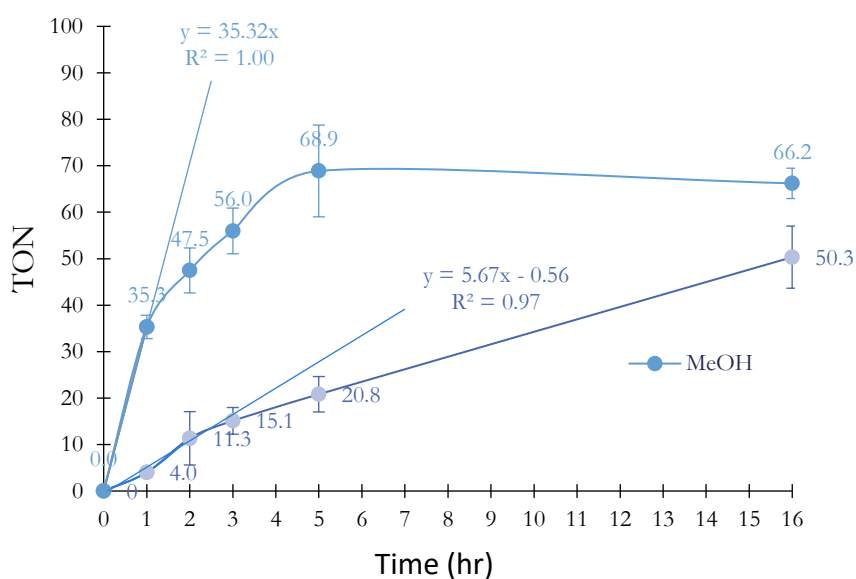


**Figure 29. Production (in TON) of formaldehyde in methanol (MeOH) and deuterated methanol (MeOD-d4) with respect to time. The slopes are taken for each and the equations as well as the  $R^2$  are reported.**

The reaction was also studied in  $^{13}\text{C}$ -labelled ethanol in the  $\alpha$  position. Since ethanol is labelled on the  $\alpha$ -carbon, there are three possible combinations of exact mass for ethylformate:

- $m/z = 74$  without any labelled atom
- $m/z = 75$  with one labelled atom

- $m/z = 76$  with two labelled atoms

Solutions were prepared using incremental amounts of the labelled ethanol, 0 %, 18 %, 35 % and 53% (Figure 30). As the amount of labelled ethanol increases, the heavier products ( $m/z = 75$  and 76) increase as well, while the non-labelled product ( $m/z = 74$ ) decreases. The mass distributions ( $m/z$  74, 75 and 76) were compared to the statistical expected distributions for the different  $^{13}\text{C}$ -ethanol content and found to match rather well. This correlation supports that the solvent, ethanol, is the origin of formate and ethyl-formate in solution. This also means that the reaction taking place involves C-H abstraction at the  $\alpha$  position followed by C-C cleavage to produce formate.

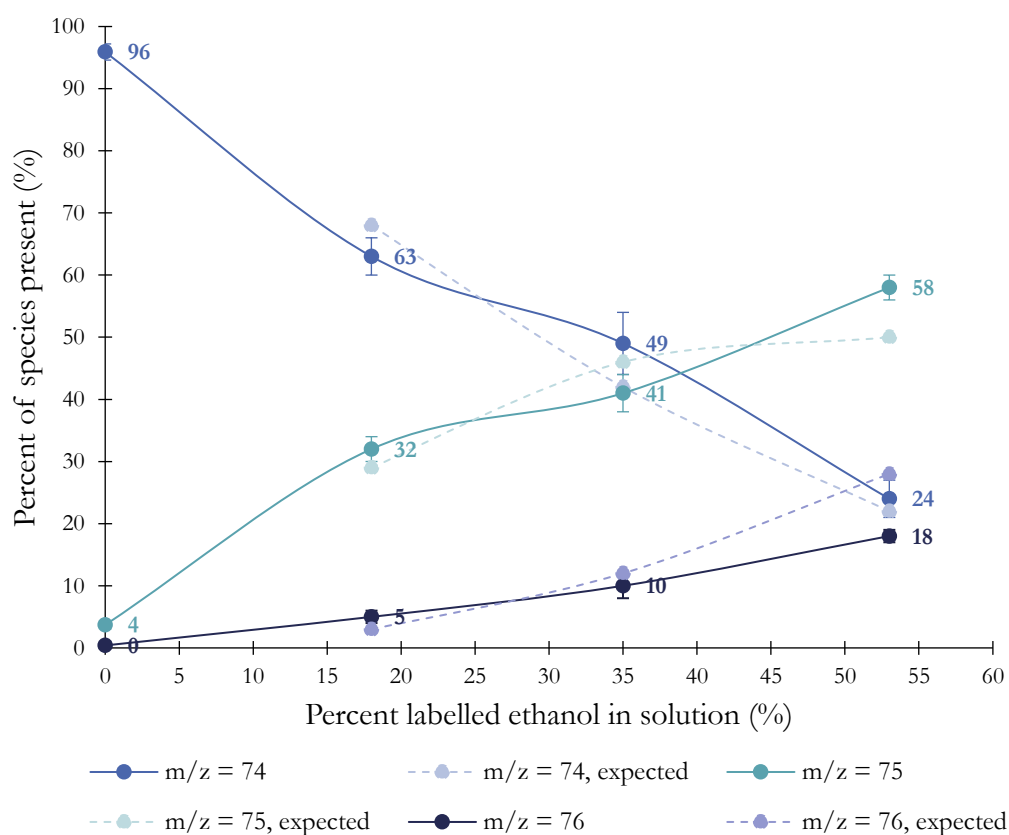


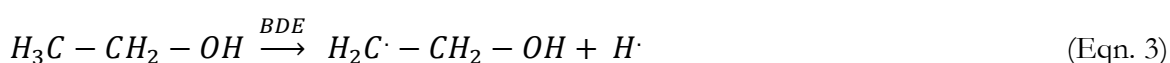
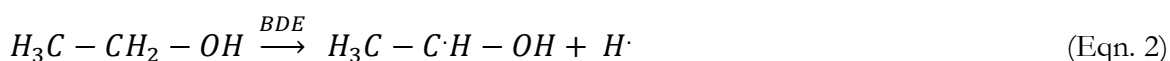
**Figure 30.** Percentages of species ( $m/z = 74$ , 75 or 76, blue, green, and dark blue, respectively) present at the ethyl formate retention time with respect to percentage of labelled ethanol found in solution during the reaction. The expected probabilities are shown in dotted lines.

## 2.4 – Bond dissociation energies

To evaluate the oxidative capacities of complex **1**, the C-H bond dissociation energies of both methanol and ethanol were calculated. Geometry optimizations and vibrational frequency calculations were performed with the ORCA program package to obtain the free energies of the

C-H and C• molecules. Absence of imaginary modes confirmed that true minima were obtained. These geometry optimizations were carried with the B3LYP functional and the def2-TZVP basis set, in combination with corresponding auxiliary basis sets.

The bond dissociation energy was obtained by evaluating the free energies of the radical form of the deprotonated molecule plus that of the radical proton subtracted from the free energy of the initial molecule.



In the case of methanol, we evaluated the H<sub>2</sub>C•-OH species and the H<sub>3</sub>C-OH one. In the case of ethanol, we evaluate the dissociation in the α-C position, H<sub>3</sub>C-CH•-OH, and the one in the β-C position, H<sub>2</sub>C•-CH<sub>2</sub>-OH. The computed bond dissociation energy was found to be 94.3 kcal/mol for methanol, 92.7 kcal/mol for the α-C position of ethanol, and 99.9 kcal/mol for the β-C position of ethanol.

## 2.5 – Proposed reaction mechanisms

The GC and GC-MS studies gave us relevant information on the origin of formate and on the nature of the reactions taking place. There is evidence for the formation of aldehydes and carboxylic acids in both solvents. The hydrogen abstraction of the C-H bond is likely involved in the rate determining step while the C-H is a strong bond to activate (BDEs greater than 90 kcal/mol). The oxidized ligand/complex ([Cu(POPA)(H<sub>2</sub>O)(NO<sub>3</sub>))] does not produce formate nor other products indicating that the oxidation of the ligand reduces the oxidizing power of the reactive Cu-oxygen species involved in solvent oxidations.

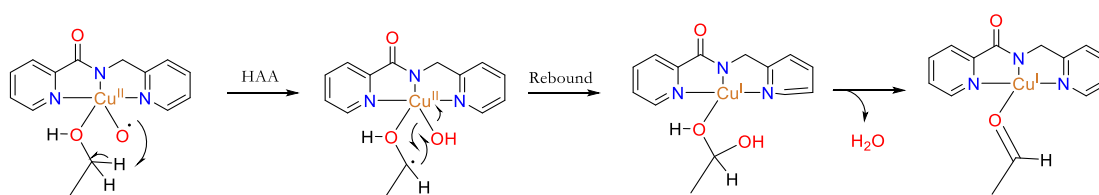
In methanol, there is evidence of formaldehyde and formate. In ethanol, there is evidence of formate produced from the α-C after C-C cleavage of the alcohol. The corresponding aldehyde, ethanal, was also observed, as well as the carboxylic acid in the form of ethylacetate. More importantly, methanol was also identified in the reaction.

## Ethanol oxidation

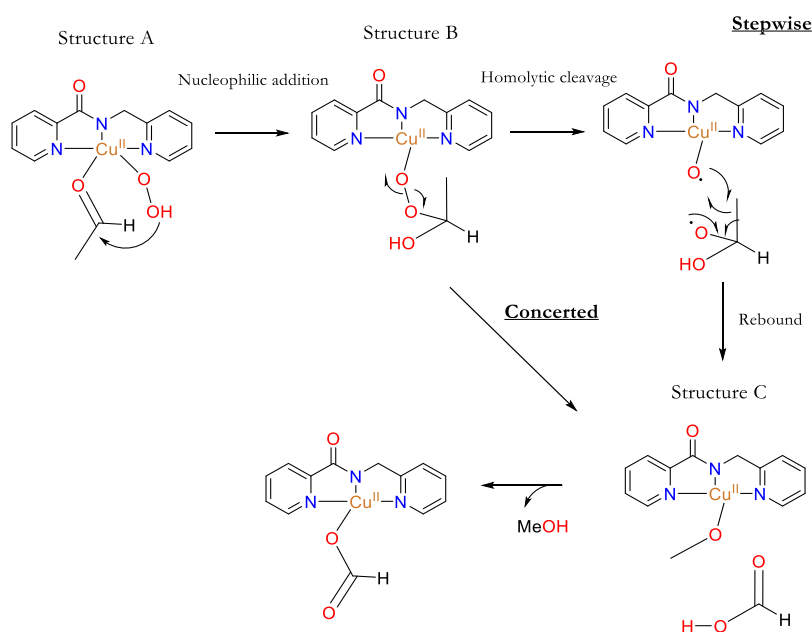
The oxidation of ethanol was envisioned as a two-part reaction. First, there would be the oxidation of the alcohol to the corresponding aldehyde, ethanal (Scheme 11, 1). This first step is a common one when considering the reactivity in methanol which leads to methanal that can be over-oxidized to formate. In the case of ethanol, we propose the second step to be a deformylation reaction of ethanal to produce formate and methanol (Scheme 11, 2). [35]

Concerning the first step: since the BDE of the C-H bond of the  $\alpha$ -C position of ethanol is quite high, and since metal-centered species are likely involved in the H-abstraction step given the KDIE values, we propose the involvement of a copper-oxyl species responsible for the H-abstraction step. The produced R-C $\cdot$  species can recombine with the copper(II)-hydroxide resulting complex to yield an acetal species that can subsequently be converted into the aldehyde (ethanal) and water.

### 1) Formation of ethanal



### 2) Deformylation



**Scheme 11.** Proposed reaction mechanism for the formation of ethanal and subsequent deformylation to produce formic acid and methanol.

Concerning the second step: it has been shown that aldehyde deformylation can be carried out by nucleophilic metal-oxygen intermediates. In the case of copper chemistry, copper-superoxo and copper-peroxo species have been shown to display nucleophilic reactivities when ligated by electron-rich ligands. [36] Some copper-hydroperoxo species were also shown to have nucleophilic character. [35] In the present case, it is highly probable that Cu(II)-OOH species are formed upon reaction of the Cu(II) complex with hydrogen peroxide via a peroxide shunt mechanism. Our ligand was designed to stabilize high-valent metal species therefore promoting the nucleophilicity of the hydroperoxo species. The proposed mechanism involves nucleophilic addition of the hydroperoxo to the aldehyde, generating a Cu-alkylperoxo species. Such species are known to undergo O-O bond cleavage. Further rebound-like reaction could then occur between the released radical species (Cu-oxyl and O-centered radical) and be followed by proton exchange to produce formate and methanol. A concerted step is also possible.

#### *Computational investigations*

DFT calculations were employed to investigate the second step of the reaction mechanism, the deformylation reaction. The optimized geometries as well as the free energies of structures A, B, and C (Figure 31) were evaluated using the BP86 functional in combination with def2-TZVP basis set and the ethanol solvent through the CPCM solvation model. A putative energy pathway was obtained with the highest energy structure being the initial one (structure A) and the lowest one was found to be the final product (structure C). In between these two, we find structure B as an intermediate of the reaction.

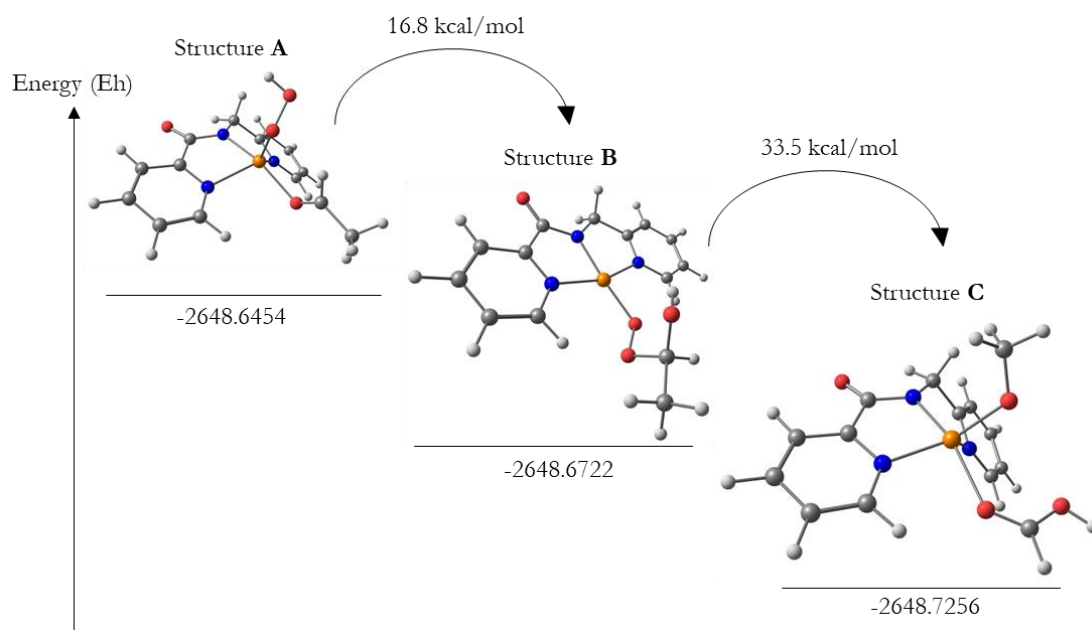


**Figure 31.** Free energies of structures A, B, and C, involved in the deformation reaction.

Based on the non-negligible free energy difference connecting structure B to structure C, we attempted to calculate a transition state using structure B as starting point (Figure 32). By scanning the appropriate reaction coordinate, the the O<sub>1</sub>-C<sub>2</sub> bond, from 3.65 to 1.40 Å, we obtained a high-energy structure for a distance of 1.72 Å that was further optimized leading to a single positive vibrational frequency consistent with a transition state. The latter specifically display a four-atom structure that will further evolve to a complex bearing a methoxy anion and formic acid as seen after the rebound mechanism proposed in Scheme 11, part B. However, based on the large free energy difference existing between the calculated transition state and structure C, another step will indeed be necessary and likely involve the formation of radical species due to O-O homolytic bond breaking. More efforts in elucidating the nature of copper-oxygen species involved in the formation of formate in ethanol are currently underway.

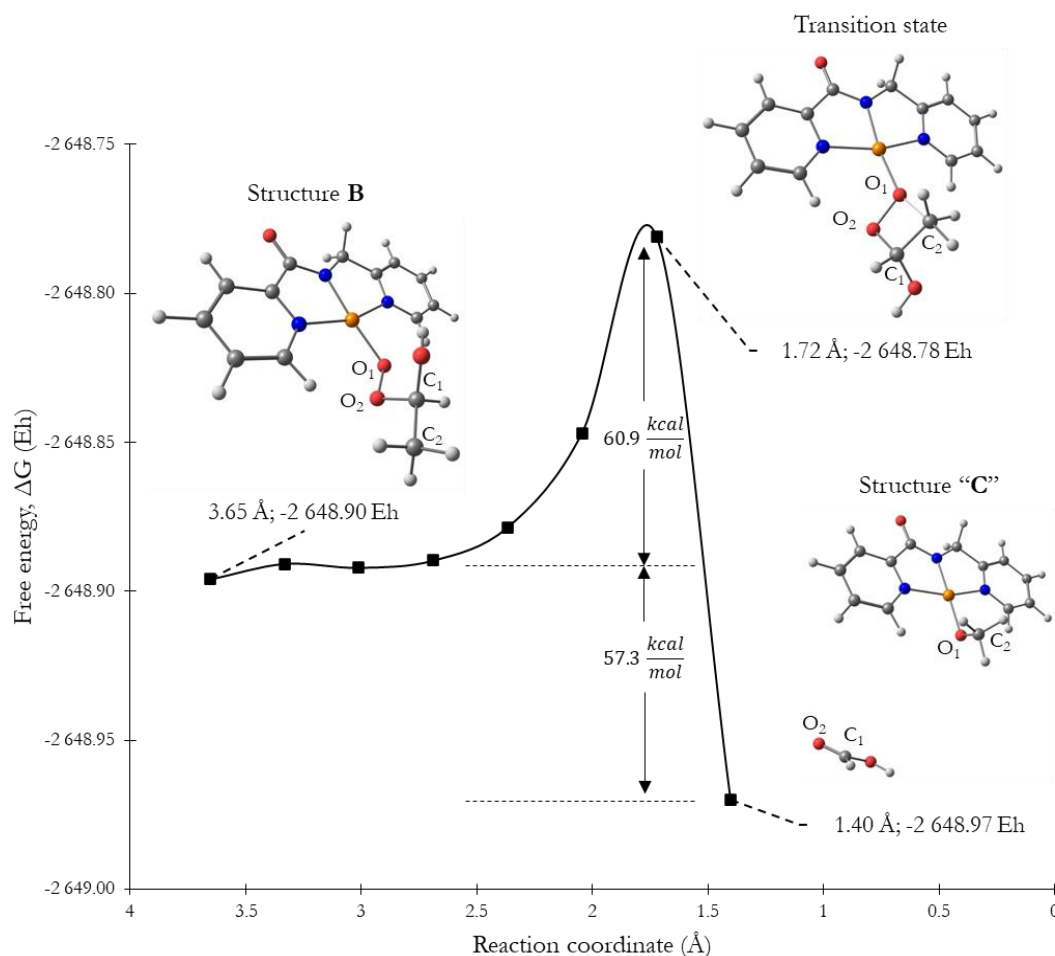


Figure 32. Calculated free energies with respect to the reaction coordinate obtained by scan through the O<sub>1</sub>-C<sub>2</sub> bond starting at 3.65 till 1.40 Å.

## 2.6 – Conclusion

Our initial hypothesis of CO<sub>2</sub> sequestration and reduction pathway was completely erroneous. However, the C-H activation of alcohol solvents is not trivial since the bond dissociation energies are quite high. Also, the KDIE suggests the involvement of metal-centered species in the H-abstraction step. We propose a mechanism implying the formation of a copper-oxyl intermediate responsible for H atom abstraction step. This reactivity supports that complex **1**, which can stabilize high-valent species and has an open reactive space, can perform highly oxidative reactions. This capability was thus further exploited with other substrates such as p-nitrophenyl- $\alpha$ -D-glucopyranoside, model-substrate for LPMO's reaction.

### 3 – Other reactivity of the [Cu(PMPA)(H<sub>2</sub>O)(NO<sub>3</sub>)] complex

Following the study of the reactivity of complex **1** in presence of base and hydrogen peroxide, we investigated the reaction in other conditions. To start, we simply moved away from alcohol solvents and studied the reaction in acetonitrile. We also subjected the reaction mixture to an LPMO model substrate in aqueous phase.

#### 3.1 – Reactivity in acetonitrile

The reaction of [Cu(PMPA)(H<sub>2</sub>O)(NO<sub>3</sub>)] (0.5 mM) in presence of 2 eq. of triethylamine and 20 eq. hydrogen peroxide was carried in acetonitrile at room temperature. The reaction mixture was left to evaporate to produce suitable crystals for XRD analysis (Figure 33). The high-resolution crystal diffraction at -140°K showed that complex **1** underwent modifications to produce a new complex: [Cu(POPA)(H<sub>2</sub>O)(NCO)] (**5**). Complex **5** is bound to the POPA ligand, *i.e.* the oxidation of the PMPA amide moiety to an imide also occurs in acetonitrile. In addition, a cyanate anion is found in the coordination sphere of the metal.

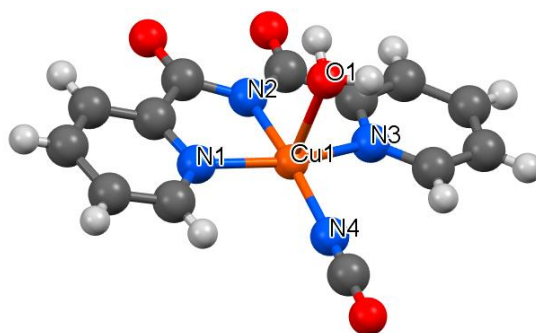
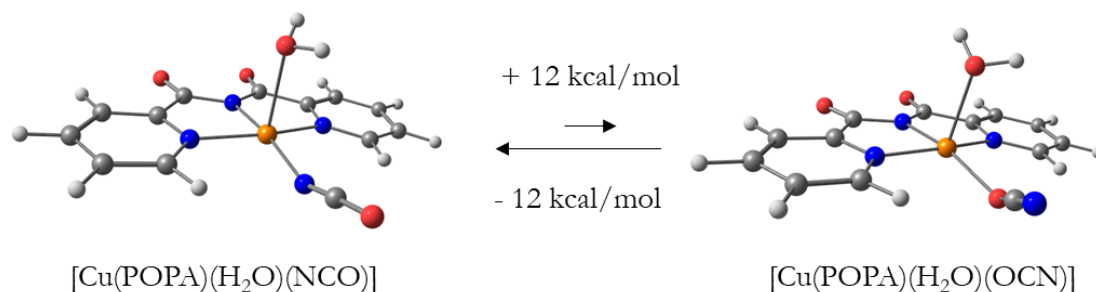


Figure 33. XRD structure of [Cu(POPA)(H<sub>2</sub>O)(NCO)], complex **5**, obtained by slow evaporation of the reaction mixture. Empirical formula: C<sub>13</sub>H<sub>10</sub>CuN<sub>4</sub>O<sub>4</sub>, Formula weight: 349.79, Temperature: 140°K.

Quantum refinement of the XRD data of complex **5** were performed with both N or O-bound cyanate and analysis of the residual densities suggested that the cyanate preferentially binds via the nitrogen atom. The binding mode of the cyanate ligand in complex **5** was also investigated by means of DFT calculations. The considered structures included a bound cyanate either through the O- or the N- atoms cyanate ligands and their geometries were optimized (BP86/def2-TZVP).



The computed free energies showed that the N-binding cyanate was more stable than the O-binding one by more than 12 kcal/mol (Figure 34), in agreement with XRD data.



**Figure 34.** Optimized structures of the N- and O- binding cyanate structures of complex 5.

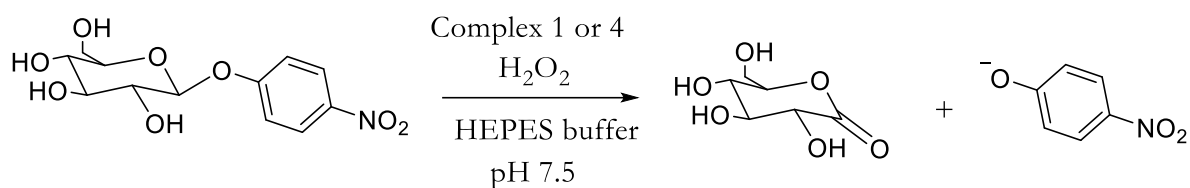
Cyanate probably arises from oxidation of acetonitrile. The BDE of the C-H bond of acetonitrile was therefore calculated. Geometry minimization and vibrational frequency calculations (B3LYP/def2-TZVP) were performed to obtain the free energies of the C-H and C<sup>•</sup> molecules. Absence of imaginary modes confirmed that true minima were obtained. The BDE was evaluated as the sum of the free energies of the radical form of the deprotonated molecule plus that of the radical proton subtracted from the free energy of the initial molecule.



The computed BDE was 95.1 kcal/mol which is greater than the ones obtained for methanol and for α-C-H bond of ethanol. This BDE result points towards the proposed metal-centered reaction via the formation of a copper-oxyl species responsible for the H-abstraction step.

### 3.2 – Reactivity with the model substrate: PNPG

The oxidation of p-nitrophenyl-α-D-glucopyranoside (PNPG) was used as a model for the activity of LPMO. [36] [37] The evolution of the reaction is easily monitored by following the characteristic absorption band of p-nitrophenol product at 415 nm (Scheme 12). The reaction is carried out in presence of hydrogen peroxide and a catalyst in aqueous medium. Here, complexes **1** and **4** were tested as catalysts.



**Scheme 12.** Reaction scheme of the oxidation of PNPG to the corresponding aldehyde and *p*-nitrophenolate in presence of complex and H<sub>2</sub>O<sub>2</sub> in HEPES buffer at pH 7.5. HEPES: (2-[4-(2-hydroxyethyl)piperazin-1-yl]ethanesulfonic acid)

The reaction was carried out either at pH 7.5 (HEPES buffer) or at pH 10.5 (carbonate buffer). The complex was placed at 50  $\mu$ M concentration in the presence of 10 mM of PNPG and 10 mM hydrogen peroxide. The amount of *p*-nitrophenol produced was obtained by UV-vis absorption measurements at 15 min and 24 hours of reaction (Figure 35).

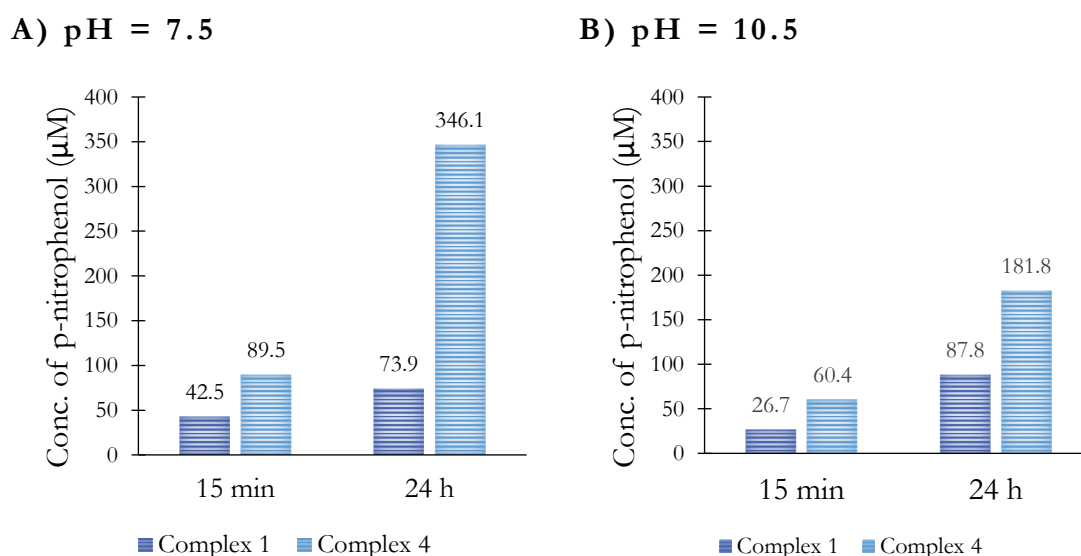


**Figure 35.** Concentration of *p*-nitrophenol obtained in buffers at A) pH = 7.5 and B) pH = 10.5, for complexes 1 (purple) and 4 (blue) after 15 min and 24 h.

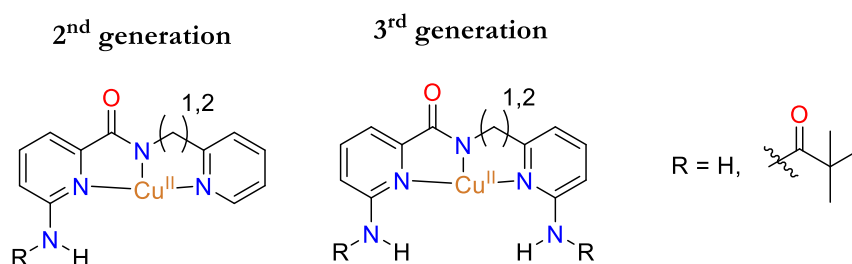
Complex **1**, with the non-oxidized PMPA ligand, produces less *p*-nitrophenol than the oxidized complex **4** in all tested conditions. In general, the yields are lower for both complexes at pH = 10.5 indicative that the structure of the complexes probably changes at high pH. Deprotonation of the bound water molecules may occur. Further work will soon be conducted to understand the origin of this pH effect. The difference between complex **1** and **4** is greater at longer reaction times

(24h). These results may be related to the instability of the  $[\text{Cu}(\text{PMPA})(\text{H}_2\text{O})(\text{NO}_3)]$  complex in presence of excess of hydrogen peroxide. Indeed, oxidation to imide as well as degradation of the ligand were observed when the complex was left to react with  $\text{H}_2\text{O}_2$  in the presence of a base. Therefore, the  $[\text{Cu}(\text{POPA})(\text{H}_2\text{O})(\text{NO}_3)]$  complex, which turned out to be unreactive towards methanol or ethanol, shows enhanced reactivity and stability for the oxidation of the saccharide model substrate, working as a potential model for the LPMO active site.

## 4 – Perspectives

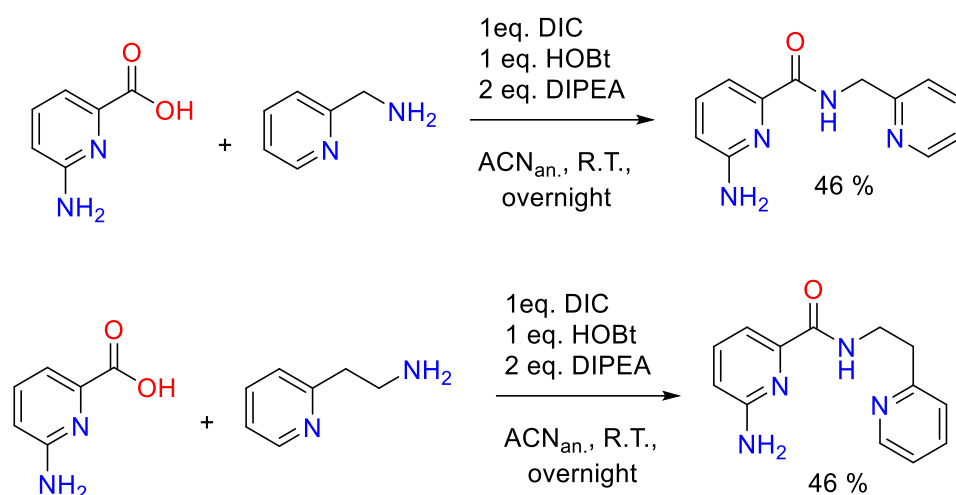
In this chapter, we have focused our studies on the reactivity of the 1<sup>st</sup> generation of ligand and complex  $[\text{Cu}(\text{PMPA})(\text{H}_2\text{O})(\text{NO}_3)]$ . This complex is bearing the  $n=1$  ligand of the alkyl chain while an in-depth study of the  $n=2$  counterpart, PEPA, remains to be conducted.

In addition, two more generations of ligands are envisioned in the future with the single or double decoration at the ortho-position (*o*-) of both the PMPA or PEPA ligands (Scheme 13).



Scheme 13. 2<sup>nd</sup>, and 3<sup>rd</sup> generation of ligands and complexes.

The synthesis of the 2<sup>nd</sup> generation PMPA and PEPA ligands with the *o*- $\text{NH}_2$  decoration, denoted  $\text{PMPA}(o\text{-NH}_2)$  and  $\text{PEPA}(o\text{-NH}_2)$  was performed by coupling the *o*- $\text{NH}_2$ -picolinic acid and 2-(aminomethyl)pyridine or 2-(2-aminoethyl)pyridine in anhydrous acetonitrile at room temperature overnight (Scheme 14). The acid was activated with  $N,N'$ -diisopropylcarbodiimide (DIC) and hydroxybenzotriazole (HOBT), in presence of diisopropylethylamine (DIPEA).



Scheme 14. Synthesis of ligands and complexes involving the PMPA(*o*-NH<sub>2</sub>) and the PEPA(*o*-NH<sub>2</sub>).

The complexation reactions were carried with either the copper nitrate or the copper perchlorate salts in methanol for three hours at room temperature. The addition of the ligands to the copper solution turned the reaction solution from light blue to green. After slow evaporation of the solutions, suitable crystals for XRD formed in the case of the PEPA(*o*-NH<sub>2</sub>) complex (Figure 36).

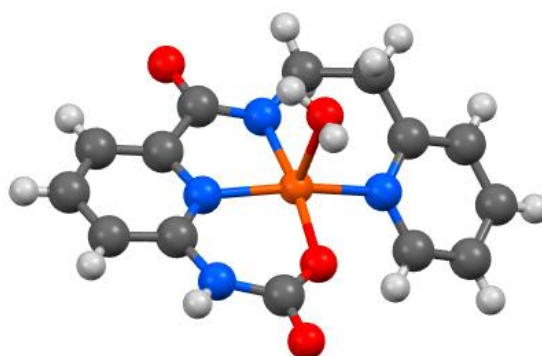
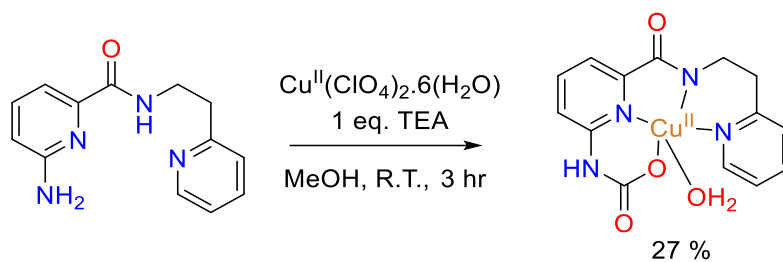


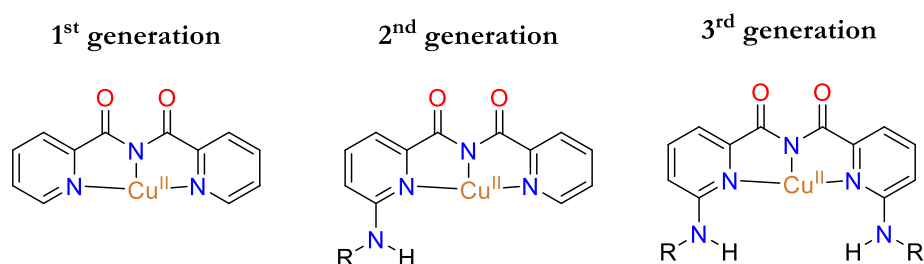
Figure 36. XRD structure of the [Cu(PEPA(*o*-carbamate))(H<sub>2</sub>O)] complex obtained by slow evaporation of the reaction mixture. Empirical formula: C<sub>14</sub>H<sub>18</sub>CuN<sub>4</sub>O<sub>6</sub>, Formula weight: 401.87, Temperature: 295°K.

Looking at the resulting crystal structure, we see that the primary amine of the ligand has been transformed into a carbamate moiety (Scheme 15). This carbamate is found coordinating the metal center. The origin of the carbamate (CO<sub>2</sub> capture?) is still unknown and further studies will be necessary. The primary amine of the ligand is reactive under these conditions and may need to be protected before complexation. The *o*-NH-CO-*t*Bu protective moiety is a good precursor to the coupling of the 2-(2-aminoethyl)pyridine before complexation.



**Scheme 15.** Reaction of ligand with copper perchlorate in methanol to form the carbamate ligand coordinating the metal center.

Our reactivity studies also pointed to the design of a new ligand based on the imide moiety of PMPA. This ligand was denoted POPA and gives rise to three new generations of ligands to synthesize and characterize (Scheme 16). This ligand is expected to be less electron donating than the PMPA family which may jeopardize the formation of high-oxidation states of copper. Additional decoration can be added on the para-position (*p*-) of the ligand to tune the electron withdrawing/donating effect of the ligand to the metal center.



**Scheme 16.** 1<sup>st</sup>, 2<sup>nd</sup>, and 3<sup>rd</sup> generations of ligands based on the POPA parent ligand and obtained by reactivity of PMPA with hydrogen peroxide.

In conclusion, the study of the PMPA ligand and complex is only the beginning. Its reactivity with solvents made it difficult to capture and to isolate the targeted copper-oxyl or copper-hydroxide species. However, other complexes envisioned within this family may provide more stability to these species by means of H-bonding and steric hindrance. In addition, the formation of the POPA ligand exhibited a weak point of the PMPA ligand at the benzylic position. Starting from the POPA ligand may indeed decrease the reactivity and improve the stability of the high-oxidation copper species.

## REFERENCES

- [1] V. G. H. Eijsink, D. Petrovic, Z. Forsberg, S. Mekasha, A. K. Rohr, B. Bissaro and G. Vaaje-Kolstad, "On the functional characterization of lytic polysaccharide monooxygenases (LPMOs)," *Biotechnology for Biofuels*, vol. 12, no. 58, 2019.
- [2] G. R. Hemsworth, E. M. Johnston, G. J. Davies and P. H. Walton, "Lytic polysaccharide monooxygenases in biomass conversion," *Trends Biotechnology*, vol. 33, pp. 747-761, 2015.
- [3] G. Vaaje-Kolstad, B. Westereng, S. J. Horn, Z. Liu, H. Zhai, M. Sorlie and V. G. H. Eijsink, "An oxidative enzyme boosting the enzymatic conversion of recalcitrant polysaccharides," *Science*, vol. 330, pp. 219-222, 2010.
- [4] T. Isaksen, B. Westereng, F. L. Aachman, J. W. Agger, D. Kracher, R. Kittl, R. Ludwig, H. Dietmar, V. G. H. Eijsink and S. J. Horn, "A C4-oxidizing lytic polysaccharide monooxygenase cleaving both cellulose and cello-oligosaccharides," *Journal of Biological Chemistry*, vol. 289, no. 5, pp. 2632-2642, 2014.
- [5] B. Westereng, J. W. Agger, S. J. Horn, G. Vaaje-Kolstad, F. L. Aachmann, Y. H. Stenstrom and V. G. H. Eijsink, "Efficient separation of oxidized cello-oligosaccharides generated by cellulose degrading lytic polysaccharide monooxygenases," *Journal of Chromatography A*, vol. 1271, pp. 144-152, 2013.
- [6] Z. Forsberg, A. K. Mackenzie, M. Sorlie, A. K. Rohr, R. Helland, A. S. Arvai, G. Vaaje-Kolstad and V. G. H. Eijsink, "Structural and functional characterization of a conserved pair of bacterial cellulose-oxidising lytic polysaccharide monooxygenases," *Proceedings of the National Academy of Sciences*, vol. 111, no. 23, pp. 8446-8451, 2014.
- [7] B. Bissaro, A. K. Rohr, G. Muller, P. Chylenski, M. Skaugen, Z. Forsberg, S. J. Horn, G. Vaaje-Kolstad and V. G. H. Eijsink, "Oxidative cleavage of polysaccharides by monocopper enzymes depends on H<sub>2</sub>O<sub>2</sub>," *Nature Chemical Biology*, vol. 13, pp. 1123-1130, 2017.
- [8] L. Bertini, R. Breglia, M. Lambrugh, P. Fantucci, L. De Gioia, M. Borsari, M. Sola, C. A. Bortolotti and M. Bruschi, "Catalytic mechanism of fungal lytic polysaccharide monooxygenases investigated by first-principles calculations," *Inorganic Chemistry*, vol. 57, pp. 86-97, 2018.

- [9] A. J. Simaan, A. L. Concia, A. Munzone, M.-C. Kafentzi, A. Kochem, M. Réglie and C. Decroos, "Modeling the Mononuclear Copper Monooxygenase Active Site," in *Bioinspired Chemistry*, Marseille, World Scientific, 2019, pp. 185-263.
- [10] S. Kim, J. Stahlberg, M. Sandgren, R. S. Paton and G. T. Beckham, "Quantum mechanical calculations suggest that lytic polysaccharide monooxygenase use a coper-oxy, oxygen-rebound mechanism," *Proceedings of the National Academy of Sciences of the United States of America*, vol. 111, no. 1, pp. 149-154, 2014.
- [11] S. Kim, C. Saracini, M. A. Siegler, N. Drichko and K. D. Karlin, "Coordination chemistry and reactivity of a cupric-hydroperoxide species featuring a proximal H-bonding substituent," *Inorganic Chemistry*, vol. 51, no. 23, pp. 12603-12605, 2012.
- [12] A. Kunishita, M. Kubo, H. Ishimaru, T. Ogura, H. Sugimoto and S. Itoh, "H<sub>2</sub>O<sub>2</sub>-reactivity of copper(II) complexes supported by tri[(pyridin-2-yl)methyl]amine ligands with 6-phenyl substituents," *Inorganic Chemistry*, vol. 47, pp. 12032-12039, 2008.
- [13] T. Fujii, A. Naito, S. Yamaguchi, A. Wada, Y. Funahashi, K. Jitsukawa, S. Nagatomo, T. Kitagaza and H. Masuda, "Construction of a square-planar hydroperoxo-copper(II) complex inducing a higher catalytic reactivity," *Chemical Communications*, no. 21, pp. 2700-2701, 2003.
- [14] C. E. Elwell, N. L. Gagnon, B. D. Neisen, D. Dhar, A. D. Spaeth, G. M. Yee and W. B. Tolman, "Copper-oxygen complexes revisited: structures, spectroscopy, and reactivity," *Chemical Reviews*, vol. 117, no. 3, pp. 2059-2107, 2017.
- [15] P. J. Donoghue, J. Tehranchi, C. J. Cramer, R. Sarangi, E. I. Solomon and W. B. Tolman, "Rapid C-H activation by a monocopper(III)-hydroxide complex," *Journal of the American Chemical Society*, vol. 133, pp. 17602-17605, 2011.
- [16] C.-Y. Wu and C.-C. Su, "Electronic and bonding properties of mixed-ligand copper(II) complexes of N-(2-picolyl)picolinamide (pmpa). X-raycrystal structures of [Cu(pmpa)(4-methylimidazole)(H<sub>2</sub>O)](H<sub>2</sub>O)(ClO<sub>4</sub>) and [Cu(pmpa)(4-methylpyridine)(H<sub>2</sub>O)](H<sub>2</sub>O)(ClO<sub>4</sub>)," *Polyhedron*, vol. 16, no. 3, pp. 383-392, 1997.
- [17] C.-Y. Wu and C.-C. Su, "Electronic and bonding properties of mixed-ligand copper(II) complexes of N-(2-pyridylethyl)polinamide (pepa). Molecular structures of [Cu(pepa)(3-

methyl-pyridine)(H<sub>2</sub>O)](ClO<sub>4</sub>), [Cu(pepa)(4-methylpyridine)(H<sub>2</sub>O)](ClO<sub>4</sub>) and [Cu(pepa)(4-methylimidazole)(H<sub>2</sub>O)]," *Polyhedron*, vol. 16, no. 14, pp. 2465-2474, 1997.

- [18] F. Neese, F. Wennmohs, U. Becker and C. Riplinger, "The ORCA quantum chemistry program package," *Journal of Chemical Physics*, vol. 152, no. 22, 2020.
- [19] C. Adamo and V. Barone, "Toward reliable density functional methods without adjustable parameters: The PBE0 model," *Journal of Chemical Physics*, vol. 110, no. 13, pp. 6158-6170, 1999.
- [20] F. Weigend and R. Ahlrichs, "Balanced basis sets of split valence, triple zeta valence and quadruple zeta valence quality for H to Rn: Design and assessment of accuracy," *Physical Chemistry Chemical Physics*, vol. 7, no. 18, pp. 3297-3305, 2005.
- [21] F. Weigand, "Accurate Coulomb-fitting basis sets for H to Rn," *Physical Chemistry Chemical Physics*, vol. 8, no. 9, pp. 1057-1065, 2006.
- [22] A. D. Becke, "Density-functional thermochemistry .3. The role of exact exchange," *Journal of Chemical Physics*, vol. 98, no. 7, pp. 5648-5652, 1993.
- [23] J. P. Perdew and Y. Wang, "Accurate and simple analytic representation of the electron-gas correlation-energy," *Physical Review B*, vol. 45, no. 23, pp. 13244-13249, 1992.
- [24] F. Weigend and R. Ahlrichs, "Balanced basis sets of split valence, triple zeta valence and quadruple zeta valence quality for H to Rn: Design and assessment of accuracy," *Physical Chemistry Chemical Physics*, vol. 7, no. 18, pp. 3297-3305, 2005.
- [25] L. Yan, Y. Lu and X. Li, "A density functional theory protocol for the calculation of redox potentials of copper complexes," *Physical Chemistry Chemical Physics*, vol. 7, no. 18, pp. 5529-5536, 2015.
- [26] J. Huot, F. Cuevas, S. Deledda, K. Edalati, Y. Filinchuk, T. Grosdidier, B. C. Hauback, M. Heere, T. Jensen, M. Latroche and S. Sartori, "Mechanochemistry of metal hydride: Recent advances," *Materials*, vol. 12, no. 17, p. 2778, 2019.
- [27] C. Weidenthaler, "Crystal structure evolution of complex metal aluminum hydrides upon hydrogen release," *Journal of Energy Chemistry*, vol. 42, pp. 133-143, 2020.



- [28] X.-P. Lee, T. Kumazawa, K. Kondo, K. Sato and O. Suzuki, "Analysis of methanol or formic acid in body fluids by headspace solid-phase microextraction and capillary gas chromatography," *Journal of Chromatography B*, vol. 734, pp. 155-162, 1999.
- [29] C. Abolin, J. D. McRae, T. N. Tozer and S. Takki, "Gas chromatographic head-space assay of formic acid as methyl formate in biologic fluids: potential application to methanol poisoning," *Biochemical Medicine*, vol. 23, pp. 209-218, 1980.
- [30] A. R. Sokoro, D. Lehotay and J. Eichhorst, "Quantitative endogenous formate analysis in plasma using headspace gas chromatography without a headspace analyzer," *Journal of Analytical Toxicology*, vol. 31, pp. 342-346, 2007.
- [31] O. Yishai, S. N. Lindner, J. Gonzalez de la Cruz, H. Tenenboim and A. Bar-Even, "The formate bio-economy," *Current Opinion in Chemical Biology*, vol. 35, pp. 1-9, 2016.
- [32] K. B. Wiberg, "The Deuterium Isotope Effect," *Chemical Reviews*, vol. 55, no. 4, pp. 713-743, 1955.
- [33] M. Bonifacic, D. A. Armstrong, I. Stefanic and K.-D. Asmus, "Kinetic isotope effect for hydrogen abstraction by  $^{\bullet}\text{OH}$  radicals from normal and carbon-deuterated ethyl alcohol and methylamine in aqueous solutions," *Journal of Physical Chemistry B*, vol. 107, no. 30, pp. 7268-7276, 2003.
- [34] R. Gonzalez-Olmos, F. Holzer, F.-D. Kopinke and A. Georgi, "Indications of the reactive species in a heterogeneous Fenton-like reaction using Fe-containing zeolites," *Applied Catalysis A: General*, vol. 398, no. 1-2, pp. 44-53, 2011.
- [35] B. Kim, D. Jeong, T. Ohta and J. Cho, "Nucleophilic reactivity of a copper(II)-hydroperoxo complex," *Communications Chemistry*, vol. 2, no. 81, pp. 1-6, 2019.
- [36] A. L. Concia, M. R. Beccia, M. Orio, F. Terra Ferre, M. Scarpellini, F. Biaso, B. Guigliarelli, M. Réglér and A. J. Simaan, "Copper complexes as bioinspired models for lytic polysaccharide monooxygenases," *Inorganic Chemistry*, vol. 56, no. 3, pp. 1023-1026, 2017.
- [37] T. P. Binder and J. F. Robyt, "p-nitrophenyl  $\alpha$ -D-glucopyranoside, a new substrate for glucanases," *Carbohydrate Research*, vol. 124, no. 2, pp. 287-299, 1983.

- [38] F. Neese, "Efficient and accurate approximations to the molecular spin-orbit coupling operator and their use in molecular g-tensor calculations," *Journal of Chemical Physics*, vol. 122, no. 3, p. 034107, 2005.
- [39] B. A. Hess, C. M. Marian, U. Wahlgren and O. Gropen, "A mean-field spin-orbit method applicable to correlated wavefunctions," *Chemical Physics Letters*, vol. 251, no. 5-6, pp. 365-371, 1996.
- [40] E. van Lenthe, E. J. Baerends and J. G. Snijders, "Relativistic regular 2-component hamiltonians," *Journal of Chemical Physics*, vol. 99, no. 6, pp. 4597-4610, 1993.
- [41] E. van Lenthe, E. J. Baerends and J. G. Snijders, "Relativistic total-energy using regular approximations," *Journal of Chemical Physics*, vol. 101, no. 11, pp. 9783-9792, 1994.
- [42] E. van Lenthe, J. G. Snijders and E. J. Baerends, "The zero-order regular approximation for relativistic effects: The effect of spin-orbit coupling in closed shell molecules," *Journal of Chemical Physics*, vol. 105, no. 15, pp. 6505-6516, 1996.
- [43] R. J. Gómez-Piñeiro, D. A. Pantazis and M. Orio, "Comparison of density functional and correlated wave function methods for the prediction of Cu(II) hyperfine coupling constants," *Chem. Phys. Chem.*, vol. 21, no. 24, pp. 2667-2679, 2020.
- [44] E. D. Hedegard, J. Kongsted and S. P. A. Sauer, "Optimized basis sets for calculation of electron paramagnetic resonance hyperfine coupling constants: aug-cc-pVTZ-J for the 3d atoms Sc-Zn," *Journal of Chemical Theory and Computation*, vol. 7, no. 12, pp. 4077-4087, 2011.
- [45] E. D. Hedegard, J. Kongsted and S. P. A. Sauer, "Improving the calculation of electron paramagnetic resonance hyperfine coupling tensors for d-block metals," *Physical Chemistry Chemical Physics*, vol. 14, no. 30, pp. 10669-10676, 2012.
- [46] A. Kunishita, M. Kubo, H. Sugimoto, T. Ogura, K. Sato, T. Takui and S. Itoh, "Mononuclear copper(II)-superoxo complexes that mimic the structure and reactivity of the active center of PHM and DBM," *Journal of the American Chemical Society*, vol. 131, pp. 2788-2789, 2009.
- [47] A. Kunishita, M. Z. Ertm, Y. Okubo, T. Tano, S. Hideki, K. Ohkubo, N. Fujieda, S. Fukuzumi, C. J. Cramer and S. Itoh, "Active site models for the CuA site of peptidylglycine  $\alpha$ -hydroxylating monooxygenase and dopamine- $\beta$ -monooxygenase," *Inorganic Chemistry*, vol. 51, pp. 9465-9480, 2012.

- [48] R. L. Peterson, R. A. Himes, H. Kotani, T. Suenobu, L. Tian, M. A. Siegler, E. I. Solomon, S. Fukuzumi and K. D. Karlin, "Cupric superoxo-mediated intermolecular C-H activation chemistry," *Journal of the American Chemical Society*, vol. 133, pp. 1702-1705, 2011.
- [49] S. Kim, J. Y. Lee, R. E. Cowley, J. W. Ginsbach, M. A. Siegler, E. I. Solomon and K. D. Karlin, "A N3S(thioether)-ligated Cu(II)-superoxo which enhances reactivity," *Journal of the American Chemical Society*, vol. 137, no. 8, pp. 2796-2799, 2015.
- [50] K. Nakatomo, Infrared and Raman spectra of inorganic and coordination compounds. Part B., Hoboken: Wiley, 2009.
- [51] F. Neese, F. Wennmohs, U. Becker and C. Riplinger, "The ORCA quantum chemistry program package," *Journal of Chemical Physics*, vol. 152, no. 22, 2020.
- [52] A. D. Becke, "Density-functional exchange-energy approximation with correct asymptotic-behavior," *Physical Review A*, vol. 38, no. 6, pp. 3098-3100, 1988.
- [53] J. P. Perdew, "Density-functional approximation for the correlation-energy of the inhomogeneous electron-gas," *Physical Review B*, vol. 33, no. 12, pp. 8822-8824, 1986.



---

## CLOSING COMMENTS AND GENERAL PERSPECTIVES

---



## CLOSING COMMENTS AND GENERAL PERSPECTIVES

In this Ph.D. thesis manuscript, we have covered both theoretical and experimental analysis of mononuclear copper metal centers. The different axes of my research project led to multiple conclusions and developments to build for future work. In the Closing Comments and General Perspectives, I summarize the individual conclusions as well as the perspectives for the project.

In Chapter II, we conducted theoretical investigations for the prediction of magnetic properties in mononuclear copper centers with a focus on EPR parameters. We used a large set of mononuclear copper complexes, for which structural and magnetic data were reported in the literature, to benchmark our methods. First, we studied the influence of the basis sets in the prediction of hyperfine coupling constants. We defined a computationally optimal basis set for Cu, with decontracted  $s$  functions, that can be used with the quantum chemical methods tested in the study. We evaluated the prediction of the hyperfine couplings constants using density functional theory (DFT) as well as wave function methods. We found that the hybrid functional B3PW91 performs best but other functionals (TPSSH, B3LYP, and PBE0) also provide reliable results, albeit to a lesser extent. Wave function based methods did not deliver reliable hyperfine coupling constants but among these methods, DLPNO-CCSD provided the best results. It does not compete however with hybrid nor hybrid meta-GGA functionals. Second, we investigated the prediction of  $g$ -tensor values. In general, hybrid functionals provide accurate  $g$ -tensors despite having an evident deficiency in the calculation of the  $g_z$  values (that are often lower than experimental values). This has been previously reported in literature and was suggested to be related either to an underestimated metal-ligand covalency or to overestimated energy gaps between the singly occupied molecular orbital (SOMO) to the lower metal-based orbitals. Preliminary results suggest that increasing the Hartree-Fock admixture using a hybrid functional leads to an increase of the  $g$ -tensor values, addressing the observed deficiency, mainly by influencing the covalency of the system as opposed to the poor evaluation of the energy gaps. However, this manipulation is not without repercussions since the hyperfine coupling values are negatively affected. The  $g$ -tensor evaluation will be further addressed in the future by studying its decomposition and the precise origin of the observed effect.

In Chapter III, we applied our theoretical methodologies and investigated two systems to elucidate and rationalize experimental observations, mainly in terms of their magnetic properties extracted by EPR. In the first part, we addressed the possible structures co-existing in one mononuclear copper-containing LPMO enzyme. Indeed, the enzyme *p*/AA10, studied in the group, exhibits two distinct EPR signals in solution, one of rhombic character and another one being axial. We built multiple models of the LPMO active site with different modulations and modifications around the copper center. Notably we investigated the effect of (i) the number of coordinated exogenous ligands (one or two) (ii) the deprotonation of one or two coordinated water molecules (iii) the presence of chloride ions in the coordination sphere of the metal and (iv) decoordination or change of geometry of the protein ligands. The EPR parameters were computed for all the models and compared to experimental results. We observed that the rhombic character was indeed predicted for the original coordination sphere of LPMO active site (3N from the protein and two water molecules in the coordination sphere). Similar rhombic species were obtained upon decoordination of a water molecule, decoordination of the primary amine of the histidine brace, or distortion of the imidazole rings. However, an axial EPR character was obtained by deprotonation of one water molecule, forming a hydroxyl ligand coordinating the copper center. We therefore postulate that the formation of this species is responsible for the minor species observed in experimental conditions. The origin of this deprotonation remains unclear and will be investigated using greater models. In the second part, we investigated an LPMO-inspired tripeptidic system (Histidine-Proline-Histidine) denoted HPH-Cu. Multiple model structures were constructed with different coordination motifs around the copper including the coordination or non-coordination of the imidazole ring of the second histidine of the HPH ligand. Free energies as well as spectroscopic parameters, mainly EPR but also UV-vis, were computed and compared to experimental results. Our studies suggest that the coordination of the imidazole ring of the HPH ligand is not present at pH 5.0 but is highly probable at pH 7.5 suggesting that HPH-Cu is a good structural model for the histidine-brace ligation in LPMO active-center (at pH 7.5).

These two examples illustrate the fact that the use of DFT studies in correlation to experimental observations is a relevant approach for the study of bioinorganic systems. These examples also suggest that the magnetic properties calculations developed in Chapter II are rather well converged and can be used to elucidate and rationalize experimental conundrums.

In Chapter IV, we investigated the a LPMO model complex,  $[\text{Cu}(\text{PMPA})(\text{H}_2\text{O})(\text{NO}_3)]$ , and its reactivity in the presence of hydrogen peroxide. When exposed to hydrogen peroxide in methanol



or ethanol solvent, the complex was found to easily produce formate. A crystal structure of the reaction mixture was obtained, and three modifications were observed: oxidation of the PMPA ligand, coordination of a hydroxyl group, and coordination of a formate anion. This formally produced a putative stable Cu(III) species. However, high-resolution X-ray diffraction, EPR and SQUID measurements, as well as DFT calculations, all pointed towards a +II oxidation state of the copper possibly stabilized by the presence of  $H^+$ . In solution, we postulate that the hydroxyl group is in fact a water ligand. We then demonstrated that formate is coming from oxidation of the alcohol solvent (methanol or ethanol), and other oxidation products were also detected such as the aldehydes (formaldehyde and ethanal). Kinetic isotope effect studies suggest that rate-determining step involves C-H abstraction performed by metal-centered active species. Additionally, when using the oxidized ligand in the reaction, no formate was obtained. With this information, we envisioned a two-step process for the oxidation of ethanol to produce formic acid undergoing strong C-H activation and C-C bond cleavage: 1) the oxidation of ethanol to ethanal, and 2) an ethanal deformylation reaction. Preliminary theoretical calculations were performed using DFT methods to rationalize the latter deformylation step considering a concerted mechanism option. However, a very high activation energy is predicted indicating that a stepwise mechanism is more probable. These mechanistic studies are still on-going for the deformylation step as well as the oxidation of ethanol to ethanal. The reactivity was also tested in acetonitrile which yielded a cyanate ligand, as well as the oxidation of the PMPA ligand. More studies are necessary to elucidate the formation of the cyanate ligand but a simple look at the bond dissociation energies of the tested solvents suggest that  $[Cu(PMPA)(H_2O)(NO_3)]$  complex possesses the oxidative potential to produce cyanate upon oxidation of acetonitrile. More interestingly, this complex and the oxidized counterpart,  $[Cu(POPA)(H_2O)(NO_3)]$ , were tested in the oxidation of an LPMO model substrate, *p*-nitrophenol-glucose in aqueous solutions and in the presence of hydrogen peroxide. Even though both were found capable to produce *p*-nitrophenol, the ligand-oxidized  $[Cu(POPA)(H_2O)(NO_3)]$  complex led to higher oxidation yields and higher stability after 24h of reaction. This efficiency is probably coming from the stabilization of the ligand evidenced in the imide moiety as opposed to having the amide alone. Further studies are underway for the synthesis of decorated POPA ligands with multiple electron-donating/withdrawing groups to modulate the electronic properties of the metal center as well as H-bond donating substituents for stabilizing high-valent copper-oxygen species.



---

# MATERIALS AND METHODS

---



## MATERIALS AND METHODS

In this chapter, the reader will find the Materials and Methods of the Ph.D. thesis. The Materials and Methods are divided by chapter and takes into account two of the main chapters of the thesis: Chapter III. Prediction of EPR Parameters for the LPMO Active Site and a Synthetic LPMO-Like Peptide, and Chapter IV. Synthesis, Characterization, and Reactivity Study of N-(pyridine-2-ylmethyl)picolinamide, PMPA, Copper(II) complex and Its Derivatives.

### 1 – Chapter III. Prediction of EPR parameters of the LPMO active site and an LPMO-like tripeptidic complex using model systems

All structures presented in sets A, B and C of the HPH-peptide were investigated using DFT methods and geometry optimizations were performed with the ORCA program package. [1] These optimizations were carried with the PBE0 functional [6] and the def2-TZVP basis sets, [4] in combination with corresponding auxiliary basis sets. [5] Increased integration grids were employed (Grid4 in ORCA nomenclature), tight energy and slow convergence settings were applied in combination with the Direct Inversion in the Iterative Subspace (DIIS) algorithm (DIISmaxequation 10 in ORCA nomenclature). These optimizations were carried in the solvent phase by using the CPCM model and water as a solvent. Vibrational frequencies were computed for all optimized structures and the absence of imaginary modes confirmed that local minima on the potential energy surfaces were obtained.

The DFT method used in the calculation of EPR parameters is done with the B3PW91 functional. [7] [8] Computation of hyperfine coupling constants used increased general integration grids (Grid6 in ORCA convention), further increased radial integration accuracy (IntAcc 6.0) and specially enhanced grids for the metal center (SpecialGridIntAcc 11). For all ligand atoms, the def2-TZVP basis sets [4] were used. In the case of Cu, a home-made basis set, named aug-cc-pVTZ-Jmod, was used and consists of a modified version of aug-cc-pVTZ-J [9] [10] with decontracted *s* functions and removal of innermost *s* primitives. It was found to be a robust, flexible, and generally applicable basis set for the prediction of hyperfine coupling constants [11] and g-factors. No approximations to two-electron integrals were used when calculating hyperfine coupling constants to exclude any possible error related to density fitting approximations. Spin-orbit contributions were included through mean-field and effective potential approaches. The spin-orbit coupling operator was treated by an accurate mean-field (SOMF) approximation to the

Breit–Pauli operator (SOCType 3 in ORCA). [12] [13] The potential was constructed to include one-electron terms, compute the Coulomb term in a semi-numeric way, incorporate exchange via one-center exact integrals including the spin-other orbit interaction, and include local DFT correlation (SOCFlags 1,2,3,1 in ORCA). Scalar relativistic calculations were performed with the zeroth-order regular approximation (ZORA) [14] [15] [16] Hamiltonians. Picture change effects were applied as appropriate. The effect of considering the solvent via a continuum solvation model was investigated using the CPCM. [17]

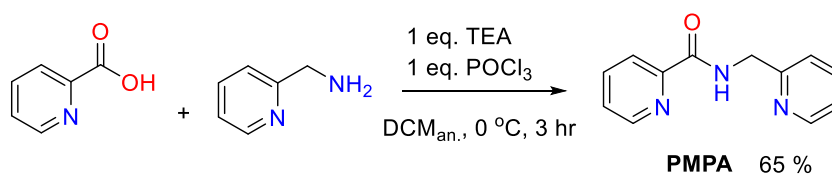
The functional used in the calculation of UV-vis spectrum is the PBE0 [6] functional. For all atoms, the def2-TZVP basis sets [4] were used. The TD-DFT methodology computed the first 50 excited states, with the corresponding maximum dimension of the expansion space in the Davidson procedure at 300 (nroots 50 and maxdim 300 in ORCA). Triplet excitation states were set to true to determine these energies in addition to the singlets. The effect of considering the solvent via a continuum solvation model was investigated using the CPCM. [17] To plot the UV-visible spectra, the orca\_mapscp program is used. The plots were built from 200 to 800 nm in wavelength, with a  $3750\text{ cm}^{-1}$  width at half height and 2000 points.

Geometry optimizations for the HMePH structures were performed with ORCA. [1] The optimizations were carried with the PBE0 [6] functional and the def2-TZVP basis sets, [4] in combination with corresponding auxiliary basis sets. [5] Increased integration grids were employed (Grid4 in ORCA nomenclature), tight energy and slow convergence settings were applied in combination with the Direct Inversion in the Iterative Subspace (DIIS) algorithm (DIISmaxequation 10 in ORCA nomenclature). These optimizations were carried in the solvent phase by using a continuum solvation model. The Natural Population Analysis [18] was used for population analysis (NPA in ORCA). In addition, unrestricted HF natural orbitals, UNO, were computed using the orca\_plot program in ORCA. Vibrational frequencies were computed for all optimized structures and the absence of imaginary modes confirmed that true minima were obtained.

## 2 – Chapter IV. Bioinspired mononuclear copper complexes: synthesis, characterization, and reactivity

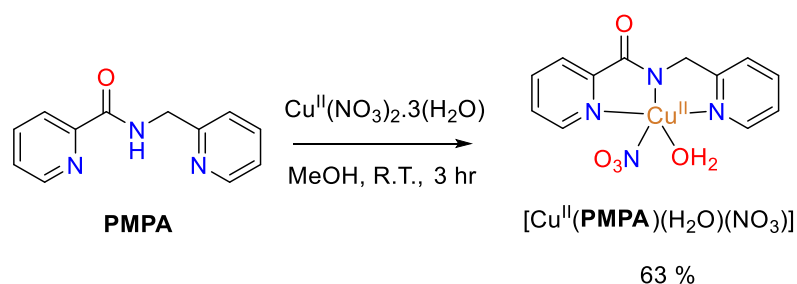
For the synthesis of ligands and complexes, the starting materials are all commercially available, as well as the solvents used.  $^1\text{H}$  and  $^{13}\text{C}$  NMR spectra were recorded in solution on a BRUKER Avance III nanobay at 300 MHz. ESI-MS was performed in a SYNAPTH G2 HDMS (Waters) equipment. Infrared experiments were performed using a Bruker Tensor 27 instrument on powder samples. X-ray diffraction (XRD) techniques used a SuperNova (Dual source), Rigaku Oxford Diffraction, diffractometer. The acquired crystallographic data for new complexes is gathered into one crystallographic data table. The UV-vis spectra were obtained using a Varian CARY 60 spectrophotometer and a 1-cm pathlength quartz cuvette or using a Hellma optical fiber probe (0.5-cm pathlength). The EPR spectra were recorded in standard X-band, continuous-wave (cw) EPR on frozen solutions using an ELEXSYS Bruker instrument equipped with a BVT 3000 digital temperature controller. Typical parameters were temperature at 120 °K, microwave power: 10-20 mW, modulation frequency 100 kHz and modulation 1-3 G. Spectra simulations were performed using Matlab program package Easyspin. Cyclic voltammetry measurements were performed using a Biologic SP-150 potentiostat controlled with the EC-Lab software version 10.10. The experiments were conducted using a three-electrode configuration cell, with a glassy carbon electrode as a working electrode, a platinum wire as auxiliary electrode, and an Ag/AgCl electrode as reference. The GC equipment is an FID Shimadzu GC-14A equipped with a C-R5A chromatopak. The column installed is a Supelco Analytical fused silica capillary column (60 m x 0.2 mm x 0.5  $\mu\text{m}$  film thickness). The GC oven temperature was set at 80 °C. The GC was in splitless mode, and the time of acquisition varied from 5 to 10 minutes. The GC-MS equipment is Shimadzu GC-2010 plus coupled with the Shimadzu GCMS-AP2010SE. The column installed is a Zebron phase ZB-5MS (60 °C, 60 m x 0.25 mm x 0.25  $\mu\text{m}$  film thickness).  $\text{H}_2$  was used as the carrier gas.

### 1. Synthesis of the PMPA ligand



To an anhydrous dichloromethane solution (9 mL) of picolinic acid (375 mg, 3.1 mmol), triethylamine (3.1 mmol, 308 mg), and 2-(aminomethyl)pyridine (3.1 mmol, 329 mg) in an ice bath, phosphorous oxychloride (3.1 mmol, 467 mg) in dichloromethane (3 mL) was added dropwise with constant stirring. After a couple of minutes, an additional amount of triethylamine (6.1 mmol, 616 mg) was added. After 3 h, the reaction medium was neutralized with aqueous potassium bicarbonate. The organic layer was extracted and dried over MgSO<sub>4</sub>. The solvent was evaporated yielding a viscous yellow residue (420 mg, 65%). <sup>1</sup>H NMR (MeOD; 300 MHz) δ in ppm: 4.74 (s, 2H), 7.30 (t, 1H), 7.43 (d, 1H), 7.56 (t, 1H), 7.80 (t, 1H), 7.96 (t, 1H), 8.13 (d, 1H), 8.51 (d, 1H), 8.66 (d, 1H). <sup>13</sup>C NMR (MeOD; 300 MHz) δ in ppm: 15.57, 45.57, 123.04, 123.34, 123.94, 127.99, 138.90, 138.95, 150.1, 151.07, 159.07, 167.12.

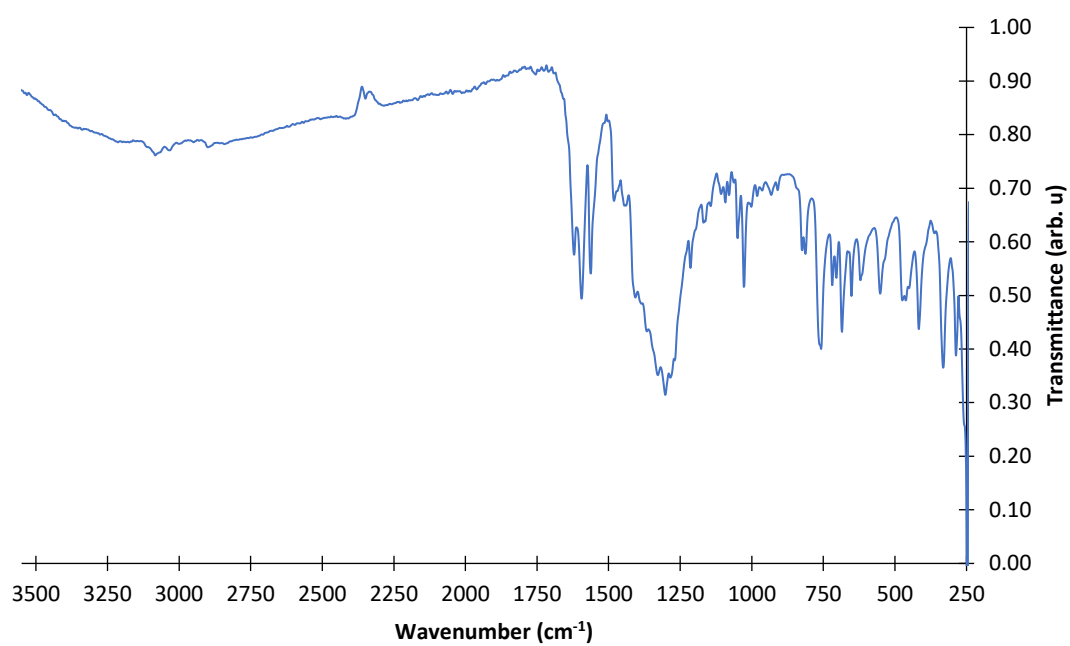
## 2. Synthesis of complex **1**, [Cu(PMPA)(H<sub>2</sub>O)(NO<sub>3</sub>)]



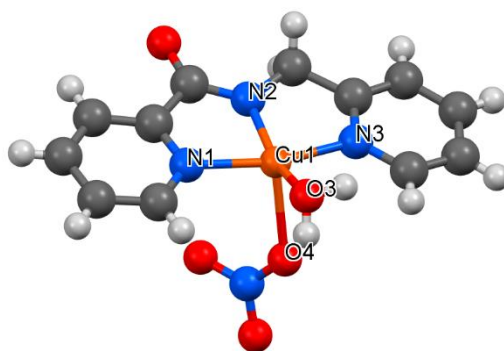
Complex **1** was prepared by mixing a solution of PMPA ligand (0.5 mmol, 107 mg) in methanol (3 mL) to a copper nitrate trihydrate (0.5 mmol, 119 mg) solution in methanol (4 mL) with constant stirring at room temperature. The reaction was left running for 3 hours. The initial light blue solution turned dark blue and precipitated. The powder was recovered by filtration. It was then resolubilized in methanol and suitable crystals for XRD were obtained by slow evaporation (55 mg, 0.15 mmol, 63%). IR: amide 1600, 1620 cm<sup>-1</sup>. λ/nm (ε /M<sup>-1</sup>.cm<sup>-1</sup>) : 295 (3790) 625 (110). ESI-MS in acetonitrile (1.2 mM NaF): 275 corresponding to [Cu(PMPA)]<sup>+</sup>. EPR (MeOH): g<sub>min</sub> = 2.05, g<sub>mid</sub> = 2.08, g<sub>max</sub> = 2.24, A<sub>max</sub><sup>Cu</sup> = 545 MHz.



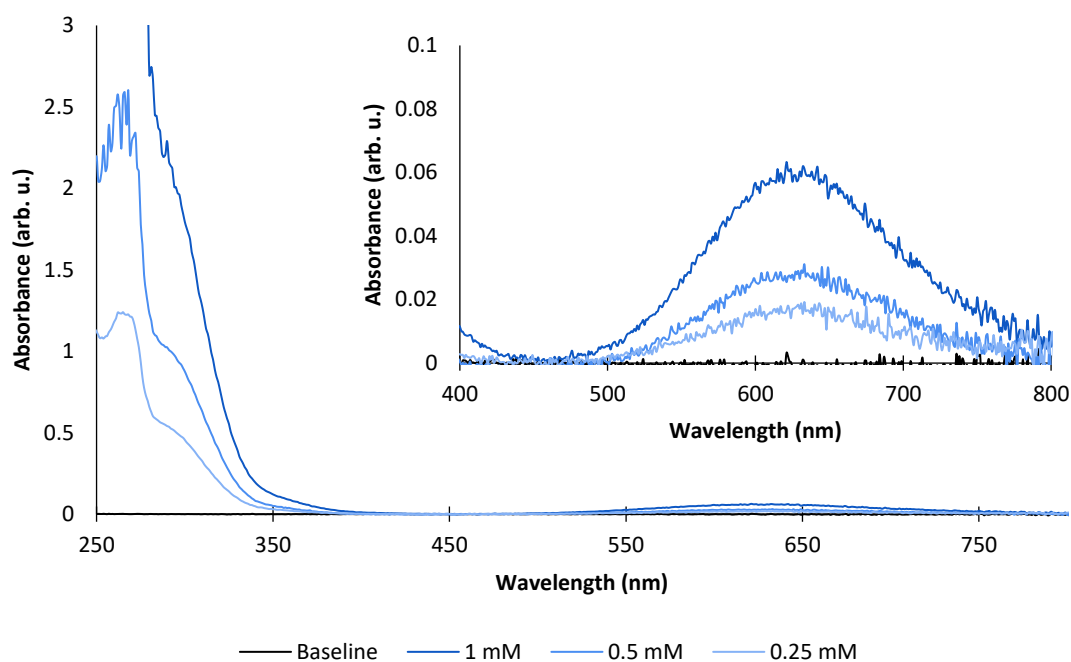
IR spectrum of complex 1 powder.



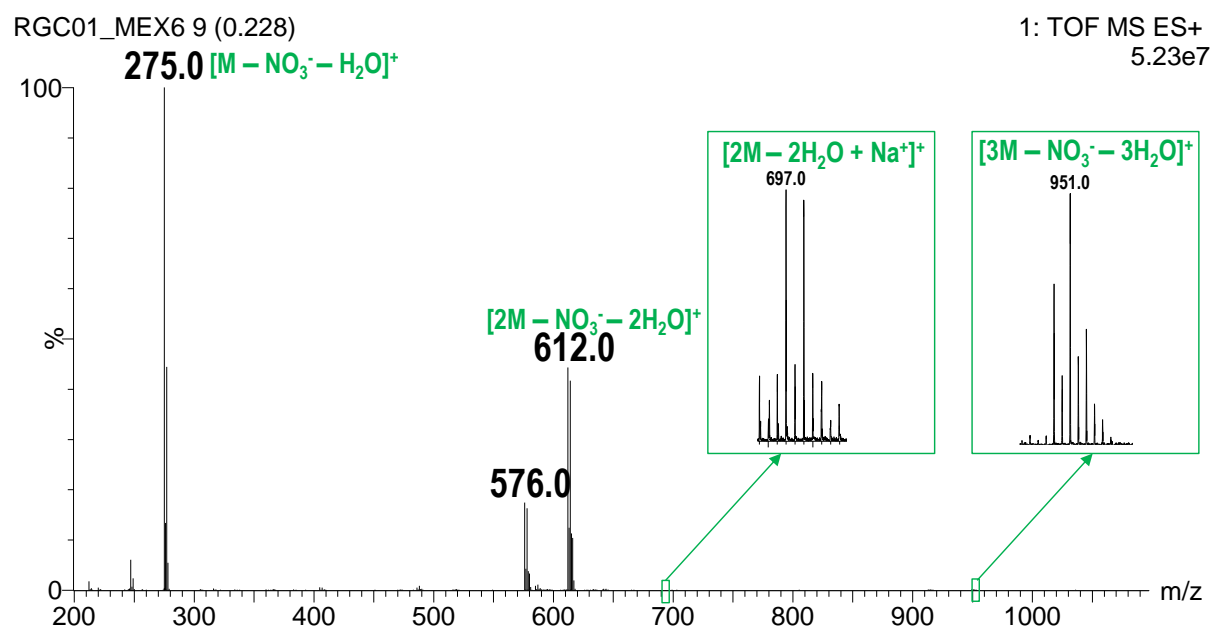
XRD of complex 1.



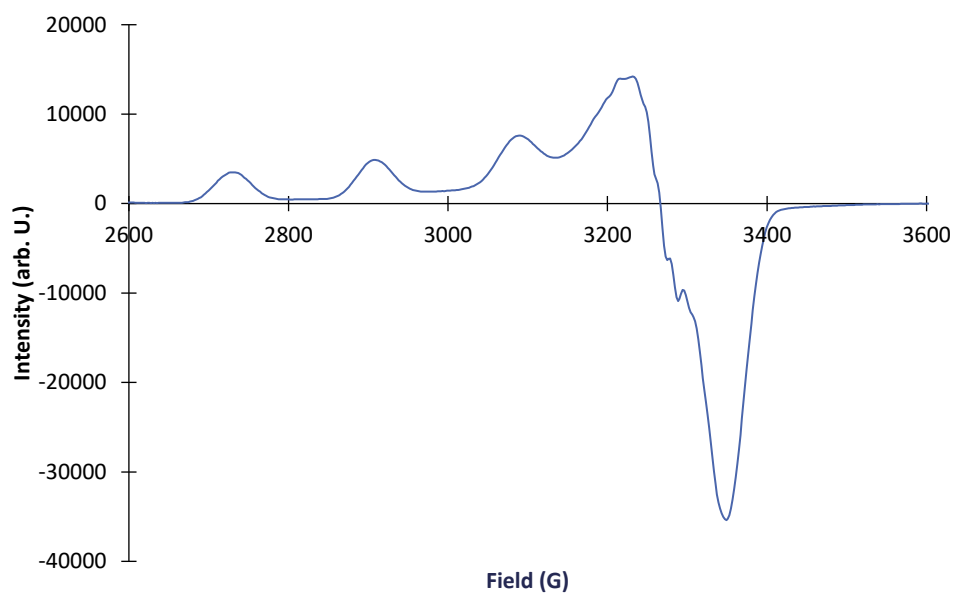
UV-vis spectra of complex **1** at different concentrations in methanol.



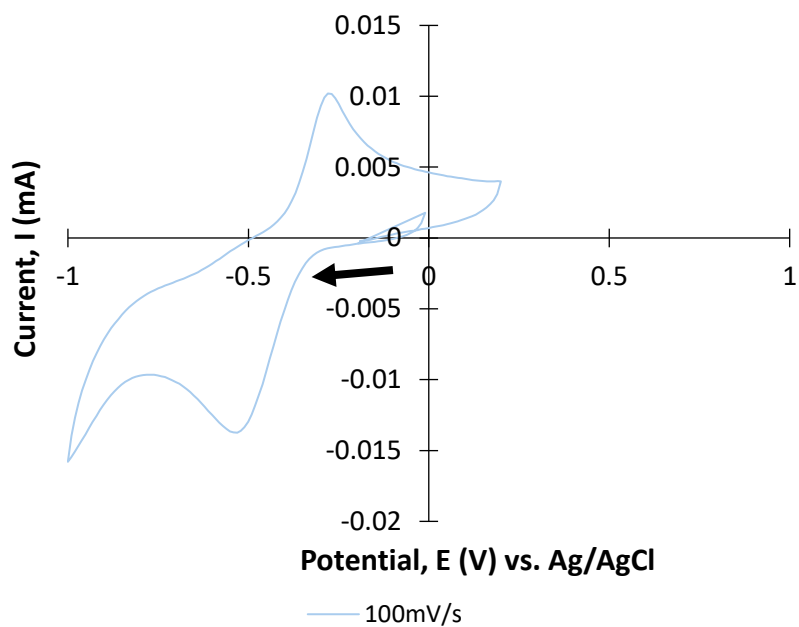
ESI-MS of complex **1** in acetonitrile solution (1.2 mM NaF). M corresponds to the Cu(PMPA) entity. A Dinuclear species was also observed at 612 bridged by a nitrate anion.



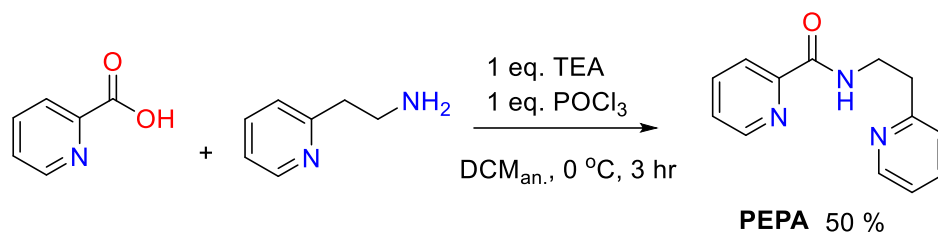
X-band EPR of complex **1** (0.5 mM) in MeOH.



Cyclic voltammetry of complex **1** (5 mM) in sodium nitrate buffer (100 mM) at pH 7.5. Glassy carbon electrode was used as a working electrode, a platinum wire as auxiliary electrode, and an Ag/AgCl electrode as reference.

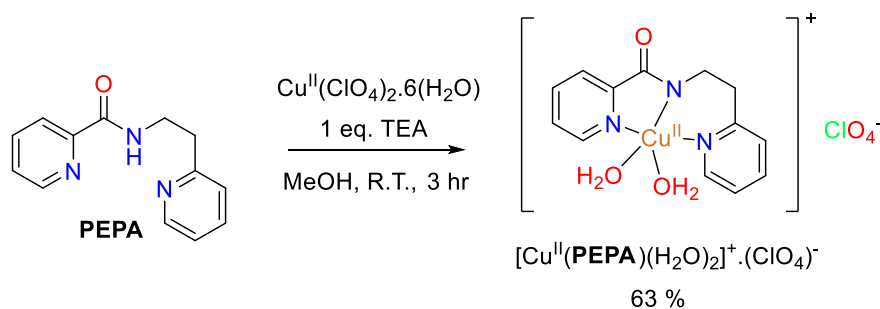


### 3. Synthesis of the PEPA ligand



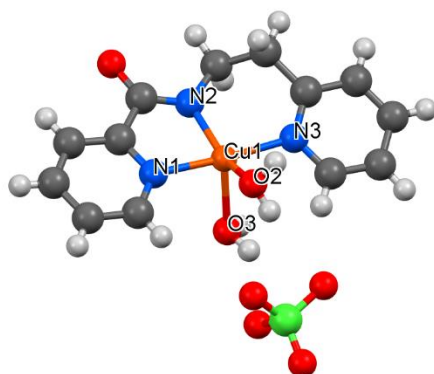
To an anhydrous dichloromethane solution (5 mL) of picolinic acid (250 mg, 2.0 mmol), triethylamine (2.0 mmol, 202 mg), and 2-(2-aminoethyl)pyridine (2.0 mmol, 244 mg), phosphorous oxychloride (2.0 mmol, 306 mg) in dichloromethane (3 mL) was added dropwise with constant stirring at 0 °C. After a couple of minutes, an additional amount of triethylamine (2.0 mmol, 202 mg) was added. After 3 h, the reaction medium was neutralized with aqueous potassium bicarbonate. The organic layer was extracted and dried over  $\text{MgSO}_4$ . The solvent was evaporated and the product was placed under vacuum. A viscous yellow oil was recovered after 6 hours (241 mg, 50%).  $^1\text{H}$  NMR (MeOD; 300 MHz)  $\delta$  in ppm: 3.11 (t, 2H), 3.79 (t, 2H), 7.27 (t, 1H), 7.38 (d, 1H), 7.53 (t, 1H), 7.75 (t, 1H), 7.93 (t, 1H), 8.04 (d, 1H), 8.47 (d, 1H), 8.60 (d, 1H).  $^{13}\text{C}$  NMR (MeOD; 300 MHz)  $\delta$  in ppm: 36.88, 38.98, 53.45, 121.65, 121.90, 123.76, 126.35, 137.38, 137.43, 148.38, 149.49, 158.73, 165.35.

### 4. Synthesis of the complex **2**, $[\text{Cu}(\text{PEPA})(\text{H}_2\text{O})_2]^+(\text{ClO}_4)^-$

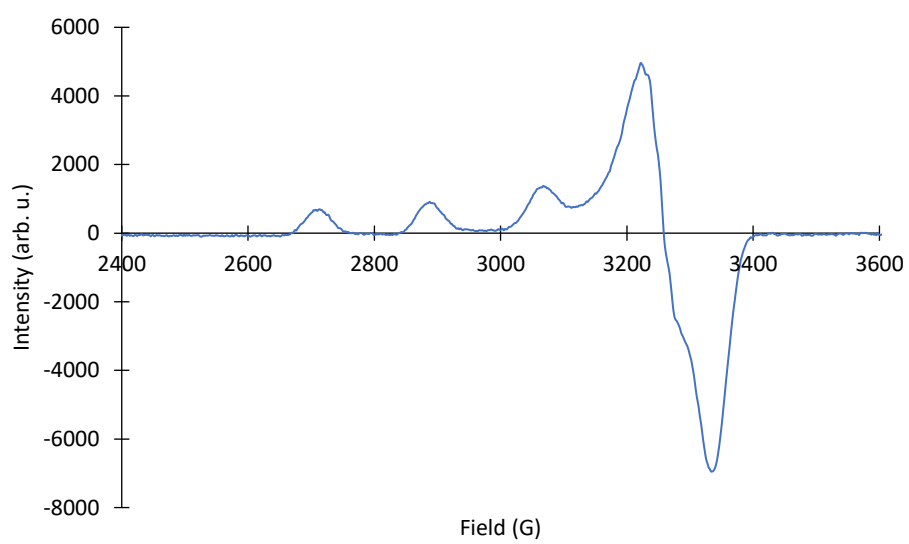


The PEPA ligand (42 mg, 0.19 mmol) and triethylamine (19 mg, 0.19 mmol) in methanol (4 mL) was added dropwise to a copper perchlorate hexahydrate (70.3 mg, 0.19 mmol) solution in methanol (4 mL) with constant stirring at room temperature. The reaction was left running for 3 hours at room temperature. The initial light blue solution turned dark green. Diethyl ether was added to the concentrated mixture to form a blue precipitate. The blue powder was recovered by filtration. It was then resolubilized in a methanol/water mixture (1:1) to produce suitable crystals for X-ray diffraction (XRD) by slow evaporation (yield = 63%). UV-vis: 298, 645 nm. EPR:  $g_{\text{min}} = 2.05$ ,  $g_{\text{mid}} = 2.07$ ,  $g_{\text{max}} = 2.26$ ,  $A_{\text{max}}^{\text{Cu}} = 2.26$ . CV:  $E_{1/2}(\text{Cu}^{\text{II}}/\text{Cu}^{\text{I}}) = 0.260$  mV vs. Ag/AgCl.

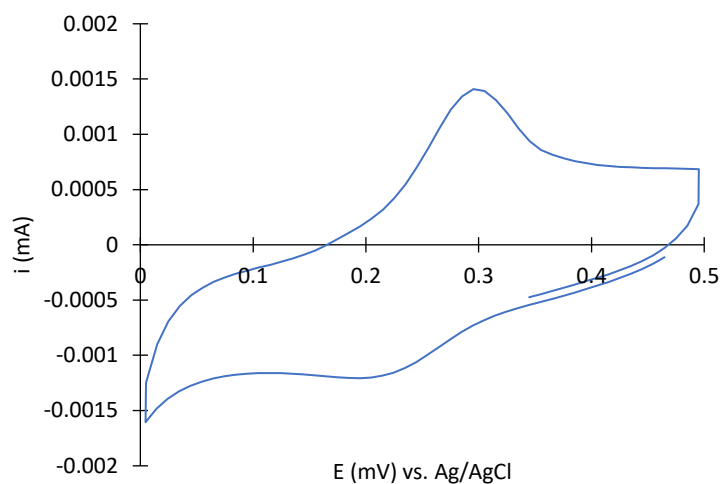
## XRD of complex **2**



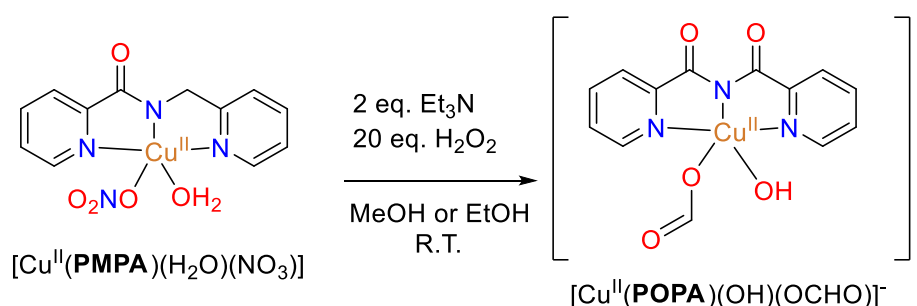
## X-band EPR of complex **2**



Cyclic voltammetry of complex **2** (1 mM) in methanol. Glassy carbon electrode was used as a working electrode, a platinum wire as auxiliary electrode, and an Ag/AgCl electrode as reference.

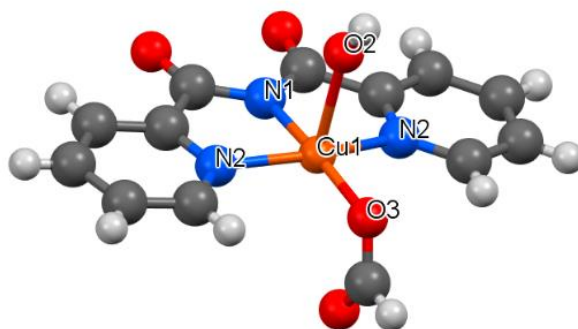
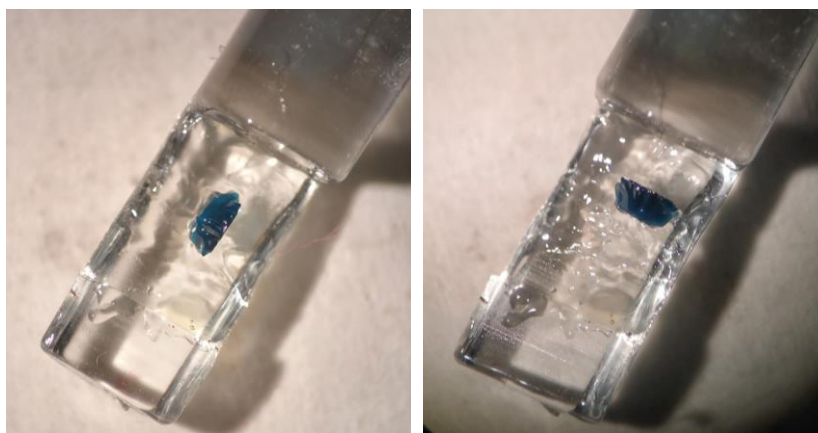


#### 5. Formation of complex **3** $[\text{Cu}^{\text{II}}(\text{POPA})(\text{OH})(\text{OCHO})]^-$

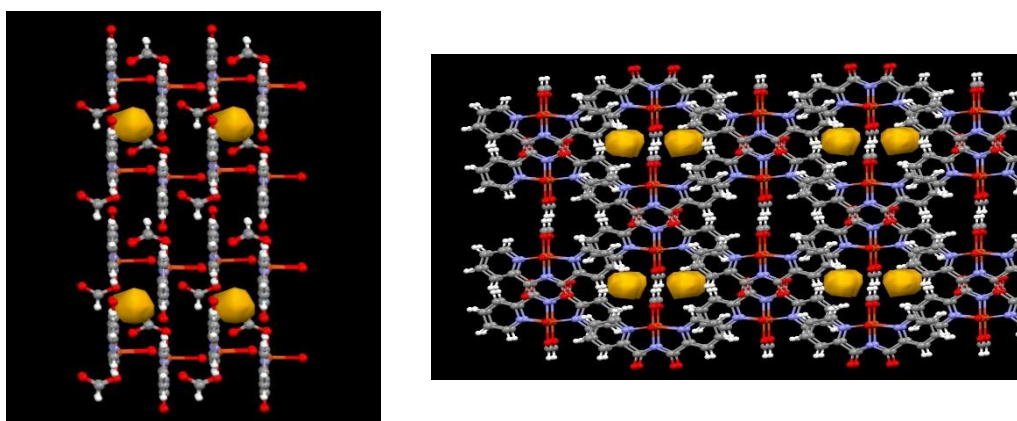


To a solution of complex **1** (1 mM) in methanol or ethanol, 2 equivalents of triethylamine (0.12 M) were added. Then, 20 equivalents of hydrogen peroxide (0.60 M) were added. The initial blue solution turns green and eventually becomes blue again. After slow evaporation of the reaction mixture, a single crystal was hand-picked for XRD confirm the structure of complex **3**. IR: imide 1580, 1624, 1710  $\text{cm}^{-1}$ . EPR:  $g_{\text{min}} = 2.06$ ,  $g_{\text{mid}} = 2.08$ ,  $g_{\text{max}} = 2.24$ .

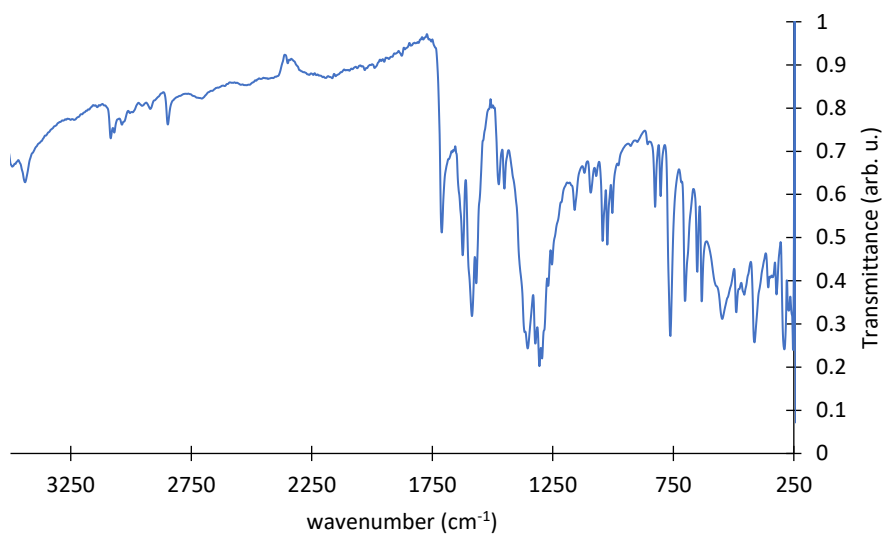
XRD of complex 3 on single crystal



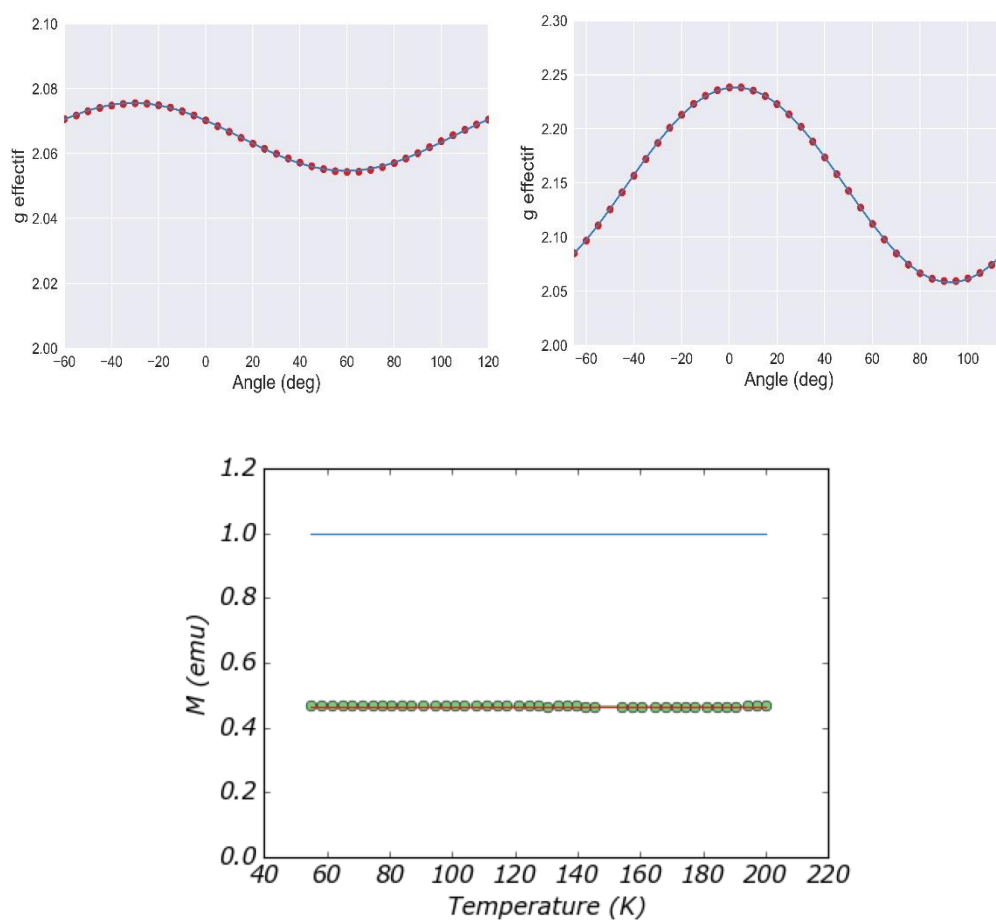
High-resolution low temperature XRD of single crystal



IR of complex 3 powder

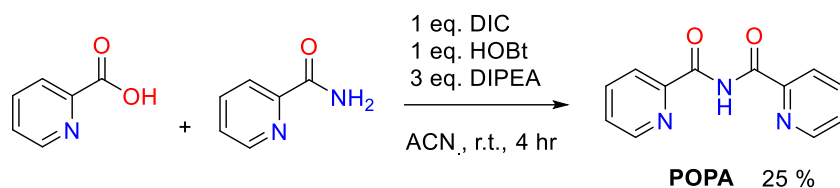


EPR and SQUID measurements of complex 3 single crystal



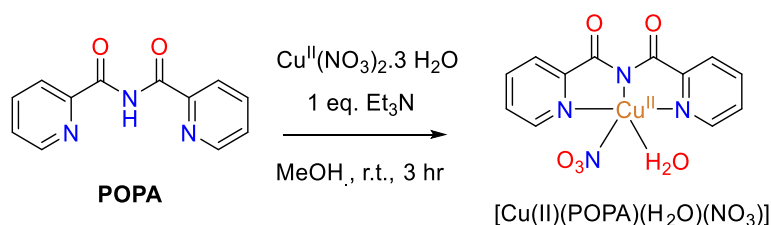


## 6. Synthesis of the POPA ligand



To a solution of picolinic acid (190 mg, 1.55 mmol) in acetonitrile (12 mL), N'-diisopropylcarbodiimide (195 mg, 1.55 mmol), hydroxybenzotriazole (209 mg, 1.55 mmol), and diisopropylethylamine (600 mg, 4.65 mmol) were added and left running for 1 hour at room temperature with constant stirring. Then, a solution of picolinamide (189 mg, 1.55 mmol) in acetonitrile (6 mL) was added dropwise and left running for an additional 3 hours. Aqueous potassium bicarbonate was then added. The organic layer was extracted using ethylacetate and dried over  $\text{Na}_2\text{SO}_4$ . Column chromatography was employed for purification using a DCM/ethyl acetate mixture (4:1) as eluent to yield the POPA ligand. (420 mg, 50%).  $^1\text{H}$  NMR (MeOD; 300 MHz)  $\delta$  in ppm: 4.74 (s, 2H), 7.30 (t, 1H), 7.43 (d, 1H), 7.56 (t, 1H), 7.80 (t, 1H), 7.96 (t, 1H), 8.13 (d, 1H), 8.51 (d, 1H), 8.66 (d, 1H).  $^{13}\text{C}$  NMR (MeOD; 300 MHz)  $\delta$  in ppm: 15.57, 45.57, 123.04, 123.34, 123.94, 127.99, 138.90, 138.95, 150.1, 151.07, 159.07, 167.12.

## 7. Synthesis of complex **4**, $[\text{Cu}(\text{POPA})(\text{H}_2\text{O})(\text{NO}_3)]$

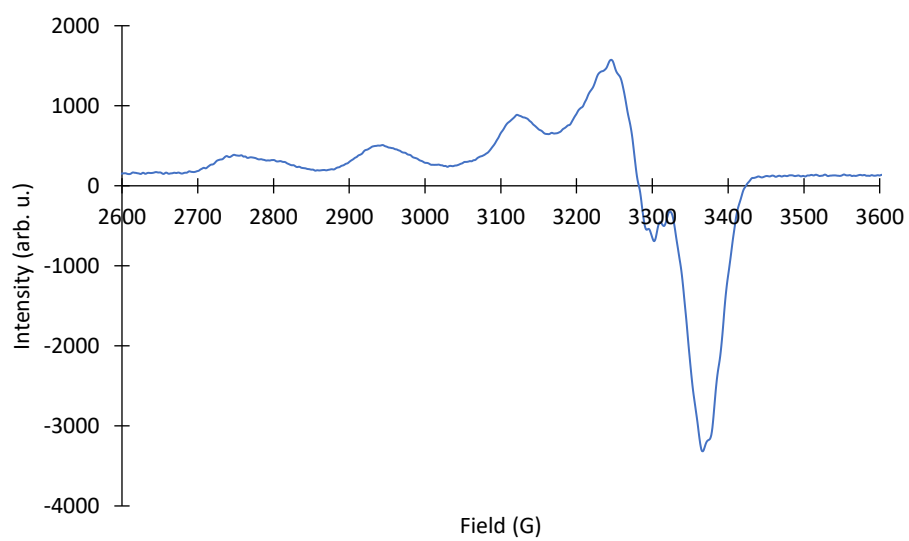


To a solution of the POPA ligand (100 mg, 0.44 mmol) in methanol (4 mL), a copper nitrate trihydrate (83 mg, 0.34 mmol) solution in methanol (4 mL) was added dropwise with constant stirring at room temperature. Triethylamine (44 mg, 0.44 mmol) was added to the reaction mixture which was left running for 3 hours. The initial light purple solution turned blue in presence of the base. Diethyl ether was added to the concentrated solution to form a precipitate. The powder was recovered by filtration. It was then resolubilized in methanol and suitable crystals for X-ray diffraction (XRD) were obtained by slow evaporation (67 mg, 0.18 mmol, 25%). IR: imide 1716, 1604, 1593  $\text{cm}^{-1}$ . EPR:  $g_{\text{min}} = 2.040$ ,  $g_{\text{mid}} = 2.060$ ,  $g_{\text{max}} = 2.220$ ,  $A_{\text{max}}^{\text{Cu}} = 560$  MHz.

IR of complex 4 powder.



X-band EPR of complex 4 (0.5 mM) in methanol



Impurities were observed in the EPR spectrum.

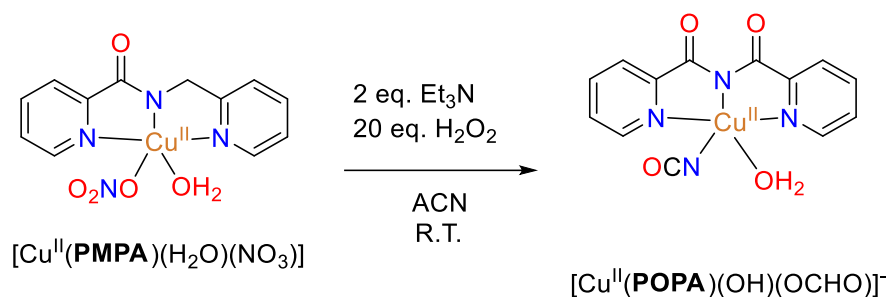
## 8. GC experiments

GC measurements of the complexes **1** and **4** in presence of triethylamine and hydrogen peroxide in multiple conditions were performed in 2 mL sealed vials with a reaction volume of 100  $\mu\text{L}$ . Methanol and ethanol were used as solvents. Concentrated sulfuric acid (25  $\mu\text{L}$ ) was added to the reaction mixture at the end of the reaction. After stabilization of the gas/liquid phases in the sealed vial (ca. 30 s), gas from the headspace (4  $\mu\text{L}$ ) was withdrawn with gas-tight syringe and injected to the GC for analysis.

## 9. GC-MS experiments

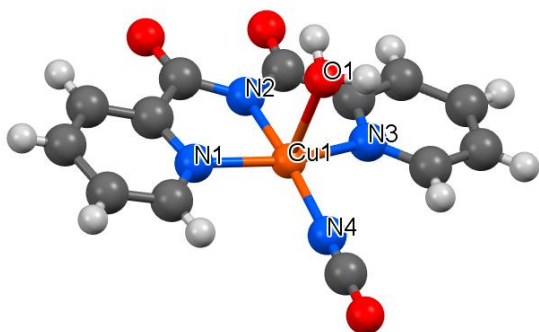
GC-MS measurements of complexes **1** and **4** in presence of triethylamine and hydrogen peroxide in multiple conditions were performed in 2 mL sealed vials. Methanol and ethanol were used as solvents. The labeled  $\alpha$ - $^{13}\text{C}$  of ethanol was also used. Concentrated sulfuric acid (25  $\mu\text{L}$ ) was added to the reaction mixture at the end of the reaction. After stabilization of the gas/liquid phases in the sealed vial (20 to 30 s), the headspace (15  $\mu\text{L}$ ) was withdrawn with gas-tight syringe and injected to the GC-MS instrument for analysis.

## 10. Formation of complex **5**, $[\text{Cu}(\text{POPA})(\text{H}_2\text{O})(\text{NCO})]$

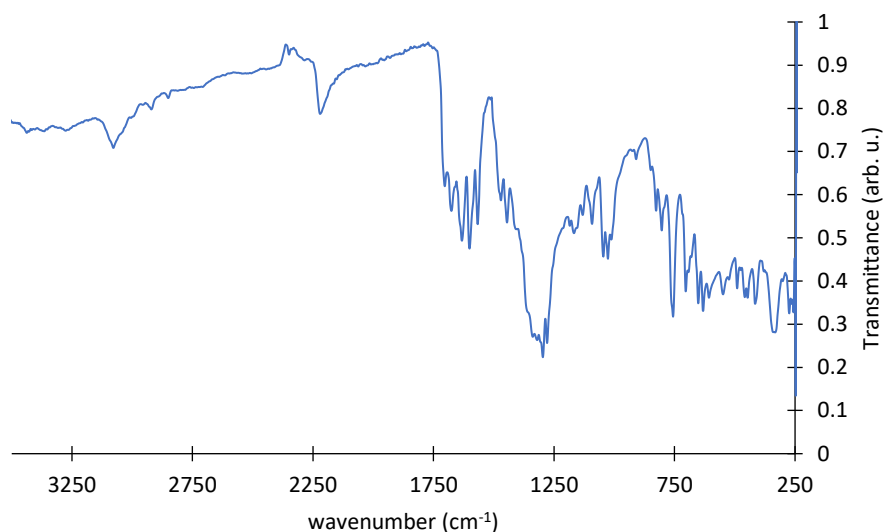


To a solution of complex **1** (1 mM) in acetonitrile, 2 equivalents of triethylamine (0.12 M) were added. Then, 20 equivalents of hydrogen peroxide (0.60 M) were added. The initial blue solution turns green and eventually becomes blue again. After slow evaporation of the reaction mixture, suitable crystals for XRD formed. IR: imide 1597-1685  $\text{cm}^{-1}$ , cyanate 2220  $\text{cm}^{-1}$ .

## XRD of complex 5



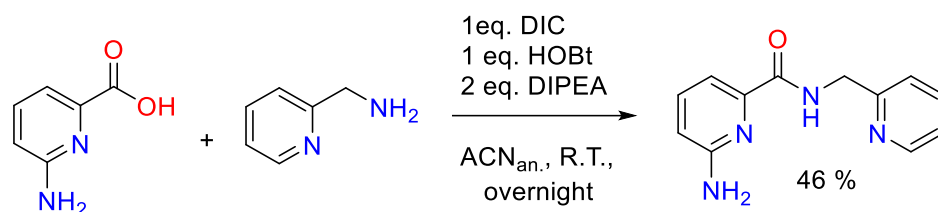
## IR of complex 5 powder



## 11. Oxidative cleavage of PNPG model substrate

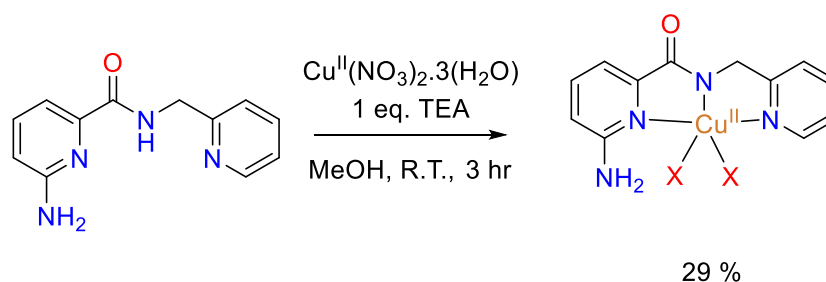
The experiments were conducted in 96-well plates using a BioTek Synergy MX microplate reader. Solutions of PNPG (0.1 M), complex **1** (1 mM), complex **4** (1 mM), and H<sub>2</sub>O<sub>2</sub> (0.1 M) were prepared in HEPES buffer (25 mM) at pH 7.5 or carbonate buffer (50 mM) at 10.5. The total volume was set to 200  $\mu$ L and the substrate (PNPG) and H<sub>2</sub>O<sub>2</sub> concentrated solutions were added in 20  $\mu$ L. Different volumes of complex (**1** or **4**) were added to vary the concentration in solution. The data acquisition was initiated after addition of H<sub>2</sub>O<sub>2</sub>. The microplate reader temperature was set at 25 °C, with stirring between each acquisition, which were taken at 420 nm wavelength every minute.

## 12. Synthesis of the PMPA-*o*-NH<sub>2</sub> ligand



A solution of 6-aminopicolinic acid (95 mg, 0.69 mmol) was prepared in acetonitrile (10 mL) and stirred at 65°C for 15 minutes. The heating was turned off and N,N'-diisopropylcarbodiimide (87mg, 0.69 mmol), hydroxybenzotriazole (93 mg, 0.69 mmol), and diisopropylethylamine (89 mg, 0.69 mmol) were added. The reaction mixture was left under stirring for 1 hour. A solution of 2-(aminomethyl)pyridine (75 mg, 0.69 mmol) and diisopropylethylamine (89 mg, 0.69 mmol) in acetonitrile (10 mL) was added slowly. The reaction mixture was left overnight at room temperature. Aqueous potassium bicarbonate was added and the mixture was left stirring for an additional hour. Ethyl acetate was added for extraction. The organic layers were washed with brine and dried over MgSO<sub>4</sub>. After removal of the solvent, a yellow powder was recovered (73 mg, 0.32 mmol, 46%). <sup>1</sup>H NMR (MeOD; 300 MHz)  $\delta$  in ppm: 4.62 (s, 2H), 6.65 (d, 1H), 7.24 (t, 1H), 7.27 (d, 1H), 7.34 (d, 1H), 7.72 (t, 1H), 8.42 (d, 1H). <sup>13</sup>C NMR (MeOD; 300 MHz)  $\delta$  in ppm: 41.30, 43.95, 110.76, 111.83, 121.45, 122.40, 137.75, 147.40, 148.80, 157.70, 158.75, 166.30.

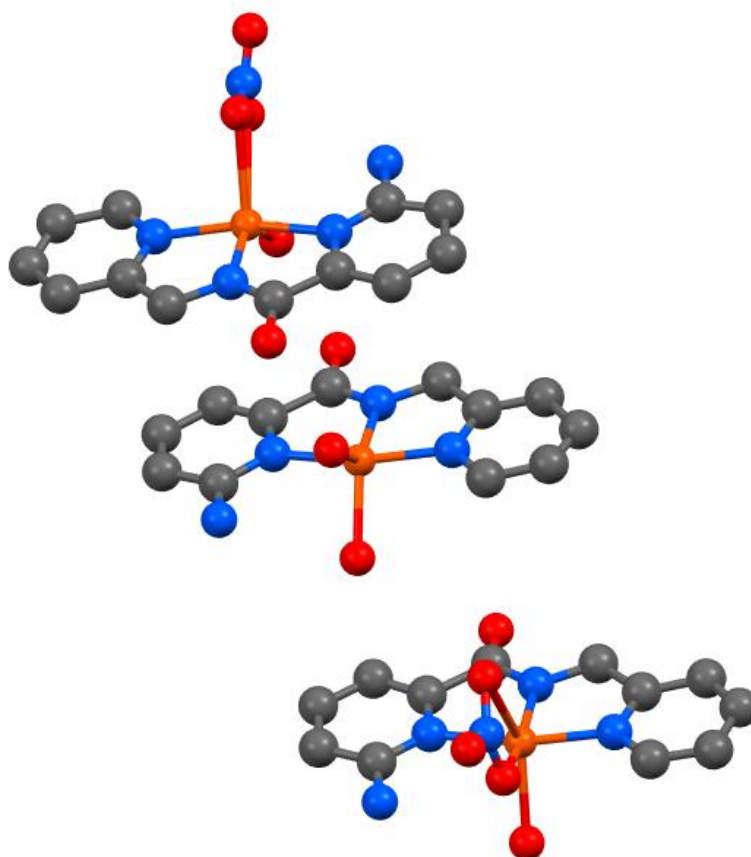
## 13. Synthesis of complex **6**, [Cu(PMPA-*o*-NH<sub>2</sub>)(X)<sub>2</sub>] (X = NO<sub>3</sub>, or H<sub>2</sub>O)



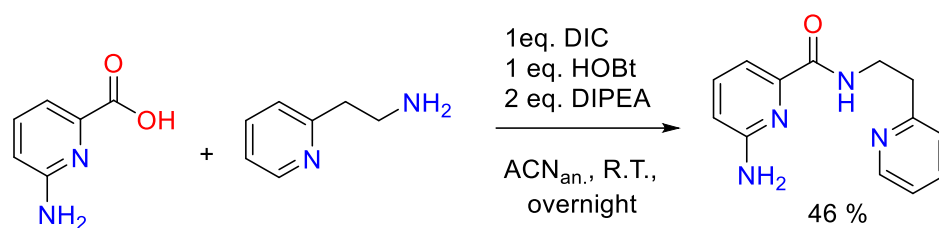
To a solution of PMPA(*o*-NH<sub>2</sub>) ligand (40 mg, 0.18 mmol) and triethylamine (in methanol (5 mL), a solution of copper nitrate trihydrate (44 mg, 0.18 mmol) in methanol (2 mL) was added dropwise. The reaction solution turned dark green. The reaction was left running for 3 hours at room temperature. The reaction mixture was concentrated by rotaevaporation and diethyl ether was added to form a green suspension. The oily suspension was resolubilized in a MeOH/water mixture (1:1) for crystallization (19.6 mg, 0.053 mmol, 29% yield). An initial analysis of the crystal

by XRD yielded multiple coordination spheres due to different exogeneous ligands found in the crystal matrix. A refined structure was not obtained.

XRD structures of complex **6**

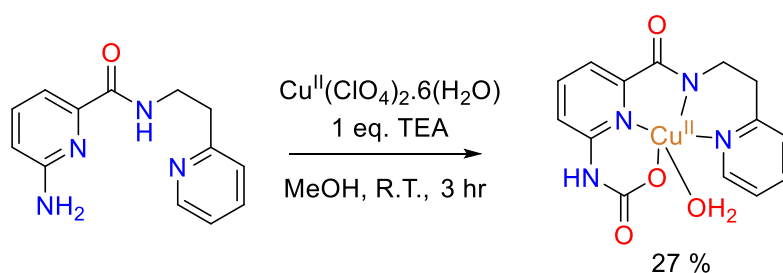


#### 14. Synthesis of the PEPA-*o*-NH<sub>2</sub> ligand



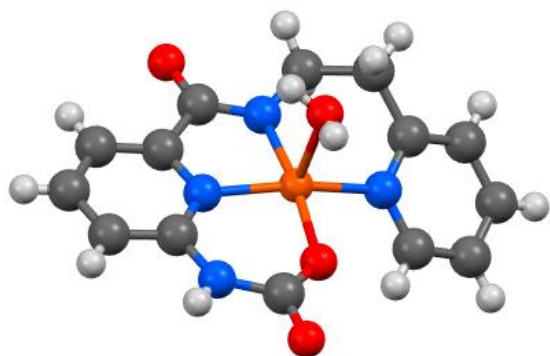
A solution of 6-aminopicolinic acid (95 mg, 0.69 mmol) was prepared in acetonitrile (10 mL) and stirred at 70°C for 5 to 10 minutes. N,N'-diisopropylcarbodiimide (87mg, 0.69 mmol), hydroxybenzotriazole (93mg, 0.69 mmol), and diisopropylethylamine (89 mg, 0.69 mmol) were added. The reaction mixture was left running for 1 hour. A solution of 2-(2-aminoethyl)pyridine (75 mg, 0.69 mmol) and diisopropylethylamine (84 mg, 0.69 mmol) in acetonitrile (10 mL) was added slowly. The reaction mixture was left running overnight with constant stirring. Aqueous potassium bicarbonate was added and the resulting solution was left stirring for 30 minutes. Ethyl acetate was added for extraction. The organic layers were washed with brine and dried over Na<sub>2</sub>SO<sub>4</sub>. After removal of the solvent, a viscous oil was recovered and placed under vacuum for 3 hours. (77 mg, 0.32 mmol, 46%). <sup>1</sup>H NMR (MeOD; 300 MHz)  $\delta$  in ppm: 3.01 (t, 2H), 3.72 (m, 2H), 6.61 (d, 1H), 7.18 (t, 1H), 7.21 (d, 1H), 7.28 (t, 1H), 7.44 (d, 1H), 7.67 (t, 1H), 8.41 (d, 1H). <sup>13</sup>C NMR (MeOD; 300 MHz)  $\delta$  in ppm: 37.00, 38.89, 110.54, 111.68, 121.84, 123.70, 137.34, 137.98, 147.49, 148.45, 158.54, 158.82, 166.06.

#### 15. Synthesis of complex **7**, [Cu(PEPA-*o*-NHCO<sub>2</sub>)(H<sub>2</sub>O)] complex



To a solution of copper perchlorate hexahydrate salt (122 mg, 0.33 mmol) in methanol (3 mL), a solution of PEPA (79 mg, 0.33 mmol) and triethylamine (33 mg, 0.33 mmol) in methanol was added dropwise. The reaction mixture turned green and was left running for 3 hours at room temperature and diethyl ether was added. The powder was recovered by filtration (32 mg, 0.09 mmol, 27%). Suitable crystals for XRD were formed upon slow evaporation of a methanol/water (1:1) solution.

## XRD of complex 7



## 16. Computational methods

Calculation of EPR parameters: The DFT method used in the calculation of EPR parameters is done with the B3PW91 functional. [7] [8] The calculation used increased general integration grids (Grid6 in ORCA convention), further increased radial integration accuracy (IntAcc 6.0) and specially enhanced grids for the metal center (SpecialGridIntAcc 11). For all ligand atoms, the def2-TZVP basis sets [4] were used. In the case of Cu, a home-made basis set, named aug-cc-pVTZ-Jmod, was used and consists of a modified version of aug-cc-pVTZ-J [9] [10] with decontracted *s* functions and removal of innermost *s* primitives. No approximations to two-electron integrals were used when calculating hyperfine coupling constants to exclude any possible error related to density fitting approximations. Spin-orbit contributions were included through mean-field and effective potential approaches. The spin-orbit coupling operator was treated by an accurate mean-field (SOMF) approximation to the Breit–Pauli operator (SOCType 3 in ORCA). [12] [13] The potential was constructed to include one-electron terms, compute the Coulomb term in a semi-numeric way, incorporate exchange via one-center exact integrals including the spin-other orbit interaction, and include local DFT correlation (SOCFlags 1,2,3,1 in ORCA). The effect of considering the solvent via a continuum solvation model was investigated using the CPCM. [17]

Calculation of UV-vis absorption spectrum: The functional used for TD-DFT was PBE0. [6] For all atoms, the def2-TZVP basis sets [4] were used. The TD-DFT methodology computed the first 50 excited states, with the corresponding maximum dimension of the expansion space in the Davidson procedure at 300 (nroots 50 and maxdim 300 in ORCA). Triplet excitation states were set to true to determine these energies in addition to the singlets. The effect of considering the



solvent via a continuum solvation model was investigated using the CPCM. [17] To plot the UV-visible spectra, the `orca_mapscp` program is used. The plots were built from 200 to 800 nm in wavelength, with a  $3750\text{ cm}^{-1}$  width at half height and 2000 points.

Reactivity calculations: For these calculations, we carried out the geometry optimizations using the BP86 functional. [2] [3] For all atoms, the def2-TZVP basis sets [4] were used. The scan was realized along the O<sub>1</sub>-C<sub>2</sub> bond, starting at 3.65 Å and finishing at 1.40 Å, in a total of 8 steps. Next steps will be to re-optimize the obtained putative transition state and obtain its numerical frequencies.

## 17. Crystallographic data table

	Complex 1	Complex 2	Complex 3	Complex 4
Empirical formula	C <sub>12</sub> H <sub>12</sub> CuN <sub>4</sub> O <sub>5</sub>	C <sub>13</sub> H <sub>16</sub> ClCuN <sub>3</sub> O <sub>7</sub>	C <sub>13</sub> H <sub>10</sub> CuN <sub>3</sub> O <sub>5</sub>	C <sub>12</sub> H <sub>11.33</sub> CuN <sub>4</sub> O <sub>5.33</sub>
Formula weight	355.80	425.28	351.78	360.40
Temperature/K	298	295	139.98(11)	295
Crystal system	triclinic	monoclinic	orthorhombic	triclinic
Space group	P-1	P2 <sub>1</sub> /n	Cmc2 <sub>1</sub>	P-1
a/Å	7.2429(3)	7.1191(2)	15.4318(3)	7.2491(4)
b/Å	7.4975(3)	21.9498(5)	13.4730(3)	7.5175(4)
c/Å	13.5881(7)	11.1326(2)	6.47320(10)	13.5695(7)
α/°	86.942(4)	90	90	87.007(4)
β/°	75.737(4)	92.289(2)	90	75.908(5)
γ/°	79.177(3)	90	90	79.310(5)
Volume/Å <sup>3</sup>	702.40(6)	1738.22(7)	1345.86(4)	704.75(7)
Z	2	4	4	2
ρ <sub>calc</sub> /cm <sup>3</sup>	1.682	1.625	1.736	1.698
μ/mm <sup>-1</sup>	1.585	3.575	1.652	1.583
F(000)	362.0	868.0	712.0	366.0
Crystal size/mm <sup>3</sup>	0.4x0.26x0.1	0.42x0.24x0.06	0.22x0.12x0.12	0.1x0.08x0.05
2θ range for data collection/°	5.9 to 57.68	8.056 to 142.332	7.466 to 58.948	7.278 to 56.27
Index ranges	-9 ≤ h ≤ 9, -8 ≤ k ≤ 10, -17 ≤ l ≤ 18	-8 ≤ h ≤ 8, -26 ≤ k ≤ 26, -10 ≤ l ≤ 13	-20 ≤ h ≤ 19, -18 ≤ k ≤ 17, -8 ≤ l ≤ 8	-9 ≤ h ≤ 8, -9 ≤ k ≤ 9, -16 ≤ l ≤ 17
Reflections collected	20930	18477	14742	6027
Independent reflections	3238 [R <sub>int</sub> = 0.0416, R <sub>sigma</sub> = 0.0264]	3335 [R <sub>int</sub> = 0.0646, R <sub>sigma</sub> = 0.0303]	1781 [R <sub>int</sub> = 0.0239, R <sub>sigma</sub> = 0.0133]	2955 [R <sub>int</sub> = 0.0250, R <sub>sigma</sub> = 0.0457]
Data/restraints/parameters	3238/0/208	3335/0/228	1781/1/110	2955/0/210
Goodness-of-fit on F <sup>2</sup>	1.061	1.074	1.051	1.139
Final R indexes [I ≥ 2σ (I)]	R <sub>1</sub> = 0.0349, wR <sub>2</sub> = 0.0850	R <sub>1</sub> = 0.0804, wR <sub>2</sub> = 0.2370	R <sub>1</sub> = 0.0262, wR <sub>2</sub> = 0.0702	R <sub>1</sub> = 0.0446, wR <sub>2</sub> = 0.1071
Final R indexes [all data]	R <sub>1</sub> = 0.0423, wR <sub>2</sub> = 0.0895	R <sub>1</sub> = 0.0860, wR <sub>2</sub> = 0.2461	R <sub>1</sub> = 0.0265, wR <sub>2</sub> = 0.0705	R <sub>1</sub> = 0.0576, wR <sub>2</sub> = 0.1161
Largest diff. peak/hole / e Å <sup>-3</sup>	0.39/-0.26	1.16/-0.61	0.73/-0.25	0.33/-0.34

	Complex 5	Complex 7
Empirical formula	C <sub>13</sub> H <sub>10</sub> CuN <sub>4</sub> O <sub>4</sub>	C <sub>14</sub> H <sub>18</sub> CuN <sub>4</sub> O <sub>6</sub>
Formula weight	349.79	401.87
Temperature/K	139.7(9)	295
Crystal system	triclinic	triclinic
Space group	P-1	P-1
a/Å	7.30060(10)	7.39520(10)
b/Å	10.1469(2)	14.7268(2)
c/Å	10.3148(2)	11.1326(2)
α/°	111.990(2)	77.8300(10)
β/°	95.873(2)	84.886(2)
γ/°	109.420(2)	84.886(2)
Volume/Å <sup>3</sup>	645.34(2)	1630.78(5)
Z	2	2
ρ <sub>calc</sub> /cm <sup>3</sup>	1.800	1.637
μ/mm <sup>-1</sup>	1.718	2.270
F(000)	354.0	828.0
Crystal size/mm <sup>3</sup>	0.26x0.26x0.26	0.22x0.18x0.05
2θ range for data collection/°	6.556 to 60.57	6.146 to 141.96
Index ranges	-10 ≤ h ≤ 10, -13 ≤ k ≤ 13, -14 ≤ l ≤ 13	-9 ≤ h ≤ 8, -18 ≤ k ≤ 18, -19 ≤ l ≤ 19
Reflections collected	22821	25251
Independent reflections	3403 [R <sub>int</sub> = 0.0217, R <sub>sigma</sub> = 0.0120]	6175 [R <sub>int</sub> = 0.0281, R <sub>sigma</sub> = 0.0184]
Data/restraints/parameters	3403/0/200	6175/0/465
Goodness-of-fit on F <sup>2</sup>	1.079	1.048
Final R indexes [I>=2σ (I)]	R <sub>1</sub> = 0.0222, wR <sub>2</sub> = 0.0595	R <sub>1</sub> = 0.0367, wR <sub>2</sub> = 0.1013
Final R indexes [all data]	R <sub>1</sub> = 0.0231, wR <sub>2</sub> = 0.0601	R <sub>1</sub> = 0.0380, wR <sub>2</sub> = 0.1028
Largest diff. peak/hole / e Å <sup>-3</sup>	0.43/-0.36	0.48/-0.45

## REFERENCES

- [1] F. Neese, F. Wennmohs, U. Becker and C. Riplinger, "The ORCA quantum chemistry program package," *Journal of Chemical Physics*, vol. 152, no. 22, 2020.
- [2] A. D. Becke, "Density-functional exchange-energy approximation with correct asymptotic-behavior," *Physical Review A*, vol. 38, no. 6, pp. 3098-3100, 1988.
- [3] J. P. Perdew, "Density-functional approximation for the correlation-energy of the inhomogeneous electron-gas," *Physical Review B*, vol. 33, no. 12, pp. 8822-8824, 1986.
- [4] F. Weigend and R. Ahlrichs, "Balanced basis sets of split valence, triple zeta valence and quadruple zeta valence quality for H to Rn: Design and assessment of accuracy," *Physical Chemistry Chemical Physics*, vol. 7, no. 18, pp. 3297-3305, 2005.
- [5] F. Weigand, "Accurate Coulomb-fitting basis sets for H to Rn," *Physical Chemistry Chemical Physics*, vol. 8, no. 9, pp. 1057-1065, 2006.
- [6] C. Adamo and V. Barone, "Toward reliable density functional methods without adjustable paramters: The PBE0 model," *Journal of Chemical Physics*, vol. 110, no. 13, pp. 6158-6170, 1999.
- [7] A. D. Becke, "Density-functional thermochemistry .3. The role of exact exchange," *Journal of Chemical Physics*, vol. 98, no. 7, pp. 5648-5652, 1993.
- [8] J. P. Perdew and Y. Wang, "Accurate and simple analytic representation of the electron-gas correlation-energy," *Physical Review B*, vol. 45, no. 23, pp. 13244-13249, 1992.
- [9] E. D. Hedegard, J. Kongsted and S. P. A. Sauer, "Optimized basis sets for calculation of electron paramagnetic resonance hyperfine coupling constants: aug-cc-pVTZ-J for the 3d atoms Sc-Zn," *Journal of Chemical Theory and Computation*, vol. 7, no. 12, pp. 4077-4087, 2011.
- [10] E. D. Hedegard, J. Kongsted and S. P. A. Sauer, "Improving the calculation of electron paramagnetic resonance hyperfine coupling tensors for d-block metals," *Physical Chemistry Chemical Physics*, vol. 14, no. 30, pp. 10669-10676, 2012.
- [11] R. J. Gómez-Piñeiro, D. A. Pantazis and M. Orio, "Comparison of density functional and correlated wave function methods for the prediction of Cu(II) hyperfine coupling constants," *Chem. Phys. Chem.*, vol. 21, no. 24, pp. 2667-2679, 2020.

- [12] F. Neese, "Efficient and accurate approximations to the molecular spin-orbit coupling operator and their use in molecular g-tensor calculations," *Journal of Chemical Physics*, vol. 122, no. 3, p. 034107, 2005.
- [13] B. A. Hess, C. M. Marian, U. Wahlgren and O. Gropen, "A mean-field spin-orbit method applicable to correlated wavefunctions," *Chemical Physics Letters*, vol. 251, no. 5-6, pp. 365-371, 1996.
- [14] E. van Lenthe, E. J. Baerends and J. G. Snijders, "Relativistic regular 2-component hamiltonians," *Journal of Chemical Physics*, vol. 99, no. 6, pp. 4597-4610, 1993.
- [15] E. van Lenthe, E. J. Baerends and J. G. Snijders, "Relativistic total-energy using regular approximations," *Journal of Chemical Physics*, vol. 101, no. 11, pp. 9783-9792, 1994.
- [16] E. van Lenthe, J. G. Snijders and E. J. Baerends, "The zero-order regular approximation for relativistic effects: The effect of spin-orbit coupling in closed shell molecules," *Journal of Chemical Physics*, vol. 105, no. 15, pp. 6505-6516, 1996.
- [17] M. Cossi and V. Barone, "Quantum calculation of molecular energies and energy gradients in solution by a conductor solvent model," *Journal of Physical Chemistry A*, vol. 102, no. 11, pp. 1995-2001, 1998.
- [18] A. E. Reed, R. B. Weinstock and F. Weinhold, "Natural population analysis," *The Journal of Chemical Physics*, vol. 83, no. 2, pp. 735-746, 1985.



---

# SUPPORTING INFORMATION

---





## SUPPORTING INFORMATION

In this chapter, the reader will find the compiled supporting information of the Ph.D. thesis Experimental and Theoretical Investigation of LPMO-inspired Mononuclear Copper Complexes. The Supporting Information, S.I., is divided by chapter and takes into account the core chapters of the thesis, i.e. Chapter II. Theoretical Methods and their Application in EPR Spectroscopy of Mononuclear Copper(II) Centers, Chapter III. Prediction of EPR Parameters for the LPMO Active Site and a Synthetic LPMO-Like Peptide, and Chapter IV. Synthesis, Characterization, and Reactivity Study of N-(pyridine-2-ylmethyl)picolinamide, PMPA, Copper(II) complex and Its Derivatives.

## 1 – Supporting information regarding Chapter II.

**Table S1.** Calculated HFCs (individual components and detailed contributions, in MHz) of  $[\text{Cu}(\text{NH}_3)_4]^{2+}$  obtained with the B3PW91 functional with different basis sets.

<i>Basis set</i>	$A_{11}$	$A_{22}$	$A_{33}$	$A^{FC}$	$A^{PC}$	$A_{11}^{SD}$	$A_{22}^{SD}$	$A_{33}^{SD}$	$A_{11}^{S,dip}$	$A_{22}^{S,dip}$	$A_{33}^{S,dip}$
aug-cc-pVTZ-Junc	-20.7	-21.1	-590.6	-339.2	128.3	247.4	246.9	-494.3	-57.2	-57.2	114.5
aug-cc-pVTZ-J	-19.0	-19.4	-587.5	-338.1	129.5	247.4	246.9	-494.2	-57.8	-57.7	115.3
CP(PPP)	-28.2	-28.6	-583.3	-336.8	123.4	239.8	239.4	-479.3	-54.7	-54.6	109.3
aug-cc-pVTZ	-272.7	325.4	325.8	-5.7	131.8	-515.3	257.4	257.9	116.4	-58.1	-58.2
aug-cc-pwCVTZ	213.0	213.4	-356.1	-104.5	127.9	246.7	247.2	-493.9	-57.1	-57.2	114.4
cc-pwCVTZ	213.9	214.3	-354.7	-103.2	127.7	246.4	246.8	-493.2	-56.9	-57.0	114.1
def2-TZVP	-246.3	332.5	332.9	9.2	130.5	-499.5	249.5	250.0	113.5	-56.7	-56.8
def2-TZVP-uncS	-1.0	-1.3	-580.4	-324.9	130.7	250.1	249.7	-499.8	-56.9	-56.8	113.7
aug-cc-pVTZ-Jmod	-19.2	-19.6	-591.2	-337.9	127.9	248.1	247.6	-495.7	-57.3	-57.2	114.4
<i>Exp.</i>	<i>68.8</i>	<i>68.8</i>	<i>586.5</i>								

**Table S2.** APDs of  $A_{33}$ ,  $A_{iso}$  and  $\Delta A$  of  $[\text{Cu}(\text{NH}_3)_4]^{2+}$  for calculated hyperfine coupling constants obtained with the B3PW91 functional using different basis sets and compared to experimental values.

<i>Basis set</i>	$A_{33}$	$A_{iso}$	$\Delta A$	$APD(A_{33})$	$APD(A_{iso})$	$APD(\Delta A)$
aug-cc-pVTZ-Junc	-590.6	210.8	569.9	1	13	10
aug-cc-pVTZ-J	-587.5	208.6	568.5	0	14	10
CP(PPP)	-583.3	213.4	555.1	1	12	7
aug-cc-pVTZ	325.8	126.2	598.5	44	48	16
aug-cc-pwCVTZ	-356.1	23.4	569.5	39	90	10
cc-pwCVTZ	-354.7	24.5	569.0	40	90	10
def2-TZVP	332.9	139.7	579.2	43	42	12
def2-TZVP-uncS	-580.4	194.2	579.4	1	20	12
aug-cc-pVTZ-Jmod	-591.2	210.0	572.0	1	13	10
<i>Exp.</i>	<i>586.5</i>	<i>241.4</i>	<i>517.7</i>			

**Figure S1.** Graphical representation of APDs of  $A_{33}$ ,  $A_{iso}$  and  $\Delta A$  of  $[\text{Cu}(\text{NH}_3)_4]^{2+}$  for calculated hyperfine coupling constants obtained with the B3PW91 functional and different basis.

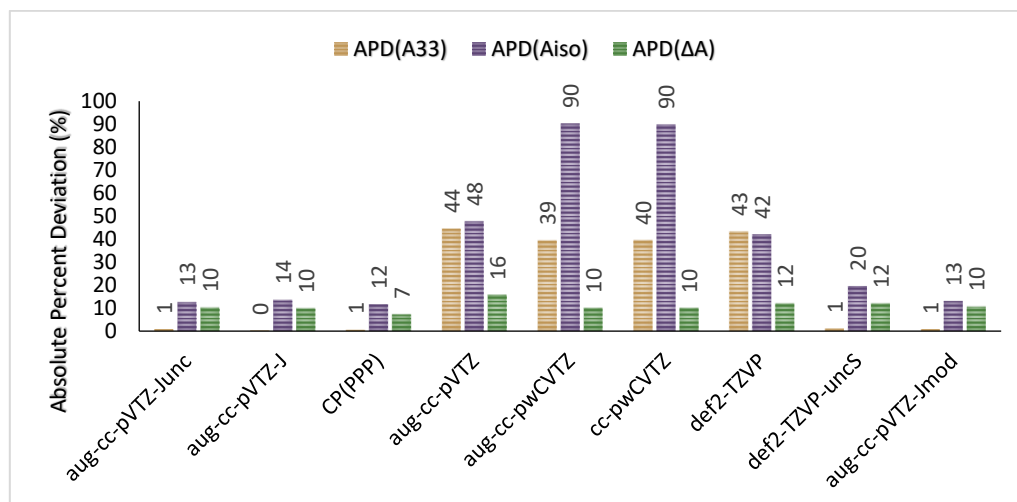


**Table S3.** Calculated HFCs (individual components and detailed contributions, in MHz) of  $[\text{Cu}(\text{NH}_3)_4]^{2+}$  obtained with the TPSSh functional with different basis sets.

<i>Basis set</i>	$A_{11}$	$A_{22}$	$A_{33}$	$A^{FC}$	$A^{PC}$	$A_{11}^{SD}$	$A_{22}^{SD}$	$A_{33}^{SD}$	$A_{11}^{S,dip}$	$A_{22}^{S,dip}$	$A_{33}^{S,dip}$
aug-cc-pVTZ-Junc	-2.4	-2.8	-580.0	-294.7	99.6	235.5	235.1	-470.6	56.7	56.8	185.4
aug-cc-pVTZ-J	-13.7	-14.1	-589.3	-306.2	100.5	235.2	234.7	-469.9	57.4	57.4	186.8
CP(PPP)	-18.8	-19.1	-580.3	-303.1	97.0	228.9	228.5	-457.4	55.4	55.5	180.2
aug-cc-pVTZ	-292.9	314.2	314.6	9.3	102.6	-491.9	245.7	246.2	189.6	59.1	59.1
aug-cc-pwCVTZ	184.7	185.0	-393.5	-107.0	99.1	235.2	235.7	-471.0	56.4	56.3	184.4
cc-pwCVTZ	188.5	188.9	-388.9	-102.8	99.0	234.9	235.3	-470.2	56.4	56.3	184.2
def2-TZVP	-261.8	324.8	325.2	27.1	102.3	-476.8	238.2	238.6	187.9	59.5	59.5
def2-TZVP-uncS	19.5	19.8	-567.5	-278.5	102.4	238.4	238.7	-477.1	59.6	59.5	188.1
aug-cc-pVTZ-Jmod	-5.4	-5.8	-586.3	-298.0	98.8	236.5	236.0	-472.5	56.1	56.2	184.1
<i>Exp.</i>	<i>68.8</i>	<i>68.8</i>	<i>586.5</i>								

**Table S4.** APDs of  $A_{33}$ ,  $A_{iso}$  and  $\Delta A$  of  $[\text{Cu}(\text{NH}_3)_4]^{2+}$  for calculated hyperfine coupling constants obtained with TPSSh functional using different basis sets and compared to experimental values.

<i>Basis set</i>	$A_{33}$	$A_{iso}$	$\Delta A$	$APD(A_{33})$	$APD(A_{iso})$	$APD(\Delta A)$
aug-cc-pVTZ-Junc	-580.0	195.1	577.6	1	19	12
aug-cc-pVTZ-J	-589.3	205.7	575.6	0	15	11
CP(PPP)	-580.3	206.1	561.5	1	15	8
aug-cc-pVTZ	314.6	112.0	607.5	46	54	17
aug-cc-pwCVTZ	-393.5	7.9	578.5	33	97	12
cc-pwCVTZ	-388.9	3.8	577.8	34	98	12
def2-TZVP	325.2	129.4	587.0	45	46	13
def2-TZVP-uncS	-567.5	176.1	587.3	3	27	13
aug-cc-pVTZ-Jmod	-586.3	199.2	580.9	0	17	12
<i>Exp.</i>	<i>586.5</i>	<i>241.4</i>	<i>517.7</i>			

**Figure S2.** Graphical representation of APDs of  $A_{33}$ ,  $A_{iso}$  and  $\Delta A$  of  $[\text{Cu}(\text{NH}_3)_4]^{2+}$  for calculated hyperfine coupling constants obtained with TPSSh functional and different basis.

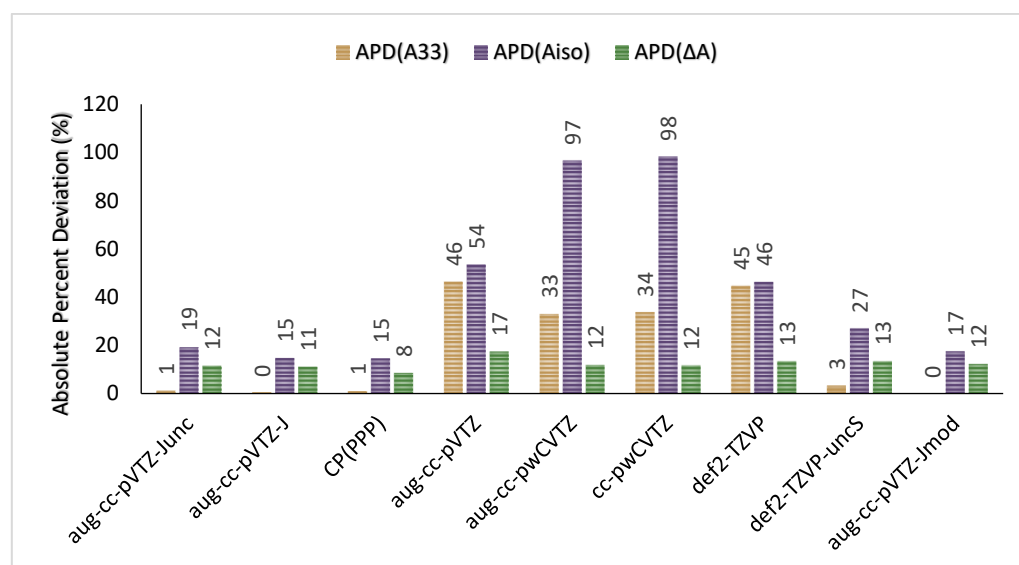


**Table S5.** Calculated HFCs (individual components and detailed contributions, in MHz) for **[Cu(dtc)<sub>2</sub>]** obtained with the PBE0 functional with different basis sets.

<i>Basis set</i>	$A_{11}$	$A_{22}$	$A_{33}$	$A^{FC}$	$A^{PC}$	$A_{11}^{SD}$	$A_{22}^{SD}$	$A_{33}^{SD}$	$A_{11}^{S,dip}$	$A_{22}^{S,dip}$	$A_{33}^{S,dip}$
aug-cc-pVTZ-Junc	-111.1	-116.7	-528.4	-330.6	78.5	176.1	172.5	-348.7	-35.1	-37.2	72.4
aug-cc-pVTZ-J	-110.1	-115.7	-526.4	-329.9	79.1	176.1	172.5	-348.6	-35.4	-37.4	73.0
CP(PPP)	-111.1	-116.6	-519.1	-324.2	75.3	171.6	167.7	-339.2	-33.7	-35.4	69.1
aug-cc-pVTZ	136.1	141.6	-296.0	-86.9	80.8	180.3	183.8	-364.1	-38.1	-36.1	74.2
aug-cc-pwCVTZ	42.7	48.4	-368.9	-170.6	78.0	172.5	176.1	-348.7	-37.2	-35.2	72.4
cc-pwCVTZ	43.4	49.1	-367.2	-169.3	77.7	172.0	175.7	-347.6	-37.0	-35.0	72.0
def2-TZVP	133.0	138.2	-281.4	-82.0	78.6	173.1	176.2	-349.3	-36.6	-34.7	71.3
def2-TZVP-uncS	-94.6	-99.8	-514.6	-315.1	78.8	176.5	173.3	-349.8	-34.8	-36.7	71.5
aug-cc-pVTZ-Jmod	-109.3	-114.8	-525.5	-329.0	79.1	176.1	172.5	-348.6	-35.4	-37.4	73.0
<i>Exp.</i>	<i>140.1</i>	<i>140.1</i>	<i>487.3</i>								

**Table S6.** APDs of  $A_{33}$ ,  $A_{iso}$  and  $\Delta A$  of **[Cu(dtc)<sub>2</sub>]** for calculated hyperfine coupling constants obtained with PBE0 functional using different basis sets and compared to experimental values.

<i>Basis set</i>	$A_{33}$	$A_{iso}$	$\Delta A$	$APD(A_{33})$	$APD(A_{iso})$	$APD(\Delta A)$
aug-cc-pVTZ-Junc	-528.4	252.1	417.3	8	1	20
aug-cc-pVTZ-J	-526.4	250.7	416.3	8	2	20
CP(PPP)	-519.1	248.9	408.0	7	3	18
aug-cc-pVTZ	-296.0	6.1	437.6	39	98	26
aug-cc-pwCVTZ	-368.9	92.6	417.3	24	64	20
cc-pwCVTZ	-367.2	91.6	416.3	25	64	20
def2-TZVP	-281.4	3.4	419.6	42	99	21
def2-TZVP-uncS	-514.6	236.3	420.0	6	8	21
aug-cc-pVTZ-Jmod	-525.5	249.9	416.2	8	2	20
<i>Exp.</i>	<i>487.3</i>	<i>255.8</i>	<i>347.2</i>			

**Figure S3.** Graphical representation of APDs of  $A_{33}$ ,  $A_{iso}$  and  $\Delta A$  of **[Cu(dtc)<sub>2</sub>]** for calculated hyperfine coupling constants obtained with PBE0 functional and different basis sets.

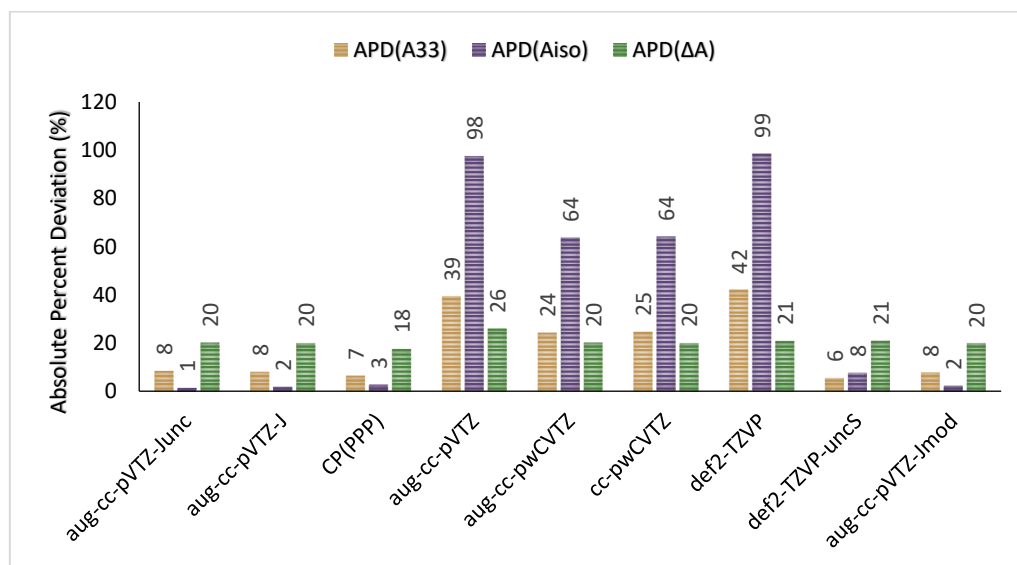


**Table S7.** Calculated HFCs (individual components and detailed contributions, in MHz) for **[Cu(dtc)<sub>2</sub>]** obtained with the B3PW91 functional with different basis sets.

<i>Basis set</i>	$A_{11}$	$A_{22}$	$A_{33}$	$A^{FC}$	$A^{PC}$	$A_{11}^{SD}$	$A_{22}^{SD}$	$A_{33}^{SD}$	$A_{11}^{S,dip}$	$A_{22}^{S,dip}$	$A_{33}^{S,dip}$
aug-cc-pVTZ-Junc	-98.9	-104.6	-495.3	-302.7	69.7	165.2	161.7	-326.9	-31.2	-33.3	64.6
aug-cc-pVTZ-J	-97.9	-103.5	-493.2	-301.9	70.3	165.1	161.7	-326.8	-31.5	-33.6	65.2
CP(PPP)	-99.4	-104.9	-487.7	-297.8	67.1	161.3	157.5	-318.8	-30.0	-31.8	61.8
aug-cc-pVTZ	128.1	133.7	-281.0	-78.0	71.6	168.6	172.1	-340.7	-34.1	-32.0	66.1
aug-cc-pwCVTZ	47.5	53.1	-342.9	-150.1	69.3	161.6	165.2	-326.8	-33.3	-31.2	64.7
cc-pwCVTZ	48.2	53.9	-341.4	-148.9	69.1	161.2	164.8	-326.0	-33.2	-31.2	64.4
def2-TZVP	126.6	131.8	-266.0	-72.1	69.6	161.9	165.1	-327.0	-32.8	-30.7	63.5
def2-TZVP-uncS	-84.3	-89.5	-482.5	-288.6	69.8	165.3	162.1	-327.4	-30.8	-32.9	63.6
aug-cc-pVTZ-Jmod	-97.3	-102.9	-492.6	-301.2	70.3	165.1	161.7	-326.8	-31.5	-33.6	65.2
<i>Exp.</i>	<i>140.1</i>	<i>140.1</i>	<i>487.3</i>								

**Table S8.** APDs of  $A_{33}$ ,  $A_{iso}$  and  $\Delta A$  of **[Cu(dtc)<sub>2</sub>]** for calculated hyperfine coupling constants obtained with the B3PW91 functional using different basis sets and compared to experimental values.

<i>Basis set</i>	$A_{33}$	$A_{iso}$	$\Delta A$	$APD(A_{33})$	$APD(A_{iso})$	$APD(\Delta A)$
aug-cc-pVTZ-Junc	-495.3	232.9	396.4	2	9	14
aug-cc-pVTZ-J	-493.2	231.5	395.3	1	9	14
CP(PPP)	-487.7	230.7	388.3	0	10	12
aug-cc-pVTZ	-281	6.4	414.7	42	97	19
aug-cc-pwCVTZ	-342.9	80.8	396.0	30	68	14
cc-pwCVTZ	-341.4	79.8	395.3	30	69	14
def2-TZVP	-266	2.5	397.8	45	99	15
def2-TZVP-uncS	-482.5	218.8	398.2	1	14	15
aug-cc-pVTZ-Jmod	-492.6	230.9	395.3	1	10	14
<i>Exp.</i>	<i>487.3</i>	<i>255.8</i>	<i>347.2</i>			

**Figure S4.** Graphical representation of APDs of  $A_{33}$ ,  $A_{iso}$  and  $\Delta A$  of **[Cu(dtc)<sub>2</sub>]** for calculated hyperfine coupling constants obtained with the B3PW91 functional and different basis.

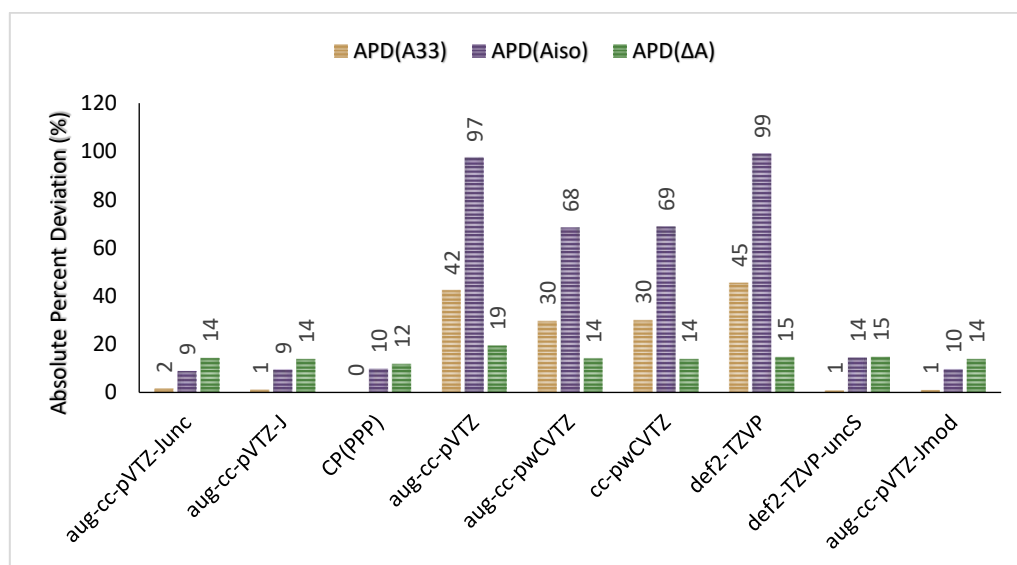


**Table S9.** Calculated HFCs (individual components and detailed contributions, in MHz) for **[Cu(dtc)<sub>2</sub>]** obtained with the TPSSh functional with different basis sets.

<i>Basis set</i>	$A_{11}$	$A_{22}$	$A_{33}$	$A^{FC}$	$A^{PC}$	$A_{11}^{SD}$	$A_{22}^{SD}$	$A_{33}^{SD}$	$A_{11}^{S,dip}$	$A_{22}^{S,dip}$	$A_{33}^{S,dip}$
aug-cc-pVTZ-Junc	-70.2	-74.5	-463.7	-261.5	58.7	158.1	155.4	-313.5	-25.5	-27.1	52.5
aug-cc-pVTZ-J	-77.6	-81.9	-469.7	-268.9	59.2	157.8	155.1	-312.9	-25.7	-27.3	53.0
CP(PPP)	-75.8	-80.1	-461.8	-263.2	57.3	154.9	151.9	-306.8	-24.8	-26.1	50.9
aug-cc-pVTZ	135.3	139.6	-272.9	-59.7	60.3	162.3	165.0	-327.3	-27.7	-26.1	53.8
aug-cc-pwCVTZ	42.8	47.2	-347.0	-143.8	58.1	155.5	158.3	-313.9	-27.0	-25.4	52.6
cc-pwCVTZ	45.8	50.2	-343.3	-140.5	58.0	155.2	158.1	-313.3	-26.9	-25.4	52.4
def2-TZVP	138.2	142.4	-253.9	-50.4	59.2	156.3	158.8	-315.1	-26.9	-25.3	52.3
def2-TZVP-uncS	-52.2	-56.3	-448.9	-245.2	59.4	159.0	156.4	-315.4	-25.4	-27.0	52.3
aug-cc-pVTZ-Jmod	-69.8	-74.1	-461.9	-261.1	59.2	157.8	155.1	-312.9	-25.7	-27.3	53.0
<i>Exp.</i>	140.1	140.1	487.3								

**Table S10.** APDs of  $A_{33}$ ,  $A_{iso}$  and  $\Delta A$  of **[Cu(dtc)<sub>2</sub>]** for calculated hyperfine coupling constants obtained with the TPSSh functional using different basis sets and compared to experimental values.

<i>Basis set</i>	$A_{33}$	$A_{iso}$	$\Delta A$	$APD(A_{33})$	$APD(A_{iso})$	$APD(\Delta A)$
aug-cc-pVTZ-Junc	-463.7	202.8	393.5	5	21	13
aug-cc-pVTZ-J	-469.7	209.7	392.1	4	18	13
CP(PPP)	-461.8	205.9	386.0	5	20	11
aug-cc-pVTZ	-272.9	0.7	412.5	44	100	19
aug-cc-pwCVTZ	-347	85.7	394.2	29	67	14
cc-pwCVTZ	-343.3	82.4	393.5	30	68	13
def2-TZVP	-253.9	8.9	396.3	48	97	14
def2-TZVP-uncS	-448.9	185.8	396.7	8	27	14
aug-cc-pVTZ-Jmod	-461.9	201.9	392.1	5	21	13
<i>Exp.</i>	487.3	255.8	347.2			

**Figure S5.** Graphical representation of absolute percent deviation of  $A_{33}$ ,  $A_{iso}$  and  $\Delta A$  of **[Cu(dtc)<sub>2</sub>]** for calculated hyperfine coupling constants obtained with the TPSSh functional and different basis sets.

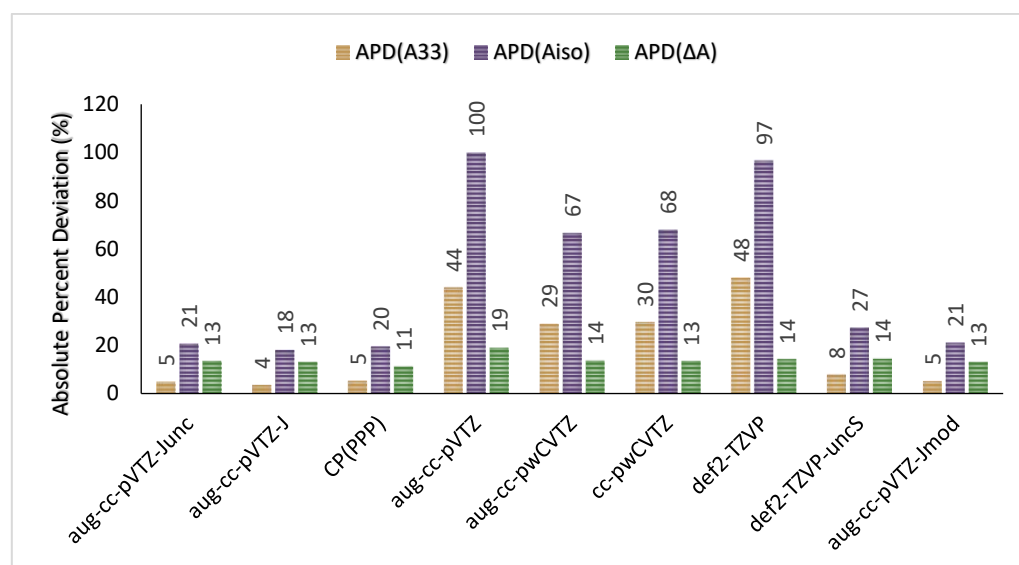


**Table S11.** Calculated HFCs (individual components and detailed contributions, in MHz) for **[Cu(acac)<sub>2</sub>]** obtained with the PBE0 functional with different basis sets.

<i>Basis set</i>	$A_{11}$	$A_{22}$	$A_{33}$	$A^{FC}$	$A^{PC}$	$A_{11}^{SD}$	$A_{22}^{SD}$	$A_{33}^{SD}$	$A_{11}^{S,dip}$	$A_{22}^{S,dip}$	$A_{33}^{S,dip}$
aug-cc-pVTZ-Junc	-49.2	-50.8	-644.2	-386.5	138.4	263.4	261.7	-525.1	-64.4	-64.4	129.0
aug-cc-pVTZ-J	-47.8	-49.4	-641.2	-385.7	139.5	263.3	261.8	-525.1	-64.9	-65.0	130.0
CP(PPP)	-58.8	-60.2	-637.2	-384.3	132.2	254.9	252.5	-507.4	-61.6	-60.6	122.3
aug-cc-pVTZ	-307.9	314.0	315.7	-34.8	142.1	-547.1	272.9	274.2	131.9	-66.1	-65.8
aug-cc-pwCVTZ	188.4	190.0	-404.5	-146.4	137.7	261.9	263.0	-524.8	-64.7	-64.3	129.0
cc-pwCVTZ	191.9	193.5	-399.6	-141.9	137.1	260.9	262.2	-523.2	-64.2	-64.0	128.3
def2-TZVP	-288.0	313.8	315.2	-27.4	141.0	-530.5	264.4	266.1	128.9	-64.3	-64.4
def2-TZVP-uncS	-26.4	-27.9	-629.9	-369.3	141.2	266.2	264.6	-530.8	-64.5	-64.4	129.0
aug-cc-pVTZ-Jmod	-46.7	-48.4	-640.1	-384.6	139.5	263.3	261.8	-525.1	-64.9	-65.1	130.0
<i>Exp.</i>	35.0	35.0	520.0								

**Table S12.** APDs of  $A_{33}$ ,  $A_{iso}$  and  $\Delta A$  of **[Cu(acac)<sub>2</sub>]** for calculated hyperfine coupling constants obtained with the PBE0 functional using different basis sets and compared to experimental values.

<i>Basis set</i>	$A_{33}$	$A_{iso}$	$\Delta A$	$APD(A_{33})$	$APD(A_{iso})$	$APD(\Delta A)$
aug-cc-pVTZ-Junc	-644.2	248.1	595.0	24	26	23
aug-cc-pVTZ-J	-641.2	246.1	593.4	23	25	22
CP(PPP)	-637.2	252.1	578.4	23	28	19
aug-cc-pVTZ	315.7	107.3	623.6	39	45	29
aug-cc-pwCVTZ	-404.5	8.7	594.5	22	96	23
cc-pwCVTZ	-399.6	4.7	593.1	23	98	22
def2-TZVP	315.2	113.7	603.2	39	42	24
def2-TZVP-uncS	-629.9	228.1	603.5	21	16	24
aug-cc-pVTZ-Jmod	-640.1	245.1	593.4	23	25	22
<i>Exp.</i>	520.0	196.7	485.0			

**Figure S6.** Graphical representation of APDs of  $A_{33}$ ,  $A_{iso}$  and  $\Delta A$  of **[Cu(acac)<sub>2</sub>]** for calculated hyperfine coupling constants obtained with the PBE0 functional.

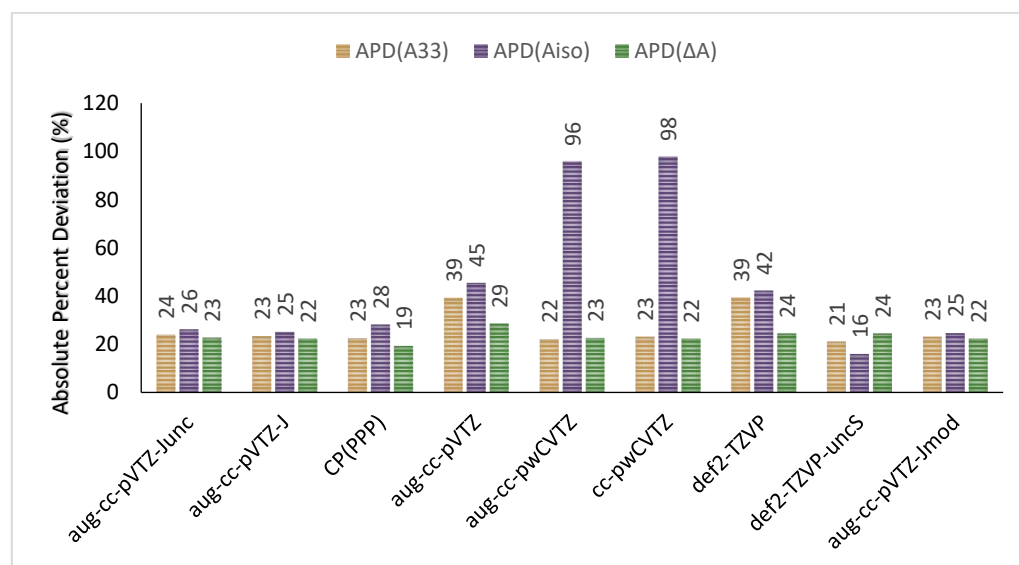


**Table S13.** Calculated HFCs (individual components and detailed contributions, in MHz) for  $[\text{Cu}(\text{acac})_2]$  obtained with the B3PW91 functional with different basis sets.

<i>Basis set</i>	$A_{11}$	$A_{22}$	$A_{33}$	$A^{FC}$	$A^{PC}$	$A_{11}^{SD}$	$A_{22}^{SD}$	$A_{33}^{SD}$	$A_{11}^{S,dip}$	$A_{22}^{S,dip}$	$A_{33}^{S,dip}$
aug-cc-pVTZ-Junc	-37.7	-38.1	-622.6	-361.0	128.2	254.2	255.2	-509.4	-59.1	-100.5	119.6
aug-cc-pVTZ-J	-36.1	-36.5	-619.4	-359.9	129.3	254.0	255.4	-509.3	-59.4	-61.2	120.6
CP(PPP)	-48.0	-48.4	-616.5	-359.8	122.2	247.0	245.0	-492.0	-57.4	-55.7	113.2
aug-cc-pVTZ	298.7	300.2	-302.3	-30.6	129.5	259.9	261.6	-521.5	-60.0	-60.4	120.3
aug-cc-pwCVTZ	188.7	190.0	-385.2	-128.0	125.8	249.8	251.2	-501.0	-58.9	-59.0	118.1
cc-pwCVTZ	191.6	192.9	-380.8	-124.1	125.3	248.9	250.5	-499.4	-58.5	-58.8	117.4
def2-TZVP	-281.6	298.7	300.1	-22.0	127.7	-504.1	251.0	253.2	116.8	-58.0	-58.9
def2-TZVP-uncS	-24.1	-25.4	-606.0	-346.3	127.8	253.3	251.1	-504.4	-58.9	-58.0	117.0
aug-cc-pVTZ-Jmod	-40.9	-42.3	-615.4	-360.4	127.5	251.6	249.8	-501.4	-59.7	-59.2	118.9
<i>Exp.</i>	35.0	35.0	520.0								

**Table S14.** APDs of  $A_{33}$ ,  $A_{iso}$  and  $\Delta A$  of  $[\text{Cu}(\text{acac})_2]$  for calculated hyperfine coupling constants obtained with the B3PW91 functional using different basis sets and compared to experimental values.

<i>Basis set</i>	$A_{33}$	$A_{iso}$	$\Delta A$	$APD(A_{33})$	$APD(A_{iso})$	$APD(\Delta A)$
aug-cc-pVTZ-Junc	-622.6	232.8	584.9	20	18	21
aug-cc-pVTZ-J	-619.4	230.7	583.3	19	17	20
CP(PPP)	-616.5	237.6	568.5	19	21	17
aug-cc-pVTZ	-302.3	98.9	602.5	42	50	24
aug-cc-pwCVTZ	-385.2	2.2	575.2	26	99	19
cc-pwCVTZ	-380.8	1.2	573.7	27	99	18
def2-TZVP	300.1	105.7	581.7	42	46	20
def2-TZVP-uncS	-606	218.5	581.9	17	11	20
aug-cc-pVTZ-Jmod	-615.4	232.9	574.5	18	18	18
<i>Exp.</i>	520.0	196.7	485.0			

**Figure S7.** Graphical representation of APDs of  $A_{33}$ ,  $A_{iso}$  and  $\Delta A$  of  $[\text{Cu}(\text{acac})_2]$  for calculated hyperfine coupling constants obtained with the B3PW91 functional and different basis sets.

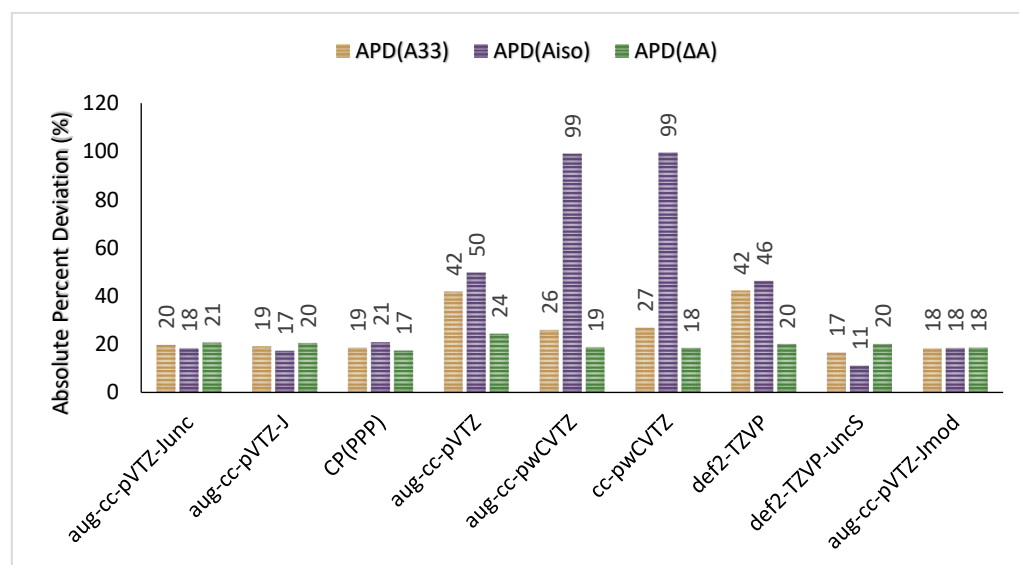




**Table S15.** Calculated HFCs (individual components and detailed contributions, in MHz) for  $[\text{Cu}(\text{acac})_2]$  obtained with the TPSSh functional with different basis sets.

<i>Basis set</i>	$A_{11}$	$A_{22}$	$A_{33}$	$A^{FC}$	$A^{PC}$	$A_{11}^{SD}$	$A_{22}^{SD}$	$A_{33}^{SD}$	$A_{11}^{S,dip}$	$A_{22}^{S,dip}$	$A_{33}^{S,dip}$
aug-cc-pVTZ-Junc	-23.7	-24.5	-606.1	-316.2	98.1	240.4	236.0	-476.5	-46.0	-42.4	88.5
aug-cc-pVTZ-J	-35.1	-36.0	-615.3	-327.8	98.9	240.0	235.7	-475.7	-46.3	-42.8	89.2
CP(PPP)	-42.8	-43.8	-607.0	-325.9	94.7	232.6	228.1	-460.7	-44.3	-40.7	84.9
aug-cc-pVTZ	279.6	281.2	-319.1	-18.9	99.5	242.4	246.5	-488.9	-43.4	-45.9	89.2
aug-cc-pwCVTZ	151.7	153.2	-420.4	-134.7	96.2	232.7	236.6	-469.3	-42.4	-44.9	87.3
cc-pwCVTZ	157.5	159.0	-412.7	-127.9	95.8	231.8	235.8	-467.6	-42.2	-44.7	87.0
def2-TZVP	281.1	282.6	-295.5	-9.2	98.7	233.9	238.3	-472.2	-42.3	-45.1	87.2
def2-TZVP-uncS	-8.2	-9.7	-586.6	-300.2	98.8	238.4	234.1	-472.5	-45.1	-42.3	87.3
aug-cc-pVTZ-Jmod	-23.2	-24.0	-603.4	-315.8	98.9	240.0	235.7	-475.7	-46.3	-42.8	89.2
<i>Exp.</i>	35.0	35.0	520.0								

**Table S16.** APDs of  $A_{33}$ ,  $A_{iso}$  and  $\Delta A$  of  $[\text{Cu}(\text{acac})_2]$  for calculated hyperfine coupling constants obtained with the TPSSh functional using different basis sets and compared to experimental values.

<i>Basis set</i>	$A_{33}$	$A_{iso}$	$\Delta A$	$APD(A_{33})$	$APD(A_{iso})$	$APD(\Delta A)$
aug-cc-pVTZ-Junc	-606.1	218.1	582.4	17	11	20
aug-cc-pVTZ-J	-615.3	228.8	580.2	18	16	20
CP(PPP)	-607	231.2	564.2	17	18	16
aug-cc-pVTZ	-319.1	80.6	600.3	39	59	24
aug-cc-pwCVTZ	-420.4	38.5	573.6	19	80	18
cc-pwCVTZ	-412.7	32.1	571.7	21	84	18
def2-TZVP	-295.5	89.4	578.1	43	55	19
def2-TZVP-uncS	-586.6	201.5	578.4	13	2	19
aug-cc-pVTZ-Jmod	-603.4	216.9	580.2	16	10	20
<i>Exp.</i>	520.0	196.7	485.0			

**Figure S8.** Graphical representation of APDs of  $A_{33}$ ,  $A_{iso}$  and  $\Delta A$  of  $[\text{Cu}(\text{acac})_2]$  for calculated hyperfine coupling constants obtained with the TPSSh functional and different basis sets.

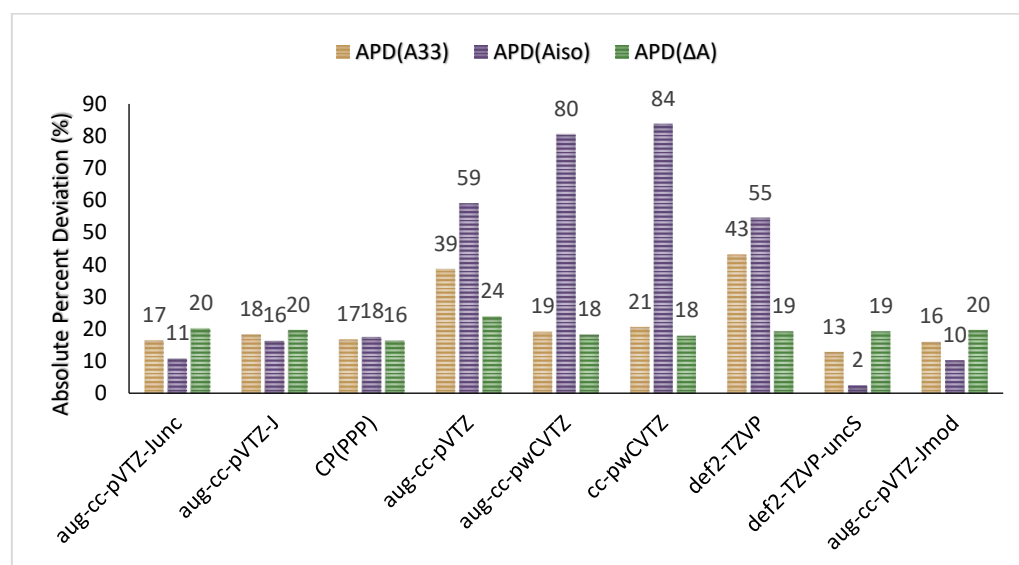


**Table S17.** Calculated HFCs (individual components and detailed contributions, in MHz) for  $[\text{Cu}(\text{NH}_3)_4]^{2+}$  obtained with the B3PW91 functional, DKH2 Hamiltonian with different basis sets.

<i>Basis set</i>	$A_{11}$	$A_{22}$	$A_{33}$	$A^{FC}$	$A^{PC}$	$A_{11}^{SD}$	$A_{22}^{SD}$	$A_{33}^{SD}$	$A_{11}^{SO,dip}$	$A_{22}^{SO,dip}$	$A_{33}^{SO,dip}$
aug-cc-pVTZ-Junc	-13.5	-14.0	-588.9	-335.0	129.5	249.4	248.9	-498.3	-57.4	-57.3	114.9
aug-cc-pVTZ-J	10.5	11.0	-562.9	-310.8	130.3	248.7	249.2	-497.9	-57.7	-57.7	115.4
CP(PPP)	-19.5	-19.8	-579.7	-330.3	124.0	241.4	241.0	-482.4	-54.6	-54.5	109.1
aug-cc-pVTZ-DK	-291.2	313.4	313.8	-21.0	133.0	-520.0	259.7	260.2	116.8	-58.3	-58.4
aug-cc-pwCVTZ-DK	198.0	198.5	-376.6	-122.4	129.1	248.7	249.2	-498.0	-57.3	-57.4	114.7
cc-pwCVTZ-DK	199.0	199.4	-375.2	-121.2	128.9	248.4	248.9	-497.3	-57.2	-57.2	114.4
DKH-def2-TZVP	-15.1	-15.5	-588.5	-332.9	126.5	247.4	246.9	-494.3	-56.1	-56.0	112.2
def2-TZVP-uncS	6.9	7.3	-578.9	-320.3	132.1	252.2	252.7	-504.9	-57.1	-57.1	114.2
aug-cc-pVTZ-Jmod	-12.1	-12.6	-591.5	-334.1	128.7	250.6	250.0	-500.6	-57.3	-57.2	114.6
<i>Exp.</i>	<i>68.8</i>	<i>68.8</i>	<i>586.5</i>								

**Table S18.** Calculated HFCs (individual components and detailed contributions, in MHz) for  $[\text{Cu}(\text{NH}_3)_4]^{2+}$  obtained with the B3PW91 functional, DKH2 Hamiltonian, and finite nucleus model with different basis sets.

<i>Basis set</i>	$A_{11}$	$A_{22}$	$A_{33}$	$A^{FC}$	$A^{PC}$	$A_{11}^{SD}$	$A_{22}^{SD}$	$A_{33}^{SD}$	$A_{11}^{SO,dip}$	$A_{22}^{SO,dip}$	$A_{33}^{SO,dip}$
aug-cc-pVTZ-Junc	0.4	0.9	-574.5	-320.6	129.5	248.9	249.4	-498.3	-57.3	-57.4	114.9
aug-cc-pVTZ-J	11.3	11.8	-562.2	-310.0	130.3	248.7	249.2	-497.9	-57.7	-57.7	115.4
CP(PPP)	-17.7	-18.1	-577.9	-328.6	124.0	241.4	241.0	-482.4	-54.6	-54.5	109.1
aug-cc-pVTZ-DK	-291.2	313.3	313.8	-21.1	133.0	-520.0	259.7	260.2	116.8	-58.3	-58.4
aug-cc-pwCVTZ-DK	198.2	198.7	-376.4	-122.3	129.1	248.7	249.2	-498.0	-57.3	-57.4	114.7
cc-pwCVTZ-DK	199.1	199.6	-375.0	-121.0	128.9	248.4	248.9	-497.3	-57.2	-57.2	114.4
DKH-def2-TZVP	-14.9	-15.4	-588.3	-332.7	126.5	247.4	246.9	-494.3	-56.1	-56.0	112.2
def2-TZVP-uncS	7.1	7.5	-578.7	-320.1	132.1	252.2	252.7	-504.9	-57.1	-57.2	114.2
aug-cc-pVTZ-Jmod	-5.2	-5.6	-584.5	-327.2	128.7	250.6	250.0	-500.6	-57.3	-57.2	114.6
<i>Exp.</i>	<i>68.8</i>	<i>68.8</i>	<i>586.5</i>								

**Table S19.** Calculated HFCs (individual components and detailed contributions, in MHz) for  $[\text{Cu}(\text{NH}_3)_4]^{2+}$  obtained with the B3PW91 functional and ZORA Hamiltonian with different basis sets.

<i>Basis set</i>	$A_{11}$	$A_{22}$	$A_{33}$	$A^{FC}$	$A^{PC}$	$A_{11}^{SD}$	$A_{22}^{SD}$	$A_{33}^{SD}$	$A_{11}^{SO,dip}$	$A_{22}^{SO,dip}$	$A_{33}^{SO,dip}$
aug-cc-pVTZ-Junc	-57.4	-57.8	-633.6	-379.0	129.4	249.6	249.1	-498.7	-57.4	-57.3	114.7
aug-cc-pVTZ-J	-34.0	-34.4	-608.9	-355.9	130.1	249.4	249.0	-498.4	-57.7	-57.6	115.2
CP(PPP)	-60.9	-61.2	-622.0	-371.8	123.8	241.6	241.3	-482.9	-54.5	-54.4	108.9
aug-cc-pVTZ	-278.6	328.0	328.3	-7.6	133.5	-521.7	260.6	261.1	117.2	-58.6	-58.7
aug-cc-pwCVTZ	235.7	236.1	-341.3	-85.1	128.6	249.3	249.7	-499.0	-57.1	-57.2	114.2
cc-pwCVTZ	237.7	238.1	-338.8	-82.7	128.4	249.0	249.4	-498.4	-56.9	-57.0	113.9
ZORA-def2-TZVP	-51.9	-52.2	626.1	-369.5	126.1	247.5	247.1	-494.5	-56.0	-55.9	111.8
def2-TZVP-uncS	-1.0	-1.4	-580.4	-325.0	130.7	250.1	249.6	-499.8	-56.9	-56.8	113.7
aug-cc-pVTZ-Jmod	-54.1	-54.4	-629.0	-376.0	130.1	249.4	249.0	-498.4	-57.7	-57.6	115.2
<i>Exp.</i>	<i>68.8</i>	<i>68.8</i>	<i>586.5</i>								

**Table S20.** APDs of  $A_{33}$ ,  $A_{iso}$  and  $\Delta A$  of  $[\text{Cu}(\text{NH}_3)_4]^{2+}$  for calculated hyperfine coupling constants obtained with the PBE0 and B3PW91 functionals, using the DKH2 and ZORA Hamiltonians and the aug-cc-pVTZ-J-mod basis.

<i>Functional</i>	<i>Relativistic Method</i>	$A_{33}$	$A_{iso}$	$\Delta A$	$APD(A_{33})$	$APD(A_{iso})$	$APD(\Delta A)$
PBE0	DKH2	-604.7	-213.6	586.9	3	12	13
	DKH2-FN	-603.4	-208.6	592.4	3	14	14
	ZORA	-651.0	-259.2	588.0	11	7	14
	None	-606.4	-218.2	582.6	3	10	13
	<i>Exp.</i>	586.5	241.4	517.7	-	-	-
B3PW91	DKH2	-591.5	-205.4	579.4	1	15	12
	DKH2-FN	-584.5	-198.4	579.3	0	18	12
	ZORA	-629.0	-245.8	574.9	7	2	11
	None	-591.2	-210.0	572.0	1	13	10
	<i>Exp.</i>	586.5	241.4	517.7	-	-	-

**Figure S9.** Graphical representation of APDs of  $A_{33}$ ,  $A_{iso}$  and  $\Delta A$  of  $[\text{Cu}(\text{NH}_3)_4]^{2+}$  for calculated hyperfine coupling constants obtained with the PBE0 functional, using the DKH2 and ZORA Hamiltonians and the aug-cc-pVTZ-J-mod basis set.

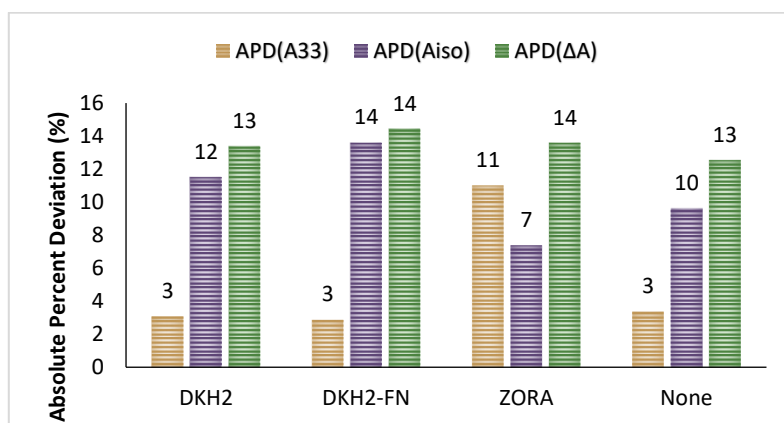


**Figure S10.** Graphical representation of APDs of  $A_{33}$ ,  $A_{iso}$  and  $\Delta A$  of  $[\text{Cu}(\text{NH}_3)_4]^{2+}$  for calculated hyperfine coupling constants obtained with the B3PW91 functional, using the DKH2 and ZORA Hamiltonians and the aug-cc-pVTZ-J-mod basis set.

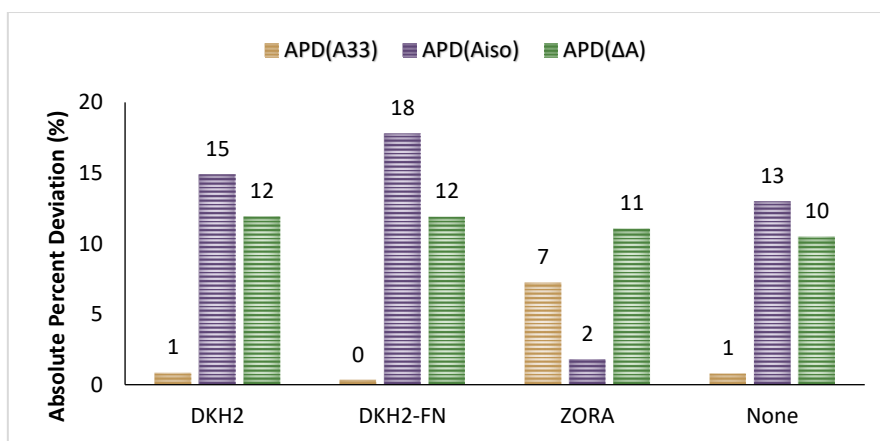


**Table S21.** Calculated HFCs (individual components, in MHz) and APDs of  $A_{33}$ ,  $A_{iso}$  and  $\Delta A$  with respect to experimental values for **[Cu(dtc)<sub>2</sub>]** obtained with the aug-cc-pVTZ-Jmod basis set with different functionals.

<i>Functional</i>	<i>A<sub>11</sub></i>	<i>A<sub>22</sub></i>	<i>A<sub>33</sub></i>	<i>A<sub>iso</sub></i>	<i>ΔA</i>	<i>APD(A<sub>33</sub>)</i>	<i>APD(A<sub>iso</sub>)</i>	<i>APD(ΔA)</i>
B3LYP	-82.7	-88.3	-476.7	215.9	394.0	2.2	15.6	13.5
B3PW91	-97.3	-102.9	-492.6	230.9	395.3	1.1	9.7	13.9
CAM-B3LYP	-121.0	-128.4	-551.1	266.8	430.1	13.1	4.3	23.9
M06	94.5	102.7	-234.0	12.3	336.7	52.0	95.2	3.0
M062X	-257.7	-264.5	-679.8	400.7	422.1	39.5	56.6	21.6
PBE	-41.1	-45.5	-384.0	156.9	342.9	21.2	38.7	1.2
PBE0	-109.3	-114.8	-525.5	249.9	416.2	7.8	2.3	19.9
SCAN	-88.4	-91.5	-516.6	232.2	428.2	6.0	9.3	23.3
TPSS	-41.5	-45.2	-405.7	164.1	364.2	16.7	35.8	4.9
TPSSh	-69.8	-74.1	-461.9	201.9	392.1	5.2	21.1	12.9
<i>Exp.</i>	<i>140.1</i>	<i>140.1</i>	<i>487.3</i>	<i>255.8</i>	<i>347.2</i>			

**Table S22.** Calculated HFCs (individual components, in MHz) and APDs of  $A_{33}$ ,  $A_{iso}$  and  $\Delta A$  with respect to experimental results for **[Cu(acac)<sub>2</sub>]** obtained with the aug-cc-pVTZ-Jmod basis set with different functionals.

<i>Functional</i>	<i>A<sub>11</sub></i>	<i>A<sub>22</sub></i>	<i>A<sub>33</sub></i>	<i>A<sub>iso</sub></i>	<i>ΔA</i>	<i>APD(A<sub>33</sub>)</i>	<i>APD(A<sub>iso</sub>)</i>	<i>APD(ΔA)</i>
B3LYP	-15.9	-16.3	-605.4	212.5	589.5	16.4	8.1	21.5
B3PW91	-40.9	-42.3	-615.4	232.9	574.5	18.3	18.4	18.5
CAM-B3LYP	-56.3	-59.4	-804.6	306.8	748.3	54.7	56.0	54.3
M06	-133.4	236.0	240.5	114.4	373.9	53.8	41.8	22.9
M062X	-298.6	-306.1	-638.8	414.5	340.2	22.8	110.8	29.9
PBE	-10.4	-10.7	-506.0	175.7	495.6	2.7	10.7	2.2
PBE0	-46.7	-48.4	-640.1	245.1	593.4	23.1	24.6	22.4
SCAN	118.2	233.4	-258.9	30.9	492.3	50.2	84.3	1.5
TPSS	-6.1	-6.8	-537.7	183.5	531.6	3.4	6.7	9.6
TPSSh	-23.2	-24.0	-603.4	216.9	580.2	16.0	10.3	19.6
<i>Exp.</i>	<i>35.0</i>	<i>35.0</i>	<i>520.0</i>	<i>196.7</i>	<i>485.0</i>			

**Table S23.** Calculated HFCs (individual components, in MHz) and APDs of  $A_{33}$ ,  $A_{iso}$  and  $\Delta A$  with respect to experimental results for **[Cu(en)<sub>2</sub>]<sup>2+</sup>** obtained with the aug-cc-pVTZ-Jmod basis set with different functionals.

<i>Functional</i>	<i>A<sub>11</sub></i>	<i>A<sub>22</sub></i>	<i>A<sub>33</sub></i>	<i>A<sub>iso</sub></i>	<i>ΔA</i>	<i>APD(A<sub>33</sub>)</i>	<i>APD(A<sub>iso</sub>)</i>	<i>APD(ΔA)</i>
B3LYP	-55.3	-56.0	-620.0	243.8	564.7	3.0	4.0	7.8
B3PW91	-72.5	-73.3	-635.0	260.3	562.5	5.5	2.5	7.3
CAM-B3LYP	-60.2	-61.6	-650.9	257.6	590.7	8.1	1.4	12.7
M06	196.2	197.3	-234.1	53.1	431.4	61.1	79.1	17.7
M062X	-296.0	-296.8	-717.6	436.8	421.6	19.2	72.0	19.5
PBE	-27.7	-28.0	-528.3	194.7	500.6	12.2	23.4	4.5
PBE0	-80.7	-81.6	-659.4	273.9	578.7	9.5	7.8	10.4
SCAN	-23.1	-25.2	-654.0	234.1	630.9	8.6	7.8	20.4
TPSS	-26.4	-26.8	-555.3	202.8	528.9	7.8	20.1	0.9
TPSSh	-50.9	-51.5	-613.2	238.5	562.3	1.9	6.1	7.3
<i>Exp.</i>	<i>78.0</i>	<i>82.0</i>	<i>602.0</i>	<i>254.0</i>	<i>524.0</i>			

**Table S24.** Calculated HFCs (individual components, in MHz) and APDs of  $A_{33}$ ,  $A_{iso}$  and  $\Delta A$  with respect to experimental results for  $[\text{Cu}(\text{mnt})_2]^{2-}$  obtained with the aug-cc-pVTZ-Jmod basis set with different functionals.

<i>Functional</i>	$A_{11}$	$A_{22}$	$A_{33}$	$A_{iso}$	$\Delta A$	$APD(A_{33})$	$APD(A_{iso})$	$APD(\Delta A)$
B3LYP	-66.0	-71.7	-488.1	208.6	422.1	1.1	12.3	14.5
B3PW91	-82.2	-87.5	-503.8	224.5	421.6	4.4	5.6	14.3
CAM-B3LYP	-101.6	-106.2	-559.2	255.7	457.6	15.8	7.5	24.1
M06	125.6	130.7	-252.0	1.4	382.7	47.8	99.4	3.8
M062X	-270.5	-271.5	-766.2	436.1	495.7	58.7	83.3	34.4
PBE	-34.0	-39.8	-390.0	154.6	356.0	19.2	35.0	3.5
PBE0	-95.3	-100.1	-538.3	244.6	443.0	11.5	2.8	20.1
SCAN	19.3	31.6	-129.2	26.1	160.8	73.2	89.0	56.4
TPSS	-35.6	-41.0	-409.9	162.2	374.3	15.1	31.8	1.5
TPSSh	-60.2	-65.4	-468.2	197.9	408.0	3.0	16.8	10.6
<i>Exp.</i>	<i>113.9</i>	<i>116.9</i>	<i>482.7</i>	<i>237.8</i>	<i>368.8</i>			

**Table S25.** Calculated HFCs (individual components, in MHz) and APDs of  $A_{33}$ ,  $A_{iso}$  and  $\Delta A$  with respect to experimental results for  $[\text{Cu}(\text{gly})_2]$  obtained with the aug-cc-pVTZ-Jmod basis set with different functionals.

<i>Functional</i>	$A_{11}$	$A_{22}$	$A_{33}$	$A_{iso}$	$\Delta A$	$APD(A_{33})$	$APD(A_{iso})$	$APD(\Delta A)$
B3LYP	-27.5	34.4	-581.6	191.6	616.0	9.8	6.7	26.5
B3PW91	16.0	-46.7	-596.5	209.1	612.5	12.6	1.8	25.8
CAM-B3LYP	32.7	-35.5	-618.1	207.0	650.8	16.6	0.8	33.7
M06	-171.6	237.3	281.0	115.6	452.6	47.0	43.7	7.0
M062X	-261.3	-300.5	-703.8	421.9	442.5	32.8	105.4	9.1
PBE	15.8	56.5	-458.5	128.7	515.0	13.5	37.3	5.8
PBE0	5.9	-61.5	-627.0	227.5	632.9	18.3	10.8	30.0
SCAN	13.1	105.4	-581.0	154.2	686.4	9.6	24.9	41.0
TPSS	14.2	61.7	-490.0	138.0	551.7	7.5	32.8	13.3
TPSSh	-21.6	37.1	-567.2	183.9	604.3	7.0	10.5	24.1
<i>Exp.</i>	<i>43.1</i>	<i>43.1</i>	<i>529.9</i>	<i>205.4</i>	<i>486.8</i>			

**Table S26.** Calculated HFCs (individual components, in MHz) and APDs of  $A_{33}$ ,  $A_{iso}$  and  $\Delta A$  with respect to experimental results for  $[\text{Cu}(\text{kts})]$  obtained with the aug-cc-pVTZ-Jmod basis set with different functionals.

<i>Functional</i>	$A_{11}$	$A_{22}$	$A_{33}$	$A_{iso}$	$\Delta A$	$APD(A_{33})$	$APD(A_{iso})$	$APD(\Delta A)$
B3LYP	-39.9	-45.1	-548.1	211.0	508.2	4.7	16.8	5.4
B3PW91	-55.9	-61.3	-562.3	226.5	506.4	2.2	10.7	5.0
CAM-B3LYP	-96.0	-101.1	-725.6	307.6	629.6	26.2	21.3	30.6
M06	192.1	200.7	-212.7	60.0	413.4	63.0	76.3	14.3
M062X	-247.6	-254.0	-683.9	395.2	436.3	18.9	55.8	9.5
PBE	-15.1	-20.2	-445.2	160.2	430.1	22.6	36.9	10.8
PBE0	-62.9	-68.3	-592.3	241.2	529.4	3.0	4.9	9.8
SCAN	-11.1	-15.8	-558.5	195.1	547.4	2.9	23.1	13.5
TPSS	-9.5	-14.0	-467.2	163.6	457.7	18.8	35.5	5.1
TPSSh	-32.2	-36.8	-530.6	199.9	498.4	7.7	21.2	3.4
<i>Exp.</i>	<i>92.9</i>	<i>92.9</i>	<i>575.1</i>	<i>253.6</i>	<i>482.2</i>			

**Table S27.** Calculated HFCs (individual components, in MHz) and APDs of  $A_{33}$ ,  $A_{iso}$  and  $\Delta A$  with respect to experimental results for **[Cu(sac)<sub>2</sub>]** obtained with the aug-cc-pVTZ-Jmod basis set with different functionals.

<i>Functional</i>	$A_{11}$	$A_{22}$	$A_{33}$	$A_{iso}$	$\Delta A$	$APD(A_{33})$	$APD(A_{iso})$	$APD(\Delta A)$
B3LYP	37.4	49.9	-566.6	159.8	616.5	20.4	18.9	50.1
B3PW91	16.7	32.0	-581.1	177.5	613.1	23.5	9.9	49.3
CAM-B3LYP	39.1	56.6	-591.5	165.3	648.1	25.7	16.1	57.8
M06	-162.4	299.1	315.9	150.9	478.3	32.9	23.4	16.5
M062X	-237.1	-271.1	-730.4	412.9	493.3	55.2	109.7	20.1
PBE	42.4	50.0	-474.3	127.3	524.3	0.8	35.3	27.7
PBE0	5.4	26.3	-607.0	191.8	633.3	29.0	2.6	54.2
SCAN	102.8	135.0	-252.1	4.8	387.1	46.4	97.6	5.7
TPSS	49.7	54.0	-499.4	131.9	553.4	6.1	33.0	34.7
TPSSh	33.2	39.7	-560.3	162.5	600.0	19.0	17.5	46.1
<i>Exp.</i>	<i>60.0</i>	<i>60.0</i>	<i>470.7</i>	<i>196.9</i>	<i>410.7</i>			

**Table S28.** Calculated HFCs (individual components, in MHz) and APDs of  $A_{33}$ ,  $A_{iso}$  and  $\Delta A$  with respect to experimental results for **[Cu(im)<sub>4</sub>]<sup>2+</sup>** obtained with the aug-cc-pVTZ-Jmod basis set with different functionals.

<i>Functional</i>	$A_{11}$	$A_{22}$	$A_{33}$	$A_{iso}$	$\Delta A$	$APD(A_{33})$	$APD(A_{iso})$	$APD(\Delta A)$
B3LYP	-6.7	-7.5	-610.9	208.4	604.2	8.4	9.4	20.7
B3PW91	-23.9	-24.6	-624.2	224.2	600.3	10.7	2.5	19.9
CAM-B3LYP	-10.2	-11.0	-636.0	219.1	625.8	12.8	4.8	25.0
M06	-181.8	254.8	256.3	109.8	438.1	54.5	52.3	12.5
M062X	-285.1	-287.2	-701.4	424.6	416.3	24.4	84.5	16.8
PBE	5.8	6.5	-534.1	173.9	540.6	5.3	24.4	8.0
PBE0	-33.1	-33.9	-646.3	237.8	613.2	14.6	3.3	22.5
SCAN	23.8	24.1	-654.2	202.1	678.3	16.0	12.2	35.5
TPSS	15.4	15.9	-554.8	174.5	570.7	1.6	24.2	14.0
TPSSh	-3.5	-4.1	-607.7	205.1	604.2	7.8	10.9	20.7
<i>Exp.</i>	<i>63.2</i>	<i>63.2</i>	<i>563.8</i>	<i>230.1</i>	<i>500.6</i>			

**Table S29.** Calculated HFCs (individual components, in MHz) and APDs of  $A_{33}$ ,  $A_{iso}$  and  $\Delta A$  with respect to experimental results for **[Cu(py)<sub>4</sub>]<sup>2+</sup>** obtained with the aug-cc-pVTZ-Jmod basis set with different functionals.

<i>Functional</i>	$A_{11}$	$A_{22}$	$A_{33}$	$A_{iso}$	$\Delta A$	$APD(A_{33})$	$APD(A_{iso})$	$APD(\Delta A)$
B3LYP	-39.7	-40.6	-602.9	227.7	563.2	7.0	3.3	9.4
B3PW91	-55.6	-56.5	-615.0	242.4	559.4	9.1	10.0	8.7
CAM-B3LYP	-43.5	-44.5	-634.2	240.7	590.7	12.5	9.2	14.8
M06	-201.1	209.8	211.5	73.4	412.6	62.5	66.7	19.8
M062X	-294.6	-297.9	-689.4	427.3	394.8	22.3	93.9	23.3
PBE	-19.1	-19.5	-509.7	182.8	490.6	9.5	17.1	4.7
PBE0	-64.1	-65.2	-640.0	256.4	575.9	13.6	16.4	11.9
SCAN	-6.7	-7.4	-631.8	215.3	625.1	12.1	2.3	21.4
TPSS	-11.2	-11.7	-531.8	184.9	520.6	5.6	16.1	1.1
TPSSh	-33.1	-33.7	-591.7	219.5	558.6	5.0	0.4	8.5
<i>Exp.</i>	<i>48.8</i>	<i>48.8</i>	<i>563.5</i>	<i>220.4</i>	<i>514.7</i>			

**Table S30.** Calculated HFCs (individual components, in MHz) and APDs of  $A_{33}$ ,  $A_{iso}$  and  $\Delta A$  with respect to experimental results for  $[\text{Cu}(\text{eta})]^{2+}$  obtained with the aug-cc-pVTZ-Jmod basis set with different functionals.

<i>Functional</i>	$A_{11}$	$A_{22}$	$A_{33}$	$A_{iso}$	$\Delta A$	$APD(A_{33})$	$APD(A_{iso})$	$APD(\Delta A)$
B3LYP	-44.9	-66.7	-525.4	212.3	480.5	1.2	10.6	8.9
B3PW91	-56.7	-78.8	-537.3	224.3	480.6	1.0	5.6	8.9
CAM-B3LYP	-60.2	-84.0	-588.0	244.1	527.8	10.6	2.7	19.6
M06	141.4	162.9	-231.2	24.4	394.1	56.5	89.7	10.7
M062X	-248.4	-267.9	-688.7	401.7	440.3	29.5	69.1	0.2
PBE	-7.4	-30.0	-401.8	146.4	394.4	24.4	38.4	10.6
PBE0	-65.2	-87.0	-572.1	241.4	506.9	7.6	1.6	14.9
SCAN	-4.3	-52.4	-572.7	209.8	568.4	7.7	11.7	28.8
TPSS	-0.8	-22.8	-422.6	148.7	421.8	20.5	37.4	4.4
TPSSh	-27.3	-48.9	-494.8	190.3	467.5	7.0	19.9	5.9
<i>Exp.</i>	<i>90.5</i>	<i>90.5</i>	<i>531.8</i>	<i>237.6</i>	<i>441.3</i>			

**Table S31.** Calculated HFCs (individual components, in MHz) and APDs of  $A_{33}$ ,  $A_{iso}$  and  $\Delta A$  with respect to experimental results for  $[\text{Cu}(\text{epa})(\text{H}_2\text{O})]^{2+}$  obtained with the aug-cc-pVTZ-Jmod basis set with different functionals.

<i>Functional</i>	$A_{11}$	$A_{22}$	$A_{33}$	$A_{iso}$	$\Delta A$	$APD(A_{33})$	$APD(A_{iso})$	$APD(\Delta A)$
B3LYP	-19.0	-21.9	-588.5	209.8	569.5	12.2	11.4	31.9
B3PW91	-34.9	-38.0	-600.9	224.6	566.0	14.5	5.2	31.1
CAM-B3LYP	-20.3	-23.7	-617.3	220.4	597.0	17.7	6.9	38.3
M06	-202.5	230.4	234.8	87.6	437.3	55.2	63.0	1.3
M062X	-275.6	-279.4	-711.6	422.2	436.0	35.6	78.3	1.0
PBE	-5.8	-7.0	-496.8	169.9	491.0	5.3	28.3	13.7
PBE0	-42.7	-45.8	-626.0	238.2	583.3	19.3	0.6	35.1
SCAN	37.1	40.6	-572.0	164.8	612.6	9.0	30.4	41.9
TPSS	2.6	3.5	-517.8	170.6	521.3	1.3	28.0	20.8
TPSSh	-14.3	-16.9	-576.2	202.5	561.9	9.8	14.5	30.2
<i>Exp.</i>	<i>92.9</i>	<i>92.9</i>	<i>524.6</i>	<i>236.8</i>	<i>431.7</i>			

**Table S32.** Calculated HFCs (individual components, in MHz) and APDs of  $A_{33}$ ,  $A_{iso}$  and  $\Delta A$  with respect to experimental results for  $[\text{Cu}(\text{atpt})]^{2+}$  obtained with the aug-cc-pVTZ-Jmod basis set with different functionals.

<i>Functional</i>	$A_{11}$	$A_{22}$	$A_{33}$	$A_{iso}$	$\Delta A$	$APD(A_{33})$	$APD(A_{iso})$	$APD(\Delta A)$
B3LYP	-32.4	-46.1	-396.8	158.4	364.4	23.7	10.8	36.6
B3PW91	-40.9	-54.6	-407.1	167.5	366.2	26.9	17.2	37.3
CAM-B3LYP	-54.8	-70.7	-456.8	194.1	402.0	42.4	35.8	50.7
M06	-117.3	136.6	155.0	58.1	272.3	51.7	59.4	2.1
M062X	-176.4	-215.3	-482.6	291.4	306.2	50.4	103.9	14.8
PBE	-5.7	-17.1	-302.6	108.5	296.9	5.7	24.1	11.3
PBE0	-47.2	-61.1	-438.1	182.1	390.9	36.6	27.4	46.5
SCAN	-3.2	0.7	-403.1	135.2	403.8	25.7	5.4	51.3
TPSS	1.6	-8.5	-321.7	109.5	323.3	0.3	23.4	21.2
TPSSh	-18.2	-30.1	-379.1	142.5	360.9	18.2	0.3	35.3
<i>Exp.</i>	<i>54.0</i>	<i>54.0</i>	<i>320.8</i>	<i>142.9</i>	<i>266.8</i>			

**Table S33.** Calculated HFCs (individual components, in MHz) and APDs of  $A_{33}$ ,  $A_{iso}$  and  $\Delta A$  with respect to experimental results for  $[\text{Cu}(\text{GGH})_2]^-$  obtained with the aug-cc-pVTZ-Jmod basis set with different functionals.

<i>Functional</i>	$A_{11}$	$A_{22}$	$A_{33}$	$A_{iso}$	$\Delta A$	$APD(A_{33})$	$APD(A_{iso})$	$APD(\Delta A)$
B3LYP	-45.8	-52.8	-599.0	232.5	553.2	3.4	7.2	0.1
B3PW91	-64.8	-72.0	-613.5	250.1	548.7	1.0	0.2	1.0
CAM-B3LYP	-38.9	-46.3	-619.6	234.9	580.7	0.1	6.3	4.8
M06	-59.8	212.9	225.2	126.1	285.0	63.7	49.7	48.6
M062X	-252.2	-267.1	-412.1	310.5	159.9	33.5	23.9	71.1
PBE	-27.7	-32.3	-438.1	166.0	410.4	29.3	33.8	25.9
PBE0	-69.1	-76.1	-631.9	259.0	562.8	1.9	3.3	1.6
SCAN	6.6	-32.9	-430.2	152.2	436.8	30.6	39.3	21.2
TPSS	-29.5	-34.4	-511.3	191.7	481.8	17.5	23.5	13.0
TPSSh	-53.5	-59.8	-608.0	240.4	554.5	1.9	4.1	0.1
<i>Exp.</i>	<i>66.0</i>	<i>66.0</i>	<i>620.0</i>	<i>250.7</i>	<i>554.0</i>			

**Table S34.** Calculated HFCs (individual components, in MHz) and APDs of  $A_{33}$ ,  $A_{iso}$  and  $\Delta A$  with respect to experimental results for  $[\text{Cu}(\text{GGG})]^-$  obtained with the aug-cc-pVTZ-Jmod basis set with different functionals.

<i>Functional</i>	$A_{11}$	$A_{22}$	$A_{33}$	$A_{iso}$	$\Delta A$	$APD(A_{33})$	$APD(A_{iso})$	$APD(\Delta A)$
B3LYP	-30.4	-40.5	-615.7	228.9	585.3	2.2	5.8	8.5
B3PW91	-46.8	-57.0	-628.7	244.2	581.9	4.3	0.5	7.8
CAM-B3LYP	-34.7	-46.2	-651.1	244.0	616.4	8.0	0.5	14.2
M06	206.4	218.9	-268.7	52.2	487.6	55.4	78.5	9.6
M062X	-296.2	-307.5	-810.3	471.3	514.1	34.5	94.1	4.7
PBE	1.1	-12.4	-497.7	169.7	498.8	17.4	30.1	7.6
PBE0	-57.8	-68.2	-658.8	261.6	601.0	9.3	7.7	11.4
SCAN	-6.0	-17.0	-626.0	216.3	620.0	3.9	10.9	14.9
TPSS	4.2	-6.7	-521.1	174.5	525.3	13.5	28.1	2.7
TPSSh	-22.8	-32.3	-592.3	215.8	569.5	1.7	11.1	5.5
<i>Exp.</i>	<i>63.0</i>	<i>63.0</i>	<i>602.6</i>	<i>242.9</i>	<i>539.6</i>			

**Table S35.** Calculated HFCs (individual components, in MHz) and APDs of  $A_{33}$ ,  $A_{iso}$  and  $\Delta A$  with respect to experimental results for  $[\text{Cu}(\text{salpn})_2]$  obtained with the aug-cc-pVTZ-Jmod basis set with different functionals.

<i>Functional</i>	$A_{11}$	$A_{22}$	$A_{33}$	$A_{iso}$	$\Delta A$	$APD(A_{33})$	$APD(A_{iso})$	$APD(\Delta A)$
B3LYP	3.0	-0.1	-571.1	189.4	574.1	8.4	8.5	19.7
B3PW91	-10.6	-21.7	-584.3	205.5	573.7	10.9	0.7	19.6
CAM-B3LYP	3.7	5.4	-601.7	197.5	607.1	14.2	4.6	26.6
M06	-150.4	245.4	263.5	119.5	413.9	50.0	42.3	13.7
M062X	-254.0	-276.1	-655.5	395.2	401.5	24.5	90.9	16.3
PBE	5.7	6.3	-471.5	153.2	477.8	10.5	26.0	0.4
PBE0	-15.8	-29.3	-610.6	218.6	594.8	15.9	5.6	24.0
SCAN	39.3	47.8	-585.1	166.0	632.9	11.1	19.8	32.0
TPSS	14.3	17.5	-495.0	154.4	512.5	6.0	25.4	6.9
TPSSh	2.1	-2.2	-560.1	186.7	562.2	6.3	9.8	17.2
<i>Exp.</i>	<i>47.1</i>	<i>47.1</i>	<i>526.7</i>	<i>207.0</i>	<i>479.6</i>			



**Table S36.** Calculated HFCs (individual components, in MHz) and APDs of  $A_{33}$ ,  $A_{iso}$  and  $\Delta A$  with respect to experimental results for **[Cu((S,S)-mnpala)<sub>2</sub>]** obtained with the aug-cc-pVTZ-Jmod basis set with different functionals.

<i>Functional</i>	$A_{11}$	$A_{22}$	$A_{33}$	$A_{iso}$	$\Delta A$	$APD(A_{33})$	$APD(A_{iso})$	$APD(\Delta A)$
B3LYP	-49.5	-55.7	-618.5	241.2	569.0	6.3	1.4	10.4
B3PW91	-66.3	-72.5	-631.6	256.8	565.3	8.6	8.0	9.6
CAM-B3LYP	-47.2	-53.8	-650.8	250.6	603.6	11.9	5.4	17.1
M06	187.3	197.6	-218.6	55.4	416.2	62.4	76.7	19.3
M062X	-302.1	-312.3	-705.0	439.8	402.9	21.2	84.9	21.9
PBE	-19.9	-26.6	-501.2	182.6	481.3	13.8	23.2	6.7
PBE0	-74.1	-80.2	-658.8	271.0	584.7	13.3	13.9	13.4
SCAN	-6.9	-14.4	-627.5	216.3	620.6	7.9	9.1	20.4
TPSS	-17.8	-23.9	-530.6	190.8	512.8	8.8	19.8	0.5
TPSSh	-44.9	-50.8	-603.5	233.1	558.6	3.8	2.0	8.3
<i>Exp.</i>	<i>66.0</i>	<i>66.0</i>	<i>581.6</i>	<i>237.9</i>	<i>515.6</i>			

**Table S37.** Calculated HFCs (individual components, in MHz) and APDs of  $A_{33}$ ,  $A_{iso}$  and  $\Delta A$  with respect to experimental results for **[Cu(salen)<sub>2</sub>]** obtained with the aug-cc-pVTZ-Jmod basis set with different functionals.

<i>Functional</i>	$A_{11}$	$A_{22}$	$A_{33}$	$A_{iso}$	$\Delta A$	$APD(A_{33})$	$APD(A_{iso})$	$APD(\Delta A)$
B3LYP	-11.8	-13.9	-609.3	211.7	597.5	0.7	22.0	16.4
B3PW91	-30.3	-32.6	-622.8	228.6	592.5	1.5	15.8	15.4
CAM-B3LYP	-10.0	-12.4	-638.3	220.2	628.3	4.0	18.9	22.4
M06	-210.0	238.6	245.8	91.5	455.8	59.9	66.3	11.2
M062X	-294.3	-304.3	-760.0	452.9	465.7	23.8	66.8	9.3
PBE	-3.3	-4.7	-508.7	172.2	505.4	17.1	36.6	1.5
PBE0	-38.8	-41.2	-649.7	243.2	610.9	5.9	10.4	19.0
SCAN	26.8	26.9	-622.1	189.5	649.0	1.4	30.2	26.4
TPSS	4.1	5.2	-531.8	174.2	537.0	13.3	35.9	4.6
TPSSh	-12.9	-14.0	-596.4	207.8	583.5	2.8	23.5	13.7
<i>Exp.</i>	<i>100.4</i>	<i>100.4</i>	<i>613.7</i>	<i>271.5</i>	<i>513.3</i>			

**Table S38.** Calculated HFCs (individual components, in MHz) and APDs of  $A_{33}$ ,  $A_{iso}$  and  $\Delta A$  with respect to experimental results for **[Cu(bipy)<sub>2</sub>(NCS)]<sup>+</sup>** obtained with the aug-cc-pVTZ-Jmod basis set with different functionals.

<i>Functional</i>	$A_{11}$	$A_{22}$	$A_{33}$	$A_{iso}$	$\Delta A$	$APD(A_{33})$	$APD(A_{iso})$	$APD(\Delta A)$
B3LYP	47.4	98.4	-475.5	109.9	573.9	1.6	40.7	35.4
B3PW91	31.9	82.8	-487.4	124.2	570.2	4.1	33.0	34.5
CAM-B3LYP	54.2	98.4	-528.0	125.1	626.4	12.8	32.5	47.8
M06	-16.2	300.9	349.2	211.3	365.4	25.4	14.0	13.8
M062X	-141.8	-166.2	-448.5	252.2	306.7	4.2	36.0	27.6
PBE	38.6	75.8	-376.9	87.5	452.7	19.5	52.8	6.8
PBE0	30.0	78.6	-519.9	137.1	598.5	11.1	26.1	41.2
SCAN	63.7	134.9	-501.4	100.9	636.3	7.1	45.6	50.1
TPSS	54.9	94.2	-396.7	82.5	490.9	15.2	55.5	15.8
TPSSh	45.8	92.6	-463.0	108.2	555.6	1.1	41.6	31.1
<i>Exp.</i>	<i>44.1</i>	<i>44.1</i>	<i>468.0</i>	<i>185.4</i>	<i>423.9</i>			

**Table S39.** Calculated HFCs (individual components, in MHz) and APDs of  $A_{33}$ ,  $A_{iso}$  and  $\Delta A$  with respect to experimental results for  $[\text{Cu}(\text{ttcn})_2]^{2+}$  obtained with the aug-cc-pVTZ-Jmod basis set with different functionals.

<i>Functional</i>	$A_{11}$	$A_{22}$	$A_{33}$	$A_{iso}$	$\Delta A$	$APD(A_{33})$	$APD(A_{iso})$	$APD(\Delta A)$
B3LYP	-18.3	-21.9	-444.0	161.4	425.7	3.2	16.3	6.8
B3PW91	-29.9	-33.8	-456.4	173.4	426.5	0.5	10.1	7.0
CAM-B3LYP	-41.4	-45.2	-509.0	198.5	467.6	11.0	2.9	17.3
M06	170.7	-172.0	178.3	59.0	350.3	61.1	69.4	12.1
M062X	-175.0	-189.4	-572.3	312.2	397.3	24.8	61.9	0.4
PBE	0.6	-2.4	-358.5	120.1	359.1	21.8	37.7	9.9
PBE0	-34.5	-38.7	-485.9	186.4	451.4	5.9	3.4	13.2
SCAN	-17.2	-21.0	-477.0	171.7	459.8	4.0	11.0	15.3
TPSS	9.6	12.5	-372.3	116.7	384.8	18.8	39.5	3.5
TPSSh	-4.4	-7.5	-424.9	145.6	420.5	7.4	24.5	5.5
$E_{xp}$ .	60.0	60.0	458.7	192.9	398.7			

**Table S40.** Calculated hyperfine contributions  $A^{FC}$  and  $A^{SD}$  (in MHz) and their APDs using the aug-cc-pVTZ-Jmod basis set and B2PLYP functional and compared to B3PW91 results.

<i>Complex</i>	<i>Functional</i>	$A^{FC}$	$A_{1r}^{SD}$	$A_{22}^{SD}$	$A_{33}^{SD}$	$APD(A^{FC})$	$APD(A_{1r}^{SD})$	$APD(A_{22}^{SD})$	$APD(A_{33}^{SD})$
$[\text{Cu}(\text{dte})_2]^{2+}$	B2PLYP	-358.9	129.8	122.3	-252.1	19.2	21.4	24.3	22.9
	B3PW91	-301.2	165.1	161.7	-326.8				
$[\text{Cu}(\text{acac})_2]$	B2PLYP	-389.2	278.5	276.0	-554.5	8.0	10.7	10.5	10.6
	B3PW91	-360.4	251.6	249.8	-501.4				
$[\text{Cu}(\text{en})_2]^{2+}$	B2PLYP	-419.4	248.7	246.7	-495.5	13.7	4.5	4.3	4.4
	B3PW91	-368.7	238.1	236.5	-474.6				
$[\text{Cu}(\text{mnt})_2]^{2-}$	B2PLYP	-321.9	130.6	128.1	-258.6	14.7	21.6	21.3	21.4
	B3PW91	-280.7	166.5	162.7	-329.2				
$[\text{Cu}(\text{gly})_2]$	B2PLYP	-371.0	309.5	217.2	-526.6	14.1	6.5	7.6	7.0
	B3PW91	-325.2	290.6	201.8	-492.4				
$[\text{Cu}(\text{kts})]$	B2PLYP	-371.8	219.2	214.4	-433.6	14.5	3.1	2.6	2.9
	B3PW91	-324.9	212.5	208.9	-421.5				
$[\text{Cu}(\text{sac})_2]$	B2PLYP	-319.1	275.6	259.7	-535.3	10.2	10.5	2.3	6.4
	B3PW91	-289.6	249.5	253.8	-503.3				
$[\text{Cu}(\text{im})_4]^{2+}$	B2PLYP	-379.1	266.4	266.3	-532.8	11.0	4.6	4.6	4.6
	B3PW91	-341.6	254.6	254.7	-509.4				
$[\text{Cu}(\text{py})_4]^{2+}$	B2PLYP	-396.0	252.3	252.0	-504.3	11.9	5.7	5.5	5.6
	B3PW91	-353.8	238.6	238.9	-477.5				
$[\text{Cu}(\text{eta})]^{2+}$	B2PLYP	-386.0	247.5	196.9	-444.4	22.3	19.7	6.1	13.3
	B3PW91	-315.6	206.8	185.5	-392.2				
$[\text{Cu}(\text{epa})(\text{H}_2\text{O})]^{2+}$	B2PLYP	-358.4	251.9	247.0	-498.9	7.3	4.9	4.8	4.9
	B3PW91	-334.0	240.1	235.7	-475.7				
$[\text{Cu}(\text{atpt})]^{2+}$	B2PLYP	-335.6	160.7	145.1	-305.8	29.4	3.2	7.8	5.5
	B3PW91	-259.4	166.0	157.4	-323.4				
$[\text{Cu}(\text{H}_2\text{GGH})_2]^{-}$	B2PLYP	-391.5	229.4	175.8	-405.2	42.7	18.9	13.3	16.4
	B3PW91	-274.4	193.0	155.1	-348.1				
$[\text{Cu}(\text{H}_2\text{GGG})]^{-}$	B2PLYP	-387.2	251.6	239.8	-491.4	12.7	4.3	4.0	4.2
	B3PW91	-343.5	241.3	230.5	-471.8				
$[\text{Cu}(\text{salpn})_2]$	B2PLYP	-359.0	269.9	254.3	-524.2	10.1	10.6	5.2	7.9
	B3PW91	-326.2	244.0	241.7	-485.7				
$[\text{Cu}(\text{S,S-mnpala})_2]$	B2PLYP	-411.9	260.5	255.3	-515.8	11.1	7.2	7.5	7.4
	B3PW91	-370.8	242.9	237.5	-480.4				
$[\text{Cu}(\text{salen})_2]$	B2PLYP	-372.1	265.7	262.4	-528.0	9.2	8.1	4.7	6.4
	B3PW91	-340.7	245.9	250.5	-496.4				

<b>[Cu(bipy)<sub>2</sub>(NCS)]<sup>+</sup></b>	B2PLYP	-304.4	299.1	241.2	-540.3	16.8	44.4	11.2	12.8
	B3PW91	-260.6	207.2	271.7	-478.8				
<b>[Cu(ttcn)<sub>2</sub>]<sup>2+</sup></b>	B2PLYP	-325.2	169.2	167.3	-336.6	25.4	5.2	5.8	5.5
	B3PW91	-259.3	178.6	177.6	-356.2				

**Table S41.** Calculated HFCs (total values, in MHz) using the aug-cc-pVTZ-Jmod basis set and B2PLYP functional, and their APDs with respect to experimental values using the B3PW91 value for the  $A^{50}$  contribution.

<i>Complex</i>	<i>A<sub>33</sub></i>	<i>A<sub>iso</sub></i>	<i>ΔA</i>	<i>MAPD(A<sub>33</sub>)</i>	<i>MAPD(A<sub>iso</sub>)</i>	<i>MAPD(ΔA)</i>
<b>[Cu(NH<sub>3</sub>)<sub>4</sub>]<sup>2+</sup></b>	-663.3	254.8	613.0	13.1	5.5	18.4
<b>[Cu(dtc)<sub>2</sub>]<sup>2+</sup></b>	-475.6	288.6	285.2	2.4	12.8	17.8
<b>[Cu(acac)<sub>2</sub>]</b>	-697.3	261.7	654.5	34.1	33.1	35.0
<b>[Cu(en)<sub>2</sub>]<sup>2+</sup></b>	-706.5	310.9	594.0	17.4	22.4	13.4
<b>[Cu(mnt)<sub>2</sub>]<sup>2-</sup></b>	-474.4	265.7	315.2	1.7	11.7	14.5
<b>[Cu(gly)<sub>2</sub>]</b>	-676.5	254.8	665.7	27.7	30.4	28.8
<b>[Cu(kts)]</b>	-621.5	273.5	525.3	8.1	7.8	8.9
<b>[Cu(sac)<sub>2</sub>]</b>	-642.6	207.0	655.8	36.5	5.1	59.7
<b>[Cu(im)<sub>4</sub>]<sup>2</sup></b>	-685.1	261.7	635.5	21.5	13.7	27.0
<b>[Cu(py)<sub>4</sub>]<sup>2+</sup></b>	-683.9	284.5	599.7	21.4	29.1	16.5
<b>[Cu(eta)<sub>2</sub>]<sup>2+</sup></b>	-659.9	294.7	573.5	24.1	24.0	30.0
<b>[Cu(epa)(H<sub>2</sub>O)]<sup>2</sup></b>	-648.4	248.9	601.0	23.6	5.1	39.2
<b>[Cu(atpt)]<sup>2+</sup></b>	-465.6	243.7	343.2	45.1	70.5	28.6
<b>[Cu(H<sub>2</sub>GGH)<sub>2</sub>]<sup>-</sup></b>	-641.0	307.3	525.5	3.4	22.6	5.1
<b>[Cu(H<sub>2</sub>GGG)]<sup>-</sup></b>	-692.0	287.9	611.8	14.8	18.5	13.4
<b>[Cu(salpn)<sub>2</sub>]</b>	-655.7	238.4	636.9	24.5	15.2	32.8
<b>[Cu(S,S-mnpala)<sub>2</sub>]</b>	-708.0	297.9	618.2	21.7	25.2	19.9
<b>[Cu(salen)<sub>2</sub>]</b>	-685.9	260.0	644.0	11.8	4.3	25.5
<b>[Cu(bipy)<sub>2</sub>(NCS)]<sup>+</sup></b>	-592.7	168.0	672.8	26.6	9.4	58.7
<b>[Cu(ttcn)<sub>2</sub>]<sup>2+</sup></b>	-502.6	239.2	397.5	9.6	24.0	0.3

**Table S42.** Calculated hyperfine contributions  $A^{FC}$  and  $A^{SD}$  (in MHz) and their APDs, using the aug-cc-pVTZ-Jmod basis set and wave function based methods, and compared to DFT results using B3PW91 functional.

<i>Complex</i>	<i>Method</i>	$A^{FC}$	$A_{1I}^{SD}$	$A_{22}^{SD}$	$A_{33}^{SD}$	$APD(A^{FC})$	$APD(A_{1I}^{SD})$	$APD(A_{22}^{SD})$	$APD(A_{33}^{SD})$
<b>[Cu(NH<sub>3</sub>)<sub>4</sub>]<sup>2+</sup></b>	DLPNO	-376.1	278.5	277.7	-556.1	11	12	12	12
	HF	-467.9	320.0	319.0	-639.0	38	29	29	29
	MP2	-458.5	301.6	300.8	-602.4	36	22	22	22
	OO-MP2	-328.3	160.1	159.9	-320.0	3	35	35	35
	OO-SCS-MP2	-275.8	208.6	208.2	-416.8	18	16	16	16
	<i>B3PW91</i>	<i>-337.9</i>	<i>248.1</i>	<i>247.6</i>	<i>-495.7</i>				
<b>[Cu(dtc)<sub>2</sub>]<sup>2+</sup></b>	DLPNO	-343.0	201.5	195.6	-397.1	13.9	22.0	21.0	21.5
	HF	-476.9	310.3	309.6	-619.9	58.3	87.9	91.5	89.7
	MP2	-473.6	266.9	260.8	-527.8	57.2	61.6	61.3	61.5
	OO-MP2	-150.1	103.6	90.9	-194.4	50.2	37.3	43.8	40.5
	OO-SCS-MP2	-96.3	115.5	117.9	-233.3	68.0	30.1	27.1	28.6
	<i>B3PW91</i>	<i>-301.2</i>	<i>165.1</i>	<i>161.7</i>	<i>-326.8</i>				
<b>[Cu(acac)<sub>2</sub>]</b>	DLPNO	-370.6	294.7	293.1	-587.8	2.8	17.1	17.3	17.2
	HF	-499.7	326.8	324.5	-651.3	38.7	29.9	29.9	29.9
	MP2	-471.1	314.1	312.6	-626.8	30.7	24.8	25.2	25.0
	OO-MP2	-115.7	123.0	128.9	-252.0	67.9	51.1	48.4	49.7
	OO-SCS-MP2	-132.2	185.1	203.0	-388.1	63.3	26.4	18.7	22.6
	<i>B3PW91</i>	<i>-360.4</i>	<i>251.6</i>	<i>249.8</i>	<i>-501.4</i>				
<b>[Cu(en)<sub>2</sub>]<sup>2+</sup></b>	DLPNO	-393.7	270.1	268.1	-538.2	6.8	13.4	13.3	13.4
	HF	-510.4	320.5	318.7	-639.1	38.4	34.6	34.7	34.7
	MP2	-500.4	298.2	296.1	-594.3	35.7	25.2	25.2	25.2
	OO-MP2	-287.4	152.0	149.2	-301.2	22.1	36.2	36.9	36.5
	OO-SCS-MP2	-225.1	191.8	191.5	-383.3	39.0	19.4	19.1	19.2
	<i>B3PW91</i>	<i>-368.7</i>	<i>238.1</i>	<i>236.5</i>	<i>-474.6</i>				
<b>[Cu(mnt)<sub>2</sub>]<sup>2-</sup></b>	DLPNO	-343.2	195.8	194.9	-390.7	22.3	17.6	19.8	18.7
	HF	-475.0	304.0	301.5	-605.6	69.2	82.6	85.3	83.9
	MP2	-451.0	237.7	235.7	-473.4	60.7	42.8	44.8	43.8
	OO-MP2	-104.1	84.4	76.1	-160.5	62.9	49.3	53.2	51.3
	OO-SCS-MP2	-123.3	120.5	92.5	-213.0	56.1	27.7	43.1	35.3
	<i>B3PW91</i>	<i>-280.7</i>	<i>166.5</i>	<i>162.7</i>	<i>-329.2</i>				
<b>[Cu(gly)<sub>2</sub>]</b>	DLPNO	-355.5	339.0	223.8	-562.8	9.3	16.7	10.9	14.3
	HF	-497.4	401.9	238.0	-639.9	52.9	38.3	17.9	30.0
	MP2	-463.8	357.9	249.1	-607.0	42.6	23.2	23.5	23.3
	OO-MP2	-122.7	122.6	136.9	-259.5	62.3	57.8	32.1	47.3
	OO-SCS-MP2	-132.5	163.6	227.8	-391.4	59.3	43.7	12.9	20.5
	<i>B3PW91</i>	<i>-325.2</i>	<i>290.6</i>	<i>201.8</i>	<i>-492.4</i>				
<b>[Cu(kts)]</b>	DLPNO	-339.4	250.9	244.7	-495.6	4.5	18.0	17.1	17.6
	HF	-477.8	320.1	313.5	-633.6	47.1	50.6	50.0	50.3
	MP2	-445.9	292.7	284.9	-577.6	37.3	37.7	36.3	37.0
	OO-MP2	-46.6	90.6	102.1	-192.7	85.7	57.4	51.1	54.3
	OO-SCS-MP2	-62.2	123.7	139.8	-263.4	80.9	41.8	33.1	37.5
	<i>B3PW91</i>	<i>-324.9</i>	<i>212.5</i>	<i>208.9</i>	<i>-421.5</i>				
<b>[Cu(sac)<sub>2</sub>]</b>	DLPNO	-323.4	298.5	270.2	-568.7	11.7	19.6	6.4	13.0
	HF	-507.3	347.5	295.8	-643.3	75.2	39.3	16.5	27.8
	MP2	149.0	252.9	-646.9	394.0	48.5	1.4	154.9	21.7
	OO-MP2	-95.6	81.9	153.5	-235.4	67.0	67.2	39.5	53.2
	OO-SCS-MP2	-113.1	163.3	207.5	-370.8	60.9	34.6	18.3	26.3
	<i>B3PW91</i>	<i>-289.6</i>	<i>249.5</i>	<i>253.8</i>	<i>-503.3</i>				

<i>Complex</i>	<i>Method</i>	<i>A<sup>FC</sup></i>	<i>A<sub>1f</sub><sup>SD</sup></i>	<i>A<sub>22</sub><sup>SD</sup></i>	<i>A<sub>33</sub><sup>SD</sup></i>	<i>APD(A<sup>FC</sup>)</i>	<i>APD(A<sub>1f</sub><sup>SD</sup>)</i>	<i>APD(A<sub>22</sub><sup>SD</sup>)</i>	<i>APD(A<sub>33</sub><sup>SD</sup>)</i>
<b>[Cu(im)<sub>4</sub>]<sup>2+</sup></b>	DLPNO	-379.3	283.2	283.0	-566.2	11.0	11.2	11.1	11.2
	HF	-499.5	321.9	321.5	-643.4	46.2	26.4	26.2	26.3
	MP2	-440.2	304.3	304.2	-608.5	28.9	19.5	19.4	19.5
	OO-MP2	-250.0	155.6	155.4	-311.0	26.8	38.9	39.0	38.9
	OO-SCS-MP2	-230.5	207.1	206.6	-413.7	32.5	18.7	18.9	18.8
	<i>B3PW91</i>	<i>-341.6</i>	<i>254.6</i>	<i>254.7</i>	<i>-509.4</i>				
<b>[Cu(py)<sub>4</sub>]<sup>2+</sup></b>	DLPNO	-375.4	274.7	274.4	-549.1	6.1	15.1	14.9	15.0
	HF	-692.1	315.3	314.8	-630.1	95.6	32.1	31.8	31.9
	MP2	111.7	313.9	314.6	-628.5	68.4	31.5	31.7	31.6
	OO-MP2	-201.6	128.8	128.3	-257.1	43.0	46.0	46.3	46.2
	OO-SCS-MP2	-171.4	176.2	177.1	-353.2	51.5	26.2	25.9	26.0
	<i>B3PW91</i>	<i>-353.8</i>	<i>238.6</i>	<i>238.9</i>	<i>-477.5</i>				
<b>[Cu(eta)]<sup>2+</sup></b>	DLPNO	-339.2	275.9	227.9	-503.8	7.5	33.4	22.9	28.5
	HF	-581.4	344.1	280.3	-624.3	84.2	66.4	51.1	59.2
	MP2	-299.8	326.3	264.4	-590.7	5.0	57.8	42.6	50.6
	OO-MP2	-38.2	73.0	138.7	-211.7	87.9	64.7	25.2	46.0
	OO-SCS-MP2	-64.3	112.0	169.2	-281.3	79.6	45.8	8.8	28.3
	<i>B3PW91</i>	<i>-315.6</i>	<i>206.8</i>	<i>185.5</i>	<i>-392.2</i>				
<b>[Cu(epa)(H<sub>2</sub>O)]<sup>2+</sup></b>	DLPNO	-353.2	271.0	266.9	-537.9	5.7	12.9	13.3	13.1
	HF	-476.9	320.9	317.9	-638.9	42.8	33.7	34.9	34.3
	MP2	-448.1	312.3	285.2	-597.5	34.2	30.1	21.0	25.6
	OO-MP2	26.8	-34.5	8.4	26.1	92.0	85.6	96.4	94.5
	OO-SCS-MP2	-60.3	81.1	85.5	-166.7	82.0	66.2	63.7	65.0
	<i>B3PW91</i>	<i>-334.0</i>	<i>240.1</i>	<i>235.7</i>	<i>-475.7</i>				
<b>[Cu(atpt)]<sup>2+</sup></b>	DLPNO	-302.1	203.0	194.0	-397.0	16.5	22.3	23.3	22.8
	HF	-410.3	308.8	307.4	-616.1	58.2	86.0	95.3	90.5
	MP2	-398.3	278.0	269.5	-547.4	53.5	67.4	71.2	69.3
	OO-MP2	-91.4	76.7	61.4	-138.1	64.7	53.8	61.0	57.3
	OO-SCS-MP2	-60.1	81.9	95.2	-177.1	76.8	50.7	39.5	45.2
	<i>B3PW91</i>	<i>-259.4</i>	<i>166.0</i>	<i>157.4</i>	<i>-323.4</i>				
<b>[Cu(H<sub>2</sub>GGH)<sub>2</sub>]<sup>-</sup></b>	DLPNO	-309.1	253.1	219.0	-472.1	12.6	31.2	41.2	35.6
	HF	-446.7	365.4	266.4	-631.8	62.8	89.4	71.8	81.5
	MP2	-423.2	306.9	273.0	-579.9	54.3	59.0	76.0	66.6
	OO-MP2	-38.0	19.9	106.6	-126.4	86.2	89.7	31.3	63.7
	OO-SCS-MP2	11.9	42.6	137.7	-180.4	95.7	77.9	11.2	48.2
	<i>B3PW91</i>	<i>-274.4</i>	<i>193.0</i>	<i>155.1</i>	<i>-348.1</i>				
<b>[Cu(H<sub>2</sub>GGG)]<sup>-</sup></b>	DLPNO	-365.6	278.3	258.9	-537.2	6.4	15.3	12.3	13.9
	HF	-509.0	350.1	288.5	-638.6	48.2	45.1	25.2	35.4
	MP2	-474.0	305.0	284.1	-589.2	38.0	26.4	23.3	24.9
	OO-MP2	-131.9	132.9	109.3	-242.2	61.6	44.9	52.6	48.7
	OO-SCS-MP2	-127.4	155.1	183.7	-338.9	62.9	35.7	20.3	28.2
	<i>B3PW91</i>	<i>-343.5</i>	<i>241.3</i>	<i>230.5</i>	<i>-471.8</i>				
<b>[Cu(salpn)<sub>2</sub>]</b>	DLPNO	-347.6	290.0	271.4	-561.4	6.6	18.9	12.3	15.6
	HF	-512.3	334.2	307.0	-641.2	57.1	37.0	27.0	32.0
	MP2	-18.8	311.1	330.7	-641.8	94.2	27.5	36.8	32.2
	OO-MP2	-82.6	83.5	108.3	-191.9	74.7	65.8	55.2	60.5
	OO-SCS-MP2	-72.3	139.0	167.4	-306.4	77.8	43.0	30.7	36.9
	<i>B3PW91</i>	<i>-326.2</i>	<i>244.0</i>	<i>241.7</i>	<i>-485.7</i>				
<b>[Cu(S,S-mnpala)<sub>2</sub>]</b>	DLPNO	-380.0	282.6	277.2	-559.7	2.5	16.3	16.7	16.5
	HF	-511.9	326.1	318.1	-644.2	38.0	34.2	33.9	34.1
	MP2	-486.2	306.4	301.0	-607.5	31.1	26.1	26.8	26.4
	OO-MP2	-145.3	131.0	118.4	-249.4	60.8	46.1	50.1	48.1
	OO-SCS-MP2	-134.6	179.3	185.6	-364.9	63.7	26.2	21.9	24.0
	<i>B3PW91</i>	<i>-370.8</i>	<i>242.9</i>	<i>237.5</i>	<i>-480.4</i>				

Complex	Method	$A^{FC}$	$A_{11}^{SD}$	$A_{22}^{SD}$	$A_{33}^{SD}$	$APD(A^{FC})$	$APD(A_{11}^{SD})$	$APD(A_{22}^{SD})$	$APD(A_{33}^{SD})$
[Cu(salen) <sub>2</sub> ]	DLPNO	-365.5	283.2	281.3	-564.5	7.3	15.2	12.3	13.7
	HF	-534.2	324.7	318.7	-643.4	56.8	32.1	27.2	29.6
	MP2	-88.8	303.8	330.4	-634.2	73.9	23.6	31.9	27.8
	OO-MP2	-92.9	108.6	115.3	-223.8	72.7	55.8	54.0	54.9
	OO-SCS-MP2	-120.4	160.6	187.2	-347.8	64.7	34.7	25.3	29.9
	B3PW91	-340.7	245.9	250.5	-496.4				
[Cu(bipy) <sub>2</sub> (NCS)] <sup>+</sup>	DLPNO	-307.9	319.3	257.2	-576.5	18.1	54.1	5.3	20.4
	HF	-395.7	361.6	292.2	-653.8	51.8	74.6	7.5	36.5
	MP2	-420.5	319.5	294.3	-613.7	61.3	54.2	8.3	28.2
	OO-MP2	-32.2	33.3	101.3	-134.7	87.6	83.9	62.7	71.9
	OO-SCS-MP2	25.8	58.3	105.6	-163.9	90.1	71.8	61.1	65.8
	B3PW91	-260.6	207.2	271.7	-478.8				
[Cu(ttcn) <sub>2</sub> ] <sup>2+</sup>	DLPNO	-318.1	222.0	217.0	-439.0	22.7	24.3	22.2	23.3
	HF	-410.4	318.3	312.7	-631.0	58.2	78.2	76.1	77.2
	MP2	-395.5	283.1	278.8	-561.9	52.5	58.5	57.0	57.7
	OO-MP2	-172.0	96.9	94.5	-191.4	33.7	45.8	46.8	46.3
	OO-SCS-MP2	-131.0	115.1	113.3	-228.4	49.5	35.6	36.2	35.9
	B3PW91	-259.3	178.6	177.6	-356.2				

**Table S43.** Calculated g-tensors (individual components) of [Cu(NH<sub>3</sub>)<sub>4</sub>]<sup>2+</sup> obtained with the PBE0 and B3PW91 functional with selected basis sets.

B3PW91	$g_x$	$g_y$	$g_z$	$\Delta g_I$	$\Delta g_{//}$	$\Delta g_{iso}$	$APD(\Delta g_I)$	$APD(\Delta g_{//})$	$APD(\Delta g_{iso})$
Aug-cc-pVTZ	2.048	2.048	2.171	45.7	168.7	86.7	2.2	29.3	20.7
Aug-cc-pVTZ-J	2.048	2.048	2.172	45.7	169.7	87.0	2.2	28.9	20.4
Aug-cc-pVTZ-Jmod	2.048	2.048	2.172	45.7	169.7	87.0	2.2	28.9	20.4
Aug-cc-pVTZ-Junc	2.048	2.048	2.172	45.7	169.7	87.0	2.2	28.9	20.4
Aug-cc-pwCVTZ	2.045	2.045	2.171	42.7	168.7	84.7	4.5	29.3	22.6
cc-pwCVTZ	2.048	2.048	2.171	45.7	168.7	86.7	2.2	29.3	20.7
CP(PPP)	2.048	2.048	2.166	45.7	163.7	85.0	2.2	31.4	22.3
Def2-TZVP	2.048	2.048	2.166	45.7	163.7	85.0	2.2	31.4	22.3
Exp.	2.047	2.047	2.241	44.7	238.7	109.3			

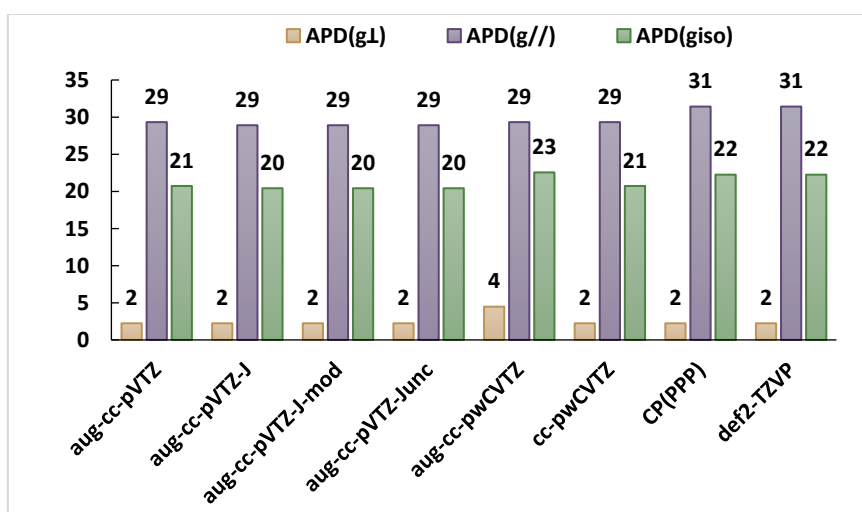


**Figure S11.** Graphical representation of APDs of  $\Delta g_I$ ,  $\Delta g_{//}$  and  $\Delta g_{iso}$  of [Cu(NH<sub>3</sub>)<sub>4</sub>]<sup>2+</sup> for calculated g-tensors obtained with the and B3PW91 functional and different basis sets.

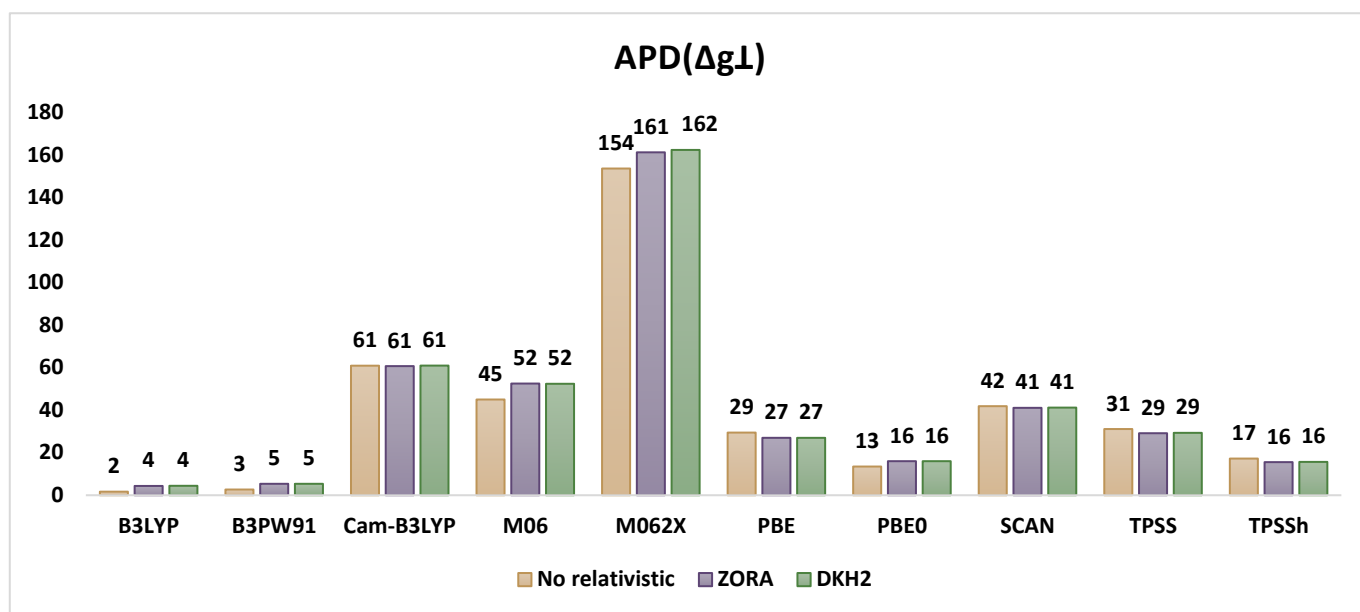


**Figure S12.** Graphical representation of APDs of  $\Delta g_{\perp}$  of  $[\text{Cu}(\text{NH}_3)_4]^{2+}$  for calculated g-tensors obtained with selected functionals and the aug-cc-pVTZ-Jmod basis, using no relativistic correction, ZORA, and DKH2.

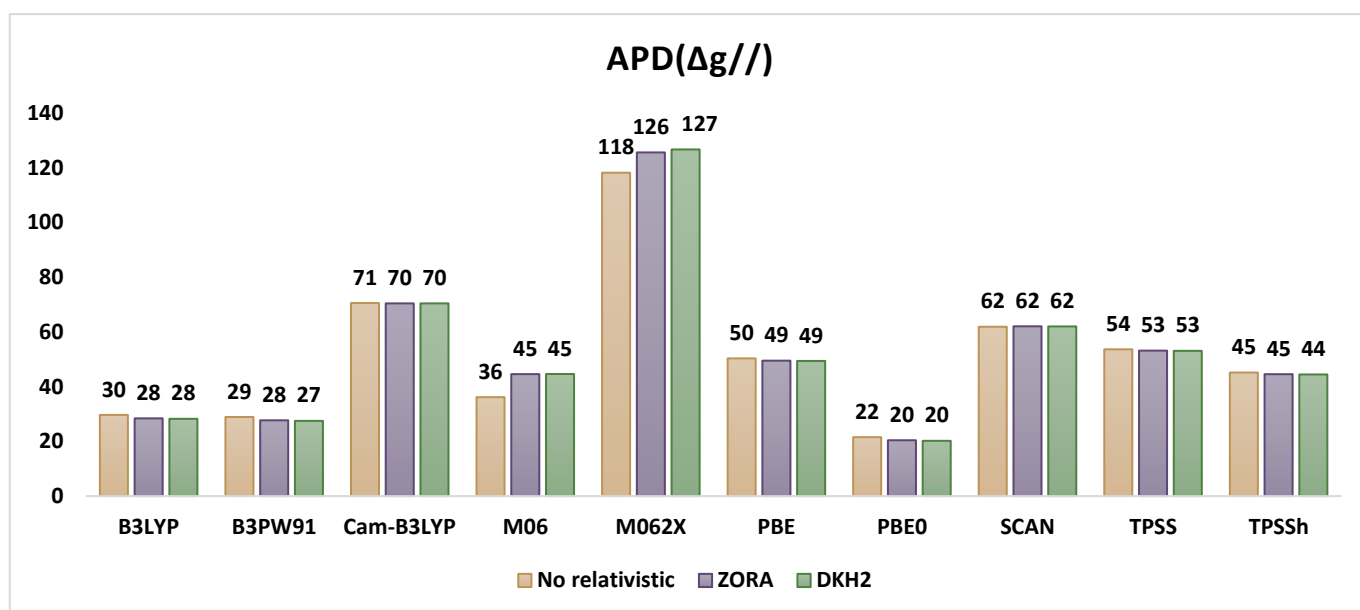


**Figure S13.** Graphical representation of APDs of  $\Delta g_{//}$  of  $[\text{Cu}(\text{NH}_3)_4]^{2+}$  for calculated g-tensors obtained with selected functionals and the aug-cc-pVTZ-Jmod basis, using no relativistic correction, ZORA, and DKH2.

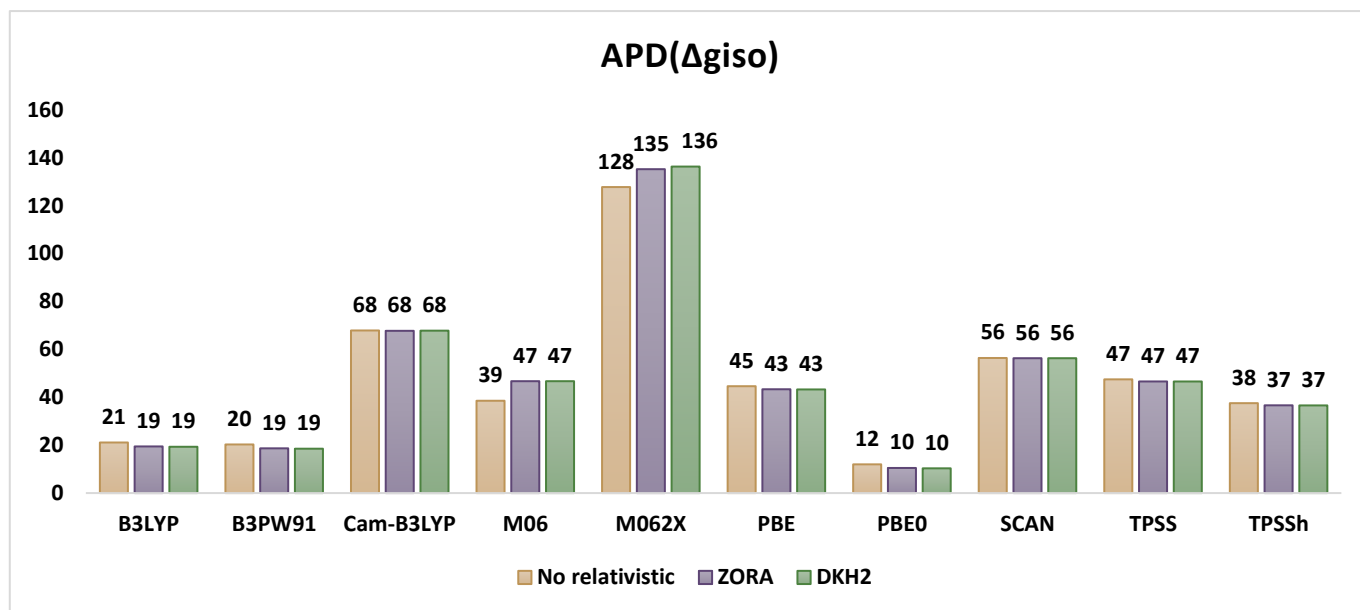


**Figure S14.** Graphical representation of APDs of  $\Delta g_{iso}$  of  $[\text{Cu}(\text{NH}_3)_4]^{2+}$  for calculated g-tensors obtained with selected functionals and the aug-cc-pVTZ-Jmod basis, using no relativistic correction, ZORA, and DKH2.

**Table S44.** Calculated g-tensors (individual components) of  $[\text{Cu}(\text{dte})_2]$  obtained with selected functionals with the aug-cc-pVTZ-Jmod basis sets.

Functional	$g_x$	$g_y$	$g_z$	$\Delta g_{\perp}$	$\Delta g_{//}$	$\Delta g_{iso}$	$APD(\Delta g_{\perp})$	$APD(\Delta g_{//})$	$APD(\Delta g_{iso})$
B3LYP	2.020	2.027	2.072	21.2	69.9	37.4	6.4	15.5	12.3
B3PW91	2.021	2.027	2.074	21.5	71.4	38.1	5.3	13.7	10.7
Cam-B3LYP	2.011	2.015	2.035	10.5	32.6	17.8	53.9	60.6	58.2
M06	2.020	2.028	2.089	21.8	87.1	43.6	3.7	5.3	2.1
M062X	2.058	2.059	2.249	56.0	246.2	119.4	146.8	197.7	179.7
PBE	2.015	2.023	2.047	16.5	44.4	25.8	27.1	46.3	39.5
PBE0	2.024	2.029	2.086	23.9	83.9	43.9	5.4	1.5	2.9
SCAN	2.016	2.022	2.048	16.7	45.8	26.4	26.2	44.6	38.1
TPSS	2.016	2.023	2.049	16.9	46.7	26.8	25.4	43.5	37.1
TPSSh	2.081	2.025	2.061	50.8	58.7	53.4	124.1	29.0	25.2
Exp.	2.025	2.025	2.085	22.7	82.7	42.7			



**Table S45.** Calculated g-tensors (individual components) of **[Cu(dtc)<sub>2</sub>]** obtained with selected functionals with the aug-cc-pVTZ-Jmod basis sets, employing ZORA Hamiltonian.

<i>Functional</i>	$g_x$	$g_y$	$g_z$	$\Delta g_{\parallel}$	$\Delta g_{\perp}$	$\Delta g_{iso}$	$APD(\Delta g_{\parallel})$	$APD(\Delta g_{\perp})$	$APD(\Delta g_{iso})$
B3LYP	2.022	2.028	2.079	22.6	76.6	40.6	0.2	7.3	4.8
B3PW91	2.023	2.028	2.080	22.9	78.1	41.3	1.1	5.6	3.2
Cam-B3LYP	2.012	2.015	2.038	11.1	35.7	19.3	51.2	56.9	54.8
M06	2.023	2.029	2.102	23.8	99.2	48.9	4.8	20.0	14.6
M062X	2.064	2.067	2.277	63.3	274.7	133.7	179.0	232.2	213.4
PBE	2.016	2.023	2.050	17.2	47.9	27.4	24.1	42.1	35.7
PBE0	2.026	2.030	2.094	25.8	91.5	47.7	13.5	10.7	11.7
SCAN	2.017	2.023	2.051	17.5	48.6	27.9	22.8	41.3	34.7
TPSS	2.017	2.024	2.052	17.7	49.9	28.4	21.8	39.7	33.4
TPSSh	2.020	2.026	2.066	20.4	63.3	34.7	10.1	23.5	18.7
<i>Exp.</i>	<i>2.025</i>	<i>2.025</i>	<i>2.085</i>	<i>22.7</i>	<i>82.7</i>	<i>42.7</i>			

**Table S46.** Calculated g-tensors (individual components) of **[Cu(dtc)<sub>2</sub>]** obtained with selected functionals with the aug-cc-pVTZ-Jmod basis sets, employing DKH2 Hamiltonian.

<i>Functional</i>	$g_x$	$g_y$	$g_z$	$\Delta g_{\parallel}$	$\Delta g_{\perp}$	$\Delta g_{iso}$	$APD(\Delta g_{\parallel})$	$APD(\Delta g_{\perp})$	$APD(\Delta g_{iso})$
B3LYP	2.022	2.028	2.079	22.6	76.8	40.6	0.5	7.1	4.8
B3PW91	2.022	2.028	2.080	22.9	78.2	41.3	0.8	5.5	3.2
Cam-B3LYP	2.012	2.015	2.038	11.0	35.6	19.2	51.7	57.0	55.1
M06	2.023	2.029	2.102	23.7	99.3	48.9	4.5	20.1	14.5
M062X	2.065	2.067	2.278	63.4	275.9	134.2	179.5	233.7	214.5
PBE	2.016	2.023	2.050	17.1	47.9	27.4	24.4	42.1	35.8
PBE0	2.026	2.030	2.094	25.7	91.7	47.7	13.2	10.9	11.7
SCAN	2.017	2.023	2.051	17.4	48.6	27.8	23.1	41.2	34.8
TPSS	2.016	2.023	2.052	17.6	49.9	28.4	22.2	39.7	33.5
TPSSh	2.020	2.026	2.066	20.3	63.4	34.7	10.4	23.4	18.8
<i>Exp.</i>	<i>2.025</i>	<i>2.025</i>	<i>2.085</i>	<i>22.7</i>	<i>82.7</i>	<i>42.7</i>			

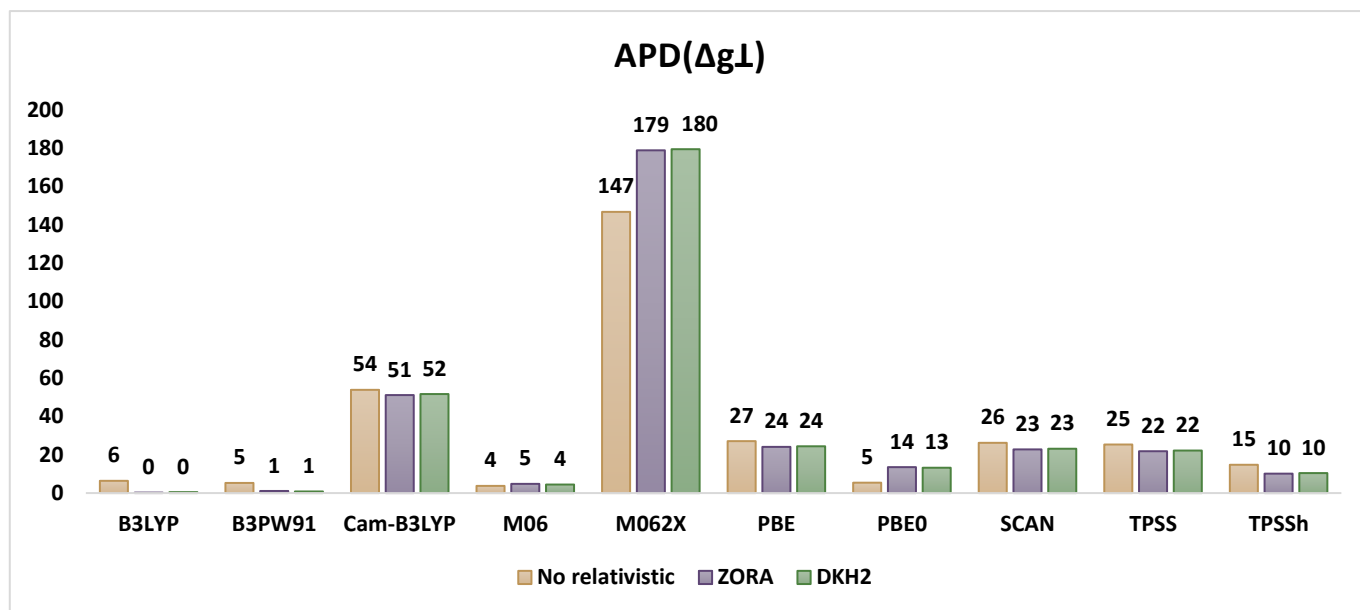


**Figure S15.** Graphical representation of APDs of  $\Delta g_{\perp}$  of  $[\text{Cu}(\text{dte})_2]$  for calculated g-tensors obtained with selected functionals and the aug-cc-pVTZ-Jmod basis, using no relativistic correction, ZORA, and DKH2.

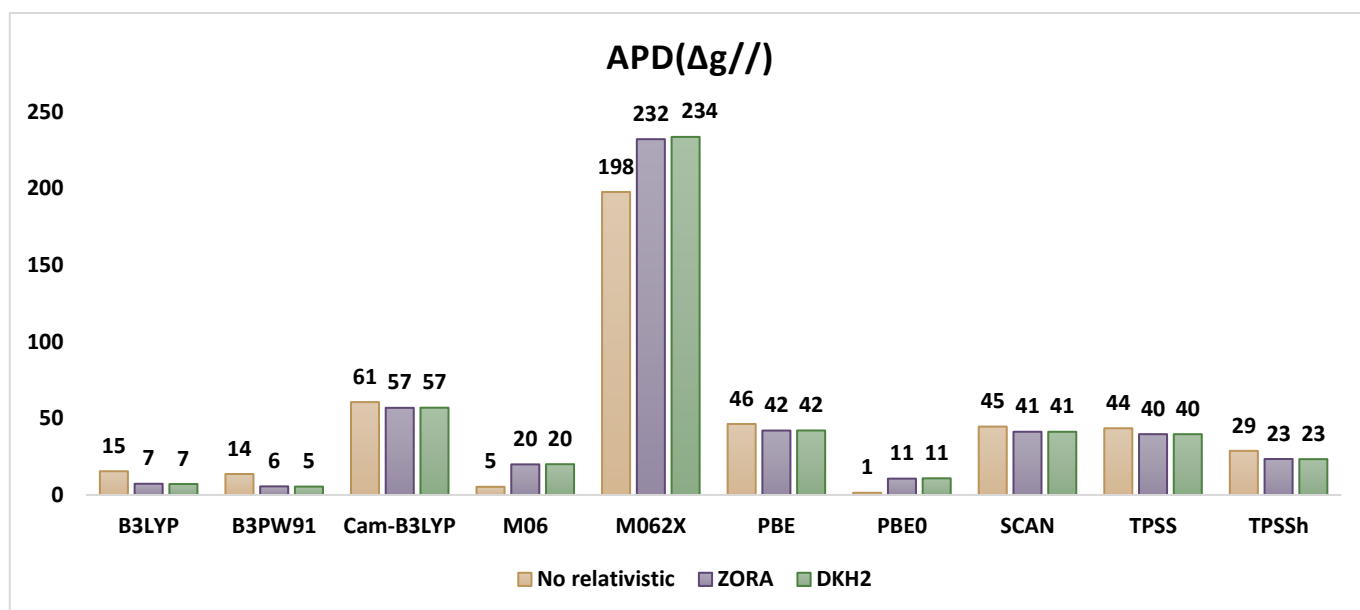


**Figure S16.** Graphical representation of APDs of  $\Delta g_{\parallel}$  of  $[\text{Cu}(\text{dte})_2]$  for calculated g-tensors obtained with selected functionals and the aug-cc-pVTZ-Jmod basis, using no relativistic correction, ZORA, and DKH2.

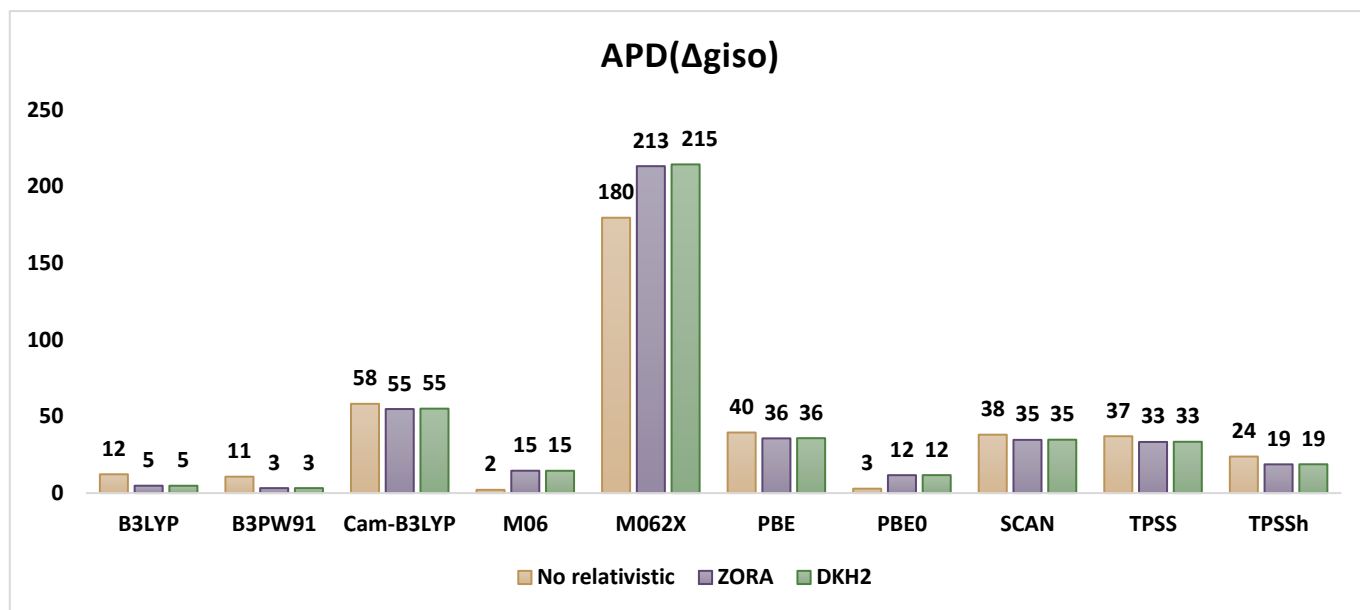


**Figure S17.** Graphical representation of APDs of  $\Delta g_{iso}$  of **[Cu(dtc)<sub>2</sub>]** for calculated g-tensors obtained with selected functionals and the aug-cc-pVTZ-Jmod basis, using no relativistic correction, ZORA, and DKH2.

**Table S47.** Calculated g-tensors (individual components) of **[Cu(acac)<sub>2</sub>]** obtained with selected functionals with the aug-cc-pVTZ-Jmod basis sets.

Functional	$g_x$	$g_y$	$g_z$	$\Delta g_I$	$\Delta g_{//}$	$\Delta g_{iso}$	$APD(\Delta g_I)$	$APD(\Delta g_{//})$	$APD(\Delta g_{iso})$
B3LYP	2.047	2.051	2.176	46.9	174.1	89.3	18.6	38.4	32.7
B3PW91	2.048	2.052	2.178	47.2	175.8	90.1	18.2	37.8	32.1
Cam-B3LYP	2.021	2.022	2.077	19.4	75.0	37.9	66.3	73.5	71.4
M06	2.066	2.071	2.344	65.9	341.4	157.7	14.2	20.8	18.9
M062X	2.113	2.113	2.531	110.6	528.6	249.9	91.7	87.0	88.4
PBE	2.032	2.035	2.113	31.0	110.9	57.6	46.3	60.8	56.6
PBE0	2.053	2.056	2.197	52.3	194.6	99.7	9.4	31.2	24.8
SCAN	2.029	2.031	2.096	27.5	93.7	49.6	52.3	66.8	62.6
TPSS	2.032	2.035	2.113	31.0	110.9	57.6	46.3	60.8	56.6
TPSSh	2.038	2.042	2.136	37.7	133.4	69.6	34.7	52.8	47.6
Exp.	2.060	2.060	2.285	57.7	282.7	132.7			

**Table S48.** Calculated g-tensors (individual components) of **[Cu(acac)<sub>2</sub>]** obtained with selected functionals with the aug-cc-pVTZ-Jmod basis sets, employing ZORA Hamiltonian.

<i>Functional</i>	$g_x$	$g_y$	$g_z$	$\Delta g_I$	$\Delta g_{//}$	$\Delta g_{iso}$	$APD(\Delta g_I)$	$APD(\Delta g_{//})$	$APD(\Delta g_{iso})$
B3LYP	2.048	2.052	2.178	47.8	176.0	90.5	17.1	37.7	31.8
B3PW91	2.049	2.052	2.180	48.1	177.6	91.2	16.6	37.2	31.2
Cam-B3LYP	2.021	2.022	2.077	19.4	74.8	37.9	66.3	73.5	71.4
M06	2.069	2.073	2.361	68.5	358.7	165.2	18.7	26.9	24.5
M062X	2.114	2.115	2.541	112.0	538.3	254.1	94.2	90.4	91.5
PBE	2.033	2.036	2.122	32.2	119.3	61.2	44.1	57.8	53.8
PBE0	2.054	2.057	2.198	53.0	195.9	100.6	8.1	30.7	24.2
SCAN	1.926	2.032	2.152	-23.6	149.6	34.1	59.1	47.1	74.3
TPSS	2.033	2.035	2.114	31.6	111.6	58.3	45.1	60.5	56.1
TPSSh	2.039	2.042	2.137	38.3	134.3	70.3	33.6	52.5	47.0
<i>Exp.</i>	<i>2.060</i>	<i>2.060</i>	<i>2.285</i>	<i>57.7</i>	<i>282.7</i>	<i>132.7</i>			

**Table S49.** Calculated g-tensors (individual components) of **[Cu(acac)<sub>2</sub>]** obtained with selected functionals with the aug-cc-pVTZ-Jmod basis sets, employing DKH2 Hamiltonian.

<i>Functional</i>	$g_x$	$g_y$	$g_z$	$\Delta g_I$	$\Delta g_{//}$	$\Delta g_{iso}$	$APD(\Delta g_I)$	$APD(\Delta g_{//})$	$APD(\Delta g_{iso})$
B3LYP	2.048	2.052	2.179	47.9	176.6	90.8	17.0	37.5	31.6
B3PW91	2.049	2.052	2.181	48.2	178.3	91.5	16.5	36.9	31.0
Cam-B3LYP	2.021	2.022	2.077	19.3	75.0	37.9	66.5	73.5	71.4
M06	2.069	2.073	2.361	68.6	358.8	165.3	18.9	26.9	24.6
M062X	2.115	2.115	2.544	112.5	541.3	255.4	95.0	91.5	92.5
PBE	2.033	2.036	2.122	32.2	119.7	61.4	44.1	57.7	53.7
PBE0	2.054	2.057	2.199	53.1	196.6	100.9	8.0	30.5	23.9
SCAN	2.029	2.031	2.096	27.8	93.2	49.6	51.9	67.0	62.6
TPSS	2.033	2.035	2.114	31.6	111.9	58.4	45.2	60.4	56.0
TPSSh	2.039	2.042	2.137	38.3	134.7	70.4	33.6	52.4	46.9
<i>Exp.</i>	<i>2.060</i>	<i>2.060</i>	<i>2.285</i>	<i>57.7</i>	<i>282.7</i>	<i>132.7</i>			

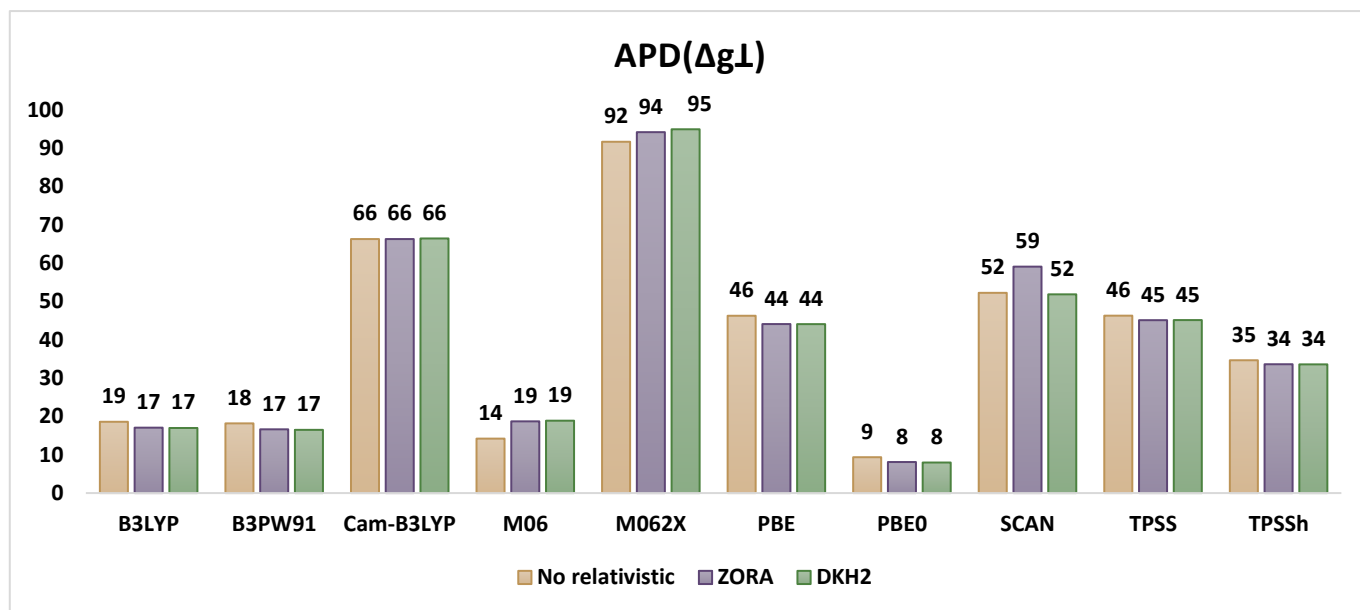


**Figure S18.** Graphical representation of APDs of  $\Delta g_{\perp}$  of  $[\text{Cu}(\text{acac})_2]$  for calculated g-tensors obtained with selected functionals and the aug-cc-pVTZ-Jmod basis, using no relativistic correction, ZORA, and DKH2.

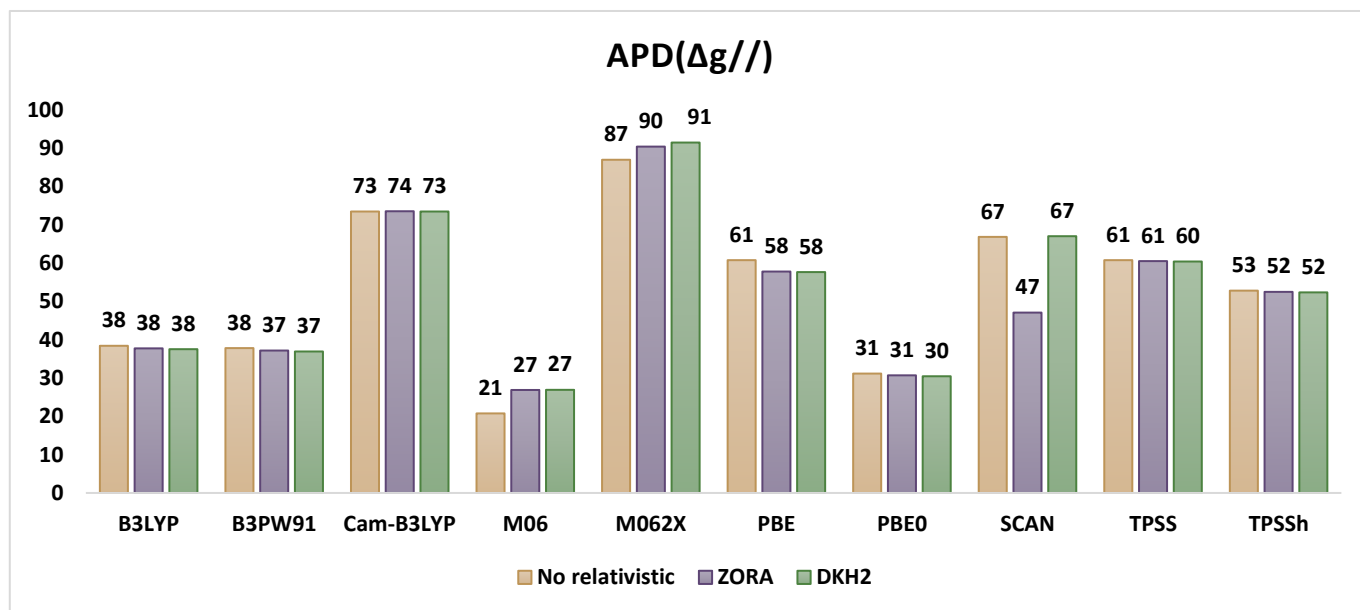


**Figure S19.** Graphical representation of APDs of  $\Delta g_{\parallel}$  of  $[\text{Cu}(\text{acac})_2]$  for calculated g-tensors obtained with selected functionals and the aug-cc-pVTZ-Jmod basis, using no relativistic correction, ZORA, and DKH2.

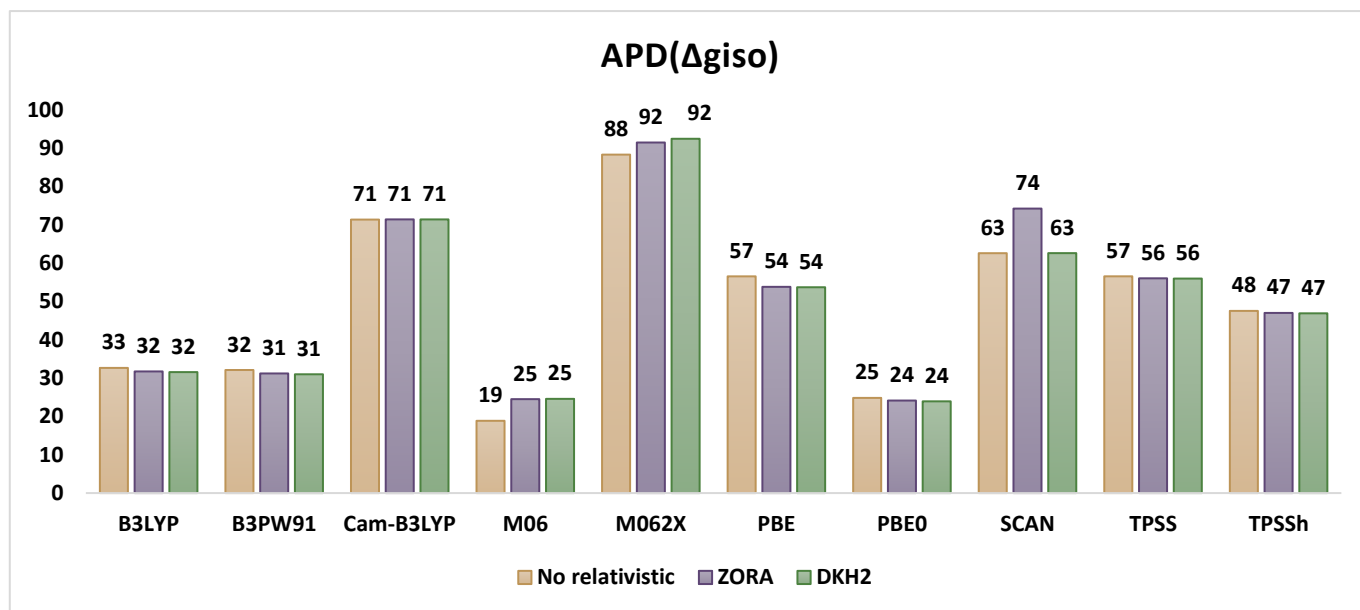


**Figure S20.** Graphical representation of APDs of  $\Delta g_{iso}$  of  $[\text{Cu}(\text{acac})_2]$  for calculated g-tensors obtained with selected functionals and the aug-cc-pVTZ-Jmod basis, using no relativistic correction, ZORA, and DKH2.

**Table S50.** Calculated g-tensors (individual components) of  $[\text{Cu}(\text{en})_2]^{2+}$  obtained with selected functionals with the aug-cc-pVTZ-Jmod basis sets.

Functional	$g_x$	$g_y$	$g_z$	$\Delta g_I$	$\Delta g_{//}$	$\Delta g_{iso}$	$APD(\Delta g_I)$	$APD(\Delta g_{//})$	$APD(\Delta g_{iso})$
B3LYP	2.039	2.039	2.135	36.5	133.0	68.7	10.2	33.4	26.7
B3PW91	2.039	2.039	2.137	36.9	134.6	69.5	9.2	32.6	25.8
Cam-B3LYP	2.018	2.018	2.063	15.8	60.6	30.7	61.3	69.7	67.2
M06	2.050	2.050	2.228	48.0	225.9	107.3	17.9	13.1	14.5
M062X	2.087	2.087	2.394	85.0	391.5	187.1	108.8	96.1	99.7
PBE	2.029	2.028	2.094	26.2	91.8	48.1	35.5	54.0	48.7
PBE0	2.043	2.043	2.152	40.9	149.8	77.2	0.5	25.0	17.6
SCAN	2.025	2.026	2.080	23.1	77.3	41.2	43.1	61.3	56.0
TPSS	2.028	2.028	2.091	25.8	88.2	46.6	36.6	55.8	50.3
TPSSh	2.033	2.033	2.108	30.6	105.5	55.5	24.8	47.2	40.7
Exp.	2.040	2.046	2.202	40.7	199.7	93.7			

**Table S51.** Calculated g-tensors (individual components) of  $[\text{Cu}(\text{mnt})_2]^{2-}$  obtained with selected functionals with the aug-cc-pVTZ-Jmod basis sets.

<i>Functional</i>	$g_x$	$g_y$	$g_z$	$\Delta g_I$	$\Delta g_{//}$	$\Delta g_{iso}$	$APD(\Delta g_I)$	$APD(\Delta g_{//})$	$APD(\Delta g_{iso})$
B3LYP	2.017	2.017	2.055	14.8	52.7	27.4	28.5	41.9	37.7
B3PW91	2.017	2.017	2.054	14.8	51.9	27.2	28.3	42.8	38.3
Cam-B3LYP	2.010	2.010	2.031	7.6	28.2	14.4	63.3	68.9	67.2
M06	2.018	2.018	2.067	15.8	64.2	31.9	23.7	29.2	27.5
M062X	2.039	2.043	2.163	38.7	161.1	79.5	87.0	77.6	80.6
PBE	2.012	2.015	2.032	11.3	29.7	17.5	45.2	67.2	60.3
PBE0	2.018	2.019	2.062	16.4	59.8	30.9	20.6	34.1	29.8
SCAN	2.014	2.015	2.036	11.8	33.3	19.0	42.8	63.3	56.9
TPSS	2.013	2.015	2.033	11.5	31.1	18.0	44.5	65.7	59.1
TPSSh	2.015	2.016	2.044	13.2	41.3	22.5	36.3	54.5	48.8
<i>Exp.</i>	2.023	2.023	2.093	20.7	90.7	44.0			

**Table S52.** Calculated g-tensors (individual components) of  $[\text{Cu}(\text{gly})_2]$  obtained with selected functionals with the aug-cc-pVTZ-Jmod basis sets.

<i>Functional</i>	$g_x$	$g_y$	$g_z$	$\Delta g_I$	$\Delta g_{//}$	$\Delta g_{iso}$	$APD(\Delta g_I)$	$APD(\Delta g_{//})$	$APD(\Delta g_{iso})$
B3LYP	2.034	2.050	2.148	39.5	145.9	75.0	20.4	44.9	38.2
B3PW91	2.034	2.051	2.149	39.9	147.1	75.6	19.7	44.4	37.7
Cam-B3LYP	2.016	2.023	2.069	17.0	66.5	33.5	65.9	74.9	72.4
M06	2.043	2.070	2.260	54.2	257.9	122.1	9.1	2.6	0.6
M062X	2.070	2.123	2.424	93.9	421.2	203.0	89.1	59.1	67.3
PBE	2.025	2.033	2.102	26.7	99.3	50.9	46.3	62.5	58.1
PBE0	2.037	2.057	2.166	44.4	163.3	84.0	10.6	38.3	30.7
SCAN	2.022	2.031	2.085	23.9	82.3	43.3	51.9	68.9	64.3
TPSS	2.025	2.033	2.097	26.4	94.6	49.1	46.8	64.3	59.5
TPSSh	2.029	2.040	2.116	32.1	113.7	59.3	35.4	57.1	51.2
<i>Exp.</i>	2.052	2.052	2.267	49.7	264.7	121.3			

**Table S53.** Calculated g-tensors (individual components) of  $[\text{Cu}(\text{kts})]$  obtained with selected functionals with the aug-cc-pVTZ-Jmod basis sets.

<i>Functional</i>	$g_x$	$g_y$	$g_z$	$\Delta g_I$	$\Delta g_{//}$	$\Delta g_{iso}$	$APD(\Delta g_I)$	$APD(\Delta g_{//})$	$APD(\Delta g_{iso})$
B3LYP	2.036	2.037	2.123	34.3	120.9	63.1	23.8	12.2	1.9
B3PW91	2.037	2.038	2.125	34.8	123.0	64.2	25.6	10.7	0.3
Cam-B3LYP	2.017	2.018	2.060	15.1	58.1	29.4	45.3	57.8	54.2
M06	2.043	2.046	2.188	42.3	185.6	90.1	52.9	34.8	40.0
M062X	2.090	2.095	2.379	90.1	376.2	185.5	225.6	173.2	188.2
PBE	2.026	2.027	2.083	24.5	80.8	43.2	11.6	41.3	32.8
PBE0	2.041	2.042	2.142	39.1	139.4	72.5	41.4	1.2	12.7
SCAN	2.042	2.026	2.075	31.8	73.1	45.5	14.7	46.9	29.2
TPSS	2.027	2.028	2.082	24.8	80.1	43.2	10.5	41.8	32.8
TPSSh	2.032	2.032	2.100	29.4	97.6	52.1	6.1	29.1	19.0
<i>Exp.</i>	2.030	2.030	2.140	27.7	137.7	64.3			

**Table S54.** Calculated g-tensors (individual components) of **[Cu(sac)<sub>2</sub>]** obtained with selected functionals with the aug-cc-pVTZ-Jmod basis sets.

<i>Functional</i>	$g_x$	$g_y$	$g_z$	$\Delta g_I$	$\Delta g_{//}$	$\Delta g_{iso}$	$APD(\Delta g_I)$	$APD(\Delta g_{//})$	$APD(\Delta g_{iso})$
B3LYP	2.039	2.046	2.147	40.5	144.9	75.3	15.2	39.0	32.2
B3PW91	2.040	2.046	2.148	40.6	145.6	75.6	14.9	38.7	31.9
Cam-B3LYP	2.019	2.021	2.068	17.4	65.8	33.5	63.6	72.3	69.8
M06	2.053	2.062	2.254	54.8	251.7	120.4	15.0	5.9	8.5
M062X	2.088	2.097	2.394	90.5	392.1	191.0	89.9	65.0	72.1
PBE	2.026	2.034	2.101	27.3	98.6	51.1	42.7	58.5	54.0
PBE0	2.044	2.050	2.163	44.8	160.6	83.4	6.1	32.4	24.9
SCAN	2.058	2.037	2.146	44.8	143.6	77.7	6.0	39.6	30.0
TPSS	2.026	2.033	2.097	27.2	94.5	49.6	43.0	60.2	55.3
TPSSh	2.032	2.039	2.116	33.0	113.5	59.8	30.9	52.3	46.1
<i>Exp.</i>	2.050	2.050	2.240	47.7	237.7	111.0			

**Table S55.** Calculated g-tensors (individual components) of **[Cu(im)<sub>4</sub>]<sup>2+</sup>** obtained with selected functionals with the aug-cc-pVTZ-Jmod basis sets.

<i>Functional</i>	$g_x$	$g_y$	$g_z$	$\Delta g_I$	$\Delta g_{//}$	$\Delta g_{iso}$	$APD(\Delta g_I)$	$APD(\Delta g_{//})$	$APD(\Delta g_{iso})$
B3LYP	2.043	2.043	2.159	40.6	156.6	79.3	9.2	39.7	31.9
B3PW91	2.043	2.043	2.161	40.8	158.3	80.0	8.6	39.0	31.3
Cam-B3LYP	2.019	2.019	2.070	17.0	68.0	34.0	62.0	73.8	70.8
M06	2.056	2.057	2.283	54.2	280.3	129.6	21.3	7.9	11.4
M062X	2.091	2.092	2.436	88.8	433.3	203.6	98.7	66.9	75.0
PBE	2.031	2.031	2.113	28.8	110.9	56.2	35.5	57.3	51.7
PBE0	2.047	2.047	2.176	44.9	173.9	87.9	0.4	33.0	24.5
SCAN	1.714	2.039	2.099	-125.6	96.2	-51.7	181.1	63.0	55.6
TPSS	2.031	2.031	2.107	28.4	105.1	54.0	36.4	59.5	53.6
TPSSh	2.036	2.036	2.127	33.8	124.2	64.0	24.3	52.2	45.0
<i>Exp.</i>	2.047	2.047	2.262	44.7	259.7	116.3			

**Table S56.** Calculated g-tensors (individual components) of **[Cu(py)<sub>4</sub>]<sup>2+</sup>** obtained with selected functionals with the aug-cc-pVTZ-Jmod basis sets.

<i>Functional</i>	$g_x$	$g_y$	$g_z$	$\Delta g_I$	$\Delta g_{//}$	$\Delta g_{iso}$	$APD(\Delta g_I)$	$APD(\Delta g_{//})$	$APD(\Delta g_{iso})$
B3LYP	2.042	2.042	2.155	39.9	152.6	77.5	21.4	41.4	35.8
B3PW91	2.042	2.043	2.157	40.2	154.2	78.2	20.7	40.9	35.2
Cam-B3LYP	2.019	2.020	2.070	17.1	67.4	33.9	66.3	74.1	71.9
M06	2.054	2.055	2.264	52.0	261.8	121.9	2.6	0.4	1.0
M062X	2.092	2.093	2.439	90.1	437.1	205.7	77.7	67.7	70.5
PBE	2.030	2.031	2.108	28.1	105.4	53.9	44.5	59.6	55.4
PBE0	2.046	2.047	2.173	44.3	170.7	86.4	12.6	34.5	28.4
SCAN	2.027	2.028	2.089	25.0	87.2	45.7	50.7	66.6	62.1
TPSS	2.030	2.031	2.104	27.9	101.3	52.4	44.9	61.1	56.6
TPSSh	2.035	2.036	2.123	33.3	121.0	62.5	34.4	53.6	48.2
<i>Exp.</i>	2.053	2.053	2.263	50.7	260.7	120.7			



**Table S57.** Calculated g-tensors (individual components) of  $[\text{Cu}(\text{eta})]^{2+}$  obtained with selected functionals with the aug-cc-pVTZ-Jmod basis sets.

<i>Functional</i>	$g_x$	$g_y$	$g_z$	$\Delta g_I$	$\Delta g_{//}$	$\Delta g_{iso}$	$APD(\Delta g_I)$	$APD(\Delta g_{//})$	$APD(\Delta g_{iso})$
B3LYP	2.039	2.045	2.130	39.9	127.4	69.1	44.1	19.2	2.8
B3PW91	2.040	2.046	2.132	40.7	129.3	70.2	47.0	18.0	1.1
Cam-B3LYP	2.017	2.019	2.060	15.8	57.7	29.8	42.8	63.4	58.0
M06	2.050	2.059	2.200	52.3	197.9	100.8	89.1	25.5	42.0
M062X	2.117	2.135	2.438	123.6	435.6	227.6	346.4	176.2	220.5
PBE	2.012	2.026	2.083	16.9	80.2	38.0	39.0	49.1	46.5
PBE0	2.046	2.053	2.150	47.0	147.5	80.5	70.0	6.5	13.4
SCAN	2.024	2.029	2.077	24.0	74.9	41.0	13.2	52.5	42.3
TPSS	2.018	2.028	2.083	21.0	80.6	40.9	24.2	48.9	42.5
TPSSh	2.032	2.037	2.104	32.1	101.2	55.1	15.9	35.8	22.4
<i>Exp.</i>	2.030	2.030	2.160	27.7	157.7	71.0			

**Table S58.** Calculated g-tensors (individual components) of  $[\text{Cu}(\text{epa})(\text{H}_2\text{O})]^{2+}$  obtained with selected functionals with the aug-cc-pVTZ-Jmod basis sets.

<i>Functional</i>	$g_x$	$g_y$	$g_z$	$\Delta g_I$	$\Delta g_{//}$	$\Delta g_{iso}$	$APD(\Delta g_I)$	$APD(\Delta g_{//})$	$APD(\Delta g_{iso})$
B3LYP	2.044	2.045	2.151	42.1	148.6	77.6	16.9	29.5	25.4
B3PW91	2.044	2.046	2.153	42.7	150.3	78.6	15.7	28.6	24.4
Cam-B3LYP	2.019	2.020	2.067	17.2	65.1	33.2	66.1	69.1	68.1
M06	2.059	2.060	2.263	57.1	260.6	124.9	12.7	23.7	20.1
M062X	2.105	2.107	2.454	103.5	451.8	219.6	104.2	114.4	111.1
PBE	2.030	2.031	2.102	28.3	99.3	52.0	44.2	52.9	50.1
PBE0	2.049	2.050	2.168	47.4	165.6	86.8	6.4	21.4	16.5
SCAN	2.027	2.028	2.085	25.3	83.1	44.6	50.0	60.6	57.1
TPSS	2.030	2.031	2.098	28.2	95.5	50.6	44.3	54.7	51.3
TPSSh	2.036	2.038	2.119	34.6	116.2	61.8	31.7	44.8	40.6
<i>Exp.</i>	2.053	2.053	2.213	50.7	210.7	104.0			

**Table S59.** Calculated g-tensors (individual components) of  $[\text{Cu}(\text{atpt})]^{2+}$  obtained with selected functionals with the aug-cc-pVTZ-Jmod basis sets.

<i>Functional</i>	$g_x$	$g_y$	$g_z$	$\Delta g_I$	$\Delta g_{//}$	$\Delta g_{iso}$	$APD(\Delta g_I)$	$APD(\Delta g_{//})$	$APD(\Delta g_{iso})$
B3LYP	2.030	2.031	2.117	28.3	114.9	57.1	71.1	50.6	60.0
B3PW91	2.030	2.032	2.119	28.7	117.0	58.1	70.6	49.7	59.3
Cam-B3LYP	2.015	2.015	2.057	12.8	55.1	26.9	86.9	76.3	81.2
M06	2.034	2.035	2.162	32.2	160.0	74.8	67.0	31.2	47.6
M062X	2.101	2.108	2.444	102.5	441.8	215.6	4.9	89.9	51.1
PBE	2.021	2.024	2.083	20.0	80.4	40.1	79.5	65.4	71.9
PBE0	2.035	2.036	2.136	32.9	133.6	66.4	66.3	42.6	53.4
SCAN	2.021	2.023	2.077	19.6	74.5	37.9	79.9	68.0	73.4
TPSS	2.022	2.024	2.082	20.4	79.8	40.2	79.1	65.7	71.8
TPSSh	2.026	2.027	2.098	24.4	95.2	48.0	75.1	59.1	66.4
<i>Exp.</i>	2.100	2.100	2.235	97.7	232.7	142.7			

**Table S60.** Calculated g-tensors (individual components) of  $[\text{Cu}(\text{GGH})]^-$  obtained with selected functionals with the aug-cc-pVTZ-Jmod basis sets.

<i>Functional</i>	$g_x$	$g_y$	$g_z$	$\Delta g_I$	$\Delta g_{//}$	$\Delta g_{iso}$	$APD(\Delta g_I)$	$APD(\Delta g_{//})$	$APD(\Delta g_{iso})$
B3LYP	2.027	2.031	2.104	26.6	101.7	51.6		40.4	
B3PW91	2.028	2.031	2.105	26.9	102.5	52.1		40.0	
Cam-B3LYP	2.015	2.016	2.056	12.9	53.3	26.4		68.8	
M06	2.029	2.034	2.134	29.6	132.1	63.7		22.6	
M062X	2.086	2.108	2.377	94.5	374.4	187.8		119.3	
PBE	2.019	2.021	2.069	17.7	66.3	33.9		61.1	
PBE0	2.032	2.036	2.122	31.7	119.4	60.9		30.1	
SCAN	2.020	2.021	2.067	18.2	64.9	33.8		62.0	
TPSS	2.019	2.022	2.069	18.1	66.3	34.2		61.2	
TPSSh	2.023	2.026	2.083	22.2	81.1	41.8		52.5	
<i>Exp.</i>			2.173		170.7				

**Table S61.** Calculated g-tensors (individual components) of  $[\text{Cu}(\text{GGG})]^{2+}$  obtained with selected functionals with the aug-cc-pVTZ-Jmod basis sets.

<i>Functional</i>	$g_x$	$g_y$	$g_z$	$\Delta g_I$	$\Delta g_{//}$	$\Delta g_{iso}$	$APD(\Delta g_I)$	$APD(\Delta g_{//})$	$APD(\Delta g_{iso})$
B3LYP	2.032	2.037	2.125	32.1	123.0	62.4		38.4	
B3PW91	2.032	2.037	2.126	32.4	123.6	62.8		38.1	
Cam-B3LYP	2.016	2.018	2.061	14.4	59.0	29.3		70.5	
M06	2.040	2.047	2.194	41.3	191.2	91.3		4.2	
M062X	2.070	2.087	2.329	76.1	326.9	159.7		63.7	
PBE	2.023	2.025	2.088	21.5	85.7	42.9		57.1	
PBE0	2.036	2.041	2.139	36.2	136.8	69.7		31.5	
SCAN	2.022	2.024	2.076	20.6	74.0	38.4		62.9	
TPSS	2.023	2.025	2.085	21.8	82.8	42.1		58.5	
TPSSh	2.027	2.031	2.101	26.6	98.5	50.5		50.7	
<i>Exp.</i>			2.202		199.7				

**Table S62.** Calculated g-tensors (individual components) of  $[\text{Cu}(\text{salpn})]$  obtained with selected functionals with the aug-cc-pVTZ-Jmod basis sets.

<i>Functional</i>	$g_x$	$g_y$	$g_z$	$\Delta g_I$	$\Delta g_{//}$	$\Delta g_{iso}$	$APD(\Delta g_I)$	$APD(\Delta g_{//})$	$APD(\Delta g_{iso})$
B3LYP	2.043	2.048	2.158	42.8	155.7	80.4	25.8	39.8	35.5
B3PW91	2.043	2.048	2.159	43.1	157.1	81.1	25.3	39.3	35.0
Cam-B3LYP	2.019	2.021	2.071	17.8	68.5	34.7	69.2	73.5	72.2
M06	2.059	2.064	2.286	59.2	283.2	133.9	2.6	9.5	7.4
M062X	2.108	2.112	2.471	107.4	468.4	227.7	86.3	81.1	82.7
PBE	2.027	2.033	2.106	27.8	103.3	53.0	51.8	60.0	57.5
PBE0	2.048	2.053	2.177	48.2	174.8	90.4	16.5	32.4	27.5
SCAN	2.026	2.029	2.088	25.4	86.0	45.6	56.0	66.8	63.4
TPSS	2.028	2.033	2.101	27.8	98.8	51.5	51.8	61.8	58.7
TPSSh	2.034	2.039	2.123	34.3	120.2	63.0	40.5	53.5	49.5
<i>Exp.</i>	2.060	2.060	2.261	57.7	258.7	124.7			

**Table S63.** Calculated g-tensors (individual components) of **[Cu(S,S-mnpala)]** obtained with selected functionals with the aug-cc-pVTZ-Jmod basis sets.

<i>Functional</i>	$g_x$	$g_y$	$g_z$	$\Delta g_I$	$\Delta g_{//}$	$\Delta g_{iso}$	$APD(\Delta g_I)$	$APD(\Delta g_{//})$	$APD(\Delta g_{iso})$
B3LYP	2.039	2.042	2.148	38.0	145.3	73.8	34.2	38.9	37.3
B3PW91	2.039	2.042	2.149	38.4	147.0	74.6	33.5	38.2	36.6
Cam-B3LYP	2.019	2.019	2.069	16.6	66.7	33.3	71.1	72.0	71.7
M06	2.051	2.054	2.257	50.5	254.2	118.4	12.4	7.0	0.6
M062X	2.094	2.096	2.440	92.6	437.6	207.6	60.5	84.1	76.4
PBE	2.026	2.029	2.100	25.5	97.6	49.5	55.8	58.9	57.9
PBE0	2.044	2.046	2.167	42.9	164.2	83.3	25.6	30.9	29.2
SCAN	2.025	2.027	2.085	23.4	82.3	43.1	59.4	65.4	63.4
TPSS	2.026	2.029	2.096	25.5	93.5	48.2	55.9	60.6	59.1
TPSSh	2.032	2.035	2.116	31.0	113.3	58.4	46.2	52.3	50.3
<i>Exp.</i>	2.060	2.060	2.240	57.7	237.7	117.7			

**Table S64.** Calculated g-tensors (individual components) of **[Cu(salen)]** obtained with selected functionals with the aug-cc-pVTZ-Jmod basis sets.

<i>Functional</i>	$g_x$	$g_y$	$g_z$	$\Delta g_I$	$\Delta g_{//}$	$\Delta g_{iso}$	$APD(\Delta g_I)$	$APD(\Delta g_{//})$	$APD(\Delta g_{iso})$
B3LYP	2.040	2.042	2.146	38.9	143.8	73.9	21.6	24.2	23.3
B3PW91	2.041	2.043	2.147	39.2	144.7	74.3	21.1	23.7	22.8
Cam-B3LYP	2.019	2.020	2.067	16.9	65.0	32.9	66.0	65.7	65.8
M06	2.054	2.056	2.252	52.4	250.0	118.3	5.5	31.8	22.8
M062X	2.091	2.093	2.398	89.5	395.5	191.5	80.1	108.5	98.7
PBE	2.027	2.029	2.099	25.8	96.9	49.5	48.0	48.9	48.6
PBE0	2.045	2.047	2.162	43.4	160.0	82.3	12.6	15.7	14.6
SCAN	2.026	2.027	2.084	24.0	81.7	43.2	51.8	56.9	55.2
TPSS	2.027	2.029	2.095	25.9	93.0	48.2	47.9	51.0	49.9
TPSSh	2.033	2.035	2.115	31.7	112.3	58.5	36.3	40.8	39.2
<i>Exp.</i>	2.052	2.052	2.192	49.7	189.7	96.3			

**Table S65.** Calculated g-tensors (individual components) of **[Cu(bipy)<sub>2</sub>(NCS)]<sup>+</sup>** obtained with selected functionals with the aug-cc-pVTZ-Jmod basis sets.

<i>Functional</i>	$g_x$	$g_y$	$g_z$	$\Delta g_I$	$\Delta g_{//}$	$\Delta g_{iso}$	$APD(\Delta g_I)$	$APD(\Delta g_{//})$	$APD(\Delta g_{iso})$
B3LYP	2.055	2.058	2.174	54.3	172.1	93.6	36.6	33.0	34.4
B3PW91	2.055	2.059	2.177	54.9	174.7	94.8	36.0	32.0	33.6
Cam-B3LYP	2.021	2.055	2.111	35.7	108.6	60.0	58.3	57.7	57.9
M06	2.075	2.088	2.333	79.1	330.7	162.9	7.7	28.8	14.2
M062X	2.142	2.165	2.598	151.1	595.7	299.3	76.3	132.1	109.7
PBE	2.034	2.055	2.113	42.5	110.6	65.2	50.4	56.9	54.3
PBE0	2.060	2.066	2.199	60.7	197.1	106.2	29.1	23.2	25.6
SCAN	2.033	2.036	2.094	32.5	91.4	52.1	62.0	64.4	63.5
TPSS	2.035	2.050	2.109	40.0	106.3	62.1	53.4	58.6	56.5
TPSSh	2.044	2.050	2.134	44.8	131.2	73.6	47.8	48.9	48.4
<i>Exp.</i>	2.088	2.088	2.259	85.7	256.7	142.7			

**Table S66.** Calculated g-tensors (individual components) of  $[\text{Cu}(\text{ttcn})_2]^{2+}$  obtained with selected functionals with the aug-cc-pVTZ-Jmod basis sets.

<i>Functional</i>	$g_x$	$g_y$	$g_z$	$\Delta g_I$	$\Delta g_{//}$	$\Delta g_{iso}$	$APD(\Delta g_I)$	$APD(\Delta g_{//})$	$APD(\Delta g_{iso})$
B3LYP	2.027	2.031	2.097	27.0	94.8	49.6	36.8	17.3	25.7
B3PW91	2.027	2.032	2.098	27.3	96.0	50.2	36.0	16.3	24.7
Cam-B3LYP	2.015	2.016	2.050	13.0	47.5	24.5	69.5	58.6	63.3
M06	2.028	2.035	2.126	29.0	123.3	60.4	32.1	7.5	9.4
M062X	2.092	2.093	2.344	90.2	341.7	174.0	111.4	197.9	161.0
PBE	2.016	2.023	2.065	17.2	62.3	32.2	59.8	45.7	51.7
PBE0	2.032	2.036	2.113	31.7	110.5	58.0	25.8	3.6	13.1
SCAN	2.020	2.023	2.064	19.2	62.0	33.5	55.0	45.9	49.8
TPSS	2.018	2.024	2.066	18.5	63.2	33.4	56.7	44.9	49.9
TPSSh	2.023	2.028	2.080	23.1	77.8	41.3	46.0	32.2	38.1
<i>Exp.</i>	2.045	2.045	2.117	42.7	114.7	66.7			

## 2 – Supporting information regarding Chapter III.

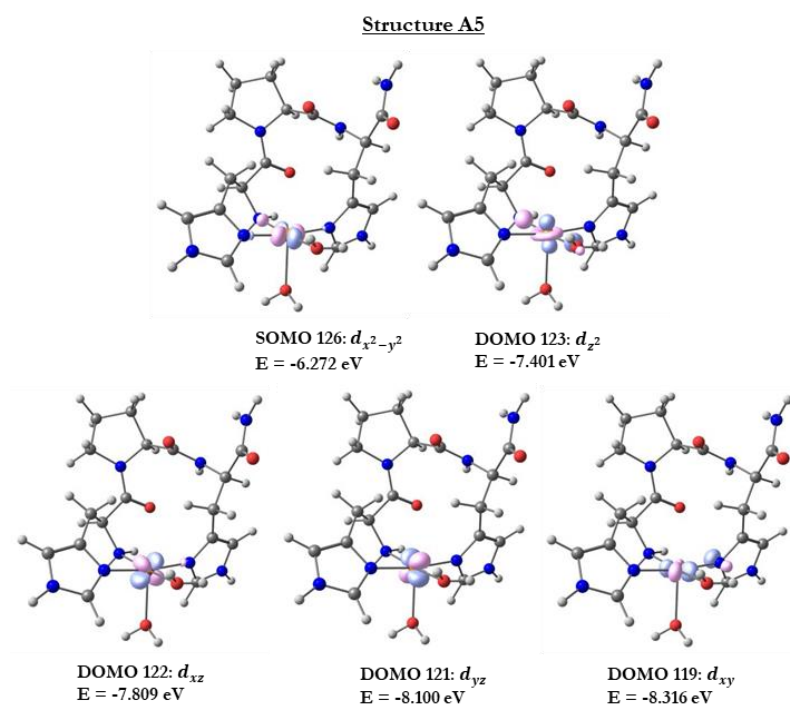


**Figure S21.** Unrestricted natural orbitals rendered for the 3d9 electrons of the copper center using structure A5. Contour value was 1.4400 for all orbitals. The energy value for each molecular orbital is reported in eV, and their occupancy is reported in singly occupied or doubly occupied (SOMO, DOMO).

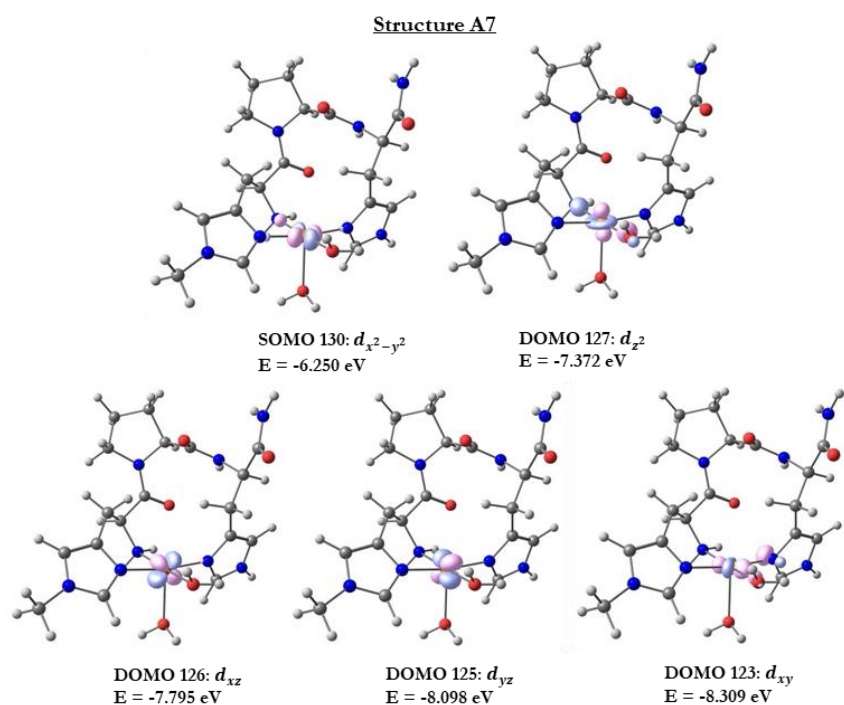


**Figure S22.** Unrestricted natural orbitals rendered for the 3d9 electrons of the copper center using structure A7. Contour value was 1.4400 for all orbitals. The energy value for each molecular orbital is reported in eV, and their occupancy is reported in singly occupied or doubly occupied (SOMO, DOMO).

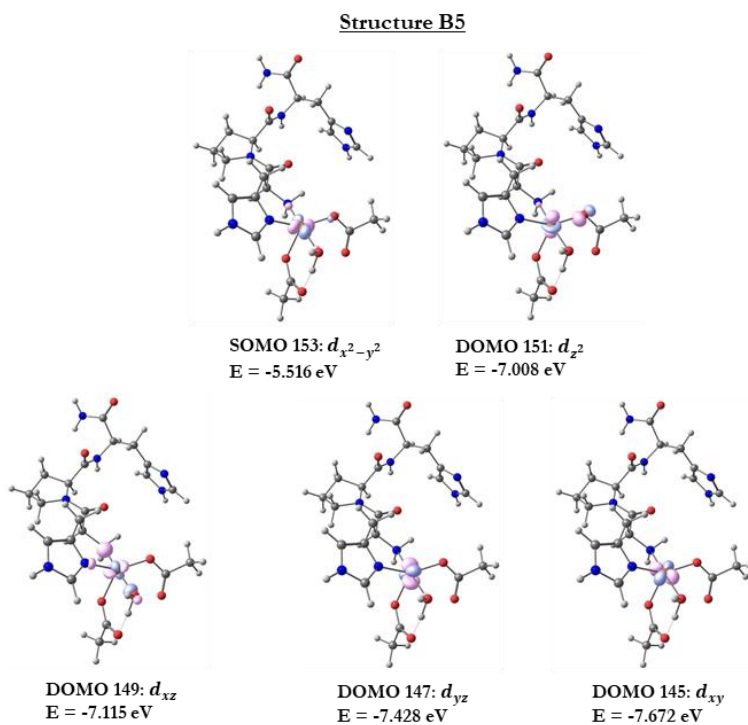


**Figure S23.** Unrestricted natural orbitals rendered for the 3d9 electrons of the copper center using structure B5. Contour value was 1.4400 for all orbitals. The energy value for each molecular orbital is reported in eV, and their occupancy is reported in singly occupied or doubly occupied (SOMO, DOMO).

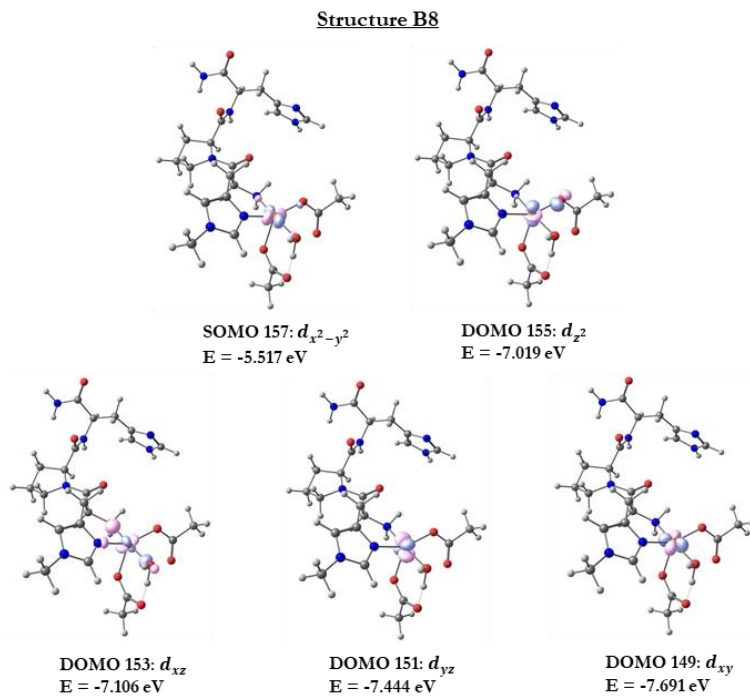


**Figure S24.** Unrestricted natural orbitals rendered for the 3d9 electrons of the copper center using structure B5. Contour value was 1.4400 for all orbitals. The energy value for each molecular orbital is reported in eV, and their occupancy is reported in singly occupied or doubly occupied (SOMO, DOMO).

Table S67. Summary of natural population analysis for selected atoms contributing to the copper center 1<sup>st</sup> coordination sphere and to the  $\tau$ -modification in structures A2 and A6. \*R = H for non-methylated structure A2, and R\* = Me for methylated structure A6.

Structure	Atom	Natural Charge	Natural Population				Natural Spin Density
			Core	Valence	Rydberg	Total	
A5	Cu	1.390	17.997	9.589	0.024	27.610	0.659
	W <sub>1</sub>	-0.970	2.000	6.953	0.017	8.970	0.043
	W <sub>2</sub>	-0.999	2.000	6.979	0.0197	8.999	0.000
	NIm <sub>1</sub>	-0.589	1.999	5.554	0.036	7.589	0.080
	NH <sub>2</sub>	-0.849	2.000	5.823	0.026	7.849	0.127
	NIm <sub>2</sub>	-0.591	1.999	5.555	0.037	7.591	0.089
	CH	0.200	1.999	3.776	0.024	5.800	-0.002
	N	-0.461	1.999	5.441	0.020	7.461	0.002
	R*	0.465	0.000	0.533	0.001	0.535	0.001
A7	Cu	1.385	17.997	9.594	0.024	27.616	0.656
	W <sub>1</sub>	-0.967	2.000	6.949	0.018	8.967	0.045
	W <sub>2</sub>	-0.996	2.000	6.976	0.021	8.996	0.000
	NIm1	-0.591	1.999	5.556	0.036	7.861	0.080
	NH <sub>2</sub>	-0.847	2.000	5.821	0.026	7.847	0.129
	NIm2	-0.594	1.999	5.559	0.036	7.594	0.090
	CH	0.205	1.999	3.772	0.024	5.795	-0.002
	N	-0.281	1.999	5.260	0.021	7.281	0.002
	R*	-0.421	1.999	4.411	0.011	6.421	0.001

Table S68. Summary of natural population analysis for selected atoms contributing to the copper center 1<sup>st</sup> coordination sphere and to the  $\tau$ -modification in structures A2 and A6. \*R = H for non-methylated structure A2, and R\* = Me for methylated structure A6.

Structure	Atom	Natural Charge	Natural Population				Natural Spin Density
			Core	Valence	Rydberg	Total	
B5	Cu	1.420	17.998	9.556	0.026	27.580	0.686
	Ac <sub>1</sub>	-0.835	2.000	6.814	0.022	8.835	0.081
	Ac <sub>2</sub>	-0.810	2.000	6.788	0.023	8.810	0.000
	W <sub>1</sub>	-1.011	2.000	6.991	0.020	9.011	0.062
	NH <sub>2</sub>	-0.848	2.000	5.821	0.027	7.848	0.106
	NIm <sub>2</sub>	-0.585	1.999	5.549	0.037	7.585	0.065
	CH	0.189	1.999	3.786	0.026	5.811	-0.004
	N	-0.465	1.999	5.446	0.020	7.465	0.001
	R*	0.462	0.000	0.537	0.001	0.538	0.000
B8	Cu	1.418	17.998	9.558	0.026	27.582	0.685
	Ac1	-0.834	2.000	6.912	0.022	8.834	0.082
	Ac2	-0.807	2.000	6.784	0.023	8.807	-0.000
	W1	-1.010	2.000	6.990	0.020	9.010	0.062
	NH <sub>2</sub>	-0.867	2.000	5.820	0.027	7.847	0.104
	NIm2	-0.586	1.999	5.550	0.036	7.586	0.067
	CH	0.195	1.999	3.780	0.025	5.805	-0.004
	N	-0.285	1.999	5.264	0.021	7.285	0.001
	R*	-0.421	1.999	4.411	0.011	6.421	0.001





# List of Figures

## Chapter I. Introduction

Figure 1. Crystal structure of Plastocyanin from spinach resolved to 1.7 Å with zoom into the active site (PDB: 1AG6). [15] .....	26
Figure 2. Crystal structure of oxyhemocyanin obtained from <i>Limulus polyphemus</i> determined at 2.4Å resolution, with zoom into the active site (PDB: 1OXY). [22].....	27
Figure 3. Crystal structure of PHM obtained from <i>Rattus norvegicus</i> , with zoom into the active site (PDB: 1OPM). [25].....	30
Figure 4. Crystal structure of TaGH61 LPMO enzyme and zoom into the first and second coordination spheres of the active site. (PDB: 2YET). [37].....	32
Figure 5. Peisach-Blumberg plot of selected LPMO enzymes showing variability in gZ and AZ values between and within AA families. The dash-lined circle of the corresponding family gives an idea of the potential region for expected EPR values. Data and references are reported in Table 1. [51].....	34
Figure 6. X-band EPR spectra of the LPMO enzyme PlAA10 (plain line) and the simulated EPR spectra (dashed line) obtained with the parameters shown in Table 2. [41].....	36
Figure 7. X-band EPR spectra of the LPMO enzyme SmAA10A (black lines): A) without substrate, B) in the presence of (NAG)6, and C) in the presence of either α- or β-chitin. In each case, the simulated spectra are reported as well (sim, gray line) using the experimental g- and A- values. Data obtained from [64].....	37
Figure 8. Overview of the possible catalytic pathways proposed for LPMOs on polysaccharide substrates (R-H). The dark blue HAA label identifies the hydrogen atom abstraction step. The reduced LPMO-Cu(I) species can bind either dioxygen first and then the substrate (blue box), or the opposite (gray box), to produce the LPMO-Cu(II)-superoxo species. Three distinct classes are derived with respect to the HAA step: I. Cu(II)-superoxo performs HAA (green box), II. Cu(II)-hydroperoxo performs HAA (yellow box), or III. Cu(II)-oxyl performs HAA (red box). Adapted from [67].....	40

Figure 9. Proposed peroxide shunt pathway for LPMO enzymes producing the copper-oxyl intermediate.....41

Figure 10. Crystal structure of  $[\text{Cu}^{\text{II}}(\text{TMG}_3\text{tren})(\text{O}_2^-)]^+$  and  $[\text{Cu}^{\text{II}}(\text{HB}(3\text{-tBu-5-iPrpz})_3)(\text{O}_2^-)]$  illustrating the end-on and side-on binding of the superoxo ligand.....42

## Chapter II. Computational EPR spectroscopy for the study of mononuclear copper(II) centers

Figure 1. Molecular structures of the Cu(II) complexes considered in the present study. Definition of ligand abbreviations: dtc = dimethyldithiocarbamate, acac = acetylacetone; en = ethylenediamine; mnt = maleonitriledithiolate; gly = glycine; kts = 2-keto-3-ethoxybutyraldehyde-bis(thiosemicarbazone); sac = salicylaldehyde imine; im = imidazole; py = pyridine; eta = N,N'-ethylenebis(thiophene-2-aldehyde); epa = N,N'-ethylenebis(pyridine-2-aldehyde); atpt = 3,4-bis(3-amino-1-thiopropyl)toluene; GGH = glycine-glycine-histidine; GGG = glycine-glycine-glycine; salpn = N,N'-bis(salicylidene)-1,2-propanediamine; (S,S)-mnpala = 2,5,8-trimethyl-5-nitro-3,7-diazanonanedioate; salen = bis(salicylidene)ethylenediamine; bipy = 2,2'-bipyridine; ttcn = 1,4,7-trithiacyclononane.....71

Figure 2. Graphical representation of the APD values of calculated A33, Aiso, and  $\Delta A$  for  $[\text{Cu}(\text{NH}_3)_4]^{2+}$  obtained with the PBE0 functional using different basis sets.....79

Figure 3. Graphical representation of the APD values of calculated A33, Aiso and  $\Delta A$  for  $[\text{Cu}(\text{NH}_3)_4]^{2+}$  obtained with the aug-cc-pVTZ-Jmod basis set using different functionals and compared to experimental results.....85

Figure 4. Graphical representation of the mean APD values of calculated A33, Aiso and  $\Delta A$  for the complete set of complexes obtained with the aug-cc-pVTZ-Jmod basis set using different functionals and compared to experimental results.....86

Figure 5. Graphical representation of the mean APD values of calculated AFC and ASD for the complete set of complexes using the aug-cc-pVTZ-Jmod basis set and different wave function methods with respect to B3PW91 values.....89

Figure 6. Graphical representation of the mean APD values of calculated A33, Aiso and  $\Delta A$  for the complete set of complexes obtained with the aug-cc-pVTZ-Jmod basis set and different wave

function methods, using ASO contributions from B3PW91, with respect to experimental results.....	90
Figure 7. Graphical representation of the APD values of calculated g-tensors for $[\text{Cu}(\text{NH}_3)_4]^{2+}$ obtained with the PBE0 functional and selected basis sets.....	95
Figure 8. Graphical representation of the calculated MAPD values for $\Delta g_L$ , $\Delta g_{//}$ and $\Delta g_{iso}$ (A) and the average MAPD (B) of the complete set of complexes using selected functionals and the aug-cc-pVTZ-Jmod basis sets.....	99

### **Chapter III. Prediction of EPR parameters of the LPMO active site and an LPMO-like tripeptidic complex using model systems**

Figure 1. X-ray crystal structure of the active site of PLAA10 and selected residues in the second coordination sphere. C-atoms are shown in teal, N-atoms in blue, O-atoms in red and Cu-atom in magenta. The amino acid residues are shown with their corresponding code and number with respect to the PDB structure. The isoleucine 113 is simulated with a contoured map at $2.8\sigma$ . Adapted from [11].....	115
Figure 2. Optimized structure of the A1 model of the PLAA10 enzyme's active site. H-, C-, N-, and O-atoms are presented in white, gray, blue, and red, respectively. Copper is presented in orange.....	123
Figure 3. Optimized structures of the models from structure set A.....	125
Figure 4. Optimized structure of the B1 model upon decoordination a water molecule from structure A1.....	125
Figure 5. Optimized structures of the modifications brought to structure B1. Structure B2 has a single deprotonated water molecule and optimized to a distorted square planar geometry. Structure B3 has a distortion around the imidazole dihedral angle leading to a distorted square planar geometry as well.....	126
Figure 6. Optimized structure of the C1 model decoordinating the primary amine from structure A1.....	127
Figure 7. Optimized structures of the models from structure set C.....	128
Figure 8. Optimized structure of the model D1 coordinating a water molecule from structure C1.....	129

Figure 9. Optimized structure of models E1 and E2 coordinating one or two Cl-anions and decoordinating the N-terminal amine.....	129
Figure 10. Optimized structures of models A2, A3, C1 and D1 obtained by inclusion of the water solvent through the CPCM solvation model.....	130
Figure 11. Optimized structures of models D2 to D8 obtained with inclusion of the water solvent through the CPCM solvation model.....	131
Figure 12. Optimized structures of model A1 in gas-phase and in aqueous-phase using CPCM and water as solvent.....	134
Figure 13. Relative binding energies calculated for selected structures in sets A (dark red), B (orange), and C (yellow). The corresponding structures and their relative free energies are indicated.....	147
Figure 14. TD-DFT-calculated UV-vis spectra for structures A2 (dark red), B2 (yellow), and B4 (brown). The experimental UV-vis spectrum (black) is also plotted for comparison. The calculated graphs were normalized to improve the qualitatively comparison.....	152
Figure 15. Natural orbitals of DFT-optimized structures A2 and A6 (non-methylated vs. methylated). Contour value was 1.4400 for all orbitals. The energy for each orbital is reported in eV, and their occupancy is specified (Singly occupied or Doubly occupied Molecular Orbital)....	157

#### **Chapter IV. Bioinspired mononuclear copper complexes: synthesis, characterization, and reactivity**

Figure 1. XRD structure of [CuII(PMPA)(H <sub>2</sub> O)(NO <sub>3</sub> )] (1) obtained by slow evaporation of a methanol solution of the complex. Empirical formula: C <sub>12</sub> H <sub>12</sub> CuN <sub>4</sub> O <sub>5</sub> , Formula weight: 355.80, Temperature: 298°K.....	170
Figure 2. XRD structure of [CuII(PEPA)(H <sub>2</sub> O) <sub>2</sub> ](ClO <sub>4</sub> ) (2) obtained by slow evaporation. Empirical formula: C <sub>13</sub> H <sub>16</sub> ClCuN <sub>3</sub> O <sub>7</sub> , Formula weight: 452.28, Temperature: 295°K.....	171
Figure 3. Optimized structures of complexes 1 and 2 obtained with PBE0 functional and def2-TZVP basis set. The crystal structure geometry was used as initial coordinates for the calculation.....	172

Figure 4. UV-vis spectra of complex 1 in methanol solutions at 1, 0.5 and 0.25 mM (dark to light blue) ranging from 200 to 800 nm. The baseline was taken with the solvent alone (black). The inset shows a magnified spectra for the 400 to 800 nm range.....	173
Figure 5. UV-vis spectrum of 0.25 mM solution of complex 1 in methanol (blue) superimposed with the calculated spectrum obtained using TD-DFT with the PBE0 functional and the def2-TZVP basis sets (green). The calculated spectrum was plotted using the orca_plot utility from ORCA. The inset shows magnified spectra for the 400 to 800 nm range.....	174
Figure 6. Difference electron densities sketches Active orbitals involved in the d-d transition and of the ligand to metal charge transfer for complex 1. The corresponding wavelength and oscillator strengths, $f$ , are reported. Contour values used are 0.011 and 0.005, respectively with the acceptor state being in light blue and the donor state in light pink.....	175
Figure 7. EPR spectrum of complex 1 obtained from a 1 mM solution in methanol at 120K...	176
Figure 8. Cyclic voltammogram of complex 1 (5mM) in aqueous solution, pH 7.5, containing 100 mM NaNO <sub>3</sub> , recorded under argon atmosphere and at 100 mV/s scan rate. GC was used as WE, Pt-wire as CE, and Ag/AgCl as RE. The arrow indicates the direction of the CV acquisition.....	177
Figure 9. Cyclic voltammograms of complex 1 (5mM) in aqueous solution, pH 7.5, containing 100 mM NaNO <sub>3</sub> , recorded under argon atmosphere and at different scan rates (100 to 500 mV/s) The arrow indicates the direction of the CV scans.....	179
Figure 10. UV-vis spectrum of complex 1 in methanol before (blue) and after reaction with triethylamine and hydrogen peroxide. The red spectra was recorded right after hydrogen peroxide addition and the one in black is obtained after a few minutes of reaction. The inset shows the temporal evolution of the intensity at 440 nm.....	181
Figure 11. EPR spectrum of complex 1 (light blue) in methanol and upon addition of hydrogen peroxide (red) recorded at different time intervals. Black arrows indicate the evolution of the spectrum over time.....	182
Figure 12. XRD structure of [Cu(POPA)(OH)(OCHO)], complex 3, obtained by slow evaporation of the reaction mixture. Empirical formula: C <sub>13</sub> H <sub>10</sub> CuN <sub>3</sub> O <sub>5</sub> , Formula weight: 351.76, Temperature: 295°K.....	183
Figure 13. Image of the single crystal of complex 3 placed on the goniometer device used for solid-state EPR analysis.....	183

Figure 14. Effective g-value of complex 3 obtained at each rotating angle for two different orientations of the single crystal.....	184
Figure 15. Magnetization of the single crystal of complex 3 (green circles) with respect to temperature. The $S = \frac{1}{2}$ and $S = 1$ magnetization values were simulated in red and blue, respectively.....	184
Figure 16. Tunnels present in the matrix of the crystal structure (yellow spheres) possibly occupied by protons.....	185
Figure 17. Optimized structures of complex 3 as different overall charges and spin states (A, D, and E). The singly occupied molecular orbital (SOMO) and the spin density plot are represented in B) and C).....	186
Figure 18. UV-vis spectrum of complex 1 in ethanol (light blue) and the reaction in presence of triethylamine (denoted TEA in the legend, dark blue) and hydrogen peroxide with respect to time (light to dark green). The inset zooms into the 300 to 850 nm range. The black arrows indicate the evolution of the absorbance spectrum over time.....	187
Figure 19. A) Crystallization of the reaction mixture displaying multiple crystal types. B) Cocrystallization of two structures with 66% of $[\text{Cu}(\text{PMPA})(\text{H}_2\text{O})(\text{NO}_3)]$ and 33% of $[\text{Cu}(\text{POPA})(\text{H}_2\text{O})(\text{NO}_3)]$ . C) Degraded PMPA ligand to the picolinic acid reagent to produce $[\text{Cu}(\text{picolinate})_2]$ .....	188
Figure 20. Production (in TON) of methyl/ethyl formate in either methanol (light blue) or ethanol (dark blue) as a function of time.....	189
Figure 21. Production (in TON) of methyl or ethyl formate in either methanol (graph A) or ethanol (graph B) as a function of complex 1 concentration. The reactions were carried out for 1h (light blue) or 3h (dark blue).....	190
Figure 22. Production (in TON) of methyl formate in methanol solvent as a function of equivalents of triethylamine.....	191
Figure 23. Production (in TON) of methyl-formate in methanol solvent as a function of equivalents of hydrogen peroxide.....	191
Figure 24. XRD structure of $[\text{Cu}(\text{POPA})(\text{H}_2\text{O})(\text{NO}_3)]$ obtained by slow evaporation of the reaction mixture. Empirical formula: $\text{C}_{13}\text{H}_{11}\text{CuN}_4\text{O}_5$ , Formula weight: 360.40, Temperature: 295°K.....	193

Figure 25. Production (in TON) of formaldehyde in methanol with respect to time.....	194
Figure 26. Production (in TON) of methyl- or ethyl-formate under air, argon, or carbon dioxide atmospheres after 3 hours of reaction in presence of triethylamine (2 eq.) and hydrogen peroxide (20 eq.).....	195
Figure 27. GC-MS mass distribution of ethyl-formate obtained after reaction of complex 1 in presence of triethylamine (2 eq.) and hydrogen peroxide (20 eq.) in ethanol under air, carbon dioxide, and labelled carbon dioxide atmospheres.....	196
Figure 28. Production (in TON) of methyl formate in methanol (MeOH) and deuterated methanol (MeOD-d4) with respect to time. The slopes are taken for each and the equations as well as the R2 are reported.....	197
Figure 29. Production (in TON) of formaldehyde in methanol (MeOH) and deuterated methanol (MeOD-d4) with respect to time. The slopes are taken for each and the equations as well as the R2 are reported.....	197
Figure 30. Percentages of species ( $m/z = 74, 75$ or $76$ , blue, green, and dark blue, respectively) present at the ethyl formate retention time with respect to percentage of labelled ethanol found in solution during the reaction. The expected probabilities are shown in dotted lines.....	198
Figure 31. Free energies of structures A, B, and C, involved in the deformylation reaction.....	202
Figure 32. Calculated free energies with respect to the reaction coordinate obtained by scan through the O1-C2 bond starting at 3.65 till 1.40 Å.....	203
Figure 33. XRD structure of $[\text{Cu}(\text{POPA})(\text{H}_2\text{O})(\text{NCO})]$ , complex 5, obtained by slow evaporation of the reaction mixture. Empirical formula: $\text{C}_{13}\text{H}_{10}\text{CuN}_4\text{O}_4$ , Formula weight: 349.79, Temperature: 140°K.....	204
Figure 34. Optimized structures of the N- and O- binding cyanate structures of complex 5.....	205
Figure 35. Concentration of p-nitrophenol obtained in buffers at A) pH = 7.5 and B) pH = 10.5, for complexes 1 (purple) and 4 (blue) after 15 min and 24 h.....	206
Figure 36. XRD structure of the $[\text{Cu}(\text{PEPA}(\text{o-carbamate}))(\text{H}_2\text{O})]$ complex obtained by slow evaporation of the reaction mixture. Empirical formula: $\text{C}_{14}\text{H}_{18}\text{CuN}_4\text{O}_6$ , Formula weight: 401.87, Temperature: 295°K.....	208





# List of Schemes

## Chapter I. Introduction

Scheme 1. Copper-oxygen species proposed as active species in the reactivity of copper monooxygenases.....	28
Scheme 2. Reactions catalyzed by dopamine $\beta$ -monooxygenase (D $\beta$ M) and peptidylglycine $\alpha$ -hydroxylating monooxygenase (PHM) in presence of dioxygen and ascorbate.....	29
Scheme 3. Proposed mechanisms for C-H bond activation involving the Cu(II)-superoxyl (A) or the Cu(II)-oxyl (B) as active species of the CuM and CuB sites in PHM and D $\beta$ M, respectively.....	31
Scheme 4. Regioselectivity on the oxidation of polysaccharide chains by LPMOs. C1 oxidation results in the formation of lactones and subsequent hydration to form aldonic acids. C4 oxidation leads to the formation of ketoaldose and the corresponding hydrated gemdiols. C1/C4 oxidations lead to oligosaccharides with both ends being oxidized. [50].....	33
Scheme 5. Equations for the oxidative reaction of LPMO enzymes mediated by A) O <sub>2</sub> , or B) H <sub>2</sub> O <sub>2</sub> . In either case, there is a priming reduction of the Cu(II) metal center to Cu(I).....	38
Scheme 6. Dinuclear copper species formed from copper-superoxo species.....	42
Scheme 7. Formation of spectroscopically characterized Cu(II)-superoxo species. A) Intramolecular benzylic oxygenation. [71] [72] B) Hydrogen bond stabilization of Cu(II)-superoxo species capable of C-H activation. [73] C) Different coordinating atoms, N <sub>3</sub> S, capable of C-H activation. [74]. Modified from [75].....	44
Scheme 8. Formation of the square-planar [Cu(BPBA)(OOH)] <sup>+</sup> complex by addition of 2 equivalents of both hydrogen peroxide and triethylamine, in an acetone solution of the [Cu(BPBA)(MeOH)] <sub>2</sub> <sup>2+</sup> complex at -78°C.....	44
Scheme 9. Copper-cumylperoxo and its reactivity products: gradual degradation, spin trapping with DMPO and oxidation of substrates (AcrH <sub>2</sub> and CHD). Modified from [77].....	45
Scheme 10. Formation of the Cu(III)-hydroxide complex and its reactivity with dihydroanthracene.....	46

### Chapter III. Prediction of EPR parameters of the LPMO active site and an LPMO-like tripeptidic complex using model systems

Scheme 1. Proposed copper coordination to the apo-SliLPMO10E with and without the N-terminal (Nt) amine in the coordination sphere. X represents either H <sub>2</sub> O or chloride ligands. The g <sub>z</sub> and A <sub>z</sub> Cu determined by EPR are reported the right-hand side of each structure. Adapted from [12].....	117
Scheme 2. LPMO models from structure set A, bearing a Cu <sub>3</sub> N <sub>2</sub> O coordinating environment and the corresponding modifications of the ligands: single deprotonation (A2 and A3), double deprotonation (A4), and imidazole distortion (A5).....	119
Scheme 3. LPMO models depicted in structure set B, bearing a Cu <sub>3</sub> N <sub>1</sub> O coordination sphere, originating from the decoordination of a water molecule from A1, and its subsequent modifications by deprotonation of the water molecule (B2) and imidazole distortion (B3).....	119
Scheme 4. LPMO models depicted in structure set C, bearing a Cu <sub>2</sub> N <sub>2</sub> O coordination sphere, originating from the decoordination of the N-terminal from A1, and its subsequent modifications: deprotonation of the water molecule(s) (C2, C3, and C4) and imidazole distortion (C5).....	120
Scheme 5. LPMO models leading to structure set D, bearing a Cu <sub>2</sub> N <sub>3</sub> O coordination sphere, originating from the coordination of an extra water ligand from structure C1 (structure D1).....	121
Scheme 6. LPMO models from structure set D, bearing a Cu <sub>2</sub> N <sub>3</sub> O coordination sphere, originating from structure D1 followed by a series of deprotonation of either one, two or all three water molecules.....	121
Scheme 7. LPMO models from structure set E, bearing a Cu <sub>2</sub> N <sub>1</sub> O <sub>1</sub> Cl and Cu <sub>2</sub> N <sub>2</sub> Cl coordination sphere, originating from replacing once or twice a water molecule by a Cl-anion from structure C1.....	122
Scheme 8. Proposed structures for major and minor species referring to model system A1 and B2.....	141
Scheme 9. Synthesized HPH peptide and its methylated analogues mimicking the coordination sphere of the LPMO's active site with the histidine brace and the imidazole ring. The MeHPH and HMePH are N-methylated analogues of HPH with methyl groups at the peptidic amide and at the imidazole ring of the histidine brace positions.....	142

Scheme 10. Structures included in set A. Structure A1 has a 4-member coordination sphere of the Cu<sub>3</sub>N<sub>1</sub>O type bearing an acetate ligand. Structures A2 to A5 have a 5-member coordination sphere of the type Cu<sub>3</sub>N<sub>2</sub>O with a combination of acetate and water molecule coordinating the copper center. Structures A6 and A7 are the N-methylated counterparts of structures A2 and A5.....143

Scheme 11. Structures included in set B. Structures B1 to B3 have a 4-member coordination sphere of the Cu<sub>2</sub>N<sub>2</sub>O type. Structures B4 to B7 have a 5-member coordination sphere of the type Cu<sub>3</sub>N<sub>2</sub>O with a combination of acetate and water molecules coordinating the copper center. Structure B8 is the N-methylated counterpart of structure B5.....144

Scheme 12. Structures included in set C. All structures have a 4-member coordination sphere of the Cu<sub>2</sub>N<sub>2</sub>O type, with a combination of acetate and water molecules coordinating the copper center.....145

Scheme 13. Proposed structures together with the modifications most susceptible to exist in solution.....154

Scheme 14. Structures considered for Mayer bond order and NPA analyses. Involved atoms and corresponding bonds are in bold and colored with Ac standing for acetate and W standing for water.....155

#### **Chapter IV. Bioinspired mononuclear copper complexes: synthesis, characterization, and reactivity**

Scheme 1. A) Square-planar copper-hydroperoxo complex [13] B) copper(III)-hydroxide species [15].....168

Scheme 2. Design of three generations of complexes based on PMPA (n=1) or PEPA (n=2) ligands with tunable space around the active metal center. R = H, COtBu.....168

Scheme 3. Synthesis of PMPA and PEPA ligands via activation of picolinic acid in presence of POCl<sub>3</sub> and addition of primary amine. Anhydrous dichloromethane (DCMan.) is used as solvent in an ice bath.....169

Scheme 4. Synthesis of [Cu<sup>II</sup>(PMPA)(H<sub>2</sub>O)(NO<sub>3</sub>)] (complex 1) by addition of the PMPA ligand to a solution of copper nitrate trihydrate salt in methanol.....170

Scheme 5. Synthesis of $[\text{Cu}^{\text{II}}(\text{PEPA})(\text{H}_2\text{O})_2](\text{ClO}_4)$ (complex 2) by addition of the PEPA ligand to a copper perchlorate hexahydrate salt in presence of 1 equivalent of triethylamine in methanol.....	170
Scheme 6. Formation of the square-planar $[\text{Cu}(\text{BPBA})(\text{OOH})]^+$ complex by addition of 2 equivalents of both hydrogen peroxide and triethylamine, in an acetone solution of the $[\text{Cu}(\text{BPBA})(\text{MeOH})]^{2+}$ complex at $-78^\circ\text{C}$ .....	180
Scheme 7. Formation of $[\text{Cu}(\text{POPA})(\text{OH})(\text{OCHO})]^-$ in methanol or ethanol from $[\text{Cu}(\text{PMPA})(\text{H}_2\text{O})(\text{NO}_3)]$ in presence of 2 eq. of triethylamine and 20 eq. hydrogen peroxide at room temperature.....	185
Scheme 8. Pathway to quantify the formate produced by GC via esterification into methyl or ethyl formate.....	189
Scheme 9. Synthesis of the POPA ligand via activation of picolinic acid in presence of DIC, HOBt and DIPEA and addition of primary amide. Acetonitrile (ACN) is used as solvent at room temperature.....	192
Scheme 10. Synthesis of $[\text{Cu}^{\text{II}}(\text{POPA})(\text{H}_2\text{O})(\text{NO}_3)]$ , complex 4, by addition of POPA to a copper nitrate trihydrate salt in methanol in presence of 1 equivalent of triethylamine.....	193
Scheme 11. Proposed reaction mechanism for the formation of ethanal and subsequent deformylation to produce formic acid and methanol.....	200
Scheme 12. Reaction scheme of the oxidation of PNPG to the corresponding aldehyde and p-nitrophenolate in presence of complex and $\text{H}_2\text{O}_2$ in HEPES buffer at pH 7.5. HEPES: (2-[4-(2-hydroxyethyl)piperazin-1-yl]ethanesulfonic acid).....	206
Scheme 13. 2nd, and 3rd generation of ligands and complexes.....	207
Scheme 14. Synthesis of ligands and complexes involving the $\text{PMPA}(\text{o-NH}_2)$ and the $\text{PEPA}(\text{o-NH}_2)$ .....	208
Scheme 15. Reaction of ligand with copper perchlorate in methanol to form the carbamate ligand coordinating the metal center.....	209
Scheme 16. 1st, 2nd, and 3rd generations of ligands based on the POPA parent ligand and obtained by reactivity of PMPA with hydrogen peroxide.....	209

# List of Tables

## Chapter I. Introduction

Table 1. EPR gZ and AZ values used for the Peisach-Blumberg plot.....	35
Table 2. Spin-Hamiltonian parameters for selected enzymes showing two EPR species parameters with rhombic and axial features.....	36
Table 3. Spin-Hamiltonian parameters (parallel region) for selected enzymes and in interaction with the substrate.....	37

## Chapter II. Computational EPR spectroscopy for the study of mononuclear copper(II) centers

Table 1. List of the Cu(II) complexes considered in the present study and their experimentally determined $^{63}\text{Cu}$ hyperfine coupling constants (absolute values, in MHz).....	72
Table 2. Calculated HFCs (individual components and detailed contributions, in MHz) of $[\text{Cu}(\text{NH}_3)_4]^{2+}$ obtained with the PBE0 functional with selected basis sets and varying the computational approach to compute the Coulomb term.....	74
Table 3. Calculated HFCs (individual components and detailed contributions, in MHz) of $[\text{Cu}(\text{NH}_3)_4]^{2+}$ obtained with the B3PW91 functional and the aug-cc-pVTZ-J-mod basis set, using different solvents and the CPCM model.....	74
Table 4. Calculated HFCs (individual components and detailed contributions, in MHz) for $[\text{Cu}(\text{NH}_3)_4]^{2+}$ obtained with the PBE0 functional using different basis sets.....	77
Table 5. Core and valence-shell spin contributions to the isotropic HFCs (in MHz) for $[\text{Cu}(\text{NH}_3)_4]^{2+}$ obtained with the PBE0 functional using different basis sets.....	77
Table 6. APD values of A33, Aiso, and $\Delta A$ for calculated HFCs of $[\text{Cu}(\text{NH}_3)_4]^{2+}$ obtained with the PBE0 functional using different basis sets and compared with experimental data.....	79
Table 7. Calculated HFCs (individual components and detailed contributions, in MHz) for $[\text{Cu}(\text{NH}_3)_4]^{2+}$ obtained with the PBE0 functional and the DKH2 Hamiltonian with different basis sets.....	81

Table 8. Calculated HFCs (individual components and detailed contributions, in MHz) for [Cu(NH <sub>3</sub> ) <sub>4</sub> ] <sup>2+</sup> obtained with the PBE0 functional, DKH2 Hamiltonian, and finite nucleus model with different basis sets.....	81
Table 9. Calculated HFCs (individual components and detailed contributions, in MHz) for [Cu(NH <sub>3</sub> ) <sub>4</sub> ] <sup>2+</sup> obtained with the PBE0 functional and ZORA Hamiltonian with different basis sets.....	81
Table 10. Calculated HFCs (total values and individual components, in MHz) for [Cu(NH <sub>3</sub> ) <sub>4</sub> ] <sup>2+</sup> obtained with the aug-cc-pVTZ-Jmod basis set using different functionals.....	83
Table 11. Core and valence-shell spin contributions (in MHz) for [Cu(NH <sub>3</sub> ) <sub>4</sub> ] <sup>2+</sup> obtained with the aug-cc-pVTZ-Jmod basis set using different functionals.....	83
Table 12. APD values of A <sub>33</sub> , A <sub>iso</sub> and ΔA for calculated HFCs obtained with the aug-cc-pVTZ-Jmod basis set using different functionals with respect to experimental HFCs for [Cu(NH <sub>3</sub> ) <sub>4</sub> ] <sup>2+</sup> .....	84
Table 13. MAPD values of A <sub>33</sub> , A <sub>iso</sub> and ΔA with respect to experimental results for the complete set of complexes obtained with the aug-cc-pVTZ-Jmod basis set while using different functionals.....	86
Table 14. Hyperfine contributions A <sub>FC</sub> and A <sub>SD</sub> (total values and individual components, in MHz) using the aug-cc-pVTZ-Jmod basis set and the B2PLYP functional and absolute APD values for [Cu(NH <sub>3</sub> ) <sub>4</sub> ] <sup>2+</sup> with respect to B3PW91 values.....	87
Table 15. Mean APDs of A <sub>33</sub> , A <sub>iso</sub> and ΔA with respect to experimental results for the complete complex set obtained with B2PLYP using B3PW91 A <sub>SO</sub> values and the aug-cc-pVTZ-Jmod basis set.....	87
Table 16. Mean APDs for the complete set of complexes using the aug-cc-pVTZ-Jmod basis set and different wave function methods, with respect to B3PW91 values.....	89
Table 17. MAPD values of A <sub>33</sub> , A <sub>iso</sub> and ΔA with respect to experimental results for the complete complex set obtained with different wave function methods using B3PW91 A <sub>SO</sub> values and the aug-cc-pVTZ-Jmod basis set.....	90
Table 18. List of the Cu(II) complexes considered in this study together with their experimental g-tensors.....	92

Table 19. Calculated g-tensors of $[\text{Cu}(\text{NH}_3)_4]^{2+}$ obtained with PBE0 functional and selected basis sets.....	94
Table 20. Calculated g-tensors (individual components, g-shifts, and APDs) of $[\text{Cu}(\text{NH}_3)_4]^{2+}$ obtained with selected functionals with the aug-cc-pVTZ-Jmod basis set without applying any scalar relativistic corrections.....	96
Table 21 Calculated g-tensors (individual components, g-shifts, and APDs) of $[\text{Cu}(\text{NH}_3)_4]^{2+}$ obtained with selected functionals with the aug-cc-pVTZ-Jmod basis employing the DKH2 Hamiltonian.....	97
Table 22. Calculated g-tensors (individual components, g-shifts, and APDs) of $[\text{Cu}(\text{NH}_3)_4]^{2+}$ obtained with selected functionals with the aug-cc-pVTZ-Jmod basis employing the ZORA Hamiltonian.....	97
Table 23. Calculated MAPD values for $\Delta g_L$ , $\Delta g_{//}$ and $\Delta g_{iso}$ of the complete complex set of complexes obtained with selected functionals using the aug-cc-pVTZ-Jmod basis sets.....	98

### **Chapter III. Prediction of EPR parameters of the LPMO active site and an LPMO-like tripeptidic using model systems**

Table 1. EPR simulation parameters of PlAA10 [11] and SlAA10E [12] for both the rhombic and axial species.....	116
Table 2. Selected geometrical parameters of the copper coordination sphere of the PlAA10 enzyme and comparison with those for the calculated model structure A1.....	124
Table 3. Geometrical values surrounding the copper center involving the N-atom ligands of the PlAA10 enzyme, the optimized model structure A1, and structure B1.....	126
Table 4. Evaluation of EPR parameters for structure A1 using different functionals, methods, and accounting for the solvation effect during optimization. Experimental values reported are for the major species of the PlAA10 enzyme.....	133
Table 5. Calculated EPR parameters (B3PW91/aug-cc-pVTZ-Jmod) for structures A1, B1, C1 and D1. Experimental values of the major and minor species found in PlAA10 [11] are reported as axial and rhombic, respectively.....	134

Table 6. Calculated EPR parameters (B3PW91/aug-cc-pVTZ-Jmod) for structures A2, B2, C2, and C3. Experimental values of the major and minor species found in PLAA10 [11] are reported.....	136
Table 7. EPR parameters (B3PW91/aug-cc-pVTZ-Jmod) for structures A4 and C4. Experimental values of the major and minor species found in PLAA10 [11] are reported.....	137
Table 8. EPR parameters (B3PW91/aug-cc-pVTZ-Jmod) for structures C1, E1, and E2. Experimental values of the major and minor species found in SliAA10E [12] are reported.....	137
Table 9. EPR parameters (B3PW91/aug-cc-pVTZ-Jmod) for structures A5, B3, and C5. The EPR values of the corresponding non-distorted structures are also presented: A1, B1, and C1. Experimental values of the major and minor species found in PLAA10 [12] are reported.....	139
Table 10. Gibbs free energies and binding energies for structures in set A. LCu represents the common coordination sphere shared between all structures.....	145
Table 11. Gibbs free energies and binding energies for structures in set B. LCu represents the common coordination sphere shared between all structures.....	146
Table 12. Gibbs free energies and binding energies for structures in set C. LCu represents the common coordination sphere shared between all structures.....	147
Table 13. DFT-calculated (B3PW91/aug-cc-pVTZ-Jmod) EPR parameters of selected structures in sets A and B. Experimental values are reported MOPS buffer at pH 7.5.....	148
Table 14. TD-DFT calculated electronic transitions (PBE0/def2-TZPV) for structure set A. The experimental absorption band obtained is also reported at pH 7.5 in MOPS buffer.....	151
Table 15. TD-DFT calculated (PBE0, def2-TZPV) electronic transitions for structure set B. The experimental absorption band obtained is also reported at pH 7.5 in MOPS buffer.....	151
Table 16. Calculated relative free energy differences (PBE0, def2-TZVP), predicted EPR parameters (B3PW91, aug-cc-pVTZ-Jmod), and electronic transitions (PBE0, def2-TZPV) for selected structures A2, A4, A5, B2 and B4.....	153
Table 17. Mayer bond order obtained for the selected bonding atoms in methylated and non-methylated DFT-optimized structures A2, A6, A5, A7, B5, and B8. The bonding atoms consists of those in the first coordination sphere of copper and those involved in the Me modification. *R = H for A2, A5, and B5 and R= Me for A6, A7 and B8.....	156



Table 18. Natural population analysis for selected atoms contributing to the Cu coordination sphere and to the  $\tau$ -modification in structures A2 and A6. \*R = H for A2 and R\* = Me A6.....158

#### **Chapter IV. Bioinspired mononuclear copper complexes: synthesis, characterization, and reactivity**

Table 1. Selected bond distances and angles of XRD and DFT-optimized structures of complexes 1 and 2.....172

Table 2. EPR parameters of [CuII(PMPA)(H<sub>2</sub>O)(NO<sub>3</sub>)], complex 1, obtained from experiment (1mM solution in MeOH) and using DFT (B3PW91 functional, aug-cc-pVTZ-Jmod basis sets).....176

Table 3. Calculated free energies used for the Born-Haber cycle to evaluate the redox potential of the CuII/CuI couple (PBE0/def2-TZVP/COSMO solvation model). The theoretical Ag/AgCl reference is 4.071 V.....178

